Fall 2012

Supramolecular chemistry of molecular concepts: tautomers, chirality, protecting groups, trisubstituted olefins, cyclophanes, and their impact on the organic solid state

Elizabeth Elacqua
University of Iowa

SUPRAMOLECULAR CHEMISTRY OF MOLECULAR CONCEPTS: TAUTOMERS, CHIRALITY, PROTECTING GROUPS, TRISUBSTITUTED OLEFINS, CYCLOPHANES, AND THEIR IMPACT ON THE ORGANIC SOLID STATE

by

Elizabeth Elacqua

An Abstract

Of a thesis submitted in partial fulfillment
of the requirements for the Doctor of
Philosophy degree in Chemistry
in the Graduate College of
The University of Iowa

December 2012

Thesis Supervisor: Professor Leonard R. MacGillivray

ABSTRACT

The research presented in this thesis is founded upon the ability to mimic Nature by using highly directional forces to influence self-assembly, while achieving the formation of desired supramolecular structures. The successful engineering of such solids relies upon a full comprehension of supramolecular synthons, so as to apply them to design complex architectures. We have studied synthon formation in multifunctional pharmaceutical solids. Through the formation of salts and co-crystals, we uncovered a role of tautomers in the salt – co-crystal continuum. From a solid-state perspective, one can envisage that tautomers could promote co-crystal formation since an inherent flexibility to interconvert can accommodate geometries of different co-formers, as well as increase the number of synthons able to support a multicomponent solid. We have also employed co-crystallization to ibuprofen as a means to exploit solid-state properties. We have shown that co-crystallization with bipyridines can result in the formation of both co-crystal solid solutions and co-crystal conglomerates.

Supramolecular chemistry can also be utilized to construct target organic and metal-organic frameworks. Solid-state synthesis has emerged as a means to achieve the formation of molecular targets that are usually inaccessible *via* solution phase synthesis through the exploitation of molecular recognition and self-assembly. In particular, utilizing a combinatorial template strategy can facilitate a [2+2] photodimerization in the solid state. Although the template-directed strategy has helped circumvent problems associated with crystal packing, the solid state is still not routinely used for synthesis, owing, in part, to a lack of expansion to multifunctional olefins and molecular targets.

We have introduced a method to direct the reactivity of multifunctional olefins that contain two robust hydrogen bonding elements to produce heteropolytopic molecules that are of interest for the formation of metal-organic frameworks. Specifically, we developed a protecting group strategy that affords a supramolecular regiochemistry to

attain the desired self-assembly. We have also extended our template approach to more conformationally-complex molecules to gain a further understanding of the rules regarding reactivity in highly substituted systems.

The end of this thesis is focused upon the solid-state synthesis of a series of molecular targets known as cyclophanes. Cyclophanes have a very rich history however, their immersion in all aspects of chemistry has suffered from a lack of high yielding synthetic techniques, as well as novel methodologies that target substitution on the aliphatic bridges. We have shown that a series of laterally-substituted [2.2]cyclophanes can be synthesized in quantitative yields utilizing template-directed self-assembly. The cyclophanes also exhibit optical properties that are influenced by a nonconventional internal charge transfer process, stemming from the strained cyclobutane core. We have also developed a sonochemical method to produce nanocrystals of cyclophanes, resulting in enhanced and red-shifted emissions.

Overall, the results described herein detail the use of supramolecular chemistry to achieve the formation of target architectures that differ in topology, connectivity, and/or physiochemical properties. The entirety of this thesis represents the undeveloped interplay between traditional synthetic organic chemistry and supramolecular solid-state chemistry. While the precision afforded by the crystalline phase provides access to molecular targets with high fidelity, expansion to multifunctional molecules that are desirable in the context of emergent properties bodes well for the continued development and exploitation of molecular recognition to generate novel functional materials.

Abstract Approved: _____
Thesis Supervisor

_____
Title and Department

_____
Date

SUPRAMOLECULAR CHEMISTRY OF MOLECULAR CONCEPTS: TAUTOMERS, CHIRALITY, PROTECTING GROUPS, TRISUBSTITUTED OLEFINS, CYCLOPHANES, AND THEIR IMPACT ON THE ORGANIC SOLID STATE

by

Elizabeth Elacqua

A thesis submitted in partial fulfillment
of the requirements for the Doctor of
Philosophy degree in Chemistry
in the Graduate College of
The University of Iowa

December 2012

Thesis Supervisor: Profeesor Leonard R. MacGillivray

Graduate College
The University of Iowa
Iowa City, Iowa

CERTIFICATE OF APPROVAL

PH.D. THESIS

This is to certify that the Ph.D. thesis of

Elizabeth Elacqua

has been approved by the Examining Committee
for the thesis requirement for the Doctor of Philosophy
degree in Chemistry at the December 2012 graduation.

Thesis Committee:
Leonard R. MacGillivray, Thesis Supervisor

F. Christopher Pigge

Christopher M. Cheatum

Daniel M. Quinn

Geoff G. Z. Zhang

To Daniel Louis, Flora Domenica, Joseph Ceasar, and Mary Karpe

It is not the critic who counts, nor the man who points out how the strong man stumbled, or where the doer of deeds could have done them better. The credit belongs to the man who is actually in the arena; whose face is marred by dust and sweat and blood; who strives valiantly; who errs and comes short again and again; who knows the great enthusiasms, the great devotions, and spends himself in a worthy cause; Who, at the best, knows in the end, the triumph of high achievement; and who, at the worst, if he fails, fails while daring greatly, so that his place shall never be with those cold and timid souls who know neither victory nor defeat…

T.R. Roosevelt
Citizenship in a Republic

ACKNOWLEDGMENTS

As Albert Schweitzer noted, “in everyone’s life, at some time, our inner fire goes out. It is then burst into flame by an encounter with another human being. We should be thankful for those people who re-kindle the inner spirit.”

The results depicted in this thesis would have been undoubtedly impossible to achieve if not for the unwavering help and support of many people. Contrary to popular thought, although a thesis is only authored by a single entity, an entire ensemble or supporting cast is needed to accomplish the many results portrayed within a single dissertation. All of these people deserve my sincere gratitude.

First and foremost, I would like to thank my advisor, Professor Len MacGillivray for the opportunity to work in his dynamic research group. In some respects, the choice of an advisor for a Ph.D. is even more taxing than choosing the university itself since one can argue that there is limitless information about the school that can be accessed, however, you don’t necessarily know if your advisor’s personality meshes with your own until a year or two into the program. Having said that, I am extremely lucky to have been chosen by Len; his group gave me the freedom to pursue several different projects without begging. His more ‘hands off’ approach and self-professed research environment akin to that of a postdoctoral appointment augmented my aptitude to become a more independent researcher, while giving me the opportunity to say things such as ‘Len, I found a way to turn this one result into a thesis chapter, and here are the results,’ or ‘Hey, Len - I have this great idea for unsymmetrical cyclophanes’ without encountering even the subtlest degree of resistance. I will admit that some fear was present when I had my first meeting with Len after joining his group, and he told me he wanted me to write a review paper on something I, at the time knew nothing about, but now feel inundated with knowledge about. I am also indebted to him for passing on his wisdom and experiences on several occasions, as well as providing a tremendous degree of patience,

understanding, guidance, and support amongst several other things that could easily take another 100 pages to express my gratitude for. Thank you.

I would also like to extend my thanks to several faculty members. Without the enthusiasm of Dr. David Wiemer at my first ACS National Meeting poster, I still would not know where Iowa was, and base everything I know about it on the movie 'Field of Dreams.' I don't think I ever would've applied to Iowa if not for his constant support and help when I was still an undergraduate. I will always be grateful he stumbled upon my poster, while I stumbled through explaining a mess of signals in a 60 MHz NMR. I am also extremely indebted to Dr. Ned Bowden for his guidance and advice in teaching and research, as well as in life. I sincerely appreciate all the support (and well-timed jokes and laughter) throughout my career at Iowa. If I could have selected another committee member, if would've been Ned (though he is probably lucky I cannot…). I consider myself very fortunate to have encountered such a supportive department in Iowa.

I would also like to thank the other members of my thesis committee – Dr. Chris Pigge, Dr. Chris Cheatum, Dr. Dan Quinn, and Dr. Geoff G. Z. Zhang – for their unwavering support, advice, enthusiasm, and guidance in all of my research endeavors.

I am also indebted to several other members of the chemistry department. Sharon Robertson and Janet Kugley are acknowledged for easing the NY-to-IA transition in my career, and also for the constant advice, support, and quick responses to all of my inquiries. I am also grateful to Dr. Dale Swenson to has contributed to this thesis in many ways, most notably, but not limited to, his assistance with crystal structures and advice along the way. Dr. Jonas Baltrusaitis is also acknowledged for assistance with the SEMs and calculations that make up a large portion of the cyclophane story, as well as for several other discussions about organic molecules and research that sometimes even took place on the basketball courts.

I would also like to thank several collaborators. Dr. Geoff G. Z. Zhang, Rodger F. Henry, and Dr. Shuang Chen, who have contributed to this thesis in many ways

ranging from collecting crystal structures to analyzing data and providing manuscript suggestions and advice. Dr. Eric W. Reinheimer is acknowledged for collecting and analyzing several of the crystal structures in the latter portion of this thesis. His willingness to jump on board with our research and enthusiasm for collecting structures has led to very quick results. At this point, it is possible he knows more about molecular motion in co-crystals than he ever thought possible. Additional thanks are also given to Dr. Yulia Skvortsova and Dr. M. Lei Geng for fruitful discussions about fluorescence spectroscopy. Dr. Ryan Groeneman and Dr. Claude Mertzenich are acknowledged for constant support and research advice throughout the years.

During my studies at Iowa, I had the pleasure of meeting and working with several talented colleagues. Dr. Dejan-Krešimir Bučar helped me when I first joined the group, and has, essentially, had a hand in the several of the chapters of this thesis. I am thankful to him for several things, mostly, but not limited to, providing research advice, crystallographic guidance, and perspectives. Dr. Poonam Kaushik is also acknowledged for jump-starting what has become a great story in chapter 4. Additional thanks are given to Paul Jurgens and Bradley Loren for remaining enthusiastic about research in general, despite any number of complicated projects I put in from of them. I couldn't have asked for a better pair of undergraduates to share my research endeavors with.

I owe many thanks to great colleagues in the past 5 years: Thank you Kreso, Poonam, Joe, Saikat, Manza, John, Jelena, Paul, Brad, Kristin, Nam, Ryan, Claude, Charley, Michael, Katie, Becca and Jake. Additional thanks are given to past group members: Tomislav, Tony, and Tamara for support, advice, and their recollection of graduate school experiences and stories. Dave, Reba, Jake, Lindsay, Matt, Tara (and Dan), Joe C, Kristin (and Ryan), Travis, CJ, Phil, Caitlin, Justine, and others I've forgotten from Iowa… Thanks for all the good times, the support, the laughter, and the friendships.

I also owe sincere appreciation and gratitude to some faculty members at Le Moyne College for supervising the beginning of my scientific career. I thank Dr. Michael Masingale for being willing to let me work in his organometallics lab as a freshman, and allowing me synthesize compounds I would've never dared to handle, nor could I draw at the time. My gratitude is also extended to Dr. Joseph Mullins, who gave me the keys to his research lab and left me to work every chance I got for 2 years (ironically, I still have those keys…). Thanks for all the constant support, advice, and for preferring to talk about the chemistry of a fine red wine, as opposed to research, while in the lab.

Lastly (though surely not of least importance), I would like to thank my family and friends in NY for supporting me throughout this journey. I do not have to list them, for I am certain they know who they are. Without their constant support through all of my endeavors and endless encouragement along the way, none of this journey would be possible.

ABSTRACT

The research presented in this thesis is founded upon the ability to mimic Nature by using highly directional forces to influence self-assembly, while achieving the formation of desired supramolecular structures. The successful engineering of such solids relies upon a full comprehension of supramolecular synthons, so as to apply them to design complex architectures. We have studied synthon formation in multifunctional pharmaceutical solids. Through the formation of salts and co-crystals, we uncovered a role of tautomers in the salt – co-crystal continuum. From a solid-state perspective, one can envisage that tautomers could promote co-crystal formation since an inherent flexibility to interconvert can accommodate geometries of different co-formers, as well as increase the number of synthons able to support a multicomponent solid. We have also employed co-crystallization to ibuprofen as a means to exploit solid-state properties. We have shown that co-crystallization with bipyridines can result in the formation of both co-crystal solid solutions and co-crystal conglomerates.

Supramolecular chemistry can also be utilized to construct target organic and metal-organic frameworks. Solid-state synthesis has emerged as a means to achieve the formation of molecular targets that are usually inaccessible *via* solution phase synthesis through the exploitation of molecular recognition and self-assembly. In particular, utilizing a combinatorial template strategy can facilitate a [2+2] photodimerization in the solid state. Although the template-directed strategy has helped circumvent problems associated with crystal packing, the solid state is still not routinely used for synthesis, owing, in part, to a lack of expansion to multifunctional olefins and molecular targets.

We have introduced a method to direct the reactivity of multifunctional olefins that contain two robust hydrogen bonding elements to produce heteropolytopic molecules that are of interest for the formation of metal-organic frameworks. Specifically, we developed a protecting group strategy that affords a supramolecular regiochemistry to

attain the desired self-assembly. We have also extended our template approach to more conformationally-complex molecules to gain a further understanding of the rules regarding reactivity in highly substituted systems.

The end of this thesis is focused upon the solid-state synthesis of a series of molecular targets known as cyclophanes. Cyclophanes have a very rich history however, their immersion in all aspects of chemistry has suffered from a lack of high yielding synthetic techniques, as well as novel methodologies that target substitution on the aliphatic bridges. We have shown that a series of laterally-substituted [2.2]cyclophanes can be synthesized in quantitative yields utilizing template-directed self-assembly. The cyclophanes also exhibit optical properties that are influenced by a nonconventional internal charge transfer process, stemming from the strained cyclobutane core. We have also developed a sonochemical method to produce nanocrystals of cyclophanes, resulting in enhanced and red-shifted emissions.

Overall, the results described herein detail the use of supramolecular chemistry to achieve the formation of target architectures that differ in topology, connectivity, and/or physiochemical properties. The entirety of this thesis represents the undeveloped interplay between traditional synthetic organic chemistry and supramolecular solid-state chemistry. While the precision afforded by the crystalline phase provides access to molecular targets with high fidelity, expansion to multifunctional molecules that are desirable in the context of emergent properties bodes well for the continued development and exploitation of molecular recognition to generate novel functional materials.

TABLE OF CONTENTS

LIST OF TABLES

LIST OF FIGURES

CHAPTER 1. INTRODUCTION

The motivation behind chemistry research continues to focus upon the complete comprehension of how matter is put together and how it interacts with other forms of matter. Specifically, there is an ongoing push to synthesize valuable materials in the form of natural products,[1] active drugs,[2] nanostructures,[3] and electrical devices.[4] The synthesis of such structurally-exquisite molecules is a challenging task, wherein every group and atom has a precise destination within a targeted framework. The targeted making and breaking of covalent bonds has been exhaustively studied, and correspondingly, well-documented in terms of mechanisms and synthesis.[1] Owing to the breadth and wealth of knowledge of reactions, a chemist invariably desires to exert precise control over matter and its reactivity in an attempt to synthesize molecules by design.[5] The nature of covalent bonding has been well-established since Linus Pauling's work in the 1930's,[6] yet, researchers are still unable to control the interactions of chemicals. Biological systems are capable of influencing molecules and building more complex entities by exerting dynamic control over noncovalent interactions with a definite precision.[7] In an effort to comprehend and mimic Nature,[8] chemists now strive to fully understand the noncovalent forces that control molecular assemblies and their functions.

1.1 Supramolecular Chemistry

In 1969, Jean-Marie Lehn coined the term 'supramolecular chemistry.'[9] Lehn classified supramolecular chemistry as the branch of chemistry concerned with the interplay between designed molecular assemblies and intermolecular bonds, or more colloquially referred to as "chemistry beyond the molecule."[10] Supramolecular chemistry focuses on the design and synthesis of molecular architectures by relying on the complementary recognition, and subsequent assembly, of well-defined subunits. The products of complementary synthesis, the so-called 'supermolecules,'[11] are sustained by

noncovalent interactions such as hydrogen bonding,[12] halogen bonding,[13] coordination forces[14] and/or π···π stacking.[15] As natural products are strung together by covalent bonds between adjacent functionalities, supramolecular complexes are linked by complementary intermolecular interactions (Figure 1).[16]

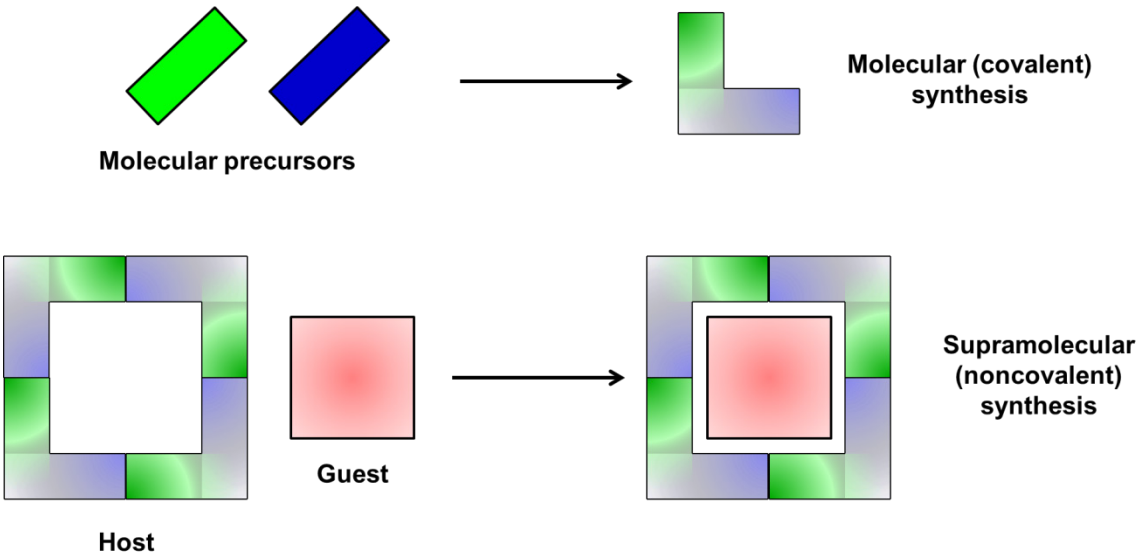

Figure 1: Construction of target molecules using covalent synthesis and noncovalent synthesis.

The emergence of supramolecular chemistry has directly influenced how efficiently chemists can design and synthesize desired frameworks.[17] The development and application of this 'bottom up' approach is widely successful, owing to the noncovalent forces that dictate structural and morphological properties, while producing structures that were previously inaccessible. Such secondary interactions provide a reliable element of control in the design of molecular architectures. The idea of molecular recognition[18] and self-assembly[19] stems from biological systems, wherein complementary molecules showcase the precision and specificity of noncovalent bonds needed to form larger architectures. As chemists have slowly recognized the advantages

of mimicking biological systems, there remains a push to synthetically design structures with the same control and precision as demonstrated by Nature. This can only be accomplished by comprehending how molecular recognition and self-assembly co-operate within biological systems, and applying this knowledge towards targeted organic synthesis.

1.2 Molecular Recognition and Self-Assembly

Molecular recognition and self-assembly are at the cornerstone of supramolecular chemistry.[20] Molecular recognition is a process in which molecules can utilize complementary functionalities to interact in a well-defined and precise manner *via* intermolecular forces. This concept has been well-established within biological systems, being utilized as early as the 1890's, when Emil Fisher described the idea of a lock-and-key interaction.[21] Accordingly, molecular recognition was said to be an analogous process to fitting a key within a lock in the context of complementarity. The lock acts as the molecular receptor, and the key is a substrate. This same 'lock and key' principle also governs enzyme recognition in the context of substrate-specific binding. Molecular recognition also plays an essential role in the synthesis of the biomacromolecules[22] responsible for life in both prokaryotes and eukaryotes (e.g. DNA, RNA, proteins). Intermolecular interactions are, in part, responsible for the helical structure of DNA, as the bases adenine, thymine, guanine, and cytosine are all polar aromatic N-heterocycles that possess recognition elements that are orthogonal to each other and interact *via* specific hydrogen bonds and π-π stacking.[23] Specifically, a purine base (adenine – A or guanosine – G) recognizes and interacts with a complementary pyrimidine base (thymine – T or cytosine – C) *via* hydrogen bonding such that A—T and G—C pairs stack along each strand of the DNA helix (Figure 2).

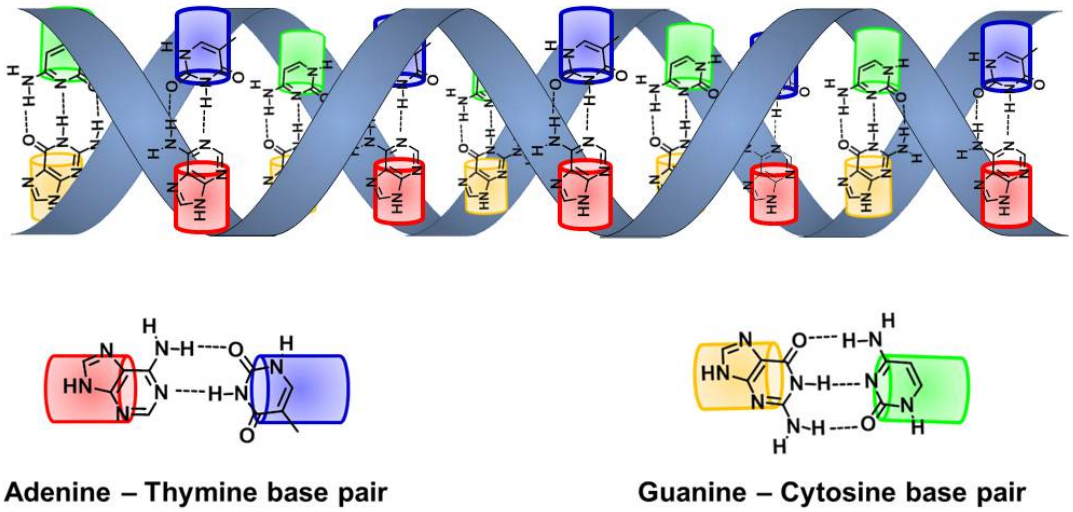

Figure 2: Self-assembly of nucleobases to generate DNA.

Another process that is integral to the formation of functional supramolecular architectures is self-assembly. Defined by George Whitesides, self-assembly is "the spontaneous assembly of molecules into structured, stable, noncovalently joined aggregates" (Figure 3).[19] The process of self-assembly is known to be reversible, thus, any mismatched subunits or assemblies can be eliminated from the final structure.[20] The idea of self-assembly is founded in biological studies of the tobacco mosaic virus (TMV).[24] TMV is formed when a protein sheath composed of 2130 identical protein subunits encloses single-stranded RNA. The protein sheath provides the shape of the helix, while the RNA strand controls the length. Studies of TMV have demonstrated that the components can disassemble and *in vitro*, reassemble to form the active virus. Essential principles of self-assembly were provided by TMV, the most significant being: 1) the control of associations through multiple reversible interactions, 2) the economy of molecular information of subunits, 3) self-correcting information, and 4) overall efficiency of molecular assembly.

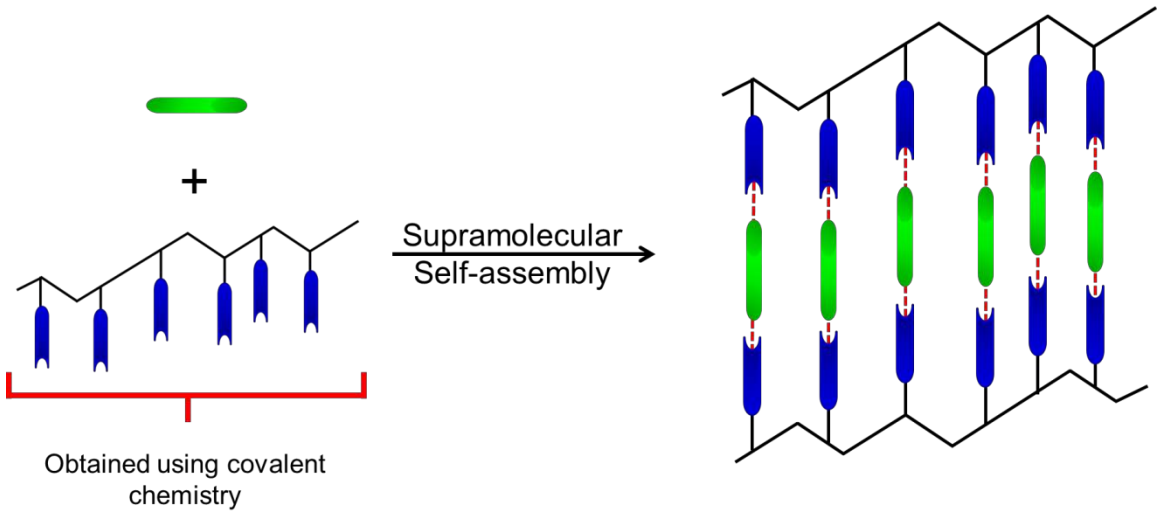

Figure 3: Self-assembly of hydrogen bonding reactants to generate a side-chain supramolecular polymer aggregate.

1.3. Molecular vs. Supramolecular Organic Synthesis

Advancements in synthetic organic chemistry rely upon the development and application of novel methodologies to synthesize target molecules.[1] Currently, organic synthesis portrays the pursuit of target molecules as a significant problem that can be solved through the meticulous formation of a series of covalent bonds and functional group interconversions in a linear fashion.[25] With the increasing complexity of desirable structures, the number of steps needed to achieve the target increases, and thus, attaining the desired regio- and stereochemistry in the product remains a noteworthy challenge. To combat the challenge, a systematic approach to molecular organic synthesis, known as target-driven synthesis, was developed by E. J. Corey.[26] The target-driven approach introduced the concept of target 'synthons' or structural units within molecules attainable *via* retrosynthetic analysis.[27] Retrosynthesis is essentially a conceptual tool that facilitates the breakdown of a target molecule into smaller discrete units and enables the recognition of synthons. A key component of a retrosynthetic analysis involves the

design of multiple plausible synthetic routes, as well as the comparison of any possible pathways in a very straightforward fashion. Upon recognition of molecular synthons, the target molecule can then be synthesized in, ideally, the most direct route with the fewest number of steps and, in theory, the highest possible yield. The success of a retrosynthetic analysis relies upon an endless library of chemical reactions that can be applied to reactants with a variety of geometries and multiple functionalities.[27] Application of a retrosynthetic approach has led to the successful synthesis of a variety of complex molecular targets, although at times, in less than desirable yields.[28]

Whereas targets in organic synthesis are defined in the context of the connectivity of covalent bonds, supramolecular targets are described in terms of their interactions and topologies.[16] Although originally applied to construct molecular targets, the concept of a target-driven synthesis[1] can still be used to provide a rational entry to the development of supramolecular structures. In particular, the retrosynthetic analysis of a solid architecture can allow for the identification of multiple supramolecular synthons that have the capacity to self-assemble and sustain the target framework. As coined by Guatum Desiraju, "Supramolecular synthons are structural units within supermolecules which can be formed and/or assembled by known or conceivable synthetic operations involving intermolecular interactions. . . and play the same focusing role in supramolecular synthesis that conventional synthons do in molecular synthesis."[16] In contrast to a molecular target, a supramolecular target can be furnished by two distinct types of synthons: homosynthons and heterosynthons.[16, 29] Whereas a homosynthon is a supramolecular entity sustained by two or more identical hydrogen-bonding functional groups, a heterosynthon consists of two or more different, yet still complementary, hydrogen-bonding functionalities (Figure 4).

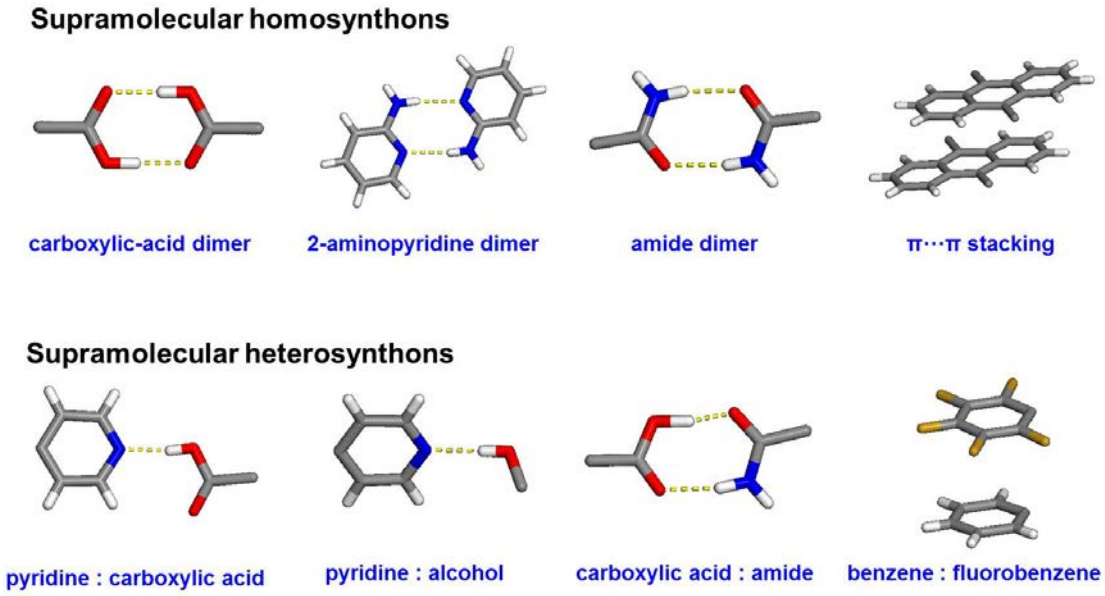

Figure 4: Examples of supramolecular synthons.

1.4 Functional Supramolecular Chemistry

Since the inception of supramolecular chemistry in 1969, the area has developed in somewhat of an architectural science focused broadly upon 'the chemistry beyond the molecule.'[10] Initial studies focused on understanding the basic interactions of molecular recognition and how those interactions dictated self-assembly.[19] As engineers of target assemblies, the paramount challenge afflicting supramolecular chemists stems from designing systems that echo sophistication, yet are as simple and efficient as those produced by Nature. The impetus behind comprehending the complex interplay between molecular interactions and self-organization remains centered in the potential to reliably predict, and thus, control intermolecular forces leading to the construction of target frameworks with desired physical and/or chemical properties.[30] The area of supramolecular chemistry has, thus, evolved to encompass the notion of controlled engineering of supramolecular entities *by design*,[5] providing access to functional

supramolecular materials, such as supramolecular polymers[31] and liquid crystals[32] that exploit the dynamic nature[33] of noncovalent interactions.

1.4.1 Supramolecular Polymer Science

The coalescence of supramolecular chemistry and materials science has resulted in the development of polymers, with a focus on subsequent self-assembly. Owing to the ability of Nature to design macromolecules utilizing molecular recognition (vide supra), supramolecular polymers emerged as attractive modules capable of sustaining a precise assembly, while providing building blocks for functional materials.[31] There are two classes of supramolecular polymers, organized by the domain containing the noncovalent interaction. If the interactions comprise the polymer backbone, it is termed a main-chain supramolecular polymer,[34] while materials containg noncovalent interactions within the pendant units are coined side-chain supramolecular polymers.[35] Both classes have exhibited unique properties, and their development bodes well for materials science.[36] To date, main-chain supramolecular polymers have garnered the most interest, whereas side-chain functionalization has only emerged as a mainstream target in the past 15 years.

In the 1990's, Jean-Marie Lehn reported the first well-defined main-chain supramolecular polymers[37] based upon the complementary recognition of ditopic uracil and 2,6-diaminopyridine monomeric organic building blocks (Figure 5a),[38] while Fréchet reported the first noncovalently functionalized side-chain polymers based upon poly(siloxanes) and poly(acyrlates) with liquid crystalline domains comprising (acid) O—H···N (imidazole) hydrogen bonds in the pendant chains (Figure 5b).[39] Aided by the understanding of the directional hydrogen bonds manifested throughout nature, specifically present in the biopolymers DNA and RNA,[23] supramolecular polymer science after Lehn and Fréchet's groundbreaking work has developed into a rich and mature area. By the late 1990's, 2-ureido-4[1H]-pyrimidinone (UPy) units emerged as strong self-complementary monomers, owing to their ability to sustain four highly

directional hydrogen bonds.[40] Extensive work utilizing UPy motifs to control the formation of main-chain supramolecular polymers has been accomplished by Meijer,[41] Zimmerman,[42] and others[43] (Figure 5c-5d). Such materials have demonstrated both high degrees of polymerization and rigidity,[44] as well as potential in tissue engineering.[45] In the late 1990's, an additional approach emerged to exhibit architectural control in side-chain supramolecular materials. This approach involves utilizing ring-opening metathesis polymerization (ROMP)[46] to synthesize hydrogen bonding motifs within the side-chain, and has been extensively studied by both Weck[47] and Rotello.[48]

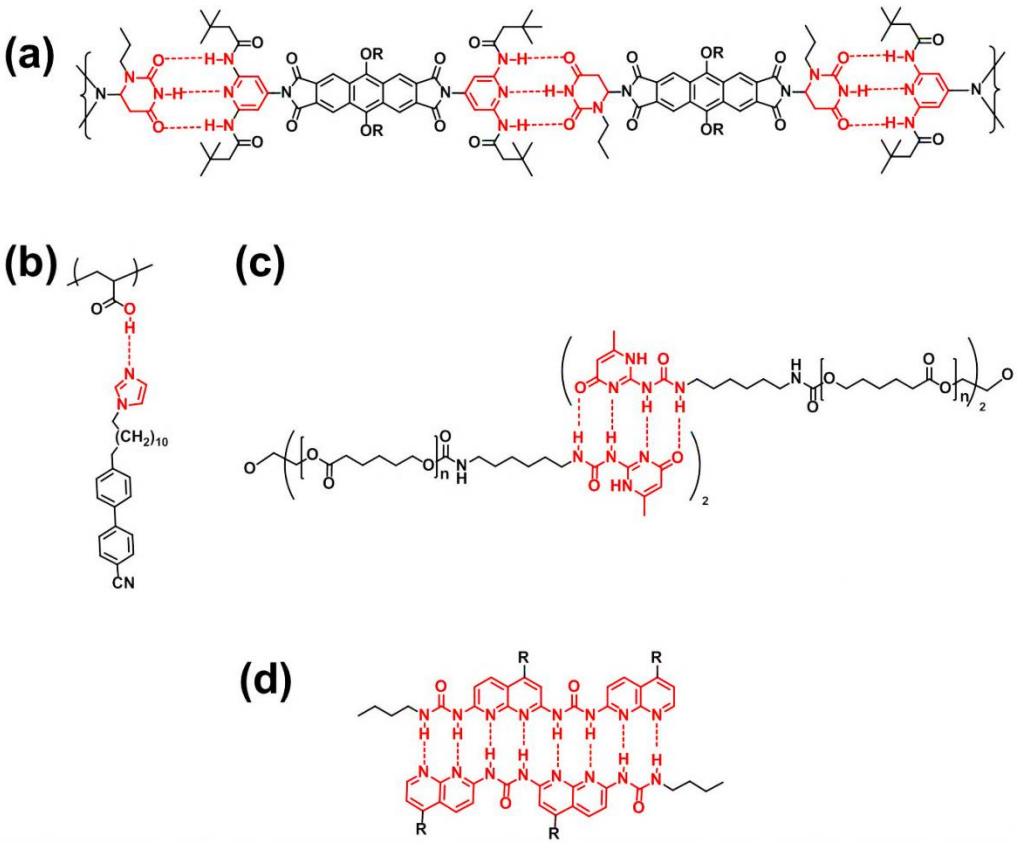

Figure 5: Supramolecular polymers with molecular recognition elements in red: (a) Lehn's uracil and diamidopyridine main-chain polymer, (b) Fréchet's poly(acrylate) liquid crystalline side-chain polymer, (c) Meijer's self-complementary UPy polymer, and (d) Zimmerman's ureido-naphthyridine self-complementary oligomer.

In a fashion similar to obtaining other supramolecular architectures, metal coordination has also been investigated in the context of polymer self-assembly,[49] owing to the highly directional and orthogonal nature of the interaction, as well as the capacity to form much stronger interactions in side-chain functionalized materials.[50] In addition, utilization of metal-ligand bonds could afford materials exhibiting optical, chemiluminescent, electrical, and/or photochemical properties. The majority of metallosupramolecular polymers reported to date are based upon bipyridine (bipy)[51] and terpyridine (terpy)[52] ligands, owing to their multidentate nature and ability to lead to orthogonal functionalization. Recent work by Rowan has also utilized bis(benzimidazolyl)pyridine units to generate stimuli-responsive shape-memory polymers,[53] as well as optically-healable[54] materials using europium and zinc, respectively (Figure 6a). Additional utilization of pincer ligand-based scaffolds[55] has been demonstrated by Weck and coworkers.[56] The combination of multiple supramolecular interactions in the form of both coordination bonds and hydrogen bonds has also been pioneered by Weck to sustain polymeric structures (Figure 6b).[57] Specifically, a combinatorial approach[58] was developed that allowed for the supramolecular functionalization along a polymer backbone, so as to encompass multiple different noncovalent motifs equally (i.e. using both metal coordination and/or multiple hydrogen bonding sites), while providing access to a unique library of materials.

Although still in their infancy, the emergence of supramolecular polymers has undoubtedly led to well-defined materials that are reminiscent of biomolecules. The seminal work of Lehn[38] and Fréchet,[39] as well as the availability of multiple recognition elements[40-45] has spurred the development of this field. Additional efforts, spearheaded largely by Weck[47] and Rotello[48] to circumvent the vexatious nature of uncontrollable polymerizations, led to the utilization of ROMP to afford well-defined architectures with a high degree of precision. With the breadth of supramolecular interactions that can be utilized to afford novel architectures, the field undeniably has a very promising future.

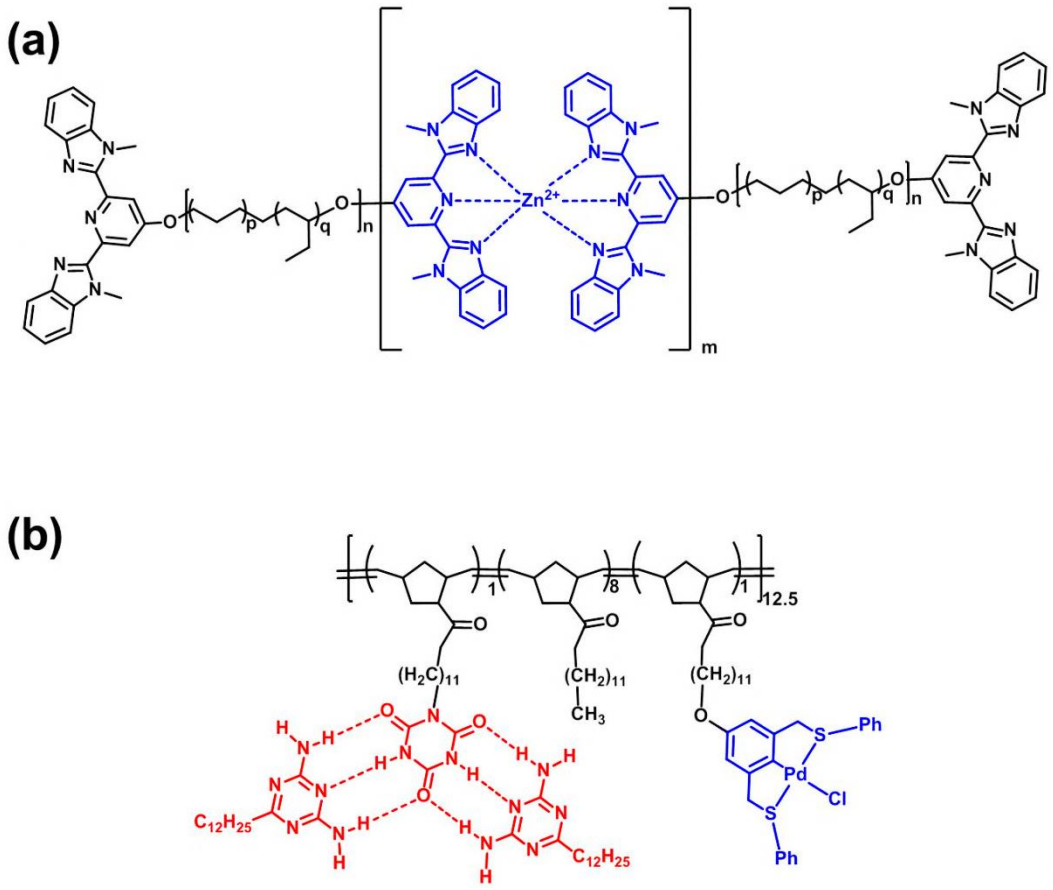

Figure 6: Supramolecular polymers with metal coordination (blue) and hydrogen bonding (red) elements: (a) Rowan's bis(benzimidazolyl)pyridine system and (b) Weck's mixed coordination and hydrogen bonding system.

1.5. Crystal Engineering

The central paradigm of solid-state supramolecular organic chemistry is founded upon crystal engineering,[30] the ability to make molecules by design. Crystal engineering is the 'new organic synthesis,'[16] using both analysis and synthesis to engineer new, functionalized, and robust materials. Akin to traditional syntheses that rely on reason and ingenuity to breakdown a target molecule into discrete synthons, crystal engineers can innovatively assess target architectures in the context of patterns of intermolecular interactions. In effect, a crystal engineer endeavors to identify and design building

blocks and synthons that can ultimately guarantee predictability within a homologous set of structures,[16] owing to the robust ability to be reliably and effectively applied to each molecule within a given set. The establishment of such structural predictability can be expected to culminate with the deliberate development of solids with very specific physical and/or chemical properties *via* a bottom up approach.

Although it is generally impossible to predict the structure of the simplest crystals,[59] even if one is given all possible knowledge of the chemical constituents, the early persistent efforts of Desiraju,[60] Etter,[61] Robson,[62] Wuest,[63] and others,[64] combined with the current work of Zaworotko,[65] Braga,[66] MacGillivray,[67] and Aakeröy[68] have led to the emergence of crystal engineering as a practical method to construct target architectures such as metal-organic frameworks,[69] pharmaceutical materials,[70] devices,[71] and organic semiconductors.[72]

The building blocks of a functionalized crystal are held together by intermolecular interactions[50] that are weaker than the covalent bonds within the individual components. Aside from coordination bonds and ionic interactions, such as dipole-dipole, the strongest interactions in crystal engineering are hydrogen bonds. Owing to the strength, directionality, and overall ubiquity of the interactions in organic molecules, hydrogen bonds are the most exploited interactions in crystal engineering.[73] In the context of hydrogen-bonded complexes, supramolecular adducts known as co-crystals are widely studied to impart desired physiochemical properties within a multicomponent solid.

Although there are several different definitions of a co-crystal, and indeed, the community cannot even converge on whether it is a 'co-crystal' or a 'cocrystal,'[74] Aakeröy has provided an explanation that is not widely accepted by crystal engineers. According to Aakeröy, a co-crystal is a "structurally homogenous crystalline material that contains two or more neutral building blocks that are present in definite stoichiometric amounts."[75] In co-crystals, two or more distinct chemical entities are held together by one of multiple intermolecular interactions.

Co-crystals are of particular interest to not only study solid-state reactivity,[76] but also develop robust pharmaceutical solids[70] and optical devices.[71] Co-crystals are utilized in the context of solid-state reactivity to circumvent issues arising from an unpredictable crystal packing.[77] Within the pharmaceutical industry, co-crystals have been investigated to overcome solubility, hydration, stability, and toxicity issues in drugs. In addition, co-crystals provide an effective way to tailor the properties (e.g. melting point, solid-state behavior, hygroscopicity, compressibility) of active pharmaceutical ingredients (APIs).[78] Recently, co-crystallization has been applied to manipulate the luminescent and/or non-linear optic (NLO) properties of organic molecules.[79] Co-crystals are also different from solid solutions, wherein two or more components are present, yet one of the components is randomly distributed within the crystal lattice of the other.

1.6 Organic Solid-State Reactivity

1.6.1 Introduction and Principles

Covalent bond-forming reactions lie at the core of synthetic organic chemistry.[80] Such reactions are utilized to construct simple and complex frameworks with variable yields. Within this field, chemists continually search for conditions to control the formation of covalent bonds, while obtaining high yields and limiting byproducts. In this context, the organic solid state has emerged as an exciting medium that provides control over the formation of such bonds.[81] The solid state maintains an environment which is flexible enough to allow some atoms to move and react, yet rigid enough to facilitate quantitative and stereospecific covalent bond formation. Additionally, conducting reactions within crystals enables molecules to adopt previously unknown geometries, resulting in the formation of products that are inaccessible in the liquid phase.

The most studied solid-state reaction remains the [2+2] cycloaddition.[82] Pioneering work on this reaction was achieved by Schmidt in the 1960's and 70's.[83] Based upon structural analyses of cinnamic acids, Schmidt identified the geometrical

criteria for a pair of carbon-carbon double bonds to undergo a solid-state [2+2] photodimerization.[83] Following this work, it was determined that solid-state reactions are topochemically-controlled with a minimal amount of molecular movement.[83] Thus, the [2+2] cycloaddition is dictated in part by the alignment and parallel overlap of the olefins and the relevant nonbonding orbitals. The desired olefin distance in the crystal lattice is thought to be within 4.2 Å.[83] The validity of the topochemical postulate is illustrated through the reactivity of cinnamic acid polymorphs. In particular, *o*-ethoxycinnamic acid exists as three polymorphs, labeled as α, β, and γ (Figure 7). The α- and β- forms are photoreactive, stacking with the double bonds of neighboring molecules aligned and within 4.2 Å, while the γ-form has neighboring molecules aligned, yet separated by > 4.2 Å and is photostable. Whereas the α-polymorph adopts alternating orientations within each stack, the β-polymorph adopts identical orientations in each stack. Consequently, the [2+2] photodimerization of the α- and β-forms affords the head-to-tail and head-to-head truxillic acids, respectively.[83]

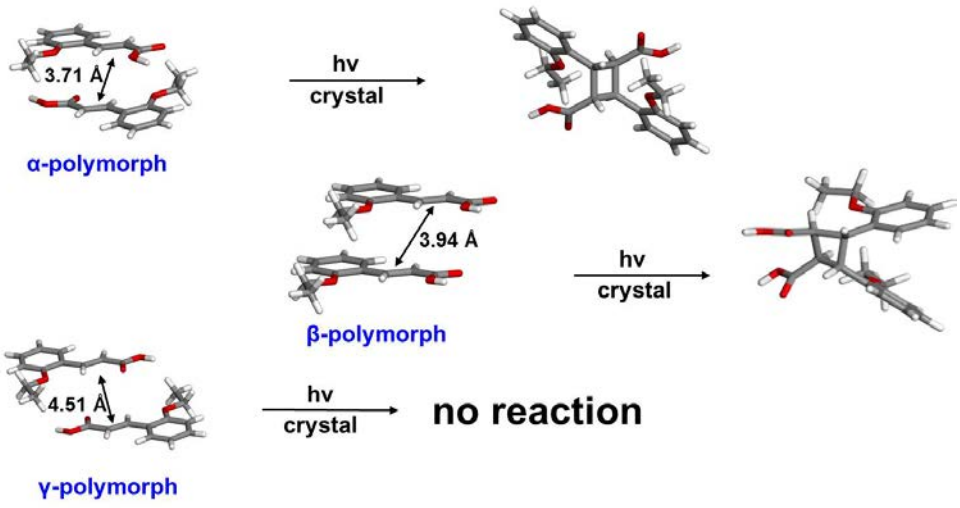

Figure 7: Crystal structures and solid-state reactivity of α, β, and γ polymorphs of *o*-ethoxycinnamic acid.

Several advances have been made to circumvent the problems associated with crystal packing to facilitate reactivity within the solid state. More specifically, intermolecular forces in the field of supramolecular chemistry have been exploited. Initially, directing effects of covalently-attached functionalities (e.g. Cl-atoms) were employed to steer packing.[84] Forces such as π –π stacking, charge-transfer complexation, and hydrogen bonding then followed. Despite successes, however, somewhat limited control was achieved since the functional groups lacked an ability to compete with crystal packing.

Whereas initial work to control reactivity involved the use of covalently-attached substituents to promote olefins in a suitable geometry to react, chemists in more recent years have turned to a dynamic combinatorial chemistry approach,[58] wherein a library of auxiliaries that function as templates is screened to direct reactivity.[77] Specifically, organic molecules and metal-complexes have been utilized to assemble and organize reactants *via* directional forces (e.g. cation-π stacking, hydrogen bonding, metal coordination) in a geometry appropriate for reaction. By exerting supramolecular control over the solid-state topology that is independent of crystal packing, relatively complex molecules (e.g. ladderanes and paracyclophanes) have been effectively synthesized in up to quantitative yields (Figure 8).[81]

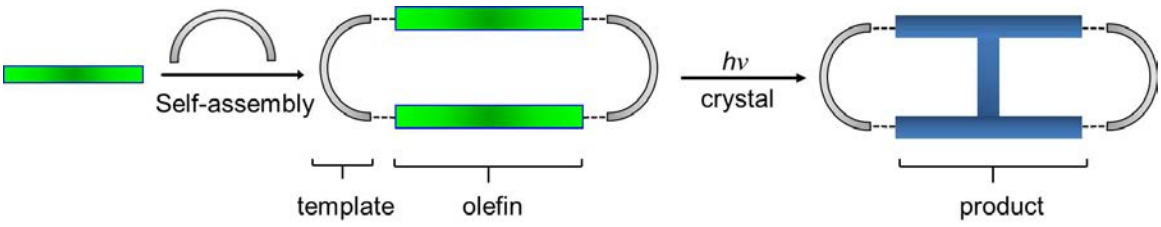

Figure 8: Combinatorial template-directed approach to control reactivity in the solid state.

In line with Schmidt's work, studies were aimed at identifying molecules that could crystallize in a reactive assembly. Owing to the topochemical postulate[83] and the abundance of studies, the [2+2] cycloaddition is the most well-known solid-state reaction. Although not much has been studied in the context of topochemistry for other cycloadditions, several other reactions have been pursued with good success in the solid state. The second most studied solid-state reaction is the [4+2] cycloaddition.[85] Other reactions, such as the [4+4] and [3+2] cycloadditions,[86] are sparking some interest in the context of solid-state reactivity. Several lesser known solid-state reactions (e.g. 1,3-dipolar cycloadditions, S_N^2 reactions)[87] have also been demonstrated to occur. Despite the breadth of known solid-state reactions, the [2+2] cycloaddition remains the focus of studies, owing to a strong topochemical foundation.

1.6.2 Hydrogen Bond-Driven [2+2] Cycloadditions

Templates that operate *via* hydrogen bonding to preorganize reactive molecules have been utilized to control [2+2] photodimerizations of olefins mainly functionalized with pyridyl groups.[77, 81] The approach relies on the formation of organic co-crystals. MacGillivray introduced the co-crystallization approach to control and direct the reactivity of substituted olefins in the solid state. Specifically, it was demonstrated that the photostable olefin *trans*-1,2-bis(4-pyridyl)ethylene (4,4'-bpe), when co-crystallized with 1,3-dihydroxybenzene (res), forms a discrete four-component molecular assembly sustained by O—H···N hydrogen bonds wherein the double bonds of 4,4'-bpe are aligned parallel, and separated by 3.65 Å (Figure 9).[88] The resulting photoreactive discrete assembly produces *rctt*-tetrakis-(4-pyridyl)cyclobutane (*rctt*-4,4'-tpcb) stereospecifically and in quantitative yield. In essence, the use of the ditopic res template essentially decoupled the effects of solid-state reactivity from crystal packing.

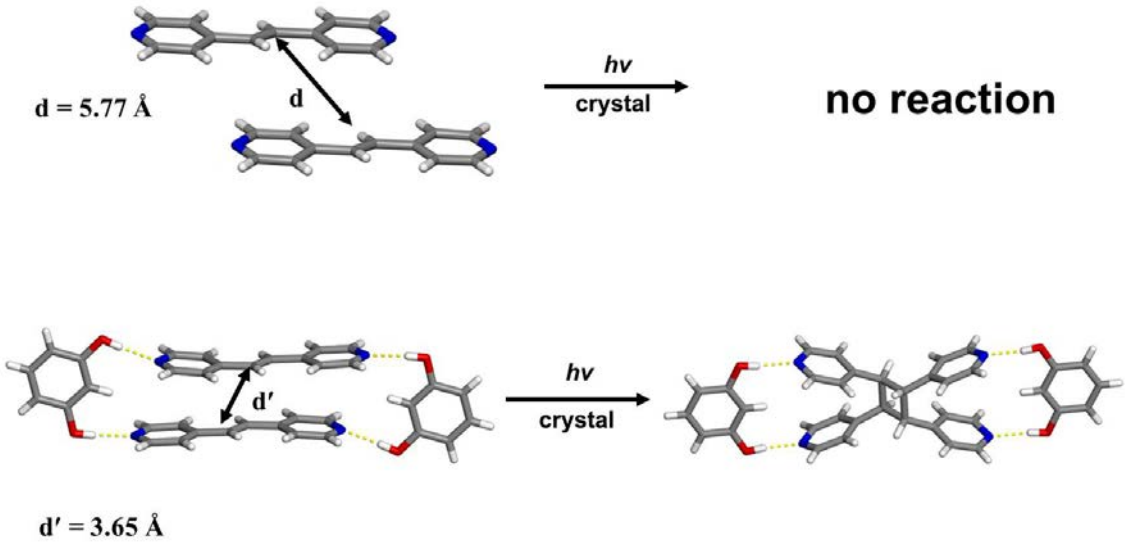

Figure 9: Application of a template-directed approach to synthesize 4,4′-tpcb using res as an organic template.

A template based on a crown ether was subsequently used to organize C=C bonds within a 0D complex in a solid for a [2+2] photoreaction.[89] Specifically, Garcia-Garibay, Stoddart and co-workers demonstrated that reaction of a bisparaphenylene-34-crown-10 (bpp-34-crown-10) with a bis(dialkylammonium)-substituted stilbene (amm-stilb) produced the four-component complex 2(bpp-34-crown-10)·2(amm-stilb) held together by eight $^{+}$N—H···O hydrogen bonds. The cavity of the crown ether was filled with end of the two reactants, with the olefinic bonds being parallel and separated by approximately 4.20 Å. UV irradiation resulted in a dimerization of amm-stilb to give a single diastereomer in approximate 80% yield.

MacGillivray demonstrated that co-crystallization of 1,8-naphthalenedicarboxylic acid (nda) with either 4,4'-bpe or 2,2'-bpe produced a discrete four-component assembly sustained by O—H···N hydrogen bonds (Figure 10a).[90] Each carboxylic acid group also participated in a C—H···O interaction with each pyridine ring. The olefins in each assembly were organized parallel and separated by 3.73 and 3.91 Å, respectively, which

rendered both 4,4'-bpe and 2,2'-bpe photoreactive. UV irradiation of each solid produced the corresponding *rctt* isomers in quantitative yield. Expanding on this idea, Jones has also demonstrated that carboxylic acid templates can also direct the reactivity of 4,4'-bpe.[91] Specifically, tricarballylic acid (tca) was co-crystallized with 4,4'-bpe, affording a supramolecular tape, wherein the C=C bonds are separated by <3.85 Å (Figure 10b).

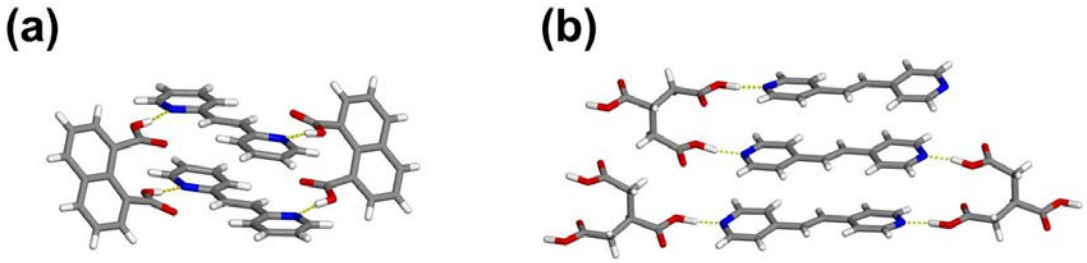

Figure 10: Co-crystals of photoactive (a) 2(nda)·2(2,2'-bpe) and (b) (tca)·2(4,4'-bpe).

In addition to symmetrical hydrogen bond donor templates that interact *via* O—H···N hydrogen bonds, MacGillivray and co-workers have demonstrated the ability of unsymmetrical Rebek's imide (Reb-im) to direct a [2+2] photodimerization (Figure 11).[92] Specifically, co-crystallization of Reb-im with 4,4'-bpe produced a four-component assembly with stacked olefins parallel and separated by 3.78 Å. The assembly was held together by both O—H···N and N—H···N hydrogen bonds. The photoreaction also proceeded *via* a single crystal to single crystal (SCSC) transformation to give 4,4'-tpcb stereospecifically and in 100% yield.

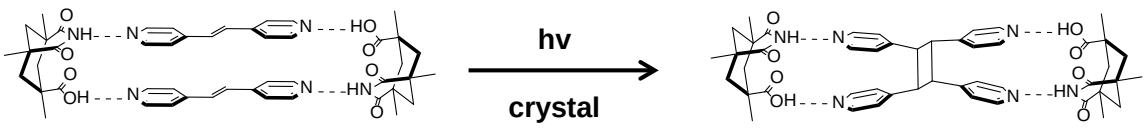

Figure 11: Synthesis of 4,4′-tpcb using Reb-im as a heteroditopic template

Organic templates have also been utilized to pre-organize monopyridyl olefins into more complex architectures. Co-crystallization of 4-chlorostilbazole (4-Cl stilbz) with resorcinol or 4-ethylresorcinol affords a three-component assembly that is held together by two O—H···N hydrogen bonds.[93] Both molecular assemblies result in the quantitative formation of *rctt*-1,2-bis(4-pyridyl)-3,4-bis(*p*-chlorophenyl)cyclobutane. Recently, Ramamurthy demonstrated that additional stilbazoles (e.g. 4-CN, 4-F, 4-Br stilbz) undergo stereospecific photodimerizations using thiourea as a template.[94] Specifically, co-crystallization of 4-F stilbz afforded an infinite assembly sustained by N—H···N hydrogen bonds. Thiourea tapes are formed that position the olefins like rungs of a ladder in an antiparallel orientation (Figure 12). UV-irradiation of the co-crystals afforded afforded the head-to-tail dimer in near quantitative yield.

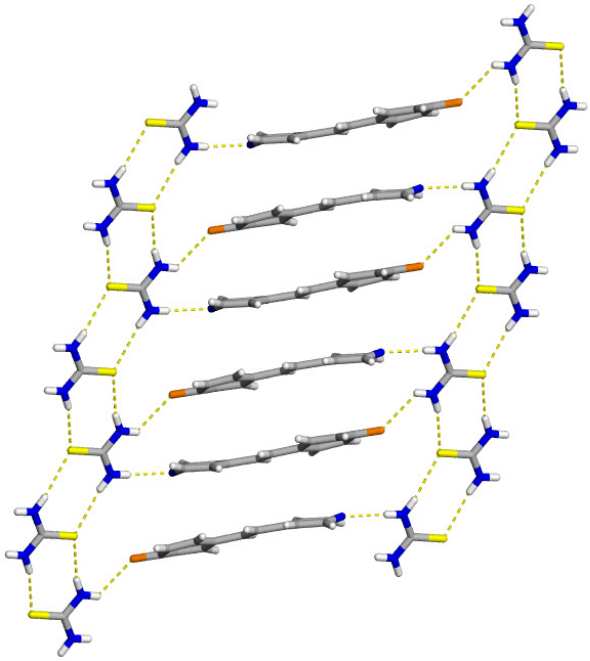

Figure 12: Self-assembly of thiourea and 4-F stilbz displaying the position the olefins like rungs of a ladder in a parallel head-to-head orientation

Hydrogen bond-driven self-assembly has also been utilized to direct the reactivity of di- and triolefinic reactants. Specifically, 5-OCH_3 res has been utilized as a linear template to organize both *trans*-1,4-(4-pyridyl)-1,3-butadiene and *trans*-1,6-(4-pyridyl)-1,3,5-hexatriene into a photoreactive four-component assembly, wherein the C=C bonds lie parallel and separated by <4.2 Å, and in a position suitable for photoreaction.[95] The photoreaction results in the stereospecific and quantitative formation of [3] and [5]ladderanes (Figure 13).

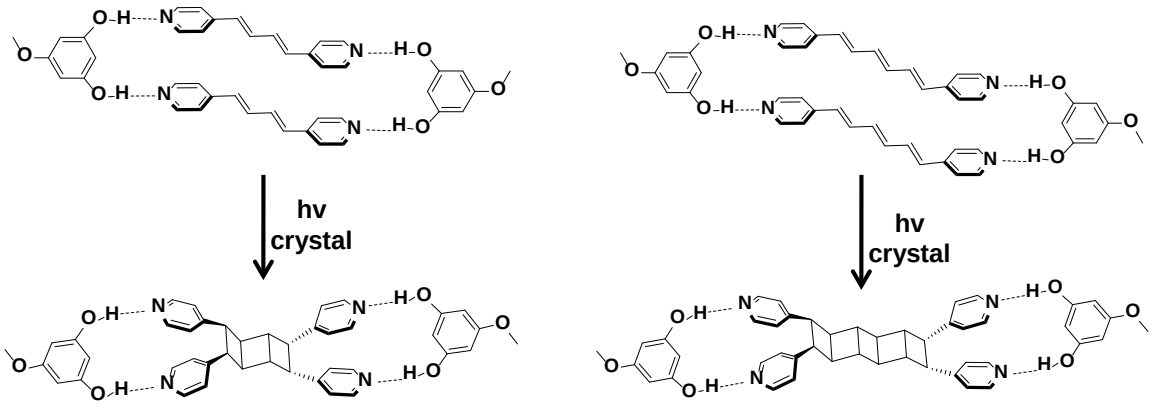

Figure 13: Template-directed solid-state reactivity to generate a [3]- and [5]-ladderane.

Similarly, co-crystallizing 4-benzylresorcinol (4-Bn res) with *p*-di-[2-(4-pyridyl)ethenyl]benzene affords co-crystals wherein both sets of double bonds are positioned for a double photoreaction (Figure 14a).[96] 4-Bn res controls the positioning of the olefins *via* strong O—H···N hydrogen bonds, affording a bridge-substituted [2.2]paracyclophane (tpcp) stereospecifically, and in quantitative yields (Figure 14b). This same approach has also been used by Brunklaus to direct the reactivity of *p*-di-[2-(4-pyridyl)ethenyl]-2-fluorobenzene (bpef).[97] Co-crystallization of bpef with 2,4-dihydroxybenzaldehyde (4-CHO res) affords a similar four-component assembly that

affords a [2.2]paracyclophane *via* a rare single-crystal to single-crystal (SCSC) reaction (Figure 14c).

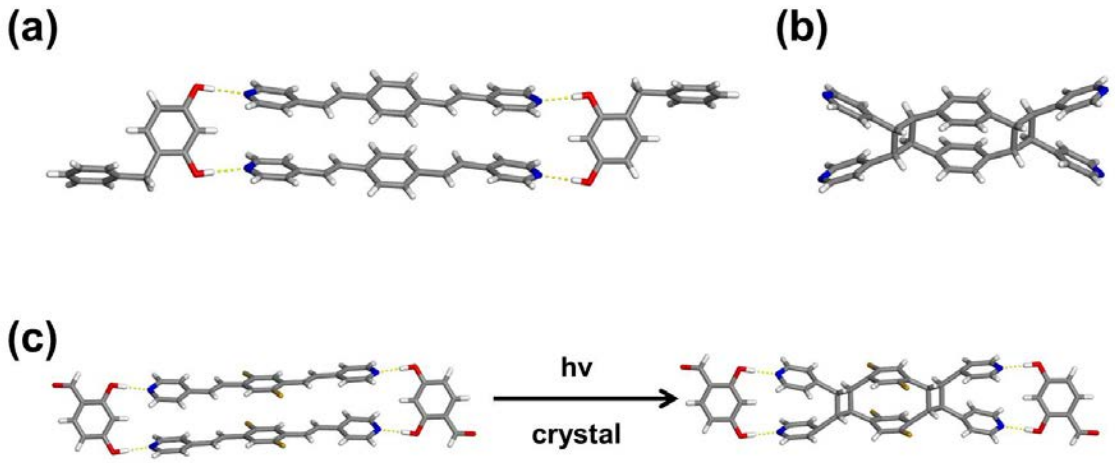

Figure 14: Template-directed [2+2] photodimerizations affording [2.2]paracyclophanes: (a) co-crystal 2(4-Bn res)·2(bpeb) that affords product (b) tpcp, and (c) solid-state synthesis of substituted tpcp from co-crystal 2(4-CHO res)·2(bpef).

In related work, Santra and Birahda have reported that the reactivity of 1,5-bis(4-pyridyl)-1,4-pentadiene-3-one (1,5-bppo) can be directed using the tritopic phloroglucinol (pg).[98] The resulting ladder-like network is sustained *via* the expected O—H···N hydrogen bonds with two of the –OH groups, while the additional phenolic –OH is bonded to a CH_3CN molecule. Adjacent double bonds in the 1D network are separated by 3.60 and 3.85 Å. The photoreaction results in 100% yield of a tricyclo[6.2.0.0]decane ring system (Figure 15).

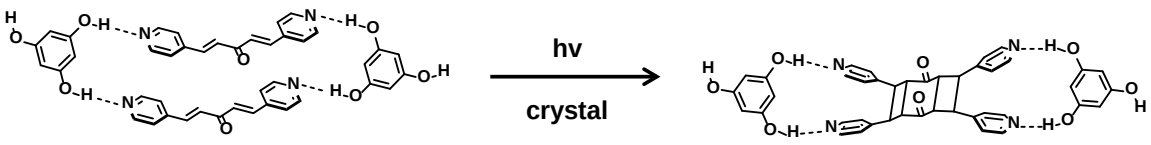

Figure 15: Photoactive ladder-like network of (1,5-bppo)·(pg).

All of the above assemblies rely on olefins substituted with hydrogen bond-accepting pyridines, along with hydrogen bond-donating templates. In principle, the supramolecular code can also be reversed, such that the olefins are functionalized with carboxylic acids, while the templates are substituted with pyridines. This was first demonstrated by MacGillivray using fum as the reactive olefin and 2,3-bis(4-methylenethiopyridyl)naphthalene (2,3-nap) as the ditopic template (Figure 16a).[99] As expected, a four-component assembly dominated by strong O—H···N hydrogen bonds resulted from co-crystallization. The olefins were aligned and approximately parallel with a C=C separation of 3.84 Å and reacts in a SCSC manner to give ctba in up to 70% yield. A similar approach was developed by Wolf to further direct the reactivity of fum, wherein 1,8-bis(4-pyridyl)naphthalene (dpn) was used as a template (Figure 16b).[100] This supramolecular approach resulted in the quantitative formation of ctba.

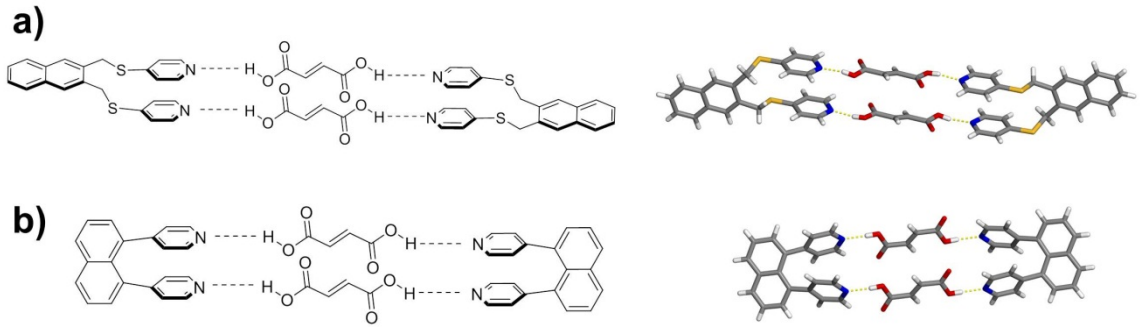

Figure 16: Solid-state reactivity of fum by 'reversing the code' of the template approach.

1.6.3 Halogen Bond-Driven [2+2] Cycloadditions

In addition to templates that enforce stacking, ditopic halogen bond donors have been used to assemble olefins within a photoreactive assembly. Metrangolo and coworkers have also shown that reactivity in the solid state could be controlled using templates based on halogen bonding, and π-π stacking.[101] Specifically, they

demonstrated the first use of a tetratopic template to complex 4,4'-bpe in a reactive assembly. Co-crystallization of 4,4'-bpe and a halogenated pentaerythritol derivative (ery) afforded an infinite 1D ribbon sustained by I···N halogen bonds (Figure 17). The directionality resulting from the halogen bonds and π-π stacking preorganized the olefins into a reactive alignment. The photoreaction afforded *rctt*-4,4'-tpcb stereospecifically and in quantitative yield.

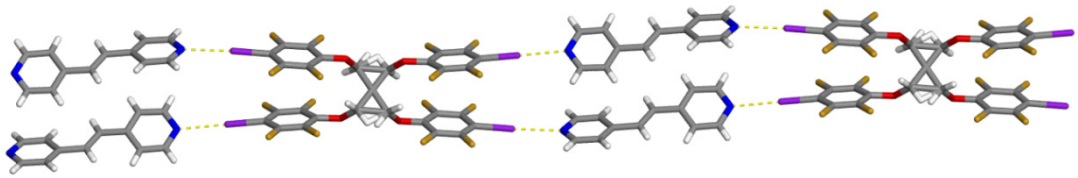

Figure 17: Halogen-bonding erythritol template employed by Metrangolo to direct the reactivity of 4,4′-bpe.

1.6.4 Coordination-Driven Self-Assembly in [2+2] Cycloadditions

Transition metal-ion complexes have been introduced as templates to direct [2+2] photoreactions in the solid state.[102] The photoreaction has been achieved in both discrete complexes and metal-organic frameworks (MOFs). MOFs are intriguing platforms to control the photodimerization owing to changes to bulk physical properties that can occur in the porous frameworks.

MacGillivray and co-workers reported the first metal complex to control a [2+2] photodimerization in a solid.[103] A Schiff-base complex involving Zn(II) ions pre-organized 4,4'-bpe into a discrete tetranuclear complex that, upon photoreaction, underwent a change in fluorescence. Two dinuclear $[Zn_2L(OH)]^{2+}$ (where: L = 2,6-bis[*N*-(2-pyridylethyl)formimidoyl]-4-methylphenol) units stacked two molecules of 4,4'-bpe into a polygon based on a rectangular geometry. The olefins were assembled parallel and

separated by 3.64 Å (Figure 18). Upon UV-irradiation, the bipyridines formed *rctt*-4,4'-tpcb in a SCSC reaction stereospecifically and in quantitative yield.

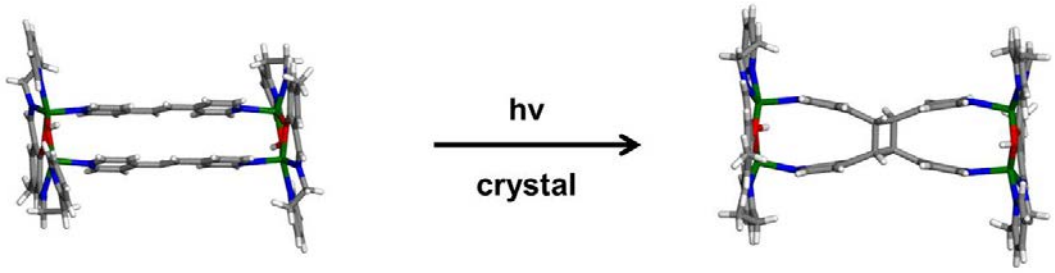

Figure 18: X-ray crystal structure of tetranuclear Zn(II) complex that directs reactivity of 4,4'-bpe to afford 4,4'-tpcb in a SCSC reaction (Zn = green).

Jin and coworkers reported the ability of rectangular tetranuclear Ir(II) and Rh(II) complexes to direct a photodimerization of 4,4'-bpe. Bridging oxalato ligands enabled two 4,4'-bpe molecules to coordinate adjacent sites, leading to the C=C bonds being parallel and separated by 3.79 Å (Figure 19).[104] UV-irradiation produced *rctt*-4,4'-tpcb in up to quantitative yield. The *rtct*-isomer was also generated in the Ir(II)-based solid. The tetranuclear assembly supported SCSC reactivity.

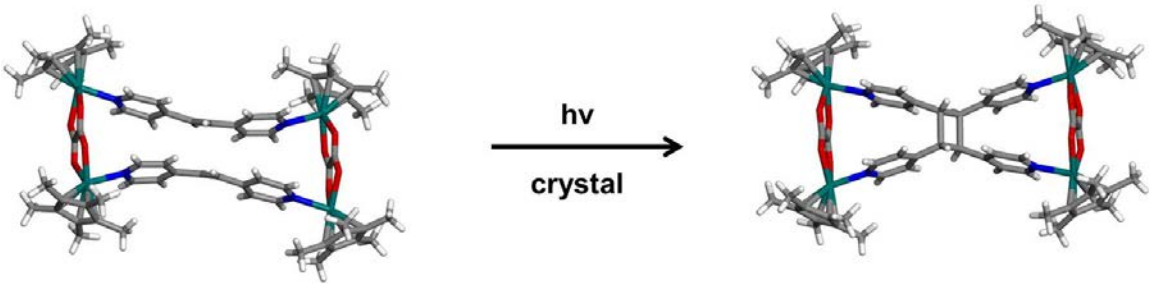

Figure 19: Controlled SCSC synthesis of 4,4'-tpcb using an iridium based macrocyclic template (Ir = turquoise).

Ag(I) ions have been used to direct [2+2] photodimerizations in solids. Argentophilic forces (i.e. Ag···Ag interactions) were exploited by MacGillivray and co-workers to assemble and stack a stilbazole (4-stilbz) for reaction. Reaction of Ag(I) trifluoroacetate with 4-stilbz produced a disilver complex that organized two pairs of 4-stilbz.[105] The Ag···Ag interaction displayed a metal-metal separation of 3.41 Å while the C=C bonds were criss-crossed and separated by 3.82 Å (Figure 20a). The corresponding head-to-head cyclobutane was generated quantitatively in a SCSC reaction. The formation of the photoproduct was ascribed to pedal-like rotation of the C=C bonds in the solid. A similar complex was subsequently used to achieve the first photodimerization of terminal olefins in a solid. Reaction of Ag(I) chlorate with 4-vinylpyridine (4-vp) afforded a disilver complex (Figure 20b) that generated *cis*-1,2-bis(4-pyridyl)cyclobutane stereospecifically and in quantitative yield.[106]

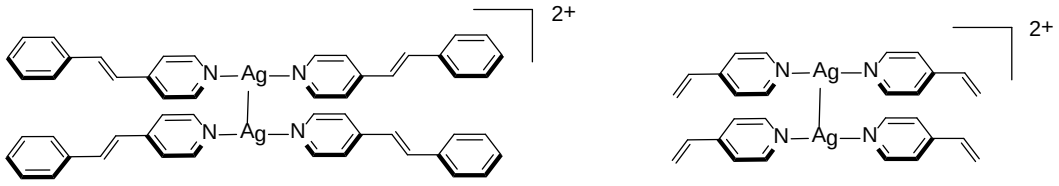

Figure 20: Schematic of Ag-based assembly of (a): with 4-stilbz and (b) with 4-vp.

The sizes and shapes of the cavities and pores of MOFs are defined by both the metals and organic bridges. Changes to the structures of the components results in changes to properties and functions of the pores. It, thus, follows that a change in structure that accompanies a [2+2] photodimerization in the solid state can be considered a means to affect the properties of MOF materials.

In this context, Michaelides and coworkers were the first to describe a photoreaction integrated into a MOF.[107] The framework was based on Cd(II) ions connected to fumarate (fum) ions that produced a rectangular grid network. The C=C

bonds were parallel and separated by 3.37 Å between adjacent layers, which enabled the olefins to react to give ctba. Although the network did not possess cavities, the study established that reactive components can be incorporated into a MOF.

In related work, Vittal and coworkers subsequently described the photoactive ladder-like coordination polymer $[Zn\{CF_3CO_2)(\mu\text{-}O_2CCH_3)\}_2(\mu\text{-}4,4'\text{-bpe})_2]_\infty$.[108] Each Zn(II) center adopted a distorted octahedral geometry, with two acetate ions bridging a pair of Zn(II) ions in $[Zn_2(\mu\text{-bpe})_2]_\infty$ with Zn···Zn distances of 3.85 Å. Each metal was chelated by a trifluoroaceate ion (Figure 21). The C=C bonds of parallel chains were separated by 3.75 Å. UV-irradiation afforded 4,4'-tpcb quantitatively *via* a SCSC transformation.

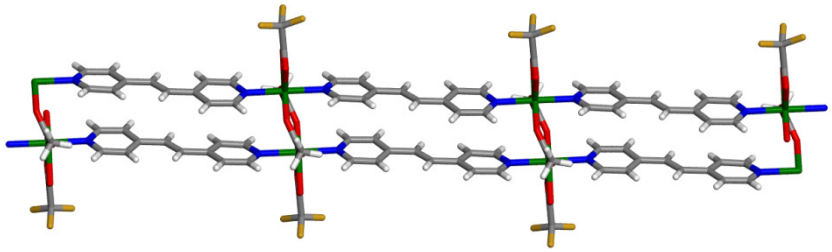

Figure 21: Representation of $[\{(CF_3CO_2)(\mu\text{-}O_2CCH_3)Zn\}_2(\mu\text{-bpe})_2]_\infty$ (Zn = green).

Following the work of Vittal, MacGillivray and coworkers described the ability of the Schiff-base complex $\{[Zn_2L(OH)(4,4'\text{-bpe})_2](ClO_4)_2\}_\infty$ to support a linear photoreactive ladder-like coordination polymer (Figure 22).[109] The metals were tetra-coordinated by L in the basal plane while the apical sites were coordinated by the bipyridines. The olefins were, thus, coordinated to neighboring dinuclear complexes, being stacked parallel and separated by 3.71 Å. UV-irradiation generated 4,4'-tpcb stereospecifically in up to 95% yield.

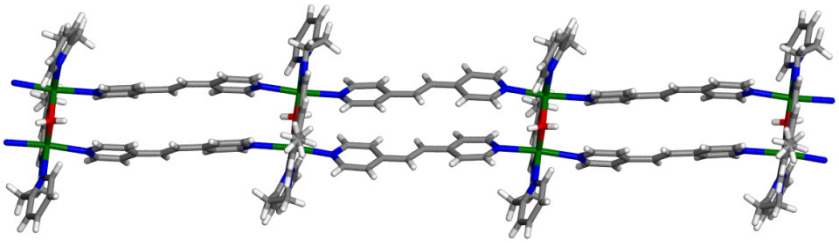

Figure 22: Crystal structure of $[Zn_2L(OH)(4,4'\text{-bpe})_2](ClO_4)2\cdot 4H_2O$ (Zn = green).

Whereas argentophilic forces supported reactive discrete complexes, Vittal and coworkers reported a [2+2] photodimerization involving the solvated 1D coordination polymer $[Ag(4,4'\text{-bpe})(H_2O)](CF_3CO_2)\cdot CH_3CN$.[110] Adjacent 1D polymers produced a 2D brickwall structure sustained by Ag···Ag forces and hydrogen bonds. Olefins of two consecutive layers were misaligned and separated at 5.15 Å. UV-irradiation, however, resulted in an unusual solid-state reorganization that led a photodimerization of the C=C bonds in up to quantitative yield. Similar observations were made by the same group involving the 1D double- and triple-stranded polymers $[Cd(4,4'\text{-bpe})(CH_3COO)_2(H_2O)]_\infty$ and $[Pb_3(4,4'\text{-bpe})_3(O_2CCF_3)_4(O_2CCH_3)_2]_\infty$ (Figure 23), respectively.[111,112] For the former, adjacent polymers exhibited C=C bonds separated on the order of 4.33 Å. A dehydration of the solid, however, afforded a photoactive material that reacted to give 4,4'-tpcb upon UV-irradiation in 100% yield. For the latter, the reaction proceeded in a two-step pathway wherein UV-irradiation followed by mortar-and-pestle grinding facilitated quantitative conversion of 4,4'-bpe to 4,4'-tpcb.

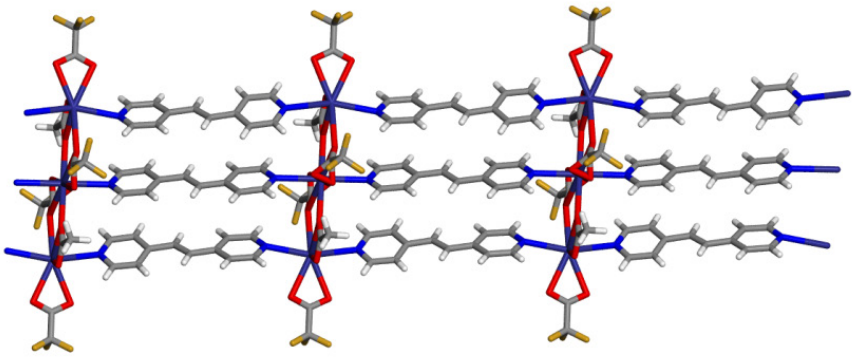

Figure 23: Representation of adjacent layers of $[Pb_3(4,4'\text{-bpe})_3(O_2CCF_3)_4(O_2CCH_3)_2]_\infty$ (Pb = indigo)

Miao and Zhu have described the integration of a [2+2] photodimerization into a 2D MOF.[113] The components of $\{[Cd_2(CH_3COO)_2(3\text{-sulfobenzoate})(4,4'\text{-bpe})_{2.5}(H_2O)]\cdot 4H_2O\}_\infty$ generated a 2D MOF with one edge based on stacked 4,4'-bpe in a ladderlike chain and the other edge being a single 4,4'-bpe linker. The 2D structures assembled into 3D networks *via* interpenetration. UV-irradiation generated 4,4'-tpcb in quantitative yield. An isostructural solid involving the photoproduct 4,4'-tpcb also formed upon reaction of the individual components.

Michaelides *et al*. reported the first photodimerization in a 3D MOF. The solid was based on reported 2D layered structure composed of Cd(II) dimers linked by fum. The 2D layers were pillared using 4,4'-bpe to give a 3D MOF with a structure that conforms to a quasi α-Po topology.[114] The fum ions, thus, were bridging ligands in a 2D grid while double columns of 4,4'-bpe ligands acted as linkers. The close proximity between pairs of Cd(II) ions assembled 4,4'-bpe parallel and separated by 3.95 Å. UV-irradiation afforded 4,4'-tpcb stereospecifically and in quantitative yield. Vittal later reported that reaction of Zn(II) ions and either fum, muconic acid (muco), or 1,4-benzene dicarboxylic acid (bdca) affords a series of interpenetrated 3D MOFs (Figure 24).[115] The MOFs involving muco and bcda reacted to generate 4,4'-tpcb *via* SCSC transformations.

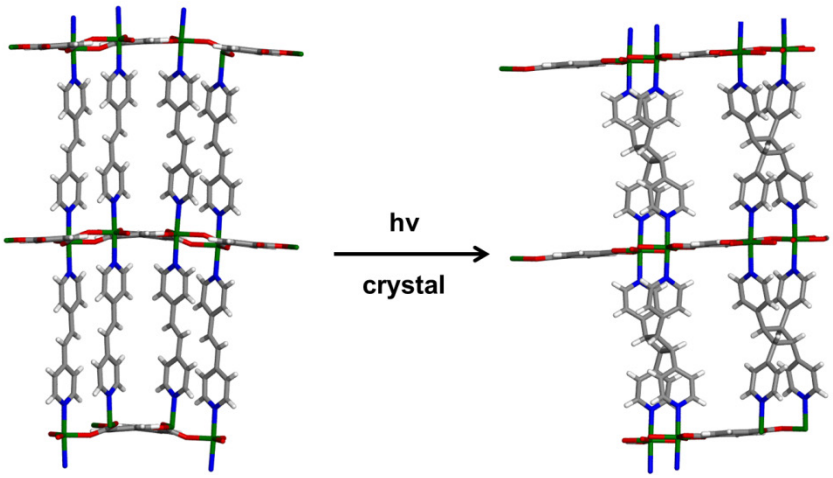

Figure 24: Perspective of a cubic net of (a) [Zn(bpe)(bdca)]·DMF before photoreaction and (b) $[Zn(tpcb)_{0.5}(bdca)]$·DMF after SCSC reaction (Zn = green).

Dienes have been assembled to react in MOFs. In particular, Eddaoudi and co-workers employed Cu(II) ions to assemble the anion of the heterocyclic diolefin chelidonic acid (cdo) for a [2+2] photodimerization (Figure 25).[116] The dicarboxylate reacted *via* a SCSC transformation to give an unusual cage-like photodimer.

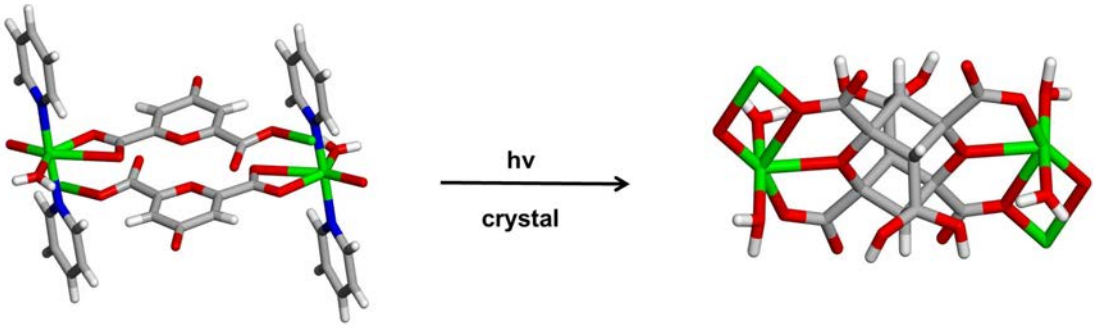

Figure 25: Solid-state photodimerization of $Cu(cdo)(py)_2(H_2O)$ (Cu = bright green).

Lang and co-workers have reported an extension of the MOF approach to the diene 1,4-bpep.[117] Hydrothermal treatment of 1,4-bpep with Zn(II) ions with 5-

sulfoisophthalic acid or 1,4-bpep with Cd(II) ions and 1,3-phenylenediacetic acid afforded the photoactive 2D and 3D MOFs $[Zn_4(\mu_3\text{-}OH)_2(5\text{-sufoisophthalate})_2(1,4\text{-bpeb})_2]_\infty$ and $[Cd_2(1,3\text{-pda})_2(1,4\text{-bpeb})_2]_\infty$, respectively. For the former, the stacked olefins were aligned offset or 'out-of-phase'. UV-irradiation of the solid produced the corresponding offset cyclobutane dimer in 100% yield. For the latter, the olefins were eclipsed or 'in-phase', with the photoreaction generating the paracyclophane tpcp (Figure 26). Both solids reacted *via* a SCSC transformation.

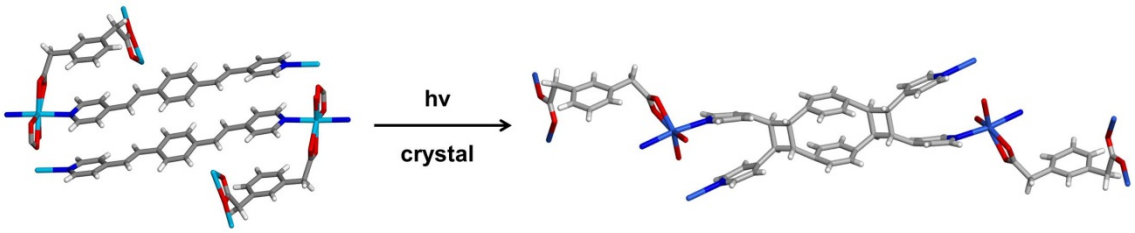

Figure 26: Photodimerization of $[Cd_2(1,3\text{-pda})_2(1,4\text{-bpeb})_2]_\infty$ generating $[Cd_2(1,3\text{-pda})_2(tpcp)]_\infty$ (Cd = aqua).

1.6.5 Mixed Hydrogen Bond and Coordination-Driven Self-Assembly in [2+2] Cycloadditions

The self-assembly process to direct [2+2] photodimerizations in the solid state has been extended to combinations of coordination and hydrogen bonds. More specifically, Hill and Briceño reported that both crystalline $[Mn(2,4\text{-bpe})_2(OH_2)_4](ClO_4)_2\cdot 2(2,4\text{-bpe})\cdot 2H_2O$ and $[Mn(2,4\text{-bpe})_2(NCS)_2(OH_2)_2]$ possess olefins organized by Mn–N coordination and O—H···N hydrogen bonds that involve coordinated H_2O molecules that conform to geometries for photoreaction (Figure 27).[118-119] UV-irradiation of both solids resulted in the regioselective formation of the head-to-tail photodimer *rctt*-2,4-tpcb. In related work, Vittal has described the ability of stacked olefins in $[Zn(4,4'\text{-bpe})_2(H_2O)_4(NO_3)_2\cdot 8/3(H_2O)\cdot 2/3(4,4'\text{-bpe})$ to undergo a photodimerization to afford 4,4'-

tpcb in 100 % yield.[120] The components formed a 1D hydrogen-bonded complex wherein the reactive olefins participated in a combination of Zn–N coordination and O—H···N hydrogen bonds that involved coordinated H_2O molecules.

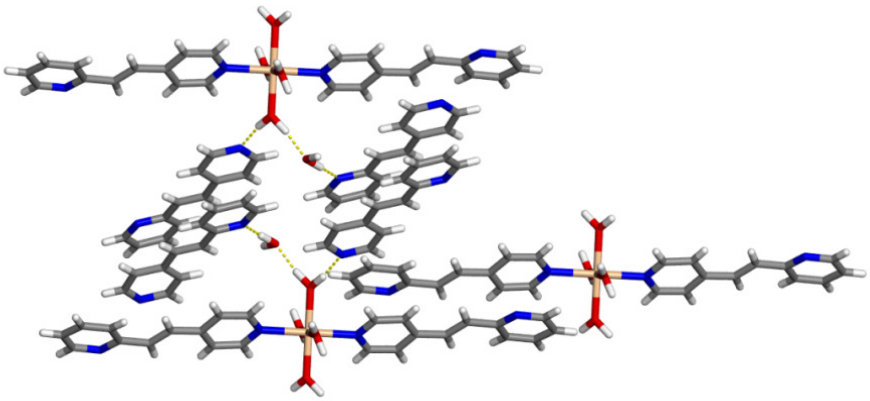

Figure 27: View of $[Mn(2,4\text{-bpe})_2(OH_2)_4](ClO_4)_2 \cdot 2(2,4\text{-bpe}) \cdot 2H_2O$ (Mn = tan).

1.6.6 Charge-Driven [2+2] Cycloadditions

In principle, hydrogen bonds involving cations and anions, as well as cation-π interactions[121] can help drive the solid-state packing such that the olefins are aligned for photoreaction. Ito originally demonstrated that cinnamic acids undergo [2+2] photodimerization in the solid state mediated by salt formation.[122] Diammonium fumarates and ammonium cinnamates displayed photoreactivity owing to strong hydrogen bonding to the cations (Figure 28). The salt formation with several amines was explored to better understand how anion identity impacts stereospecificity and product formation. In most cases, greater than 50% yield was observed, affording the head-to-head dimers with moderate to high stereoselectivity.

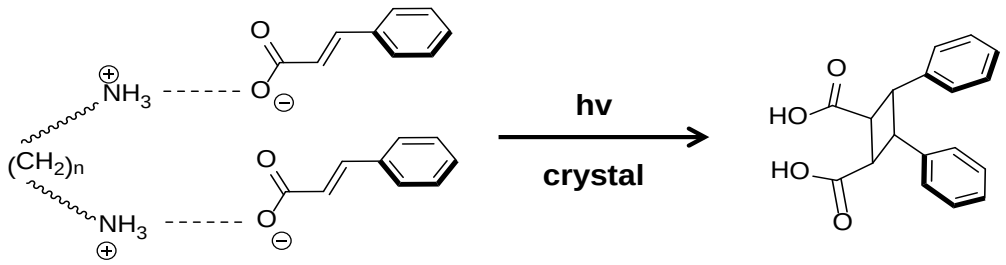

Figure 28: Solid-state [2+2] photodimerization of trans-cinnamates *via* double salt formation.

Photodimerizations with charged compounds have been studied in several styryl dyes, wherein a N-heterocycle (e.g. pyridine, benzothiazole) was alkylated to generate the salt. Gromov and coworkers have also shown that when the styryl dye contains a crown ether, stereospecific [2+2] reactions can be conducted since crown ethers normally interact with cations (Figure 29).[123] Additionally, Gromov determined that the presence of the counteranion controls the assembly process to give specific dimer complexes.

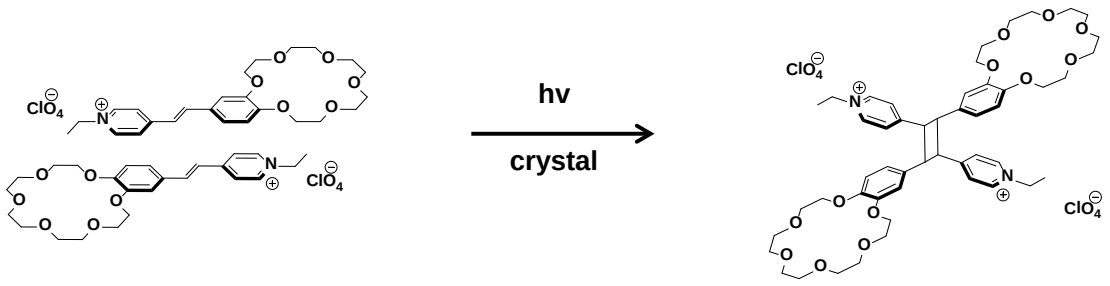

Figure 29: Solid-state [2+2]photodimerization of a stilbazole-based dye containing a 18-C-6 substituent.

Vittal and coworkers have recently shown that salts can undergo photoreactions stereospecifically, and that the stereochemistry is anion-controlled.[124] Specifically, formation of the trifluoroacetate and hydrogen sulfate salts of (E)-3-(4-pyridyl)acrylic acid (4-pa), and subsequent photoreactions generated the head-to-tail and head-to-head

dimers, respectively. In both cases, the C=C bonds were aligned within 3.7 Å. The salt formed between 4-pa and trifluoroacetic acid (tfa) crystallizes in a head-to-tail fashion (Figure 30a), whereas the salt formed between 4-pa and H_2SO_4 crystallizes in head-to-head fashion (Figure 30b). The effect of the anion is demonstrated in the (4-pa)(tfa) salt, as C—H···F hydrogen bonding interactions between the anion and pyridine ring helped control the packing. The photoreaction of this salt afforded the cyclobutane dimer quantitatively, whereas the HSO_4^- salt demonstrated a 66% yield, as every third olefin is crisscrossed within the assembly.

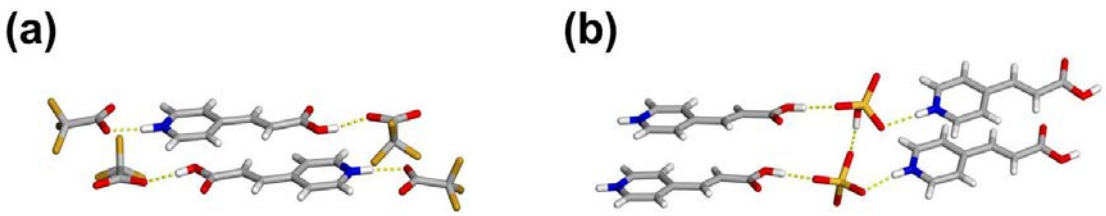

Figure 30: Anion-directed solid-state photodimerization of 4-pyridineacrylic acid.

Vittal has also demonstrated that (E)-4,4'-stilbenedicarboxylic acid, when ground with 1,3-diaminopropane, the resulting salt undergoes [2+2] photodimerization quantitatively, affording *rctt*-tetrakis-(4'-carboxyphenyl)cyclobutane after protonation of the salt dimer.[125] Cation-π interactions between pyridinium and aromatic rings have also directed reactivity in [2+2] photodimerizations. Specifically, cation-π interactions have been used to direct the photodimerization of 4-azachalcone and 4'-methoxy-4-azachalcone, as well as their respective HCl salts. In all four compounds, at least 90% of the olefin was converted to the cyclobutane. The neutral compounds did not show stereoselectivity, as all four possible dimers were obtained; however, the two salts demonstrated nearly quantitative formation of the *syn* head-to-tail product. Briceño has

also studied charge-assisted hydrogen bonds in supramolecular ionic assemblies of protonated asymmetric olefins (e.g. 2,4'-bpe, 4-hydroxy and 4-Cl stilbz) with the dicarboxylate salt of 1,2,4,5-benzenetetracarboxylic acid.[126] The salt formation heavily influences the packing as, in all cases, the head-to-tail photodimers form.

1.6.7 Substituent-Controlled [2+2] Cycloadditions

It should not go without mention that earlier studies of the [2+2] photodimerization revealed that additional supramolecular forces could be exploited to control reactivity, such that olefins are aligned in a photoreactive assembly. Hydrogen bonding has been utilized to organize J-shaped olefinic diacids into "fish hook" assemblies that preorganize C=C bonds in the solid state for photoreaction. Initial work by Feldman reported a 'J'-shaped naphthalene dicarboxylic acid to self-assemble *via* carboxylic acids to form a dimer sustained by O-H···O hydrogen bonds (Figure 31).[127] The naphthalene unit preorganized the C=C bonds parallel and separated by 3.62 Å. UV irradiation produced the corresponding cyclobutane in quantitative yield.

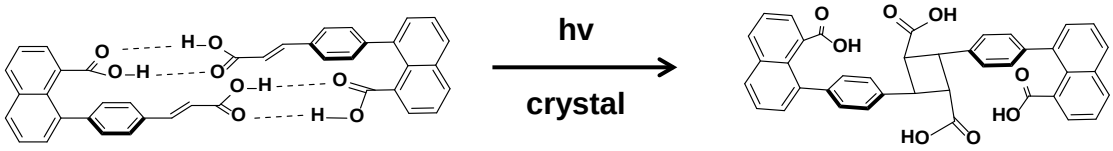

Figure 31: Photoactive assembly of a J-shaped naphthalene dicarboxylic acid.

Later, Wheeler demonstrated that chiral sulfonamidecinnamic acids self-assemble into hydrogen-bonded dimers wherein the olefins lie parallel, with C=C bonds separated by 3.68 Å.[128] The approach was expanded to cross-photoreactions that generate heterodimers. Upon UV irradiation, the quasiracemate co-crystals underwent asymmetric photodimerizations to afford a single enantiomeric α-truxillic acid photoproduct (Figure 32).

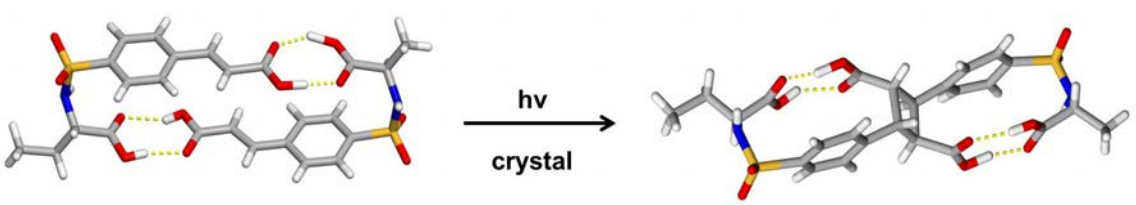

Figure 32: [2+2] Photodimerization of a sulfonamidecinammic acid quasiracemates.

In addition to hydrogen bonding, additional forces such as perfluoro-phenyl stacking[129] and π-π stacking have also displayed the ability to control solid-state packing. As demonstrated by Desiraju, engineering a crystal such that donor-acceptor interactions are present also can afford a photoreactive assembly through charge-transfer.[130] Although the utility of multiple inter- and intramolecular forces has been shown to direct reactivity, olefins that do not rely on auxiliaries to lock the C=C bonds in place show limited control over solid-state packing, and thus, insufficient control over product formation and stereochemistry. Despite a lack of reliable control, non-templated [2+2] photodimerizations still have demonstrated interesting results and have provided a better understanding of supramolecular interactions and how they can be manipulated for applications.

1.6.8 Applications and Properties of Products

The products of a template-driven [2+2] photodimerization are studded with, in the minimal case, two hydrogen bond accepting groups, such as pyridyl or carboxylic acid moieties.[77,81] The products are generally formed in quantitative yields, and gram amounts can be produced with relative ease and without byproducts. These combined features warranted the utilization of the photoproducts as attractive ligands in coordination-driven self-assembly. In particular, the pyridine-based photoproducts synthesized in our studies could serve as ditopic or polytopic organic linkers in metal-

organic frameworks (MOFs) or other such materials. Whereas the utilization of molecules synthesized in the liquid phase to materials science has been invariably studied, importantly, the application of solid-state products to materials science is largely undeveloped. This can be attributed to difficulties associated with engineering target architectures within the solid state, as well as the limited utility of [2+2] cycloadditions reactions.

1.6.8.1 Applications: Metal-Organic Frameworks

The major driving force behind the utilization of photoproducts as MOF ligands spawns from the potential to generate materials with tailored magnetic, electronic, semiconducting, and/or optical properties[131] akin to that of zeolites and mesoporous materials.[132] MOFs typically consist of metal ions that form vertices of a porous framework and organic linkers that form struts. An advantage of MOFs is an easily-modifiable synthesis to control pore connectivities, topologies, and dimensions by varying the ligands, metals, and/or counterions. Thus, MOFs are expected to have applications in areas such as gas storage, separations, and catalysis.

Upon template-directed synthesis of 2,2′-tpcb, subsequent treatment with $CuSO_4 \cdot 5H_2O$ generated a 1D MOF of the formulation $[Cu_2(\mu\text{-}2,2'\text{-tpcb})(H_2O)_2]_\infty$, wherein 2,2′-tpcb served as a bis-chelating ligand (Figure 33).[133] A square pyramidal coordination environment was exhibited by each Cu(II) ion, with two of the pyridyl N-atoms and two O-atoms (one from a sulfate ion and one from a water molecule) in the basal plane, and an O-atom of a second sulfate ion occupying the apical site. The polymer assembles in both offset and parallel strands, with the interstitial space occupied by water molecules. It was demonstrated that the self-assembly process is sensitive to changes in counterion, as the 1D MOF generated using 2,2'-tpcp and $Cu(NO_3) \cdot 2.5H_2O$ exhibits an octahedral coordination sphere consisting of the bi-chelating 2,2'-tpcb and two chelating nitrate ions.

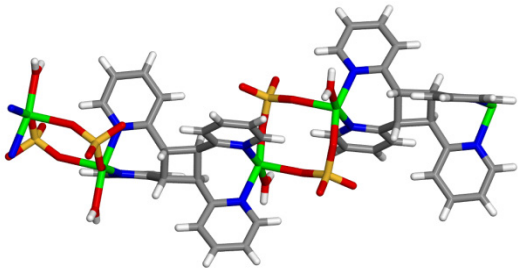

Figure 33: 1D polymer $[Cu_2(\mu_2\text{-}SO_4)_2(\mu\text{-}2,2'\text{-tpcb})(H_2O)_2]_\infty$ (Cu = bright green).

Incorporation of 4,4′-tpcb as an organic linker resulted in the generation of a porous 2D MOF. In particular, treatment of 4,4′-tpcb with the Cu-paddle wheel complex $[Cu_2(O_2CCH_3)_4(H_2O)_2]$ afforded the 2D MOF $[Cu_4(O_2CCH_3)_8(4,4'\text{-tpcb})]_\infty$.[134] The complex resulted in the production of a 2D grid with identical rhombic cavities (*ca*. 17.2 Å × 17.2 Å). The stacking of 2D grids afforded a 3D framework with isolated 1D channels (*ca*. 10 Å × 12 Å) that were occupied by benzene molecules that assembled in a herringbone manner. In a different report, it was demonstrated that treatment of 4,4′-tpcb with $[Co(O_2CCH_3)_2(H_2O)_4]$ also afforded a 2D MOF of the composition $[Co_4(O_2CCH_3)_2(4,4'\text{-tpcb})]_\infty$ (Figure 34).[135] Similar to 2D MOF $[Cu_4(O_2CCH_3)_8(4,4'\text{-tpcb})]_\infty$, the Co-based framework possessed rhombic cavities with edge lengths of 7.3 Å. In contrast to the Cu-based MOF, the framework exhibited two different rhombic cavities.

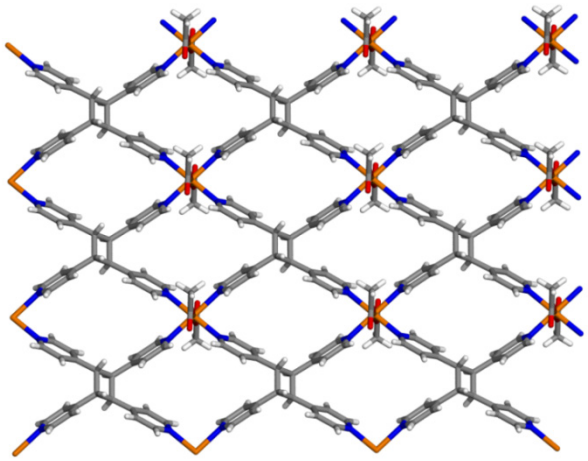

Figure 34: Perspective view of $[Co(O_2CCH_3)_2(4,4'\text{-tpcb})]_\infty$ that illustrates the different cavities of the 2D MOF (Co = orange).

In addition to tpcb-based MOFs, we have demonstrated that the [2.2]paracyclophane tpcp forms a 2D MOF with a topology that conforms to a nonregular net upon treatment with $Co(O_2CCH_3)_2 \cdot 4H_2O$.[136] The topology of the grid was unusual in that the network was based on a combination of 3- and 4-connected 'nodes' wherein two 3-connected nodes were covalently fused *via* tpcp (Figure 35). As a result of the assembly process, the 2D grid contained both rhombic and hexagonal cavities, each of which hosted different solvent molecules as guests. Specifically, a methanol molecule filled hydrophilic square cavities, while toluene molecules filled hydrophobic hexagon cavities. By effectively serving as two 3-connected nodes, tpcp provided a unique means to 'code' the design and formation of a MOF structure.

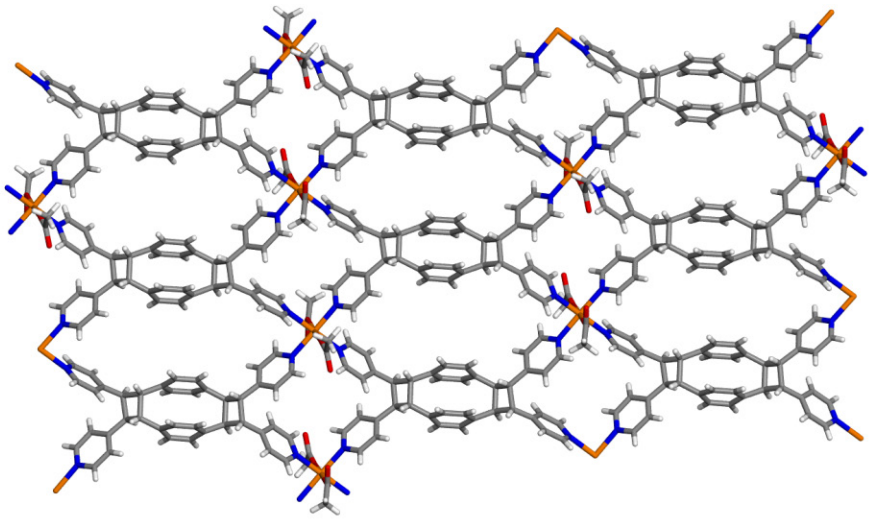

Figure 35: Perspective view of $[Co(O_2CCH_3)_2(4,4'\text{-tpcp})]_\infty$ (Co = orange).

1.6.8.2 SCSC-Controlled Properties

In a single-crystal to single-crystal reaction,[137] the structural integrity of the crystal is maintained throughout the course of reaction. In contrast, the intrinsic properties (e.g. optical, electrical, mechanical) of the crystal can change continually as the reaction proceeds, making the phenomenon attractive for materials-based applications, such as data storage and photoswitches.[138] Despite the significance of SCSC reactions in materials science, there remains a lack of knowledge regarding the design of materials that exhibit such reactivity. Consequently, most SCSC reactions are recognized by discovery rather than design.

Recently, we have demonstrated that SCSC reactivity may be attained in nano co-crystal systems even in cases where the macro co-crystals do not display this phenomenon.[139] The potential to induce SCSC reactions upon size reduction of reactive co-crystal systems can lead to several new possibilities in the development of functional materials and devices. In addition, the crystals can exhibit further size-dependent properties (e.g. optical, mechanical) that sharply contrast those of macroscopic co-

crystals. The ability to induce SCSC reactivity within nano co-crystals can likely be attributed to an increased surface area-to-volume ratio that leads to a more efficient stress and strain relaxation mechanism that may not be present in larger crystals.

1.6.8.2.1 Photocontrolled Fluorescence

During the course of our studies involving the tetranuclear $[Zn_4\mathbf{L}(OH)_2(4,4'\text{-bpe})_2](ClO_4)_2$, (where: L = 2,6-bis[*N*-(2-pyridylethyl)formimidoyl]-4-methylphenol) we determined that the photoreaction proceeded *via* a SCSC transformation that was accompanied by a significant change in fluorescence.[103] Specifically, excitation of the crystals using 290 nm light prior to the photoreaction produced a blue emission at 464 nm, while the fully reacted solid produced a green emission at 520 nm. Laser scanning confocal microscopy revealed that a consistent difference in fluorescence of the reactants and products *via* comparison of the ratios of fluorescence at 480 and 510 nm at different depths in each crystalline solid (Figure 36).

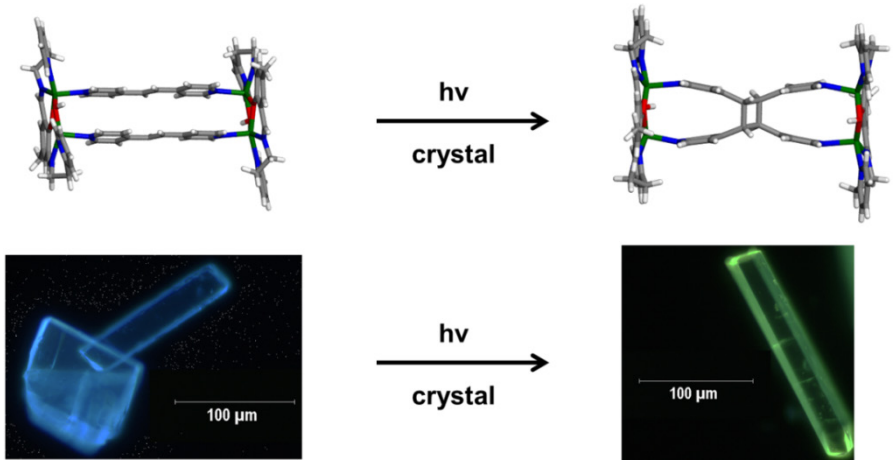

Figure 36: Photocontrolled fluorescence in single-crystalline $[Zn_4L_2(OH)_2(4,4'\text{-tpcb})](ClO_4)_4\cdot 4H_2O$ (Zn = green).

1.6.8.2.2 Size and Photocontrolled Softening or Hardening

During our studies of co-crystals that undergo SCSC transformations, we observed that the co-crystal system 2(5-CN res)·2(4,4′-bpe) underwent a size-dependent softening or hardening upon conversion to the cyclobutane product (Figure 37).[140] Whereas the millimeter sized co-crystals formed *via* slow solvent evaporation, the nano co-crystals were grown using sonochemistry-assisted reprecipitation methods. Atomic Force Microscopy (AFM) was utilized to quantify the change in relative stiffness of both millimeter and nanometer-sized co-crystals. Specifically, AFM nanoindentation analysis revealed that unreacted single co-crystals of millimeter dimensions are not only extremely soft, but become 40% softer after photodimerization. The reactant nanodimensional co-crystals undergo an 85% increase in stiffness upon size-reduction and become 40% harder following the photoreaction. The remarkable changes in the mechanical properties are accompanied by a < 0.1 % change in density, which can be attributed to the close spatial arrangement of the reactants and minimal movement that occurs during the single-crystal transformation.

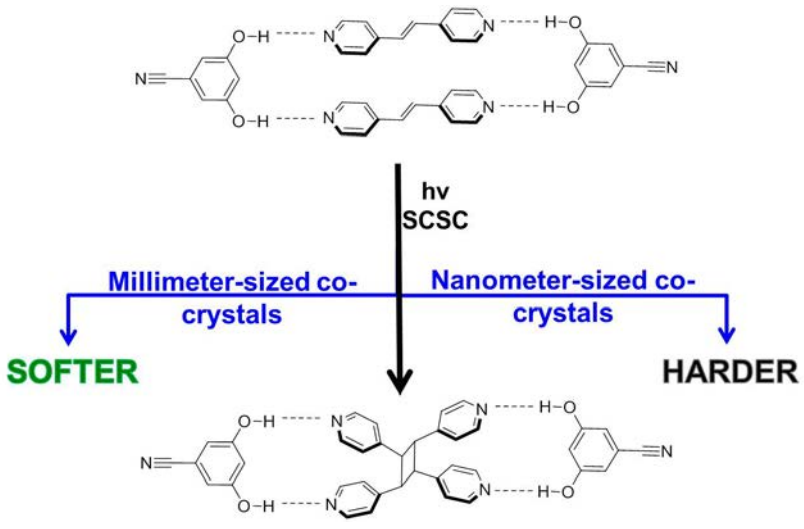

Figure 37: Size-dependent softening and hardening of co-crystals in a SCSC reaction.

1.7 Pharmaceutical Co-Crystals

The lack of essential physicochemical properties for drug candidates (e.g. solubility, bioavailability, stability) represents a serious problem in drug formulation and product manufacturing.[141] In an effort to circumvent undesirable properties and/or stability issues, potential drugs are subjected to intensive screening processes to identify salts and polymorphs with improved physicochemical properties.[142] Yet, such approaches are somewhat limited in their scope, since, salt screening can only be performed on APIs containing readily ionizable functional groups. Polymorph formation also exhibits serious limitations, since it is very much a serendipitous event that is not only unpredictable, but lacks a true design approach.[143] Polymorphs are also prone to undergo phase transitions that can be accompanied by undesirable physiochemical property changes. With such limitations in mind, the pharmaceutical industry has turned to crystal engineering, and in particular, co-crystallization as a means to design and synthesize new and robust solids not limited to APIs with ionizable functionalities.

Over the past 10 years, pharmaceutical co-crystals have emerged as a viable means to tailor the physiochemical properties of an active pharmaceutical ingredient (API).[78] Whereas crystalline forms of APIs have generally been limited to polymorphs, salts, hydrates, and solvates, the richness of functional groups within a target API suggests that such drugs would be amenable to the formation of co-crystals sustained using multiple synthons.[144] In addition, APIs represent a great opportunity to study synthon hierarchies.

Recent studies have demonstrated that co-crystallization of APIs can, indeed, form robust solid forms that exhibit physiochemical properties that are superior to that of the parent API. In particular, solubility, bioavailability, hygroscopicity, and mechanical properties of APIs have all been improved upon utilization of a co-crystallization approach.[78]

1.7.1 Co-crystal Screening Techniques

For a successful application of co-crystal strategies to the development of new pharmaceutical agent (PA)-based solids, suitable co-crystal formers must be identified quickly and efficiently. In particular, techniques reminiscent of a dynamic combinatorial approach, wherein one can screen several different potential co-formers simultaneously, would be essential to improve efficiency within a pharmaceutical environment. Currently two widely used practical techniques for screening constitute solid-state and/or liquid assisted grinding,[145] as well as a slurry-based technique founded upon physical stability.[146]

1.7.1.1 Co-crystal Screening *via* Mechanochemistry

The simultaneous engineering of several novel solid forms of a given PA is essential in drug formulation, as it provides a greater probability of designing a form that exhibits enhanced and/or optimal physiochemical properties. In this context, mechanochemistry has emerged as one of the most widely-utilized methods to form pharmaceutical co-crystals.[147] The popularity of this technique is founded upon the ease in which it can be conducted, as well as the high success rate using both 'neat' and 'liquid-assisted' methods. Mechanochemistry, and in particular, ball milling, has been shown to yield co-crystals in very short periods of time, and in near-quantitative yields.[148] The short reaction times and efficiency associated with the method is highly essential considering the functional group diversity of a given PA and correspondingly, the vast number of pharmaceutically-acceptable co-formers that can yield co-crystals of both clinical and commercial relevance.

1.7.1.2 Co-crystal Screening *via* Solution-Mediated Phase Transformation (SMPT)[146]

Recently, a suspension/slurry-based screening technique designed to engineer co-crystals was described by Zhang, and applied to efficiently generate pharmaceutical co-

crystals. The slurry approach is founded upon the thermodynamic understanding of the physical stability of hydrates and solvates and extended to co-crystals with solid co-formers (Figure 38).[146] The success of the approach relies on the presupposition that a molecular complex (i.e. co-crystal) composed of a PA and a secondary component (i.e. co-crystal former, CCF) that have the same thermodynamic stability as the solid drug if the activity of co-former in the surrounding environment is at a critical value ($0 < a_{c,CCF} \leq 1$). When the critical value is exceeded, the co-crystal stability is greatest, causing it to spontaneously crystallize when given a sufficient time for nucleation, and provided co-crystal formation between the two components is possible. The same equilibrium exists between the corresponding solid co-crystal and CCF. When the activity of both components is high, co-crystal nucleation readily occurs in a slurry of the components. The subsequent conversion from a physical mixture of the components to a solid co-crystal then proceeds *via* a solution-mediated phase transformation (SMPT) process until the activity of either component reaches the critical value. The SMPT method maximizes the screening efficiency, while providing relatively facile and rapid access to a variety of multicomponent crystalline solids.

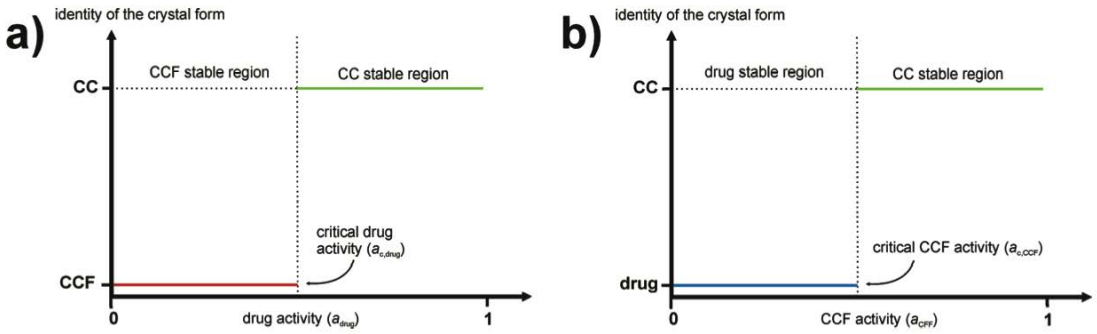

Figure 38: Phase diagrams depicting physical stability of: (a) co-crystals with respect the activity of the drug, and (b) co-crystals with respect to the activity of the co-crystal former (CCF).

1.8 Crystal Engineering at the Nanoscale

At the forefront of nanoscience lies the development of inorganic materials[149] with a vast array of potential applications ranging from medicine to electronics and materials science. Currently, there is a high demand for materials that can, not only be produced efficiently and quickly, but have enhanced physical properties (e.g. flexibility, optics, conductivity), thus prompting the development of nanomaterials.[150] However, the expense associated with the production of inorganic or metal-based materials has, at times, overridden the demand for such materials, and has instead spurred the development of more cost-effective targets. Notably, organic targets possess desirable properties that are different in comparison to inorganic or polymer-based materials.[151] The incorporation of organic molecules into the nanorealm over the past 15 years has been facile with the continued development of the reprecipitation method to facilitate the production of nano- and microcrystals with mild conditions.

Recent studies have demonstrated that organic nanocrystals of small molecules (e.g. perylene, β-carotene) exhibit different optical properties in comparison to dilute solution, and generally demonstrate a size-dependent absorption and emission.[152] While investigating size-dependent luminescence of nanocrystals, Park and others observed an enhanced emission for nanoparticles in comparison to dilute solution,[153] which was thought to be somewhat unusual since organic molecules tend to have a quenched fluorescence in the solid state.[154] The phenomenon, however, is well-known in polymers, and initially reported in poly(*p*-phenyleneethylenes) studied by Swager.[155] It is generally the case that when polymer chains aggregate, undesirable side effects occur that lead to fluorescence quenching within materials. To circumvent this issue and become capable of exploiting the emissive properties of polymeric architectures, one must exert some control over the solid-state structure. During the course of studying poly(*p*-phenyleneethylenes), Swager noted that spin-cast thin films exhibited an aggregated phase that corresponded to a higher quantum yield.[155] In the few years that followed,

other conjugated polymers studied by Garcia-Garibay,[156] Jones,[157] and Tang[158] have demonstrated similar and consistent solid-state behavior.

In light of this phenomenon, since termed 'aggregation-induced enhanced emission' (AIEE),[159] the behavior of small molecule organic nanoparticles has been more thoroughly understood. Conjugated organic molecules, like polymers, are known to self-quench in the solid state, owing to an aggregation motif that facilitates nonradiative decay, and thus, the polymers lack an appreciable emission. Specifically, a pi-pi stacked, or face-to-face motif is known to accelerate quenching and lead to blue-shifted absorbances and/or emissions that are typical of H-aggregates.[160] In contrast, a herringbone, or edge-to-face packing motif promotes a higher intensity fluorescence, owing to a J-type aggregation.[161] Although organic nanocrystals are still in their infancy, the potential to tune the optical properties in lieu of covalent modification could result in their incorporation into more optoelectronic devices.

1.9 Dissertation Scope and Overview

The foundation of the work presented in this dissertation lies in the ability to manipulate highly directional noncovalent forces (e.g. hydrogen bonding, metal coordination) to achieve the formation of desired supramolecular architectures. The engineering of such structures relies upon the comprehension of supramolecular synthons, and in particular, synthon hierarchy in complex multifunctional groups, such as pharmaceutical agents (PAs). After fully comprehending how a molecule interacts in the presence of different functionalities within the organic solid state, one can move to design architectures that have different solid-state behavior and/or physiochemical properties. Such a design can also lead to functional materials, prepared within hydrogen bonding frameworks that are deemed synthetically inaccessible *via* conventional organic synthesis. *Accordingly, so too flows this dissertation.*

In chapter 2, sulfa drug-based PAs are analyzed in the context of multicomponent supramolecular complexes.[162-163] Although the prevalence of sulfonamides and sulfoxides in drug delivery and development compounds is quite high, the ways in which they interact in the solid state in the presence of other hydrogen-bonding components remain largely unexplored. Through studies with sulfadiazine and pyridine-based co-formers, we have not only reported the first co-crystals and salts of sulfadiazine,[162] but we have, perhaps more importantly, uncovered a role of tautomers in the salt – co-crystal continuum. In the context of sulfonamide geometry, effectively *all of the S–N lengths of the imidine – or higher energy and more polar tautomer – sit in between the S–N lengths of salts and the amidine tautomer*.[162] To our knowledge, such a structural relationship of tautomers as related to the salt – co-crystal boundary has not been reported. In the second portion of the chapter, we also examine the sulfa drug Sulfamethazine (SMT),[163] which is known to form multicomponent complexes with the imidine tautomer.

In chapter 3, a well-studied PA, ibuprofen, is utilized to form co-crystals with pyridine-based co-formers. Previous studies have established the reliability of the robust O—H···N supramolecular synthon. In this chapter, the focus is placed on understanding the effect of co-crystallization on the solid-state behavior of a chiral PA. In particular, we demonstrate that the well-known racemate-forming system, ibuprofen, can be exploited, so as to achieve the formation of solid solution and conglomerate systems.[164] Solid-solution systems are extremely rare, and thus, not well studied; however, conglomerate systems can ultimately result in chiral resolution, since the end result is enantiopure crystals. Understanding the interplay between solid-state structure and emergent properties of chiral PAs is essential to provide novel opportunities for chiral resolution.

In chapter 4, the focus is placed on exploiting directional noncovalent forces to confer reactivity upon a photostable compound. In this chapter, we introduce an additional challenge into the self-assembly and reaction process. In particular, the aim is

to produce heteropolytopic ligands that comprise both pyridine and carboxylic acid functionalities *via* a template-directed [2+2] photodimerization. Owing to the sensitivity of the molecular recognition process towards additional hydrogen bond motifs, we have introduced a protecting group strategy that affords 'supramolecular regiochemistry' throughout our combinatorial template-directed approach.[165]

In chapter 5, the focus is placed on how to control reactivity in the presence of steric complexity proximal to the olefinic center. Specifically, we pursued the photodimerization of trisubstituted conformationally-frustrated olefins.[166] We demonstrate the advantage to having both organic and metal-based templates to direct the reactivity of three isomeric trisubstituted olefins. To our knowledge, the [2+2] photodimerization of this series of trisubstituted olefins are the first by design.

In chapter 6, the focus is placed upon the optoelectronic properties of a series of products obtained *via* our template-directed approach.[167] In particular, we examine a series of [2.2]cyclophanes afforded in the solid state[168] in the context of absorbance and fluorescence properties. Cyclophanes are well-studied hydrocarbon architectures that exhibit intriguing properties in light of their structural simplicity, owing to their face-to-face stacked nature. Although they are visually simplistic, cyclophanes themselves are hard to synthesize *via* traditional organic approaches. We have synthesized a series of [2.2]cyclophanes using our template-directed approach, and are able to achieve the syntheses in quantitative yields.[167] The synthesis and approach will be reviewed in chapter 6, however, the focus is placed upon the properties the molecules exhibit. In particular, in wake of having chromophores being connected *via* saturated cyclobutyl bridges, the cyclophanes demonstrate non-conventional internal charge transfer (ICT) indicative of interchromophore communication through the saturated bridges.[169] We also show that, through simple post-synthetic modification of the distal pyridines, each cyclophane exhibits a red-shifted absorbance and emission.[169] Additionally, through the use of sonochemistry, we have produced nanocrystals of [2.2]cyclophanes that

demonstrate unique properties in comparison to the macromolecular counterparts.[171] We believe that the coalescence of nanotechnology and cyclophane chemistry can lead to interesting methods to fine-tune optical properties of small organic molecules in lieu of covalent modification.

Chapter 7 represents the author's attempts to incorporate several aspects of the previous chapters into one conceptual goal: the solid-state synthesis of unsymmetrical paracyclophanes.[170] In particular, it was envisaged that unsymmetrical cyclophanes could be produced in the solid state, perhaps aided by well-established pedal motion[165] within a stilbene framework. In addition, utilization of terminal ester groups[170] would allow for deprotection to a diacid framework that is expected to demonstrate different optical properties, as well as lend itself to post-synthetic modification processes, and the possibility of providing an organic ligand for metal-organic frameworks that can exhibit unique properties.

Altogether, the research described in this dissertation details the use of crystal engineering and supramolecular synthon hierarchies to achieve the formation of target architectures. The resulting frameworks differ in topology, dimensionality, connectivity, and emergent solid-state and/or physiochemical properties. An additional underlying focus is established in that each project within this dissertation assesses a common covalent chemistry theme from a supramolecular solid-state perspective. It is the intent of the author of this dissertation to present the research with an eye to leave readers of all areas, and in particular, traditional synthetic chemists, intrigued by the many facets of supramolecular chemistry.

CHAPTER 2. CRYSTAL ENGINEERING OF SULFA DRUGS

A portion of this chapter was published as a full paper in *Crystal Growth and Design* and is adapted with permission from [E. Elacqua, D.-K. Bučar, R. F. Henry, G. G. Z. Zhang, L. R. MacGillivray, *Cryst. Growth Des.* **2013**. (DOI: 10.1021/cg301745x)].

2.1 Introduction

The design of multicomponent pharmaceutical crystalline materials is based on reliable noncovalent interactions in the form of supramolecular synthons.[12, 172] The development of synthon hierarchies[173] is achieved *via* extensive co-crystallization[78, 84, 174] studies of a model pharmaceutical agent (PA) with a structurally-analogous group of co-formers that can participate in specific hydrogen bonding motifs. Caffeine[175] and carbamazepine (CBZ)[176] have been utilized as prototypical PAs to identify robust supramolecular synthons based on (amide) N—H···O=C (carboxy), (acid) O—H···O=C (carboxy), (acid) O—H···N (imidazole) and (phenol) O—H···O=C (urea) forces in co-crystals. Whereas the number of supramolecular synthons employed in crystal engineering continues to rapidly grow, there remains a need to investigate roles of organic functionalities that can affect processes of drug discovery and development.[177]

Despite a widespread presence in pharmaceutical compounds, sulfoxides ($-SO_2$) are less studied in the context of crystal engineering.[178] Although a search of the Cambridge Structural Database (CSD) reveals that supramolecular synthons exhibit a tendency to compete in solid-state materials based on sulfonates,[179] less is known about how sulfa drugs (SDs)[180] behave in co-crystals and salts.[181] SDs are the original class of PAs with an aniline ring covalently attached to a sulfonamide moiety as a structural core. SDs were the first compounds used to systematically treat and prevent bacterial and microbial infections, thriving on synergistic effects that spawn from a mixture of at least two PAs (e.g. co-trimoxazole: 1:5 mix of sulfamethoxazole and trimethoprim).[182] Owing

to a drive by the field of pharmaceutics and the pharmaceutical industry to investigate how intermolecular interactions between drug molecules dictate therapeutic efficacy, novel solid forms of SDs merit consideration to develop pharmaceutical co-crystals.[183]

2.2 Sulfadiazine (SDZ) as a Model PA

To efficiently generate multicomponent pharmaceutical solids, it is of fundamental importance to analyze a target PA, evaluate how the molecule interacts in the solid state, and identify dominant supramolecular synthons. In this context, the SD sulfadiazine (SDZ) possesses both hydrogen bond donor and acceptor groups. SDZ self-assembles *via* a self-complementary (amidine) N—H···N (pyrimidine) synthon, generating dimers that interact *via* secondary (aniline) N—H···O_2S (sulfoxide) forces (Figure 39).[184] Such two-point interactions are well-documented in the field of molecular recognition.[185] To date, multicomponent complexes of SDZ have not been reported, likely owing to a markedly low solubility in common organic solvents compared to other SDs. To achieve multicomponent solids based on SDZ, the use of a co-former with stronger hydrogen-bond-donors and/or -acceptors that compete with the hydrogen bond accepting pyrimidine functionality would be useful to limit dimer formation.[186]

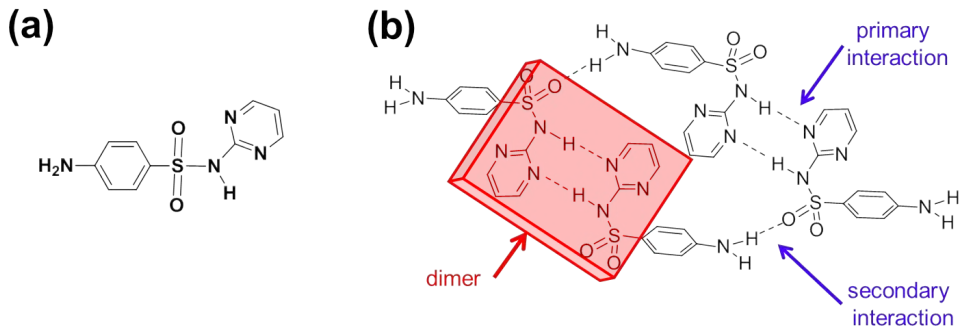

Figure 39: Schematic of (a) SDZ and (b) self-assembly involving (sulfonamide) N—H···N (pyrimidine) and (aniline) N—H···O_2S (sulfoxide) forces.

Co-crystallization strategies that aim to disrupt dimer formation and generate multicomponent solids have been reported with CBZ.[187] The goal was accomplished by introducing carboxylic acids that act as stronger hydrogen bond donors and effectively compete with CBZ dimer formation by forming (acid) O—H···O=C (amide) hydrogen bonds.[178] The work involving CBZ suggested to us that a similar strategy could be applied in the case of SDZ and pyridines (Figure 40a-b). Specifically, pyridine co-formers would provide a hydrogen bond acceptor to interact with the acidic sulfonamide (pK_a = 5.69)[188], while breaking the dimer. An investigation of the CSD reveals 35 co-crystals and 8 salts that comprise a SD.[189] Most structures contain a (sulfonamide) N—H···O=C (carboxy) or a (pyrimidinium) $^{+}$N—H···N^{-} (sulfonamide) hydrogen bond as a primary interaction between the components. Most complexes contain secondary interactions in the form of N—H···O_2S hydrogen bonds, suggesting that the sulfoxide group can be integrated into hydrogen-bonded motifs of supramolecular complexes (Figure 40c). The sulfoxide has recently emerged as a group able to readily sustain synthon formation in solids.[178c]

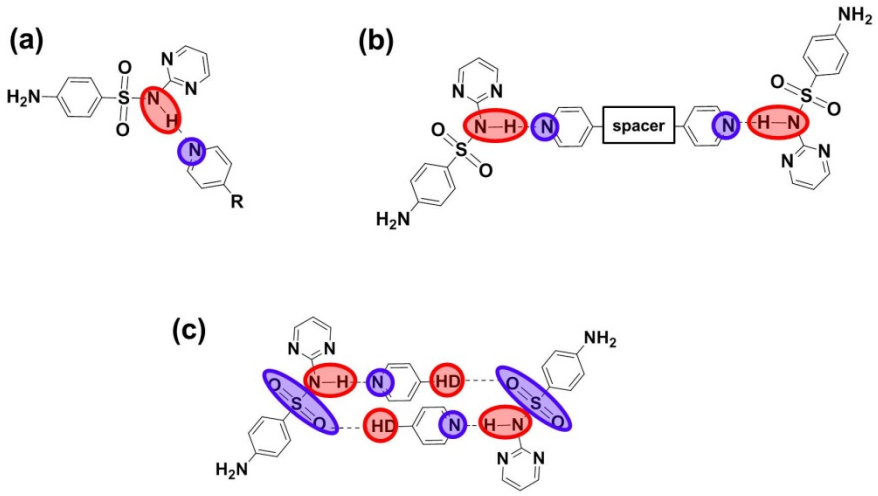

Figure 40: Approaches to multicomponent solids involving SDZ and pyridines: (a) monofunctional pyridines, (b) bifunctional pyridines, and (c) pyridines with added hydrogen bond donor (HD) groups.

In this study, we designed and constructed multicomponent crystalline solids involving SDZ and a series of mono- and bipyridines. The solids were formed using our reported co-crystal screening technique that is based on solution-mediated phase transformation (SMPT).[146] The pyridines comprise N,N-dimethyl-4-aminopyridine (dmap), 4-aminopyridine (4-ap), 4-picoline (pico), 4,4'-bipyridine (bipy), *trans*-1,2-bis(4-pyridyl)ethylene (bpe), 1,2-bis(4-pyridyl) acetylene (bpa), and 4-(pyridin-4-yl)piperazine (4-pypip) (Figure 41). We demonstrated that both co-crystals and salts form using the pyridines as co-formers, with the formation of a co-crystal or salt being related to a difference in pK_a[190] of SDZ and pyridine. We observed that the solids formed structural motifs involving dyads, rings, and chains based upon Etter's graph sets.[191] The co-formers that preserve the pyrimidine dimer, namely, bpe and bpa, were also shown to afford novel 'host-guest' solids wherein the pyridine interrupts the formation of secondary N—H···O_2S synthons.

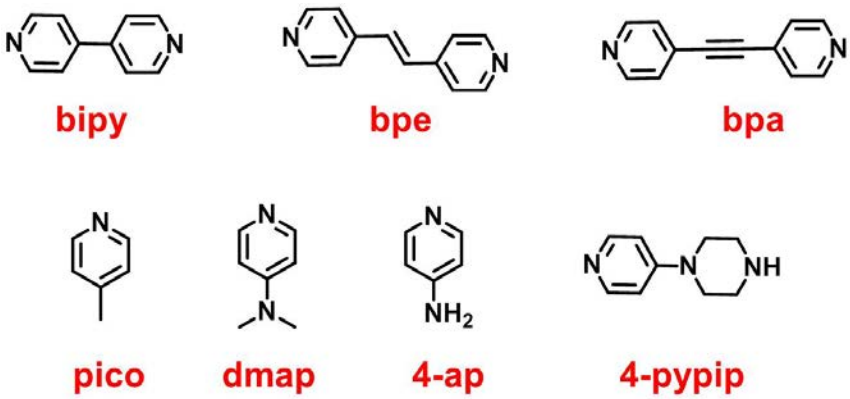

Figure 41: Chemical structures of all pyridine co-formers used with SDZ

From our efforts to investigate the co-crystal – salt continuum of complexes involving SDZ, we reveal that each solid can be classified according to the geometry of the sulfonamide moiety.[190] In particular, the structures of the co-crystals and salts are

classified according to the ΔpK_a of the components. Moreover, an analysis of our structural data along with data from the CSD reveals a trend between S–N bond length and nature of complex formed, with longer and shorter S–N bond lengths being present in neutral and anionic SDs, respectively. Whereas effects of proton transfer on C-O bond length has been established in RCO_2H/RCO_2^- systems,[191] an analysis of S–N bond geometry as related to the formation of co-crystals and salts has not been reported.

In our analysis of the X-ray data involving SDs, we have also discovered tautomers to occupy a previously unaddressed position within the co-crystal – salt continuum. Tautomers are constitutional isomers that rapidly interconvert by a chemical reaction between two or more forms.[192] A tautomeric form of a molecule can, in principle, be either neutral or charged (i.e. cation or anion). Consequently, a tautomer can serve as an integral and defining component of either a salt or co-crystal, while recent reviews suggest that a vast majority of tautomers present in the solid state exist as a neutral form.[193] Tautomers will, *de facto*, exhibit different relative energies, which will invariably affect the polarity of a molecule,[194] which can make tautomers more akin to a charged species (i.e. cation or anion). Here, we show that tautomers of SDs fall within the co-crystal regime, yet are based on geometries that lie between co-crystals and salts. We expect our identification of a role of tautomers in multicomponent solids to provide further guidelines on understanding the nature of the co-crystal – salt continuum.[190]

2.3 Experimental

SDZ (98%) and pico (98%) were purchased from Alfa Aesar (Ward Hill, MA, USA) and used without further purification. dmap (98%), 4-ap (98%), bipy (97%), and bpe (98%) were purchased from Sigma Aldrich Chemical (St. Louis, MO, USA). 4-pypip (97%) was purchased from Matrix Scientific (Columbia, SC, USA). All components were used without further purification. bpa was synthesized according to a literature procedure.[185] N,N-dimethylformamide (99.9%) was obtained from Fisher

Scientific (Pittsburgh, PA, USA). Single crystals of each solid were obtained by slow evaporation from solution. In a typical procedure, SDZ (4 mmol) and pyridine (1.0 mol. eq. for monopyridines, and 0.5 mol. eq. for bipyridines) were dissolved in DMF (5.0 - 7.0 mL) at 85 °C. Single crystals suitable for X-ray diffraction were grown upon cooling each solution to ambient temperature and then allowing the solvent to slowly evaporate. Single crystals formed within a period of approximately 10 days.

Single crystal X-ray diffraction experiments were performed on a Bruker SMART system equipped with an APEX2 CCD camera (co-formers: pico, bipy, bpe, bpa, 4-pypip), or on a Nonius Kappa CCD diffractometer (co-formers: dmap and 4-ap). Data was collected at 100 K or 293 K with graphite-monochromated MoK_α radiation (λ = 0.71073 Å). The data was collected and processed using either SaintPlus[196] (co-formers: pico, bipy, bpe, bpa, 4-pypip), or a combination of Collect[197] and HKL Scalepack/Denzo[198] (co-formers: dmap and 4-ap). All structures were solved using direct methods that generated non-hydrogen atoms. All hydrogen atoms were located in Fourier-difference electron density maps. All non-hydrogen atoms were refined anisotropically. Hydrogen atoms associated with carbon atoms were refined in geometrically constrained riding positions. Hydrogen atoms associated with nitrogen atoms were included in the located positions. Refinement was achieved with the use of SHELX-97.[199] The details of the structural analysis of all solids are summarized in Tables A-1 and A-2.

The CSD database survey was accomplished using version 5.32 (including update 5, November 2011) with ConQuest[200] (version 1.13). The CSD was searched for mono-N-substituted sulfonamides comprising a sulfanilamide substructure that satisfies the following criteria: (a) crystallographic *R* factor < 0.075, (b) not polymer structure,[201] (c) no powder structure, (d) 3D coordinates fully determined,[202] and (e) purely organic components.

The regions of S–N length and SNC angle that support salt or co-crystal formation were analyzed by calculating the mean ($\overline{X}$) and standard deviation (σ) for each variable. The calculated σ values for S–N length of each complex type were generally low in comparison to the range of observed values (S–N range = 0.089 Å; σ_{salt} = 0.007 Å (7.9%); $\sigma_{co\text{-}crystal}$ = 0.018 Å (20.2%)), the σ values for SNC angle were much larger (SNC range = 9.53°; σ_{salt} = 2.55° (26.8%); $\sigma_{co\text{-}crystal}$ = 1.83° (19.2%)). The SNC angles displayed more variation, thus, S–N lengths were used to assess salt and co-crystal regions. The boundaries for each region were depicted on the graph such that each region represented $\overline{X} \pm 2\sigma$.

2.4 Results

Seven solid forms of SDZ were obtained from the co-crystal screening[190] with the selected pyridines. The crystal structure of each solid was determined using single-crystal X-ray diffraction. Four solids were determined to be co-crystals while the remaining three solids were salts, as evidenced by proton transfer. In each SDZ solid, the sulfonamide crystallizes as either an amidine or amidide for co-crystals and salts, respectively.

(1) (SDZ)·(pico). (SDZ)·(pico) crystallizes from a neat mixture of the components in the triclinic space group $P\overline{1}$. The asymmetric unit consists of one molecule of SDZ and one molecule of pico (Figure 42a). The two components interact in a discrete assembly *via* (amidine) N—H···N (pyridine) hydrogen bonds that constitute a $D_1^1(2)$ graph set. The assembly is sustained by intermolecular (aniline) N—H···N (pyrimidine) interactions between face-to-face stacked SDZ molecules in a $R_2^2(20)$ ring. The N–H group also interacts with the SO_2 group ($d_{N\cdots O}$ = 3.34 Å),[179] however the distance is larger than cited cutoffs for significant hydrogen bonding. Additional π···π interactions between adjacent aniline rings ($d_{\pi\cdots\pi}$ = 3.23 Å) contribute to the extended packing of the solid (Figure 42b).

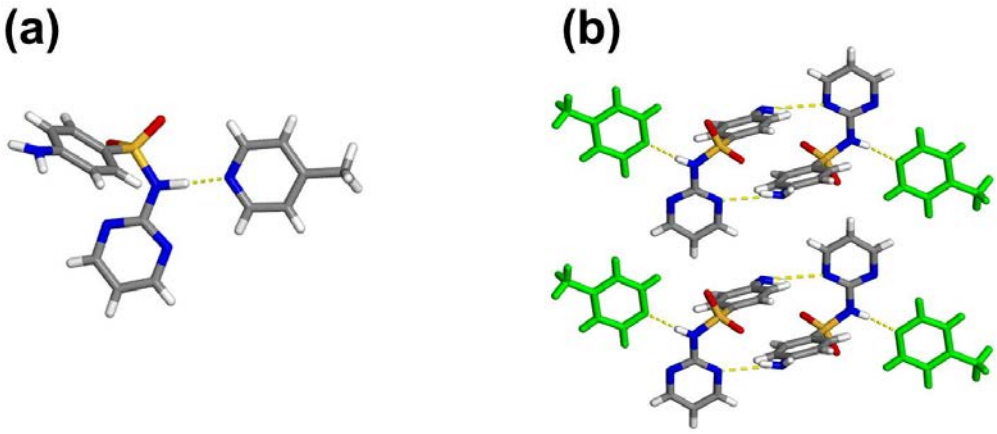

Figure 42: View of (SDZ)·(pico): (a) primary synthon and (b) extended structure highlighting (aniline) N—H···N (pyrimidine) hydrogen bonds and π···π interactions between adjacent aniline rings.

(2) 2(SDZ)·3(bipy). Co-crystallization of a 2:1 molar ratio of SDZ and bipy from DMF resulted in a co-crystal of 2:3 stoichiometry, respectively. The components crystallize in the triclinic space group $P\bar{1}$. Two molecules of SDZ and three molecules of bipy are present in the asymmetric unit. SDZ and bipy interact *via* intermolecular (amidine) N—H···N (pyridine) and (aniline) N—H···N (pyridine) hydrogen bonds. The 2:3 assembly forms a 2D polymer sustained by a combination of sulfonamide and aniline N—H···N hydrogen bonds in a $C_2^2(17)$ chain, as well as (aniline) N—H···O_2S (sulfoxide) forces based on a C(8) graph set (Figure 43). The N—H···O_2S interactions link each SDZ in the heteromolecular chain to individual (bipy)–(SDZ)–(bipy) 'bridges' that join two parallel chains, wherein each bipy participates in a single hydrogen bond with a 'free' pyridine in each unit. The free pyridines interact with the main chain aniline groups *via* C—H···N forces ($d_{C\cdots N}$ = 3.40 Å). In each molecule of bipy, the pyridines are twisted *ca*. 31-33º from co-planarity and participate in face-to-face π···π interactions ($d_{\pi\cdots\pi}$ = 3.37, 3.39, and 3.71 Å) with the stacked bipy molecules.

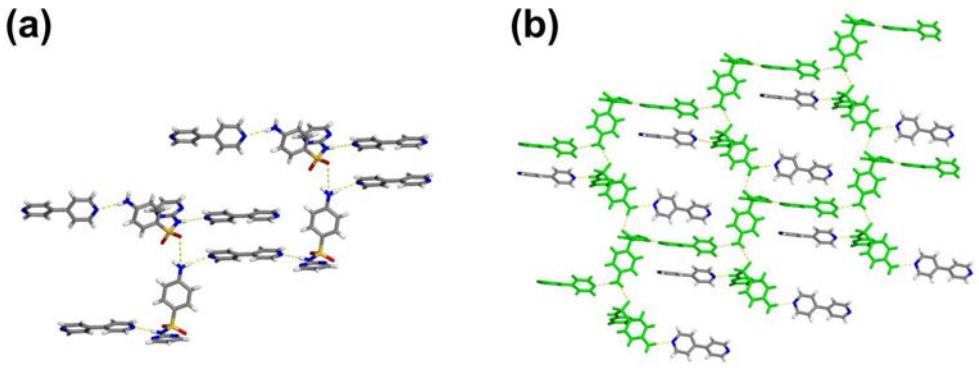

Figure 43: Views of 2(SDZ)·3(bipy) highlighting (a) hydrogen bond synthons and (b) polymer backbone.

(3) 2(SDZ)·(bpe). 2(SDZ)·(bpe) crystallizes from DMF in the triclinic space group $P\bar{1}$ with one molecule of SDZ and a ½ bpe molecule in the asymmetric unit. SDZ and bpe form a 2D hydrogen-bonded polymer. The components interact *via* intermolecular (aniline) N—H···N (pyridine) hydrogen bonds, classified as a $D_1^1(2)$ graph set (Figure 44). The sulfonamide -NH group participates in dimer formation with a second molecule of SDZ based on a $R_2^2(8)$ array of (amidine) N—H···N (pyrimidine) interactions. The NH_2 group of SDZ is involved in an intermolecular N—H···O_2S hydrogen bond. Additional π···π interactions between adjacent pyrimidine rings ($d_{\pi\cdots\pi}$ = 3.63 Å) and stacked pyridines ($d_{\pi\cdots\pi}$ = 3.43 Å) contribute to the extended structure.

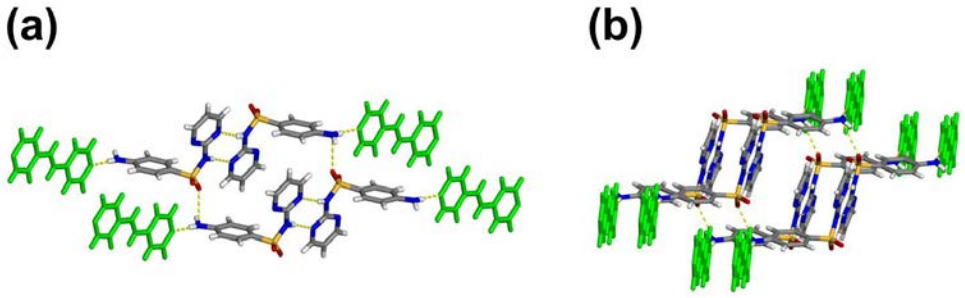

Figure 44: View of 2(SDZ)·(bpe) highlighting: (a) amidine-pyrimidine dimers and (b) π···π interactions between adjacent pyrimidine rings and pyridine co-formers.

(4) 2(SDZ)·(bpa). SDZ and bpa co-crystallize from DMF in the triclinic space group $P\bar{1}$ with one molecule of SDZ and a ½ bpa molecule in the asymmetric unit. The components form a 2D hydrogen-bonded polymer held together by (aniline) N—H···N (pyridine) hydrogen bonds. SDZ and bpa assemble similar to 2(SDZ)·(bpe), wherein adjacent SDZ molecules form hydrogen-bonded dimers *via* amidine) N—H···N (pyrimidine) forces in a $R_2^2(8)$ ring. The NH_2 group of SDZ also participates in intermolecular N—H···O_2S hydrogen bonds (Figure 45). Additional π···π interactions are present between stacked pyrimidine ($d_{\pi\cdots\pi}$ = 3.66 Å) and pyridine rings ($d_{\pi\cdots\pi}$ = 3.50 Å).

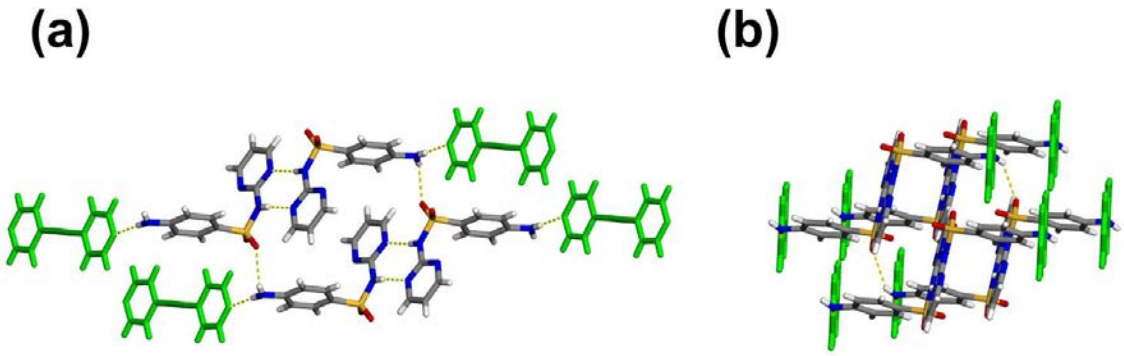

Figure 45: View of 2(SDZ)·(bpa) highlighting: (a) amidine-pyrimidine dimers and (b) π···π interactions between adjacent pyrimidine rings and pyridine co-formers.

(5) ($dmap^+$)·(SDZ^-). SDZ and dmap form a salt that crystallizes in the monoclinic space group $P2_1/n$ with one $dmap^+$ cation and one SDZ^- anion in the asymmetric unit. The components form a 2D hydrogen-bonded assembly linked *via* a primary intermolecular (pyridinium) $^+$N—H···N^- (amidide) hydrogen bond (Figure 46a). The extended structure is held together by intermolecular N—H···O_2S interactions, as well as face-to-face π···π interactions of pyrimidine rings ($d_{\pi\cdots\pi}$ = 3.29 Å) (Figure 46b).

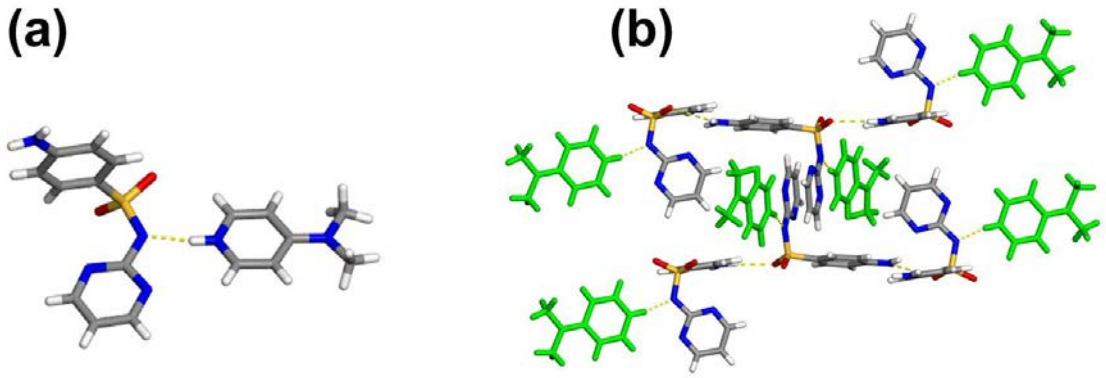

Figure 46: Views of $(dmap^{+})\cdot(SDZ^{-})$: (a) primary interaction and (b) extended structure.

(6) $(4\text{-}ap^{+})\cdot(SDZ^{-})$. SDZ and 4-ap form a salt that crystallizes from DMF in the monoclinic space group $P2_1/c$. The asymmetric unit consists of one $4\text{-}ap^{+}$ cation and one SDZ^{-} anion that assemble *via* intermolecular (pyridinium) $^{+}N—H\cdots N^{-}$ (amidide) and (amine) $N—H\cdots O_2S$ (sulfoxide) hydrogen bonds in a $R_2^2(20)$ ring (Figure 47a). The components form a 2D polymer with π···π interactions between pairs of stacked pyrimidine and pyridine rings ($d_{\pi\cdots\pi}$ = 3.80 Å) (Figure 47b).

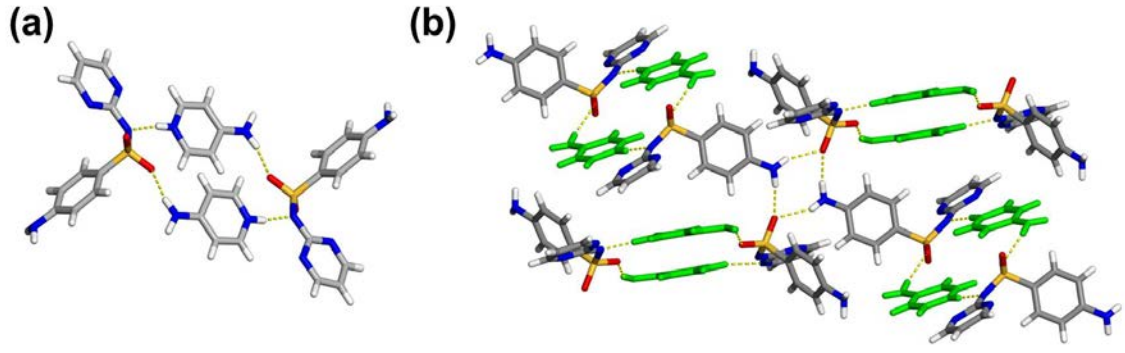

Figure 47: Views of $(4\text{-}ap^{+})\cdot(SDZ^{-})$: (a) primary interaction and (b) extended structure.

(7) (4-pypip$^+$)·(SDZ$^-$). SDZ and 4-pypip form a salt that crystallizes from DMF in the monoclinic space group $P2_1/n$. The asymmetric unit consists of one 4-pypip$^+$ cation and one SDZ$^-$ anion that self-assemble to form a 3D hydrogen-bonded polymer. Intermolecular (pyridinium) $^+$N—H···N$^-$ (amidide) and (amine) N—H···O_2S (sulfoxide) hydrogen bonds in a $C_2^2(13)$ chain, as well as (aniline) N—H···O_2S (sulfoxide) forces in a C(8) chain, form a 2D network (Figure 48). The NH_2 of SDZ$^-$ is also involved in an array of (aniline) N—H···N (pyrimidine) hydrogen bonds in a $R_2^2(20)$ graph set.

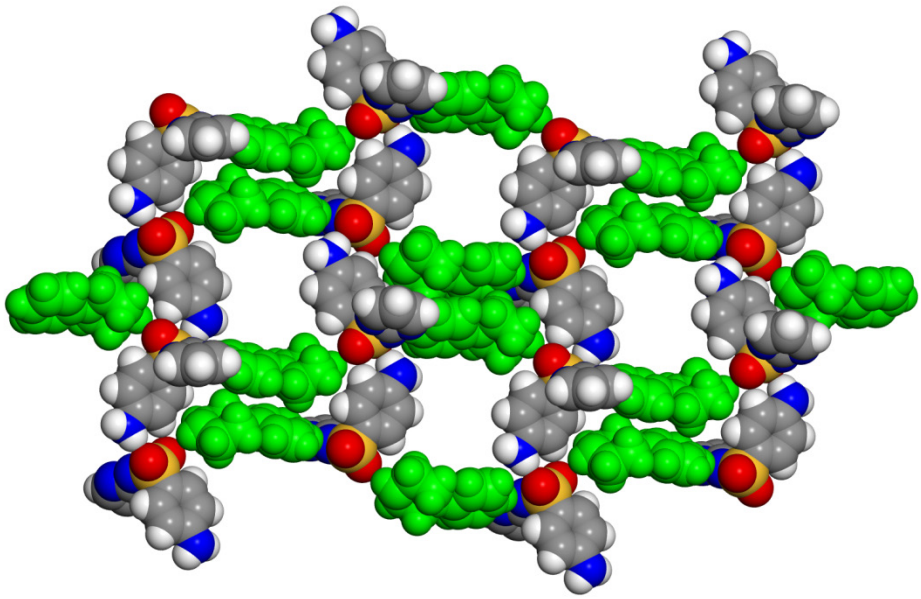

Figure 48: Space filling model of (4-pypip$^+$)·(SDZ$^-$): 2D network of $^+$N—H···N$^-$ and N—H···O_2S hydrogen bonds.

2.5 Discussion

SDZ has a mixture of hydrogen bond-donor and -acceptor groups, which make the molecule a useful target and component for crystal engineering. The -NH_2 and -NH groups are donors, whereas the -SO_2 and pyrimidine N-atoms are acceptors (Figure 49). The relative proximity of the sulfonamide -NH group to both the acceptor sulfoxide and

pyrimidine ring also makes the molecule exploitable for two-point synthon interactions. Two-point interactions in the form of (amidine) N—H···N (pyrimidine) synthons sustain the hydrogen-bonded dimer in the pure solid. Similar two-point interactions involving pyrimidines are prevalent within the field of molecular recognition and play a prominent role in biology.[203] The introduction of a co-former that can compete with dimer formation can also promote the formation of additional intermolecular forces (e.g. (amidine) N—H···O_2S (sulfoxide)). Thus, SDZ represents an attractive model SD for studies of synthon hierarchies and the generation of supramolecular complexes sustained by targeted hydrogen-bonded patterns.

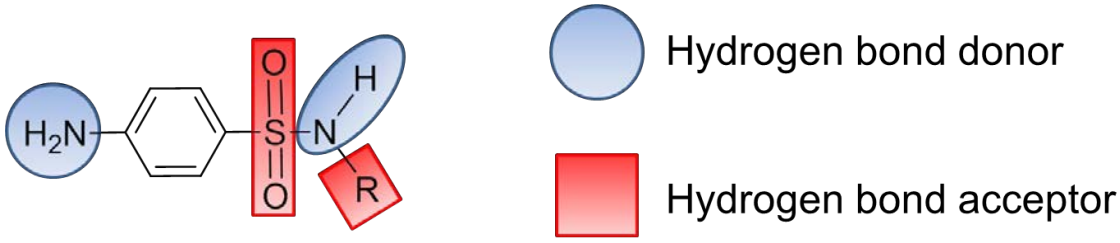

Figure 49: General schematic of a SD, viewed from a crystal engineering perspective.

2.5.1 Co-Crystals and Salts

Given that the pK_a of pyridine is larger than pyrimidine (pK_a = -1.3),[188] it was expected that the co-formers would interact with the sulfonamide and result in either neutral N—H···N interactions or proton transfer. In particular, four of the seven co-formers resulted in co-crystals while three co-formers involved proton transfer (Figure 50). Specifically, when the pK_a of the co-former exceeded 5.7, proton transfer between sulfonamide and pyridine N-atom occurred. When the pK_a was less than 5.7, co-crystal formation resulted. A division of co-crystals and salts can also be assigned using the rules regarding the ΔpK_a of components.[190] Specifically, for the co-formers, $\Delta pK_a < 0$ resulted in co-crystal formation, while $\Delta pK_a > 0$ resulted in proton transfer. Indeed,

recognizing combinations of components that exhibit both salt and co-crystal formation is important when assembling specific supramolecular architectures, as recently discussed by Aakeröy.[204]

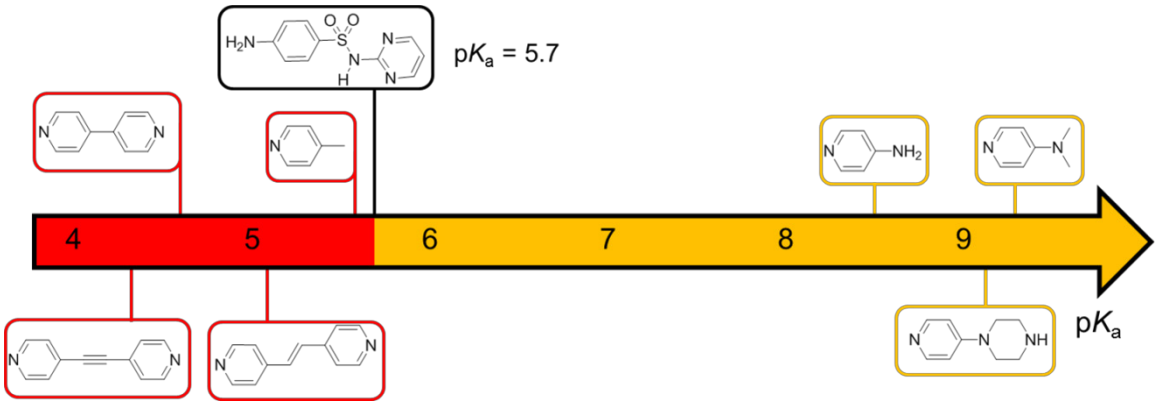

Figure 50: p*K*a values of co-formers in relation to SDZ. The red region depicts co-formers that facilitated co-crystal formation, while the yellow region facilitated proton transfer.

2.5.2 From Motifs to Graph Sets

The use of pyridines in the self-assembly process was to compete with the primary N—H···N (pyrimidine) synthon *via* a N—H···N (pyridine) hydrogen bond to the sulfonamide. Dimer formation would be interrupted by a pyridine that serves as a better hydrogen bond acceptor than pyrimidine. In the context of crystal engineering, there are a wide variety of pyridines (pK_a pyridine = 5.2)[205] that can be used to disrupt dimer formation of SDZ while supporting the formation of a either a co-crystal or salt. Supramolecular complexes formed using pyridines that are either more basic (pK_a > 5.7) or more acidic (pK_a < 5.7) than the sulfonamide group would not only provide a means to investigate how pK_a influences co-crystal or salt formation in SD-based solids but support the formation of different supramolecular synthons.

The large number of hydrogen bond groups coupled with the conformational mobility of the sulfonamide suggests that numerous hydrogen-bond synthons can be

achieved in supramolecular complexes based on SDZ.[180a] While SDZ contains more acceptor than donor groups, the use of pyridine co-formers adds to an imbalance of acceptors and, thus, would be expected to expand the number of motifs in resulting solid-state complexes. In five out of seven of our solids, the pyridine co-former interrupted dimer formation. For the co-crystals, the dimer of SDZ was both disrupted and maintained. Whereas both pico and bipy disrupted the dimer, solids involving bpe and bpa maintained the (amidine) N—H···N (pyrimidine) synthon. For the more basic pyridines (i.e. 4-ap, dmap, 4-pypip), dimer disruption was accompanied by proton transfer to the pyridine N-atom.

Five different graph sets can be ascribed to the seven solids; namely, $D_1^1(2)$ dyad, $R_2^2(8)$ ring, $R_2^2(20)$ ring, $C_2^2(17)$ chain, and $C_2^2(13)$ chain. The most frequent pattern is a single interaction between either the amido or amino N–H of SDZ and the pyridine N-atom, as described by the $D_1^1(2)$ notation. The pattern occurred in four out of seven solids, with one of three synthons (Figure 51). Specifically, (amidine) N—H···N (pyridine), (aniline) N—H···N (pyridine), and (pyridinium) $^+$N—H···N$^-$ (amidide) hydrogen bonds all comprise the $D_1^1(2)$ graph set. The $R_2^2(8)$ ring describes the two-point interaction present between the sulfonamide and pyrimidine ring that affords the dimer (Figure 51). The two structures that contain the hydrogen-bonding ring also generate interactions between the aniline N–H and pyridine N-atom, being classified as $D_1^1(2)$ notation. The $R_2^2(20)$ ring is present in two different types, each being promoted by a 'bidentate' nature of SDs. Specifically, a homomolecular[196] ring sustained by (amidine) N—H···N (pyridine) hydrogen bonds is present in the co-crystal (SDZ)·(pico) while a heteromolecular ring is present in (4-ap$^+$)·(SDZ) (Figure 51). The hydrogen-bond pattern in the salt (4-ap$^+$)·(SDZ$^-$) is based on an array of (pyridinium) $^+$N—H···N$^-$ (amidide) and (amine) N—H···O_2S (sulfonamide) forces.

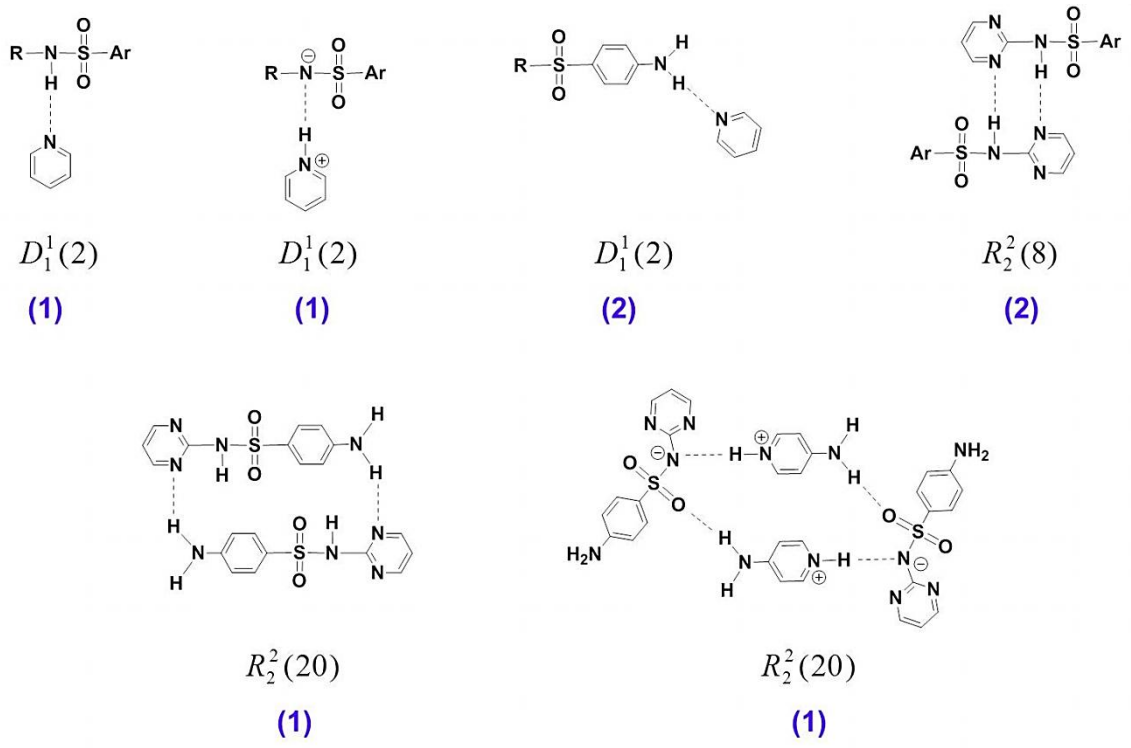

Figure 51: Finite graph sets with pyridine co-formers (number of occurrences in blue).

The remaining motif is a heteromolecular chain (Figure 52). In 2(SDZ)·3(bipy), SDZ interacts with bipy at both hydrogen-bond donor sites, which affords a $C_2^2(17)$ chain. The salt (4-pypip$^+$)·(SDZ$^-$) demonstrates similar structural behavior to 2(SDZ)·3(bipy), despite the addition of a donor site in the form of the piperazine group. Salt formation results in the 4-pypip$^+$ cation interacting with the strongest two acceptor sites of SDZ, which gives a $C_2^2(13)$ chain. Both structures also contain homomolecular C(8) chains between aniline N-H and SO_2 groups.[180a]

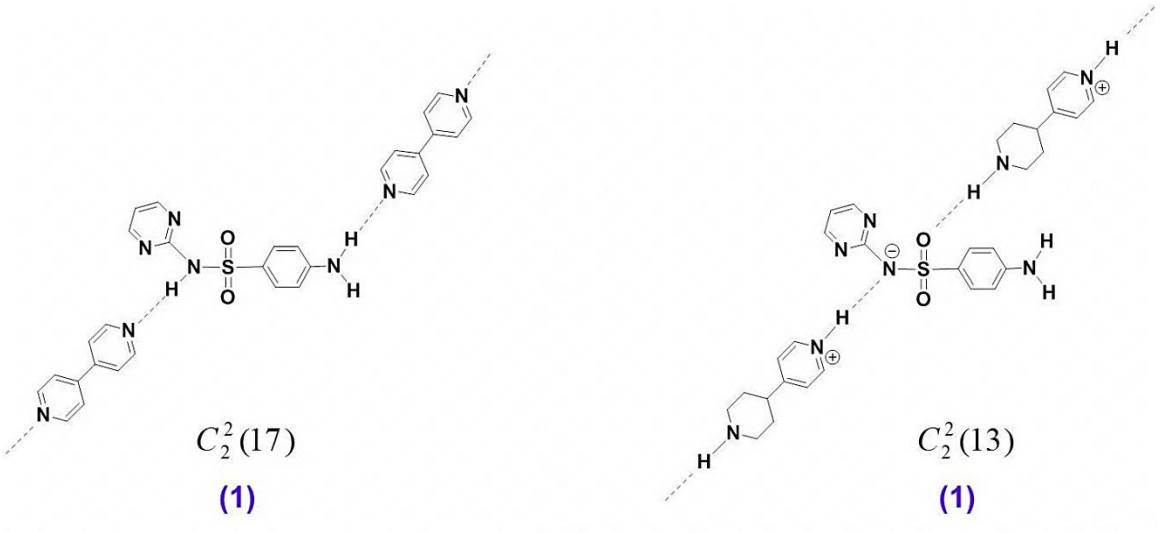

Figure 52: Chains with pyridine co-formers (number of occurrences in blue).

2.5.3 Host-Guest Co-Crystals

In co-crystals based on bpe and bpa, the co-former only competed with the formation of secondary hydrogen-bond synthons so as to enable the sulfonamide-pyrimidine $R_2^2(8)$ ring dimer to be preserved. Specifically, bpe and bpa disrupted the formation of N—H···O_2S hydrogen bonds that link pairs of dimers (Figure 53). Thus, effectively half of the N—H···O_2S interactions were retained in both solids. Both co-crystals also contain π···π interactions between adjacent stacks of dimers that are analogous to those in pure SDZ, as well as additional π···π interactions between stacked pyridines. The co-formers are, thus, akin to guest molecules within hosts, wherein the bipyridines are inserted into frameworks that do not disturb primary interactions in pure SDZ. Surprisingly, the 'better donor' does not hydrogen bond with the 'better acceptor' in each solid.[207] Energy differences between the two different hydrogen bond motifs (e.g. ring dimer and expected chain) may be minimal and overcome by a more favorable close packing, as well as additional intermolecular forces.

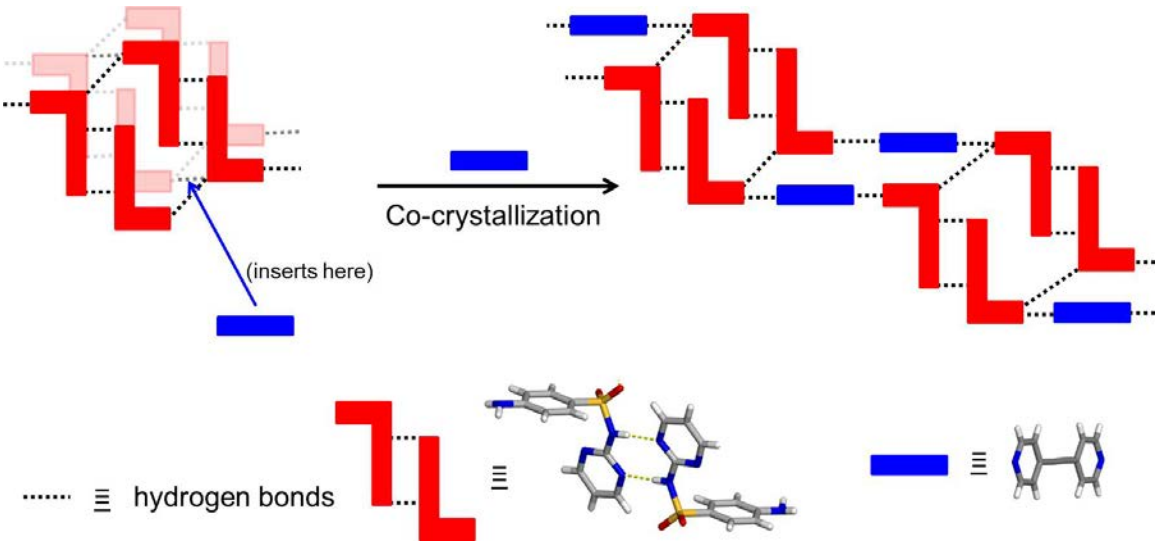

Figure 53: Schematic of interactions in pure SDZ and the 'host-guest' co-crystal with bpa.

2.5.4 Unexpected Stoichiometry

The co-crystal involving SDZ and bipy is unexpected in the context of stoichiometry. Specifically, an as prepared 2:1 ratio of SDZ and bipy co-crystallized as 2(SDZ)·3(bipy) while affording a mixed assembly with both the sulfonamide N-H group and aniline N-H group participating in hydrogen bonds. Within the co-crystal, there are two distinct 'classes' of bipy molecules. The first type of bipy participates in two different N—H···N interactions that extend the polymer framework (Figure 54, polymer-extending bipy). The second type is part of the pendant (bipy)–(SDZ)–(bipy) units and form hydrogen bonds to only one strong donor. The pendant bipy molecules each contain a non-hydrogen bonding pyridine unit that acts similar to polymer end-caps that terminate a polymer (Figure 54, end-cap bipy). The free pyridines, instead, participate in C—H···N interactions with an adjacent SDZ molecule (Figure 54).

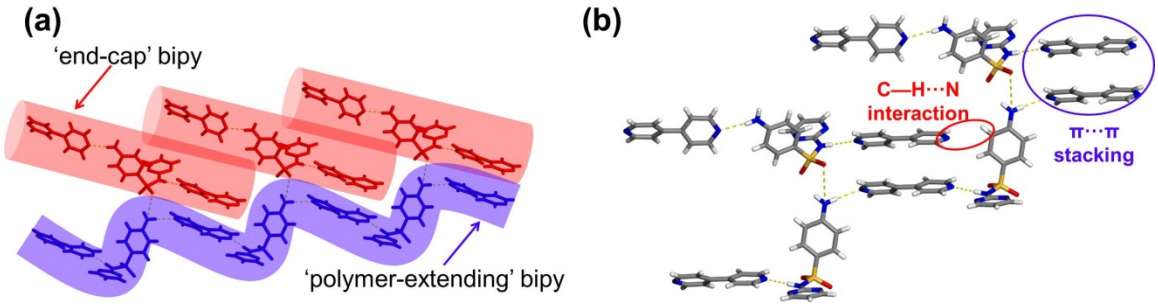

Figure 54: Co-crystal 3(SDZ)·2(bipy) highlighting: (a) 'end-cap' and 'polymer-extending' bipys and secondary interactions with unbound ends of bipy molecules.

We note that a search of the CSD reveals that free 4-pyridyl groups involving bipy and co-formers similar to SDZ (i.e. with OH or NH as hydrogen bond donor) have been reported.[208] A total of 248 such solids have been observed, with 16 (6.45%) containing bipy molecules with only one 4-pyridyl group that participates in a single hydrogen bond.[209] The unbound bipy molecules often participate in weak C—H···N or C—H···π forces.[208]

2.5.5 Geometry of the Sulfonamide

Although SDs are gaining interest as building blocks in crystal engineering,[181] relatively little effort has been extended to compare SD-based co-crystals and salts involving a series of co-formers. Having generated both co-crystals and salts of SDZ, we examined the solids with a view to understand possible geometric changes associated with the sulfonamide moiety. Proton transfer from the SD to the co-former was expected to result in an increase of the sp^2 character of the sulfonamide N-atom and, thus, lead to a decrease in the S–N bond length and, concomitantly, smaller SNR bond angle (i.e. higher S=N character) (Figure 55). Conversely, co-crystals were expected to exhibit longer S–N bond lengths and larger SNR bond angles. The geometry of biologically-active

sulfonamides has been examined in the gas phase and compared to the anionic form.[210] Computational studies reveal the sulfonamide group to exhibit partial S=N character upon deprotonation.

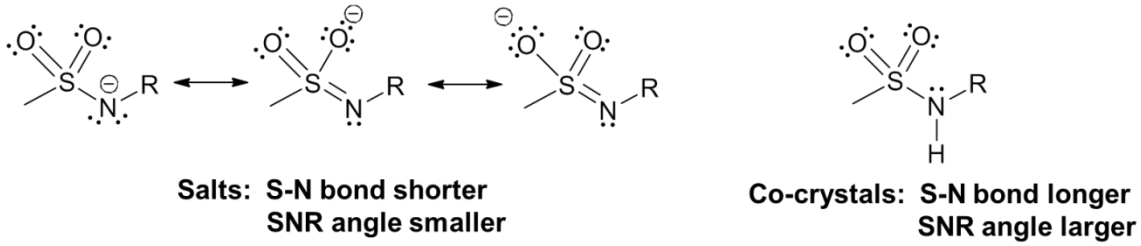

Figure 55: Schematic of sulfonamide geometries in (a) anionic and (b) neutral forms.

From our work involving pyridines, S–N bond lengths and SNC (pyrimidine) angles were determined to be different in co-crystals and salts. The salts exhibited shorter S–N bond lengths with a range of 1.56 to 1.60 Å, which is consistent with greater S=N character. The co-crystals exhibited longer S–N bonds in the range of 1.61 to 1.65 Å. Additionally, the SNC bond angles were generally smaller for the salts (122 - 124º) as compared to the co-crystals (126 - 128º) (Figure 56). From these observations, we conclude that both S–N bond length and SNC angle can serve to identify multicomponent solids based on SDZ as being either a co-crystal or salt.

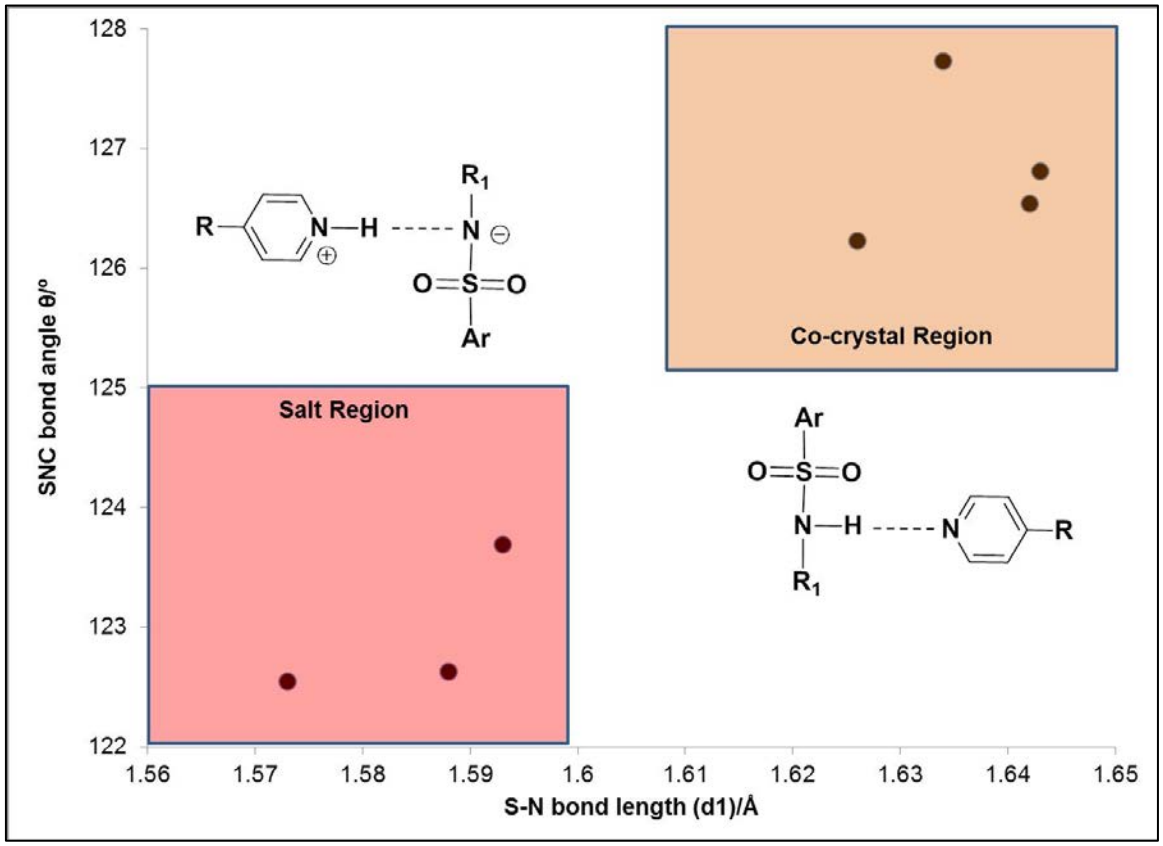

Figure 56: Plot of S–N bond length vs. SNC angle for our SDZ-based solids.

We next turned to the CSD to examine related SD-based solids. A search of the CSD revealed 43 multicomponent solids of SDs, with 35 (71%) being co-crystals and eight (19%) being salts. The majority of co-formers used to form the solids were based on N-heterocyclic amines and carboxylic acids, as well as amides (Figure 57). One pyridine, namely picolinamide, has been used in complex formation with a SD to form a co-crystal. The solid was sustained by (sulfonamide) N—H···O (carboxy) interactions. In this solid, the pyridine participates in the formation of secondary (alkyl) C—H···N (pyridine) forces. In 24 complexes, the co-former interacts with the sulfonamide N–H group *via* either (sulfonamide) N—H···N (pyrimidine) or (sulfonamide) N—H···O (carbonyl) forces in the form of two-point interactions.

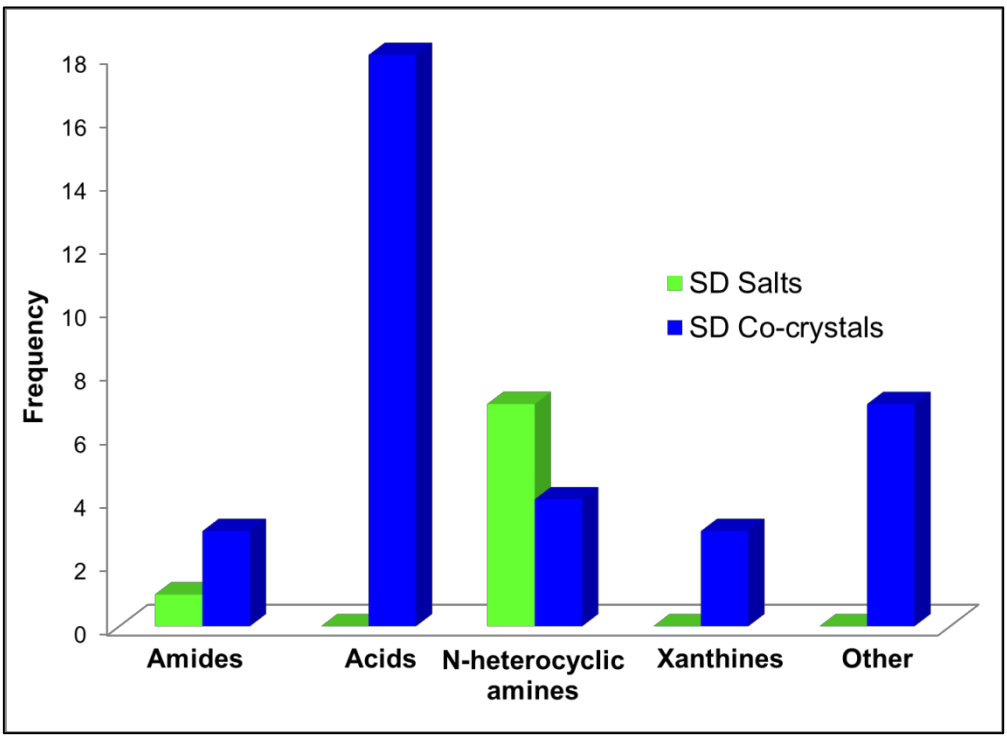

Figure 57: Frequency of primary co-former functional groups utilized in construction of multicomponent complexes involving SDs.

The S–N bond lengths and SNC angles of our pyridine-based co-crystals generally fall within the ranges of the reported SD complexes (Table 1). The S–N bond lengths and sulfonamide SNC angles of the reported complexes range from 1.56 to 1.67 Å and 118 to 127º, respectively. The larger differences compared to our SDZ-based solids can be attributed to the larger variety of co-formers and sample size, since different SDs and co-formers can be expected to accommodate a wider array of S–N lengths and SNC angles. Indeed, there are 10 SDs that differ in electronic character of the R group (R = pyridazine, pyrimidine, oxazole, thiadiazole, quinoxaline, and acetyl). Moreover, the different R groups are expected to affect delocalization involving the sulfonamide N-atom, and in turn, affect S=N character.

Table 1: Geometric parameters for all SD-based supramolecular complexes.

Sulfa Drug	Complex Former	θ/º	d1/Å	Co-crystal/Salt	Reference
sulfamethoxypyridazine	trimethoprim, H_2O	125.19	1.571	salt	[211]
sulfadiazine	ampyr	122.55	1.573	salt	[162]
sulfamethoxazole	trimethoprim	123.47	1.573	salt	[212]
sulfametrole	tetroxoprim, MeOH	118.83	1.576	salt	[213]
sulfametrole	tetroxoprim, H_2O	119.43	1.577	salt	[213]
sulfametrole	tetroxoprim, H_2O	119.63	1.581	salt	[213]
sulfamethazine	4-hydroxybenzamide	122.80	1.584	co-crystal*	[181b]
sulfametrole	tetroxoprim, EtOH	118.20	1.585	salt	[213]
sulfametrole	trimethoprim	118.30	1.585	salt	[214]
sulfamethazine	4-hydroxybenzamide	123.26	1.585	co-crystal*	[181b]
sulfadiazine	4-pypip	122.63	1.588	salt	[162]
sulfadiazine	dmap	123.69	1.593	salt	[162]
sulfamethoxypyridazine	trimethoprim	121.68	1.598	co-crystal*	[213]
sulfamethazine	picolinamide	121.38	1.602	co-crystal*	[181b]
sulfamethazine	4-hydroxybenzoic acid	122.81	1.608	co-crystal*	[181b]
sulfamethazine	theopylline	120.13	1.618	co-crystal*‡	[215]
sulfamethazine	trimethoprim, MeOH	124.22	1.622	co-crystal	[216]
sulfamethazine	indole-2-carboxylic acid	125.55	1.623	co-crystal	[217]
sulfamethazine	4-aminosalicylic acid	125.32	1.624	co-crystal	[218]
sulfadiazine	4-pico	126.23	1.626	co-crystal	[162]
sulfamethazine	4-aminobenzoic acid	123.58	1.627	co-crystal	[219]
sulfamethazine	2,4-dihydroxybenzoic acid	126.98	1.628	co-crystal	[217]
sulfamethazine	3-hydroxy-2-naphthoic acid	121.40	1.629	co-crystal*	[181b]
sulfadiazine	bipy	127.73	1.634	co-crystal	[162]
sulfamethazine	fumaric acid, CH_3CN	125.84	1.635	co-crystal	[181b]
sulfamethazine	4-chlorobenzoic acid	124.74	1.637	co-crystal	[220]
5-methoxysulfadiazine	acetylsalicylic acid	124.05	1.641	co-crystal	[221]
sulfamethazine	salicylic acid	126.58	1.641	co-crystal	[222]

Table 1. Continued

sulfamethazine	2-aminobenzoic acid	125.92	1.641	co-crystal	[219]
sulfamethazine	theophylline	125.78	1.642	co-crystal‡	[215]
5-methoxysulfadiazine	(18-C-6), CH_3CN	125.88	1.642	co-crystal	[223]
sulfadiazine	bpe	126.54	1.642	co-crystal	[162]
sulfamethazine	acetylsalicylic acid	125.94	1.643	co-crystal	[218]
sulfadiazine	bpa	126.81	1.643	co-crystal	[162]
sulfapyridine	oxalic acid, dibutyl ester	122.79	1.644	co-crystal	[224]
sulfamethazine	3,4-dichlorobenzoic acid	126.92	1.644	co-crystal	[181b]
sulfamethazine	sorbic acid	127.15	1.644	co-crystal	[181b]
sulfamerazine	(18-C-6), CH_3CN	125.65	1.645	co-crystal	[223]
5-methoxysulfadiazine	dioxane	126.23	1.646	co-crystal	[225]
sulfamethazine	MeOH	124.78	1.647	co-crystal	[226]
sulfamethazine	trimethoprim, H_2O	125.49	1.647	co-crystal	[227]
chlorsulfaquinoxaline	CH_3CN	124.62	1.648	co-crystal	[228]
5-methoxysulfadiazine	THF	125.55	1.648	co-crystal	[225]
sulfamethazine	2,4-dinitrobenzoic acid	126.18	1.650	co-crystal	[217]
sulfamethazine	salicylic acid	126.20	1.651	co-crystal	[229]
N-acetylsufanilamide	caffeine	124.85	1.652	co-crystal	[230]
sulfamethazine	benzoic acid	126.54	1.652	co-crystal	[231]
sulfamethazine	saccharin	125.56	1.656	salt†	[232]
sulfamethazine	1-hydroxy-2-naphthoic acid	126.77	1.658	co-crystal	[181b]
sulfaproxyline	caffeine	124.39	1.660	co-crystal	[233]

* Denotes complexes containing the imidine tautomer of the sulfonamide.

‡ Entries found in same crystal structure.

† Denotes salt containing a cationic SD and anionic co-former (excluded from geometry study).

The SD-based solids in the CSD reveal that the salts exhibit S–N bond lengths of 1.57 - 1.60 Å while co-crystals exhibit S–N bond lengths of 1.58 - 1.66 Å. In contrast to our pyridine-based solids, there is slight overlap in S–N bond distances of the reported salts and co-crystals from 1.58 to 1.60 Å. The overlap involves five co-crystals and six salts. The SNC angles ranged from 118 to 125º for salts and 120 to 128º for co-crystals. There is, thus, also overlap of SNC bond angles from 120 to 125º. The solids in that region comprise 17 co-crystals and four salts. As discussed by Childs in the context of C–O bond length and ΔpK_a,[190] such an overlap is likely representative of a boundary between co-crystal and salt formation.

2.5.6 Tautomers in the Co-Crystal – Salt Continuum

From our analysis of the SD-based co-crystals in the CSD, seven sulfonamide moieties exist as the imidine tautomer. The tautomer is present in six sulfamethazine (SMT) co-crystals and one co-crystal of sulfamethoxypyridazine. Both SDs contain a N-heterocyclic ring atom adjacent to the sulfonamide and can generate two tautomers (Figure 58). Relative energies of tautomeric forms have been investigated in the case of SMT, with DFT calculations revealing the amidine to be more stable than the imidine by 33.2 kJ mol^{-1}.[215] The higher energy of the imidine form has been attributed to less aromatic character of the adjacent pyrimidine ring.[215] The seven co-crystals with the imidine tautomer possess S–N bond lengths and SNC angles of 1.58 to 1.63 Å and 120 - 124°, respectively. The remaining amidine-based co-crystals in the CSD, along with our co-crystals, exhibit S–N bond lengths of 1.62 - 1.66 Å. The SNC bond angles of the amidine co-crystals span from 122 - 128°. For comparison, our salts and the salts in the CSD, exhibited S–N lengths of 1.57 - 1.60 Å and SNC angles of 118 - 125°.

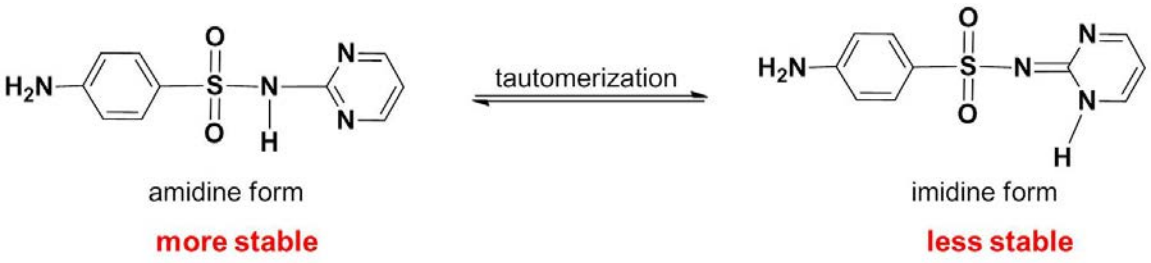

Figure 58: Schematic showing sulfonamide tautomers of SDZ.

It is clear that the ranges of S–N length for salts and amidine co-crystals do not overlap. Remarkably, however, effectively *all of the S–N lengths of the higher energy imidine tautomer sit in between the S–N lengths of salts and the amidine tautomer.* The observation is supported by an analysis of S–N bond lengths for each type of complex. Using the mean ($\overline{X}$) S–N length and standard deviation (σ) for co-crystals and salts, we analyzed the S–N distribution of each type, so as to display each region as $\overline{X} \pm 2\sigma$. From the data, the salts covered a range of 1.571 - 1.593 Å, while the co-crystal region was represented by 1.594 - 1.673 Å (Figure 59). To separate the imidine and amidine sections within the co-crystal region, $\overline{X} \pm 2\sigma$ was calculated for the amidine form. The range for amidine co-crystal S–N bond length was 1.622 - 1.660 Å, and thus, the imidine-amidine boundary is assigned at 1.622 Å. (Figure 59, dashed line). To our knowledge, a delineation of tautomers as related to S–N bond length has not been reported.

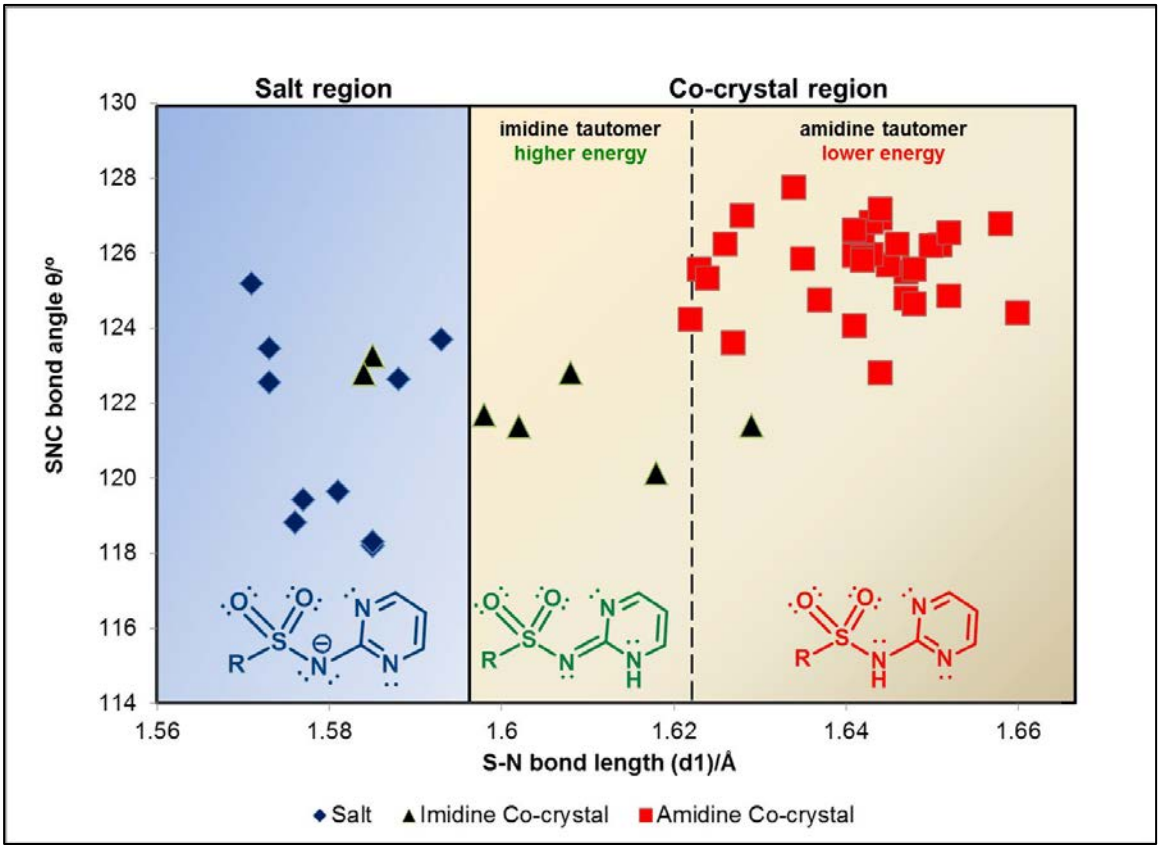

Figure 59: A plot of S–N bond length vs. SNC bond angle for SD-based complexes.

2.6 Sulfamethazine (SMT) as a Model PA

From the results related to SDZ, as well as the analysis of structures in the CSD, we turned to look at Sulfamethazine (SMT) as a model PA to generate pharmaceutical co-crystals while further studying the geometrical differences associated with tautomerizarion of SDs (Figure 60). We envisioned that SMT would provide a better opportunity to study the S–N bond length of the two tautomeric forms since the imidine tautomer of SMT has been reported most frequently (six out of seven reported imidine-based SD co-crystals, 86%). SMT is also the most well-studied SD to date, having been reported in 25 out of 42 SD-based complexes, six of which contain the imidine tautomer (24%).[234] In addition, SMT has been reported to readily form co-crystals and salts with a

variety of co-formers (e.g. N-heterocycles, carboxylic acids, amides), likely owing to a markedly-higher solubility in common organics.

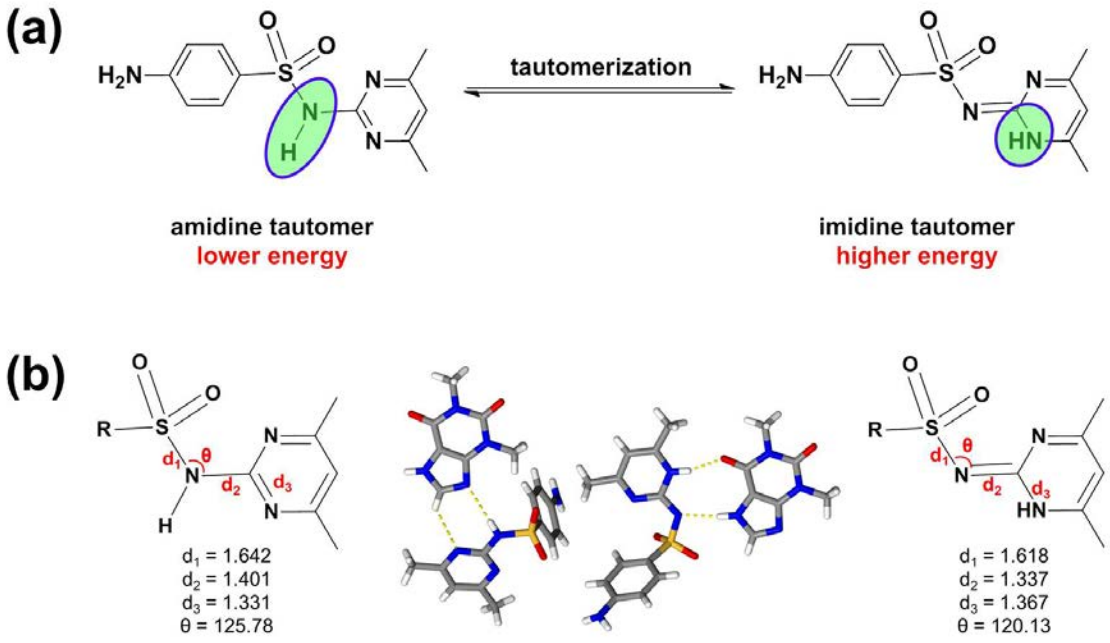

Figure 60: Schematic showing (a) two tautomeric forms of SMT and (b) geometrical differences related to the reported (SMT)·(theophylline) co-crystal containing both tautomers.[215]

SMT, similar to SDZ, is a bacteriostatic agent used to treat a variety of infections and diseases in both human and veterinary medicine. SMT, in the pure form, self-assembles *via* complementary (amidine) N—H···O_2S (sulfoxide) and (aniline) N—H···N (pyrimidine) synthons that afford C(4) chains and $R_2^2(20)$ motifs, respectively (Figure 61).[235] Previous studies with SMT have revealed both carboxylic acids and amides to co-crystallize with SMT, wherein SMT crystallizes in the imidine form.

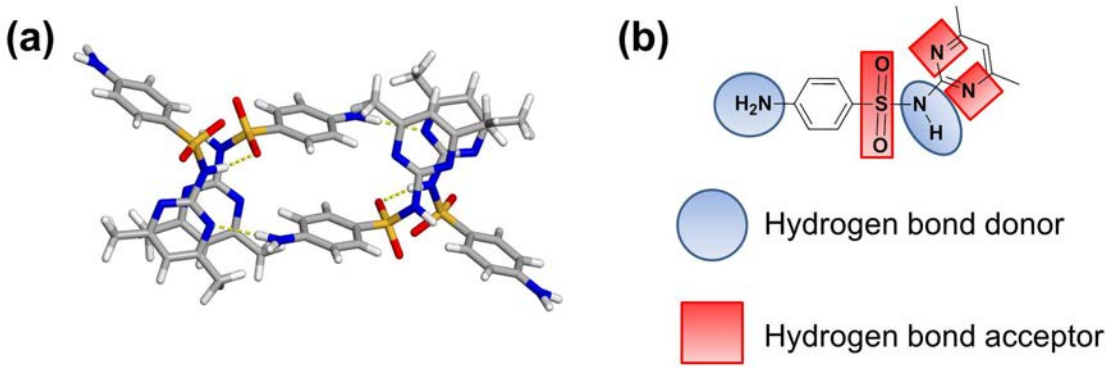

Figure 61: Schematic of SMT highlighting (a) self-assembly of complementary (amidine) N—H···O_2S (sulfoxide) and (aniline) N—H···N (pyrimidine) synthons and (b) hydrogen bonding functionalities.

In an extension of our studies with SDZ, we designed and constructed multicomponent crystalline solids involving SMT and a series of bipyridines, benzoic acids, and aromatic amides. The bipyridines comprise 4,4'-bipyridine (bipy), *trans*-1,2-bis(4-pyridyl)ethylene (bpe), and 1,2-bis(4-pyridyl) acetylene (bpa). The acid and amide co-formers used consisted of 3-hydroxybenzoic acid (3-hba), 4-hydroxybenzoic acid (4-hba), 2,5-dihydroxybenzoic acid (2,5-dhba), 2,6-dihydroxybenzoic acid (2.6-dhba), 2.4-dihydroxybenzoic acid (2,4-dhba), 3,5-dihydroxybenzoic acid (3,5-dhba), 2-aminoterephthalic acid (2-ata), benzamide (ba), 4-aminobenzamide (4-aba), 4-methoxybenzamide (4-mba), and 4-pyridylthioamide (4-pta) (Figure 62). The resulting structures consist of 13 co-crystals and one salt with SMT. Of the 13 co-crystals, four crystallize as the imidine tautomer of SMT. Extending our efforts to investigate the co-crystal – salt continuum[190] of complexes involving SDs, we reveal that the geometry of each SMT-based solid is in accordance within our earlier delineations in the context of S–N bond length.

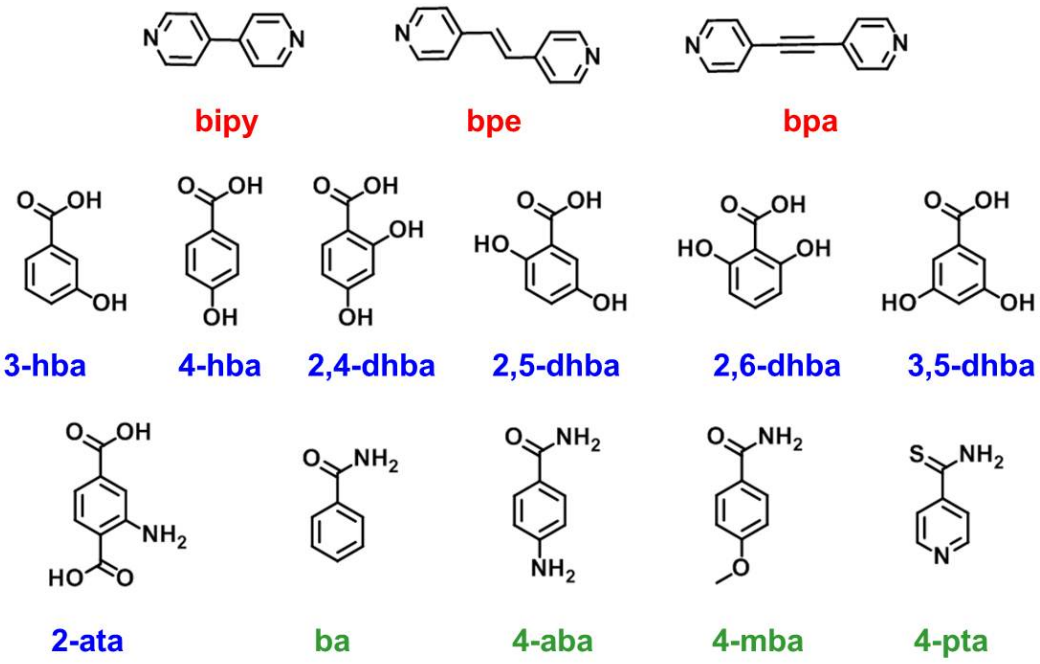

Figure 62: Chemical structures of all co-formers used with SMT comprising pyridine (red) benzoic acid (blue) and aromatic amide (green) derivatives.

2.7 Experimental

SMT (98%), bipy (97%), bpe (98%), ba (99%), 4-aba (98%), 4-mba (98%), 4-hba (99+%), 2,5-dhba (98%), and 3,5-dhba (97%) were purchased from Sigma Aldrich Chemical (St. Louis, MO, USA). 3-hba (99%), 2,4-dhba (97%), 2,6-dhba (97%), and 2-ata (99.9%) were purchased from ACROS Organics (Morris Plains, NJ, USA). 4-pta (96%) was purchased from Oakwood Products, Inc (West Columbia, SC, USA). bpa was synthesized according to a literature procedure.[195] Acetonitrile (99.9%) and Ethanol (99.98%, absolute grade) were obtained from Fisher Scientific (Pittsburgh, PA, USA) and Pharmco-AAPER (Brookfield, CT, USA), respectively. All components were used as purchased, unless specified. Single crystals of each solid were obtained by slow evaporation from solution. In a typical procedure, SMT (4 mmol) and a co-former (1.0 mol. eq. for monopyridines, monoacids, and benzamides, and 0.5 mol. eq. for

bipyridines, diacids, and 4-pta) were dissolved in CH_3CN or EtOH (5.0 - 7.0 mL) at 75 °C. Single crystals suitable for X-ray diffraction were grown upon cooling each solution to ambient temperature and then allowing the solvent to slowly evaporate. Single crystals formed within a period of approximately 5 days.

Single crystal X-ray diffraction experiments were performed on a Bruker SMART system equipped with an APEX2 CCD camera. Data was collected at 100 K with graphite-monochromated Mo*K*α radiation (λ = 0.71073 Å). The data was collected and processed using SaintPlus.[196] All structures were solved using direct methods that generated non-hydrogen atoms. All hydrogen atoms were located in Fourier-difference electron density maps. All non-hydrogen atoms were refined anisotropically. Hydrogen atoms associated with carbon atoms were refined in geometrically constrained riding positions. Hydrogen atoms associated with nitrogen and oxygen atoms were included in the located positions. Refinement was achieved with the use of SHELX-97.[199] The details of the structural analysis of all solids are summarized in Tables A-3 through A-6.

2.8 Results

14 new solid forms of SMT were obtained using co-crystal screening[146] with the selected co-formers. The crystal structure of each solid was determined using single-crystal X-ray diffraction. 13 solids were determined to be co-crystals while the remaining solid was a salt, as evidenced by proton transfer. In ten solids, the sulfonamide crystallizes as either an amidine (co-crystals) or amidide (salt) functionality, while the remaining four crystallize as the higher energy imidine species.[225]

(8) (SMT)·(bipy)·(CH_3CN). Co-crystallization of a 2:1 molar ratio of SMT and bipy in CH_3CN afforded a co-crystal solvate of 1:1:1 stoichiometry. The components crystallize in the monoclinic space group $P2_1/c$. The asymmetric unit consists of one molecule of SMT, one bipy molecule, and one CH_3CN. SMT and bipy interact *via* alternating intermolecular (sulfonamide) N—H···N (pyridine) and (aniline) N—H···N

(pyridine) hydrogen bonds in a $C_2^2(17)$ chain. The 1:1 assembly forms a 2D polymer sustained by a combination of amidine and aniline N—H···N hydrogen bonds, as well as (aniline) N—H···N (pyrimidine) and N—H···O_2S hydrogen bonds (Figure 63). The CH_3CN molecule also participates in weak (aniline) C—H···N (nitrile) interactions with SMT.

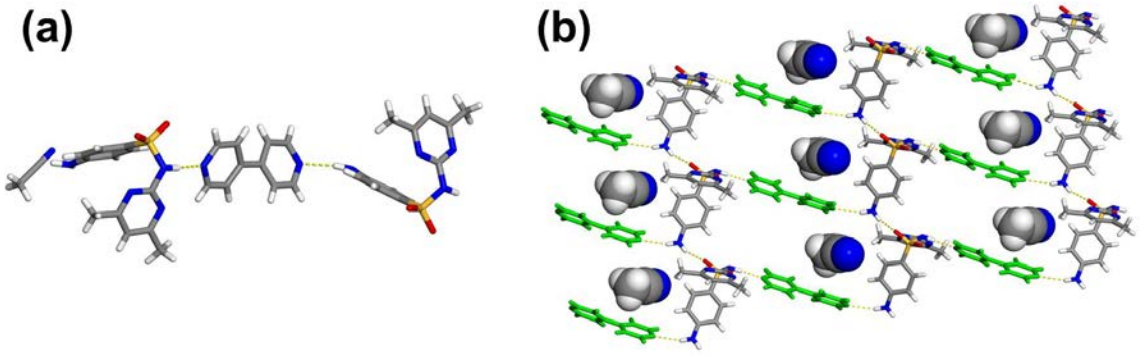

Figure 63: View of (SMT)·(bipy)·(CH_3CN) highlighting: (a) alternating amidine and aniline N—H···N hydrogen bonds and (b) 2D sheet formed with additional N—H···O_2S forces.

(9) (SMT)·(bpe)·(CH_3CN). SMT and bpe crystallize as a co-crystal solvate in the triclinic space group $P\bar{1}$. Crystallization from a 2:1 molar ratio in CH_3CN in a solid of 1:1:1 stoichiometry, wherein the asymmetric unit consists of one molecule of SMT, one bipy molecule, and one CH_3CN. SMT and bipy interact *via* alternating intermolecular (amidine) N—H···N (pyridine) and (aniline) N—H···N (pyridine) hydrogen bonds in a $C_2^2(17)$ chain. The 1:1 assembly forms a 2D polymer, wherein the extended structure is also sustained by a combination of (aniline) N—H···N (pyrimidine) and (aniline) N—H···O_2S (sulfoxide) hydrogen bonds (Figure 64). The CH_3CN molecule also participates in weak (aniline) C—H···N (nitrile) and (alkyl) C—H···π (aniline) interactions with SMT.

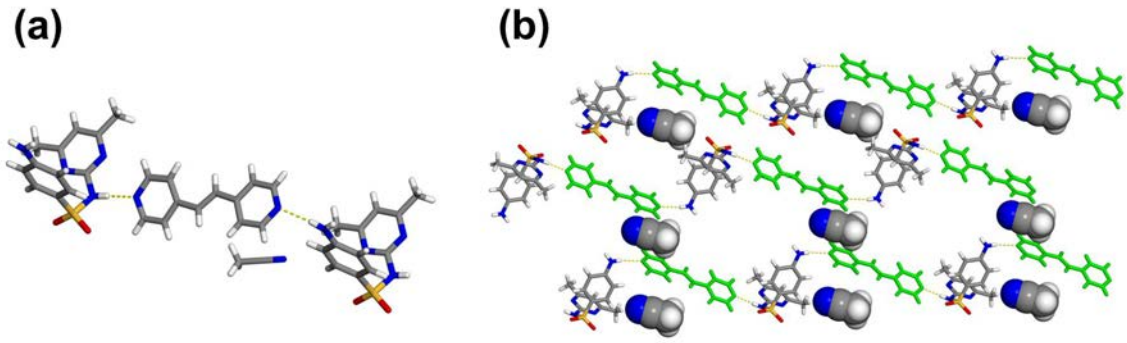

Figure 64: View of (SMT)·(bpe)·(CH_3CN) highlighting: (a) alternating amidine and aniline N—H···N hydrogen bonds and (b) 2D polymer formed with additional N—H···O_2S interactions.

(10) (SMT)·(bpa)·(CH_3CN). Co-crystallization of a 2:1 molar ratio of SMT and bpa from CH_3CN resulted in a co-crystal solvate of 1:1:1 stoichiometry. The components crystallize in the triclinic space group $P\bar{1}$. The asymmetric unit consists of one molecule of SMT, one bipy molecule, and one CH_3CN. Similar to (SMT)·(bpe)·(CH_3CN), SMT and bipy interact *via* alternating intermolecular (amidine) N—H···N (pyridine) and (aniline) N—H···N (pyridine) hydrogen bonds in a $C_2^2(19)$ chain. The components assemble to form a 2D polymer wherein (aniline) N—H···N (pyrimidine) forces and (aniline) N—H···O_2S (sulfoxide) hydrogen bonds contribute to the overall structure (Figure 65). Weak (aniline) C—H···N (nitrile) and (alkyl) C—H···π (aniline) interactions between the CH_3CN molecule and SMT are also observed.

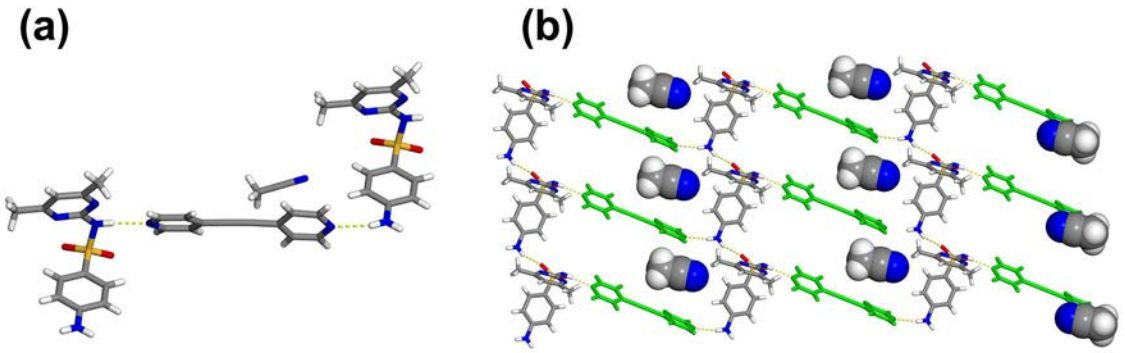

Figure 65: View of (SMT)·(bpa)·(CH_3CN) highlighting: (a) alternating amidine and aniline N—H···N hydrogen bonds and (b) hydrogen bonding interactions between SMT and CH_3CN.

(11) (SMT)·(3-hba). (SMT)·(3-hba) crystallizes from EtOH in the orthorhombic space group P*bca* with one molecule of SMT and one molecule of 3-hba in the asymmetric unit. SMT and 3-hba assemble to form zig-zag chains consisting of a two-point (acid) O—H···N (pyrimdine) and (amidine) N—H···O (carboxy) forces in a $R_2^2(8)$ motif, as well as (phenol) O—H···N (aniline) interactions. Additional forces in the form of (aniline) N—H···O_2S (sulfoxide) interactions link adjacent chains, so as to form a 2D hydrogen bonded polymer (Figure 66).

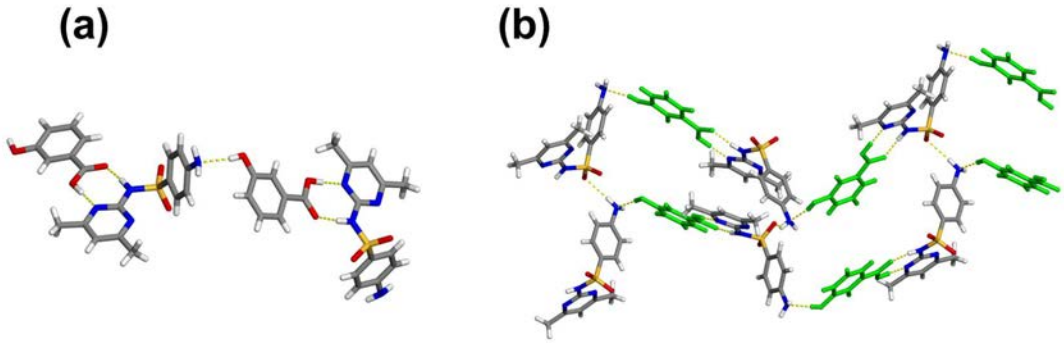

Figure 66: View of (SMT)·(3-hba): (a) primary two point (acid) O—H···N (pyrimdine) and (amidine) N—H···O (carboxy) synthon and (b) extended structure.

(12) (SMT)·(4-hba). (SMT)·(4-hba) crystallizes from an ethanolic solution in the triclinic space group $P\bar{1}$. The asymmetric unit consists of one molecule of SMT and one molecule of 4-hba. In contrast to (SMT)·(3-hba), (SMT)·(4-hba) co-crystallizes with the imidine tautomer of SMT, and is sustained by a $R_2^2(8)$ arrangement of (imidine) N—H···O (carboxy) and (acid) O—H···N (imidine) hydrogen bonds. Additional (phenol) O—H···N (aniline) and (aniline) N—H···O_2S (sulfoxide) interactions contribute to the extended structure, generating a 2D hydrogen bonded polymer (Figure 67).

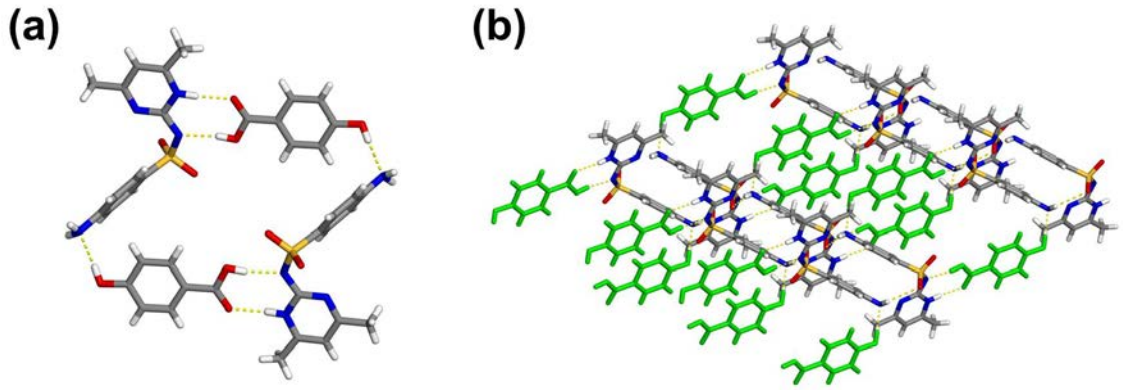

Figure 67: View of (SMT)·(4-hba): (a) primary two point (acid) O—H···N (imidine) and (imidine) N—H···O (carboxy) synthon and (b) extended 2D structure.

(13) (SMT)·(2,4-dhba). SMT and 2,4-dhba form a 1:1 co-crystal that crystallizes from ethanol in the triclinic space group $P\bar{1}$ with one molecule of SMT and one molecule of 4-hba in the asymmetric unit. (SMT)·(2,4-dhba) crystallizes as the amidine tautomer of SMT, and is sustained by a $R_2^2(8)$ arrangement of (amidine) N—H···O (carboxy) and (acid) O—H···N (amidine) hydrogen bonds. The two components assemble with additional (aniline) N—H···O_2S (sulfoxide), (phenol) O—H···O (carboxy/phenol) and (phenol) O—H···N (aniline) interactions that give rise to a 2D hydrogen bonded polymer (Figure 68).

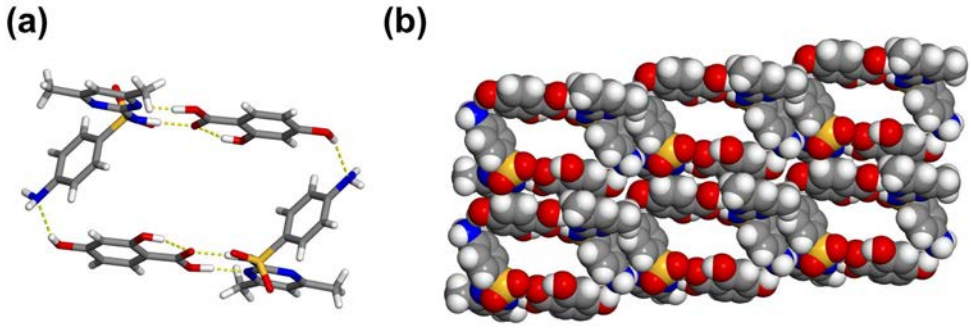

Figure 68: Views of (SMT)·(2,4-dhba): (a) primary two point (acid) O—H···N (imidine) and (imidine) N—H···O (carboxy) synthon and (b) extended 2D structure.

(14) (SMT)·(2,5-dhba). Co-crystals of the composition (SMT)·(2,5-dhba) crystallize from EtOH in the orthorhombic space group Pbca with one molecule of SMT and one molecule of 2,5-dhba in the asymmetric unit. The primary interaction between SMT and 2,5-dhba consists of the $R_2^2(8)$ motif based upon a two-point (acid) O—H···N (pyrimdine) and (amidine) N—H···O (carboxy) forces. The two components assemble to generate a 3D hydrogen-bonded polymer sustained by additional (phenol) O—H···N (aniline) and (aniline) N—H···O_2S (sulfoxide) interactions (Figure 69).

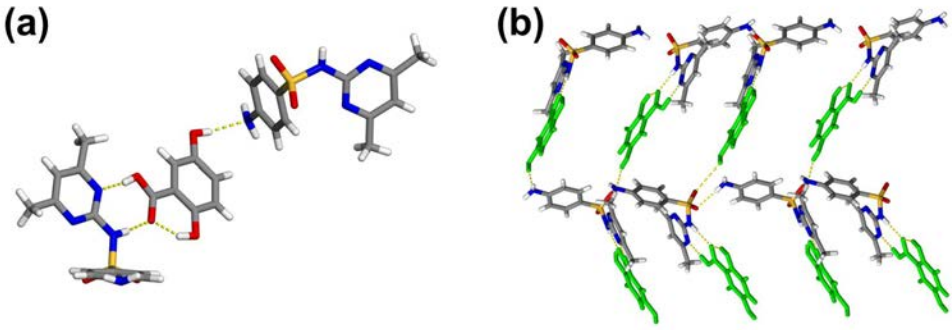

Figure 69: Views of (SMT)·(2,5-dhba): (a) primary two point (acid) O—H···N (pyrimidine) and (amidine) N—H···O (carboxy) synthon and (b) extended 2D structure.

(15) (SMT^+)·($2,6\text{-}dhba^-$). SMT and 2,6-dhba crystallize from ethanol in the orthorhombic space group P*bca* as a salt in the form of (SMT^+)·($2,6\text{-}dhba^-$). The asymmetric unit contains one SMT^+ cation and one $2,6\text{-}dhba^-$ anion that self-assemble to form a 2D polymer (Figure 70). The two-component assembly is sustained by primary (pyrimidinium) ^+N—H···O^- (carboxylate) and (amidine) N—H···O (carboxy) hydrogen bonds, arranged in a $R_2^2(8)$ motif, as well as (aniline) N—H···O_2S (sulfoxide) hydrogen bonds that form a zig-zag C(8) chain. Additional (aniline) N—H···O_2S (sulfoxide) interactions, as well as π···π interactions between aniline and pyrimidine rings of neighboring chains contribute to the overall structure. ($d_{\pi\cdots\pi}$ = 3.33 Å).

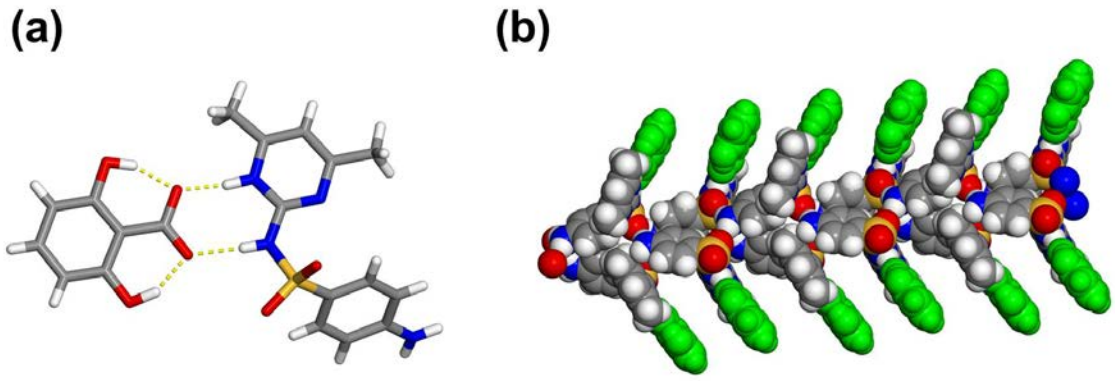

Figure 70: Views of (SMT^+)·($2,6\text{-}dhba^-$): (a) primary two point (pyrimidinium) ^+N—H···O^- (carboxylate) and (amidine) N—H···O (carboxy) synthon and (b) extended structure.

(16) (SMT)·(3,5-dhba). (SMT)·(3,5-dhba) crystallizes from an ethanolic solution in the monoclinic space group $P2_1/c$ with one molecule of SMT and one molecule of 3,5-dhba in the asymmetric unit. Similar to (SMT)·(4-hba), (SMT)·(3,5-dhba) co-crystallizes with the imidine tautomer of SMT, and thus, is sustained by a $R_2^2(8)$ arrangement of (imidine) N—H···O (carboxy) and (acid) O—H···N (imidine) hydrogen bonds. Additional (phenol) O—H···O_2S (sulfoxide), (aniline) N—H···O_2S

(sulfoxide), and (aniline) N—H···N (pyrimidine) interactions, as well as π···π stacking between benzene and pyrimidine rings ($d_{\pi\cdots\pi}$ = 3.72 Å) contribute to the extended structure, generating a 2D hydrogen bonded polymer (Figure 71).

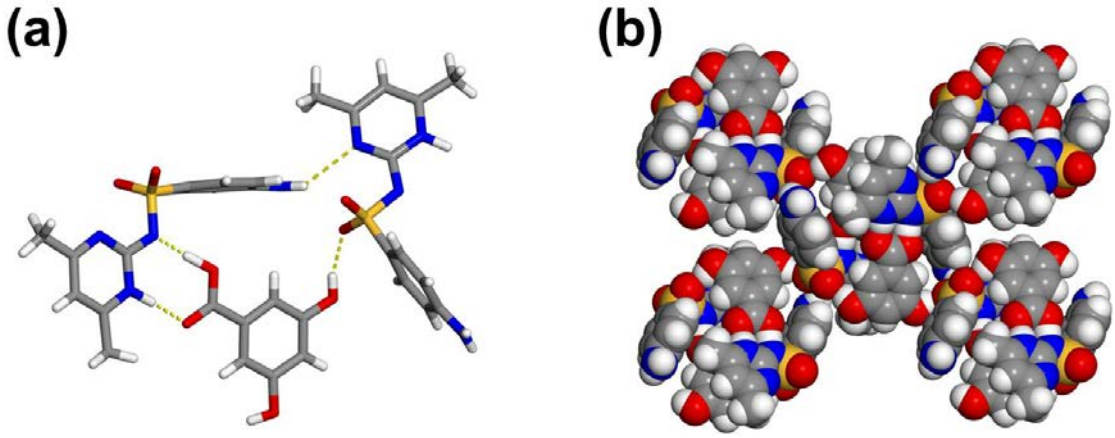

Figure 71: Views of (SMT)·(3,5-dhba): (a) primary two point (acid) O—H···N (imidine) and (imidine) N—H···O (carboxy) synthon and (b) extended 2D structure.

(17) (SMT)·(2-ata). Crystallization of a 2:1 ratio of SMT and 2-ata results in the formation of a 1:1 co-crystal. (SMT)·(2-ata) crystallizes from EtOH in the monoclinic space group $P2_1/n$ with one molecule of SMT and one molecule of 2-ata in the asymmetric unit. SMT and 3-ata assemble to form sheets consisting of a pair of two-point $R_2^2(8)$ motifs, specifically (acid) O—H···N (pyrimdine) and (amidine) N—H···O (carboxy) forces, as well as an (acid) O—H···O (carboxy) dimer (Figure 72) and (phenol) O—H···N (aniline) interactions. Additional forces in the form of (aniline) N—H···O_2S (sulfoxide) interactions link adjacent sheets, generating a 3D hydrogen bonded polymer.

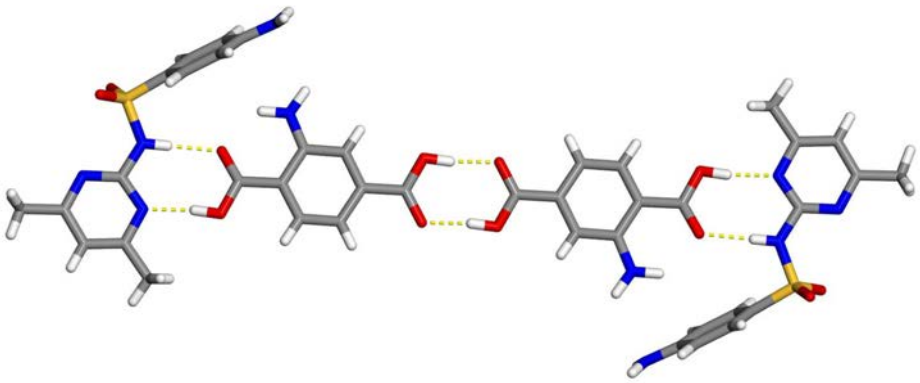

Figure 72: View of 2(SMT)·2(2-ata) highlighting (acid) O—H···N (pyrimdine) and (amidine) N—H···O (carboxy) forces, as well as an (acid) O—H···O (carboxy) dimer.

(18) (SMT)·(4-pta). SMT and 4-pta form a 1:1 co-crystal that crystallizes from ethanol in the monoclinic space group $P2_1/n$ with one molecule of SMT and one molecule of 4-pta in the asymmetric unit. (SMT)·(4-pta) crystallizes as the amidine tautomer of SMT, sustained by a $R_2^2(8)$ arrangement of (amidine) N—H···S (thiocarboxamide) and (amide) N—H···N (pyrimidine) hydrogen bonds. The two components assemble with additional (aniline) N—H···O_2S (sulfoxide) and (aniline) N—H···N (pyridine) interactions that give rise to a 3D hydrogen bonded polymer (Figure 73).

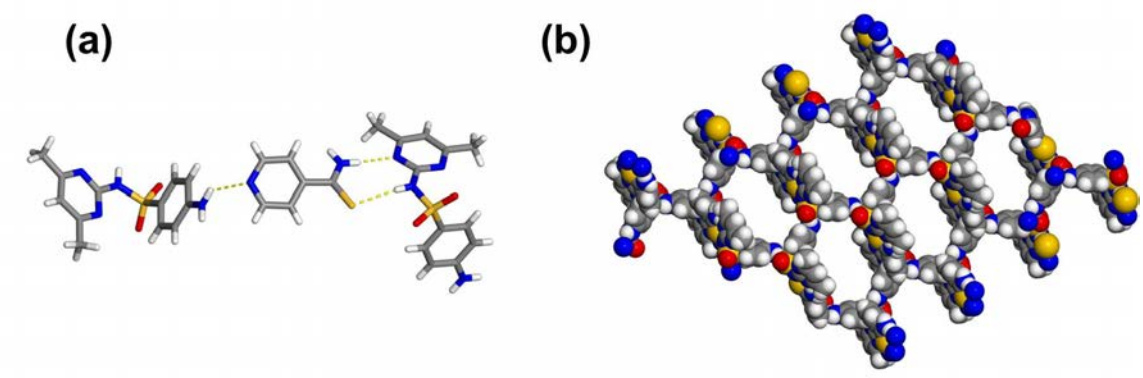

Figure 73: Views of (SMT)·(4-pta): (a) primary two point (amidine) N—H···S (thiocarboxamide) and (amide) N—H···N (pyrimidine) synthon and (b) extended 2D structure.

(19) (SMT)·(ba). SMT and ba co-crystallize in the monoclinic space group $P2_1/c$. The asymmetric unit consists of one molecule of SMT in the imidine form and one ba molecule that interact *via* intermolecular (amide) N—H···N (imidine) and (imidine) N—H···O (carboxy) hydrogen bonds in a $R_2^2(8)$ motif. The 1:1 assembly forms a 2D polymer grid, wherein the extended structure is also sustained by (aniline) N—H···O_2S (sulfoxide) hydrogen bonds (Figure 74).

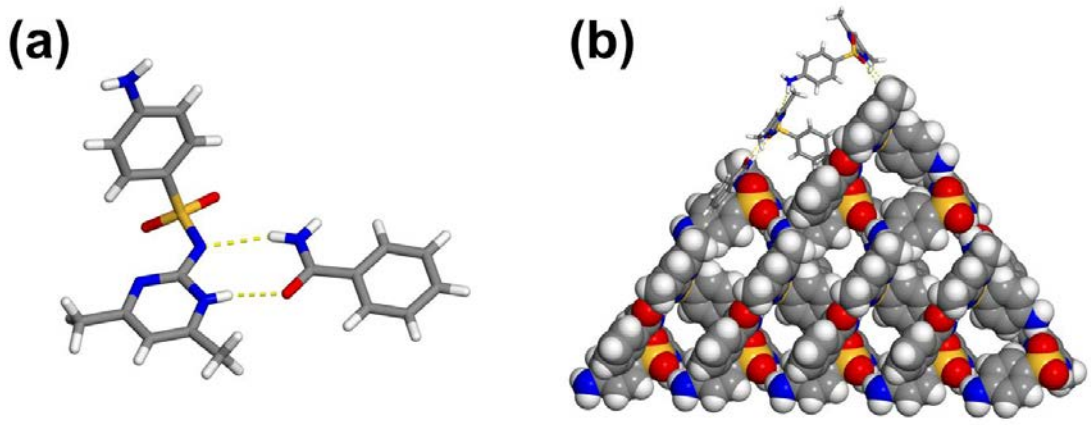

Figure 74: View of (SMT)·(ba) highlighting: (a) (amide) N—H···N (imidine) and (imidine) N—H···O (carboxy) two point interaction and (b) resulting 2D polymer with (aniline) N—H···O_2S (sulfoxide) forces.

(20) (SMT)·(4-aba). Crystallization of SMT and 4-aba results in a co-crystal of the composition (SMT)·(4-aba). The complex crystallizes in the monoclinic space group $P2_1/c$ with one molecule of SMT and one 4-aba molecule in the asymmetric unit. The two components interact *via* (amide) N—H···N (pyrimidine) and (amidine) N—H···O (carboxy) forces arranged in a $R_2^2(8)$ motif. Additional (aniline) N—H···O_2S (sulfoxide) hydrogen bonds contribute to the overall 3D polymer structure (Figure 75).

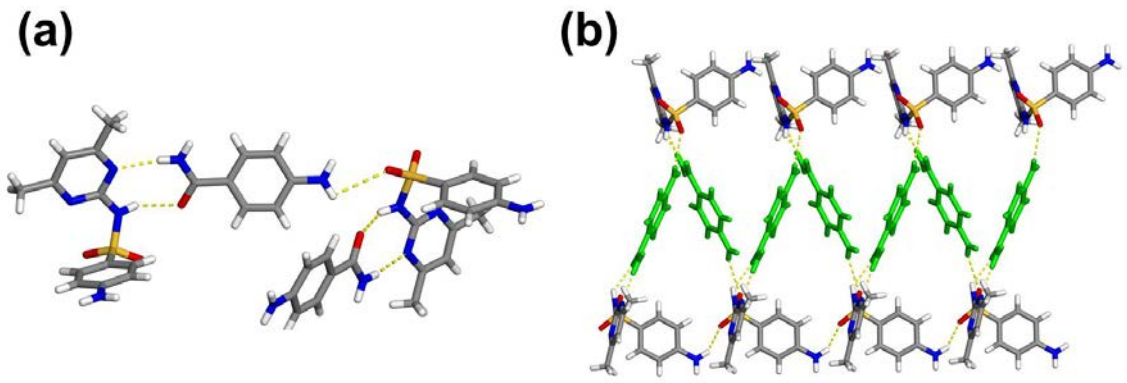

Figure 75: Views of (SMT)·(4-aba): (a) primary two point (amidine) N—H···O (carboxy) and (amide) N—H···N (pyrimidine) synthon and (b) extended structure.

(21) (SMT)·(4-mba)·(H_2O). SMT and 4-mba crystallize as a monohydrate in the triclinic space group $P\bar{1}$ with one molecule of SMT, one molecule of 4-mba, and one water molecule in the asymmetric unit. Similar to (SMT)·(ba), (SMT)·(4-mba)·(H_2O) co-crystallizes as the imidine tautomer and is sustained by a $R_2^2(8)$ arrangement of (imidine) N—H···O (carboxy) and (acid) O—H···N (imidine) hydrogen bonds. The water molecule effectively interrupts the formation of expected N—H···O_2S interactions, instead generating (hydroxyl) O—H···O_2S (sulfoxide) and (aniline) N—H···O (hydroxy) interactions that alternate in a 1D polymer $C_2^2(10)$ chain (Figure 76). The amide N–H also participates in (amide) N—H···O_2S (sulfoxide) forces.

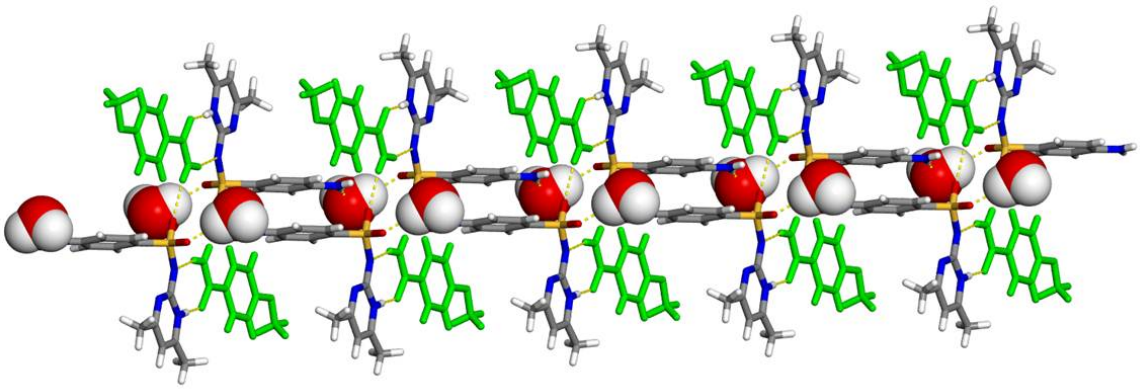

Figure 76: Perspective view of (SMT)·(4-mba)·(H_2O) highlighting primary two point (amidine) N—H···O (carboxy) and (amide) N—H···N (pyrimidine) synthon and interactions of water molecules with SMT.

2.9 Discussion

Similar to SDZ, SMT contains a mixture of hydrogen bonding motifs that make the molecule desirable for engineering co-crystals. Prior to our studies, 26 SD-based supramolecular complexes (salts, co-crystals, solvates) had been reported with SMT (63% of the SD-based complexes).[234] Of those 27 complexes, 6 exhibit the higher energy imidine tautomer. Out of the 13 new SMT-based solids we obtained, four contained the higher energy tautomer.

2.9.1 Unexpected Stoichiometry

The co-crystal involving SMT and 2-ata affords an unexpected stoichiometry. In particular, an as prepared 2:1 ratio of SMT and 2-ata co-crystallized as (SMT)·(2-ata), while giving rise to an unexpected assembly.[236] It was thought that a 2:1 ratio would engineer a co-crystal containing two $R_2^2(8)$ hydrogen bond patterns composed of (acid) O—H···N (pyrimdine) and (amidine) N—H···O (carboxy) forces per molecule of 2-ata. However, within the co-crystal two distinct two-point $R_2^2(8)$ motifs form (Figure 77). In addition to the expected (acid) O—H···N (pyrimdine) and (amidine) N—H···O (carboxy)

heterodimer, an (acid) O—H···O (carboxy) homodimer is present, giving rise to the 1:1 stoichiometry. The coexistence of a carboxylic acid homodimer in the presence of a heterosynthon is rare,[236] having only been realized in a few systems to date.[237]

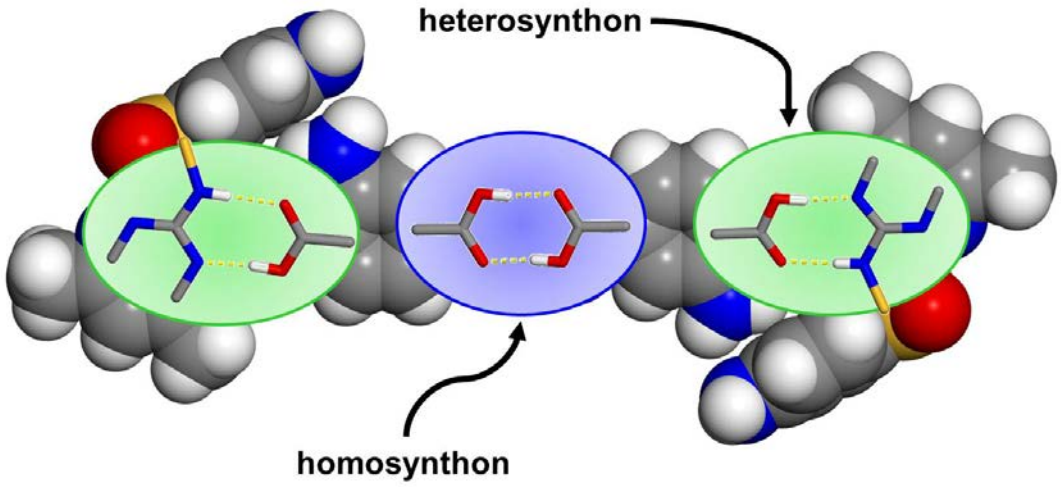

Figure 77: Schematic of (SMT)·(2-ata) highlighting heterosynthon and homosynthon interactions within the asymmetric unit.

2.9.2 Supramolecular Synthon Disruption

The co-crystal afforded with SMT and 4-mba is a hydrate (Figure 78). Interestingly enough, the water molecule interferes with the formation of the expected (aniline) N—H···O_2S (sulfoxide) interactions that are exhibited in not only all of the SDZ- and other SMT-based solids described here, but also present in over 80% of the reported SD-based solids in the CSD. Although co-crystal hydrates are commonly reported (nearing 600 in the CSD), it is relatively uncommon to observe a multicomponent system wherein complementary supramolecular synthons are engineered in a system, yet their interaction is interrupted by water molecules.[238]

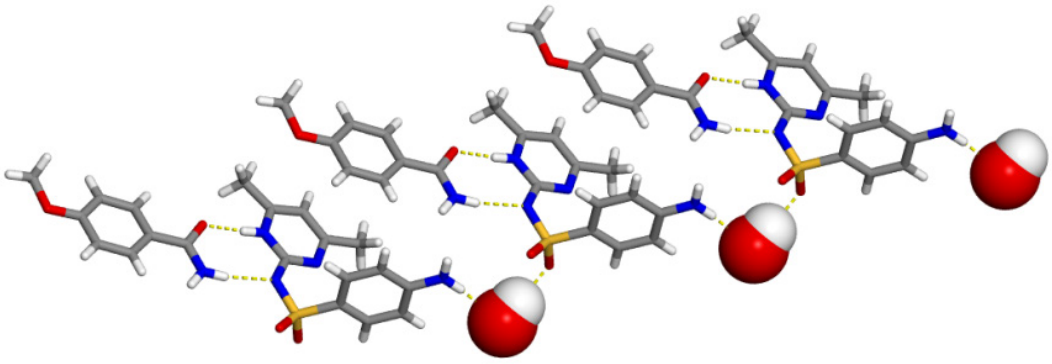

Figure 78: Perspective view of (SMT)·(4-mba)·(H_2O) highlighting water molecules engaging in synthon breakdown.

2.9.3 Geometry of the Sulfonamide

As uncovered previously, the geometry around the sulfonamide, specifically the S–N bond length, can be used to aid in assessment of salt or co-crystal formation for SDs. In addition to that, the S–N lengths of the higher energy tautomers appear to trend towards salt-like geometries. From a statistical analysis of the SD-based structures and the CSD, we observed that the salt region covered a range of 1.571 - 1.593 Å, while the co-crystal region was represented by the range of 1.594 - 1.622 Å for the imidine-based co-crystals and 1.622 - 1.673 Å for the amidine-based co-crystals (Figure 59). Extending our analysis to include our SMT-based solids, we observed that all of our SMT complexes (Table 2) lie within our previously delineated regions (Figure 79, fully-filled markers).

Table 2: Select geometrical parameters of our SMT-based complexes

Entry	Sulfa Drug	Complex Former	θ/º	d1/Å	Co-crystal/Salt
1	sulfamethazine	4-mba	119.38	1.596	Co-crystal*
2	sulfamethazine	ba	124.74	1.599	Co-crystal*
3	sulfamethazine	4-hba	121.95	1.607	Co-crystal*
4	sulfamethazine	3,5-dhba	120.59	1.620	Co-crystal*
5	sulfamethazine	2,4-dhba	126.39	1.630	Co-crystal
6	sulfamethazine	3-hba	124.44	1.637	Co-crystal
7	sulfamethazine	2-ata	126.88	1.639	Co-crystal
8	sulfamethazine	4-aba	124.35	1.640	Co-crystal
9	sulfamethazine	4-pta	125.37	1.643	Co-crystal
10	sulfamethazine	2,5-dhba	126.84	1.643	Co-crystal
11	sulfamethazine	bpa	123.37	1.644	Co-crystal
12	sulfamethazine	bpe	122.74	1.645	Co-crystal
13	sulfamethazine	bipy	120.63	1.649	Co-crystal
14	sulfamethazine	2,6-dhba	124.92	1.662	Salt†

† Denotes salt containing a cationic SD and anionic co-former (excluded from geometry study).

* Denotes complexes containing the imidine tautomer of the sulfonamide.

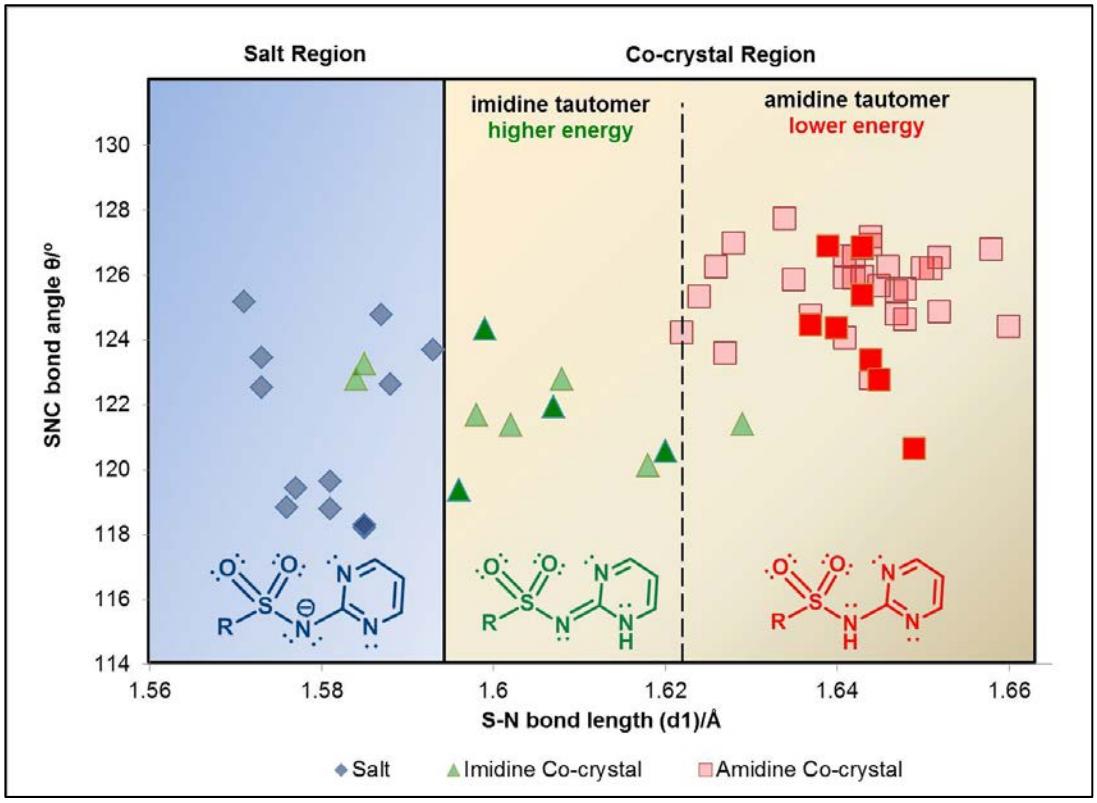

Figure 79: A revised plot of S–N bond length vs. SNC bond angle for SD-based complexes, including the SMT complexes (solid shapes) reported in this section.

2.9.4 Tautomers: Implications in Solids

The co-crystals of SDs described here (i.e. CSD and our results) reveal that the geometries of the higher energy imidine tautomers lie in between the salts and the amidine co-crystals. The positioning enables the imidine tautomers to effectively lie at the co-crystal – salt boundary. Indeed, we believe that the relative positioning of the tautomers along the salt – co-crystal continuum can be considered significant owing to the following. First, different tautomers of the same compound will exhibit different relative energies. Moreover, the differences in energy will, *de facto*, correspond to forms that exhibit different polarities.[239] From semi-empirical calculations involving SMT, for example, we have determined the imidine tautomer to exhibit a larger dipole moment (9.8

D vs. 4.9 D) than the amidine tautomer (Figure 80).[240] From a solid-state chemistry perspective, one can envisage that a higher energy (i.e. higher dipole) form of a tautomer may promote the formation of a more stable crystal lattice or a lattice akin to that of a salt. Second, molecules that exhibit tautomeric forms may be particularly useful to promote co-crystal formation since an inherent flexibility to interconvert between forms can be employed to accommodate geometric demands of different co-formers. A molecule that exhibits tautomeric forms, thus, can increase the number of possible synthons able to support a multicomponent solid. From a crystal engineering perspective, the chameleon-like behavior of tautomers, thus, enhances the crystallographic landscape[241] by increasing the number of potential synthons within a multicomponent solid, since tautomerizarion effectively converts hydrogen-bond donors to acceptors, and hydrogen-bond acceptors to donors. Moreover, the ability of tautomers to exhibit reconfigurable exteriors, or display chameleon-like behavior[242] may, in effect, be employed as a tool for the crystal engineer to increase the probability of obtaining co-crystals of a given target molecule.

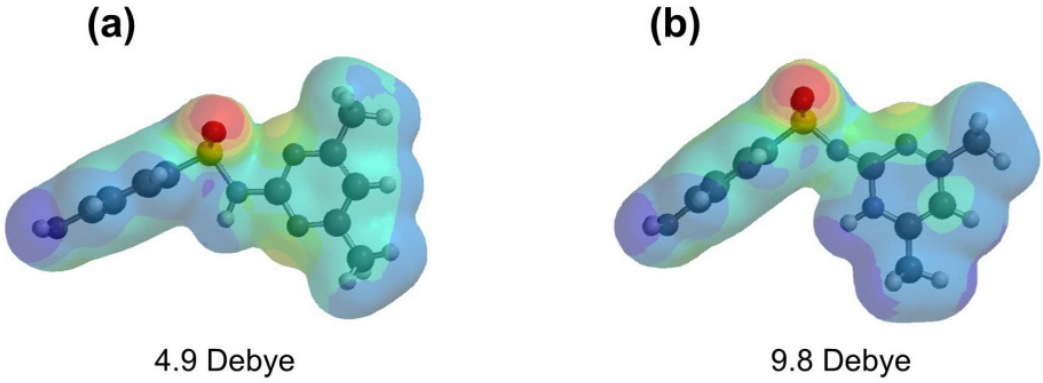

Figure 80: Electrostatic potential maps of (a) the amidine tautomer of SMT and (b) the imidine tautomer of SMT.

2.10 Conclusion

We have described 17 pharmaceutical co-crystals and 4 salts involving SDZ or SMT, with pyridines, acids, or amides as primary functional groups within the chosen co-formers. Upon analysis of the existing SD-based complexes in the CSD, as well as our SDZ-based solids, we determined that geometric differences were present upon salt and co-crystal formation. In particular, the salts display shorter S–N bonds owing to the sp^2 nature of the sulfonamide N-atom whereas co-crystals exhibit longer S–N bonds. While the imidine tautomers of SDs are co-crystals, the geometry of the imidine exclusively lies at the co-crystal – salt boundary. Moreover, we anticipate that the identification of a role of tautomers to support multicomponent solids outlined here may provide further insight on understanding and exploiting the co-crystal – salt continuum, particularly as related to co-crystal formation.[190]

CHAPTER 3. CRYSTAL ENGINEERING OF CHIRAL PHARMACEUTICAL AGENTS

3.1 Introduction

Crystal engineering,[30] a process originally used in the context of stereocontrolled-photochemical reactions,[76] has recently gained widespread interest, due to intriguing applications in solid-state and materials chemistry alike. Owing to the potential to tailor physiochemical properties (e.g. stability, bioavailability), crystal engineering has been utilized recently in the pharmaceutical industry as a method to construct novel solid forms of pharmaceutical agents (PAs). In particular, comprehending the structure-activity relationship of chiral PAs is of utmost importance for chiral resolution.[243] Resolution of chiral PAs is traditionally accomplished *via* preferential or diastereomeric crystallization. When a racemate crystallizes, three possible systems can result: (1) a true racemate forms if both enantiomers crystallize into the same unit cell and are related by symmetry; (2) a conglomerate forms if each enantiomer crystallizes separately as enantiomerically-pure crystals; (3) a solid solution forms if both enantiomers coexist in the crystal in a randomly-distributed manner. Among these systems, racemates are the most prominent, while conglomerates are rare, and solid-solutions are even rarer. To successfully identify a method for resolution, it is important to understand the chiral nature of the PA.

Recent focus in the pharmaceutical industry has led to the design and application of pharmaceutical co-crystals as a means to manipulate the chemical and physical properties of PAs *via* co-crystallization with a co-crystal former (CCF).[78, 84, 174] The resulting multicomponent crystals are held together by noncovalent interactions (e.g. hydrogen bonding, π-π stacking). Co-crystallization has been shown to alter properties such as solubility, melting point, and stability in a way comparable to ionic salts and amorphous solids of APIs.[78]

Pharmaceutical co-crystals of chiral APIs and achiral CCFs can crystallize as three different systems in a manner analogous to that of the racemate crystals (Figure 81).[244] Similarly, a co-crystal racemate forms if both enantiomers of the chiral API and CCF co-crystallize in the same unit cell, with the opposite-handed enantiomers related by symmetry. A co-crystal conglomerate can form if an enantiomer of the API and a CCF co-crystallizes into enantiomerically-pure co-crystals owing to spontaneous resolution. If both API enantiomers are present in the co-crystal in a less-defined stochastic manner, a solid solution forms.[244] Owing to the large quantity of marketed APIs (>70%) that are chiral, the understanding of such interplay between structure and properties is of fundamental importance for the application of co-crystallization to chiral APIs.

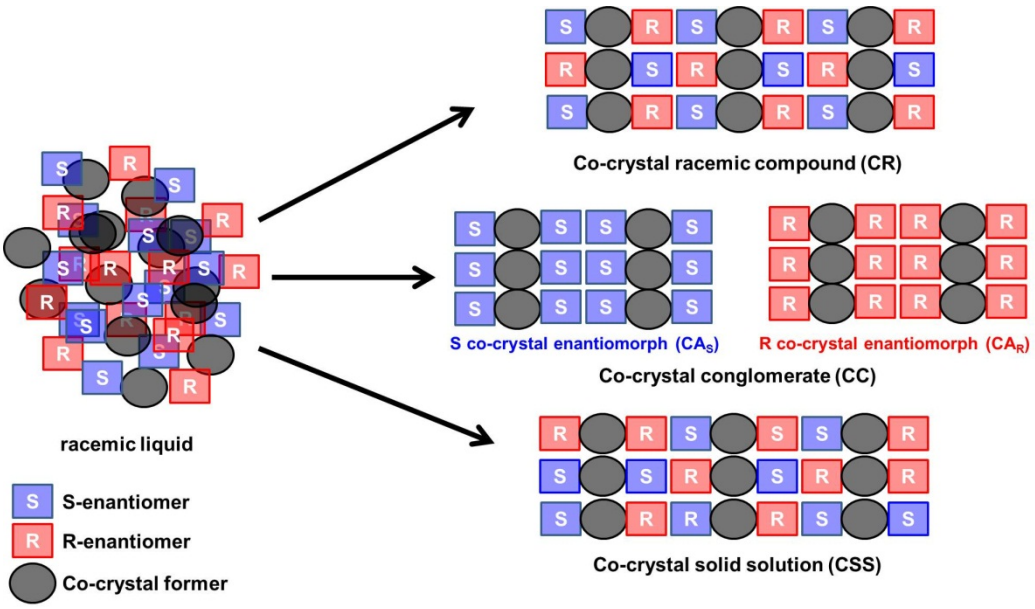

Figure 81: Possible results from the co-crystallization of a chiral pharmaceutical agent (PA) and achiral co-crystal former (CCF).

Ibuprofen solid forms are well-studied in the context of crystallization, with the structures and thermodynamic data corresponding to the formation of a racemic compound.[245] The sodium salt of ibu, however, crystallizes as a stable conglomerate.[246]

Owing to the ability to influence solid-state behavior *via* subtle structural changes, it is important to study the influence of chirality upon crystallization for different solid forms. Recently, we demonstrated that co-crystals of ibu and 4,4'-bipy[247] crystallize as a solid solution.[244] Here, we extend the scope of our study to structurally-related bipyridines comprising: (*E*)-1,2-bis(4-pyridyl)ethylene (bpe), 1,2-bis(4-pyridyl)ethane (bpeth), 1,2-bis(4-pyridyl)acetylene (bpa), (1*E*, 3*E*, 5*E*)-1,6-bis(4-pyridyl)hexatriene (bph), (*E*)-1,2-bis(2-pyridyl)ethylene (2,2′-bpe), and (*E*)-[1-(4-pyridyl)-2-(2-pyridyl)]ethylene (2,4-bpe) as co-formers in the preparation and characterization of chiral pharmaceutical co-crystals. Co-crystal mixtures of varying R:S ratios of ibu were used to gain insight into the solid-state behavior of each system. Our goal was to assess the robustness of the synthons and examine the crystallization behavior of the resulting co-crystals, and also determine if the geometry of the co-former, as well as the substitution on the pyridine ring, can influence the solid-state behavior of ibu (Figure 82). The results portrayed in this chapter can be particularly important in the field of crystal engineering, wherein constructing a system that achieves predictable structures and/or properties remains a noteworthy struggle.

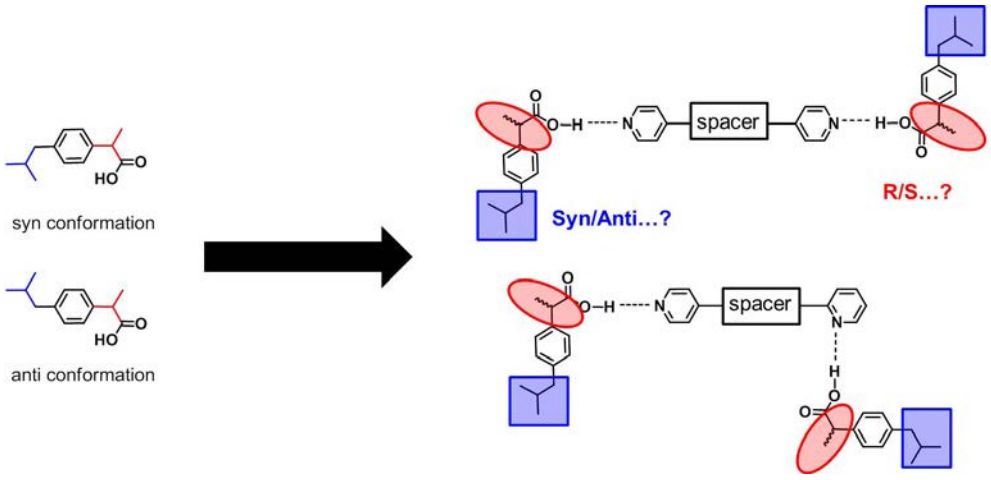

Figure 82: Subtle differences within each co-crystallization attempt that could lead to various solid-state behaviors.

3.2 Experimental

Ibu (98%), bipy (97%), bpe (98%), bpeth (97%), and 2,4′-bpe (97%) were purchased from Sigma Aldrich Chemical (St. Louis, MO, USA). 2,2′-bpe (97%) was purchased from TCI America (Portland, OR, USA). 2,4-bpe and bpeth were sublimed prior to use. bpa and bph were synthesized according to a literature procedure. Acetonitrile (99.9%) and N,N-dimethylformamide (99.9%) were obtained from Fisher Scientific (Pittsburgh, PA, USA), while ethanol (99.98%, absolute grade) was obtained from Pharmco-AAPER (Brookfield, CT, USA). Single crystals of each solid were obtained by slow evaporation from solution. In a typical procedure, (±)-ibu (48 mmol) and pyridine (0.5 mol. eq.) were dissolved in EtOH, CH_3CN, or 1:1 DMF:CH_3CN (5.0 - 7.0 mL) at 70 °C. Single crystals suitable for X-ray diffraction were grown upon cooling each solution to ambient temperature and then allowing the solvent to slowly evaporate. Single crystals formed within a period of approximately 2 - 5 days. For the enantiopure co-crystals, (+)-ibu was used as the starting material and EtOH was used as the solvent.

Single crystal X-ray diffraction experiments were performed on a Bruker SMART system equipped with an APEX CD camera. Data was collected at 173 K with graphite-monochromated Mo Kα radiation (λ = 0.71073 Å). Data was collected in four sets using ω-ϕ scans with ω steps of 0.5 and ϕ steps of 90 . A total c collected with 20 s frame exposures. Data was processed using SaintPlus.[196] Corrections for Lorentz polarization effects were applied. Absorption was negligible. All structures were solved using direct methods that yielded the non-hydrogen atoms. All presented hydrogen atoms were located in Fourier-difference electron density maps. All non-hydrogen atoms were refined anisotropically. Hydrogen atoms associated with carbon atoms were refined in geometrically constrained riding positions. Hydrogen atoms associated with oxygen atoms were included in the located positions. Refinement was achieved with the use of SHELX-97.[199] The details of the structural analysis of all solids are summarized in Tables A-7 and A-8.

Our recently reported SMPT-based suspension method[146] was used to screen for co-crystals of achiral pyridines with either (±)-ibu or (+)-ibu. In a typical screening experiment, ibu (2.0 mmol) was mixed a pyridine co-former (1.0 mmol) and a minimal volume of solvent to form a slurry. The resulting suspension was either vortexed using an analog vortex mixer (VWR VM-3000) or sonicated using a sonicator bath (Branson 2510R-DTM) to facilitate the SMPT process. The slurries were continually agitated and equilibrated for at least 24 hours at ambient conditions to ensure complete conversion. Each suspension was then filtered and the residual solid was examined by powder X-ray diffraction (PXRD) and analyzed in comparison to the individual component PXRDs. All new crystalline phases were studied further using single crystal X-ray diffraction.

For the co-crystal systems with bpe and bpeth, the powder X-ray diffractograms were obtained using a G3000 (Inel Corp. Artenary, France) diffractometer equipped with a curved position sensitive detector and parallel beam optics. The instrument was operated with a copper-anode tube (1.5kW, fine focus) at 40kV and 30mA. An incident-beam germanium monochrometer was utilized to obtain monochromatic $K_{\alpha 1}$ irradiation. The diffractometer was calibrated using the attenuated direct beam at 1° intervals. The calibration was established using a Si standard reference material (i.e. NIST 640c). The instrument was operated using the Symphonix[248] program, whereas the data was analyzed using the Jade[249] software (version 6.5). The samples was loaded onto an aluminum sample holder and leveled with a glass slide. The remaining co-crystal systems powder X-ray data were collected on a Bruker D-5000 diffractometer equipped with a Bruker SOL-X energy-sensitive detector using Cu$K_{\alpha 1}$ radiation (λ = 1.54056 Å). Representative PXRD overlays for co-crystal systems using bpe or bpeth as co-formers are displayed below (Figure 83).

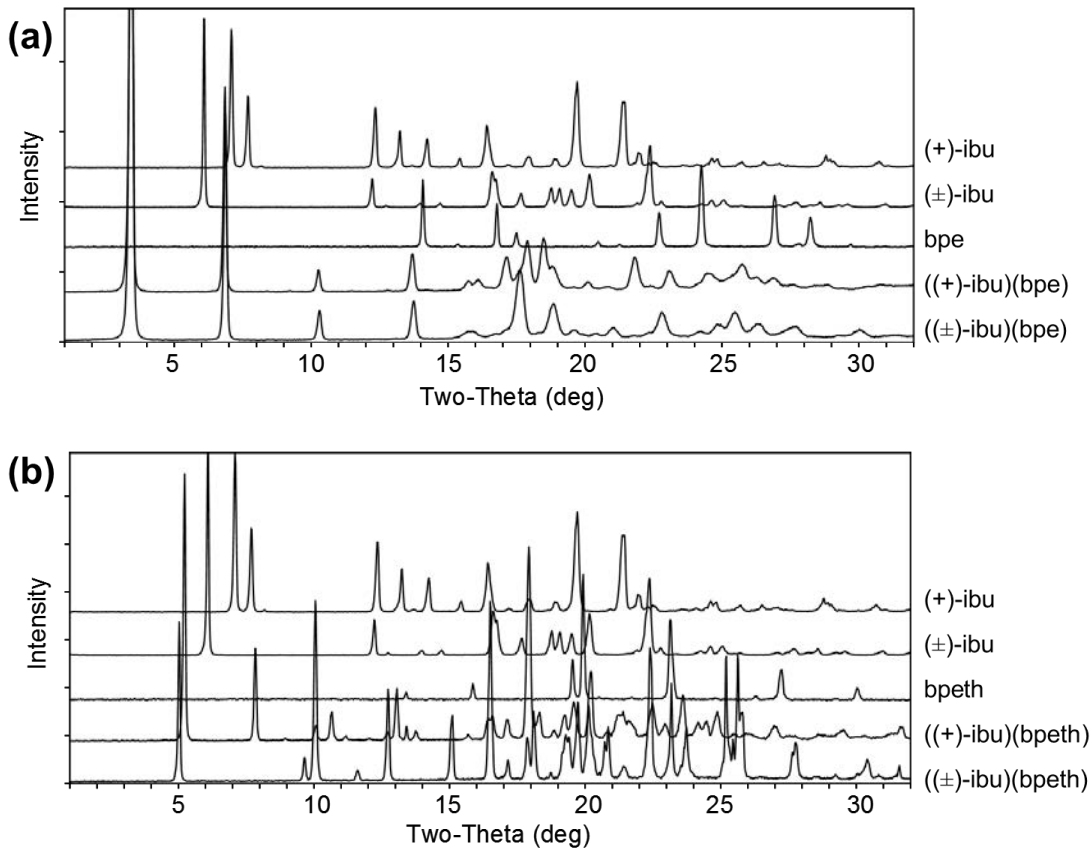

Figure 83: Powder X-ray diffraction patterns of solids isolated from SMPT co-crystal screening of ibu and (a) bpe; (b) bpeth.

Mixtures of varying enantiopurities were prepared by grinding a mixture of 2((±)-ibu)·(co-former)) and 2((+)-ibu)·(co-former)) co-crystals. Mixtures were prepared that varied from 50% to 100% S composition. DSC was performed using either a TA Instruments DSC Q2000 or Q200 under a 50 mL min^{-1} N_2 purge. Samples were scanned at 1 °C min^{-1} in Tzero aluminum hermetic pans. The temperatures and melting enthalpies were calibrated against an indium standard. The data reported are the average of 3-5 measurements unless otherwise noted.

3.3 Results

Seven new co-crystals of ibu (six with racemic ibu) were obtained using SMPT-based screening with the selected co-formers. The crystal structure of each solid was determined using single-crystal X-ray diffraction. Of the six co-crystal formers, two were fully characterized *via* construction of melting point phase diagrams as solid-solution co-crystals, while another was characterized as a co-crystal conglomerate.

(1) 2((±)-ibu)·(bpe). Co-crystal 2((±)-ibu)·(bpe) crystallizes from acetonitrile in the achiral triclinic space group, $P\bar{1}$ with two molecules of ibu and one molecule of bpe in the asymmetric unit. The compounds form a discrete three-component assembly sustained by (acid) O—H···N (pyridine) hydrogen bonds [O···N distances (Å), 2.651(5) and 2.665(5)] between each ibu and bpe. The three-component assembly adopts two different conformations (Figure 84), wherein the isobutyl units of each ibu within the assembly are either *syn* or *anti* to the hydrogen-bonding acid group. For both conformations, the two pyridine rings of bpe are coplanar. The components assemble with adjacent assemblies interacting *via* (pyridine) C—H···O (carboxy) (3.732(7) and 3.689(7) Å) and (alkyl) C—H···N (pyridine) hydrogen bonds on the order of 3.17 Å.

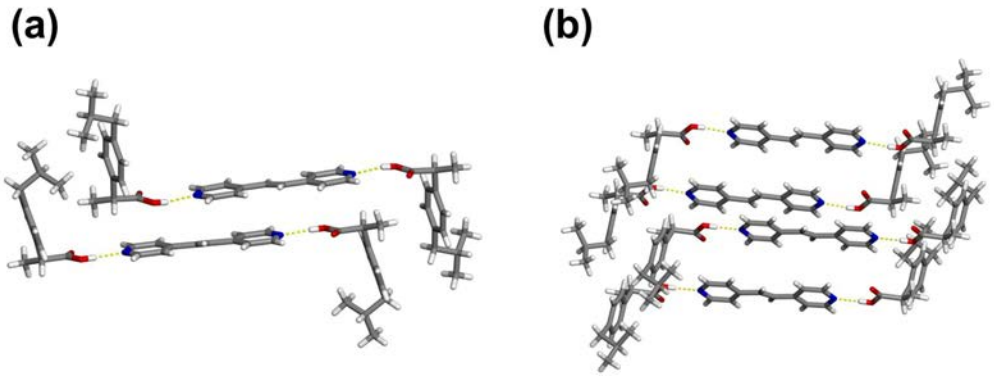

Figure 84: Views of 2((±)-ibu)·(bpe) highlighting: (a) two different three component assemblies and (b) extended packing.

(2) 2((+)-ibu)·(bpe). (+)-Ibuprofen and bpe co-crystallize from ethanol in the chiral monoclinic space group, $P2_1$ with four molecules of (+)-ibu and two molecules of bpe in the asymmetric unit. The three-component assembly is sustained by (acid) O—H···N (pyridine) hydrogen bonds [O···N distances (Å), 2.670(5), 2.621(5), 2.673(6), and 2.618(5)]. Similar to the racemic co-crystal, the assembly adopts two different conformations (Figure 85a), wherein the isobutyl units are *syn* or *anti* to the acid (Figure 73a). The two pyridines of each bpe are twisted 7.28º and 4.88º from coplanarity for the *syn* and *anti* assemblies, respectively. The *b* and *c* axis of the enantiomeric pure co-crystal can be respectively considered the *c* and *b* axis of the racemate, with the *b* axis being nearly double in length; thus, the cell volume is approximately double that of the racemate co-crystal. The components assemble such that 1D chains form along the *a* axis (Figure 85), with assemblies within the chain interacting *via* (alkyl) C—H···O (carboxy) C4 chains. Adjacent chains interact *via* (pyridine) C—H···O=C (carboxy) forces in a $C_2^2(11)$ pattern, as well as (alkenyl) C—H···O (carboxy), and (alkyl) C—H···O=C (carboxy) hydrogen bonds on the order of 3.14 - 3.73 Å.

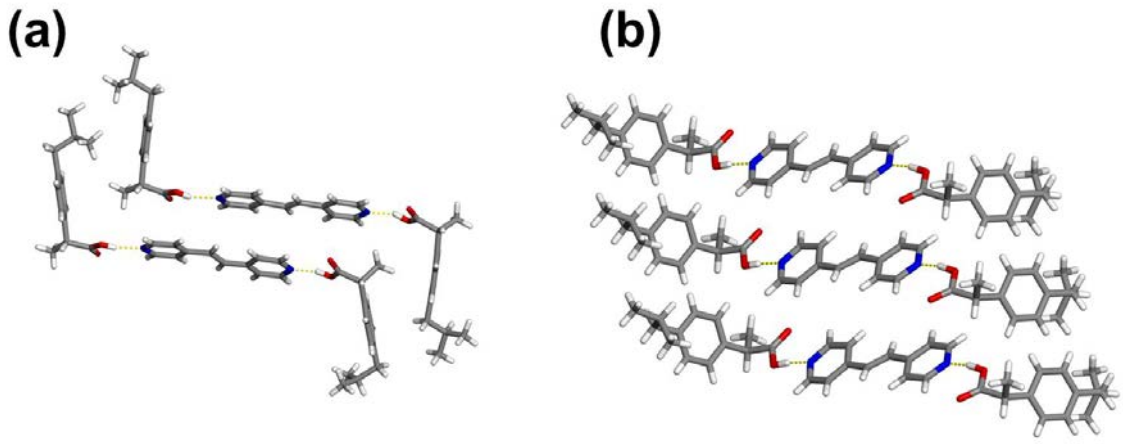

Figure 85: Views of 2((+)-ibu)·(bpe) highlighting: (a) three component assembly and (b) extended packing.

(3) 2((±)-ibu)·(bpeth). Ibu and bpeth co-crystallize from acetonitrile in the achiral triclinic space group, $P\bar{1}$ with one molecule of bpeth and two molecules of ibu in the asymmetric unit (Figure 86a). The three-component assembly is sustained by (acid) O—H···N (pyridine) hydrogen bonds [O···N distance (Å), 2.654(3)] between each ibu enantiomer and bpeth. The three-component assembly adopts one conformation, wherein the isobutyl units of ibu are *anti* to the hydrogen-bonding acid (Figure 86b). Within each assembly, the pyridines assume a conformation similar to that of pure bpeth, wherein the pyridines lie nearly orthogonal to the ethane (dihedral angle = 77.76º). Additionally, the three components assemble to form chains with adjacent assemblies interacting *via* C—H···O (carboxy) hydrogen bonds (3.690(3) Å).

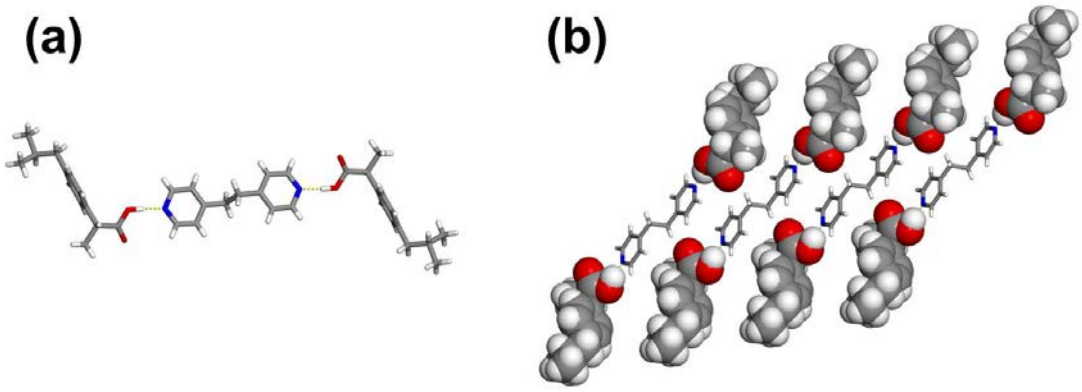

Figure 86: Views of 2((±)-ibu)·(bpeth) highlighting: (a) three component assembly and (b) extended packing.

(4) 2((±)-ibu)·(bph). Crystallization of ibu and bph from 1:1 DMF:acetonitrile (v/v) results in co-crystals of the formulation 2((±)-ibu)·(bph). The two components crystallize in the achiral triclinic space group, $P\bar{1}$ with one molecule of bph and two molecules of ibu in the asymmetric unit (Figure 87). The three-component assembly is sustained by (acid) O—H···N (pyridine) hydrogen bonds [O···N distance (Å), 2.6239(16)] between each ibu enantiomer and bph. The three-component assembly adopts one

conformation, similar to ((±)-ibu)$_2$(bpeth), wherein the isobutyl units of ibu are *anti* to the hydrogen-bonding acid (Figure 87). Additional interactions, such as (pyridine) C—H···O (carboxy) hydrogen bonds in a $C_2^2(11)$ arrangement, and π···π interactions contribute to the overall structure.

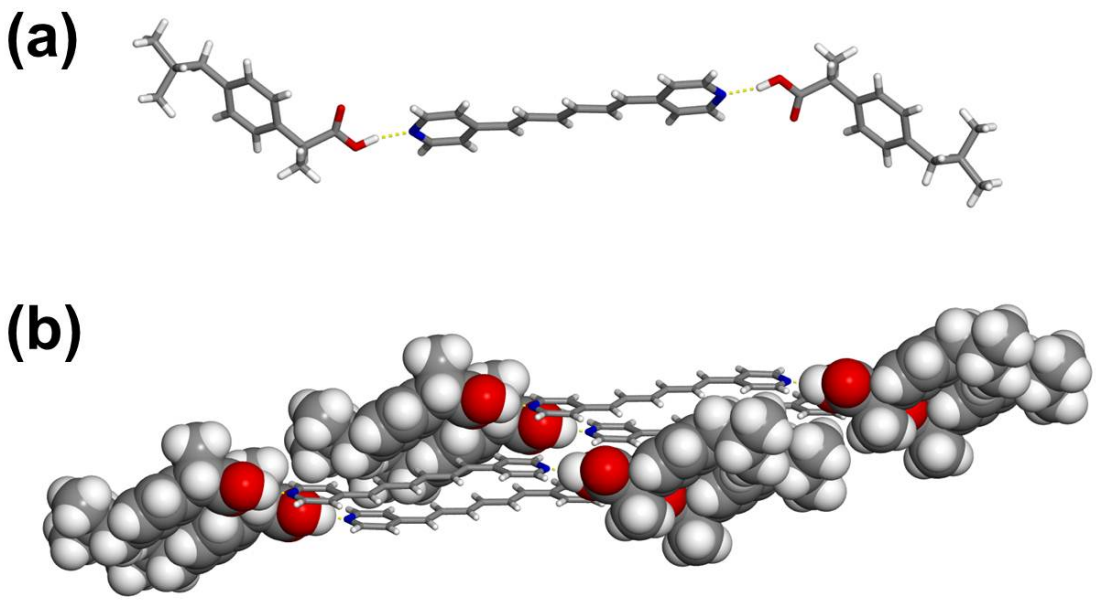

Figure 87: Views of 2((±)-ibu)·(bph) highlighting: (a) three component assembly and (b) extended packing.

(5) 2((±)-ibu)·(2,2′-bpe). Ibuprofen and 2,2′-bpe co-crystallize from ethanol in the monoclinic space group, P2$_1$/c with one molecule of ibu and one molecule of 2,2′-bpe in the asymmetric unit. The discrete three-component assembly is sustained by (acid) O—H···N (pyridine) hydrogen bonds [O···N distance (Å), 2.6774(15)]. The co-crystal assembly adopts one conformation with the isobutyl units arranged *anti* to the acid (Figure 88). The components assemble with additional (alkenyl) C—H···O (carboxy) and (alkyl) C—H···π (pyridine) hydrogen bonds, as well as π···π stacking between pyridines.

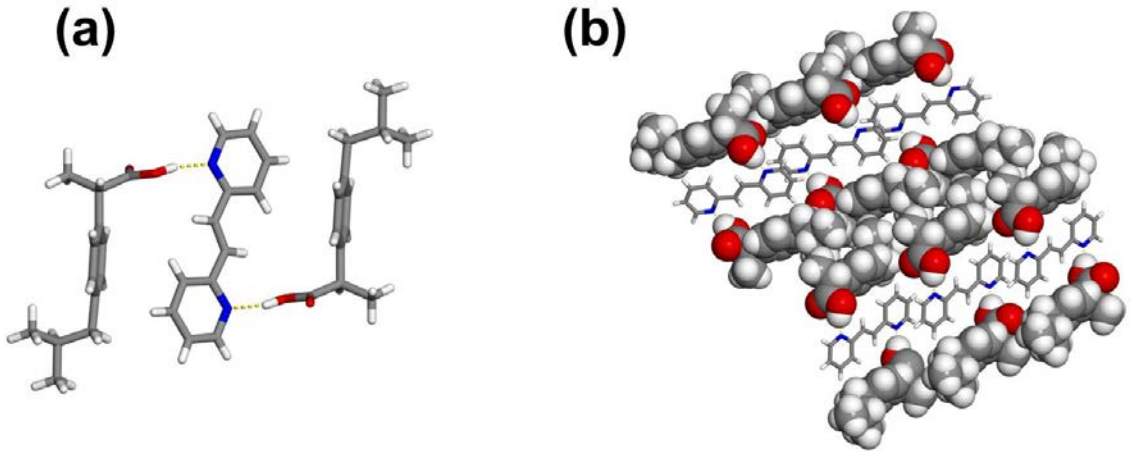

Figure 88: Views of 2((±)-ibu)·(2,2′-bpe) highlighting: (a) three component assembly and (b) extended packing.

(6) 2((±)-ibu)·(bpa). Co-crystal 2((±)-ibu)·(bpa) crystallizes from 1:1 DMF:acetonitrile (v/v) in the monoclinic space group, C2/c with one molecule of ibu and one molecule of bpa in the asymmetric unit. The compounds form a discrete three-component assembly sustained by (acid) O—H···N (pyridine) hydrogen bonds [O···N distance (Å), 2.6501(13)] between each ibu and bpe (Figure 89). Surprisingly, unlike all previous structures, ((±)-ibu)$_2$(bpa) crystallizes with chiral assemblies, such that both ibu molecules within a three-component assembly are of the same handedness. The three-component assembly adopts a single conformation wherein the isobutyl units of each ibu within the assembly are *anti* to the hydrogen-bonding acid group. Additionally, the two pyridine rings of bpa are twisted in a semi-herringbone manner, as the rings lie 44.5° apart. The components assemble with adjacent assemblies interacting *via* (pyridine) C—H···O (carboxy) (3.2047(15) Å) interactions that are arranged in a $C_2^2(11)$ motif.

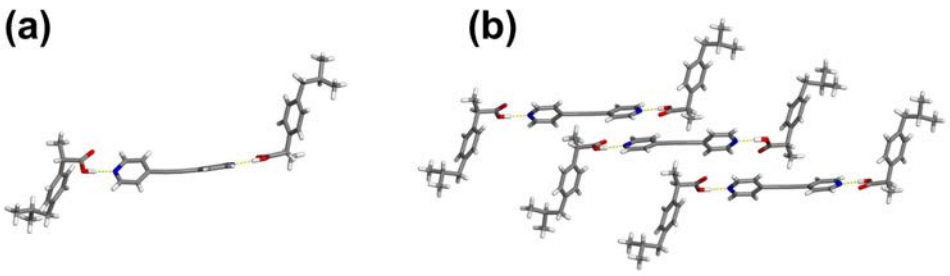

Figure 89: Views of 2((±)-ibu)·(bpa) highlighting: (a) three component assembly and (b) extended packing.

(7) ((+)-ibu)·(2,4-bpe). Co-crystallization of a 2:1 molar ratio of (±)-ibu and 2,4-bpe in ethanol afforded a co-crystal of 1:1:1 stoichiometry. The components crystallize in the monoclinic space group $P2_1$. The asymmetric unit consists of one molecule of (+)-ibu and one molecule of 2,4-bpe with the isobutyl unit of ibu in the *syn* conformation. The two-component assembly is sustained by a single (acid) O—H···N (pyridine) hydrogen bond [O···N distance (Å), 2.6213(16)] exclusively at the 4-pyridyl terminus, leaving a non-hydrogen bonding 2-pyridine unit (Figure 90). The non-hydrogen bonding pyridine participates in weaker C—H···N interactions with adjacent 4-pyridyl moieties ($d_{C—H···N}$ = 3.568 Å). The components assemble with additional (alkyl) C—H···N (pyridine) forces, as well as π···π stacking between pyridyl and alkenyl groups.

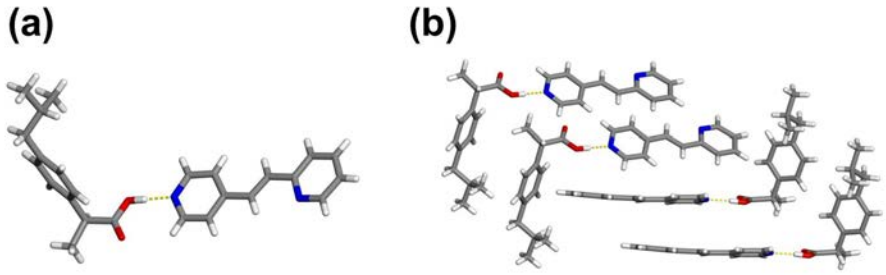

Figure 90: Views of ((±)-ibu)·(2,4-bpe) highlighting: (a) two component assembly and (b) extended packing.

3.4 Solid-State Behavior

Co-crystals of chiral APIs with achiral CCFs can form three distinct types of co-crystals: racemates, conglomerates, and solid-solutions. The crystal types were first characterized by Roozeboom in 1899, with the construction of melting point phase diagrams (Figure 91).[250] A further classification was also described for different types of solid solutions, whereby the melting points of the solid solution and the racemate dictate which sub-category they fall into. Previously, we reported that co-crystals formed between ibu and 4,4'-bipy form type II solid solutions, with a maximum melting point at the racemic composition. The 2(ibu)·(4,4'-bipy) co-crystals not only lacked a eutectic melting that would correspond to the formation of a racemate, but the co-crystal melting points decreased as the amount of S-enantiomer increased, signaling the formation of a co-crystal solid solution.

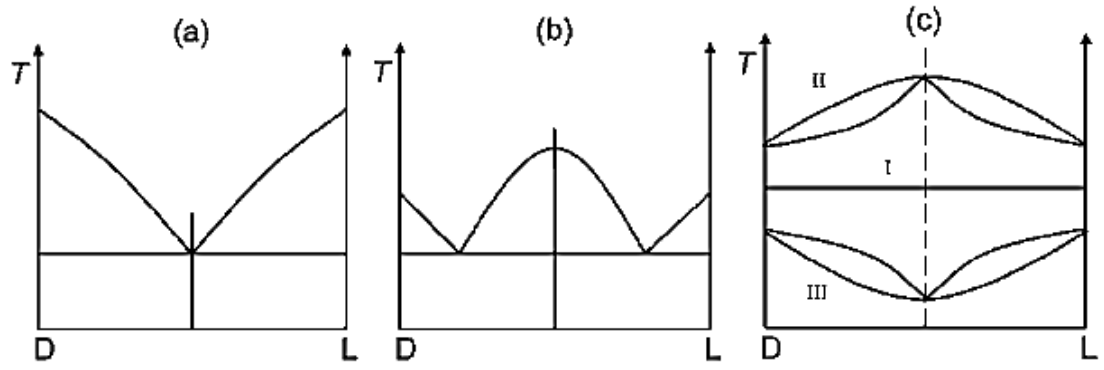

Figure 91: Melting point phase diagrams illustrating (a) conglomerate systems (b) racemates and (c) solid solutions.

3.4.1 Solid Solution Co-crystals

To evaluate the solid-state behavior of the co-crystals of ibu with structurally-related CCFs, 4,4'-bpe, and 4,4'-bpeth, we examined the melting point of the co-crystal mixtures with differing levels of enantiomeric purity (i.e. total sample compositions of

50% to 100% S). Based on the melting endotherms and DSC onsets obtained, a melting point phase diagram was constructed for each system (solid lines, Figure 92a and 92b, respectively). Each phase diagram is also overlaid with the calculated phase diagrams for racemate- and conglomerate-forming systems (dashed lines). In both systems, the melting onset decreases with gradual increases in X_S, and the melting point behavior mirrors that of a solid-solution-forming system. Indeed, analogous to 2(ibu)·(4,4'-bipy), the highest melting point for both co-crystals exists at $X_S = 0.5$, or at the racemic composition; thus, both systems demonstrate Roozeboom type II behavior.[250]

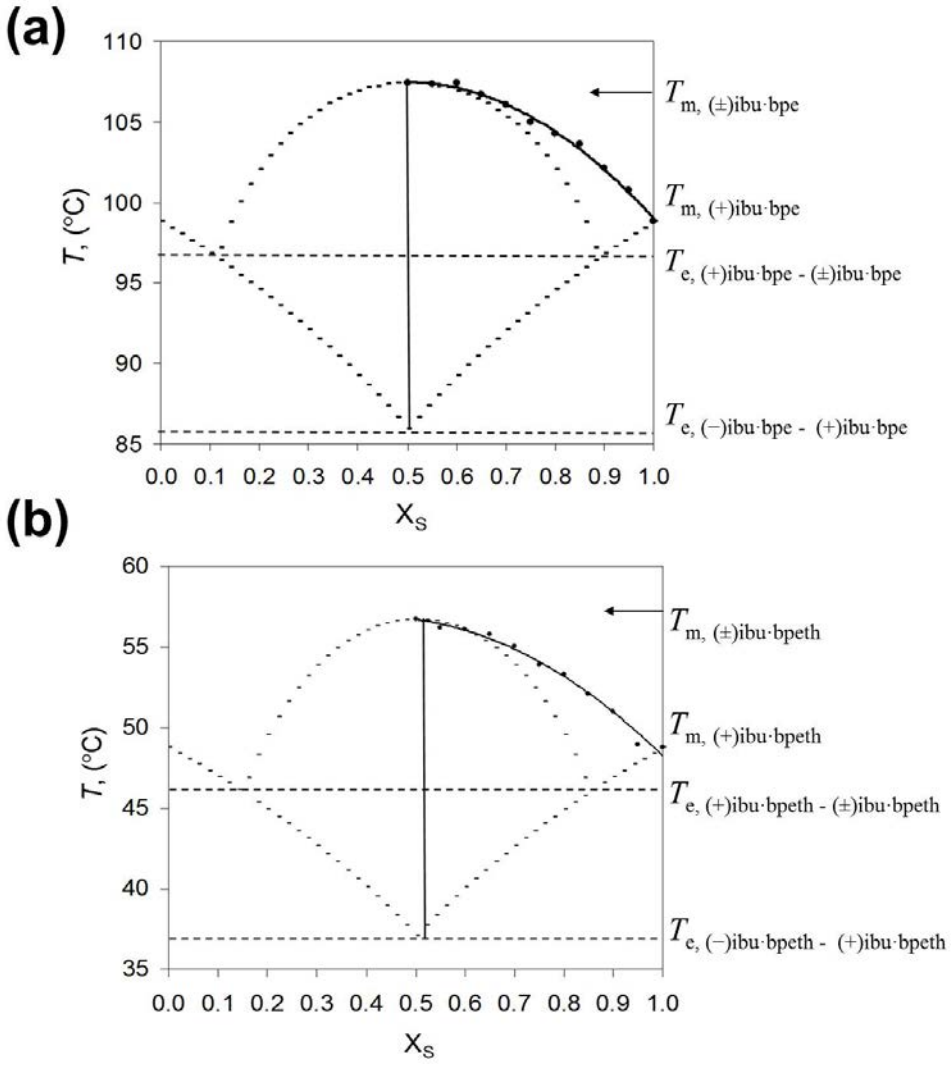

Figure 92: Melting point phase diagrams obtained for (a) 2(ibu)·(bpe) co-crystal system and (b) 2(ibu)·(bpeth) co-crystal system.

3.3.2 Conglomerate Co-crystals

Upon observing the structure of ((±)-ibu)·(2,4-bpe), we noticed that the 1:1 ratio of the two components was also consistent with the formation of enantiopure co-crystals (i.e. each crystal only contains one enantiomer in the unit cell). To evaluate the solid-state behavior of these co-crystals, we prepared physical mixtures of each type of co-crystal (i.e. co-crystals formed using (±)-ibu and co-crystals prepared with (+)-ibu), so as

to have mixtures that varied in total S composition. Based on the melting endotherms and DSC onsets (Figure 93) obtained for samples of varying enantipurities, the solid-state behavior was evaluated for the (ibu)·(2,4-bpe) co-crystal system. In contrast to the previous systems, the melting onset steadily increases with gradual increases in X_S, while two separate endotherms can be observed as the X_S increases. This behavior, combined with the obtained melting point behavior mirrors that of a conglomerate-forming system.

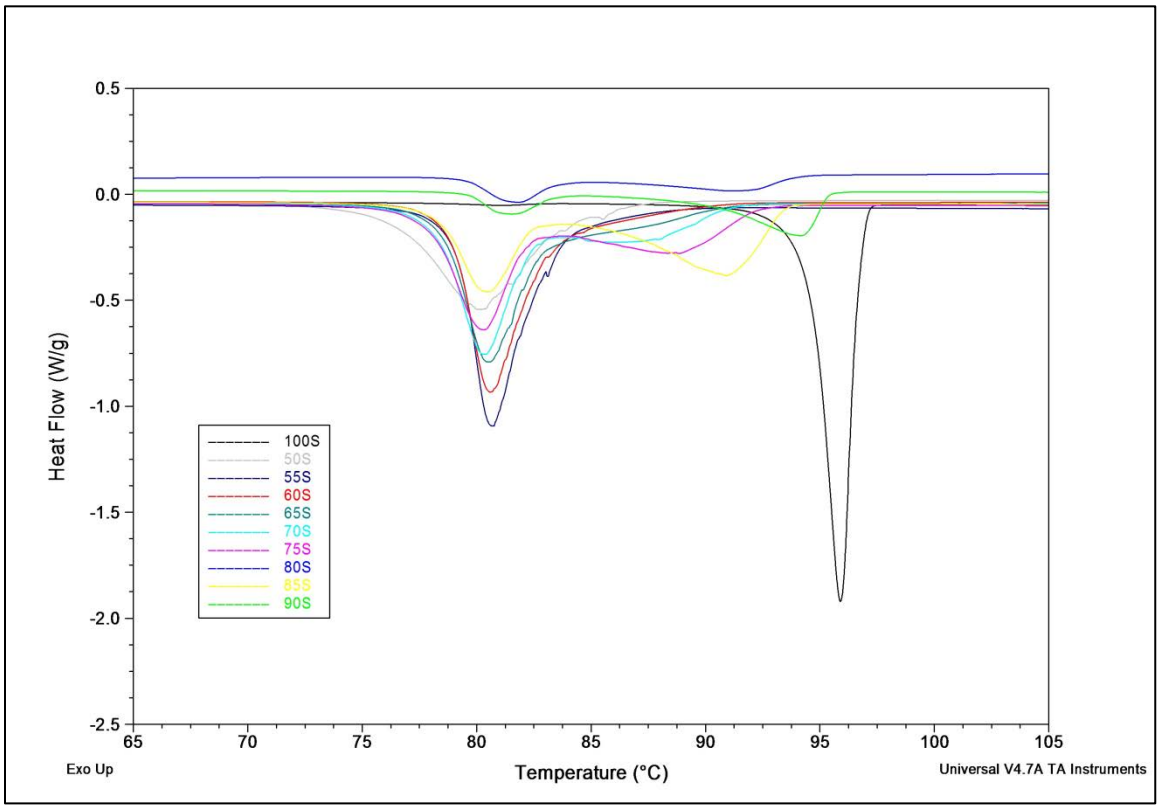

Figure 93: Thermal behavior of (ibu)(2,4-bpe) co-crystal system: DSC onsets obtained for samples with differing enantiopurities.

3.4 Conclusion

In this chapter, we have reported three additional co-crystal systems: 2(ibu)·(bpe), 2(ibu)·(bpeth), and (ibu)·(2,4-bpe). Thermal studies demonstrate that

enantiomeric mixtures of 2(ibu)·(bpe) and 2(ibu)·(bpeth) behave as solid solutions. In addition, both co-crystal systems fall into the Roozeboom type II sub-category, analogous to that of the previously reported co-crystal system of ibu with 4,4'-bipy. Thermal studies on the co-crystal obtained with the unsymmetrical system 2,4-bpe reveal that the system exhibits conglomerate-forming tendencies. To our knowledge, this is the first report of a co-crystal conglomerate system.

The combined observations suggest that ibu co-crystals with symmetrical bipyridines exhibit a rather predictable solid-state behavior, regardless of the nature (i.e. rigidity or flexibility) of the CCF, whereas the addition of an unsymmetrical achiral co-former with a subtle structural difference exhibits less predictable behavior. In this context, these results are a significant addition to the field of crystal engineering, where there remains a considerable intellectual challenge towards designing novel materials with specific architectures and/or expected properties.

CHAPTER 4. TOLERANCE OF SOLID-STATE REACTIVITY TO THE INTRODUCTION OF ADDITIONAL FUNCTIONALITIES

A portion of this chapter was published in *Angewandte Chemie, International Edition*, and is adapted with permission from John Wiley and Sons, Copyright 2012 [E. Elacqua, P. Kaushik, R. H. Groeneman, J. C. Sumrak, D.-K. Bučar, L. R. MacGillivray, *Angew. Chem.* **2012**, *124*, 1061; *Angew. Chem. Int. Ed.* **2012**, *51*, 1037.].

4.1 Introduction

The principles of crystal engineering have been reliably used to facilitate reactivity in the organic solid state and synthesize target molecules by design.[5] Previous exploits utilizing a combinatorial[58] template-directed approach[77] have resulted in the photodimerization of disubstituted olefins that are, almost invariably, planar and studded with a pair of either hydrogen bond donors or hydrogen bond acceptors,[76] with stilbazole-based molecules being notable exceptions.[93-94] In addition to involving hydrogen bonding motifs, it is often desirable to have olefins that exhibit somewhat predictable molecular recognition with the template molecule. Following initial reports of the template-directed methodology, more complex olefins have been studied, generating architecturally-exquisite molecules, such as [2.2]paracyclophanes[96] and [3]- and [5]-ladderanes.[95] As a consequence of this methodology, it can be difficult to generate multifunctional products that can be utilized postsynthetically to generate intricate target frameworks.

To expand the applicability of this approach, we have attempted to incorporate olefins with different functionalities, so as to test the tolerance of the method to additional functional groups. Previous studies by us and others have resulted in the successful installation of terminal olefins[106] and halobenzene moieties,[93-94] both of which have proven to be tolerant to the self-assembly process. Intrigued by the promise of using the products of the template-driven reactions as secondary organic building blocks

to construct metal-organic frameworks (MOFs),[69] and having already achieved the synthesis of MOFs with tetrapyridyl ligands (e.g. 4,4′-tpcb),[133-136] we sought to incorporate additional groups (e.g. acids) in the self-assembly process with pyridines.

The synthesis of MOFs[69] is of interest, owing to potential application in materials science areas ranging from gas storage[251] and catalysis[252] to diagnostic imaging.[253] Significant progress with MOFs has been made by both Yaghi and Lin in the areas of gas storage and catalysis, respectively (Figure 94). Specifically, Yaghi revealed that the 3D cubic MOF $Zn_4O(BDC)_3$ (BDC=1,4-benzenedicarboxylate) (MOF-5) exhibited both hydrogen uptake at 78 K (4.5 weight percent) and 293 K (1.0 weight percent), as well as demonstrating a high thermal stability (300° to 400°C).[251] Lin has also utilized iodinated BCD-based frameworks as potential computed tomography contrast agents,[253] while also exploiting MOF structures to direct catalysis.[252] In particular, Lin demonstrated that the BINOL-based chiral MOF $[L_1Cu_2(H_2O)_2]\cdot 21DMF\cdot 12H_2O$ (where L_1 = (R)-3,3′,6,6′-tetrakis(4-benzoic acid)-1,10-binaphthyl phosphate) denoted CMOF-1 was an active catalyst for the Friedel Crafts reaction between indole and imines. CMOF-1 exhibited an ability to afford the opposite major enantiomer as the product when compared to the corresponding heterogeneous catalyst. The combined attractive work of Yaghi, Lin, and others in the MOF field has allowed for the heightened interest of both supramolecular and solid-state chemists alike in generating novel organic building blocks that could give rise to MOFs with unique connectivities and topologies, as well as different properties.

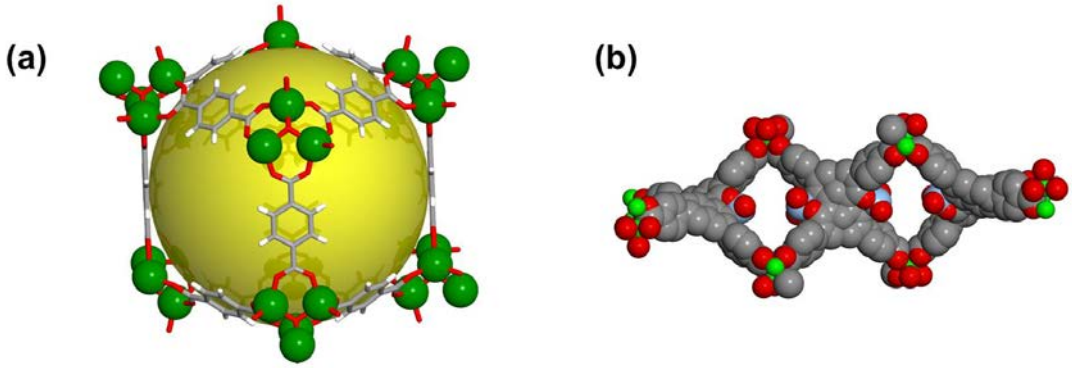

Figure 94: Structures of (a) Zn-based MOF-5 and (b) and Cu-based CMOF-1 (green = Zn, bright green = Cu, light blue = P).

4.2 'Supramolecular Regiochemistry'

A major impediment when planning reactions in the organic solid state is unpredictable structure effects of crystal packing.[83] For bimolecular reactions, reactive centers must generally lie in close proximity, being separated on the order of 4 Å.[83] To achieve the goal, chemists often functionalize reactants with groups that participate in molecular recognition[18] processes that drive the solid-state assembly process to a prerequisite geometry. The idea is to identify supramolecular synthons,[16, 29] akin to molecular synthons,[26] able to overcome effects of crystal packing and, ultimately, enable molecular synthesis by design.[5]

In this context, the use of protecting groups to achieve a particular regiochemistry is a functionalization strategy replete in solution phase synthetic organic chemistry.[254] A protecting group involves temporarily derivatizing a reactant so as to mask an organic group from hindering a desired chemical reaction by participating in an unwanted *covalent bond*. In principle, the concept of a protecting group can be applied to an organic group that participates in an unwanted *noncovalent bond*.[255] In such a setting, it may be necessary to mask an organic group from participating in an intermolecular force

that disrupts an assembly process aimed to afford a covalent bond-forming supramolecular structure.[255] The field of MOFs[69] has recently benefited from protecting group strategies that involve noncovalent bonds whereby organic groups are removed in a postsynthetic step to generate MOFs of controlled dimensionalities (Figure 95).[255] Efforts to understand and exploit such interplay between noncovalent and covalent bonds, however, remain in a stage of infancy, yet can equip chemists with powerful tools for molecular and supramolecular design. Developing such interplay is especially important in the organic solid state where structural effects of noncovalent bonds are accentuated in the closely-packed environment.[16]

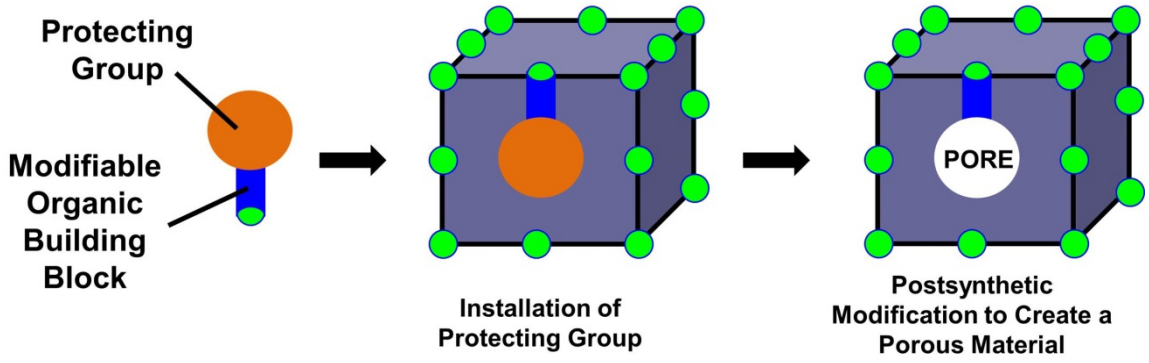

Figure 95: Application of a protecting group strategy to achieve a porous MOF.[255]

In this chapter, we introduce the concept of a protecting group strategy applied to the organic solid state (Figure 96). The strategy employs principles of supramolecular chemistry to achieve the targeted hydrogen-bond-mediated formation of C–C bonds and concomitant installation of carboxylic acid (-CO_2H) groups. We demonstrate that we can achieve a degree of 'supramolecular regiochemistry' through the use of esters as carboxylic acid protecting groups.[165]

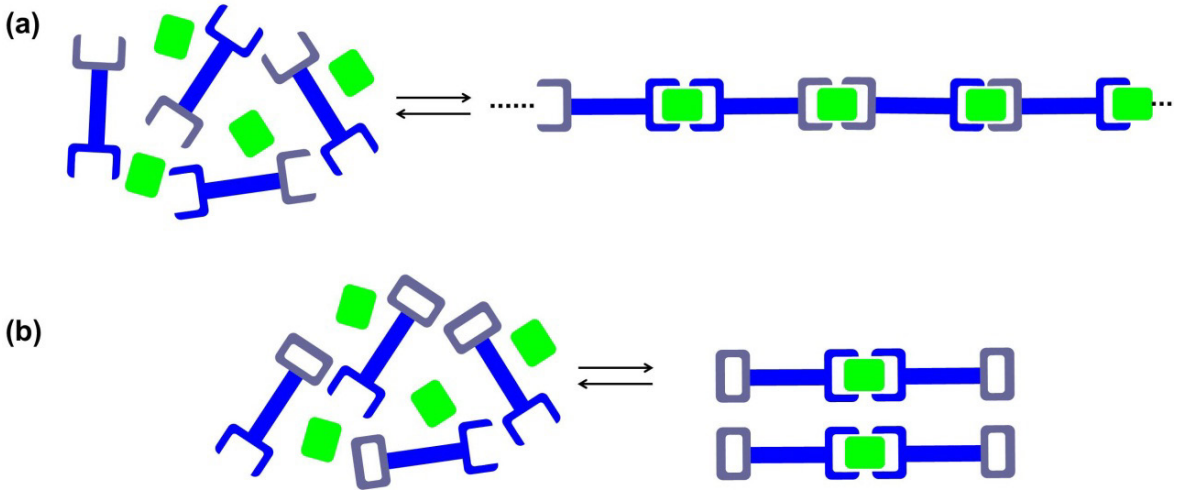

Figure 96: Protecting group strategy to achieve a targeted supramolecular framework.

4.3 Protecting Groups in Organic Solid-State Reactivity

Our interests lie in developing co-crystals based on resorcinol (res) to direct [2+2] photodimerizations in solids.[76, 77] Res acts as a ditopic hydrogen-bond-donor template that assembles and stacks olefins lined with acceptor pyridyl groups for photoreaction.[88] During studies to use res templates to direct the [2+2] cycloaddition, we developed an interest to generate head-to-head 1a (Figure 97).[124] The diacid is attractive as a building block of MOFs and related porous solids. Moreover, the presence of the 4-pyridyl groups suggested that 1a could be generated from a photodimerization of the acrylic acid 1b, wherein a res assembles 1b *via* O—H···N hydrogen bonds in a head-to-head geometry for photoreaction. To be realized, the O–H groups of a res would be required to participate in O—H···N forces and, thereby, successfully compete[256] with the O–H acid group of the olefin that directs the self-assembly of pyridine-carboxylic acids such as 1b in solids.[257] We reveal how an inability to utilize res templates to assemble 1b to form 1a can be overcome using a supramolecular protecting group strategy.[165] The strategy involves

masking the acid group[254] of 1b as an ester in 1c[258] that remains dormant in the assembly process and can be easily removed post-synthesis to generate the acid groups of 1a. The protecting strategy enables res templates to afford 1a, and a lengthened congener 2a, stereospecifically and in quantitative yield. In addition to the solid state, we are unaware of a supramolecular protecting group strategy having been applied to related hydrogen-bond-mediated syntheses developed in solution.[259] We also show how integrating a stilbene unit into a lengthened protected olefin results in strikingly enhanced reactivity that enables the generation of lengthened cyclobutane 2a, which we attribute to often overlooked pedal motion in stilbene-based solids.[260]

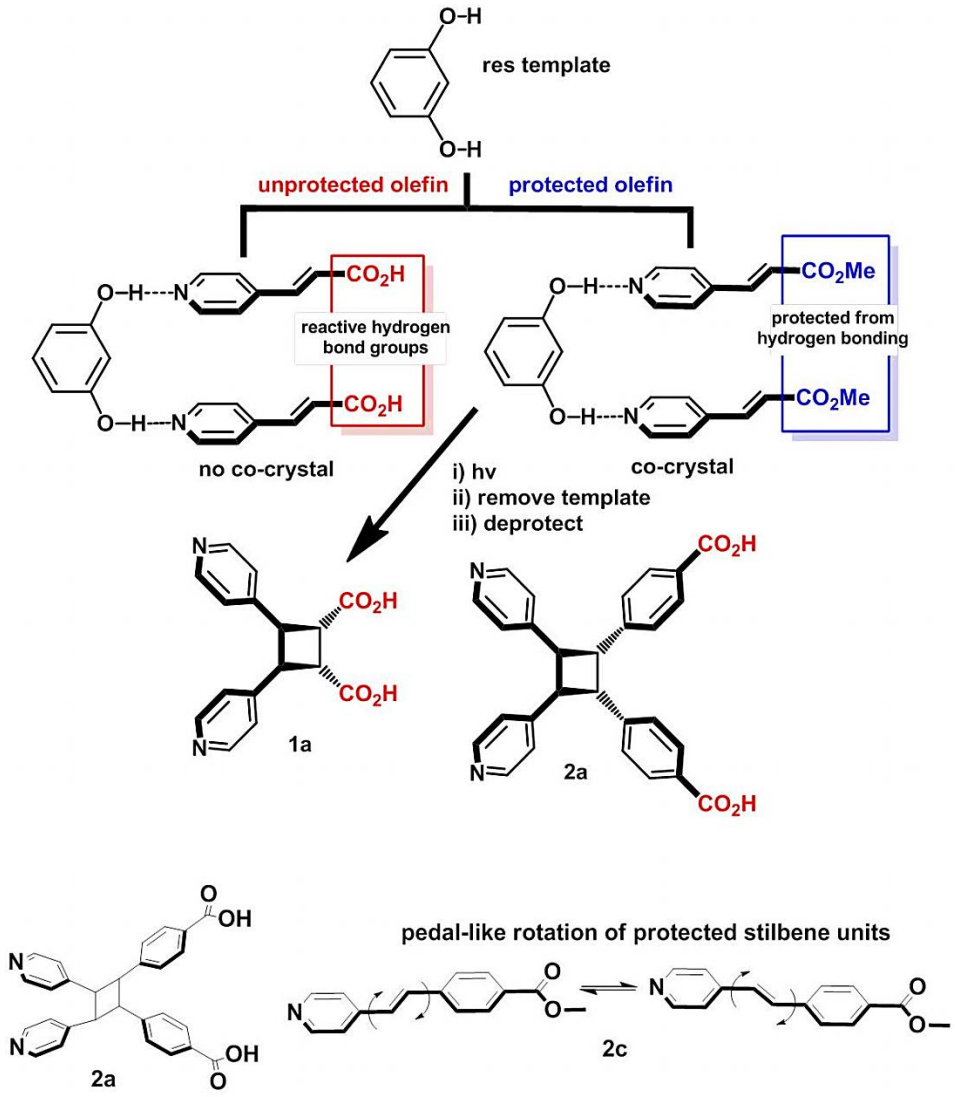

Figure 97: Supramolecuar protecting group strategy applied to the [2+2] cycloaddition of multifunctional olefins.[165]

4.4 Experimental

All reagents and solvents used were reagent grade and commercially available. Acetic anhydride, N,N-dimethylformamide (99.9%), tetrahydrofuran (99.9%), chloroform (99.8%), and methanol (>99.8%) were purchased from Fisher Scientific Company (Pittsburgh, PA, USA). 4-Carboxybenzaldehyde (97%), 4-picoline (99%), thionyl chloride (≥99%), 4-pyridinecarboxaldehyde (97%), methyl

(triphenylphosphoranylidene)acetate (98%), and dichloromethane (≥99.8%) were purchased from Sigma Aldrich Chemical (St. Louis, MO, USA). Ethanol (99.98%, absolute grade) was obtained from Pharmco-AAPER (Brookfield, CT, USA). *Trans*-3-(4-pyridyl)acrylic acid (97%) was purchased from Alfa Aesar (Ward Hill, MA, USA). All reagents were used without further purification. Substituted resorcinols were purchased commercially or synthesized *via* standard literature preparations.

^{1}H NMR spectra were collected using a Bruker Avance 300 MHz or 400 MHz spectrometer using DMSO-d_6 as a solvent. IR Spectra were recorded using KBr pellets on a Nicolet 380 single beam FT-IR spectrometer. Photoreactions were conducted using ultraviolet radiation from a 500 W medium-pressure mercury lamp in an ACE Glass photochemistry cabinet. Co-crystals were finely ground using a mortar and pestle, and then placed between a pair of pyrex glass plates. The samples were irradiated in 10-hour periods and mixed between consecutive irradiations. The product formation was monitored using ^{1}H NMR spectroscopy. Upon completion of photoreaction, the products were isolated using basic extraction with $CHCl_3$.

Single crystal diffraction data was collected on a Nonius Kappa CCD single-crystal X-ray diffractometer at both room and low temperatures using MoK_α radiation (λ = 0.71073 Å). Data collection, cell refinement and data reduction were performed using *Collect*[197] and *HKL Scalepack*/*Denzo*,[198] respectively. Structure solution and refinement were accomplished using SHELXS-97[261] and SHELXL-97,[199] respectively. The structures were solved *via* direct methods. All non-hydrogen atoms were identified from the difference Fourier map within several refinement steps. All non-hydrogen atoms were refined anisotropically. Hydrogen atoms associated with carbon atoms were refined in geometrically constrained positions with isotropic thermal parameters U_{iso}(H) = 1.5U_{eq}(C_{CH3}) and U_{iso}(H) = 1.2U_{eq}(C_{CH}). Hydrogen atoms belonging to phenolic OH groups were and refined using a riding model with isotropic thermal parameters U_{iso}(H) = 1.5U_{eq}($O_{hydroxy}$). Hydrogen atoms belonging to water molecules were indentified from the

difference Fourier and refined with isotropic thermal parameters $U_{iso}(H) = 1.5U_{eq}(O_{water})$, The details of the structural analysis of all solids are summarized in Tables A-9 through A-13. Powder X-ray data was collected on a Bruker D-5000 diffractometer equipped with a Bruker SOL-X energy-sensitive detector using CuK_α radiation (λ=1.54056 Å).

Variable temperature single crystal X-ray diffraction experiments were performed on a Rigaku SCX Mini X-ray diffractomter equipped with a Rigaku Mercury 70 CCD camera. Data were collected at 290, 250, 210 and 170 K using graphite-monochromated Mo $K_{\alpha 1}$ radiation (λ = 0.71073 Å). Data collection strategies to ensure maximum data redundancy were determined using CrystalClear.[262] Data collection, initial indexing, frame integration, Lorentz-polarization corrections and final cell parameter calculations were carried out using CrystalClear.[262] Multi-scan absorption corrections were performed using REQAB.[263] The structure was solved using direct methods and difference Fourier techniques *via* SIR92,[264] SIR2004[265] or SHELXS-97.[261] The final structural refinement included anisotropic temperature factors on all non-hydrogen atoms, with the exception of some disordered olefin carbon atoms, which could not be refined satisfactorily anisotropically. All hydrogen atoms were attached *via* the riding model at calculated positions. Structural refinement, graphics and creation of publication material were performed using SHELXL-97[199] and XSEED.[266] Space groups were unambiguously verified using PLATON.[267]

Variable temperature studies were performed on a single crystal of the desired co-crystal following this protocol: The co-crystal will be moutned and have been in the stream for one hour prior to data collection. The first collection was at 290 K. After collection, the temperature was lowered to 250 K, stabilized for 1 hour, and then collected. The temperature was then lowered to 210 K, stabilized for 1 hour, and then a third collection took place. The last collection was conducted after the temperature had been lowered to 170 K and stabilized for one hour.

4.4.1 Synthesis of (*E*)-methyl-3-(pyridine-4-yl)prop-2-enoate 1c

A solution of 4-pyridinecarboxaldehyde (4.17 g, 0.0389 mol) in 10 mL of CH_2Cl_2 was slowly added to a solution of methyl (triphenylphosphoranylidene)acetate (12.50 g, 0.0374 mol) in 30 mL CH_2Cl_2. The mixture was refluxed for 5 hours, and then cooled to ambient temp. Upon cooling to ambient temperature, pTsOH (0.0784 mol) was added with stirring to the CH_2Cl_2 solution. After stirring for 30 minutes, the acidified product was extracted with water (2x, 100 mL), basified with K_2CO_3, and re-extracted with CH_2Cl_2 (2x, 50 mL). The solution was evaporated to yield a white solid free of the $Ph_3P{=}O$ byproduct (5.5 g, 90%). ^{1}H NMR (400 MHz, DMSO-d_6): δ/ppm = 8.68 (dd, 2H), 7.76 (dd, 2H), 7.68 (d, 1H) , 6.95 (d, 1H), 3.78 (s, 3H).

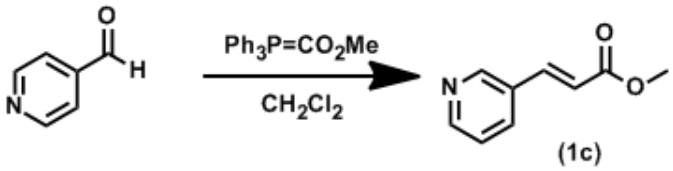

Figure 98: Synthesis of (*E*)-methyl-3-(pyridine-4-yl)prop-2-enoate *via* Wittig reaction.[268]

4.4.2 Synthesis of (*E*)-4-[(2-pyridin-4-yl)ethenyl]benzoic acid 2b

4-Picoline (5.00 g, 0.054 mol) and 4-formylbenzoic acid (8.05 g, 0.054 mol) were refluxed in 25 mL acetic anhydride for 16 hours. The mixture was cooled to ambient temperature, and poured onto 200 mL of ice water. A white powder was collected by filtration, and washed repeatedly with water, followed by aqueous ethanol, and dried to give 4-[(E)-2-(pyridine-4-yl)ethenyl]benzoic acid (2a) (10.5 g, 87%), which was used as synthesized for conversion to the ester. ^{1}H NMR (400 MHz, DMSO-d_6): δ/ppm = 8.63 (dd, 2H), 8.01 (d, 2H), 7.82 (d, 2H), 7.76 (s, 1H), 7.66 (dd, 2H), 7.44 (d, 1H).

4.4.3 Synthesis of (*E*)-methyl-4-[(2-pyridin-4-yl)ethenyl]benzoate 2c

10.04 g of [(E)-2-(pyridin-4-yl)ethenyl]benzoic acid (0.045 mol) and 80 mL of thionyl chloride were combined and stirred at room temperature for 12 hours. After 12 hours, the solution was cooled to -10 °C, and quenched *via* the slow addition of methanol. The solution was allowed to warm to room temp for another hour, then poured onto 750 mL ice water, and neutralized by the slow addition of 4M NaOH. The white precipitate formed from neutralization was filtered, washed with water, and dried to 8.75 g of the desired ester (84% overall yield). ^{1}H NMR (400 MHz, DMSO-d_6): δ/ppm = 8.58 (dd, 2H), 8.01 (d, 2H), 7.82 (d, 2H), 7.64 (d, 2H), 7.61 (dd, 2H), 7.42 (d, 1H), 3.87 (s, 3H).

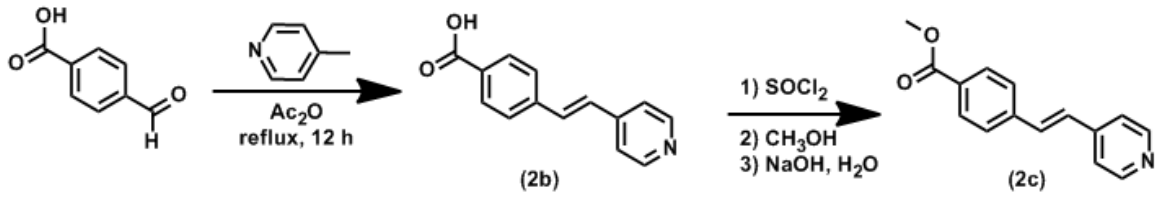

Figure 99: Synthesis of (*E*)-methyl-4-[(2-pyridin-4-yl)ethenyl]benzoate[269] *via* condensation, and subsequent one pot transformation to the methyl ester.

4.4.4 Co-crystallization Procedures

Co-crystallization of 1b was performed by dissolving 80 mg (0.54 mmol) of 1b and 0.27 mmol of a resorcinol in 10 mL of DMF (res used: res; 5-F res; 4,6-diBr res; 4,6-diI res; 4,6-diCl res; 5-OCH_3 res; 5-CO_2CH_3 res; 4-CH_2CH_3 res; 5-CH_3 res; 4-Cl res). The solution was heated to boiling and left to cool to room temperature. A precipitate formed within 1 hour. The white precipitate was filtered, dried, and analyzed using PXRD. Co-crystallization of 2b was performed by dissolving 80 mg of 2b and 0.18 mmol of a resorcinol in 10 mL of DMF. The solution was heated to boiling and left to

cool to room temperature. A precipitate formed within 30 minutes. The white precipitate was filtered, dried, and analyzed using PXRD.

Co-crystallization experiments involving 1c were performed by dissolving 50 mg of the compound in 5 mL of acetonitrile and adding 0.5 mol equivalents of a res. The solution was heated to boiling and left to cool slowly to room temperature. After standing at room temperature for 48 hours, the yellow colored co-crystals were isolated by vacuum filtration and air-dried. Co-crystallization experiments involving 2c were performed by dissolving 50 mg of the compound in 5 mL of acetonitrile or ethanol and adding 0.5 mol equivalents of a res. The solution was heated to boiling and left to cool slowly to room temperature. After standing at room temperature for 48 hours, the white colored co-crystals that formed were isolated by vacuum filtration and air-dried.

4.4.5 Photoproduct Hydrolyses

The photoproducts 1d and 2d were stirred in 2M NaOH for 2 h. 10% HCl was added until neutral by pH paper and the solutions were allowed to stir overnight. Evaporation yielded the product and sodium chloride. Trituration of the solid with 2:1 CH_3OH:$CHCl_3$ solution, followed by evaporation, afforded diacids 1a and 2a. ^{1}H NMR (1a, 300 MHz, DMSO-d_6): δ/ppm =8.36 (dd, 4H), 7.08 (dd, 4H), 4.26 (d, 2H), 3.89 (d, 2H). ^{1}H NMR (2a, AVA 400, DMSO-d_6): δ/ppm = 8.36 (dd, 4H), 7.66 (d, 4H), 7.28 (dd, 4H), 7.12 (d, 4H), 4.62 (d, 4H).

4.5 Results

In our initial studies to synthesize the target 1a, we attempted to achieve a reactive hydrogen-bonded assembly involving 1b and a res. The olefin 1b was insoluble in most organic solvents, which can be attributed to 1b participating in intermolecular (acid) O—H···N (pyridyl) hydrogen bonds in the pure solid.[257] For a res template, we employed our co-crystal screening strategy termed "template switching."[96] The strategy involves screening a pyridine-based olefin with res derivatives *via* solvent precipitation and

exposing the resulting co-crystals to UV irradiation. The method allows us to assemble the olefin into similar yet different packing environments to improve the probability of obtaining a photoreactive solid. From our studies, the application of template-switching to 1b in organic solvents (e.g. EtOH, DMF) afforded pure 1b alone as a precipitate, as evidenced by powder X-ray diffraction (PXRD) analyses (Figure 100). We attribute the inability of each res to form a co-crystal with 1b to the marked insolubility of the olefin and, corresponding, intermolecular hydrogen bonds present in the pure solid.

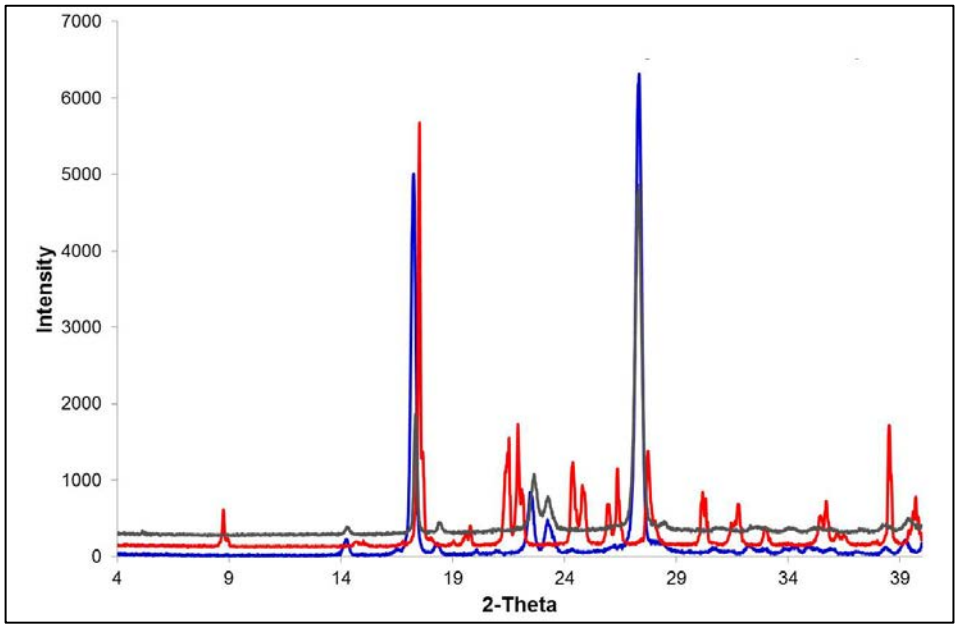

Figure 100: PXRD overlay of 1b (blue trace), 5-F res (red trace) and powder generated upon co-crystallization attempt (gray trace).

To achieve a reactive co-crystal that furnishes 1a, we designed a protecting group strategy.[165] In particular, we expected that the hydrogen-bond-donor abilities of the acid group of 1b could be rendered inactive by masking the acid proton converting as the methyl ester. Conversion of 1b to 1c was expected to result in increased solubility and, at the same time, enable a res to participate in an O—H···N hydrogen bond to the alkene. Although the sp^2-hybridized O-atom of an ester can act as a hydrogen-bond-acceptor

group, the basicity of a pyridine (pK_a = 5.2) versus an ester (pK_a = -6) suggested that the pyridyl group would selectively participate in a hydrogen bond with a res.[173b] Upon photoreaction, the resulting diester 1d would be deprotected *via* hydrolysis to generate 1a.

4.5.1 Application of Supramolecular Protecting Group Strategy to 4-Pyridine-based Olefinic Acids

Following the lack of co-crystal attained through template switching of the acrylic acid 1b, the methyl ester 1c was synthesized.[268] Our template switching method was applied to screen for reactive co-crystals of 1c and a series of resorcinols. We isolated and characterized seven co-crystals of 1c, which are described below.

(1) 2(1c)·(res). Co-crystals of the formulation 2(1c)·(res) crystallized from EtOH in the triclinic space group P$\bar{1}$ with one res and two molecules of 1c in the asymmetric unit. The components form a discrete assembly sustained by two O—H···N hydrogen bonds [O···N separations (Å): O1···N1 2.787(3), O2···N2 2.800(3)]. The C=C bonds were ordered and separated by 3.63 Å yet, adopting a crisscross conformation (Figure 101). Additional interactions in the form of (alkyl) C—H···O (carboxy) and (pyridine) C—H···O (phenol) contribute to the extended packing ($d_{C\cdots O}$ = 3.293 Å; $d_{C\cdots O}$ = 3.563 Å).

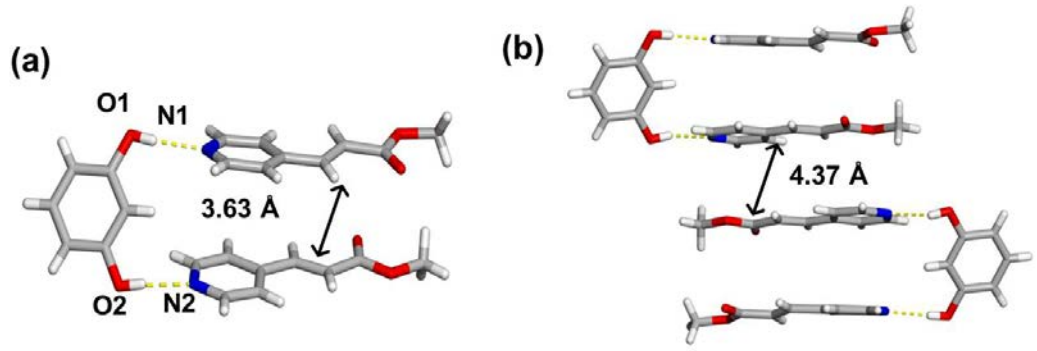

Figure 101: X-ray structure of 2(1c)·(res): (a) assembly with crisscrossed C=C bonds and (b) antiparallel packing.

(2) 2(1c)·(4-Br res). 2(1c)·(4-Br res) co-crystallizes from EtOH in the orthorhombic space group Pbca. The molecules assemble to form discrete three-component assemblies sustained through the formation of two O—H···N hydrogen bonds [O···N separations (Å): O1···N1 2.708, O2···N2 2.752] (Figure 102). The C=C bonds within each assembly are stacked parallel, aligned, and separated by 3.781 Å. The C=C bonds between neighboring assemblies are separated by 5.033 Å. Additional interactions in the form of (pyridine) C—H···O (carboxy), (alkyl) C—H···O (carboxy), and (alkyl) C—H···O (phenol) forces are present between adjacent assemblies ($d_{C\cdots O}$ = 3.375 Å; $d_{C\cdots O}$ = 3.407 Å, 3.525 Å; $d_{C\cdots O}$ = 3.484 Å, 3.501 Å).

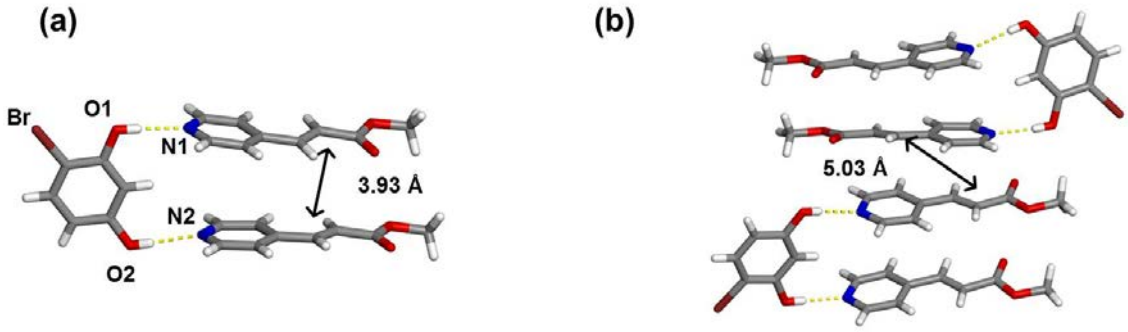

Figure 102: X-ray structure of 2(1c)·(4-Br res): (a) assembly with parallel C=C bonds and (b) antiparallel packing.

(3) 2(1c)·(4-Cl res). Co-crystals of the formulation 2(1c)·(4-Cl res) crystallize from ethanol in the orthorhombic space group Pbca with two molecules of 1c and one 4-Cl res in the asymmetric unit. The resulting three-component assembly is sustained by two O—H···N hydrogen bonds [O···N separations (Å): O1···N1 2.724, O2···N2 2.768]. Within each assembly, the C=C bonds are arranged in a parallel fashion, and aligned with a separation of 3.765 Å (Figure 103). In between adjacent assemblies, overlapping C=C bonds are arranged in an antiparallel fashion and the C···C separation is 5.010 Å.

Additional interactions in the form of (pyridine) C—H···O (carboxy), (alkenyl) C—H···O (carboxy), and (alkyl) C—H···O (phenol) forces are present between adjacent assemblies ($d_{C\cdots O}$ = 3.392 Å; $d_{C\cdots O}$ = 3.422 Å; $d_{C\cdots O}$ = 3.471 Å).

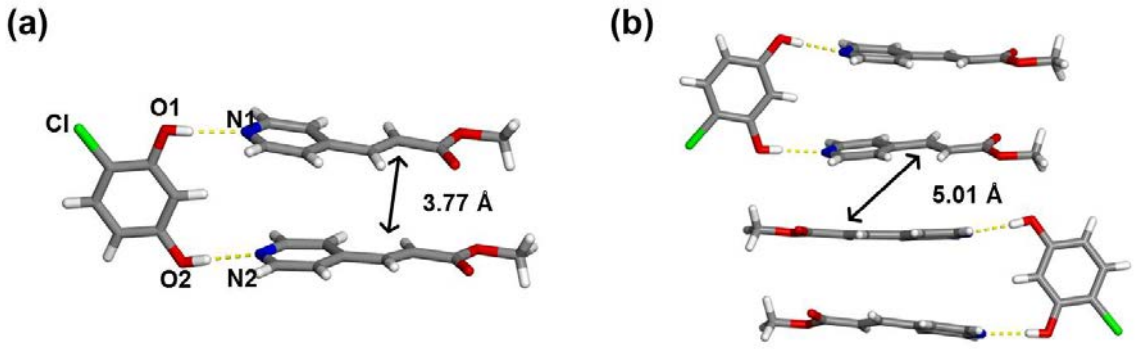

Figure 103: X-ray structure of 2(1c)·(4-Cl res): (a) assembly with parallel C=C bonds and (b) antiparallel packing.

(4) 2(1c)·(4,6-diCl res). 2(1c)·(4,6-diCl res) co-crystallizes from EtOH in the triclinic space group $P\bar{1}$ with one 4,6-diCl res and two molecules of 1c in the asymmetric unit. The resulting three-component assembly is sustained by the formation of two O—H···N hydrogen bonds [O···N separations (Å): O1···N1 2.733, O2···N2 2.790]. Within each assembly, the C=C bonds are aligned parallel with a C···C separation of 4.047 Å (Figure 104). Additionally, neighboring assemblies are positioned with the C=C moieties offset in an antiparallel manner and separated by 8.350 Å. The offset neighboring assemblies can be attributed to, in part, a degree of π···π stacking between pyridyl units ($d_{\pi\cdots\pi}$ = 3.412 Å). The extended packing contains additional (pyridine) C—H···O (carboxy), (alkenyl) C—H···O (carboxy), and Cl···Cl interactions between adjacent assemblies ($d_{C\cdots O}$ = 3.371 Å; $d_{C\cdots O}$ = 3.460 Å, 3.369 Å; $d_{Cl\cdots Cl}$ = 3.466 Å).

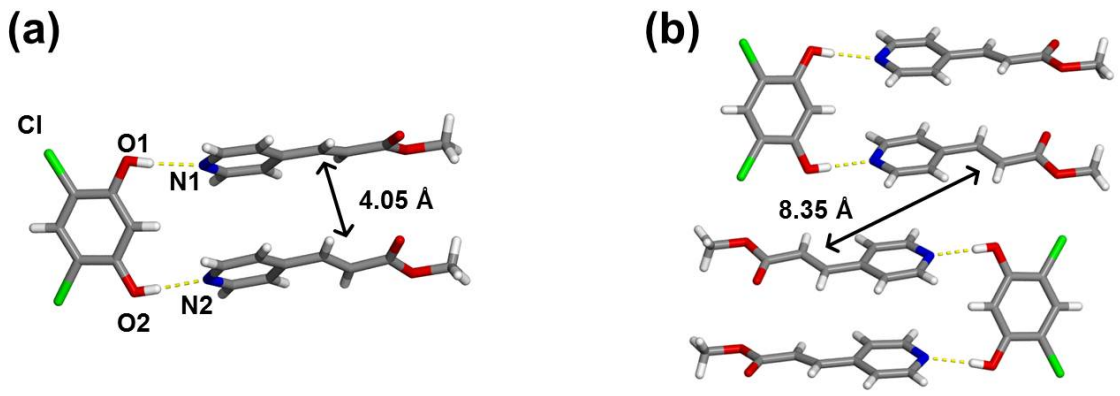

Figure 104: X-ray structure of 2(1c)·(4,6-diCl res): (a) assembly with parallel C=C bonds and (b) antiparallel offset packing.

(5) 2(1c)·(5-OCH$_3$ res). Crystallization of 1c and 5-OCH$_3$ res from EtOH affords a co-crystal in the monoclinic space group P2$_1$/n. Single crystal structure analysis reveals that the molecules assemble to form discrete three-component assemblies interacting primarily through two O—H···N hydrogen bonds [O···N separations (Å): O1···N1 2.772, O2···N2 2.790]. The C=C bonds within each assembly are parallel and separated by 3.739 Å, yet are arranged in a crisscross fashion, thus, no photoreaction is expected (Figure 105). The C=C bonds between neighboring assemblies are separated by 4.649 Å. Adjacent assemblies interact *via* (pyridine) C—H···O (phenol), (pyridine) C—H···O (carboxy), and (alkyl) C—H···O (phenol) interactions ($d_{C\cdots O}$ = 3.377 Å; $d_{C\cdots O}$ = 3.385 Å; $d_{C\cdots O}$ = 3.126 Å).

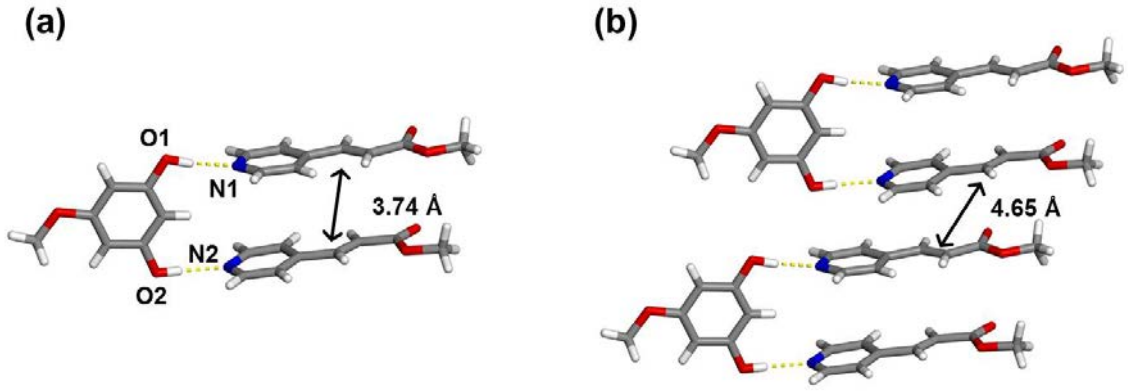

Figure 105: X-ray structure of 2(1c)·(5-OCH_3 res): (a) assembly with crisscrossed C=C bonds and (b) parallel, yet crisscrossed packing.

(6) 2(1c)·(5-CO_2CH_3 res). 2(1c)·(5-CO_2CH_3 res) crystallizes from EtOH in the monoclinic space group $P2_1/n$. The molecules assemble to form discrete three-component assemblies sustained through the formation of two O—H···N hydrogen bonds [O···N separations (Å): O1···N1 2.711, O2···N2 2.829]. The C=C bonds within each assembly are parallel and separated by 3.741 Å, yet are stacked in a crisscross manner (Figure 106). The C=C bonds between neighboring assemblies are separated by 4.920 Å. Additional interactions in the form of (pyridine) C—H···O (carboxy: 1c), (alkyl) C—H···O (carboxy), and (pyridine) C—H···O (carboxy: res) forces are present between adjacent assemblies ($d_{C\cdots O}$ = 3.348 Å; $d_{C\cdots O}$ = 3.548 Å; $d_{C\cdots O}$ = 3.467 Å).

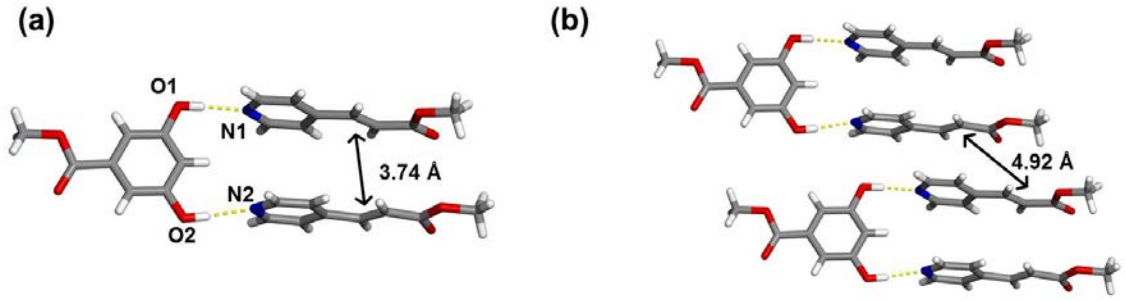

Figure 106: X-ray structure of 2(1c)·(5-CO_2CH_3 res): (a) assembly with crisscrossed C=C bonds and (b) parallel offset packing.

(7) 2(1c)·(5-F res). Co-crystals of the formulation 2(1c)·(5-F res) crystallized from CH_3CN in the orthorhombic space group Pbca. Single-crystal structure analysis revealed the formation of a discrete, three-component hydrogen-bonded assembly sustained by two O—H···N forces [O···N separations (Å): O1···N1 2.763(2), O2···N2 2.741(2)]. The stacked C=C bonds were ordered, organized parallel, and separated by 3.73 Å, geometries that conform to the criteria for photoreaction. Olefins between nearest-neighbor assemblies were antiparallel and separated by 4.87 Å (Figure 107). Adjacent assemblies also interact through the formation of (pyridine) C—H···O (carboxy) and O—H···F interactions ($d_{C\cdots O}$ = 3.293 Å; $d_{O\cdots F}$ = 2.913 Å).

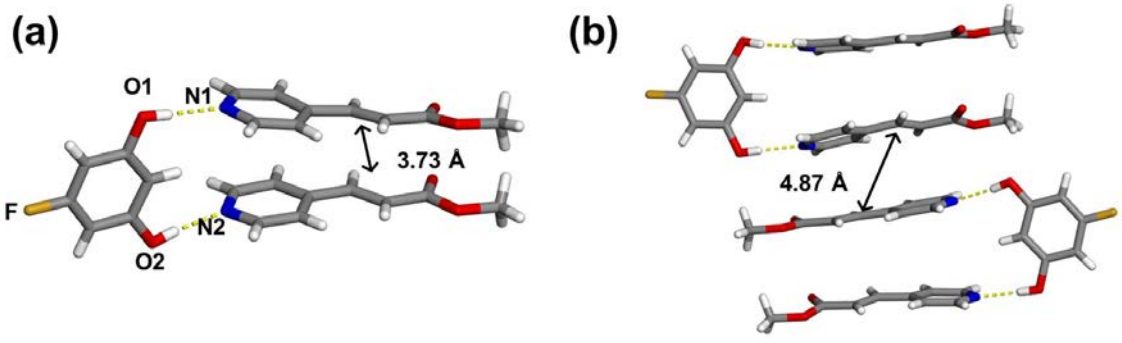

Figure 107: X-ray structure of reactive 2(1c)·(5-F res): (a) assembly with parallel C=C bonds and (b) antiparallel packing.

Of the res template screened with 1c, to our surprise, only the co-crystal 2(1c)·(5-F res) was photoactive. UV irradiation of a powdered sample of 2(1c)·(5-F res) revealed 1c to react quantitatively to give 1d, as evidenced by ^{1}H NMR spectroscopy. The photoproduct was characterized by the disappearance of the olefinic peaks at 7.65 and 6.95 ppm and the appearance of cyclobutane peaks at 4.38 and 4.15 ppm. Basic extraction and a subsequent hydrolysis afforded the unmasked diacid 1a, as confirmed by ^{1}H NMR spectroscopy (Figure 108).[124]

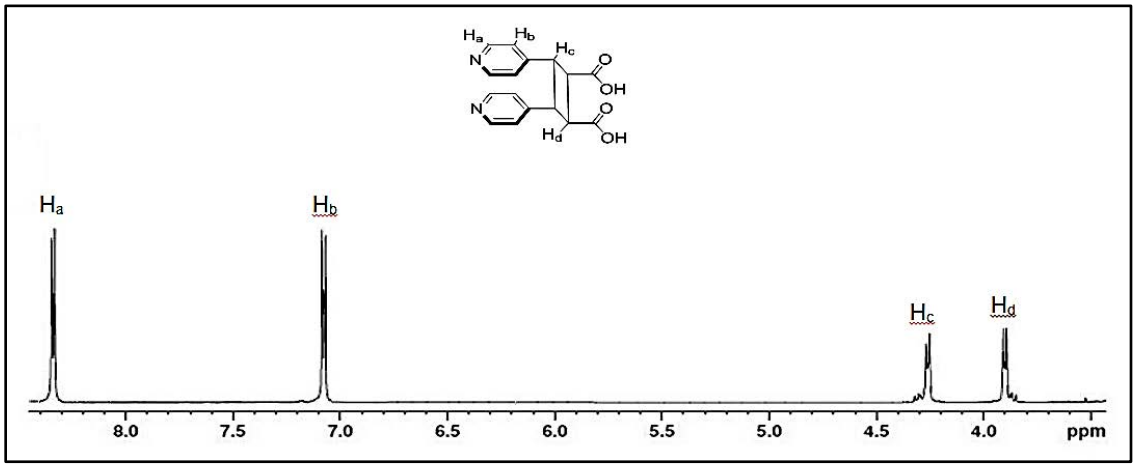

Figure 108: ^{1}H NMR spectrum of 1d obtained after hydrolysis (300 MHz, DMSO-d_6).

Given that organization of molecules in solids is extremely sensitive to subtle changes to molecular structure, we investigated the generality of the protecting group strategy through application to generate the extended cyclobutane congener 2a. As for 1b, each attempt to screen 2b for a co-crystal afforded the pure solid olefin, as confirmed by PXRD analyses (Figure 109). The corresponding protected lengthened phenyl ester 2c was, thus, prepared using a modified procedure.[269]

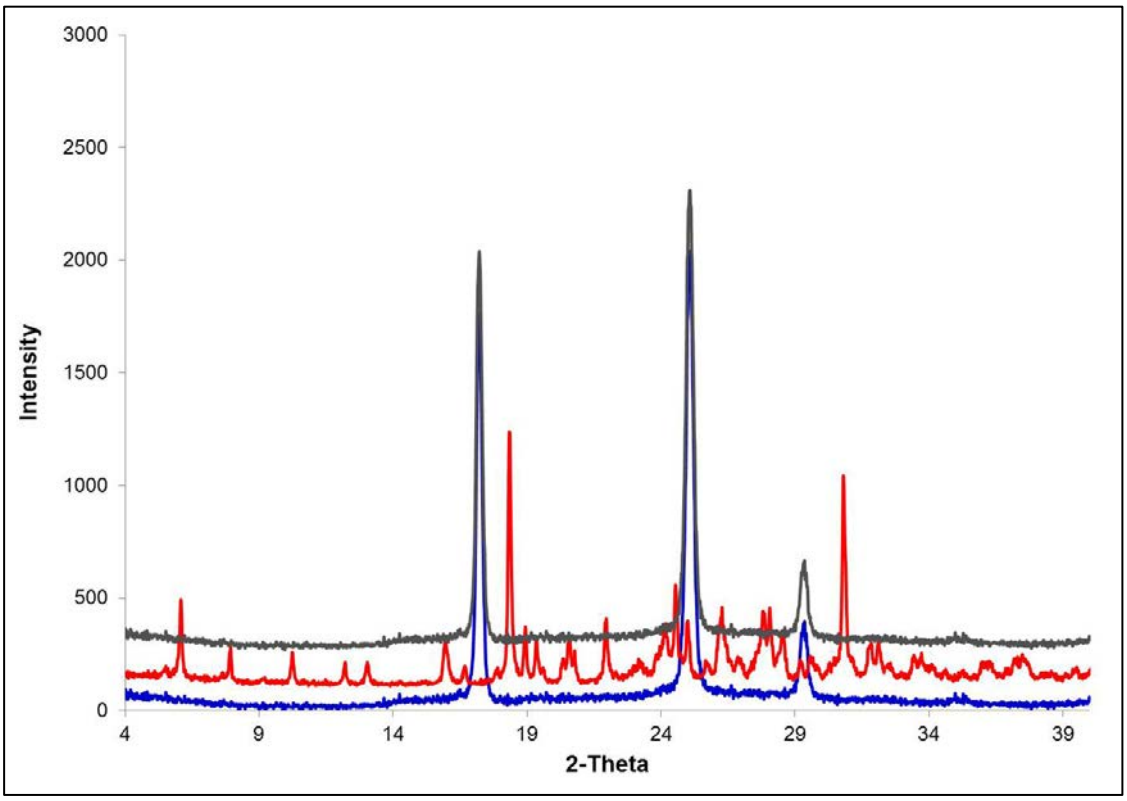

Figure 109: PXRD overlay of 2b (blue trace), 4,6-diBr res (red trace) and powder generated upon co-crystallization attempt (gray trace).

Co-crystals were generated by mixing 2c and each res (0.5 eq.) in EtOH and allowing the solution to stand. Within one week, all samples contained a precipitate that was dried and subjected to UV-irradiation. ^{1}H NMR analysis showed each solid to consist of 2c and a res (2:1 ratio) prior to UV irradiation. We isolated and characterized eight co-crystals of 1c, which are described below.

(1) 2(2c)·(5-OCH$_3$ res). Co-crystals of the formulation 2(2c)·(5-OCH$_3$ res) crystallized from EtOH in the monoclinic space group C2/c with one 5-OCH$_3$ res and two molecules of 2c in the asymmetric unit. The components form a discrete assembly sustained by two O—H···N hydrogen bonds [O···N separations (Å): O···N 2.829, O2···N2 2.895]. The C=C bonds were determined to be parallel and separated by 4.132 Å yet,

adopting a crisscross conformation (Figure 110). Olefins between neighboring assemblies were aligned parallel, but separated by 4.154 Å. Additional interactions in the form of (alkoxy) C—H···O (alkoxy) and (alkyl) C—H···O (phenol) contribute to the extended packing ($d_{C\cdots O}$ = 3.491 Å; $d_{C\cdots O}$ = 3.653 Å).

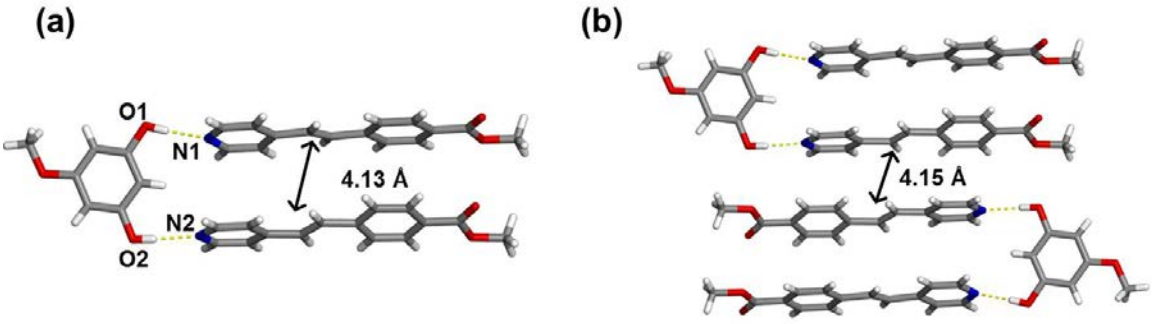

Figure 110: X-ray structure of 2(2c)·(5-OCH_3 res): (a) assembly with parallel C=C bonds and (b) antiparallel packing.

(2) 2(2c)·(5-F res). 2(2c)·(5-F res) co-crystallizes from EtOH in the triclinic space group $P\bar{1}$. The molecules assemble to form discrete three-component assemblies sustained through the formation of two O—H···N hydrogen bonds [O···N separations (Å): O1···N1 2.734, O2···N2 2.738]. The C=C bonds within each assembly are arranged parallel and separated by 4.505 Å, owing to the two reactant molecules stacking in a more edge-to-face manner (θ = 45.52°) (Figure 111). The C=C bonds between neighboring assemblies are separated by 6.629 Å. Additional interactions in the form of (pyridine) C—H···O (carboxy) forces are present between adjacent assemblies ($d_{C\cdots O}$ = 3.351 Å, 3.231 Å).

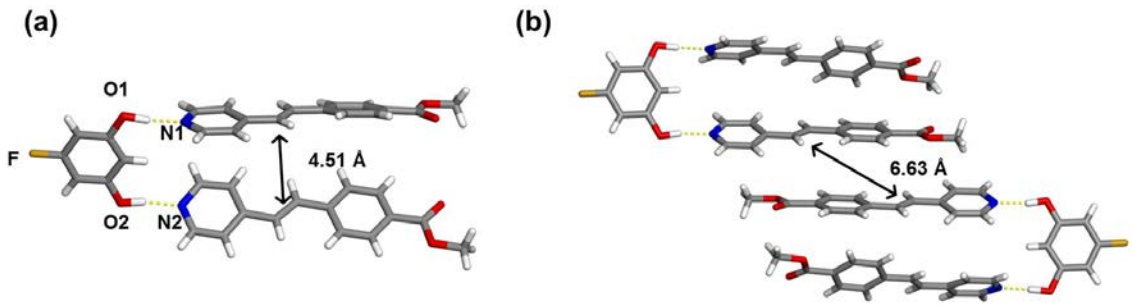

Figure 111: X-ray structure of 2(2c)·(5-F res): (a) assembly with twisted C=C bonds and (b) antiparallel packing.

(3) 2(2c)·(5-CH_3 res). Co-crystals of the formulation 2(2c)·(5-CH_3 res) crystallize from EtOH in the monoclinic space group C2/c with two molecules of 2c and one 5-CH_3 res in the asymmetric unit. The resulting three-component assembly is sustained by two O—H···N hydrogen bonds [O···N separations (Å): O1···N1 2.737(4), O2···N2 2.760(5)] (Figure 12). Within each assembly, the C=C bonds are stacked in a parallel fashion, with a C···C separation of 3.934 Å, yet are crisscross, while the C=C bonds between assemblies are aligned antiparallel, separated by 4.011 Å. Neighboring phenyl and pyridyl rings exhibit π···π stacking interactions ($d_{\pi\cdots\pi}$ = 3.587 Å). Additional interactions in the form of (alkenyl) C—H···O (carboxy) and (alkyl) C—H···O (phenol) forces are present between adjacent assemblies ($d_{C\cdots O}$ = 3.551 Å; $d_{C\cdots O}$ = 3.430 Å).

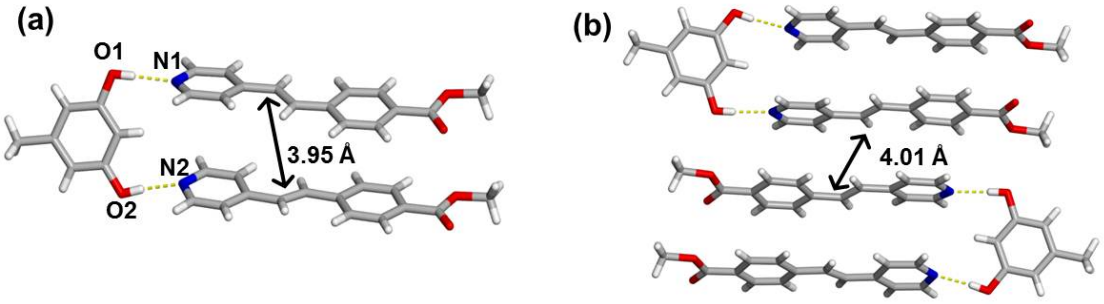

Figure 112: X-ray structure of 2(2c)·(5-OCH_3 res): (a) assembly with parallel C=C bonds and (b) antiparallel packing.

(4) 2(2c)·(4-Br res). 2(2c)·(4-Br res) co-crystallizes from EtOH in the triclinic space group $P\bar{1}$ with one 4-Br res and two molecules of 1c in the asymmetric unit. The resulting three-component assembly is sustained by the formation of two O—H···N hydrogen bonds [O···N separations (Å): O1···N1 2.682, O2···N2 2.753]. Within each assembly, the C=C bonds are aligned with a C···C separation of 3.878 Å, yet are crisscrossed (Figure 113). In between the assemblies, the C=Cs are arranged in an antiparallel manner, and separated by 4.154 Å. The extended packing contains additional (pyridine) C—H···O (carboxy) and (alkenyl) C—H···O interactions between adjacent assemblies ($d_{C\cdots O}$ = 3.391 Å; $d_{C\cdots O}$ = 3.510 Å, 3.423 Å).

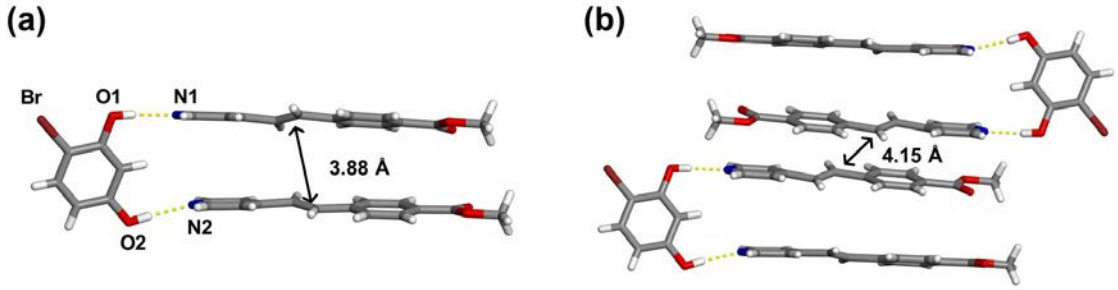

Figure 113: X-ray structure of 2(2c)·(4-Br res): (a) assembly with crisscross C=C bonds and (b) antiparallel packing.

(5) 2(2c)·(4-Cl res). Crystallization of 2c and 4-Cl res from EtOH affords a co-crystal in the triclinic space group $P\bar{1}$. Single crystal structure analysis reveals that the molecules assemble to form discrete three-component assemblies interacting primarily through two O—H···N hydrogen bonds [O···N separations (Å): O1···N1 2.713(4), O2···N2 2.725(5)]. The C=C bonds within each assembly are aligned parallel and separated by 3.934 Å, while the C=C bonds between neighboring assemblies are separated by 5.103 Å (Figure 114). The antiparallel stacking between assemblies is likely owing to significant π···π interactions between stacked phenyl and pyridine rings ($d_{\pi\cdots\pi}$ = 2.607 Å). Adjacent assemblies interact *via* (alkyl) C—H···O (phenol) and (pyridine) C—H···O interactions ($d_{C\cdots O}$ = 3.466 Å; $d_{C\cdots O}$ = 3.304 Å).

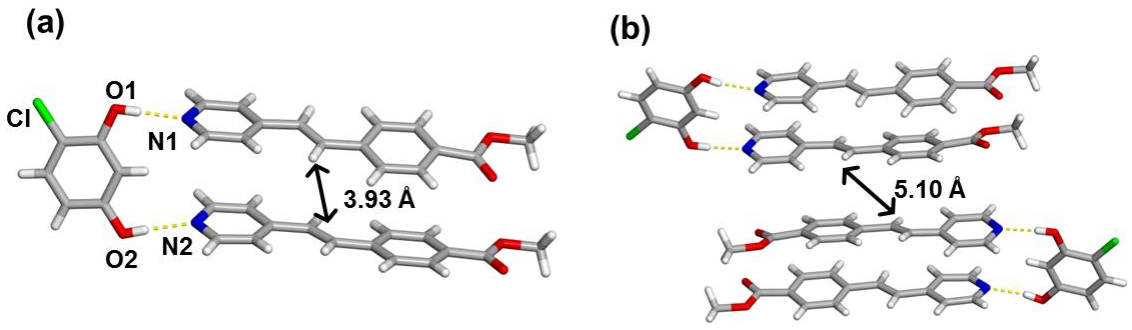

Figure 114: X-ray structure of 2(2c)·(4-Cl res): (a) assembly with parallel C=C bonds and (b) antiparallel packing.

(6) 2(2c)·(4,6-diBr res). 2(2c)·(4,6-diBr res) crystallizes from EtOH in the monoclinic space group $P\bar{1}$. The molecules assemble to form discrete three-component assemblies sustained through the formation of two O—H···N hydrogen bonds [O···N separations (Å): O1···N1 2.750(3), O2···N2 2.706(4)]. The C=C bonds within each assembly are parallel and separated by 4.100 Å, yet are stacked in a crisscross manner (Figure 115). The C=C bonds between neighboring assemblies are separated by 4.013 Å

and antiparallel, owing to π···π interactions between stacked phenyl and pyridine rings ($d_{\pi\cdots\pi}$ = 3.587 Å). Additional interactions in the form of (alkyl) C—H···O (carboxy) and (alkyl) C—H···O (phenol) forces are present between adjacent assemblies ($d_{C\cdots O}$ = 3.373 Å, 3.595 Å; $d_{C\cdots O}$ = 3.500 Å).

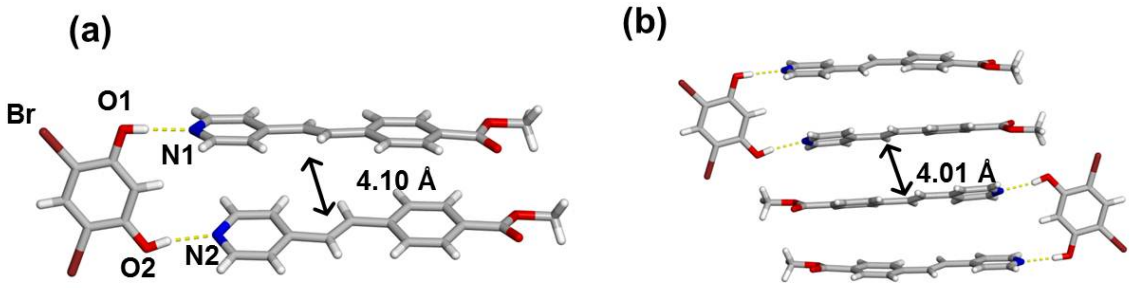

Figure 115: X-ray structure of 2(2c)·(4,6-diBr res): (a) assembly with twisted C=C bonds and (b) antiparallel packing.

(7) 2(2c)·(4,6-diI res). Co-crystals of the formulation 2(2c)·(4,6-diI res) crystallized from CH_3CN in the monoclinic space group $P2_1/c$. A structure analysis revealed the formation of a discrete, three-component hydrogen-bonded assembly sustained by two O—H···N forces [O···N separations (Å): O1···N1 2.698(4), O2···N2 2.707(3)]. The C=C bonds were aligned parallel separated by 4.239 Å, while olefins between assemblies were offset and separated by 5.417 Å (Figure 116). The olefins within an assembly are twisted 18.32° away from each other, likely contributing to the higher C···C separation. Adjacent assemblies also interact through the formation of (res) I···O (carboxy) and (res) I···O (phenol) interactions ($d_{I\cdots O}$ = 3.185 Å; $d_{I\cdots O}$ = 3.365 Å).

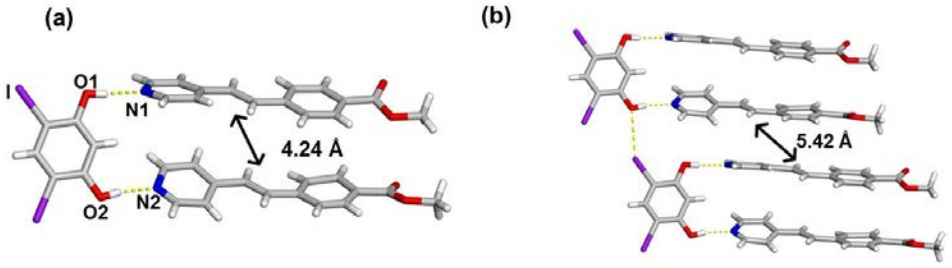

Figure 116: X-ray structure of 2(2c)·(4,6-diI res): (a) assembly with parallel C=C bonds and (b) antiparallel packing.

(8) 2(2c)·(4,6-diCl res). Co-crystals of the formulation 2(2c)·(4,6-diCl res) crystallized from EtOH in the triclinic space group $P\bar{1}$ with one 4,6-diCl res and two molecules of 2c in the asymmetric unit. The components form a discrete assembly sustained by two O—H···N hydrogen bonds [O···N separations (Å): O1···N1 2.694(6), O2···N2 2.764(5)]. The C=C bonds were determined to be ordered and separated by 3.989 Å yet, adopting a crisscross conformation (Figure 117), while the olefins between the assemblies were stacked antiparallel and aligned with a C···C separation of 3.897 Å. Additional interactions in the form of (alkyl) C—H···O (phenol) and (pyridine) C—H···O (carboxy) contribute to the extended packing ($d_{C\cdots O}$ = 3.533 Å; $d_{C\cdots O}$ = 3.180 Å).

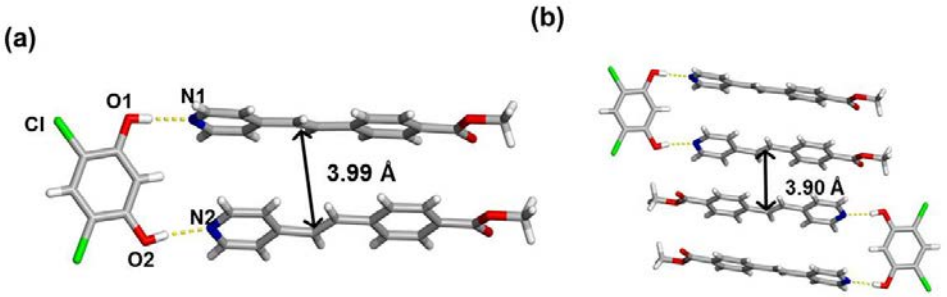

Figure 117: X-ray structure of 2(2c)·(4,6-diCl res): (a) assembly with crisscross C=C bonds and (b) antiparallel packing.

In contrast to 1c, the application of template switching to 2c, remarkably, afforded a photoactive solid *in each case* (Table 3).[165] Of the reactive solids, four solids (res = 4,6-diBr res, 4,6-diI res, 4-Cl res, and 5-CH_3 res) afforded 2d stereospecifically and in quantitative yield.

Table 3: Summary of photoreactivity studies of 2c with ten resorcinols.

entry	**res**	**time (h)**	**conv. (%)**	**yield of 2d (%)**
1	res	175	66	44[a]
2	5-F res	175	85	55[a]
3	4,6-diBr res	175	100	100
4	4,6-diCl res	75	90	90
5	4,6-diI res	175	100	100
6	4-Cl res	75	100	100
7	5-CH_3 res	130	100	100
8	4-Et res	175	52	52
9	5-OCH_3 res	175	96	64[a]
10	5-CO_2Me res	175	75	75

[a] mixture of **2d** and unidentified minor product

Single-crystal X-ray diffraction was employed to gain an understanding of the origin of the enhanced solid-state reactivity of 2c versus 1c. Moreover, a structure analysis of each solid that afforded 2d in 100% yield revealed that the C=C bonds in three

of the co-crystals were disordered [(2(2c)·(4,6-diI res): 0.51/0.49 and 0.91/0.09; 2(2c)·(4-Cl res): 0.53/0.47 and 0.50/0.50; 2(2c)·(5-CH_3 res): 0.71/0.29 and 0.66/0.34.)], with the C=C bonds being separated by 3.94, 3.94, and 3.96 Å, respectively. Olefins between the stacked assemblies were either parallel (4,6-diI res) or antiparallel (4-Cl res and 5-CH_3 res), being separated by 5.42, 5.11 and 4.01 Å, respectively (Figures 118d,f,h). For 2(2c)·(4,6-diBr res), the C=C bonds were ordered and separated by 4.10 Å, with adjacent assemblies adopting an antiparallel arrangement (Figures 118a,b). The C=C bonds between adjacent assemblies were also parallel and separated by 4.01 Å.

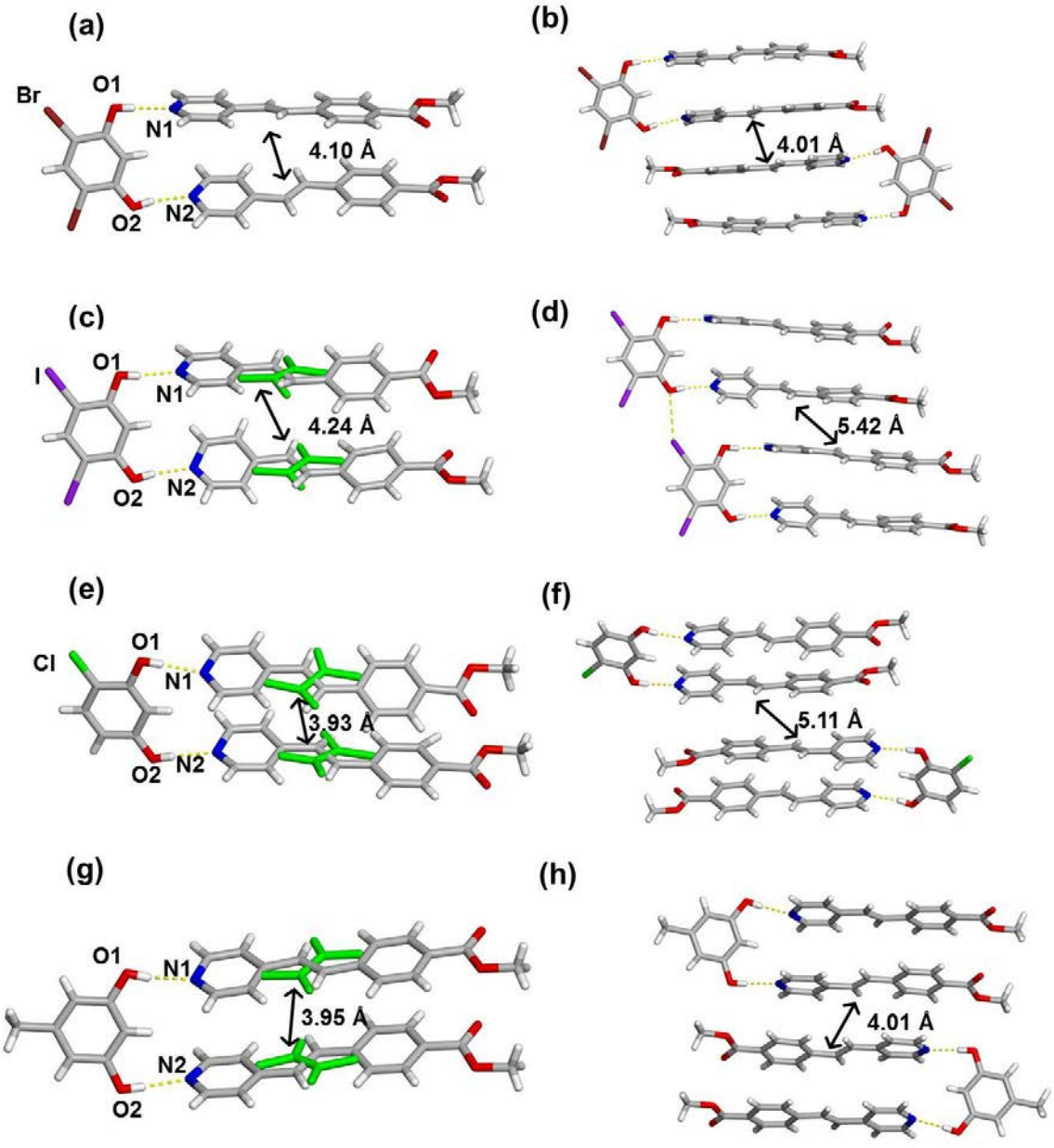

Figure 118: X-ray structures of (2c)·(res): 2(2c)·(4,6-diBr res): (a) antiparallel C=C bonds and (b) packing, 2(2c)·(4,6-diI res): (c) parallel C=C bonds and (d) packing, 2(2c)·(4-Cl res): (e) parallel C=C bonds and (f) packing, and 2(2c)·(5-CH_3 res): (g) antiparallel C=C bonds and (h) packing. Lower occupancies of each C=C bond in green.

UV irradiation of (2c)·(res) (where: res = 4,6-diBr res, 4,6-diI res, 4-Cl res, and 5-CH_3 res) revealed 2c to react stereospecifically and quantitatively in each co-crystal. The generation of the cyclobutane photoproduct was evidenced by the disappearance of the peaks at 7.65 and 7.43 ppm and appearance of peaks at 4.75 and 4.69 ppm. Basic hydrolysis, upon separation from the template, afforded the target cyclobutane 2a, as revealed by ^{1}H NMR spectroscopy. Moreover, the head-to-head structure of 2a was confirmed by an X-ray analysis of the sodium salt $[Na_4(\mu_2\text{-}OH_2)_8(C_{28}H_{20}N_2O_4)_2(OH_2)_6(OH_2)]\cdot H_2O$ (Figure 119).

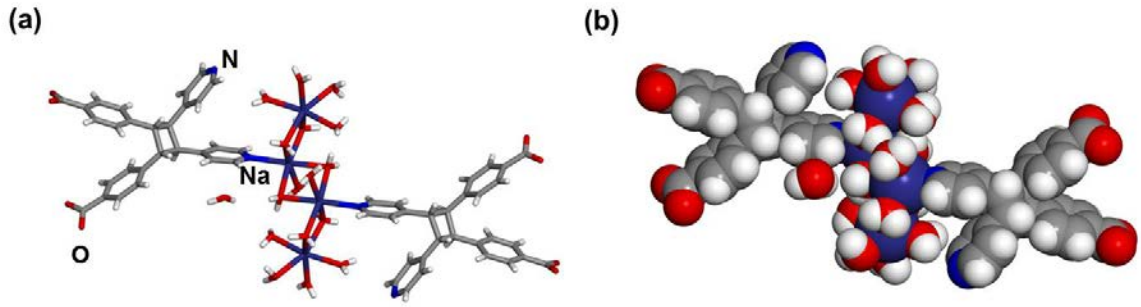

Figure 119: X-ray structure of Na carboxylate salt of 2a: (a) wireframe and (b) space-filling views of dianion of the lengthened congener 2a.

4.5.2 Pedal Motion in the Organic Solid State

Given that our structures involving 2c undergo pedal motion that mediates chemical reactivity, we sought to investigate the influence of temperature upon molecular movement in co-crystals of 2c. Variable temperature X-ray diffraction experiments have previously been reported the late 1990's by Harada and Ogawa using azobenzene as a model system.[270] In particular, it was found that the two conformer populations deviated with temperature. If the crystal structure collection was conducted at room temperature, the ratio of the two populations was determined to be 81.5/18.5.[270] When the collection was performed at 82 K, however, the motion was nonexistent, as the lower occupancy

disorder disappeared. In 2004, Harada and Ogawa also performed temperature-dependant studies on *trans*-stilbene.[271] The studies determined that the pedal motion slowed down, evidenced by the decrease in population of the minor conformer, and essentially ceased to exist at 90 K (Table 4). As the collection temperature decreased, the unit cell volume also decreased by *ca.* 1%.

Table 4: Summary of variable temperature crystallography data obtained by Harada and Ogawa for *trans*-stilbene.[271]

temperature/K	**occupancy**	**unit cell volume/Å^3**
373	0.796/0.204	1057
340	0.818/0.182	1044
300	0.846/0.154	1034
250	0.882/0.118	1023
200	0.918/0.082	1013
150	0.942/0.058	1004
90	0.945/0.055	994

4.5.3 Variable Temperature Studies of 2c and Co-crystals of 2c

The starting point for our investigation was the olefin 2c. 2c crystallizes in the orthorhombic space group $Pna2_1$ with two molecules of 2c in the asymmetric unit. The olefin is disordered over two sites (0.858/0.142) when collection is conducted at 290 K (Figure 120). The occupancies remain relatively unchanged as the collection temperature

decreases to 250 K (0.846/0.154), 210 K (0.858/0.142), and 170 K (0.865/0.135) Unlike the data collected by Harada pertaining to *trans*-stilbene,[271] 2c appears to constantly undergo pedal motion that cannot be slowed or suppressed at lower temperatures.

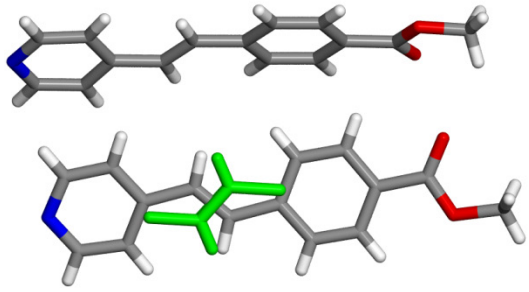

Figure 120: X-ray structure of 2c highlighting lower occupancy disorder in green.

We next turned to investigate the effects of temperature on the motion of organic co-crystals involving 2c. In particular, we studied the four co-crystals resulting in 100% photoreactivity [2(2c)·(4,6-diBr res), 2(2c)·(4,6-diI res), 2(2c)·(4-Cl res), and 2(2c)·(5-CH_3 res)]. Unlike single-component systems (e.g. *trans*-stilbene, azobenzene) that likely stack in a more rigid manner, two-component systems, such as co-crystals, could exhibit a more flexible packing motif that leads to molecular motion within the co-crystal, despite the lower temperatures.

Table 5: Summary of variable temperature data collected for 2(2c)·(4,6-diBr res) and 2(2c)·(4,6-diI res).

co-crystal	temperature/K	olefin occupancies	unit cell volume/Å^3
2(2c)·(4,6-diBr res)	290	0.861/0.139	1624
		1.000/0.000	
2(2c)·(4,6-diBr res)	250	0.871/0.129	1620
		1.000/0.000	
2(2c)·(4,6-diBr res)	210	0.876/0.124	1620
		1.000/0.000	
2(2c)·(4,6-diBr res)	170	0.898/0.102	1617
		1.000/0.000	
2(2c)·(4,6-diI res)	290	0.531/0.469	3379
		0.923/0.077	
2(2c)·(4,6-diI res)	250	0.399/0.601	3373
		1.000/0.000	
2(2c)·(4,6-diI res)	210	0.551/0.449	3367
		0.926/0.074	
2(2c)·(4,6-diI res)	170	0.536/0.464	3363
		1.000/0.000	

Table 6: Summary of variable temperature data collected for 2(2c)·(4-Cl res) and 2(2c)·(5-CH_3 res).

co-crystal	temperature/K	olefin occupancies	unit cell volume/Å^3
2(2c)·(4-Cl res)	290	0.572/0.428	1592
		0.747/0.253	
2(2c)·(4-Cl res)	250	0.506/0.494	1586
		0.561/0.439	
2(2c)·(4-Cl res)	210	0.713/0.287	1585
		0.533/0.467	
2(2c)·(4-Cl res)	170	0.497/0.503	1581
		0.587/0.413	
2(2c)·(5-CH_3 res)	290	0.704/0.296	6432
		0.792/0.208	
2(2c)·(5-CH_3 res)	250	0.710/0.290	6432
		0.773/0.227	
2(2c)·(5-CH_3 res)	210	0.719/0.281	6419
		0.771/0.229	
2(2c)·(5-CH_3 res)	170	0.658/0.342	6409
		0.782/0.218	

4.6 Discussion

The markedly enhanced reactivity of co-crystals of 2c compared to 1c with res templates can be attributed to the C=C units undergoing pedal, or crankshaft, motion in each solid. Stilbenes such as 2c can exhibit dynamic motion in the crystalline state that can interconvert C=C bonds from a criss-cross to parallel conformation that is suitable for a photodimerization (Figure 121). Here, the pedal motion of the stilbene *acts to our advantage*, compared to the acrylate 1c, to achieve reactivity within a series of res-based solids. Given that the goal here is to expand the synthetic versatility of reactivity in organic solids, these observations are important since the enhanced reactivities suggest that stilbene units and protecting groups when applied in combination can provide a route to highly-reactive olefins for the directed formation of C–C bonds in solids.

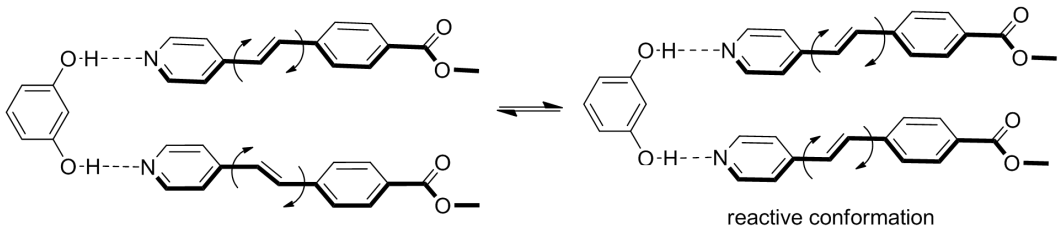

Figure 121: Enhanced reactivity of protected olefin in a co-crystal with a res template achieved through pedal motion.

The variable temperature studies demonstrate some interesting results, in the context of the four fully-reactive co-crystals. In particular, we observed that the co-crystals still exhibited a large degree of pedal motion, even after a rapid cooling cycle, the minor conformer was present in all samples, suggesting that, even at lower temperature collection, the co-crystals are constantly undergoing pedal motion that is not temperature dependant, as is the case for *trans*-stilbene[271] and azobenzene.[270] The

constant motion is, in part, attributed to the co-crystal providing a more flexibile environment that can mediate molecular motion in solids.

4.7 Extension of a Supramolecular Protecting Group Strategy to 3-Pyridine-based Olefins

3-Pyridyl-containing olefins are not as commonly studied in the context of directing solid-state reactivity, relative to their 4-pyridyl counterparts. We have reported the head-to-head [2+2] photodimerization of the co-crystal 2(1,8-naphthalenedicarboxylic acid)·2(*trans*-1-(3-pyridyl)-2-(4-pyridyl)ethylene) to afford *rctt*-1,2-bis(3-pyridyl)-3,4-bis(4-pyridyl)cyclobutane (3,4-tpcb) in quantitative yield.[272] We have also demonstrated how 3,4-tpcb can be successfully utilized in MOF chemistry. Specifically, crystallization of 3,4-tpcb in the presence of $Zn(NO_3)_2$ afforded a 2D MOF of the composition $[Zn_2(3,4\text{-tpcb})_2(NO_3)_4(H_2O)_4]_\infty$.[273] The MOF exhibited three distinct cavities, owing to the ability of the combination of pyridyl groups to sustain tiling of square cavities, whereby the cavity walls comprise combinations of 3- and 4-pyridyl groups.

Following our work on the 4-pyridyl systems, we extended our combinatorial template switching strategy to the 3-pyridyl ester analogues (Figure 122). The 3-pyridyl analogues would be of interest from a post-synthetic standpoint. In particular, the 3-pyridyl moieties are expected to lead to different topologies and connectivities, as well as dimensionalities and pore sizes if used as organic building blocks for MOFs.

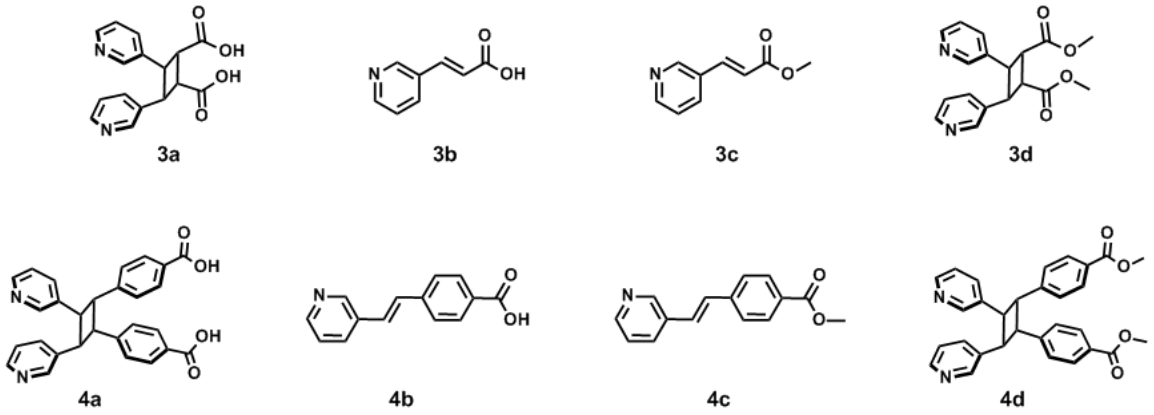

Figure 122: 3-Pyridyl starting olefins and cyclobutane products of interest in this study.

4.8 Experimental

All reagents and solvents used were reagent grade and commercially available. Acetic anhydride, N,N-dimethylformamide (99.9%), chloroform (99.8%), tetrahydrofuran (99.9%), and methanol (>99.8%) were purchased from Fisher Scientific Company (Pittsburgh, PA, USA). Ethanol (99.98%, absolute grade) was obtained from Pharmco-AAPER (Brookfield, CT, USA). 3-Pyridinecarboxaldehyde (97%), methyl (triphenylphosphoranylidene)acetate (98%), triethylphosphite (98%), sodium hydride (dry, 95%) and dichloromethane (≥99.8%) were purchased from Sigma Aldrich Chemical (St. Louis, MO, USA). Methyl-4-(bromomethyl)benzoate (>97%) was purchased from TCI America (Portland, OR, USA). All reagents were used without further purification. Substituted resorcinols were purchased commercially or synthesized *via* standard literature preparations. Silver paratoluene sulfonate (99.9+%), silver methanesulfonate (98%), silver trifluoromethanesulfonate (≥99.9%), silver nitrate (99.9+%), and silver perchlorate hydrate (99%) were purchased from Sigma Aldrich Chemical (St. Louis, MO, USA).

^{1}H NMR spectra were collected using a Bruker Avance 300 MHz or 400 MHz spectrometer using DMSO-d_6 as a solvent. IR Spectra were recorded using KBr pellets on a Nicolet 380 single beam FT-IR spectrometer. Photoreactions were conducted using ultraviolet radiation from a 500 W medium-pressure mercury lamp in an ACE Glass photochemistry cabinet. Co-crystals were finely ground using a mortar and pestle, and then placed between a pair of Pyrex glass plates. The samples were irradiated in 10-hour periods and mixed between consecutive irradiations. The product formation was monitored using ^{1}H NMR spectroscopy.

Single crystal diffraction data were collected on a Nonius Kappa CCD single-crystal X-ray diffractometer at both room and low temperatures using MoK_α radiation (λ = 0.71073 Å). Data collection, cell refinement and data reduction were performed using *Collect*[197] and *HKL Scalepack*/*Denzo*,[198] respectively. Structure solution and refinement were accomplished using SHELXS-97[261] and SHELXL-97,[199] respectively. The structures were solved *via* direct methods, while silver coordination complexes were solved using Patterson method. All non-hydrogen atoms were identified from the difference Fourier map within several refinement steps. All non-hydrogen atoms were refined anisotropically. Hydrogen atoms associated with carbon atoms were refined in geometrically constrained positions with isotropic thermal parameters U_{iso}(H) = 1.5U_{eq}(C_{CH3}) and U_{iso}(H) = 1.2U_{eq}(C_{CH}). Hydrogen atoms belonging to phenolic OH groups were and refined using a riding model with isotropic thermal parameters U_{iso}(H) = 1.5U_{eq}($O_{hydroxy}$). The details of the structural analysis of all solids are summarized in Tables A-14 through A-16. Powder X-ray data was collected on a Bruker D-5000 diffractometer equipped with a Bruker SOL-X energy-sensitive detector using CuK_α radiation (λ=1.54056 Å).

4.8.1 Synthesis of (*E*)-methyl-3-(pyridine-3-yl)prop-2-enoate 3c

A solution of 3-pyridinecarboxaldehyde (4.2 g, 0.0392 mol) in 10 mL of CH_2Cl_2 was slowly added to a solution of methyl (triphenylphosphoranylidene)acetate (12.0 g, 0.036 mol) in 60 mL CH_2Cl_2. The mixture was refluxed for 5 hours, and then cooled to ambient temp. Upon cooling to ambient temperature, pTsOH (0.0784 mol) was added with stirring to the CH_2Cl_2 solution. After stirring for 30 minutes, the acidified product was extracted with water (2x, 100mL), basified with K_2CO_3, and re-extracted with CH_2Cl_2 (2x, 50 mL). The solution was evaporated to yield a white solid free of the $Ph_3P{=}O$ byproduct (4.2 g, 72%). ^{1}H NMR (400 MHz, DMSO-d_6): δ/ppm = 8.91 (s, 1H, 8.63 (d, 1 H), 8.21 (dd, 1H), 7.74 (d, 1H), 7.48 (dt, 1H), 6.84 (d, 1H), 3.77 (s, 3H).

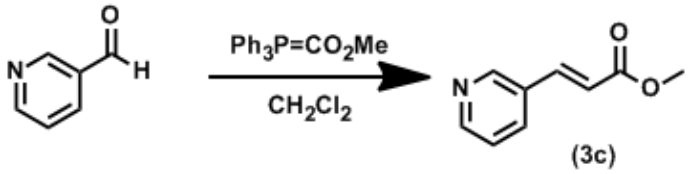

Figure 123: Synthesis of (*E*)-methyl-3-(pyridine-3-yl)prop-2-enoate *via* Wittig reaction.

4.8.2 Synthesis of (*E*)-methyl-4-[(2-pyridin-3-yl)ethenyl]benzoate 4c

Methyl-4-(bromomethyl)benzoate (5.2 g, 0.0227 mol) was refluxed in the presence of triethylphosphite (3.87 mL, 1 mol eq) for 4 hours. Upon cooling to room temperature, the cloudy solution was washed with H_2O (150 mL) and extracted with $CHCl_3$ (2x, 30 mL). After drying with Na_2SO_4, the solution was concetrated afford methyl-4-[(diethoxyphosphono)methyl] benzoate as a clear oil (6.5 g, 100%) which was

used in the subsequent step as synthesized. ^{1}H NMR (400 MHz, DMSO-d_6): δ/ppm = 7.91 (2H, d), 7.45 (2H, dd), 1.01 (4H, quintet), 3.84 (3H, s), 3.35 (2H, d), 1.16 (6H, t).

Methyl-4-[(diethoxyphosphono)methyl] benzoate (2.5 g, 0.0086 mol) was dissolved in 125 mL THF, and cooled to -10° C. Sodium hydride (0.7 g, 3.4 eq) was added slowly, followed by 0.95 g of 3-pyridinecarboxaldehyde (0.0086 mol) that was dissolved in 10 mL of THF. The resulting solution was allowed to stir to room temperature and for an additional 20 hours, followed by pouring onto 500 mL ice water. Upon vaccum filtration, (*E*)-methyl-4-[(2-pyridin-3-yl)ethenyl]benzoate was collected as a white solid (0.5 g, 24%). ^{1}H NMR (400 MHz, DMSO-d_6): δ/ppm = 8.85 (s, 1H), 8.53 (d, 1H), 8.12 (dd, 1H), 7.99 (d, 2H), 7.80 (d, 2H), 7.48 (multiplet of overlapping signals, 3H), 3.87 (s, 3H).

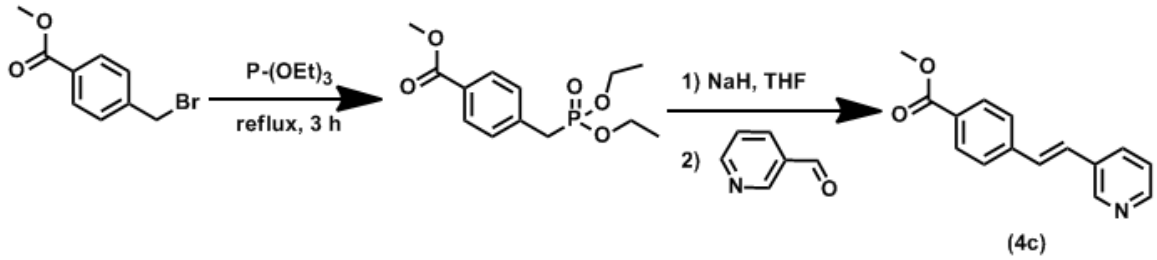

Figure 124: Synthesis of (*E*)-methyl-4-[(2-pyridin-3-yl)ethenyl]benzoate *via* Arbouzov and Horner-Wadsworth-Emmons reactions.

4.8.3 Co-crystallization Procedures

Co-crystallization experiments involving 3c were performed by dissolving 50 mg of the compound in 5 mL of ethanol and adding 0.5 mol equivalents of a res. The solution was heated to boiling and left to cool slowly to room temperature. Co-crystals formed within 72 hours and were isolated by vacuum filtration, washed with a small amount of ethanol and air-dried. Co-crystallization experiments involving 4c were performed by dissolving 50 mg of the compound in 10 mL ethanol and adding 0.5 mol equivalents of a

res. The solution was heated to boiling and left to cool slowly to room temperature. After standing at room temperature for 72 hours, the co-crystals that formed were isolated by vacuum filtration, washed with a small amount of ethanol and air-dried.

4.8.4 Silver Coordination Complex Formation

Silver complexes comprising 3c were prepared by dissolving 50 mg of 3c in 10 mL aqueous ethanol with heating and adding 0.5 mol equivalents of Ag(I)X. Individual vials were wrapped in Aluminum foil to prevent silver oxidation. Within a period of 7-10 days, crystals formed in most attempts. Single crystals were filtered, dried, and analyzed using ^{1}H NMR spectroscopy.

4.8.5 Photoproduct Hydrolyses

The photoproducts 3d and 4d were stirred in 2M NaOH for 2 h. 10% HCl was added until neutral by pH paper and the solutions were allowed to stir overnight. Evaporation yielded the product and sodium chloride. Trituration of the solid with 2:1 CH_3OH:$CHCl_3$ solution, followed by evaporation of the solvent, afforded diacids 3a and 4a. ^{1}H NMR (3a, 400 MHz, DMSO-d_6): δ/ppm =8.26 (s, 2H), 8.19 (d, 2H), 7.38 (d, 2H), 7.05 (dt, 2H), 4.41 (d, 2H), 3.63 (d, 2H). ^{1}H NMR (4a, AVA 400, DMSO-d_6): δ/ppm = 8.46 (s, 2H), 8.32 (d, 2H), 7.68 (d, 4H), 7.25 (d, 4H), 7.08 (dt, 2H), 7.00 (d, 2H), 4.80 (d, 4H).

4.9 Results

In our attempts to screen for a reactive res-based co-crystal of 3c, we encountered difficulties in that no co-crystal formed directed reactivity. In addition, we were only able to characterize one co-crystal of 3c. However, we turned to coordination-drive self-assembly mediated by Ag(I) salts to promote reactivity within 3c. We have isolated and characterized three silver complexes and one co-crystal comprising 3c, as well as a silver complex containing the ester photoproduct 3d. For the longer olefin 4c, we also used

both res templates and Ag(I) salts to direct reactivity. We have isolated and characterized one co-crystal and one silver complex consisting of 4c, both of which lead to 100% conversion to the desired diester cyclobutane 4d. The two co-crystals and six silver complexes are described below.

(1) 2(3c)·(4,6-diBr res). 2(3c)·(4,6-diBr res) crystallizes from EtOH in the monoclinic space group $P\bar{1}$. The molecules assemble to form discrete three-component hydrogen bonding assemblies sustained through the formation of two O—H···N forces [O···N separations (Å): O1···N1 2.717, O2···N2 2.748]. The C=C bonds within each assembly are parallel, aligned, and separated by 4.049 Å (Figure 125). Neighboring assemblies are stacked in an orthogonal manner, such that the C=C bonds between assemblies do not overlap effectively. Additional interactions in the form of (pyridine) C—H···O (carboxy) and (pyridne) C—H···O (phenol) forces are present between adjacent assemblies ($d_{C\cdots O}$ = 3.357 Å, 3.371 Å; $d_{C\cdots O}$ = 3.189 Å, 3.244 Å).

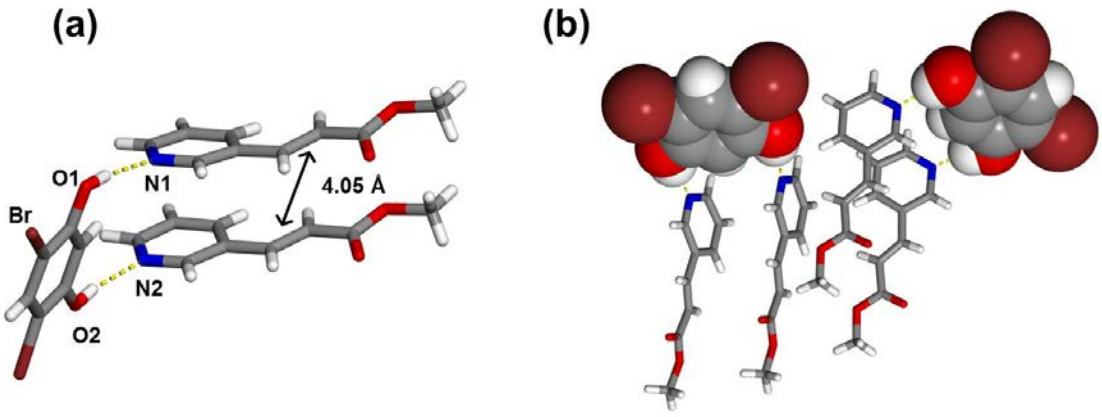

Figure 125: X-ray structure of 2(3c)·(4,6-diBr res): (a) assembly with parallel C=C bonds and (b) orthogonal packing.

(2) $[Ag_2(3c)_4][OSO_2CF_3]_2$. Reaction of 3c with $AgOSO_2CF_3$ in aqueous EtOH afforded a dinuclear Ag(I) coordination complex that crystallizes in the triclinic space

group $P\bar{1}$. The dinuclear complex is sustained by argentophilic interactions (d_{Ag-Ag} = 3.178 Å), with each Ag(I) being coordinated by two 3c ligands in a linear fashion (Figure 126). The C=C bonds within each dinuclear assembly are situated in a parallel and aligned fashion, with a C···C separation of 3.769 Å. The -OSO_2CF_3 anion lies in close proximity to the Ag(I) ion, yet is non-coordinating, and interacting with the silver *via* Ag···O interactions ($d_{Ag\cdots O}$ = 2.728 Å, 2.912 Å). The anion also participates in additional interactions in the form of (pyridine) C—H···O (triflate) and (alkenyl) C—H···O (triflate) forces ($d_{C\cdots O}$ = 3.332 Å, 3.495 Å, 3.449 Å; $d_{C\cdots O}$ = 3.426 Å). Neighboring assemblies also interact *via* (pyridine) C—H···O (carboxy) dimers and Ag···π (alkene) interactions that give rise to a 2D sheet (Figure 126b).

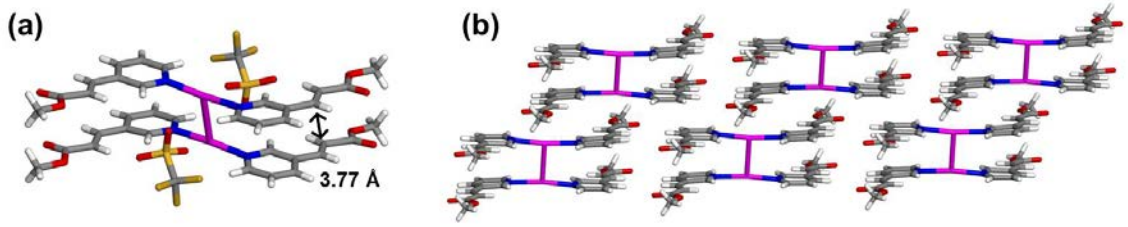

Figure 126: X-ray structure of $[Ag_2(3c)_4][OSO_2CF_3]_2$: (a) assembly with parallel C=C bonds and (b) offset extended packing.

(3) $[Ag_2(3c)_4][ClO_4]_2$. Crystallization of 3c in the presence of $AgClO_4 \cdot xH_2O$ in aqueous EtOH afforded a dinuclear Ag(I) coordination complex sustained by argentophilic interactions (d_{Ag-Ag} = 3.209 Å). The dinuclear complex crystallizes in the triclinic space group $P\bar{1}$ with each Ag(I) being coordinated by two 3c ligands in a linear fashion (Figure 127a,b). The olefins within each dinuclear assembly are aligned parallel with a C···C separation of 3.640 Å. The -ClO_4 anion lies in close proximity to the Ag(I) centers and is non-coordinating, yet interacting with the silver *via* Ag···O interactions ($d_{Ag\cdots O}$ = 2.746 Å, 3.246 Å). The perchlorate anion also participates in additional

interactions in the form of (pyridine) C—H···O forces ($d_{C\cdots O}$ = 3.527 Å, 3.576 Å). Similar to $[Ag_2(3c)_4][OSO_2CF_3]_2$, neighboring assemblies are offset, owing to (pyridine) C—H···O (carboxy) dimers and Ag···π (alkene) interactions that give rise to a 2D sheet (Figure 127c).

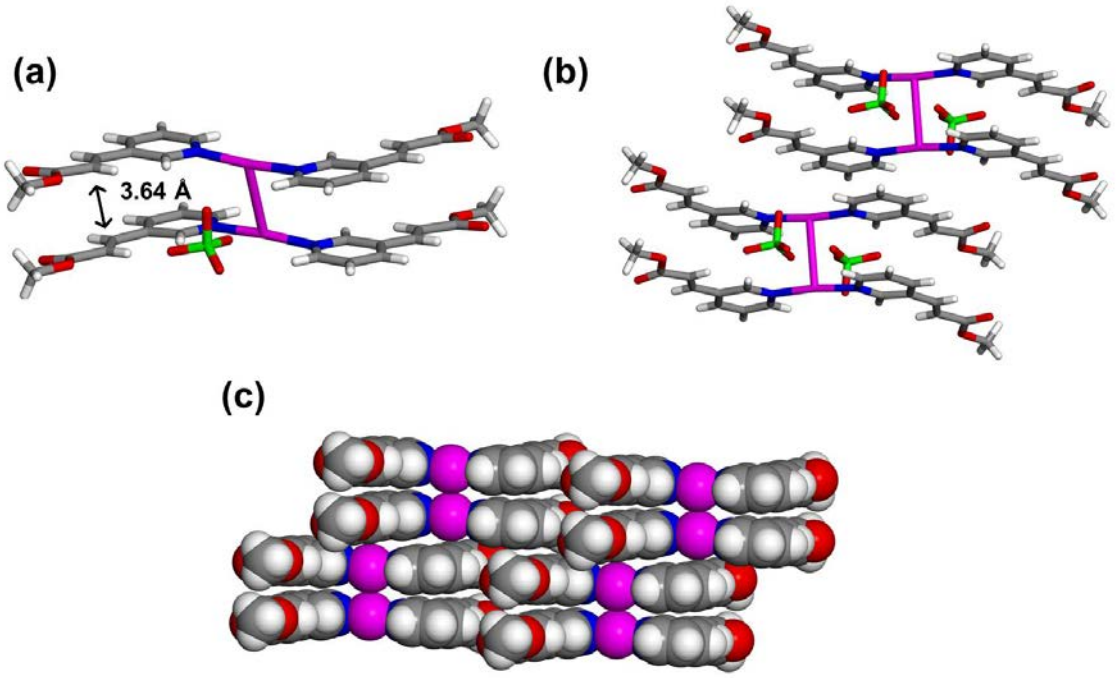

Figure 127: X-ray structure of $[Ag_2(3c)_4][ClO_4]_2$: (a) assembly with parallel C=C bonds and (b) offset extended packing.

(4) [Ag(3c)$_2$][OTs]. Reaction of 3c with AgOTs in aqueous EtOH afforded an Ag(I) coordination complex that crystallizes in the monoclinic space group $P2_1/n$. The complex interacts with another complex below it *via* argentophilic interactions ($d_{Ag\cdots Ag}$ = 3.372 Å). Each Ag(I) center is coordinated by two 3c ligands in a linear fashion (Figure 128), as well as one tosylate anion. The C=C bonds within each interacting pair are situated in a parallel and aligned fashion, with a C···C separation of 3.723Å, while neighboring C=Cs are also parallel and aligned ($d_{C\cdots C}$ = 3.842 Å). The tosylate anion also participates in Ag···O and (pyridine) C—H···O (tosylate) forces ($d_{Ag\cdots O}$ = 3.224 Å,

3.340 Å, 3.469 Å, 3.413 Å; $d_{C\cdots O}$ = 3.217 Å, 2.557 Å). Neighboring assemblies also interact *via* (pyridine) C—H···O (carboxy) forces ($d_{C\cdots O}$ = 3.747 Å, 3.842 Å).

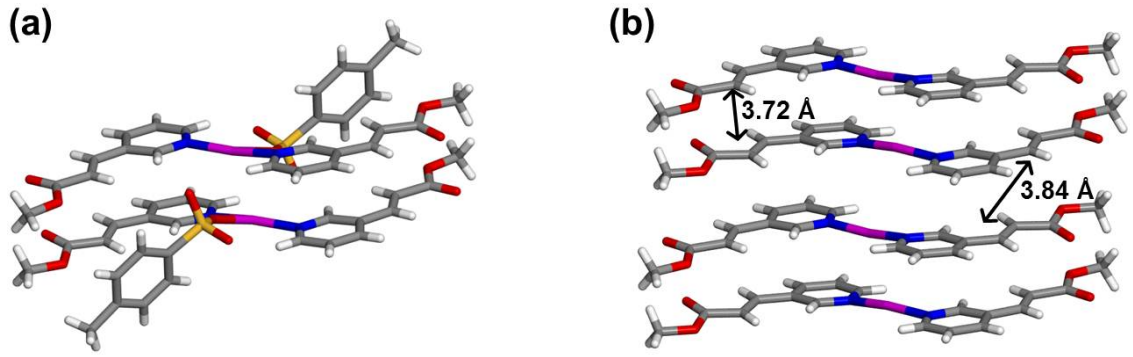

Figure 128: X-ray structure of $[Ag(3c)_2][OTs]$: (a) assembly with parallel C=C bonds and (b) extended packing with anions omitted for clarity.

(5) 2(4c)·(4,6-diCl res). 2(4c)·(4,6-diCl res) crystallizes from EtOH in the monoclinic space group $P2_1/c$. The molecules form discrete three-component assemblies sustained through the formation of two O—H···N hydrogen bonds [O···N separations (Å): O1···N1 2.774, O2···N2 2.748]. The C=C bonds within each assembly are parallel, aligned, and separated by 3.924 Å (Figure 129). Similar to 2(3c)·(4,6-diBr res), neighboring assemblies are stacked in an orthogonal manner, such that the C=C bonds between assemblies do not overlap effectively ($d_{C\cdots C}$ = 5.797 Å). Additional interactions in the form of (pyridne) C—H···Cl (res), (pyridine) C—H···O (carboxy), and (pyridne) C—H···O (phenol) forces are present between adjacent assemblies ($d_{C\cdots Cl}$ = 3.649 Å, $d_{C\cdots O}$ = 3.508 Å, 3.652 Å, 3.196 Å, 3.197 Å; $d_{C\cdots O}$ = 3.338 Å).

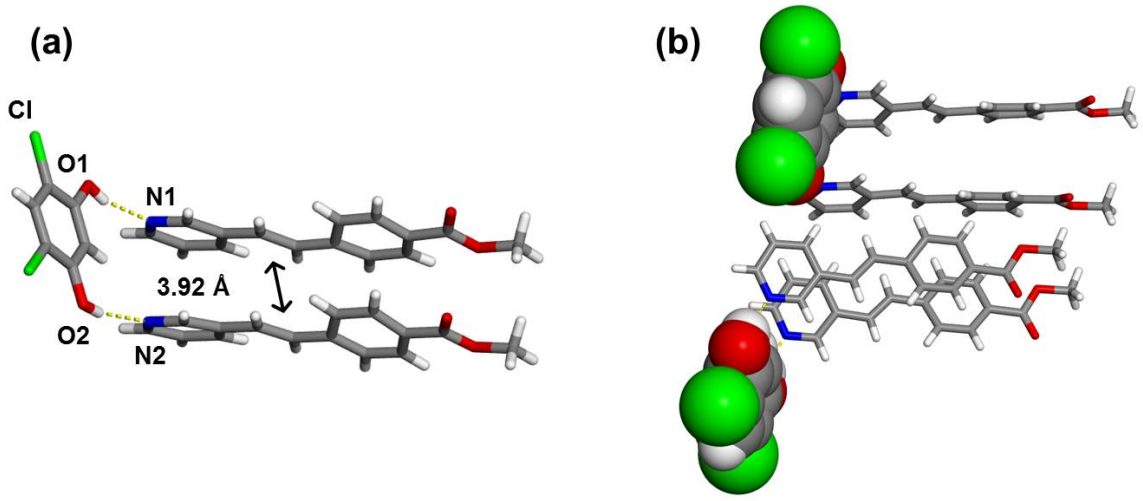

Figure 129: X-ray structure of 2(4c)·(4,6-diCl res): (a) assembly with parallel C=C bonds and (b) orthogonal packing.

(6) $[Ag(4c)_2][OSO_2CF_3]$. Reaction of 4c with $AgOSO_2CF_3$ in aqueous EtOH afforded an Ag(I) coordination complex that crystallizes in the triclinic space group $P\bar{1}$. The complex interacts with a complex under it through argentophilic interactions ($d_{Ag\cdots Ag}$ = 3.496 Å), with each Ag(I) being coordinated by two 4c ligands in a linear fashion (Figure 130). The C=C bonds within each interacting pair are situated in a parallel and aligned fashion, with a C···C separation of 3.869Å, with the next closest set of C=Cs separated by 3.996 Å. The OSO_2CF_3 anion lies in close proximity to the Ag(I) ion, yet is non-coordinating, and interacting with the silver *via* Ag···O interactions ($d_{Ag\cdots O}$ = 2.894 Å, 2.838 Å). The triflate anion also participates in additional interactions in the form of (pyridine) C—H···O (carboxy) and (alkyl) C—H···O (triflate) forces ($d_{C\cdots O}$ = 3.282 Å; $d_{C\cdots O}$ = 3.286 Å).

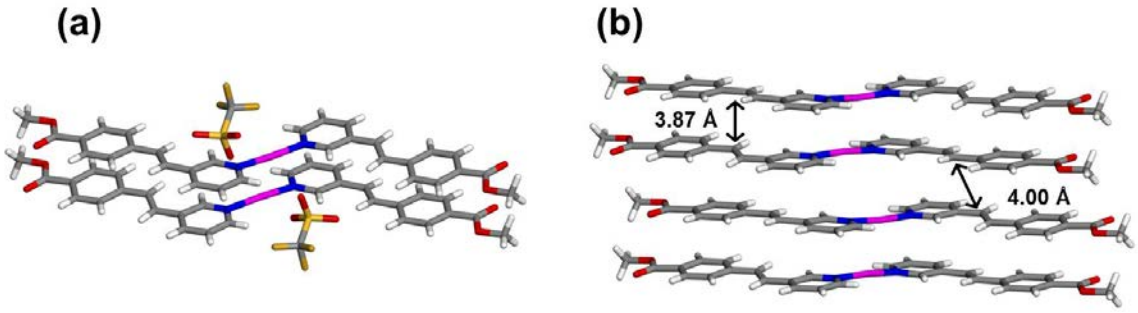

Figure 130: X-ray structure of $[Ag(4c)_2][OSO_2CF_3]$: (a) assembly with parallel C=C bonds and (b) extended parallel packing with anions omitted for clarity.

UV irradiation of powdered crystalline samples of $[Ag_2(3c)_4][OSO_2CF_3]_2$, $[Ag_2(3c)_4][ClO_4]_2$, and $[Ag(3c)_2][OTs]$, as well as $[Ag_2(3c)_4][OSO_2CH_3]_2$ afforded the desired photoproduct 3d in stereospecific and quantitative fashion. The generation of cyclobutane 3d was reflected in the resulting ^1H NMR, as the olefin peaks centered at 7.77 and 6.87 ppm had disappeared, and cyclobutyl protons at 4.18 and 4.60 ppm emerged. The structure of the photoproduct was confirmed in the case of $[Ag_2(3c)_4][OSO_2CH_3]_2$ (Figure 131).

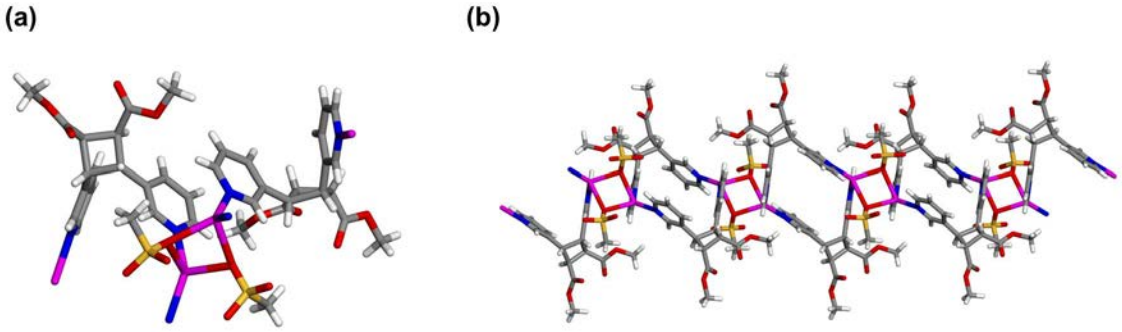

Figure 131: X-ray crystal structure of $[Ag(3d)_2][OSO_2CH_3]$ demonstrating 1D polymer network.

In the case of the extended olefin 4c, UV-irradiation of crystalline 2(4c)·(4,6-diCl res) and $[Ag(4c)_2][OSO_2CF_3]$ afforded the diester photoproduct 4d in stereospecific and quantitative yield. The quantitative photoconversion was evidenced in the ^{1}H NMR spectrum by the disappearance of the olefinic signals between 7.4 and 7.5 ppm and concomitant appearance of the cyclobutane doublets centered at 4.75 ppm (Figure 132).

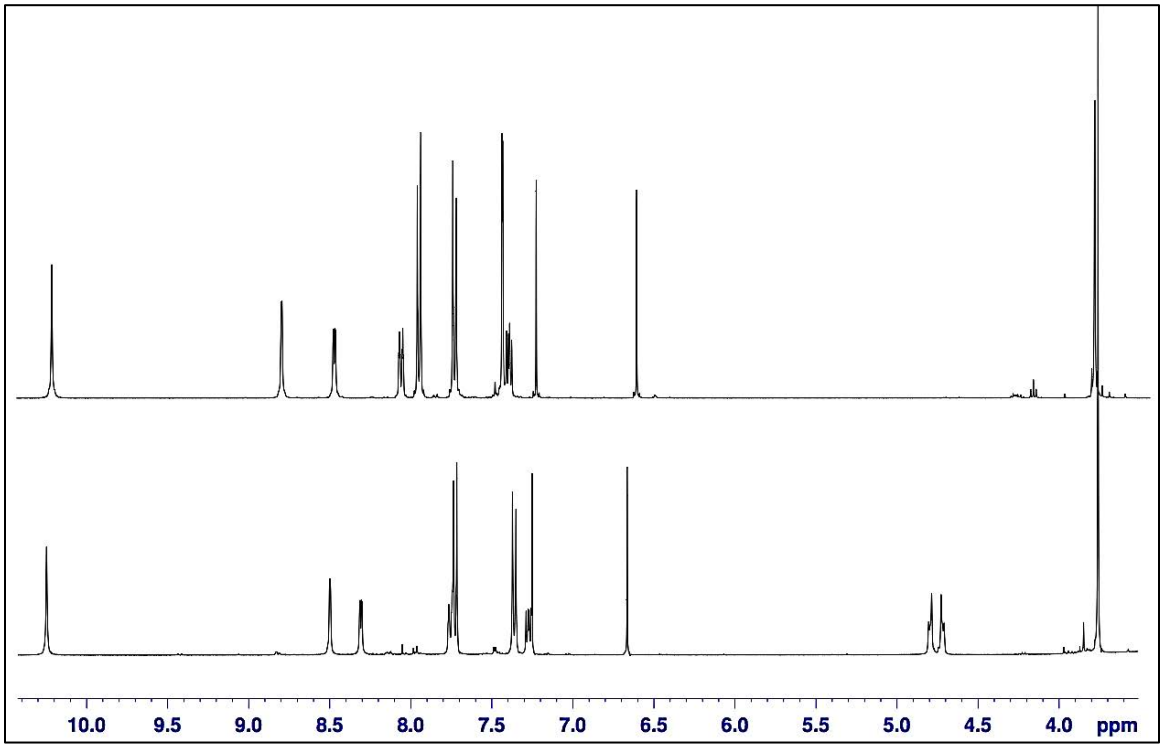

Figure 132: Comparison of the ^{1}H NMR spectrum of (top) 2(4c)·(4,6-diCl res) superimposed with (4d)·(4,6-diCl res) (bottom).

Other co-crystals and coordination complexes were tested in regards to photoreactivity of 3c and 4c. In the context of directing reactivity with resorcinol templates and 3c, none had produced photoreactions (evidenced through ^{1}H NMR), while other Ag(I) salts underwent conversion to 3d. In particular, $AgOSO_2CH_3$ also demonstrated full conversion to 3d. Interestingly, the reactivity of 4c is somewhat

similar to the 4-pyridyl analogue 2c. We observed anywhere from 20-100% conversion with both organic and Ag(I) templates tested (Table 7). Without further structural analyses, however, it cannot be ascertained why the reactivity is not as high in some cases. The enhanced reactivity of 4c in comparison to 3c, is likely due to a degree of pedal motion, although we did not examine this effect in as much detail as accomplished for the 4-pyridyl analogues.

Table 7: Summary of additional photoreactivity data obtained for 3c and 4c.

olefin	template	conv./%	time/h	yield of 3d/4d
3c	$AgOSO_2CH_3$	100	150	100
3c	4,6-di^{t}Bu res	0	150	0
3c	4,6-diI res	0	150	0
4c	AgOTs	100	100	100
4c	$AgClO_4$	0	150	0
4c	5-F res	65[a]	150	65[b]
4c	res	90	150	90[b]
4c	$AgNO_3$	90	150	90
4c	AgOMs	100	100	100

[a] photoreactions were concluded after 150 hrs since other samples exhibited full conversion in less time

[b] ^{1}H NMR shows an overlapping peak in the cyclobutane region that could affect the overall yield

Basic extraction and a subsequent hydrolysis of [Ag(3d)][OTs] and (4d)·(4,6-diCl res) afforded the unmasked diacids 3a and 4a, respectively, as confirmed by ^{1}H NMR spectroscopy.

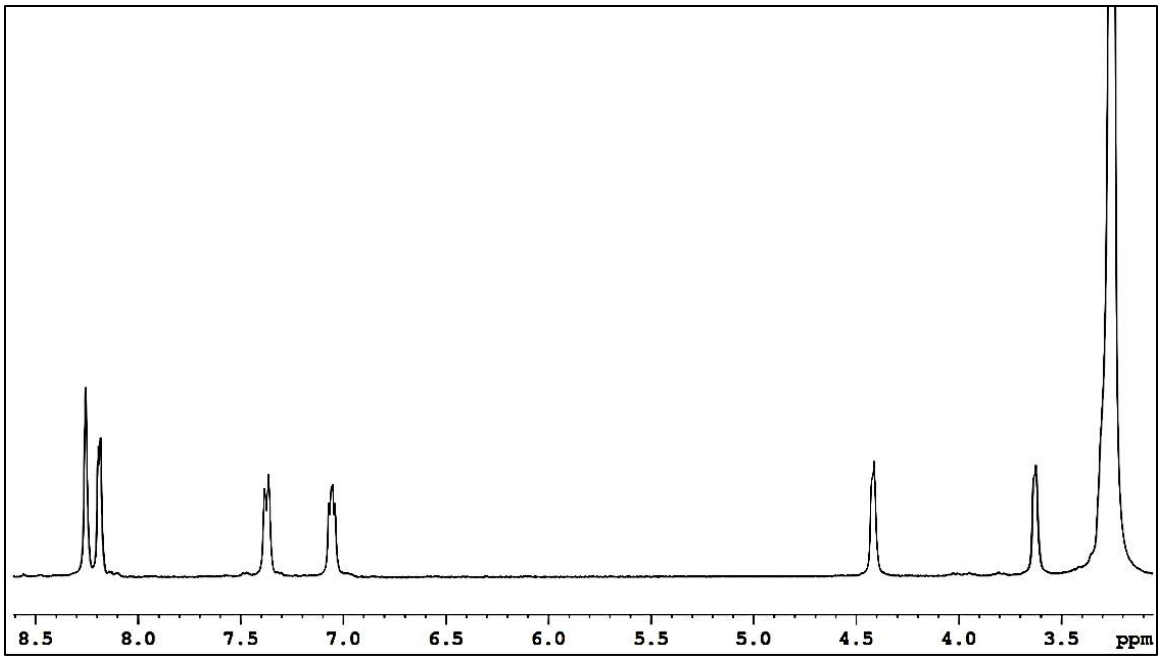

Figure 133: Representative ^{1}H NMR after hydrolysis, affording diacid 3a (large peak at ~3.3 ppm indicative of water).

4.10 Conclusion

In conclusion, we have introduced a protecting group strategy to the organic solid state that is used to direct the formation of C–C bonds mediated by principles of supramolecular chemistry. We have demonstrated that four carboxylic acid-based olefins whose photoproducts are of interest to generate novel MOFs, can be used in solid-state reactivity when the carboxylic acid proton is masked as an ester. Such a protecting group strategy essentially installs a supramolecular regiochemistry, so as to afford head-to-head photodimers that can be easily deprotected to restore the desired acid groups. We have also shown how the solid-state reactivity is enhanced using stilbenes as protected

functionalities. We have also observed that the flexible nature of an organic co-crystal appears to promote the pedal motion since the minor population is largely unaffected by rapid cooling, as is witnessed in organic stilbene crystals (i.e. *trans*-stilbene, azobenzene).[270-271] We anticipate the protecting strategy to be amenable to other protecting group strategies developed in the liquid phase and applicable to other reactions mediated by templates (e.g. hydrogen bond acceptor) in both the solid state and solution.

CHAPTER 5: TOLERANCE OF SELF-ASSEMBLY AND SOLID-STATE REACTIVITY TO THE INTRODUCTION OF CONFORMATIONALLY-FRUSTRATED OLEFINS

5.1 Introduction

Supramolecular chemistry focuses on the design of molecular architectures by relying on the complementary recognition and assembly of well-defined subunits.[274] The idea of molecular recognition stems from biology. Utilising noncovalent forces to dictate structural and morphological properties, biological systems must balance a panoply of intermolecular interactions to achieve targeted properties. In an analogous effort to mimic Nature, chemists employ noncovalent interactions to direct supramolecular self-assembly.[89]

Within the field of supramolecular chemistry, two main areas have emerged to facilitate self-assembly processes. One relies on the exploitation of hydrogen bonds[16] while the other relies on stronger metal-ligand interactions to achieve targeted frameworks.[275] In principle, both forces can be used to accomplish *the same goal* (Figure 134). This is particularly relevant for chemical reactivity, where reactants must follow specific geometries for a reaction to proceed when subjected to supramolecular control.[83] We have described how either small molecules (e.g. resorcinol) or metal complexes (e.g. Ag^{I}) can be utilized to direct reactivity within the organic solid state for [2+2] photodimerizations of olefins *via* hydrogen bonds and coordination bonds, respectively.[81] Both interactions have been shown to circumvent problems associated with crystal packing. In this context, organic templates have, thus far, been particularly successful, yielding complex products such as cyclophanes[96] and ladderanes.[95]

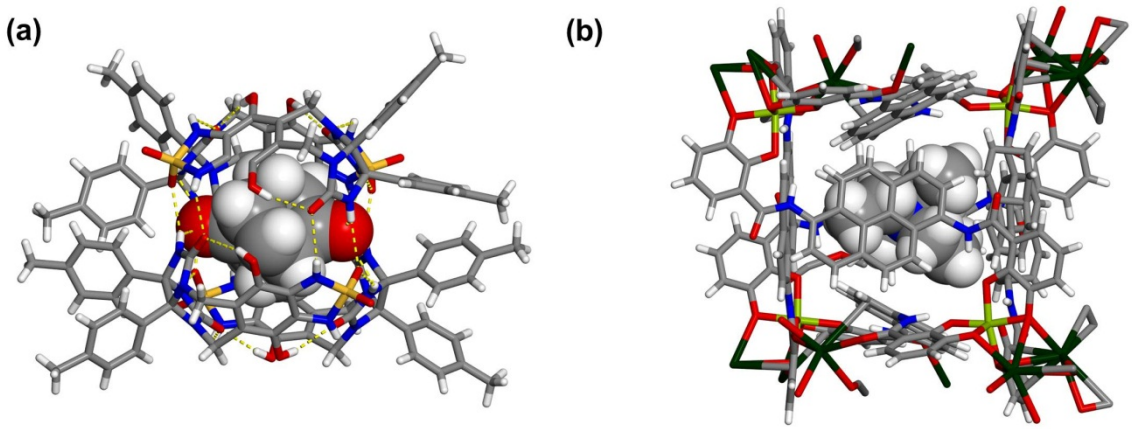

Figure 134: Supramolecular self-assembly methods employed to synthesize capsules *via* (a) hydrogen bonding and (b) metal coordination by Rebek[276] and Raymond,[277] respectively (K = dark green; Ga = lime).

To expand the applicability of the template method, we have pursued the photoreaction of trisubstituted olefins. Trisubstituted olefins are a large focus of solution-phase organic synthesis (e.g. carotenoids, terpenoids).[278] The inherent bioactivity of drugs (e.g. Mithramycin[279]) can also, for example, be rendered active *via* installation of additional substituents to C=C bonds (i.e. methyl – hydrogen substitution). Moreover, whereas trisubstituted olefins are widely studied in solution, such olefins remain relatively unexplored in solid-state reactivity. To date, reactions of trisubstituted olefins have been limited to retinoids, coumarins, quinones, and substituted cyclohexenes.[280] Importantly, trisubstitution, *de facto*, results in a steric environment that can enforce non-planarity and, thereby, pose a significant challenge to achieve face-to-face stacking in a solid.

In this chapter, we demonstrate the advantage of having templates based on hydrogen bonding and metal coordination at our disposal to direct reactivity of three trisubstituted olefins (Figure 135). We show that whereas co-crystallization of the olefins with a series of res templates invariably affords photostable solids, UV-irradiation of

crystalline Ag complexes of 3-Me-4-pyes, 3-Me-3-pyes, and 2-Me-4-pyes results in the generation of the corresponding hexa-substituted cyclobutane in quantitative yields.

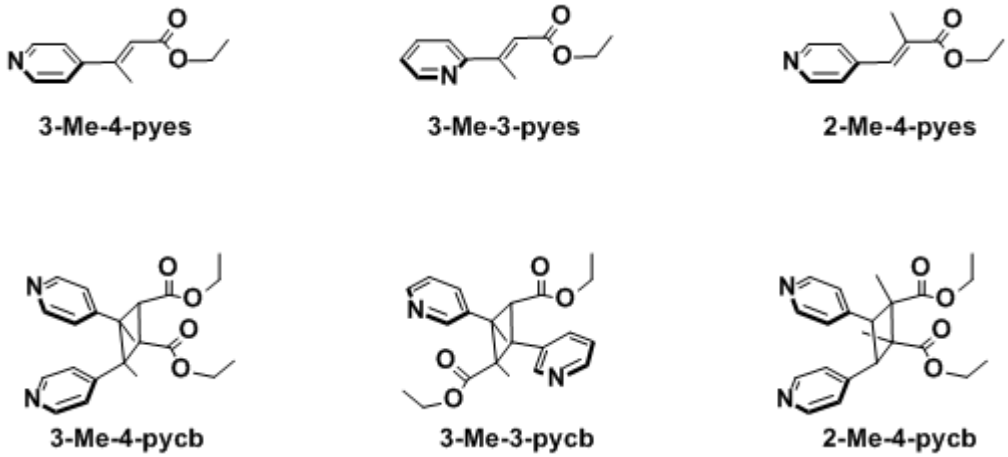

Figure 135: Trisubstituted olefins of interest and resulting cyclobutane products.

The olefins under investigation (3-Me-4-pyes, 3-Me-3-pyes, and 2-Me-4-pyes) are all liquids prepared *via* Horner Wadsworth Emmons reaction. According to molecular modelling, all three prefer a twisted geometry in the gas phase, wherein the pyridyl group is rotated on the order of 55-63° to presumably relieve steric interactions with the methyl group (Figure 136).

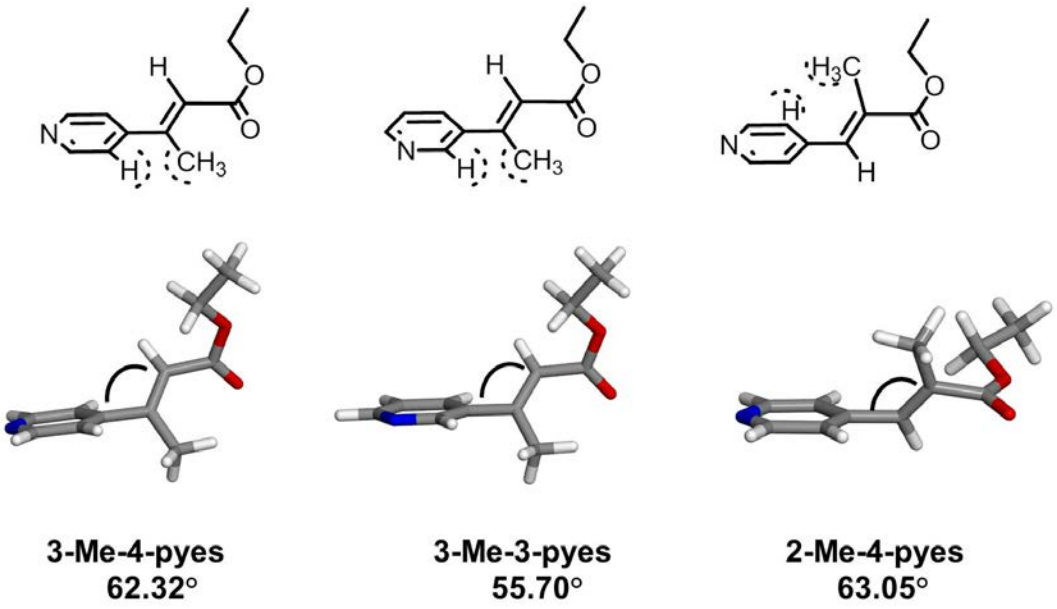

Figure 136: Spartan rendering of olefins in this study and their relative geometries and twist after energy minimization

5.2 Experimental

All reagents and solvents used were reagent grade and commercially available. N, N-dimethylformamide (99.9%) and tetrahydrofuran (99.9%), were purchased from Fisher Scientific Company (Pittsburgh, PA, USA). Ethanol (99.98%, absolute grade) was purchased from Pharmco-AAPER (Brookfield, CT, USA). 4-Pyridinecarboxaldehyde (97%), 3-pyridinecarboxaldehyde (97%), 4-acetylpyridine (97%), triethyl-2-phosphonopropionate (98%), sodium hydride (dry, 95%) and dichloromethane (≥99.8%) were purchased from Sigma Aldrich Chemical (St. Louis, MO, USA). 3-Acetylpyridine (97%) was purchased from TCI America (Portland, OR, USA). Triethylphosphonoacetate (98%) and potassium tert-butoxide (98+%) were purchased from ACROS. All reagents were used without further purification. Substituted resorcinols were purchased commercially or synthesized *via* standard literature preparations. Silver paratoluene sulfonate (99.9+%), silver heptafluorobutyrate (98%),

silver methanesulfonate (98%), silver trifluoromethanesulfonate (≥99.9%), silver nitrate (99.9+%), silver chlorate (≥99.9%), and silver perchlorate hydrate (99%) were purchased from Sigma Aldrich Chemical (St. Louis, MO, USA).

Purification of the products was accomplished using column chromatography using a gradient solvent elutant system. The column (two inches in diameter) was wet packed with *ca.* 10-12 inches of silica gel in hexanes (hex). Details on the elutants used and results are listed for each compound below:

(*E*)-ethyl-3-(pyridine-4-yl)but-2-enoate (3-Me-4-pyes): The oil was used in crude form and deposited on top of the column without further dilution. Initially, straight hexanes was used as the elutant, followed by gradual increases in polarity to hex/5% EtOAc, 6:1 hex/EtOAc, 1:1 hex/EtOAc. The hexane fractions contained the highest E:Z ratio (10:1) with the hex/5% EtOAc exhibiting ~2:1 ratio.

(*E*)-ethyl-3-(pyridine-3-yl)but-2-enoate (3-Me-3-pyes): The oil was used in crude form and deposited on top of the column without further dilution. Initially, hexanes was used as the elutant, followed by gradual increases in polarity to hex/5% EtOAc, 6:1 hex/EtOAc, 1:1 hex/EtOAc. The hexane fractions contained the highest E:Z ratio (10:1) with the hex/5% EtOAc exhibiting ~1:1 ratio.

(*E*)-ethyl-2-methyl-3-(pyridine-4-yl)prop-2-enoate (2-Me-4-pyes): The oil was dissolved in minimal 1:1 hex/EtOH and deposited on top of the column. Initially, a mixture of 7:1 hex:EtOH was used as the elutant, followed by gradual increases in polarity to 3:1 hex/EtOH, and 1:1 hex/EtOH. The initial fractions using 7:1 hex/EtOH contained the most product.

^{1}H NMR spectra were collected using a Bruker Avance 300 MHz or 400 MHz spectrometer using DMSO-d_6 as a solvent. Photoreactions were conducted using ultraviolet radiation from a 500 W medium-pressure mercury lamp in an ACE Glass photochemistry cabinet. Co-crystals were finely ground using a mortar and pestle, and then placed between a pair of pyrex glass plates. The samples were irradiated in 10-hour

periods and mixed between consecutive irradiations. The product formation was monitored using ^{1}H NMR spectroscopy.

Single crystal diffraction data were collected on a Nonius Kappa CCD single-crystal X-ray diffractometer at both room and low temperatures using MoK_α radiation (λ = 0.71073 Å). Data collection, cell refinement and data reduction were performed using *Collect*[197] and *HKL Scalepack*/*Denzo*,[198] respectively. Structure solution and refinement were accomplished using SHELXS-97[261] and SHELXL-97,[196] respectively. The resorcinol structures were solved *via* direct methods, while silver coordination complexes were solved using Patterson method. All non-hydrogen atoms were indentified from the difference Fourier map within several refinement steps. All non-hydrogen atoms were refined anisotropically. Hydrogen atoms associated with carbon atoms were refined in geometrically constrained positions with isotropic thermal parameters $U_{iso}(H) = 1.5U_{eq}(C_{CH3})$ and $U_{iso}(H) = 1.2U_{eq}(C_{CH})$. Hydrogen atoms belonging to phenolic OH groups were and refined using a riding model with isotropic thermal parameters $U_{iso}(H) = 1.5U_{eq}(O_{hydroxy})$. Hydrogen atoms belonging to water molecules were identified from the difference Fourier and refined with isotropic thermal parameters $U_{iso}(H) = 1.5U_{eq}(O_{water})$. The details of the structural analysis of all solids are summarized in Tables A-17 through A-21.

5.2.1 Synthesis of (*E*)-ethyl-3-(pyridine-4-yl)but-2-enoate

Potassium tert-butoxide (7.7 g, 1.0 mol. eq.) was added to a solution of triethylphosphonoacetate (15.2 g, 0.068 mol.) in DMF (100 mL). A solution of 4-acetylpyridine (8.5 g, 0.070 mol.) in 15 mL of DMF was then added slowly. The solution was heated to reflux for 1 day. After 1 day, the hot solution was poured onto 1 L of ice water and stirred for 3 hours. The product was then extracted using $CHCl_3$ (5x, 200 mL) and concentrated to a brown oil (10.3 g). The oil was purified using column chromatography (conditions described above), affording 8.5 g of a yellow oil (67%, E:Z

10:1). Subsequent fractions (2.5 g) contained a lower E:Z ratio. ^{1}H NMR, *E*-isomer signals (400 MHz, DMSO-d_6): δ/ppm = 8.64 (dd, 2H), 7.60 (dd, 2H), 6.34 (s, IH), 4.21 (quartet, 2H), 2.53 (s - overlap in DMSO, 1H), 1.288 (t, 3H).

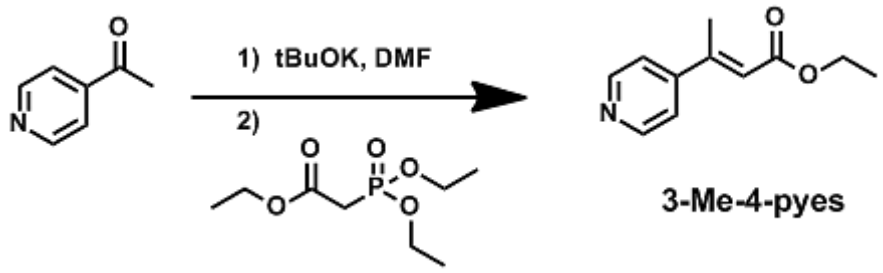

Figure 137: Synthesis of 3-Me-4-pyes *via* Horner-Wasdworth-Emmons reaction

5.2.2 Synthesis of (*E*)-ethyl-3-(pyridine-3-yl)but-2-enoate

Potassium tert-butoxide (7.7 g, 1.0 mol. eq.) was added to a solution of triethylphosphonoacetate (15.2 g, 0.068 mol.) in DMF (100 mL). A solution of 3-acetylpyridine (8.5 g, 0.070 mols) in 15 mL of DMF was then added slowly. The solution was heated to reflux for 1 day. After 1 day, the hot solution was poured onto 1 L of ice water and stirred for 3 hours. The product was then extracted using $CHCl_3$ (5x, 200 mL) and concentrated to a brown oil contaminated with some DMF (12.5 g). The oil was purified using column chromatography (conditions described above), affording 9.0 g of a yellow oil (70%, E:Z 10:1). Subsequent fractions (2.2 g) contained a lower E:Z ratio. ^{1}H NMR, *E*-isomer signals (400 MHz, DMSO-d_6): δ/ppm = 8.77 (s, IH), 8.60 (d, 1H), 7.95 (dd, 1H), 7.41 (dt, 1H), 6.20 (s, 1H), 4.16 (quartet, 2H), 2.53 (s - overlap in DMSO, 3H), 1.25 (t, 3H).

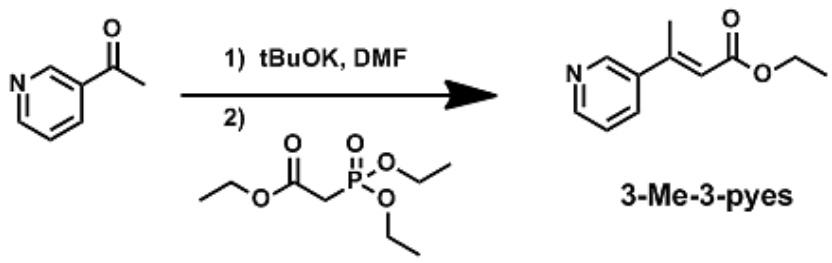

Figure 138: Synthesis of (*E*)-ethyl-3-(pyridine-3-yl)but-2-enoate *via* Horner-Wasdworth-Emmons reaction.

5.2.3 Synthesis of ((*E*)-ethyl-2-methyl-3-(pyridine-4-yl)prop-2-enoate

A solution of triethyl-2-phosphonopropionate (10.0 g, 0.0420 mol) in 200 mL of THF was cooled to -10° C. Sodium hydride (1.1 g, 1.1 mol. eq.) was added slowly to the solution. After 5 minutes, a solution of 4-pyridinecarrboxaldehyde (4.5 g, 1.0 mol. eq.) in 15 mL of THF was added slowly to cooled solution. The reaction was monitored *via* ^{1}H NMR, and was determined to be complete after 16 hours. The crude product was obtained *via* evaporation of the reaction mixture (9.6 g). Column chromatography using a hex/EtOH-based system (described above) afforded the pure product as a clear oil (6.8 g, 85%). ^{1}H NMR, *E*-isomer signals (400 MHz, DMSO-d_6): δ/ppm = 8.63 (dd, 2H), 7.52 (s, 1H), 7.36 (dd, 2H), 4.20 (quartet, 2H), 2.03 (s, 3H), 1.26 (t, 3H).

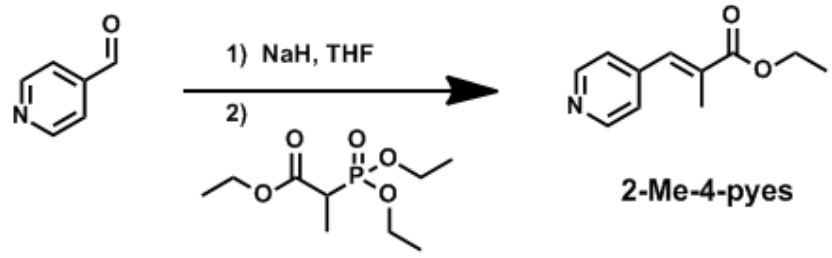

Figure 139: Synthesis of ((*E*)-ethyl-2-methyl-3-(pyridine-4-yl)prop-2-enoate *via* Horner-Wadsworth-Emmons reaction.

5.2.3 Co-crystallization Procedures

Co-crystallization of 3-Me-4-pyes, 3-Me-3-pyes, and 2-Me-4-pyes were performed by dissolving 100 mg (0.52 mmol) of the olefin and 0.26 mmol of a resorcinol in 10 mL EtOH. The solutions were heated slightly to facilitate dissolution, and then left to cool to room temperature. Upon further solvent evaporation, and within 4-7 days, each sample comprising 3-Me-4-pyes or 2-Me-4-pyes contained either single crystals or a crystalline powder that was filtered, dried, and characterized using ^{1}H NMR spectroscopy. After 4-7 days, the co-crystallization attempts of 3-Me-3-pyes invariably afforded oils that couldn't be quantified in the context of co-crystallization and/or photoreactivity.

5.2.4 Silver Coordination Complex Formation

Silver complexes comprising 3-Me-4-pyes, 3-Me-3-pyes, or 2-Me-4-pyes were prepared by dissolving 0.26 mmol of a silver salt in 10 mL aqueous ethanol with heating. 100 mg (0.52 mmol) of the desired olefin was diluted in 5 mL of ethanol and added to the silver solution. Individual vials were wrapped in Aluminum foil to prevent silver oxidation. Within a period of 7-10 days, crystals formed in most attempts. Single crystals were filtered, dried, and analyzed using ^{1}H NMR spectroscopy.

5.3 Results

In our investigations with nonplanar trisubstituted olefins, we have determined that Ag(I) templates appear better suited to direct reactivity in conformationally-complex olefins, as no resorcinol co-crystals yielded photoactive assemblies. From these studies, we have characterized six resorcinol co-crystals and eight Ag complexes with three isomeric olefins, as well as three Ag complexes with the resulting photodimers. In all of the structures, the ester unit combined with the additional -CH_3 around the reactive center adopt differing geometries, presumably to accommodate the additional sterics. The details of each of these structures will be discussed below.

5.3.1 (*E*)-ethyl-3-(pyridine-4-yl)but-2-enoate

We isolated and characterized two co-crystals and three Ag(I) coordination complexes involving 3-Me-4-pyes as a result of template switching with both resorcinols and Ag(I) salts. Although several other templates were screened (Table 8), we did not structurally characterize every attempt. To somewhat of our surprise, all of the resulting co-crystals involving a res were photostable. To gain insights into the photstability of the solids, we analysed some single crystals involving 3-Me-4-pyes. One of the three Ag(I) systems exhibited compete conversion to the desired cyclobutane product. The descriptions of the crystals mentioned above, as well as a structure of the cyclobutane complex as an Ag coordination polymer, are described below.

Table 8: Summary of additional photoreactivity data obtained using 3-Me-4-pyes.

template	**conv./%**	**time/h**	**yield of 3-Me-4--pycb**
res	0	150	0
4,6-diCl	0	150	0
4-Cl	0	150	0
5-OCH_3 res	0	100	0
$AgClO_4$	0	150	0
$AgNO_3$	0	150	0
AgOMs	0	150	0

(1) 2(3-Me-4-pyes)·(4,6-diI res). 3-Me-4-pyes and 4,6-diI res co-crystallize from EtOH in the orthorhombic space group $P2_12_12_1$ with two molecules of 3-Me-4-pyes

and 4,6-diI res in the asymmetric unit. The components assemble to form discrete three-component assemblies, sustained by two O—H···N hydrogen bonds [O···N separations (Å): O1···N1 2.720(7), O2···N2 2.741(6)]. Within each three-component assembly, the C=C are arranged in a crisscross manner ($d_{C\cdots C}$ = 3.827 Å), and the -CH_3 substituents are in a relative anti displacement, likely causing the unaligned olefins. Additionally, the pyridyl rings are twisted 35.11° and 30.16° away from the olefin. Olefins between nearest neighbour assemblies are twisted orthogonal to each other and separated greater than 7.8 Å. Additional interactions in the form of (res) I···O (carboxy), (pyridine) C—H···O (carboxy) and (alkyl) C—H···O (carboxy) interactions ($d_{I\cdots O}$ = 3.347 Å, $d_{C\cdots O}$ = 3.211 Å and 3.575 Å, respectively). Owing to the crisscross nature of the olefins, the co-crystal is photostable.

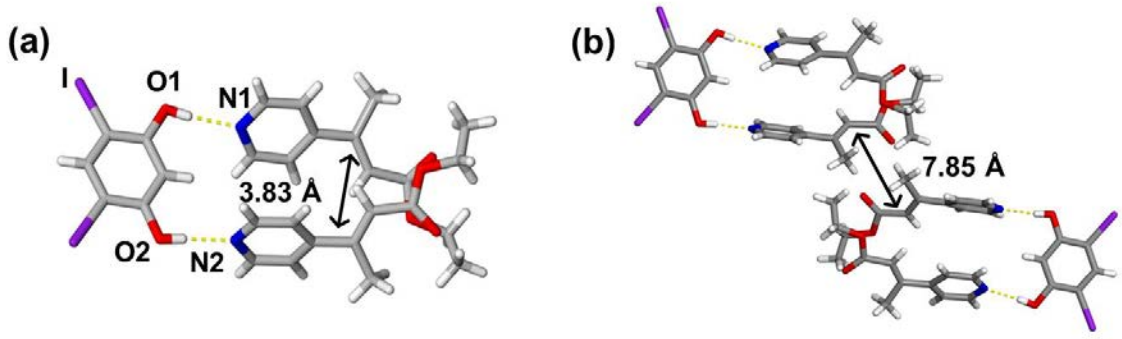

Figure 140: X-ray structure of 2(3-Me-4-pyes)·(4,6-diI res): (a) assembly with crisscrossed C=C bonds and (b) antiparallel offset packing.

(2) (3-Me-4-pyes)·(5-CH_3 res)$_\infty$. Co-crystallization of a 1:2 ratio of 5-CH_3 res and 3-Me-4-pyes in EtOH results in the formation of a 1:1 co-crystal in the monoclinic space group $P2_1/c$. Similar to the (4,6-diBr res)·2(3-Me-4-pyes) co-crystal, the primary interaction with 5-CH_3 res is an (phenol) O—H···N (pyridine) hydrogen bond [O···N

separation (Å): O1···N1 2.777(8)], however, in this co-crystal assembly, there is only one O—H···N interaction. The other phenolic OH participates in an O—H···O (carboxy) hydrogen bond [O···O separation (Å): O2···O3 2.871(3)]. Thus, the self-assembly process results in the formation of alternating O—H···N and O—H···O hydrogen bonds in an infinite ladder. The pyridyl rings are also twisted 29.63° from the plane of the olefin. The C=C bonds within the 1D ladder adopt a stacked orientation, yet are offset and separated by 5.24 Å, thus, the co-crystal is photostable.

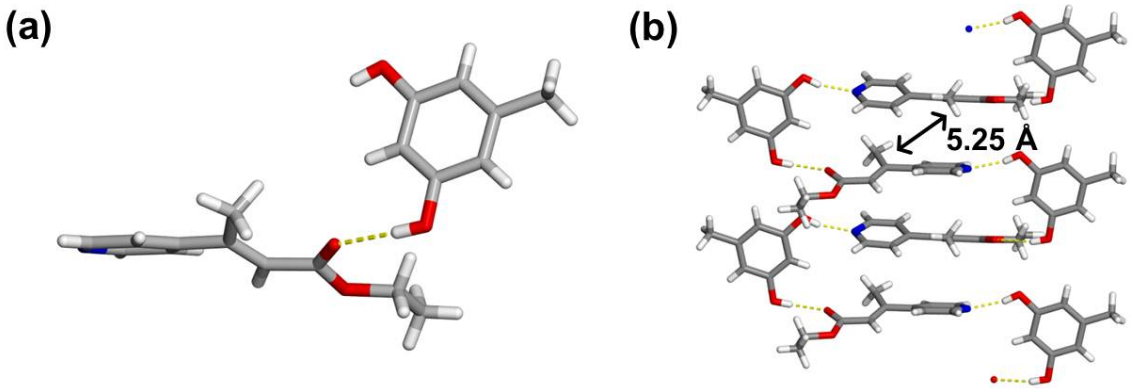

Figure 141: X-ray structure of (3-Me-4-pyes)·(5-CH_3 res)$_\infty$: (a) asymmetric unit and (b) 1D ladder with offset C=C bonds.

(3) [Ag(3-Me-4-pyes)$_2$][ClO_4]. Reaction of 3-Me-4-pyes with $AgClO_4 \cdot xH_2O$ afforded a coordination complex that crystallizes from aqueous EtOH in the monoclinic space group $P2_1/n$. Each Ag (I) ion is coordinated in a linear fashion to two molecules of 3-Me-4-pyes *via* Ag—N bonds and one ClO_4 ion in a monodentate fashion. Each Ag (I) ion also interacts with the complex below it *via* Ag···Ag interactions ($d_{Ag\cdots Ag}$ = 3.361 Å), such that the overlapping C=C bonds are parallel and aligned, however, do not satisfy Schmidt's criteria for a [2+2] photodimerization ($d_{C\cdots C}$ = 4.375 Å). The pyridyl ring is also twisted out of the plane of the olefin (θ = 13.03°, 25.32°). The -CH_3 substituents are

anti to each other within each $[Ag(3\text{-Me-4-pyes})_2][ClO_4]$ unit, and eclipsed with the $-CH_3$ groups of the stacked complex below. Additional (alkyl) C—H···O (perchlorate) and (pyridine) C—H···O (carboxy) interactions link adjacent orthogonal complexes ($d_{C\cdots O}$ = 3.591Å; $d_{C\cdots O}$ = 3.506 Å and 3.587 Å).

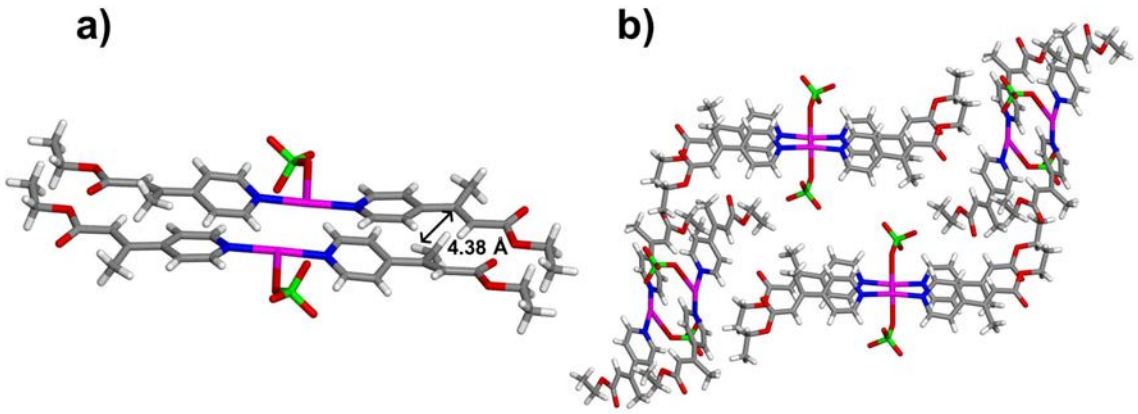

Figure 142: X-ray structure of $[Ag(3\text{-Me-4-pyes})_2][ClO_4]$: (a) overlapped C=Cs and (b) extended packing.

(4) $[Ag(3\text{-Me-4-pyes})_2][OSO_2CF_3]$. 3-Me-4-pyes and $AgOSO_2CF_3$ react in ethanol, affording a coordination complex that crystallizes in the monoclinic space group $P2_1/c$. Two 3-Me-4-pyes molecules coordinate to each Ag(I) ion in a linear fashion, with the $-CH_3$ substituents arranged in a relative anti conformation. In addition, the $-OSO_2CF_3$ anion coordinates with the Ag(I) ion. Each complex is stacked and interacts with another Ag complex *via* Ag···Ag forces ($d_{Ag\cdots Ag}$ = 3.867 Å). Within each stacked pair, the CH_3 units are eclipsed and the C=C units are aligned parallel and within Schmidt's topochemical distance criterion ($d_{C\cdots C}$ = 4.170 Å). Additionally, the pyridyl units and C=C moieties are tilted 26.80° and 17.62° from planarity. The $-OSO_2CF_3$ anion also interacts with adjacent orthogonal complexes *via* (pyridine) C—H···F (triflate) and (alkyl) C—H···O (triflate) forces ($d_{C\cdots F}$ = 3.475 Å; $d_{C\cdots O}$ = 3.548 Å, 3.196 Å). Despite

meeting the topochemical criteria, UV-irradiation of crystalline [Ag(3-Me-4-pyes)$_2$][OSO_2CF_3] does not afford the cyclobutane product.

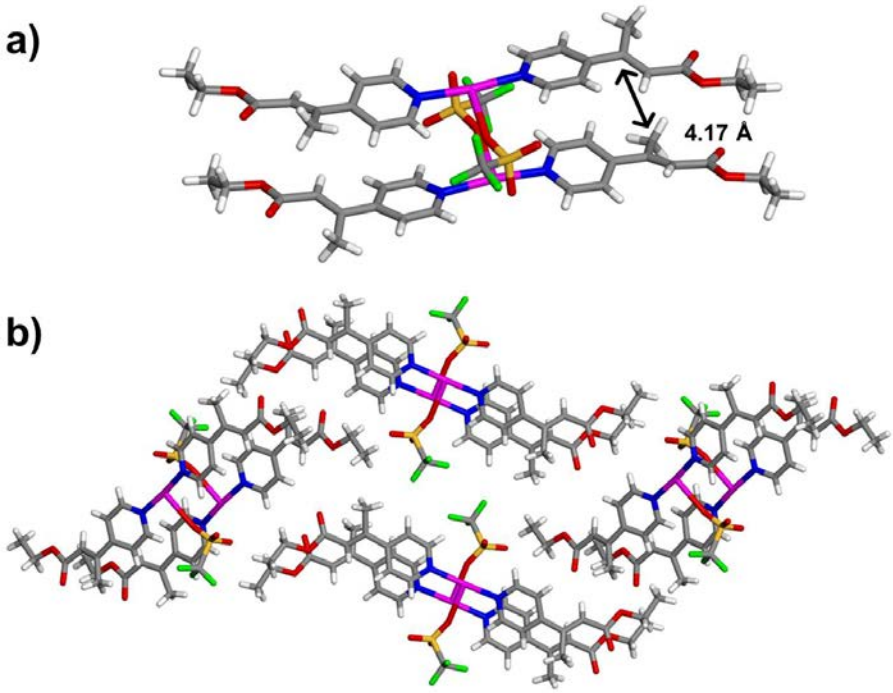

Figure 143: X-ray structure of [Ag(3-Me-4-pyes)$_2$][OSO_2CF_3]: (a) overlapped C=Cs forming a reactive assembly and (b) extended packing.

(5) [Ag(3-Me-4-pyes)$_2$][OTs]·2H$_2$O. Reaction of 2-Me-4-pyes with AgOTs in aqueous EtOH afforded a coordination complex that crystallizes in the triclinic space group $P\bar{1}$. Each Ag(I) ion is coordinated by two 3-Me-4-pyes olefins in a linear fashion, with stacked units interacting *via* argentophilic interactions ($d_{Ag\cdots Ag}$ = 3.895 Å, 3.607 Å). Two distinct pairs of interacting complexes are arranged orthogonal to each other, and with the stacked C=C units in each pair aligned and parallel for photoreaction to occur ($d_{C\cdots C}$ = 3.733 Å, 3.732 Å). The -CH_3 units are arranged in an anti orientation within [Ag(3-Me-4-pyes)$_2$][OTs], and eclipsed with the CH_3 substituents in the stacked unit, leading to the parallel orientation of the C=C bonds. The pyridine moieties are also

twisted 21.66° and 25.37° in relation to the olefin in one discrete unit, and 25.05° and 25.87° in the other. The OTs anion lies in close proximity to the Ag(I) ion, yet is non-coordinating, and interacting with the silver *via* Ag···O interactions ($d_{Ag\cdots O}$ = 2.723 Å, 2.818 Å). The Ag also interacts with an adjacent H_2O molecule ($d_{Ag\cdots O}$ = 2.997 Å, 2.964 Å). The pyridyl moiety also interacts *via* C—H···O forces with water ($d_{C\cdots O}$ = 3.302 Å, 3.328 Å) and the -OTs anion ($d_{C\cdots O}$ = 3.269 Å, 3.276 Å). UV-irradiation of crystalline powder of $[Ag(3\text{-Me-4-pyes})_2][OTs]\cdot 2H_2O$ afforded the cyclobutane product stereospecifically, and in quantitative yield.

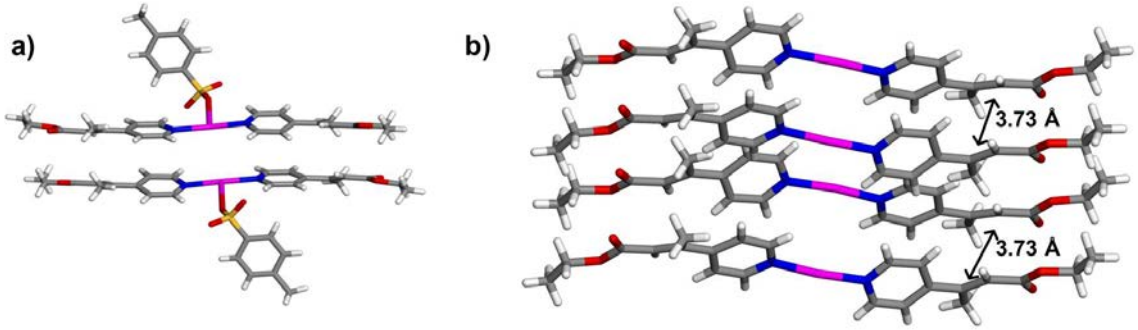

Figure 144: X-ray structure of $[Ag(3\text{-Me-4-pyes})_2][OTs]\cdot 2H_2O$: (a) overlapped C=Cs within a reactive assembly and (b) extended packing with tosylate anions omitted for clarity.

To confirm the stereochemistry around the cyclobutane, the product was isolated *via* extraction using $CHCl_3$ and NaOH. Upon subsequent filtration of the organic layer through celite and solvent evaporation, the cyclobutane product was present as a colorless oil. Given the product is an oil, we allowed the cyclobutane product to react with a fresh equivalent of AgOTs in aqueous EtOH. The resulting crystalline product of the composition $[Ag(3\text{-Me-4-pycb})][OTS]_\infty$ was analyzed using single crystal X-ray diffraction.

(6) [Ag(3-Me-4-pycb)][OTs]$_\infty$. 3-Me-4-pycb and AgOTs react to form a zig-zag 1D coordination polymer that crystallizes in the monoclinic space group $P2_1/c$. X-ray analysis confirmed that the cyclobutane adopted a head-to-head stereochemistry. The polymeric assembly is sustained, similar to the complex prior to photoreaction, by Ag—N forces, with the closest Ag atoms being between adjacent polymeric strands ($d_{Ag\cdots Ag}$ = 5.314 Å) as opposed to within one polymeric sheet ($d_{Ag\cdots Ag}$ = 6.645 Å). Similar to [Ag(3-Me-4-pyes)$_2$][OTs], the -OTs anions are not coordinated to the Ag(I) centers. The 1D polymer strands interact *via* (alkyl) C—H···O (carboxy) interactions along the periphery ($d_{C\cdots O}$ = 3.336 Å), while the -OTs anions also engage in C—H···O interactions with the pyridines ($d_{C\cdots O}$ = 3.533 Å) and the ethoxy groups ($d_{C\cdots O}$ = 3.410 Å).

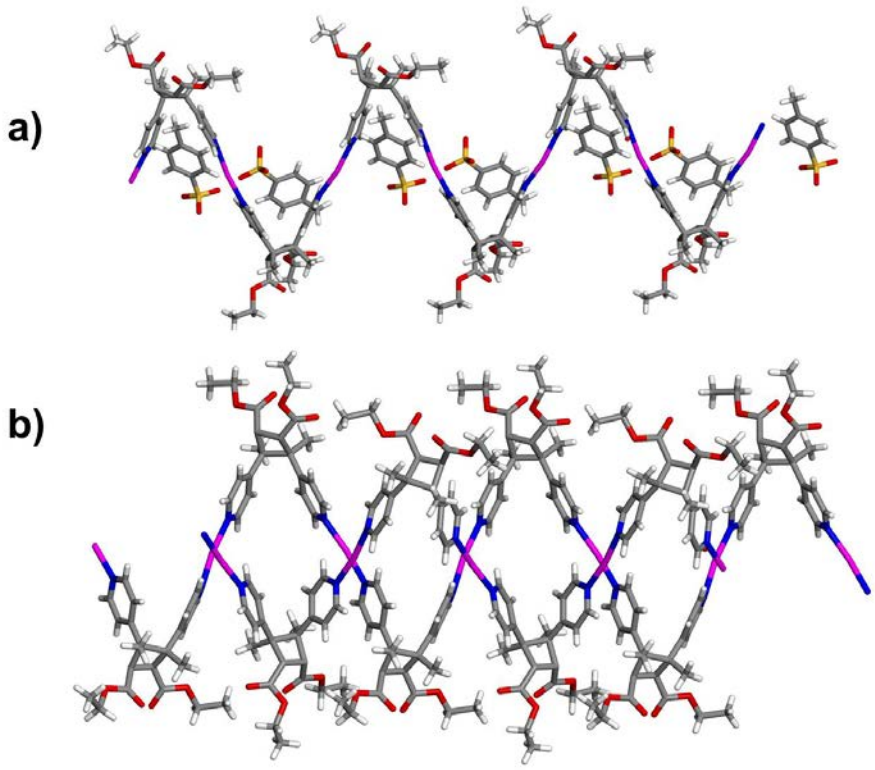

Figure 145: X-ray structure of [Ag(3-Me-4-pycb)][OTs]$_\infty$: (a) 1D zig-zag polymer strand and (b) extended packing.

5.3.2 (*E*)-ethyl-3-(pyridine-3-yl)but-2-enoate

Attempts to screen 3-Me-3-pyes using resorcinol templates in ethanol invariably afforded oils. Since the resorcinol templates and silver salts were screened simultaneously, and the silver salts afforded crystals in the solvent system with relative ease, other solvent systems were not used to probe for resorcinol co-crystals. We isolated and characterized two Ag(I) coordination complexes involving 3-Me-3-pyes. Although several other Ag(I) salts were screened and checked for photoactivity, we did not structurally characterize every attempt (Table 9). One of the two Ag(I) systems exhibited compete conversion to a cyclobutane product. The descriptions of the crystals mentioned above, as well as a structure of the cyclobutane complex as an Ag coordination polymer, are described below.

Table 9: Summary of photoreactivity data obtained using 3-Me-3-pyes.

template	**conv./%**	**time/h**	**yield of 3-Me-3--pycb**
$AgCO_2C_2F_5$	100	100	100[a]
$AgClO_3$	50[b]	150	0
$AgNO_3$	0	100	0
$AgOSO_2CH_3$	0	150	0
$AgOSO_2CF_3$	0	150	0

[a] product formed matched the ^{1}H NMR produced *via* irradiation of $[Ag(3\text{-Me-3-pyes})_2][ClO_4]$

[b] the reaction was concluded after 150 hours since the other Ag systems reacted faster

(1) $[Ag(3\text{-Me-3-pyes})_2][OTs]_\infty$. Reaction of 3-Me-3-pyes and AgOTs afforded a zig-zag 1D coordination polymer that crystallizes from aqueous EtOH in the monoclinic

space group Cc. Each Ag(I) ion is coordinated to two 3-pyridyl groups of 3-Me-3-pyes *via* Ag—N bonds, while the -OTs anion bridges two adjacent Ag(I) centers. The C=C units within two stacked molecules of 3-Me-3-pyes are arranged in a crisscross manner ($d_{C\cdots C}$ = 3.170 Å), while adjacent -CH_3 groups are arranged in a staggered conformation. The pyridine units are twisted out of the plane of the olefin (θ = 13.14°, 21.87°). The -OTs anion also interacts with neighboring pyridyl moieties *via* C—H···O forces ($d_{C\cdots O}$ = 3.207 Å). The extended structure contains additional (alkyl) C—H···O (carboxy) interactions along the periphery of multiple 1D strands ($d_{C\cdots O}$ = 3.195 Å).

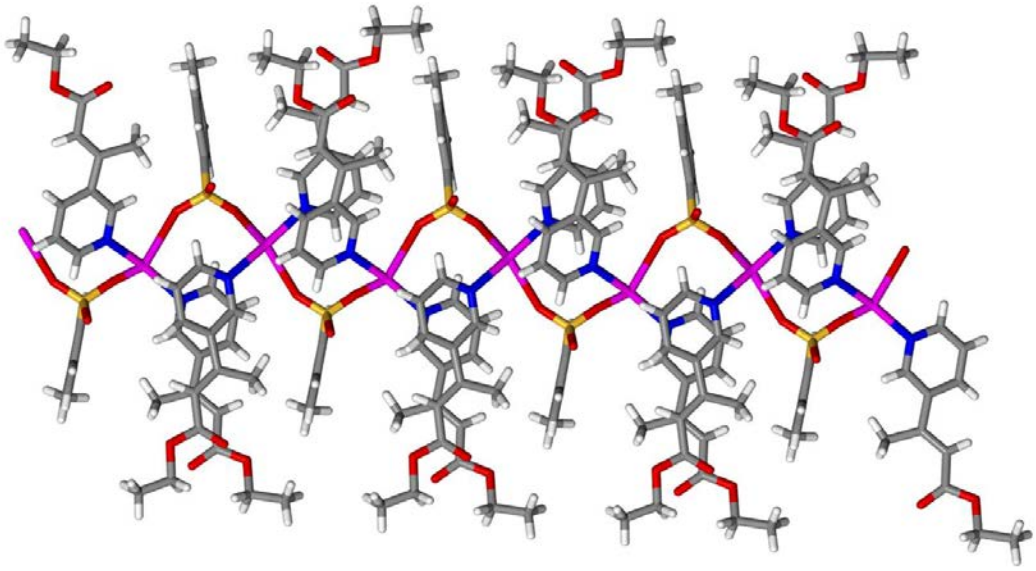

Figure 146: X-ray structure of $[Ag(3\text{-Me-3-pyes})_2][OTs]_\infty$ highlighting 1D polymer strand.

(2) $[Ag(3\text{-Me-3-pyes})_2][ClO_4]$. Reaction of 3-Me-3-pyes and $AgClO_4 \cdot xH_2O$ in aqueous EtOH afforded a mononuclear complex of composition $[Ag(3\text{-Me-3-pyes})_2][ClO_4]$ that crystallizes from the monoclinic space group C2/c. Each Ag(I) center coordinates to two 3-Me-3-pyes molecules, while the ClO_4 anion is in close proximity and interacting with the Ag (I), but not coordinated ($d_{Ag\cdots O}$ = 3.075 Å, 3.036 Å). Within

each discrete $[Ag(3\text{-Me-3-pyes})_2]^{1+}$ unit, the $-CH_3$ substituents are arranged in a relative anti conformation. The pyridyl units are tilted 28.85° from the plane of the C=C moiety. The C=C units of partially stacked complexes are overlapped and aligned in an antiparallel manner ($d_{C\cdots C}$ = 3.424 Å), and would be expected to produce the head-to-tail product upon photoirradiation. The $-ClO_4$ anion also participates in (pyridine) C—H···O and (alkyl) C—H···O interactions ($d_{C\cdots O}$ = 3.392 Å; $d_{C\cdots O}$ = 3.375 Å). UV-irradiation of a crystalline powder of $[Ag(3\text{-Me-3-pyes})_2][ClO_4]$ afforded a cyclobutane product stereospecifically, and in quantitative yield.

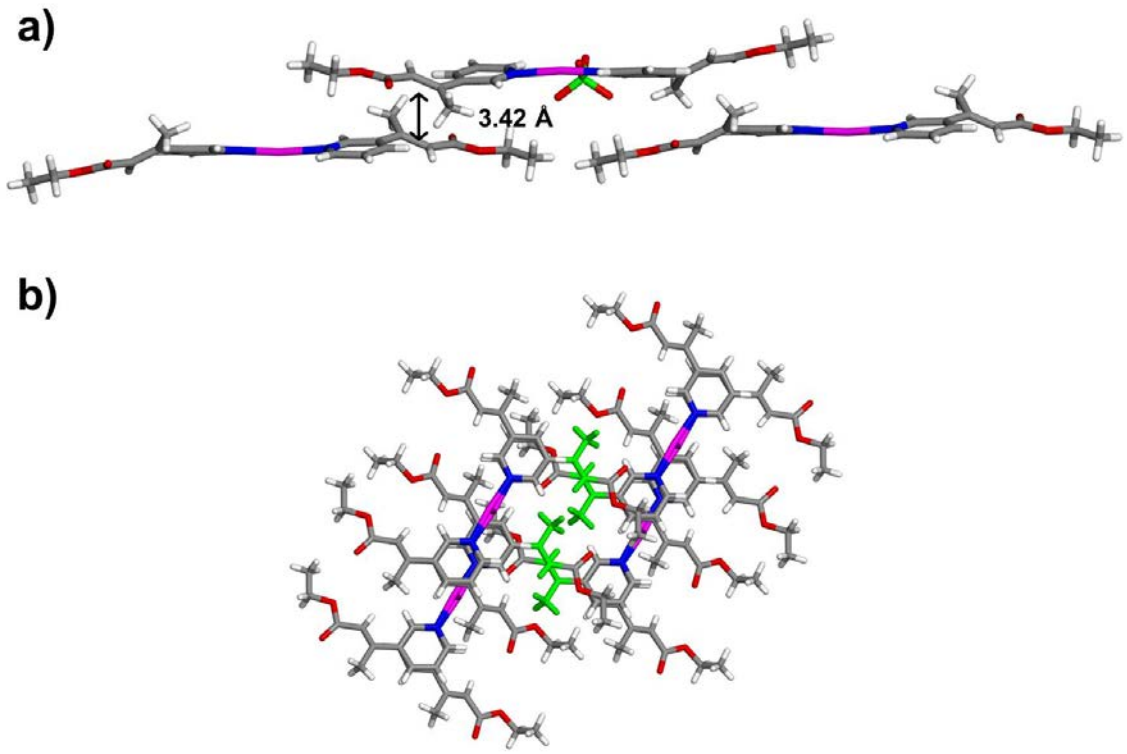

Figure 147: X-ray structure of $[Ag_2(3\text{-Me-3-pyes})_4][ClO_4]_2$: (a) offset units with antiparallel C=C overlap, and (b) extended packing with pairs of reactive olefins marked in green.

To confirm the stereochemistry around the cyclobutane, the product was isolated *via* extraction using $CHCl_3$ and NaOH. Upon subsequent filtration of the organic layer through celite and solvent evaporation, the cyclobutane product was present as a colorless oil. Given the product is an oil, we allowed the cyclobutane product to react with a fresh equivalent of $AgClO_4$ in aqueous EtOH. The resulting crystalline product of the composition $[Ag(3\text{-Me-3-pycb})][ClO_4]_\infty$ was analyzed using single crystal X-ray diffraction.

(3) $[Ag(3\text{-Me-3-pycb})][ClO_4]_\infty$. 3-Me-3-pycb and $AgClO_4$ react to form a 1D coordination polymer that crystallizes in the triclinic space group $P\bar{1}$. X-ray analysis confirmed that the cyclobutane adopted a head-to-tail stereochemistry. The polymeric assembly is sustained, similar to the complex prior to photoreaction, by Ag—N forces, with the closest Ag atoms being offset and separated by 3.728 Å. Similar to $[Ag(3\text{-Me-3-pyes})_2][ClO_4]$, the $-ClO_4$ anions are not coordinated to the Ag(I) centers, however, they interact with adjacent Ag(I) centers ($d_{Ag\cdots O}$ = 3.094 Å) and participate in weak (pyridine) C—H···O bonds ($d_{C\cdots O}$ = 3.354 Å, 3.272 Å, 3.428 Å). The 1D polymer strands interact *via* (alkyl) C—H···O (carboxy) interactions along the periphery ($d_{C\cdots O}$ = 3.353 Å).

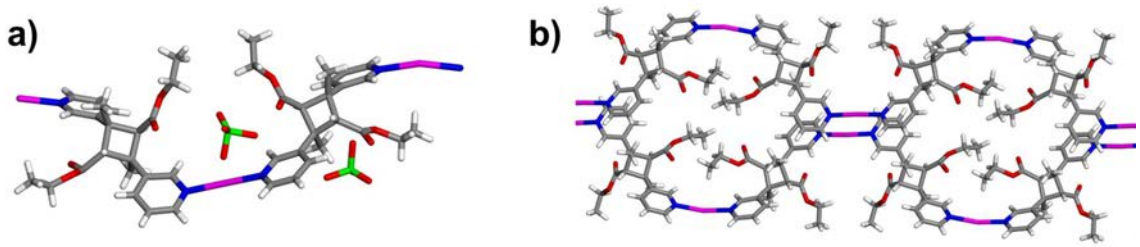

Figure 148: X-ray structure of $[Ag(3\text{-Me-3-pycb})][ClO_4]_\infty$

5.3.3 ((*E*)-ethyl-2-methyl-3-(pyridine-4-yl)prop-2-enoate

We isolated and characterized four co-crystals and three Ag(I) coordination complexes involving 2-Me-4-pyes as a result of template switching with both resorcinols and Ag(I) salts. Although several other organic and Ag(I)-based templates were screened, we did not structurally characterize every result (Table 10). Two of the three Ag(I) systems exhibited compete conversion to the desired cyclobutane product. The descriptions of the crystals mentioned above, as well as a structure of the cyclobutane complex as an Ag coordination polymer, are described below.

Table 10: Summary of additional photoreactivity data obtained using 2-Me-4-pyes.

template	**conv./%**	**time/h**	**yield of 3-Me-4--pycb**
res	0	150	0
5-OCH_3res	0	150	0
5-CH_3res	0	150	0
4,6-diI res	0	100	0
$AgClO_4$	0	150	0
$AgNO_3$	0	150	0
AgOMs	0	150	0

(1) 2(2-Me-4-pyes)·(4-Cl res). 4-Cl res and 2-Me-4-pyes co-crystallize from EtOH in the triclinic space group $P\bar{1}$ resulting in the formation of a 1:2 co-crystal. The components are arranged in a discrete three component assembly, sustained by two O—H···N hydrogen bonds [O···N separations (Å): O1···N1 2.782(3), O2···N2 2.700(4)].

Within each assembly, overlapping C=Cs are arranged in a parallel orientation ($d_{C\cdots C}$ = 3.715 Å), with the -CH_3 substituents engaged in eclipsing interactions. Furthermore, the ethoxy units are arranged in a relative staggered conformation. Additional (alkyl) C—H···Cl (res) and (pyridine) C—H···O (phenol) interactions ($d_{C\cdots Cl}$ = 3.817 Å, $d_{C\cdots O}$ = 3.497 Å) contribute to adjacent assemblies being stacked in an offset manner. Despite the favorable arrangement of the olefinic carbons, this co-crystal is photostable. The photostability is attributed to the significant twisting between the pyridine and double bond moieties (θ = 34.31°, 38.51°), likely causing the reactive pair of C=C orbitals to not be aligned.

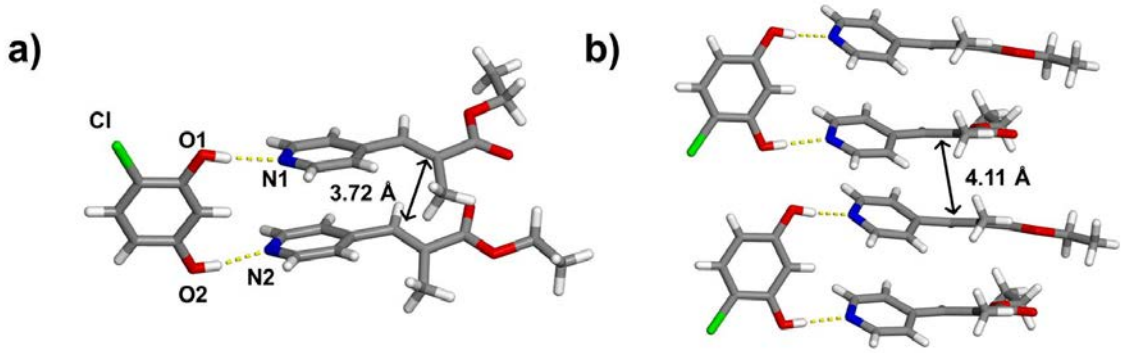

Figure 149: X-ray structure of 2(2-Me-4-pyes)·(4-Cl res): (a) twisted assembly, and (b) parallel packing of neighboring assemblies.

(2) 2(2-Me-4-pyes)·(4,6-diCl res). 4,6-diCl res and 2-Me-4-pyes form a 1:2 co-crystal that crystallizes from EtOH in the triclinic space group $P\bar{1}$. The components form a discrete three component assembly, sustained two O—H···N hydrogen bonds [O···N separations (Å): O1···N1 2.706(5), O2···N2 2.736(5)]. Within each three component assembly, overlapping C=Cs are crisscrossed ($d_{C\cdots C}$ = 3.673 Å), resulting in both the -CH_3 substituents, and the ethoxy units arranged relatively staggered to each other. Additionally, the pyridyl units and C=C moieties are tilted 24.03° and 26.41° from

planarity. Neighboring assemblies are arranged in an antiparallel and offset manner, owing to π···π stacking between overlapping pyridine units ($d_{\pi\cdots\pi}$ = 3.688 Å). Similar to the co-crystal attained with 4-Cl res, the extended structure is sustained by weaker (alkyl) C—H···Cl (res) and (pyridine) C—H···O (phenol) interactions ($d_{C\cdots Cl}$ = 3.758 Å, $d_{C\cdots O}$ = 2.566 Å). This co-crystal is also photostable, owing to the crisscross relative orientation of the C=C units.

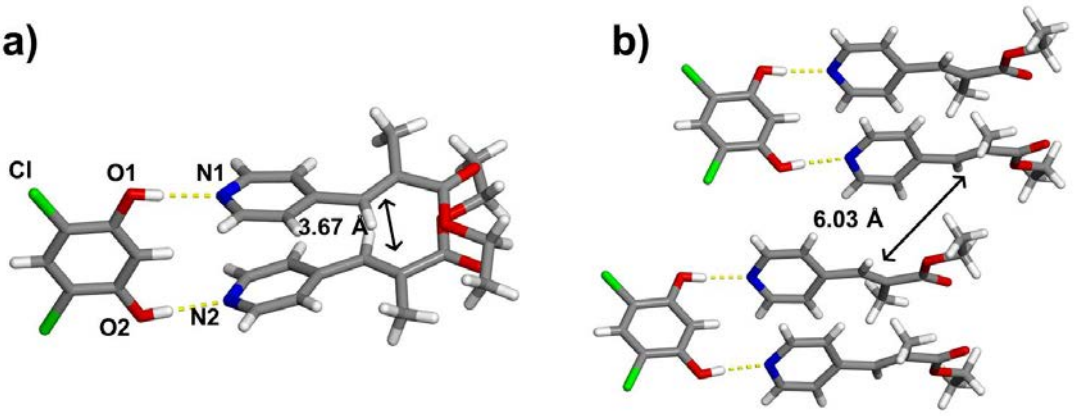

Figure 150: X-ray structure of 2(2-Me-4-pyes)·(4,6-diCl res): (a) twisted crisscross assembly, and (b) offset packing of neighboring assemblies.

(3) 2(2-Me-4-pyes)·(4-Br res). 4-Br res and 2-Me-4-pyes co-crystallize from EtOH in the triclinic space group $P\bar{1}$ with two molecules of 4-Br res and four molecules of 2-Me-4-pyes present in the asymmetric unit. Within the asymmetric unit, there are two distinct three component assemblies, one of which contains crisscrossed C=Cs, and the other with parallel aligned C=Cs ($d_{C\cdots C}$ = 3.687 Å, $d_{C\cdots C}$ = 3.719 Å for crisscross and parallel assemblies, respectively referred to as assemblies A1 and A2). Each three component assembly is sustained by two O—H···N hydrogen bonds [O···N separations, A1 (Å): O1···N1 2.744(6), O2···N2 2.731(7); O···N separations, A2 (Å): O1···N1 2.831(6), O2···N2 2.706(7)]. In A1, both the -CH_3 units and ethoxy units are relatively

arranged staggered to each other, and the pyridyl moieties are tilted away from the plane of the olefin (θ_{A1} = 29.22°, 34.57°). In contrast to A1, the -CH_3 units of A2 are eclipsed in the three-component assembly, and the ethoxy units are still in a relative staggered conformation. Additional (alkyl) C—H···Br (res), (pyridine) C—H···O (phenol), and (alkyl) C—H···O (carboxy) interactions ($d_{C\cdots Br}$ = 3.958 Å, $d_{C\cdots O}$ = 3.326 Å, 3.372 Å) are present in adjacent assemblies. Despite the favorable arrangement of the olefinic carbons in A2, this co-crystal is also photostable, likely owing to the pyridine and double bond moieties being twisted (θ_{A2} = 21.71°, 37.10°) thus causing the reactive pair of C=C orbitals to not be aligned.

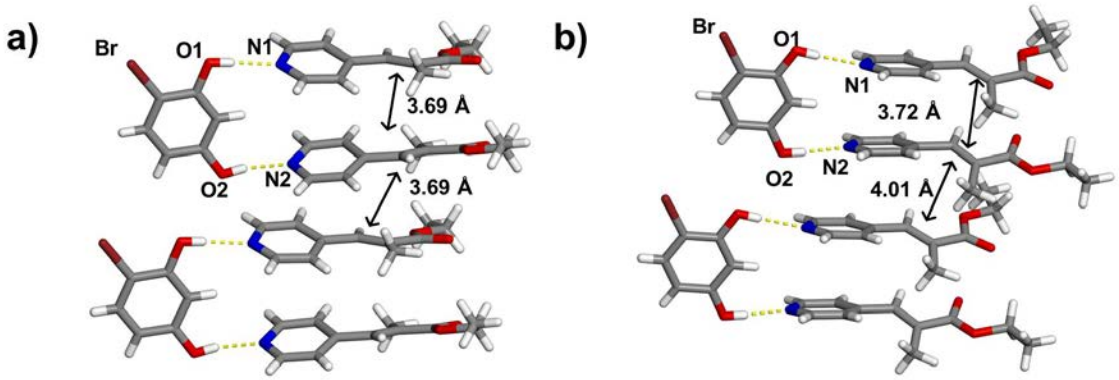

Figure 151: X-ray structure of 2(2-Me-4-pyes)·(4-Br res): (a) twisted crisscross assembly A1, and (b) parallel packing of assembly A2.

(4) 2(2-Me-4-pyes)·(4,6-diBr res). Co-crystal (4,6-diBr res)·2(2-Me-4-pyes) crystallizes from EtOH in the triclinic space group $P\bar{1}$. The components form a discrete three component assembly, sustained two O—H···N hydrogen bonds [O···N separations (Å): O1···N1 2.728(4), O2···N2 2.686(4)]. Similar to the co-crystal obtained with 4,6-diCl res, overlapping C=Cs are crisscrossed ($d_{C\cdots C}$ = 3.636 Å), resulting in both the -CH_3 substituents, and the ethoxy units arranged relatively staggered to each other in each three

component assembly. Additionally, the pyridyl units and C=C moieties are tilted 27.93° and 28.15° from planarity. Adjacent assemblies are offset and interact with each other *via* weaker (pyridine) C—H···Br (res), (pyridine) C—H···O (phenol), and (alkyl) C—H···O (carboxy) interactions ($d_{C\cdots Br}$ = 3.918 Å, $d_{C\cdots O}$ = 3.367 Å, 3.491 Å). The co-crystal is also photostable, owing to the crisscross relative orientation of the C=C units.

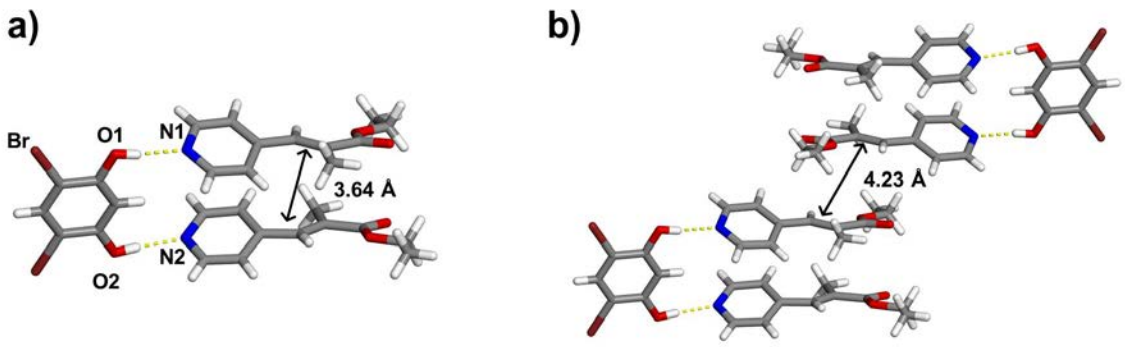

Figure 152: X-ray structure of 2(2-Me-4-pyes)·(4,6-diBr res): (a) twisted crisscross assembly, and (b) offset antiparallel packing of neighboring assemblies.

(5) [Ag(2-Me-4-pyes)$_2$][ClO$_3$]. Reaction of 2-Me-4-pyes with $AgClO_3$ in aqueous EtOH afforded a coordination complex that crystallizes in the monoclinic space group C2/c. Each Ag(I) ion is coordinated by two 2-Me-4-pyes olefins in a linear fashion. The mononuclear complex interacts with the unit below it *via* argentophilic interactions ($d_{Ag\cdots Ag}$ = 3.433 Å). The two interacting complexes are arranged with the C=C units crisscrossed ($d_{C\cdots C}$ = 3.831 Å, 3.682 Å). The -CH_3 units are arranged in a syn orientation within [Ag(2-Me-4-pyes)$_2$][ClO_3], but relative to the adjacent complex, they are anti and staggered, causing the crisscross orientation of the C=C bonds. The pyridine moieties are twisted 29.24° and 29.25° in relation to the olefin. The ClO_3 anion lies in close proximity to the Ag(I) ion, yet is non-coordinating, and interacting with the silver *via* Ag···O interactions ($d_{Ag\cdots O}$ = 3.151 Å, 3.229 Å) and the -CH_3 groups *via* C—H···O

forces ($d_{C\cdots O}$ = 3.101 Å, 3.113 Å). The latter of those two interactions effectively causes the next Ag complex to pack in an offset manner. The Ag complex is, thus, photostable.

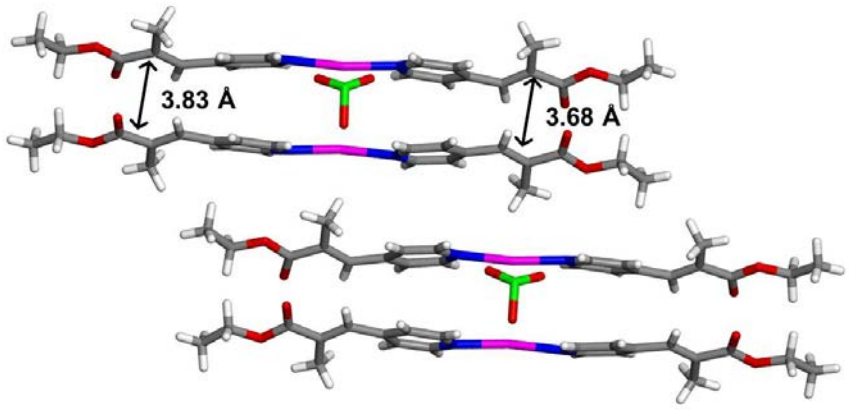

Figure 153: X-ray structure of $[Ag(2\text{-Me-4-pyes})_2][ClO_3]$ highlighting crisscross C=Cs and offset neighboring C=Cs.

(6) $[Ag_2(2\text{-Me-4-pyes})_4][CO_2C_3F_7]_2$. Reaction of 2-Me-4-pyes with $AgCO_2C_3F_7$ in aqueous EtOH afforded a dinuclear Ag(I)-coordination complex that crystallizes in the triclinic space group $P\bar{1}$. The dinuclear complex is sustained by argentophilic interactions (d_{Ag-Ag} = 3.052 Å), with each Ag(I) ion being coordinated by two 2-Me-4-pyes molecules in a linear fashion. Two $-CO_2C_3F_7$ anions are coordinated in a bridging manner between two Ag(I) centers. Within each dinuclear assembly, the C=Cs are aligned parallel and within Schmidt's criteria for [2+2] photodimerization ($d_{C\cdots C}$ = 3.914 Å). The $-CH_3$ units are arranged in a syn orientation and eclipsed with the CH_3 units below in the dinuclear assembly. In $[Ag_2(2\text{-Me-4-pyes})_4][CO_2C_3F_7]_2$, the pyridine and olefin units are twisted 23.85° and 27.48° apart. Additional (pyridine) C—H···O (carboxy) forces ($d_{C\cdots O}$ = 3.383 Å, 3.433 Å), as well as Ag···C interactions with the $-CH_3$ groups ($d_{Ag\cdots C}$ = 3.664 Å) are present between adjacent dinuclear assemblies, the latter of

which forces adjacent assemblies to pack in an offset manner. When irradiated with UV light, the Ag(I) complex photoreacts, affording the cyclobutane product in quantitative yield.

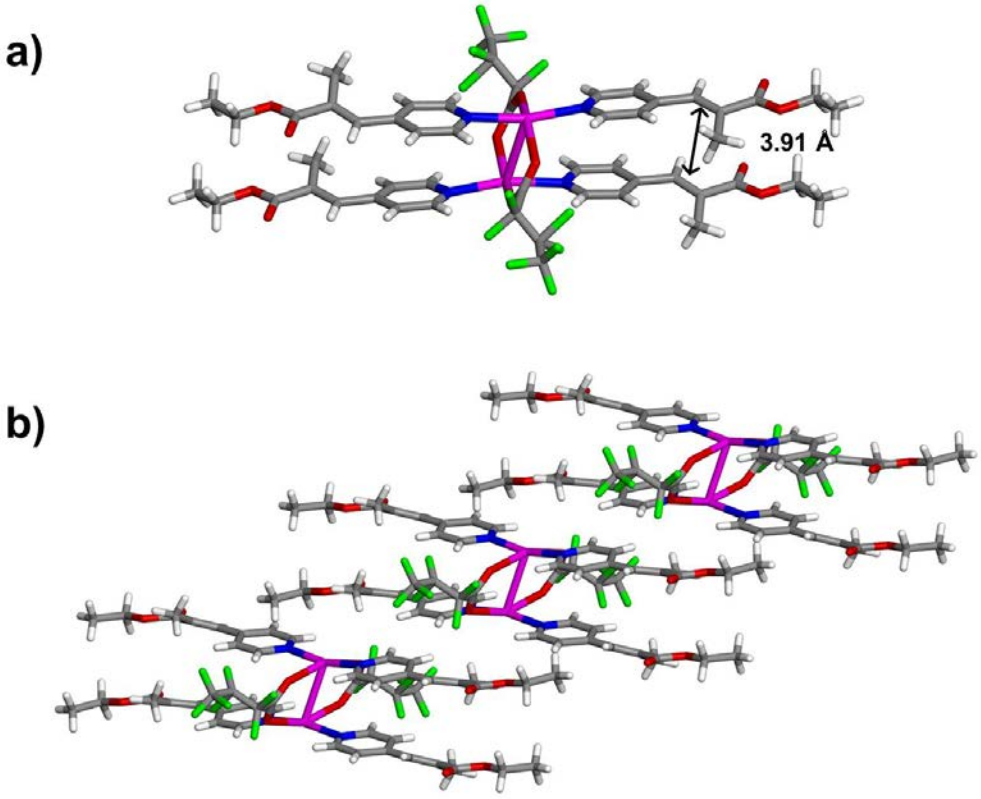

Figure 154: X-ray structure of $[Ag_2(2\text{-Me-4-pyes})_4][CO_2C_3F_7]_2$: (a) dinuclear Ag(I) complex with reactive C=C units, and (b) extended offset packing.

(7) $[Ag(2\text{-Me-4-pyes})_2][OSO_2CF_3]$. Reaction of 2-Me-4-pyes with $AgOSO_2CF_3$ from an aqueous ethanolic solution afforded an Ag(I)-coordination complex that crystallizes in the triclinic space group $P\bar{1}$. The resulting mononuclear complex is sustained by argentophilic interactions ($d_{Ag\cdots Ag}$ = 3.365 Å), with each Ag(I) ion being coordinated by two 2-Me-4-pyes molecules in a linear fashion. The pyridine moieties are twisted 40.45° and 41.69° in relation to the olefin. Within each pair of interacting

complexes, the C=Cs are aligned parallel and in position to undergo a [2+2] photodimerization ($d_{C\cdots C}$ = 3.783 Å). Unlike the complex produced with $AgCO_2C_3F_7$, the -CH_3 units are arranged in an anti orientation within each [Ag(2-Me-4-pyes)$_2$][OSO_2CF_3] unit, yet are eclipsed with the CH_3 units below. The -OSO_2CF_3 anions are in close proximity to the Ag(I) centers, interacting *via* Ag···O forces ($d_{Ag\cdots O}$ = 2.894 Å, 2.934 Å). Additional (pyridine) C—H···O (triflate) forces ($d_{C\cdots O}$ = 3.388 Å), as well as Ag···O interactions with the carboxy groups ($d_{Ag\cdots O}$ = 3.037 Å) which give rise to an offset stacking of adjacent pairs. The Ag(I) complex photoreacts upon treatment with UV-irradiation, affording the cyclobutane product stereospecifically, and in quantitative yield.

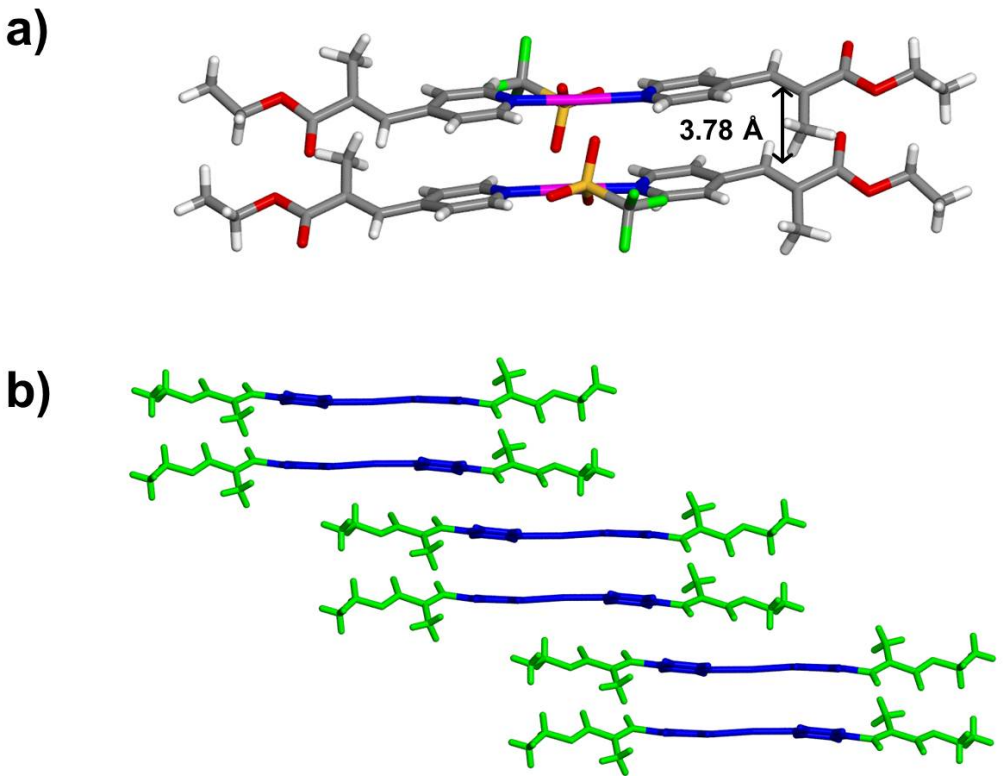

Figure 155: X-ray structure of [Ag(2-Me-4-pyes)$_2$][OSO_2CF_3]: (a) overlapping reactive C=C units and (b) extended packing highlighting twisting of pyridyl units.

To determine the stereochemistry of the resulting cyclobutane product, the cyclobutane was isolated *via* extraction using $CHCl_3$ and NaOH. Upon filtration of the organic layer through celite, the cyclobutane product was concentrated to afford a colorless oil. We allowed the cyclobutane product to react with a fresh equivalent of $AgOSO_2CF_3$ in aqueous EtOH. The resulting crystalline product of the composition [Ag(2-Me-4-pycb)][OSO_2CF_3]$_\infty$ was analyzed using single crystal X-ray diffraction.

(8) [Ag(2-Me-4-pycb)][OSO_2CF_3]$_\infty$. 2-Me-4-pycb and $AgOSO_2CF_3$ react to form a zig-zag 1D coordination polymer that crystallizes in the monoclinic space group $P2_1/c$. X-ray analysis confirmed that the cyclobutane adopted a head-to-head stereochemistry. The polymeric assembly is sustained, similar to the complex prior to photoreaction, by Ag—N forces, with the closest Ag atoms separated by 4.072 Å. In contrast to [Ag(2-Me-4-pyes)$_2$][OSO_2CF_3], the -OSO_2CF_3 ions are coordinated to the Ag(I) centers. The 1D polymer strands interact *via* (alkyl) C—H···O (carboxy) interactions along the periphery ($d_{C\cdots O}$ = 3.211).

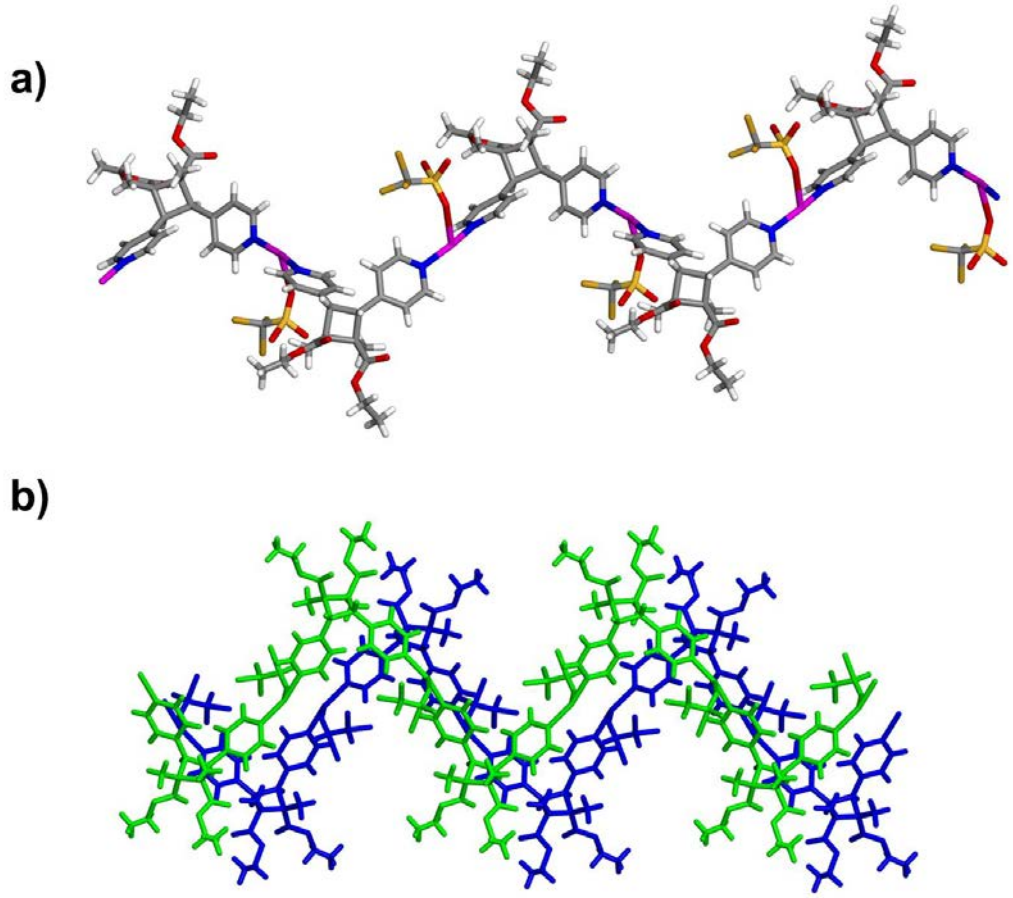

Figure 156: X-ray structure of [Ag(2-Me-4-pycb)][OSO_2CF_3]: (a) 1D polymer strand and (b) extended packing.

5.4 Hydrogen Bond-Driven vs. Coordination-Driven Self-Assembly

In the case of the resorcinol-based templates, co-crystallization with 4-pyridyl analogues was generally a successful process, as 18/20 attempts with 3-Me-4-pyes and 17/20 attempts with 2-Me-4-pyes resulted in co-crystals with the desired stoichiometry, as evidenced by ^{1}H NMR spectroscopy, and in some cases, single crystal X-ray diffraction (XRD). Despite the success rate, none of the co-crystals undergo [2+2] photodimerizations. Furthermore, in two out of six of the co-crystals whose packing was

analyzed *via* XRD, Schmidt's distance criterion for a [2+2] cycloadditions is satisfied, with olefins either within or between assemblies aligned. The twisting of the pyridyl rings and olefins is generally on the order of 20-40° in the co-crystals that satisfy all other topochemical criteria (i.e. C=C bonds overlapped, aligned, and separated by $\leq$ 4.2 Å). Within stacked assemblies, the planes of (potentially) reactive C=C pairs are twisted on the order of 7-8° (Table 11). The combination of such twists to alleviate steric frustration could lead to insufficient orbital overlap, and thus, no photoreaction is observed.

Table 11: Summary of relevant angles and twisting for co-crystals that satisfy the topochemical postulate

co-crystal	C···C/Å	pyridine twist/°	C=C pair twist/°
2(2-Me-4-pyes)·(4-Cl res)	3.72	34.31, 38.51	7.20
2(2-Me-4-pyes)·(4-Br res)	3.72	21.71, 37.10	7.56

In the Ag(I)-based complexes, quantitative reactivity is achieved in all three systems, despite the presence of similar twisting behavior. In particular, for the five Ag systems crystallographically-analyzed that met the criteria for a [2+2] photodimerizations, the pyridine rings and olefinic carbons are twisted on the order of 17-40°, similar to the resorcinol co-crystals. In these complexes, the overlapping C=Cs are twisted up to 27.5° from a perfect overlap (Table 12). The Ag(I) complex [Ag(3-Me-4-pyes)$_2$][OSO_2CF_3], which does not photoreact has the largest degree of C=C twisting (27.50°), which likely accounts for insufficient orbital overlap for a [2+2] photodimerization to occur. In all other photoreactive complexes, the reactive pair of C=C bonds more closely overlaps.

Table 12: Summary of relevant angles and twisting for Ag(I) coordination complexes that satisfy topochemical postulate.

coordination complex	C···C/Å	pyridine twist/°	C=C pair twist/°
$[Ag(3\text{-Me-4-pyes})_2][OSO_2CF_3]$[a]	4.17	17.62, 26.80	27.50
$[Ag(3\text{-Me-4-pyes})_2][OTs]\cdot 2H_2O$	3.73	21.66, 25.37	10.04
$[Ag(3\text{-Me-3-pyes})_2][ClO_4]$	3.73	28.85	0
$[Ag_2(2\text{-Me-4-pyes})_4][OCO_2C_3F_7]$	3.91	23.85, 27.48	8.73
$[Ag(2\text{-Me-4-pyes})_2][OSO_2CF_3]$	3.78	40.45, 41.69	8.43

[a] complex was photostable after UV-irradiation

5.5 Conformational Challenges in Self-Assembly

When attempting to direct reactivity in the nonplanar systems mentioned above, there are several other variables that arise within the self-assembly process, extending beyond the normal inquiries of whether or not the targeted supramolecular synthons will form, and if so, will the olefins be parallel, aligned, and separated by no more than 4.2 Å. In the case of the three target olefins, the more complex substitution around the reaction center, in essence, adds an element of challenge to the self-assembly process in that, not only does the system need to achieve Schmidt's criteria, but it also has to do so in an energetically-favorable (i.e. minimal steric factors) and efficient manner. The introduction of an additional substituent around the olefinic center, *de facto*, introduces a site wherein eclipsing interactions have to occur to achieve the targeted self-assembly and final architecture.

In the studies involving the trisubstituted olefins, the resorcinol co-crystals adopt different packing motifs to alleviate steric interactions within the assemblies. In less hindered olefin systems, the resorcinols act to juxtapose molecules in either an aligned or

crisscross manner (Figure 157a). With 3-Me-4-pyes and 2-Me-4-pyes, the conformations of both olefins in an assembly are more variable (Figure 157b), since the ester can also adopt a more staggered position that could lead to a photoactive assembly. The two co-crystals that adopt this motif also involve the most twisting about the pyridine moieties. In addition, the carboxyl moiety could participate in a more prominent hydrogen bond, as seen in the 2(3-Me-4-pyes)·(5-CH_3 res) co-crystal. Furthermore, the crisscross conformation is likely to be energetically more favorable since it positions the methyl groups and the ethoxy units anti to each other. Overall, the flexible environment provided by a co-crystal makes directing reactivity in nonplanar systems more difficult.

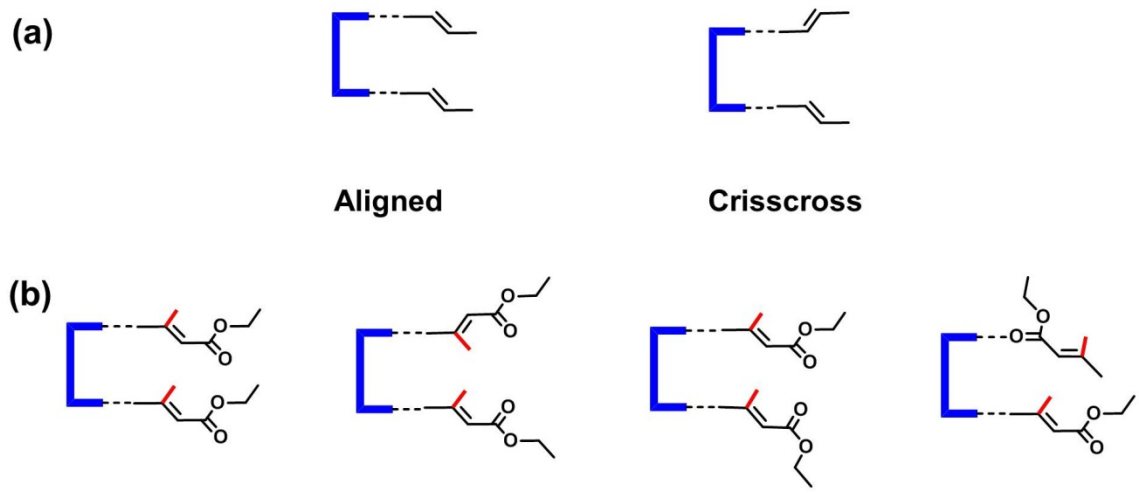

Figure 157: Resorcinol-based assembly motifs for (a) disubstituted systems and (b) trisubstituted olefins.

5.6 Conclusions

The reactivity of the nonplanar olefins within silver coordination complexes is readily achieved, likely owing to more rigid and predictable coordination forces that can force nonplanar olefins into reactive environments. Whereas resorcinol templates have successfully directed olefin reactivity in solids, more complex nonplanar olefins pose a

challenge in hydrogen bond-directed self-assembly. The observations are important since trisubstituted olefins are not as well-studied in the context of solid-state reactivity, and could be of interest for postsynthetic modification to incorporate additional functionalities around the cyclobutane core. The results suggest that metal coordination-based self-assembly can provide a more reliable method to achieve reactive assemblies of more complex, conformationally-rigid olefins. To our knowledge, this is the first example of a trisubstituted multifunctional olefin that has been photodimerized *by design*.

In this chapter, we have demonstrated the reactivity of a trisubstituted olefin in the solid state using coordination-driven self-assembly. We have shown that having both resorcinols and Ag^{I} salts is advantageous when constructing target frameworks based on self-assembly. While studying the reactivity of trisubstituted olefins, we have demonstrated that is difficult to direct solid-state reactivity in conformationally-challenged systems.

CHAPTER 6. OPTICAL PROPERTIES OF [2.2] CYCLOPHANES OBTAINED IN THE SOLID STATE

A portion of this chapter was published in *Organic Letters* and is adapted with permission from [E. Elacqua, D.-K. Bučar, Y. Skvortsova, J. Baltrusaitis, M. L. Geng, L. R. MacGillivray, *Org. Lett.* **2009**, *11*, 5106.]. Copyright 2009, American Chemical Society. The work in *Organic Letters* was reviewed as part of paper focusing on optoelectronic properties of [2.2]paracyclophanes in the *European Journal of Organic Chemistry* and is adapted with permission from John Wiley and Sons, Copyright 2010 [E. Elacqua, L. R. MacGillivray, *Eur. J. Org. Chem.* **2010**, 6883.]. A followup article focused upon the impact of nanotechnology on the optical properties of [2.2]paracyclophanes was published in *CrystEngComm* and is adapted following the rights retained by journal authors, as established by the Royal Society of Chemistry [E. Elacqua, P. T. Jurgens, J. Baltrusaitis, L. R. MacGillivray, *CrystEngComm* **2012**, *14*, 7567.].

6.1 Introduction

Much interest has been focused on the designed synthesis of molecular architectures that place chromophores into well-defined geometries.[281] [2.2]Paracyclophane (pCp) is a key building block in this regard, as the molecule provides an aromatic scaffold that can impart both unique structural and physical properties on a variety of functional groups. Indeed, the phane supports a 3D structure combined with transannular properties that organic and materials chemists have sought to develop as an organic building block in the engineering of complex molecules and materials.

From a fundamental standpoint, pCp is composed of two benzene rings covalently fixed in a face-to-face geometry by ethano bridges, wherein the two rings are stacked and distorted into a boat orientation (Figure 158).[282] The structural aberration, coupled with

intrinsic transannular effects, has resulted in pCps with a unique reactivity and intriguing spectroscopic properties.[283] Initially, pCp was coined an aromatic molecule *par excellence*, with studies focused on the comprehension of how changes in molecular structure upon simple aromatic substitution affect reactivity, physical, and spectroscopic properties. More recently, pCp has been engineered as a core for functionalization with several applications in organometallic and asymmetric synthesis[284] as chiral ligands, as well as organic scaffolds.[285] The scaffolds have invariably involved heavy substitution of the aromatic decks, leaving the aliphatic bridges largely empty. This is presumably due to the lack of reliable and diverse synthetic methods that are capable of targeting the aliphatic bridges. Additional studies have focused on the synthesis of pCp derivatives[286] and frameworks utilized for cycloadditions.[287]

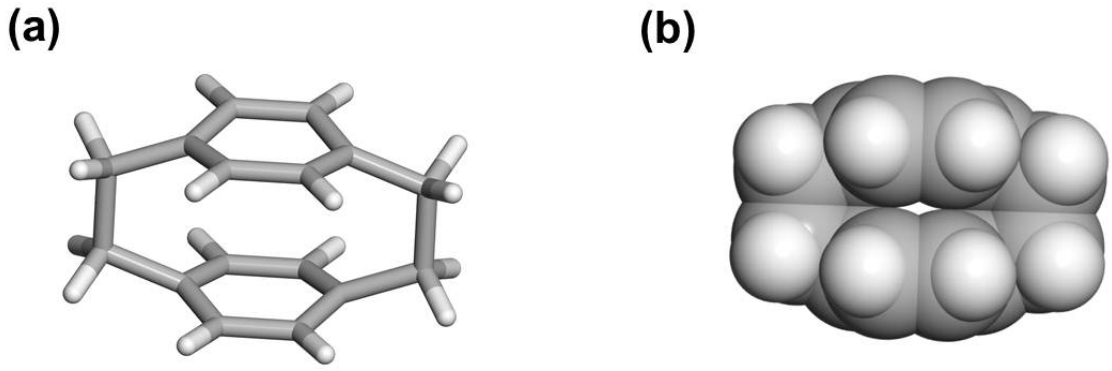

Figure 158: [2.2]Paracyclophane: (a, b) crystal structure portraying stacked aromatic framework and boat-like conformation.

pCp, and derivatives, have defined a rich area of inquiry for over 60 years.[288] The foundation lies in the unusual structure of pCp, and hence, unique and novel properties that can result from interactions within the strained architecture. In recent years, pCp has been utilized as a model to study electron delocalization, owing to the two co-facially stacked benzene rings being held in place *via* aliphatic bridges.[289] Unique optical

properties are observed when two or more π-systems are geometrically fixed in close proximity in a molecule such as pCp. In particular, transannular through-space and through-bond donation perturb the molecular π orbitals such that σ(bridge)-π(deck) interactions can lead to modulated donor-acceptor interactions.

It is well known that pCp alone exhibits an abnormal absorbance spectrum compared to simple benzene derivatives and related hydrocarbons, exhibiting bands at 225 nm, 244 nm, 286 nm, and 302 nm. The long-wavelength band has been coined the "cyclophane band," as the band is well past the absorption of simple alkyl aromatics.[285] The emission spectrum of pCp is also unexpected when compared to alkyl aromatics, as a broad band is observed at 356 nm. The spectroscopic properties are attributed to strong σ-π interactions,[290] as well as a π-π through-space delocalization that result in a smaller HOMO-LUMO gap and enhanced energy transfer throughout the entire cyclophane core.[291]

Owing to the unique optical properties conferred by the covalently-stacked aromatic rings, pCp has emerged as a prominent organic building block for the development of novel device-based applications.[291] There is an expectation that perturbations in the molecular structure of pCp can lead to an internal charge transfer (ICT) that affects device performance through electronic communication.[292] In particular, extension of the end-to-end conjugation length generates pCps with excitations and emissions up to 430 and 530 nm, respectively.[293] Termination of the chromophore with acyclic donor and acceptor groups also enhances the ICT, with absorbances and emissions near 500 and 600 nm, respectively.[294-297] Enhancement of ICT is also seen in pCp-based polymers. Polymeric systems display ICT with absorbances up to 470 nm and emissions up to 600 nm.[303-307] The changes to molecular structure, coupled with the unique structure of pCp, have produced architectures that show tunable optoelectronic properties that can lead to device-based applications.

In more general terms, understanding how molecular structure correlates to bulk properties is important when designing electronic devices. Organic semiconductors and conjugated polymers rely on the specific orientation and organization of π-networks for optimal performance. In these systems, molecular subunits are subjected to different environments that often result in poorly-defined morphologies with difficult to quantify photophysical properties.[292] In this context, the design and synthesis of well-defined pCp-based chromophoric materials has been targeted as a means to probe the effect of electronic communication on optoelectronic properties, and ultimately, incorporate tailored properties to improve device performance.

6.2 Orthogonally-Functionalized [2.2]Paracyclophanes as Model Architectures to Study Optical Properties

It is well known that electronic communication between chromophoric subunits depends on relative orientations and through-space distance. By exploiting the strained structure of pCp, and coupling chromophores orthogonally to the decks, conjugated frameworks have been developed that enhance ICT and lead to varied photophysical properties.[294] Compounds that demonstrate ICT have possessed distinct donor and acceptor groups typically connected by a π-electron conjugated path. Pioneering work involving pCp has been accomplished by Guillermo Bazan and co-workers through the synthesis of several pCps wherein stilbene-based donor and/or acceptor units (Figure 159) have studded the pCp decks.[289, 292] By coupling stilbenes to pCp, a family of molecules has been generated that provide a foundation to study the perturbations of optical properties as a function of molecular structure. By using well-known organic chromophores such as stilbenoids, comparisons have been made between a 'monomer' and pCp-based 'dimer.' Specifically, the molecular orbitals of the pCp dimer are generally known to split into symmetric and antisymmetric contributions of the monomer that result in a smaller HOMO–LUMO gap and, thus, lower energy fluorescence

compared to monomer systems. Initial studies by Bazan drew comparisons between pCp bound styryl-based chromophores of differing conjugation lengths and chromophore orientations (Figure 159). More recent investigations have led to pCps that serve as prototypes for fluorescent sensor-based applications (i.e. biological, chemical).

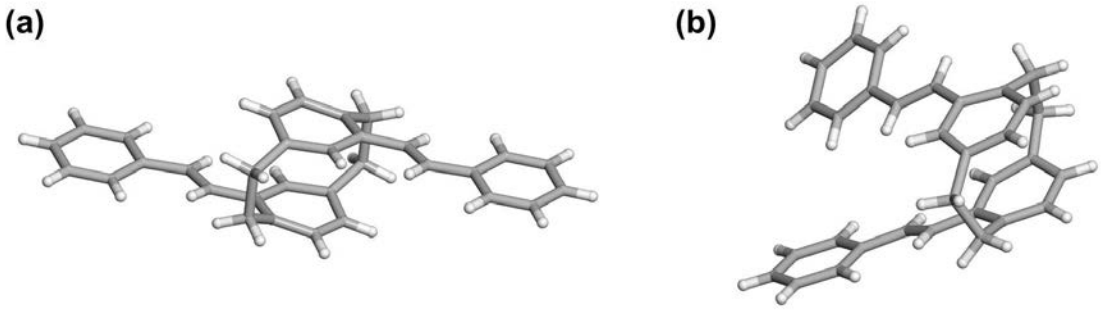

Figure 159: Stilbene-based pCps **1e-1f** studied by Bazan.

6.2.1 Influence of End-to-End Conjugation Length on Electronic Communication

pCps **1a-j** (Figure 160) have probed how conjugation length and molecular structure can be used to understand the effects of through-space delocalization on the optical properties of the pCp framework.[295] Vinyl-substituted **1a** was initially employed as the simplest chromophore, having the shortest conjugation length. The maximum excitation for the extended derivative **1a** was determined to be 281 nm, which is surprising since pCp itself exhibits a maximum absorbance at 310 nm. Additionally, **1a** showed an emission maximum at 374 nm, which is red-shifted with respect to pCp (λ_{max} = 356 nm). Bazan and co-workers also examined the properties of divinyl pCps **1b** and **1c**. The pseudo-*para* derivative demonstrated a further blue shift in absorbance (λ_{max} = 254 nm), as well as a red shift in fluorescence (λ_{max} = 394) relative to both pCp and **1a**. Conversely, the pseudo-*ortho* derivative displayed a bathochromic shift in absorbance relative to **1a** at 288 nm that corresponded to a similar bathochromic shift in fluorescence

up to 386 nm. In related studies utilizing monostyryl- and distyryl-substituted pCps (**1d-g**), absorbances and emissions up to 338 and 412 nm, respectively, were observed.

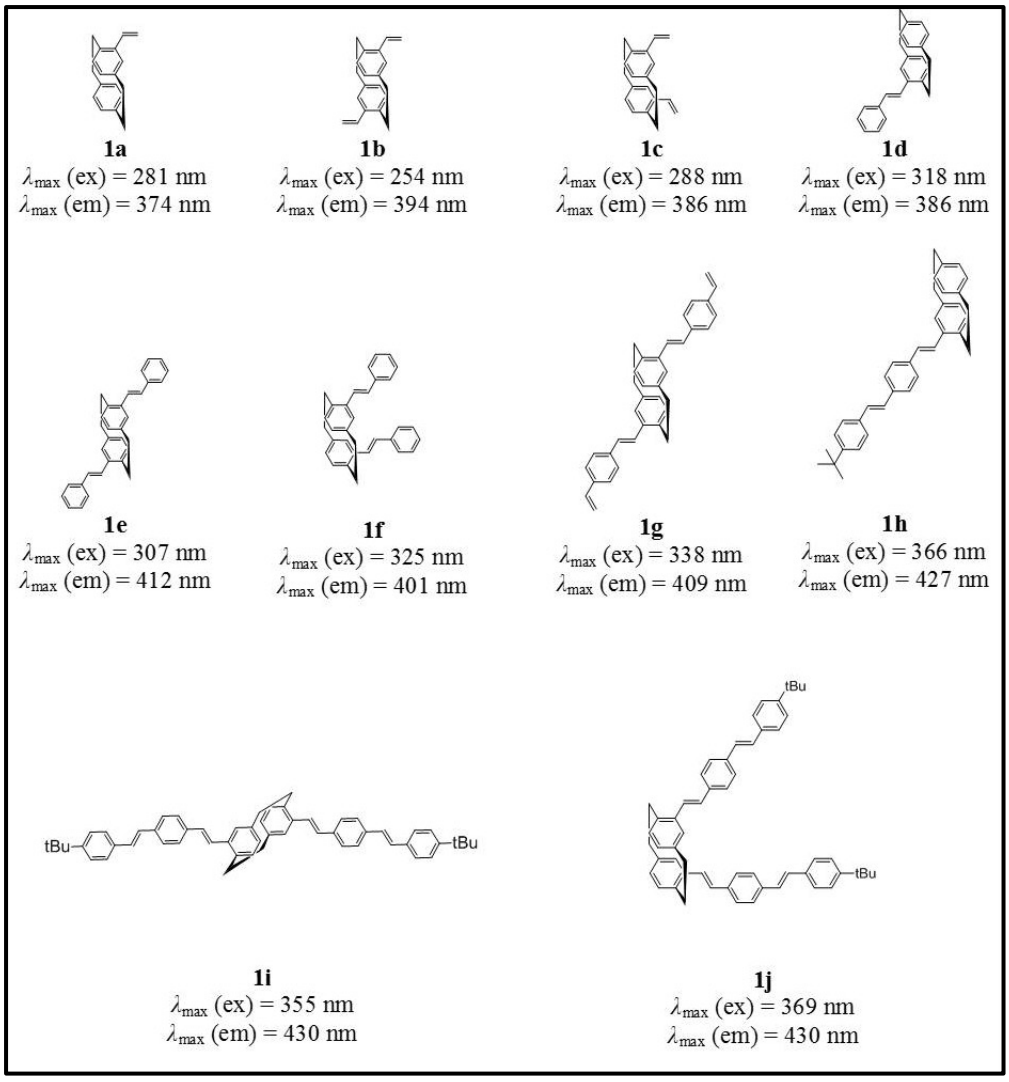

Figure 160: Substituted pCps **1a-1j** studied by Bazan.

The shifts in emissions in involving **1a-j** were consistent with increasing the end-to-end chromophore length, which increased the ability of electronic charge to be shuttled across a longer distance.[289, 295] In addition to conjugation length, substitution pattern impacted emission, as lower energy fluorescence was exhibited when the chromophores

were arranged in the pseudo-*para* orientation, effectively increasing electronic communication between chromophores, while influencing through-space delocalization.

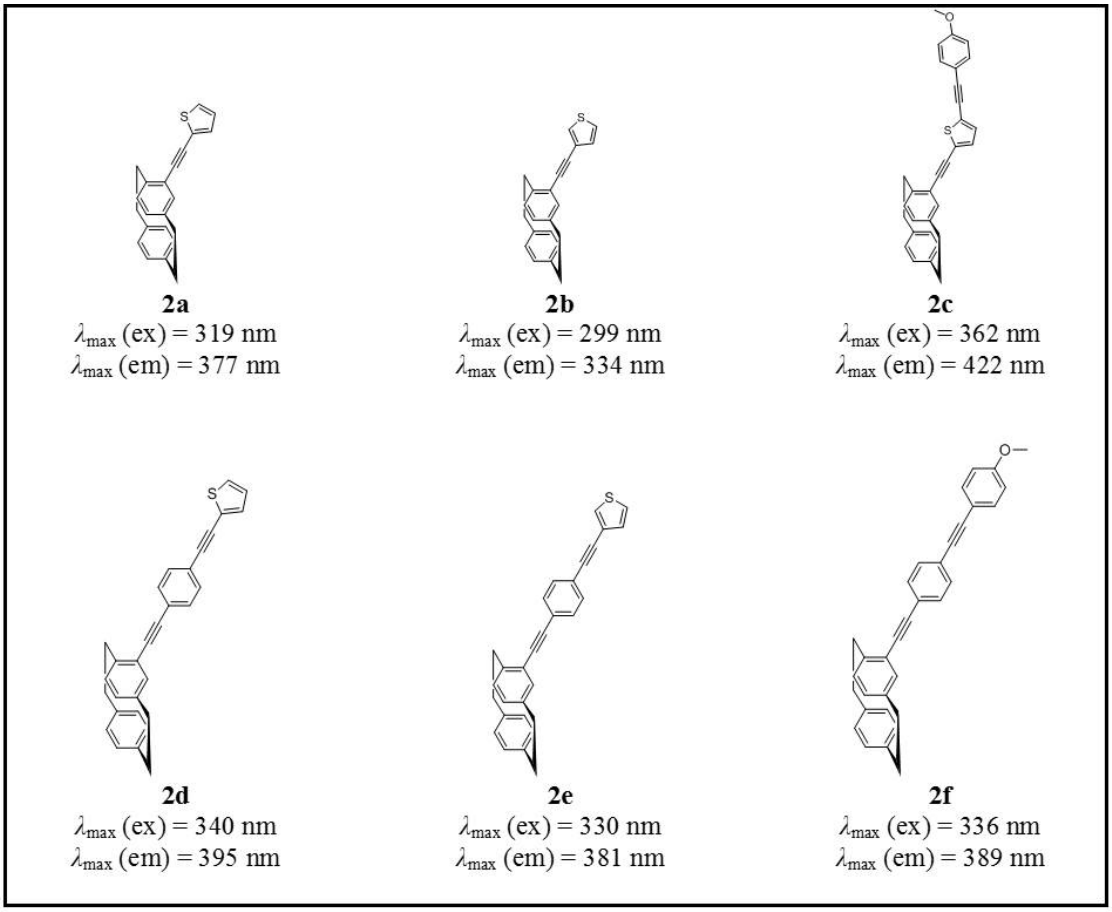

Figure 161: Substituted 4-ethynyl pCps **2a**-**2f** studied by Taticchi.

Further studies on the impact of conjugation length on electronic communication were accomplished by Taticchi and co-workers (Figure 161). Specifically, thiophene and/or benzene rings were used to extend the conjugation of 4-ethynyl[2.2]paracyclophane, affording pCps **2a**-**2f**.[296] Thiophene-substituted **2a** and **2b** were the simplest pCps investigated, differing only in connectivity to the thiophene. **2b** displayed excitation and emission maxima at 299 nm and 334 nm, respectively. In

contrast, **2a** demonstrated red-shifted absorbance and fluorescence to 319 nm and 377 nm, respectively. These observations are consistent with improved conjugation of the β-thienyl system. The more complex **2c** was investigated to study the effect of a *p*-methoxy ethynylbenzene chromophore attached at the periphery of the thiophene. Lengthening of the conjugation effectively resulted in red shifts in both absorbance and fluorescence of 50 nm, compared to **2a**. The benzene-based counterpart of **2c** was studied. Compound **2f** displayed a strong excitation of 336 nm, along with an emission at 389 nm. The results were considerably blue-shifted compared to thiophene-based **2c**. This can be attributed to increased electron delocalization facilitated by the thiophene rings. In related studies involving additional ethynylbenzene moieties within the pCp side chain (**2d**-**2e**), absorbances and emissions up to 340 nm and 395 nm, respectively, were observed.

6.2.2 Influence of Acyclic Substituents on Electronic Communication

Further perturbations to the optical properties of pCp have been achieved when a chromophore terminated in a strong acyclic donor and/or acceptor was coupled to the stacked framework. In particular, the introduction of tert-butyl, amine, and/or nitro functionalities resulted in architectures with more efficient (i.e. high wavelength emission) ICT owing to the placement of electron-donating or -withdrawing groups within the framework. Termination of the stilbenoid chromophores with tert-butyl groups, as in the cases of **1h-j**, resulted in absorbance maxima up to 370 nm and an emission maximum of 430 nm. Additional coupling of the tert-butyl styryl and stilbene-based chromophores led to tetrasubstituted donor scaffolds **3a** and **3b**. The excitation spectra displayed maxima at 380 nm and 420 nm for **3a** and **3b**, respectively, while the emission spectra revealed maxima at 450 nm and 510 nm.[297] Donor-acceptor-donor systems, such as those in **1h**-**3b**, are examples wherein electronic communication is more efficient from the donor chromophoric arms to the acceptor cyclophane core owing to the

presence of strong donor groups that give rise to lower energy excitation and emission behavior.

Unlike the ITC observed with terminal donor groups, the introduction of a combination of donor and acceptor groups promoted a more efficient charge transfer, with electronic charge being favorably shuttled throughout the entire scaffold. The coupling of a *p*-dihexylaminostyrene to one end of a substituted pCp, followed by a *p*-nitrostryryl chromophore at the other terminus (Figure 162), resulted in a donor-acceptor system with end-to-end conjugation (**4**). An excitation maximum of 383 nm and emission maximum of 570 nm were observed for **4**.[294]

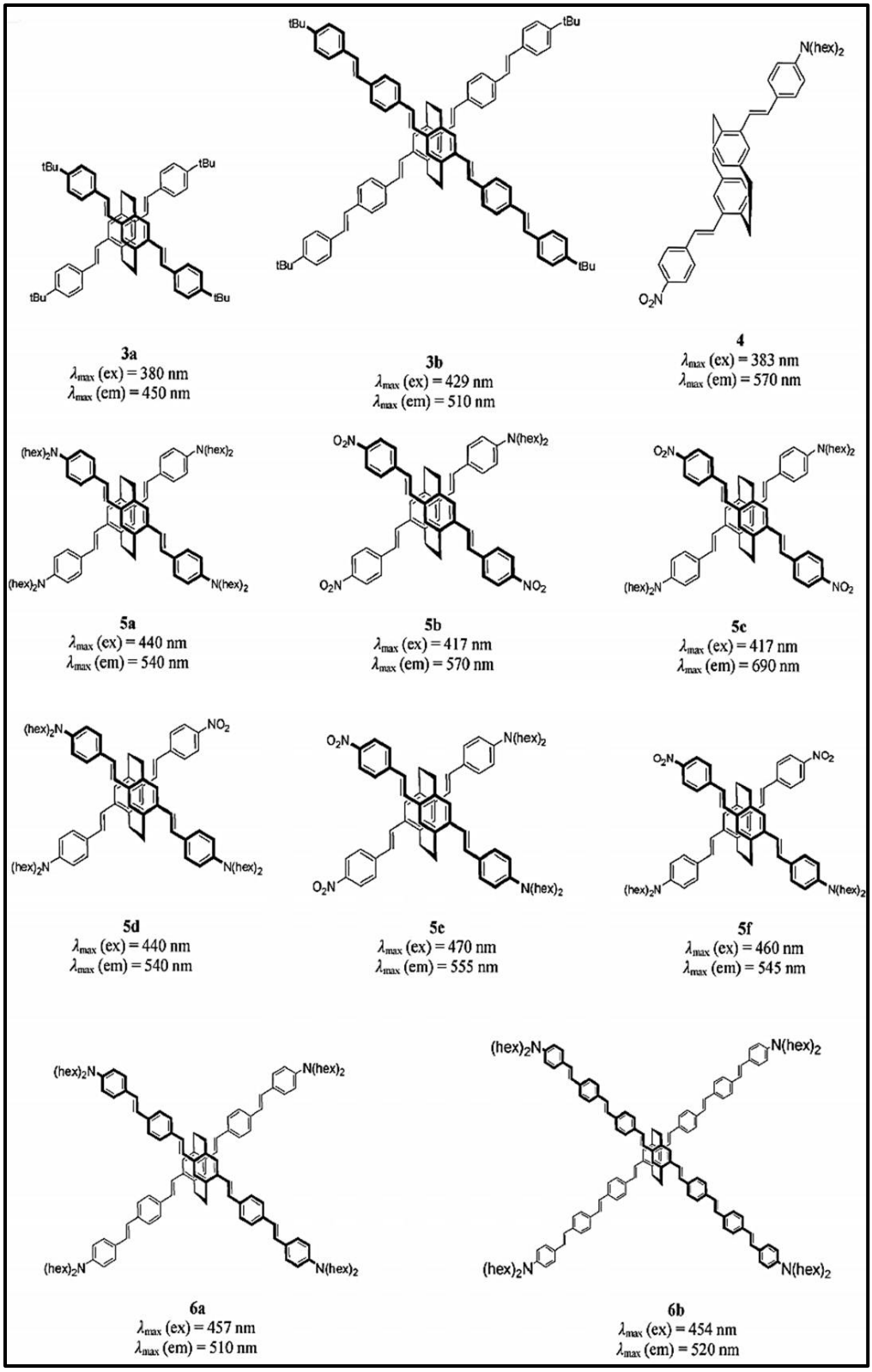

Figure 162: Tetrasubstituted pCp architectures **3a**-**6b** studied by Bazan.

An analogous class of tetrasubstituted pCps decorated with dihexylamino and/or nitro groups (**5a**-**f**) has also been reported (Figure 162-163).[308] The tetraamine **5a**, which consisted of *p*-dihexylaminostyrene branches as donor groups, exhibited an absorbance at 440 nm and an excitation at 560 nm. Comparable results were observed with either three donor or three acceptor termini (**5b** and **5d**, respectively). Compounds **5c**, **5e**, and **5f** each possessed two donor and two acceptor arms. pCps **5e** and **5f**, wherein both donor groups were placed in the pseudo-*ortho* and pseudo-*meta* positions were determined to exhibit similar absorbances up to 470 nm and emission maxima near 550 nm. Conversely, **5c** demonstrated a more unique behavior, displaying a blue-shifted absorbance at 417 nm that corresponded to two separate emission peaks at 500 nm and 690 nm. The dual emission resulted from two equally-accessible excited states, owing to coupling of the stilbenoid "parent" donor and acceptor chromophores across the transannular gap. Structurally analogous 5- and 7-ring pCp dimers **6a** and **6b** were also examined, both of which displayed an absorbance up to 457 nm with emissions at 510 and 520 nm, respectively.[309] Indeed, the introduction of donor and/or acceptor groups resulted in lower energy absorbance and fluorescence owing to the strong ICT seen associated with donor-acceptor systems.

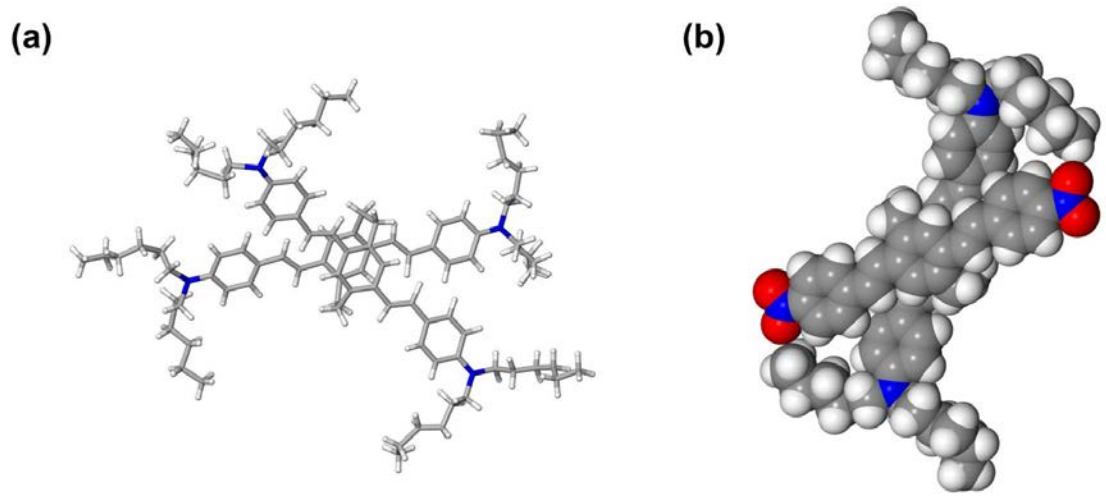

Figure 163: X-ray structures of tetrasubstituted **5a** and **5c** studied by Bazan in the context of donor-acceptor studded pCps.

6.2.3 Influence of Charged Groups on Electronic Communication

Applying pCp-based architectures for biological applications will likely require charged groups for water solubility. The molecules should contain strong interchromophore delocalization to be less susceptible to environmental factors (*e.g.* aggregation) that could affect electronic properties.[289] Efforts by Bazan to achieve water solubility led to incorporation of charged functionalities within the pCp framework.

pCps **7a-c** contain disubstituted and tetrasubstituted pCp decorated with alkyl ammonium groups (Figure 164).[298, 310] The related neutral pCps were also studied. The disubstituted pair was studied to investigate the effect of charge with direct comparison to pCp. In general, the charged compounds displayed red-shifted absorbances and emissions relative to the neutral forms. The charged compounds were also found to exhibit solvatochromism, wherein more polar solvents (e.g. DMSO, water) provided further red shifts when compared to weakly polar solvents (e.g. THF, toluene, hexanes).

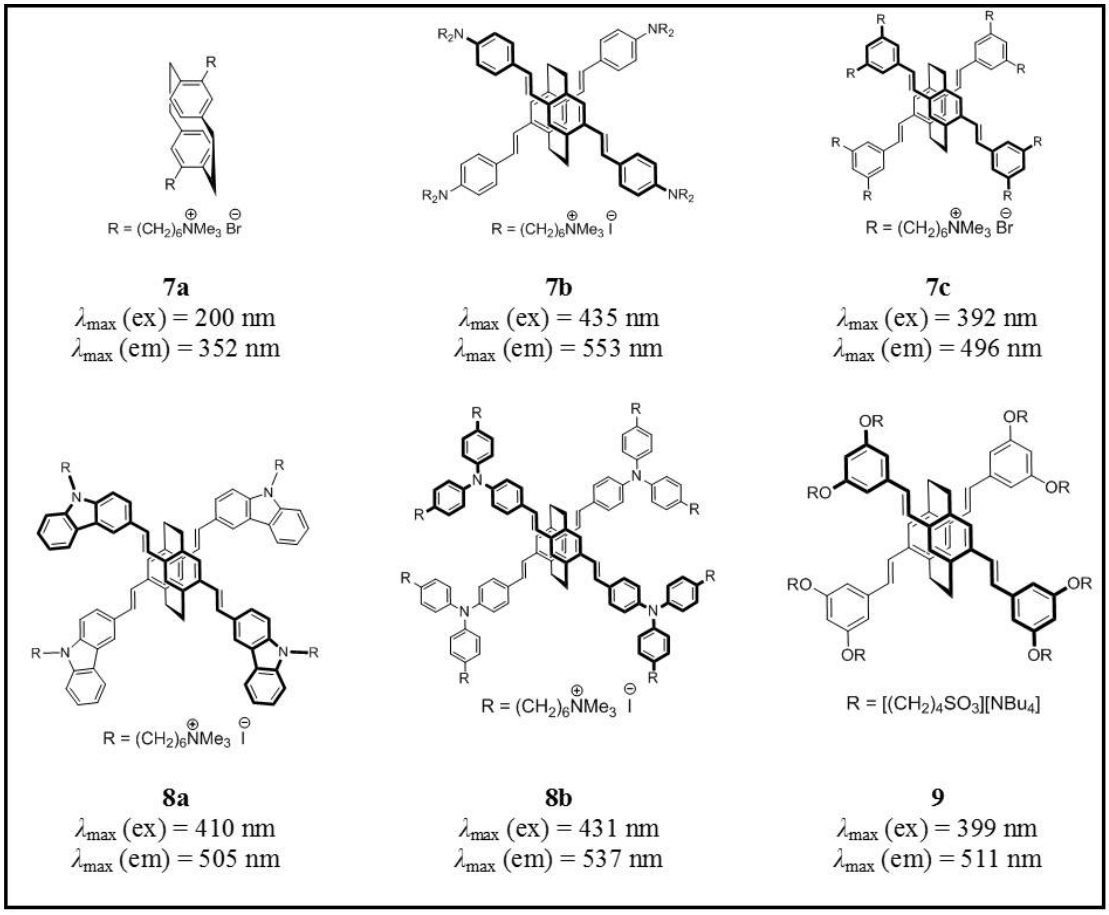

Figure 164: Charged pCp architectures studied by Bazan.

Disubstituted **7a** exhibited a maximum absorbance at 200 nm along with weaker absorbances at 227, 255, and 306 nm, which was analogous to the neutral counterpart. Excitation at 200 nm resulted in an emission at 352 nm, a slight red shift compared to the parent pCp. The optical properties of **7a** are comparable to that of pCp owing to a lack of additional chromophores and/or strong donors to increase the ICT properties. However, tetrasubstituted pCps **7b**-**c** (Figure 164), differing only by terminal groups, displayed a red-shifted shifted emission compared to neutral counterparts on the order of 20-25 nm. When N-substituted carbazoles were incorporated into structurally-analogous **8a** and **8b**, a red-shifted fluorescence of up to 45 nm was observed. The shifts are consistent with

increasing the electron accepting properties of the pendant amines *via* quaternization of the N-atoms. In the charged frameworks, ICT is optimized owing to increased electron donation from the pCp core outward to the electron-accepting arms of the frameworks. The positively charged N-atoms act as more efficient electron acceptors owing to overall electron deficiency. Bazan has also studied related O-based donors with charged groups (Figure 164). pCp **9**, which contains an ammonium sulfate moiety, displayed an absorbance of 399 nm, as well as a sharp emission at 511 nm.[299]

The studies of Bazan and Taticchi on effects of conjugation length, as well as incorporation of acyclic substituents and charged functionalities, have provided a foundation for the development of pCps with well-defined optoelectronic properties and optimized electron delocalization. Relative effects of chromophore orientation, contact site, and end-to-end conjugation length have provided an understanding of how to favorably perturb through-space delocalization and ICT to design pCp-based frameworks that provide insights into related conjugated polymers. Owing to the use of pCp as the core chromophore, and though the coupling of secondary chromophores to the core, pCp architectures were achieved that display prominent emissions. The results bode well for future incorporation of molecular pCp derivatives in materials science as electronic devices (e. g. biosensors, OLEDs, seminconductors).[289]

6.3 π-Stacked Polymers Based on [2.2]Paracyclophanes as Models to Study Optical Properties

In addition to molecules, optical properties of polymers based on pCp have been studied. Chujo and co-workers have laid a foundation by focusing on layered pCp polymers with either a 4,16-divinyl or 4,16-diethynyl[2.2]paracyclophane core. Initial studies focused on integrating pCp within a poly (*p*-phenylene-ethynylene) (PPE) or poly (*p*-phenylene-vinylene) (PPV) framework. More recently, the focus has moved to the installation of donor and/or acceptor functionalities, similar to the molecules, within the

PPE polymer backbone. To tailor properties of the polymers, donor and/or acceptor groups studied in the context of related conjugated polymers were installed along the polymeric backbone *via* covalent linkages to the decks of pCp. Integration of the groups has allowed for efficient electronic communication throughout the polymer, resulting in sharp emissions throughout the visible region on the order of 400 to 600 nm and promising charge-transfer properties compared to the "monomeric" conjugated polymers (Figure 165).

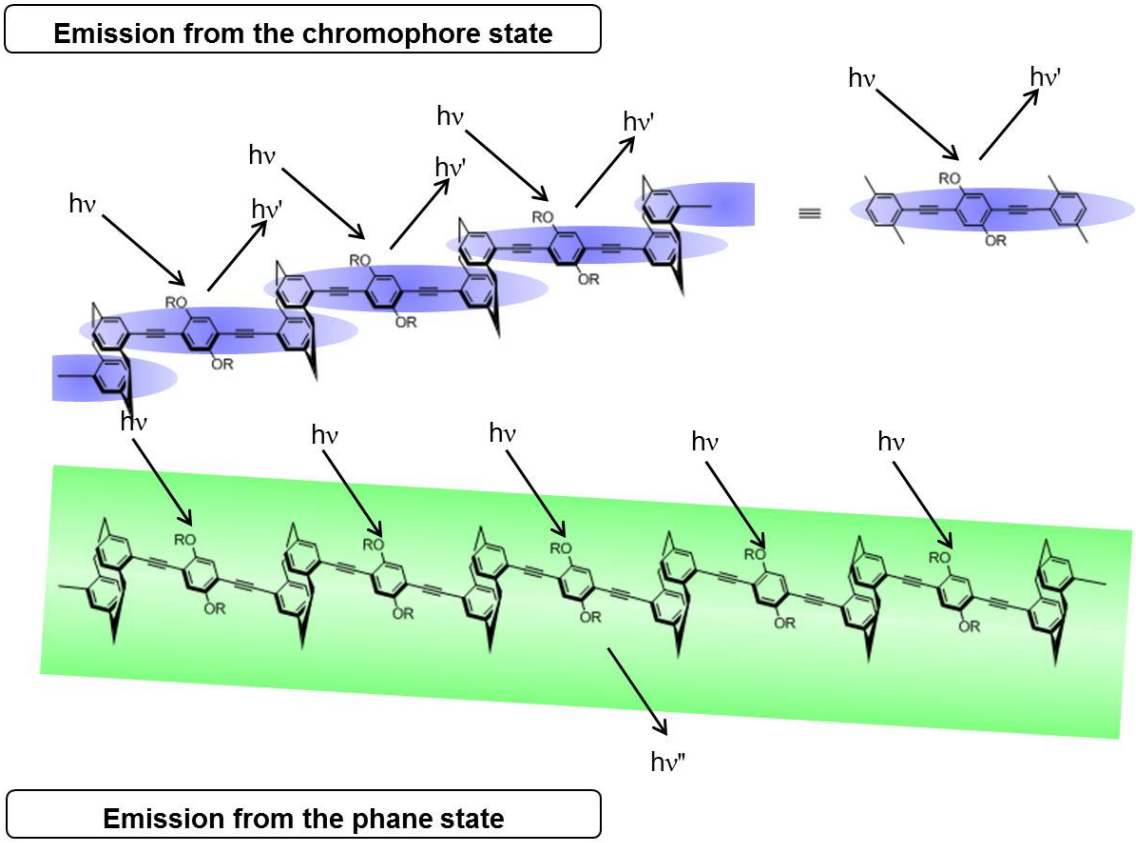

Figure 165: Chujo's proposed emission mechanism in PPE-based systems involving π-stacked pCp cores integrated in conjugated polymers.

6.3.1 [2.2]Paracyclophanes as Functional Units in PPE and PPV-Based Frameworks

The first reported pCp polymers were based on a PPV polymer backbone with a phenylene unit (**10a-c**) in the main chain (Figure 166).[300] Two intense absorbances at 340 and 398 nm, as well as a blue emission maximum at 462 nm for both **10a** and **10b**, were observed. The polymer **10c**, which contained an additional styryl unit at each terminus, exhibited an enhanced π-delocalization as evidenced by red shifts in both absorbance (λ = 362 and 423 nm) and fluorescence (λ = 487 nm).

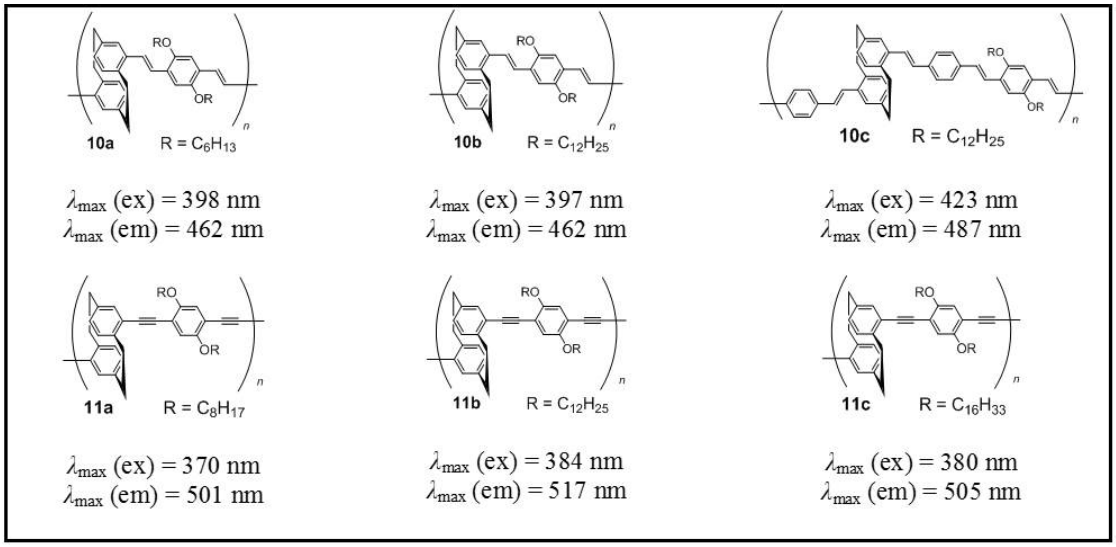

Figure 166: PPE-based (**10a-10c**) and PPV-based (**11a-11c**) pCp polymers studied by Chujo.

Analogous PPE-based frameworks **11a-c** exhibited absorbance maxima at 370-385 nm (Figure 166).[311] The emissions were red-shifted relative to the PPV frameworks, as a strong green fluorescence at 510 nm was observed in **11a-c**. Installation of a diacetylene unit as a spacer between two phenylene units in structurally related **12** resulted in a red-shifted absorbance to 406 nm and a blue emission maximum at 442 nm

(Figure 167).[312] The differences in absorbances were attributed to the effect of end-to-end chromophore length. In the PPE-based polymers, the conjugation length is larger owing to the longer alkene bonds, thus, resulting in a lower energy absorbance. In contrast, alkyne bonds are shorter with overall through-bond electron delocalization occurring over a shorter path. Owing to the shorter interchromophore distance within the PPE polymers, through space interactions are maximized with lower energy emission bands observed.

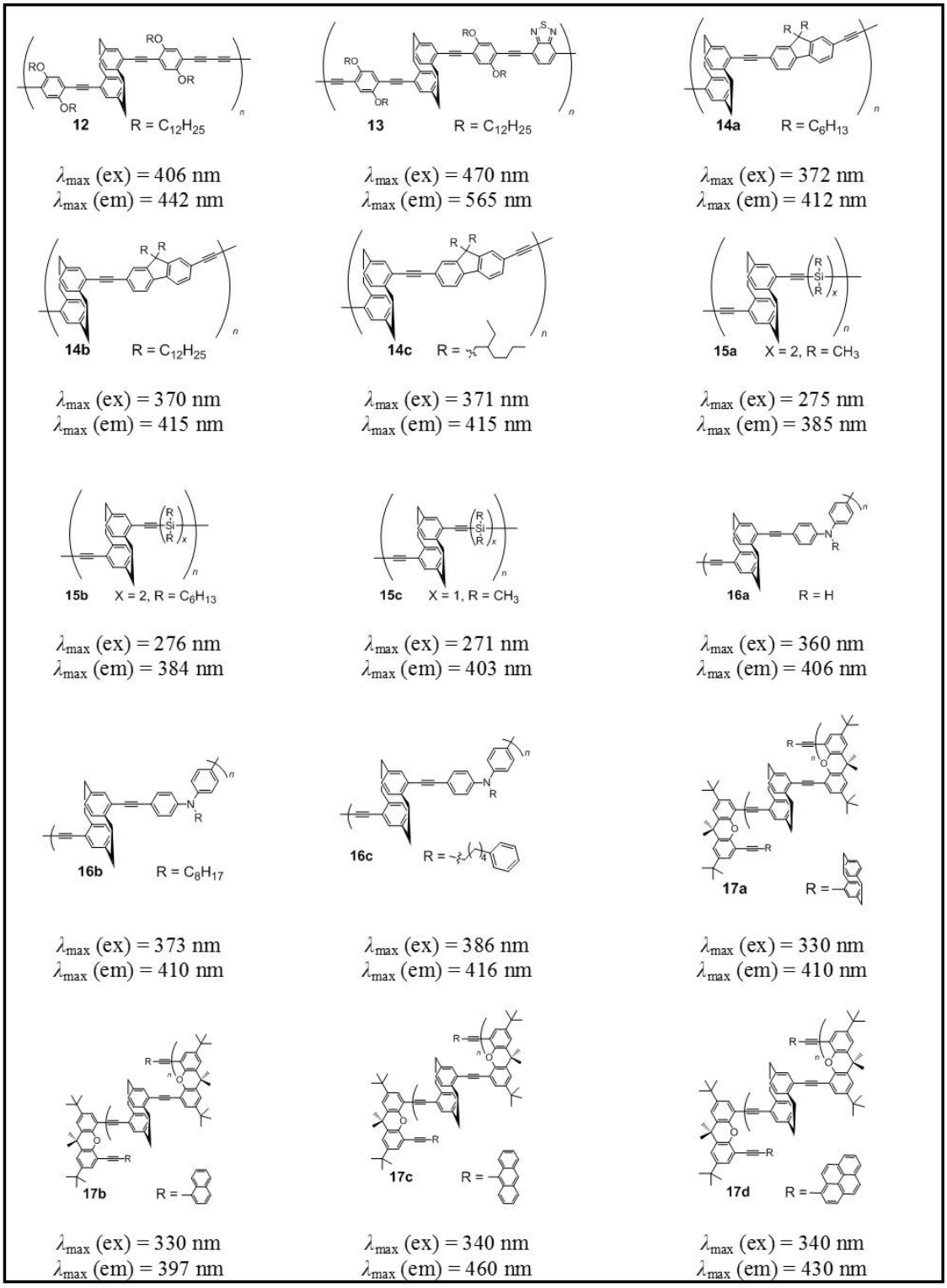

Figure 167: PPE-based pCp polymers **12-17d** studied by Chujo.

6.3.2 Installation of Donor or Acceptor Functionalities into a Polymer Backbone

Investigations of electron acceptor groups incorporated into a PPE-backbone led to benzodithiazole as a unit to facilitate electron delocalization within a pCp polymer.[301] Benzodithiazole has been used in conjugated polymers as an electron-accepting component and has successfully resulted in band gap reductions.[313] Polymer **13** displayed an absorbance maximum of 470 nm, which was attributed to a more efficient through-space delocalization and ICT between electron-accepting benzodithiazole and the electron-donating pCp. Additionally, **13** exhibited a strong orange emission at 565 nm (Figure 167).

Novel pCp-centered co-polymers containing fluorene units have also been studied.[302] Fluorene-based compounds are well known to exhibit efficient photo- and electroluminescent properties in the blue region.[302] The resulting PPE-based **14a-b** (Figure 167) displayed absorbances centered at 370 nm, along with strong blue fluorescence at 415 nm. The alkyl-substituted fluorene unit acts as a donor and participates in ICT with the adjacent pCp core, resulting in the blue fluorescence.

After investigating the impact of fluorene units within the polymeric main chain, Chujo expanded to organosilicon moieties. Organosilicon groups are of interest for semiconductor applications, as well as for photoresistors and non-linear optical (NLO) materials.[304] The resulting PPE polymers (**15a-c**, Figure 167) displayed a broad absorbance around 275 nm. A fluorescence maximum of 385 nm was observed for **15a** and **15b**, while **15c** showed a bathochromic emission at 403 nm. When phenylamine functionalities were integrated into a PPE-type structure,[305] the polymers **16a-c** exhibited a strong absorbance of 360 nm for the secondary amine, **16a** and up to 385 nm as the substitution on the amine increased in size. All the polymers exhibited a blue emission maximum around 410 nm, which resulted from ICT from the electron-donating amine unit towards the cyclophane core.

Xanthene has been recently incorporated into PPE-based scaffolds. The polymers (**17a-d**, Figure 167) exhibited strong absorbances and emissions, and in some cases, fluorescence resonance energy transfer (FRET) from the cyclophane moieties to the end-capping groups.[306] In particular, **17a-b** displayed an absorbance band at 330 nm, along with an emission up to 410 nm. **17a** and **17b** differ in structure, wherein an additional pCp or naphthalene was used as an end cap, respectively. When an anthracene unit was used as a capping agent in **17c**, a strong absorbance was observed at 340 nm, along with an emission at 460 nm. For **17c** there was a prominent overlap between the emission peak at 400 nm and the absorbance peak of 9-ethynylanthracene, which accounted for the FRET from the pCp core to the anthracene caps. When a larger pyrene system was used as an end-capping group in **17d**, an analogous absorbance was seen that also displayed a blue shift in emission at 430 nm. An additional xanthene co-polymer was prepared, wherein nitrobenzene was employed as an end-cap in **18** (Figure 168).[307] Polymer **18** exhibited an absorbance at 330 nm, as well as an additional, yet less intense, broad band at 370 nm. Nitro groups are electron-acceptors, which allows for more efficient electron transfer, and thus, lower energy absorbance. When copolymer **18** was excited at 333 nm, the molecule displayed an emission maximum at 410 nm.

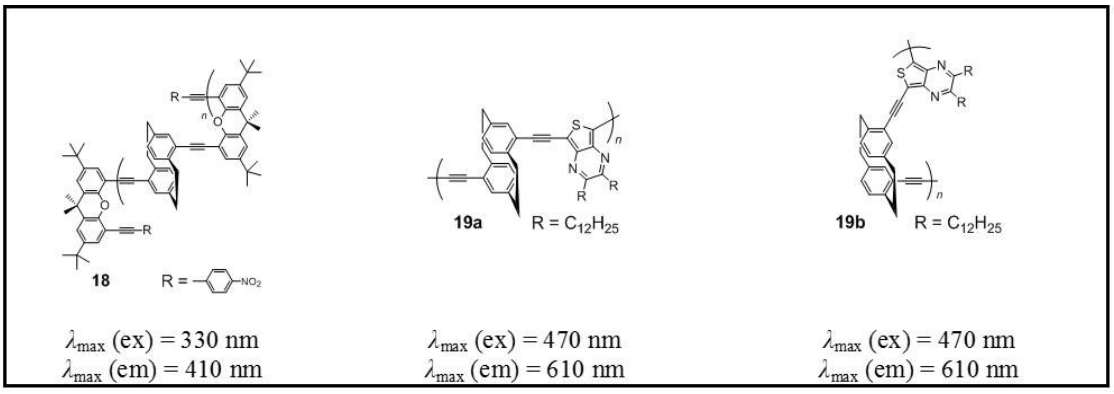

Figure 168: Additional pCp polymers **18-19b** investigated by Chujo.

To further investigate the impact of functional groups within the main chain of the pCp co-polymers, Chujo explored the influence of thieno[3,4-*b*]pyrazine. When pyrazine was used as a co-monomer in **19a-b**, an absorbance maximum at 470 nm was observed, along with an emission at 610 nm (Figure 168).[315] Thieno-[3,4-*b*]pyrazine units possess a high degree of electron withdrawing character. The co-polymers **19a-b** displayed a resulting highly efficient ICT with the polymeric main chain consisting of a donor-acceptor-donor framework.

The studies by the Chujo group have resulted in the well-defined and characterized through-space conjugated and aromatic ring-layered polymers that contain pCp units in the main chain. The PPV- and PPE-based polymers display well-defined optical properties while also demonstrating that simple structural modification can result in tailored properties with sharp emissions that span from the blue region into the orange. Collectively, the studies have demonstrated the potential incorporation of pCp-based polymers in optoelectronic device, as well as single molecular wires and NLO materials.[316]

6.4 Laterally-Substituted [2.2]Cyclophanes as Upcoming Models to Study Nonconventional Optical Properties

Despite not being well-known in the context of cyclophane chemistry, bridge-substituted [2.2]cyclophanes are emerging as viable architectures to study novel synthetic and optoelectronic properties.[169] Owing to the lack of synthetic methodologies that would target the aliphatic bridges, the solid state has surfaced as a medium to design and construct cyclophanes[96] *via* application of principles of crystal engineering and supramolecular synthesis.

6.5 Solid-State Cyclophane Synthesis *via* a Combinatorial Template Approach

Thus far, the solid state has emerged as a more reliable way to construct [2.2]cyclophanes. Solution-phase methodology generally suffers from the inability to cyclize the product, owing to the strain associated with the desired products. The solid-state essentially fixes this problem, as the reactant molecules are essentially locked with minimal movement in the crystalline state. Despite this advantage, the [2.2]cyclophanes synthesized in the solid state often times produce several different products and/or stereochemistries or suffers from modest yields. The introduction of a supramolecular template to juxtapose molecules in a reactive geometry would provide a method to exert control over product formation and stereochemistry.

Recently, we have shown that a series of [2.2]cyclophanes can be synthesized stereospecifically, and in quantitative yield, using a library of hydrogen bonding templates based upon resorcinol. In essence, the strategy is reminiscent of dynamic combinatorial chemistry,[58] wherein a series of templates are used to (reversibly)-construct co-crystals that are then tested for reactivity.

The [2.2]paracyclophane, tpcp, was generated using 4-Bn res. The success of the method suggested that the corresponding 'bent' *meta* and *ortho* analogues could be synthesized utilizing our combinatorial template-directed approach. Specifically, the [2.2]metacyclophane tpcm, and the [2.2]orthocyclophane tpco could be constructed by self-assembly of two res templates and two 'bent' diolefins m-bpeb and o-bpeb, respectively, with the res template preorganizing the diolefins for a double [2+2] photocycloaddition. Exploitation of template-switching method allowed for the generation of both of the *exo, exo* and *exo, endo* isomers of tpcm, as well as the expected *exo, exo* conformation of tpco (Figure 169).

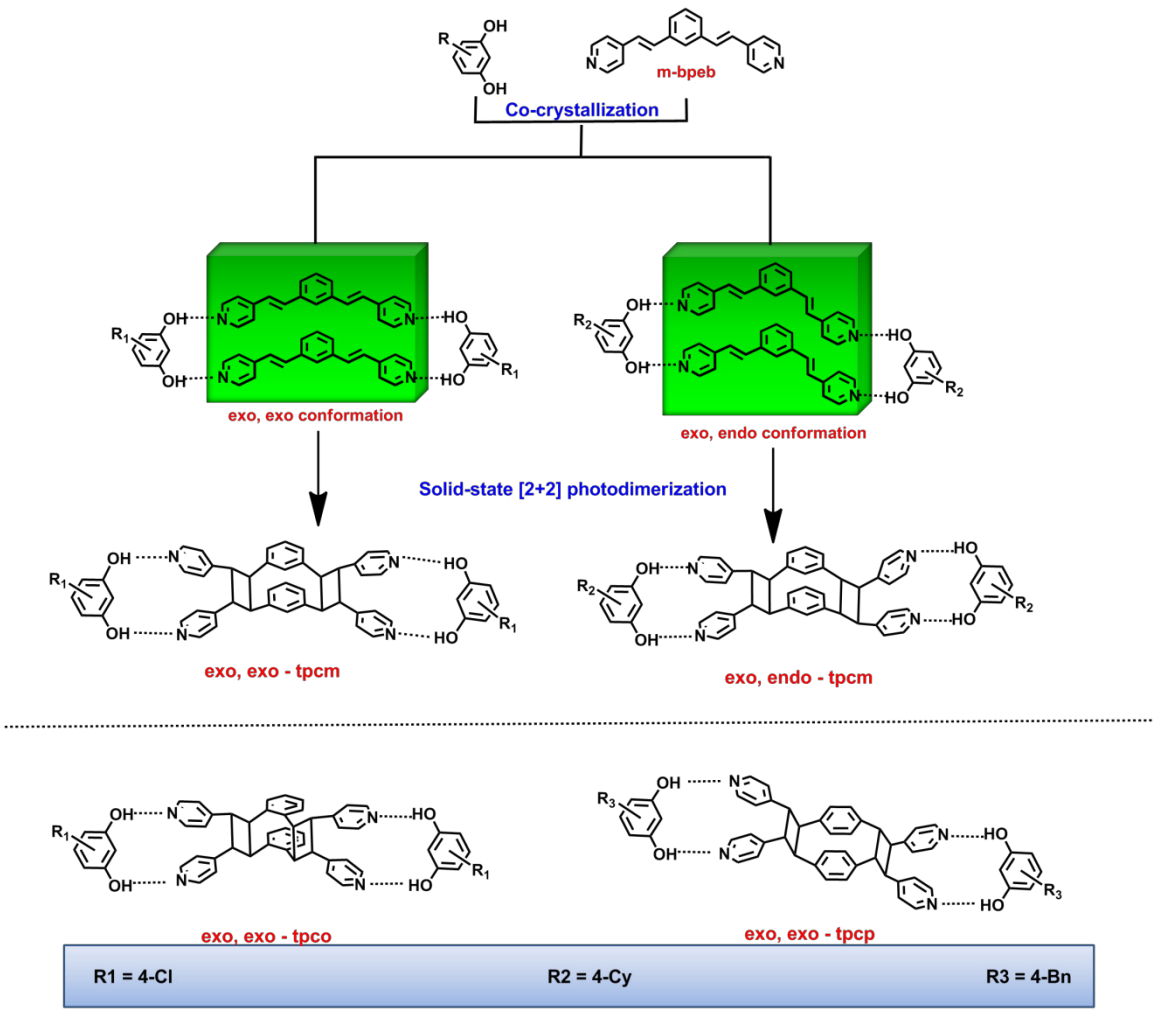

Figure 169: Supramolecular synthesis of target [2.2] cyclophanes utilizing template switching.

From these studies, 4-Cl res was determined to afford both the *exo, exo* and *endo, exo* isomers of tpcm in crystalline 2(4-Cl res)·2(m-bpeb) (Figure 170a-d). Additionally, we also determined that 4-Cy res generates the less-favored[317] *endo, exo*-tpcm stereospecifically and in 100% yield (Figure 170e-f). Given that the organization of molecules with templates is sensitive to subtle changes in molecular geometry, we applied our combinatorial template approach to generate co-crystals with the further bent o-bpeb. Co-crystals with o-bpeb were generated by dissolving equimolar amounts of res

and o-bpeb in CH_3NO_2 and allowing the solution to cool to ambient temperature. The resulting solids were dried and exposed to broadband UV radiation. 4-Cl res was found to afford tpco stereospecifically, and in quantitative yield from crystalline 2(4-Cl res)·2(o-bpeb) (Figure 170g-j).

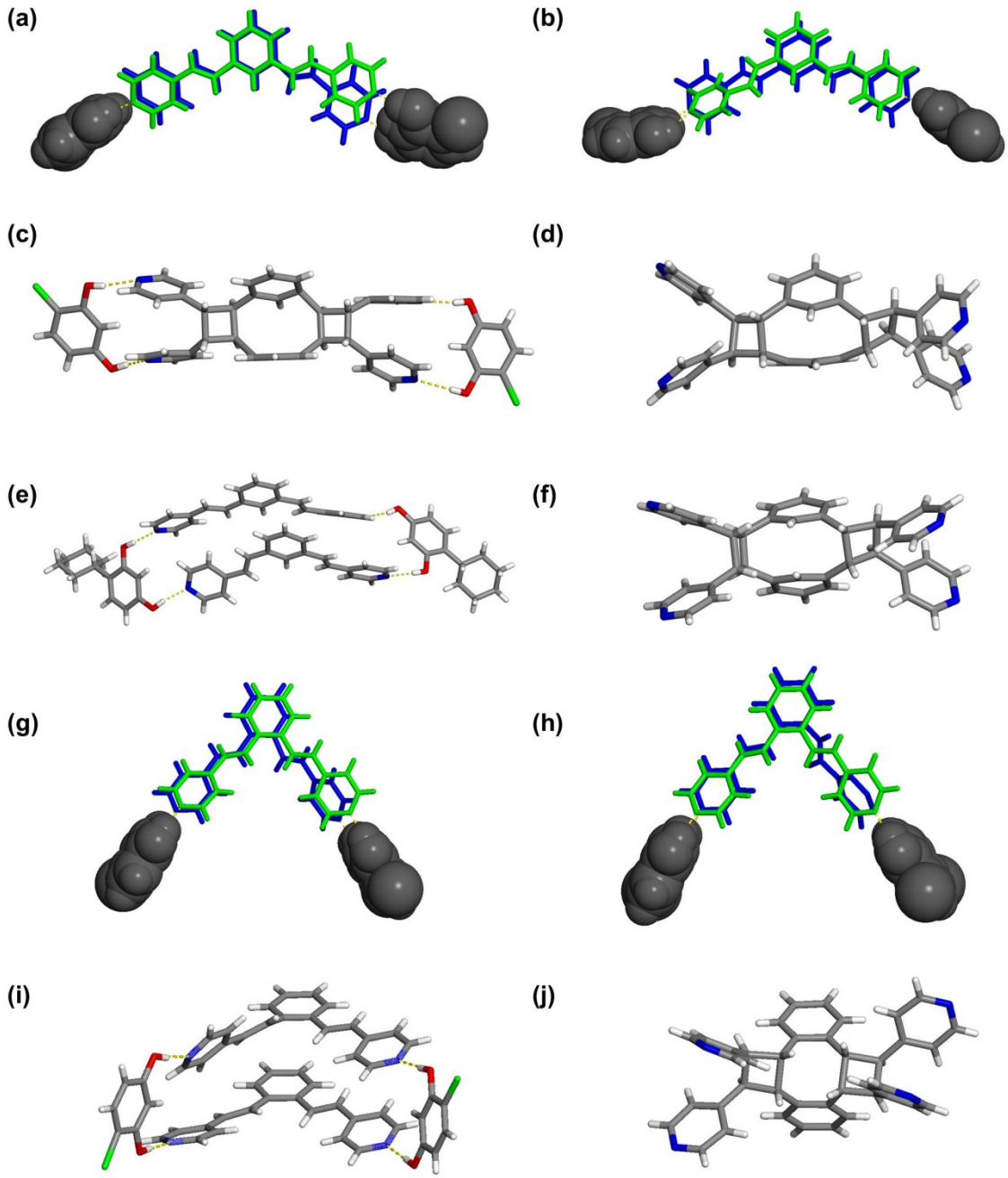

Figure 170: X-ray structures relating to the solid-state synthesis of tpcm and tpco: (a, b) *exo, exo* and *endo, exo* conformations of *m*-bpeb, (c) 2(4-Cl res)·(*endo, exo*-tpcm), (d) *exo*, *exo*-tpcm, (e) 2(4-Cy res)·(*m*-bpeb), (f) *endo, exo*-tpco, (g, h) *exo, exo* and *exo, endo* conformations of *o*-bpeb, (i) 2(4-Cl res)·(*o*-bpeb) and (j) tpco.

During our pursuits to study optoelectronic properties of our reactive solids, we developed an interest to study the optical behavior of the cyclophane products, owing to their precedence for exhibiting unique intrinsic properties. We envisioned that the distal 4-pyridyl groups could act as a chromophore to probe optical properties of the stacked cyclophane core. Owing to the high degree of sensitivity of fluorescence to molecular structure, we sought to evaluate the effect of ortho- meta- and para substitution in [2.2]cyclophane derivatives, as well as determine if the lateral 4-pyridyl groups could affect the fluorescence of the cyclophane in the wake of being attached *via* the saturated cyclobutyl bridges.[169]

In this chapter, we report the first studies of optical properties upon a series of bridge-substituted [2.2]cyclophanes derived from the organic solid state. We demonstrate that, despite the lack of continuous conjugation, the cyclophanes exhibit a nonconventional ICT, owing to the strained cyclobutanes acting as efficient through-bond donors that effectively permit withdrawl of electron density from the aromatic cyclophane core to the distal electron-poor pyridine moieties. In addition, we demonstrate that post-synthetic modification can lead to enhanced and red-shifted absorbances and emissions that are akin to fully-conjugated molecular and polymeric pCp systems.

6.6 Experimental

Iodomethane (99%) was purchased from Aldrich Chemical (St. Louis, MO, USA) and iodoethane (98%) was purchased from ACROS (Morris Plains, NJ USA) and were used as received. Tetrahydrofuran (99.9%) and N,N-dimethylformamide (99.9%) were obtained from Fisher Scientific and dried over molecular sieves before use. The cyclophanes tpcp, tpcm, and tpco were synthesized in the solid state according to literature procedures.[96, 167] All alkylations were conducted at room temperature to minimize the possibility of cyclobutane isomerizations. Single crystals of tetrakis-[(N-

methyl)-4-pyridylcyclobutyl][2.2]paracyclophane were prepared *via* dissolution of tetrakis-(4-pyridylcyclobutyl)[2.2]paracyclophane in the presence of excess iodomethane and tetrahydrofuran.

^{1}H and ^{13}C NMR specta were collected on a Bruker Avance 400 MHz spectrometer using DMSO-d_6 as a solvent. HRMS data was collected by the High Resolution Mass Spectrometry Facility at the University of Iowa. Observed HMRS values are based upon an average of three individual runs. The HRMS results are portrayed in Figures B-1 through B-4. Steady state fluorescence spectra were obtained using either a single channel AMINCO-Bowman Luminescence Spectrometer, Model FA-354 (Thermo Electron, Waltham, MA) or a HORIBA Jobin Yvon FluoroMax-4 (Edison, NJ, USA). Fluorescence Spectra were recorded in N,N-dimethylformamide at a scan rate 5 nm/s with both monochromators set to a 2 nm slit width. All optical measurements were performed using 1.0 μM solutions of the desired compound in DMF.

Single crystal diffraction data was collected on a Nonius Kappa CCD single-crystal X-ray diffractometer at both room and low temperatures using MoK_α radiation (λ = 0.71073 Å). Data collection, cell refinement and data reduction were performed using *Collect*[197] and *HKL Scalepack*/*Denzo*,[198] respectively. Structure solution and refinement were accomplished using SHELXS-97[261] and SHELXL-97,[196] respectively. The resorcinol structures were solved *via* direct methods, while silver coordination complexes were solved using Patterson method. All non-hydrogen atoms were indentified from the difference Fourier map within several refinement steps. All non-hydrogen atoms were refined anisotropically. Hydrogen atoms associated with carbon atoms were refined in geometrically constrained positions with isotropic thermal parameters U_{iso}(H) = 1.5U_{eq}(C_{CH3}) and U_{iso}(H) = 1.2U_{eq}(C_{CH}). The details of the structural analysis of tetrakis-[(N-methyl)-4-pyridylcyclobutyl][2.2]paracyclophane is summarized in Table A-22.

All calculations have been performed using Gaussian'09 program suite.[318] The long range corrected CAM-B3LYP density functional[319] combined with the 6-31G(d)

basis set was used for all ground state optimizations and frequency calculations. Minima were confirmed by zero imaginary vibrational frequency. No symmetry constraints were used during the optimization. Time-dependent density functional calculations (TDDFT) were performed at CAM-B3LYP/6-31G(d) optimized geometries using the same functional and basis set. A total of 40 excited states were calculated and only singlet excited states were considered. All calculations were performed with simulated solvation using the polarizable continuum model (PCM)[320] and N, N-dimethylformamide as a solvent. Absorption spectra were obtained using SpecDis version 1.53 software.[321] A peak broadening factor of 0.32 was used to construct the spectra. Orbitals were visualized using Chemcraft program.[322]

6.6.1 Synthesis of tetrakis-[(N-methyl)-4-pyridylcyclobutyl][2.2]paracyclophane

0.2500 g (0.44 mmol) of tetrakis-(4-pyridylcyclobutyl)[2.2]paracyclophane (tpcp) was suspended in 10 mL THF. 10 mL (22.8 g, 160 mmol) of iodomethane was added. The suspension was stirred at room temperature for 2 weeks, while reaction was monitored by ^{1}H NMR. The resultant solid was filtered, washed with acetone and chloroform, and dried to a yellow solid (0.49 g, 98%): ^{1}H NMR (400 MHz, DMSO-d_6) δ/ppm = 8.82 (dd, 8H), 8.09 (dd, 8H), 7.08 (d, 4H), 6.81 (d, 4H), 5.25 (d, 4H), 4.84 (d, 4H), 4.28 (s, 12H). HRMS (TOF-ES): Calcd for $C_{44}H_{44}N_4I_3$ (M-I): 1009.070 m/z; found: 1009.071 m/z.

6.6.2 Synthesis of tetrakis-[(N-ethyl)-4-pyridylcyclobutyl][2.2]paracyclophane

0.2500 g (0.44 mmol) of tpcp was suspended in 10 mL THF. 13 mL of iodoethane (25.35 g, 163 mmol) was added. The suspension was stirred at room temperature for 2 weeks, while reaction was monitored by ^{1}H NMR. The resultant solid was filtered, washed with acetone and chloroform, and dried to a brown solid (0.51 g,

97%): ^{1}H NMR (400 MHz, DMSO-d_6) δ/ppm = 8.82 (dd, 8H), 8.09 (dd, 8H), 7.08 (d, 4H), 6.81 (d, 4H), 5.25 (d, 4H), 4.84 (d, 4H), 4.45 (quintet, 8H), 1.43 (s, 12H). ^{13}C NMR (100 MHz, DMSO-d_6) δ = 16.72, 43.50, 49.88, 56.20, 127.70, 128.94, 132.66, 139.49, 144.45, 159.54. HRMS (TOF-ES): Calcd for $C_{48}H_{52}N_4I_3$(M-I): 1065.133 m/z; found: 1065.134 m/z.

6.6.3 Synthesis of tetrakis-[(N-methyl)-4-pyridylcyclobutyl][2.2]metacyclophane

0.2500 g (0.44 mmol) of tetrakis-(4-pyridylcyclobutyl)[2.2]metacyclophane (tpcm) was suspended in 10 mL THF. 10 mL (22.8 g, 160 mmol) of iodomethane was added. The suspension was stirred at room temperature for 3 weeks, while reaction was monitored by ^{1}H NMR. The resultant solid was filtered, washed with acetone and chloroform, and dried to a yellow solid (0.48 g, 98%): ^{1}H NMR (400 MHz, DMSO-d_6) δ/ppm = 8.90 (dd, 8H), 8.14 (dd, 8H), 6.98-6.63 (overlapping signals, 8H), 5.00 (d, 8H), 4.28 (s, 12H). (TOF-ES): Calcd for $C_{44}H_{44}N_4I_3$ (M-I): 1009.070 m/z; found: 1009.071 m/z.

6.6.4 Synthesis of tetrakis-[(N-methyl)-4-pyridylcyclobutyl][2.2]orthocyclophane

0.2500 g (0.44 mmol) of tetrakis-(4-pyridylcyclobutyl)[2.2]orthocyclophane (tpco) was suspended in 10 mL THF. 10 mL (22.8 g, 160 mmol) of iodomethane was added. The suspension was stirred at room temperature for 3 weeks, while reaction was monitored by ^{1}H NMR. The resultant solid was filtered, washed with acetone and chloroform, and dried to a yellow solid (0.49 g, 98%): ^{1}H NMR (400 MHz, DMSO-d_6) δ/ppm = 8.89 (dd, 8H), 8.19 (dd, 8H), 7.29 (m, 4H), 7.18 (m, 4H), 5.20 (d, 8H), 4.30 (s, 12H). (TOF-ES): Calcd for $C_{44}H_{44}N_4I_3$ (M-I): 1009.070 m/z; found: 1009.072 m/z.

6.7 Results

The starting point of our investigation is tpcp, which is prepared from a template-directed solid-state reaction.[96] Comparisons of the emission spectrum of tpcp with commercially available pCp and the parent diene *p*-bpeb revealed that tpcp exhibits a large red shift in fluorescence ($\lambda_{max\ (em)}$ of 414 nm as opposed to 356 nm) relative to pCp, yet at a position more comparable to *p*-bpeb ($\lambda_{max\ (em)}$ 401 nm).[323] The observations were surprising, given that the pyridine rings are attached to the cyclophane core through saturated, as opposed to delocalized, linkages while the cyclobutyl rings effectively disrupt the extended conjugation of the parent diene. The red shift in fluroresence also corresponds to a longer excitation maximum in comparison to pCp (380 nm versus 313 nm) (Figure 171). Collectively, these observations suggest that the cyclobutanes of tpcp act as efficient through-bond donors.[169]

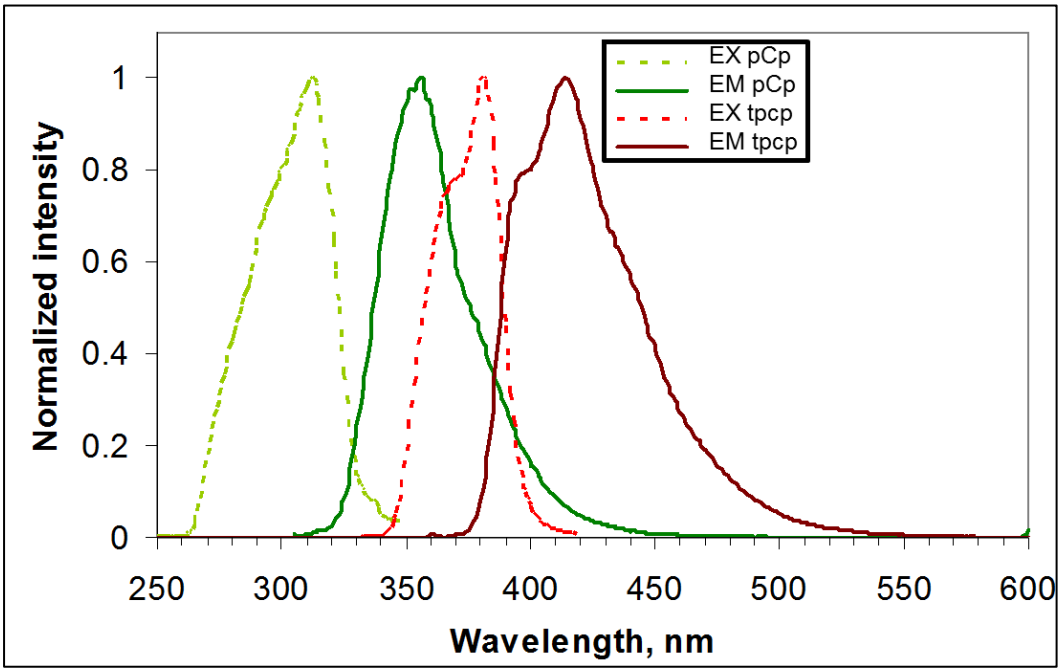

Figure 171: Normalized excitation (EX) and emission (EM) spectra of pCp compared to tpcp. The spectra were obtained in DMF using micromolar concentrations.

We next extended our studies to the related cyclophanes, tpcm and tpco. Owing to the larger twist from co-planarity of the cyclophane core exhibited by tpcm and tpco, compared to tpcp (Figure 172), it would be expected that the optical properties would, thus, be affected. In particular, it was envisioned that the further the benzene rings deviated from co-planarity, the lesser the degree of ITC that would be exhibited by the core, owing to the lack of π···π stacking achieved in the bent ortho- and metacyclophane systems.

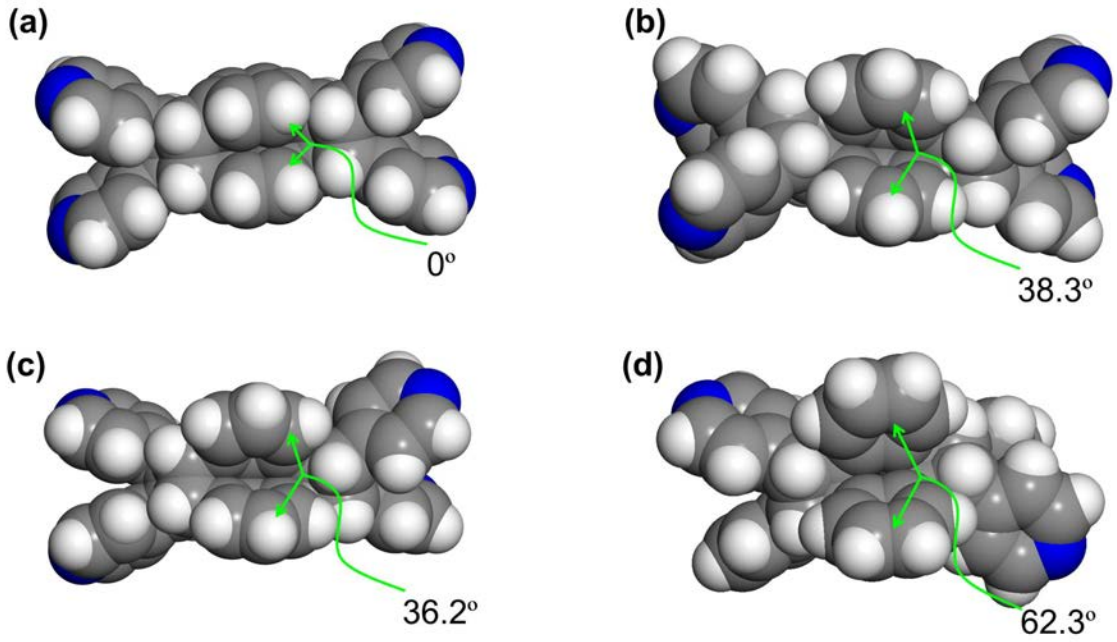

Figure 172: Space filling models of (a) tpcp, (b) *(exo, exo)*-tpcm, (c) (*endo, exo*)-tpcm and (d) tpco highlighting the degree of twisting of the core benzene rings.

As expected, the cyclophanes tpcm and tpco exhibit a hyposchromic shift in excitation relative to tpcp, reflective of the lesser degree of π···π stacking of the core (Figure 173). Specifically, tpcm exhibits an excitation at 350 nm, while tpco displays a broader excitation with two peaks of equal intensity at 347 and 365, as well as a lower intensity shoulder at 394 nm. In the context of emission properties of the two

cyclophanes, tpcm demonstrates a $\lambda_{max\ (em)} = 412$ nm, while tpco unexpectedly displays a more complex fluorescence profile (Figure 173). Excitation of tpco at 340 nm results in a broad emission that corresponds to two peaks at 387 and 419 nm. In contrast, excitation of tpco around the lower intensity absorbance of 390 nm results in a red-shifted emission of 473 nm, which is also of lower intensity.

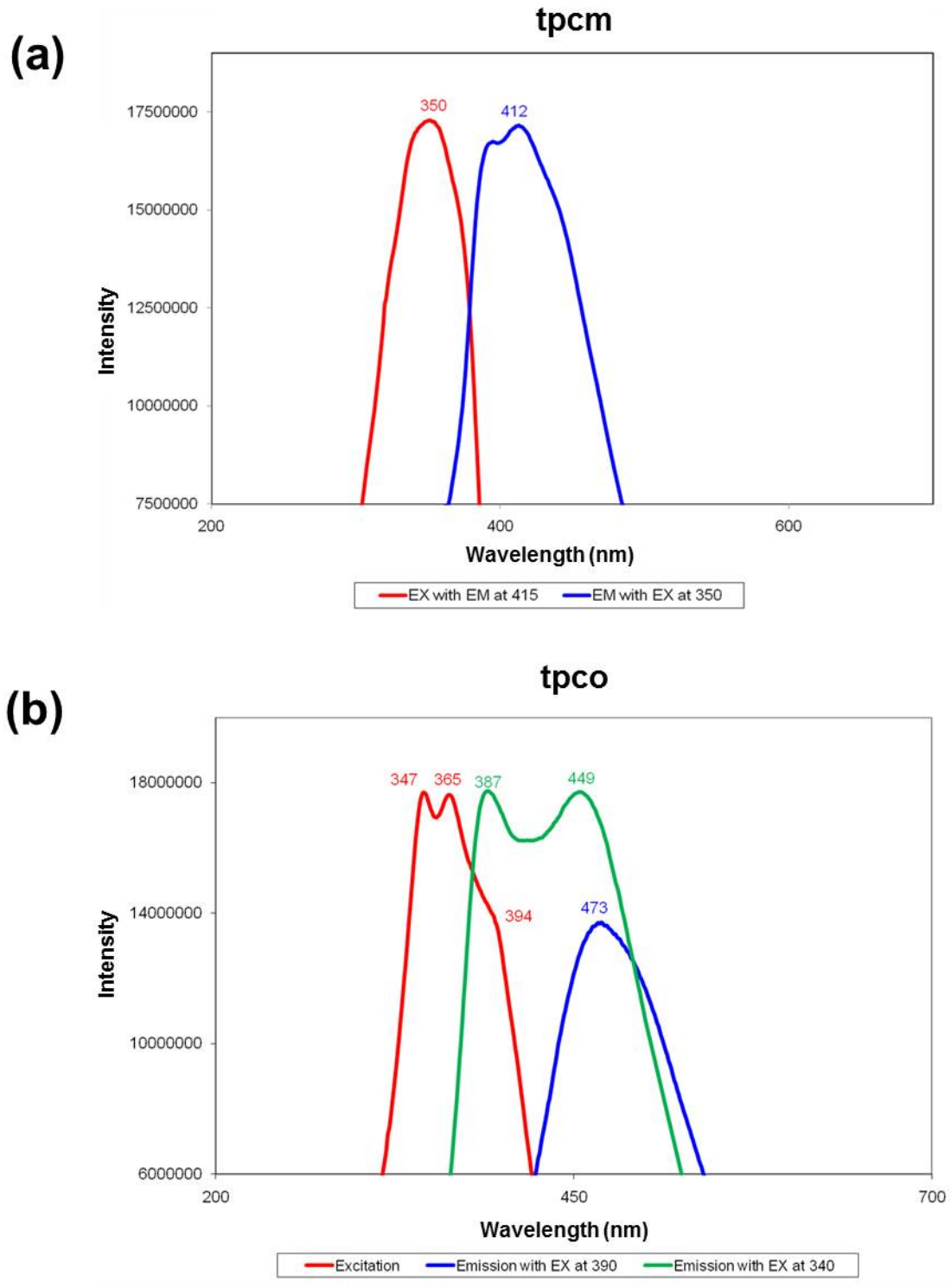

Figure 173: Excitation (EX) and emission (EM) spectra of (a) tpcm and (b) tpco obtained in DMF at micromolar concentrations.

To further evaluate the photophysical properties of the series of bridge-substituted [2.2]cyclophanes, density functional theory (DFT) calculations at the B3LYP/6-31G(d) level were conducted. In particular, we thought that assessing the optimized structures of tpcp, tpcm, and tpco in the context of HOMO and LUMO levels shoud provide insight into the effects of excitation upon the possible ICT effects (Figure 174).

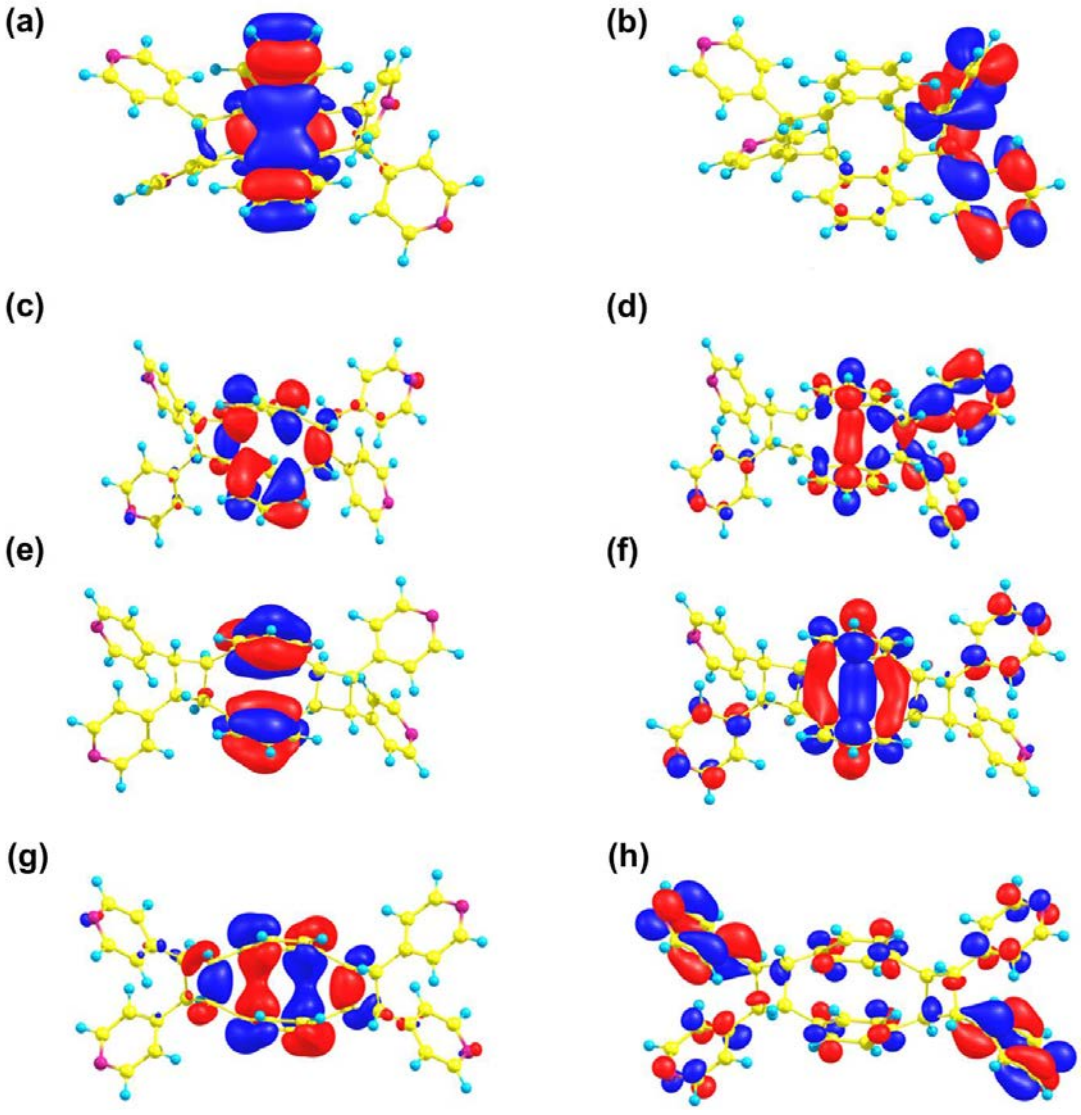

Figure 174: B3LYP/6-31G(d) calculated (left) HOMO and (right) LUMO levels for (a, b) tpco, (c, d) *endo, exo*-tpcm, (e, f) *exo, exo*-tpcm, and (g, h) tpcp.

In the optimized structure of tpco, the electron clouds remain localized mainly on the cyclophane core in the HOMO level, and spread outward to half of the pyridine moieties in the LUMO, suggesting that there is an efficient electron transfer from the core outward to the distal pyridines, however, it appears to only shuttle electron density to half of the molecule (Figure 174a-b). This could explain the dual excitation and emission behavior for tpco. If there isn't sufficient electron communication throughout the moelcule, then it is possible that each chromophore can behave as two separate species, exhibiting an individual excitation and emission reflective of two different chromophores depending on the enrgy used to excite the molecule.

In the case of tpcm, only one distinct excitation and emission peak are observed, despite the measurements being conducted with a mixture of the two isomers (Figure 173). Judging from the calculated molecular orbitals, the excitation and emission profile of the two conformational isomers shouldn't be all that different, as both isomers contain roughly the same degree of $\pi\cdots\pi$ stacking in the cyclophane core (Figure 172). In the HOMO levels of both isomers, the electron clouds are localized upon the cyclophane core, relative to the electron poor pyridine rings (Figure 174c, e), whereas the LUMO levels contain a significant (although less than half) amount of electron density upon half of the pyridine rings (Figure 174d, f), suggestive of a more efficient ICT process.

In contrast to tpco and tpcm, the molecular orbitals of tpcp imply a very efficient electron transfer process throughout the entirety of the molecule (Figure 174g-h). In particular, the HOMO level exhibits the electron density localized on the dicyclobutyl[2.2]paracyclophane core, whereas the LUMO displays electron density over the entire molecule, with the largest clouds on the pyridine rings. This observation is consistent with the cyclophane core acting as an efficient donor.[169]

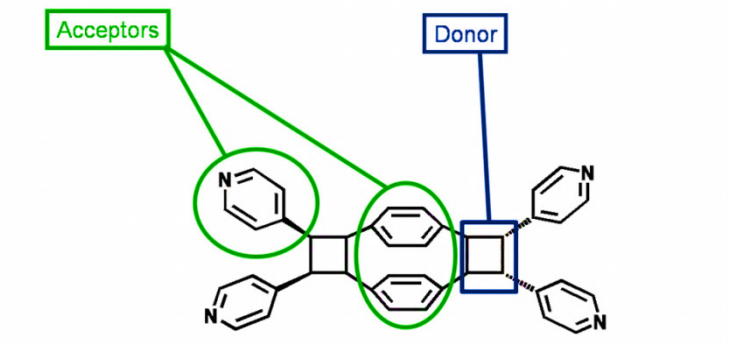

Figure 175: Rationale for observed optical properties in bridge-substituted cyclophanes.

6.8 Post-Synthethic Modification of [2.2]Cyclophanes

Given the fact that large quantities of the cyclophanes are synthetically available, and that pyridine rings can be easily derivatized, we sought to determine whether modifying the pyridines can affect donation from the dicyclobutyl cyclophane core and, thus, provide improved conditions for ICT that impact the fluorescence (Figure 176).

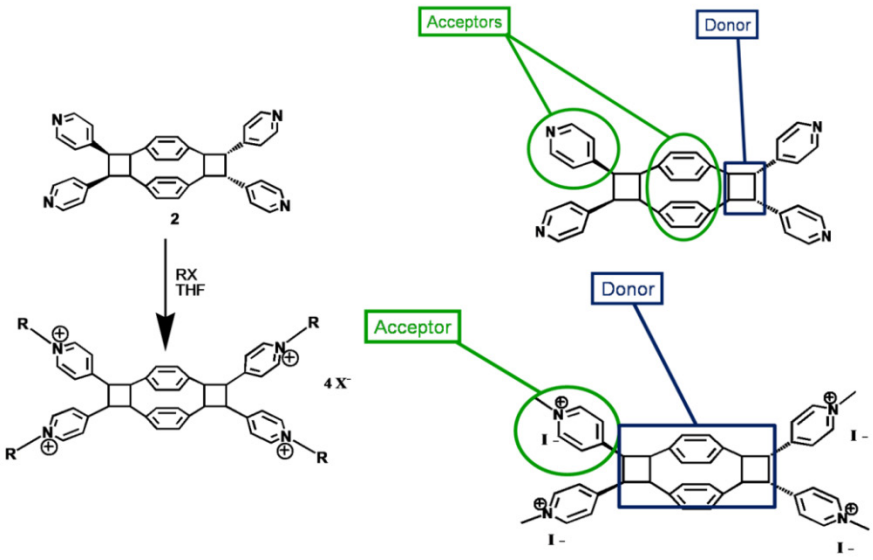

Figure 176: Post-synthetic modification strategy and theory related to donor-acceptor framework.

The starting point for our investigation is tpcp. From our previous studies, tpcp appeared to exhibit a more efficient ITC process. To determine optical effects of peripheral derivatization, tpcp was alkylated using both iodomethane and iodoethane. In a typical experiment, reaction of tpcp with the corresponding iodoalkane in tetrahydrofuran afforded the tetraiodo salt in quantitative yields. ^{1}H NMR spectroscopy confirmed that tetraalkylation occurred for both the tetra N-methylated and N-ethylated tpcp. In the resulting spectra, the α-pyridyl and β-pyridyl protons shifted to 8.82 ppm and 8.09 ppm, respectively. Additional shifts were seen for the cyclobutyl protons, which appear as sharp doublets at 5.25 ppm and 4.84 ppm (Figure 177).

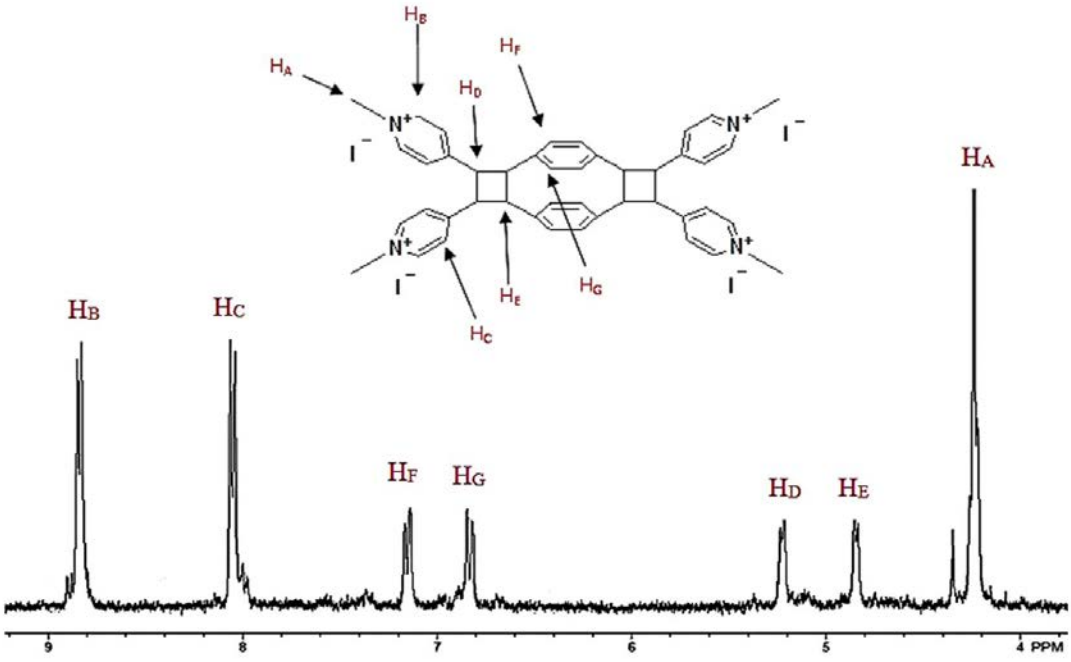

Figure 177: ^{1}H NMR of tetrakis-[(N-methyl)-4-pyridylcycobutyl][2.2]paracyclophane.

Owing to the propensity of the cyclobutane to undergo acid-induced isomerization,[324] we were interested in confirming the stereochemistry of the resulting cyclophane product, N-methyl tpcp. Initially, we were unable to form diffraction quality

crystals of the product, and turned to generating crystals of tpcp in the presence of acids to see if isomerization had occurred. To our surprise, crystals generated in the presence of the organic acids *p*-toluenesulfonic acid and camphorsulfonic acid (CSA) preserved the *rctt* stereochemistry (Figure 178). After invariably poor results in procuring single crystals of N-methyl tpcp, we turned to generate the crystals during reaction. Specifically, tpcp was dissolved in THF in the presence of copious amounts of iodomethane. In a period of three weeks, crystals more suitable for X-ray diffraction were obtained and analyzed. The stereochemistry again remained unchanged, corroborating the results obtained in the presence of the organic acids (Figure 178)

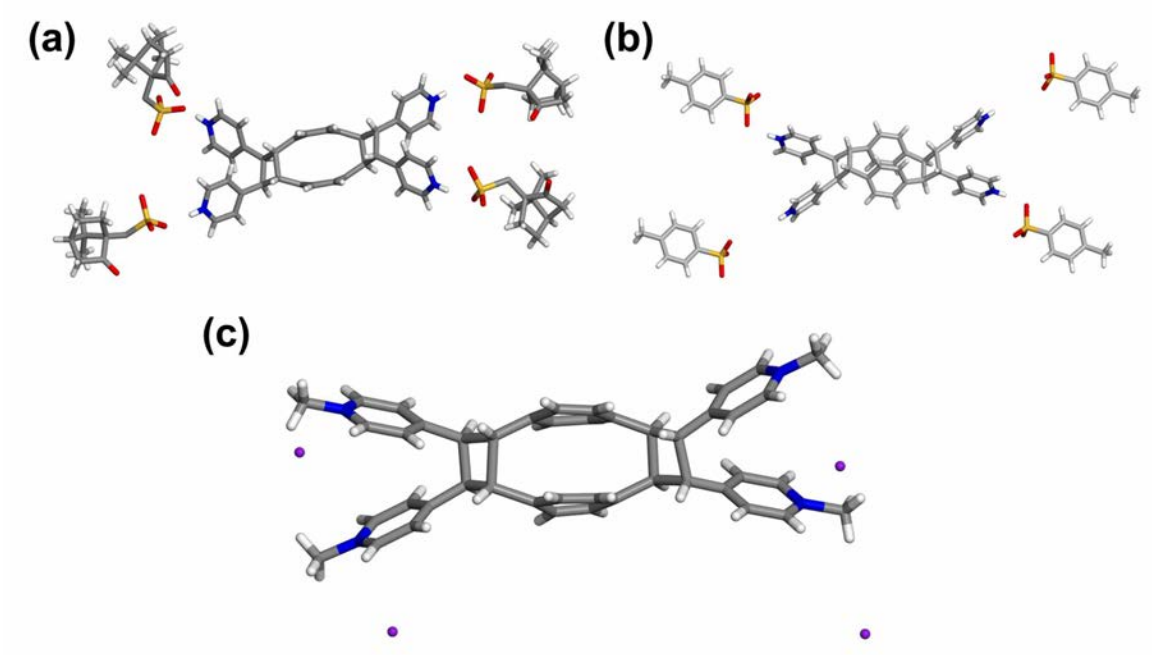

Figure 178: X-ray structures of (a) (tpcp-H^+)($^-$CSA)$_4$, (b) (tpcp-H^+)($^-$OTs)$_4$ and (c) (Me-tpcp$^+$)(I^-)$_4$.

Fluorescence spectroscopy of the derivatized paracyclophanes revealed a large bathochromic shift upon alkylation. With an excitation wavelength of 380 nm,[325] broad emission peaks for both N-methyl and N-ethyl tpcp appeared at 495 nm (Figure 179).

These observations are comparable to pCp architectures with stilbenoid chromophores *conjugated* to the stacked cyclophane decks that exhibit maximum emissions of approximately 430 nm, yet less than those involving strong acylic donor and acceptor groups (e.g. NO_2 and NR_2) attached at the termini of the stilbenoid arms.[289]

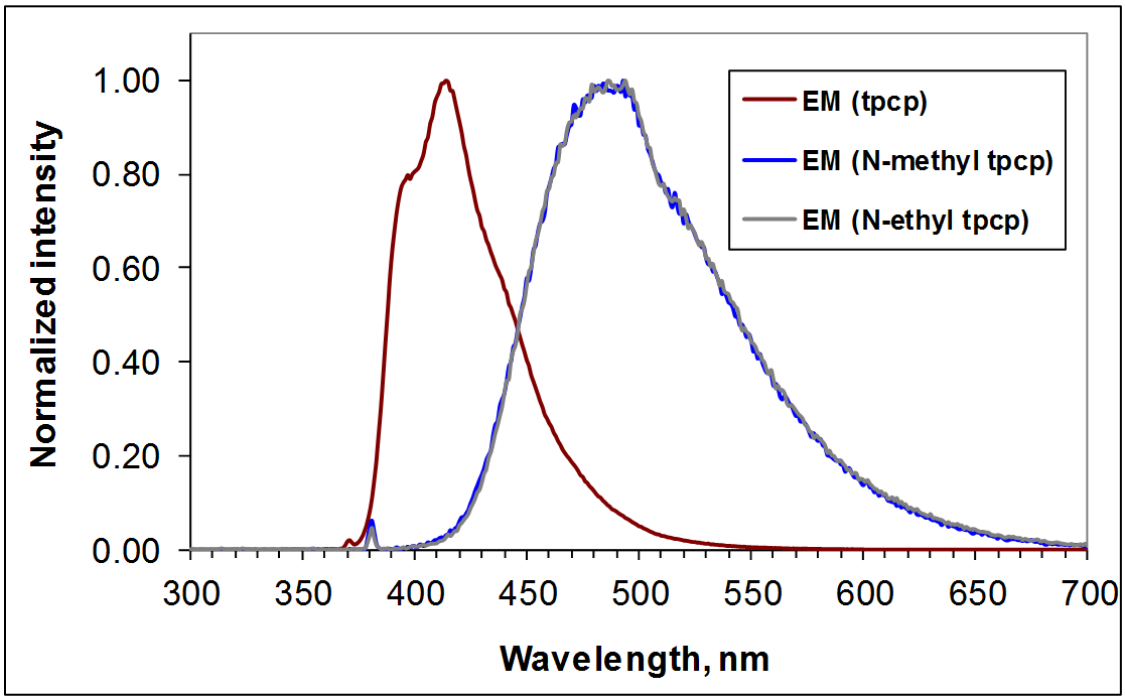

Figure 179: Normalized emission spectra of tpcp and N-alkyl tpcp derivatives in DMF at micromolar concntrations.

The emission properties of tpcp are attributed to electron donation by the dicyclobutyl-pCp core outward to the electron accepting peripheral pyridines. Indeed, the fused nature of the dicyclobutyl-pCp network is considerably strained and as a result, can be considered an electron donor scaffold. The larger red shifts in the cases of the alkylated derivatives can be attributed to the quaternization of the pyridyl N-atoms. The derivatization allows for strong polarization over the entire cyclophane molecule by

increasing the electron accepting properties of the distal 4-pyridyl groups. The alkylation of tpcp, thus, enhances ICT wherein electrostatic interactions account for the relatively large red shifts in absorption and emission. For N-alkylated tpcp, the pyridinium substituents likely withdraw electron density from the pCp fluorophore through the strained cyclobutane bridges, resulting in a nonconventional ICT. These observations involving the pyridinium ring system are consistent with optical properties of 1,8-naphthalimide-based organic dyes, wherein alkylation also resulted in bathochromic shifts of fluorescence involving a fully conjugated system.[326]

To gain further insight into the photophysical properties of the substituted cyclophanes, DFT calculations were conducted (Figure 180). The electron clouds of the HOMO and LUMO are localized on the pCp core, while the LUMO (+1) is localized almost exclusively over the pendant pyridine rings.[327] For cationic tpcp, the electron clouds of the LUMO are, in constrast to tpcp, localized on the pyridines, with the HOMO being located, similar to tpcp, on the pCp core. Collectively, these observations are consistent with the pCp core acting as an electron donor whereby electronic excitation leads to an increase in electron density toward the electron poor pyridine groups, with the relative positions of the LUMOs reflecting the gradual red shifts in fluorescence. Electron density, albeit to a less extent, is also observed on the two cyclobutane rings at both HOMO and LUMO levels, which lends a measure of support for the cyclobutanes acting as through-bond donors.

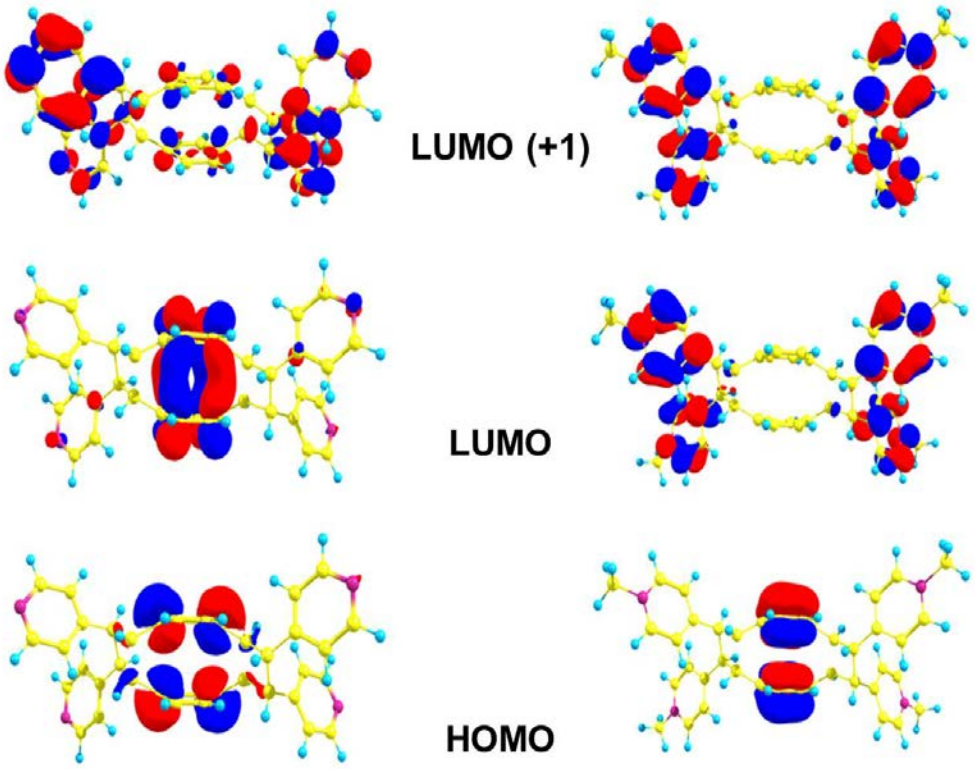

Figure 180: HOMO, LUMO, and LUMO +1 for (left) tpcp and (right) N-methyl tpcp obtained using DFT calculations at the B3LYP/6-31(d) level.

We next extended our study to investigate the effects of alkylation upon the optical properties of tpco and tpcm. In a fashion similar to tpcp and N-alkyl tpcp, we expected that the quaternization of the four pyridine rings would provide a mush stronger polarization throughout the molecule, leading to red-shifted and lower energy excitations and emissions for both cationic cyclophanes. In the case of N-methyl tpcm, a bathochromic shift of 47 nm was observed for the excitation. The red-shift also corresponded to a 78 nm shift in the emission peak (Figure 181a). Although tpco contains the least amount of $\pi\cdots\pi$ stacking within the cyclophane core, and is situated in a more edge-to-face manner, red shifts on the order of 45 and 50 nm were observed for excitation and emission, respectively (Figure 181b).

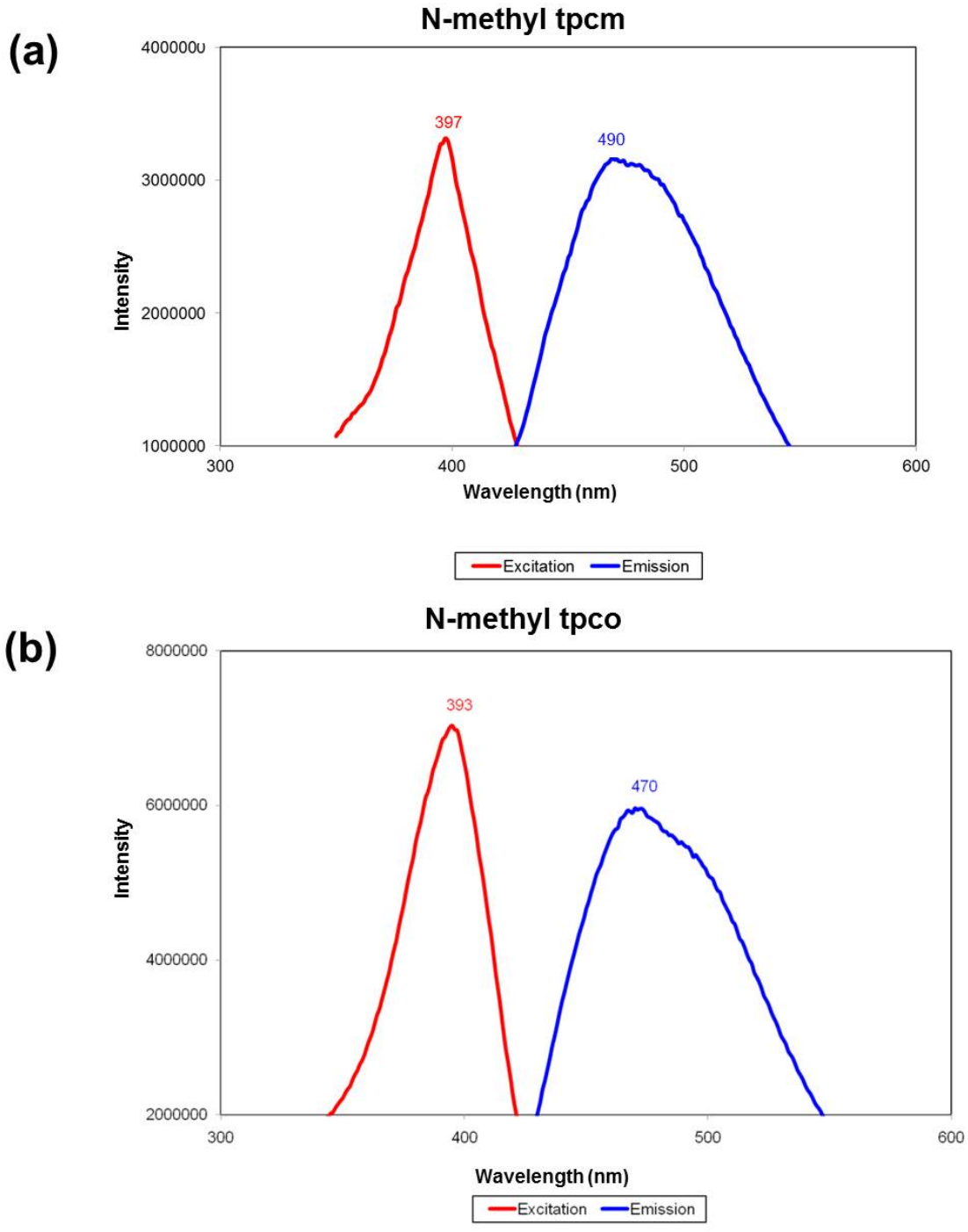

Figure 181: Excitation (EX) and emission (EM) spectra of (a) N-methyl tpcm and (b) N-methyl tpco obtained in DMF at micromolar concentrations.

6.8 Discussion

The bridge-substituted [2.2]cyclophanes described exhibit remarkable optical properties despite the chromophores being linked by saturated cyclobutane rings. In effect, the cyclobutane rings act as sufficient strained donors that aid in the shuttling of electron density across the molecule, leading to communication between the two sets of chromophores. It is interesting to note that the series of laterally-substituted cyclophanes all demonstrate lower energy excitations and emissions, in comparison to pCp itself (Table 13). Molecular orbital diagrams calculated for the HOMO and LUMO levels of tpcp, tpcm, and tpco all support the notion that the strained cyclobutanes act as efficient through bond donors.

Table 13: Summary of optical properties measured for laterally-substituted [2.2]cyclophanes relative to pCp.

cyclophane	$\lambda_{max\ (ex)}$/**nm**	$\lambda_{max\ (em)}$/**nm**
pCp	313	356
tpcp	380	414
tpcm	350	412
tpco	347, 365	387, 419
N-methyl tpcp	420	495
N-methyl tpcm	397	490
N-methyl tpco	393	470

Upon alkylation, all three cyclophanes exhibit a strong bathochromically-shifted excitation and emission maxima. In all three of these systems, it is likely that the quaternization of the pyridine rings leads to a nonconventional ICT, as the pyridinium substitutents act to withdraw electron density from the cyclophane core through the cyclobutane rings. As a result, the maximum excitations are red-shifted on the order of 40-50 nm, while the corresponding emission peaks are also red-shifted 50-80 nm. DFT calculations performed (using tpcp as a model system) lend support to the possible nonconventional ICT. The electron clouds for both tpcp and N-methyl tpcp are localized exclusively upon the cyclophane core in the HOMO level, yet are delocalized throughout the molecule in the LUMO (+1) and LUMO levels (Figure 180).

6.9 Organic Nanocrystals of [2.2]Paracyclophanes

Over the past decade, extensive research has been conducted on the controllable synthesis of nanocrystals[328] owing to correlations between size, morphology,[329] and optoelectronic properties.[152] Inorganic and polymer-based nanocrystals have garnered much interest, owing to emerging widespread applications in fields ranging from diagnostic medicine[330] to materials science.[331] Organic nanocrystals of small molecules remain relatively less studied despite a potential to modify the structures and tune optical properties of such solids[16] using methods of organic synthesis.

Early studies on the fluorescence of organic nanomaterials based on small molecules were conducted by Nakanishi[332] and Yao[333] which involved aromatics such as perylene, phthalocyanine, and pyrazoline. More recent studies by Park,[153] Diau,[334] and Yang[335] have focused on conjugated stilbenoids that exhibit strong emission, yet are weakly fluorescent in solution. Enhancements of solid-state fluorescence are quite unusual with organic materials owing to facile quenching of chromophores[154] in the condensed phase, with conjugated systems such as poly(*p*-phenyleneethynylenes),[155-156]

pseudoisocyanines,[157] and pentaphenylsilols[158] being exceptions that have been shown to exhibit enhanced emission in the solid state.

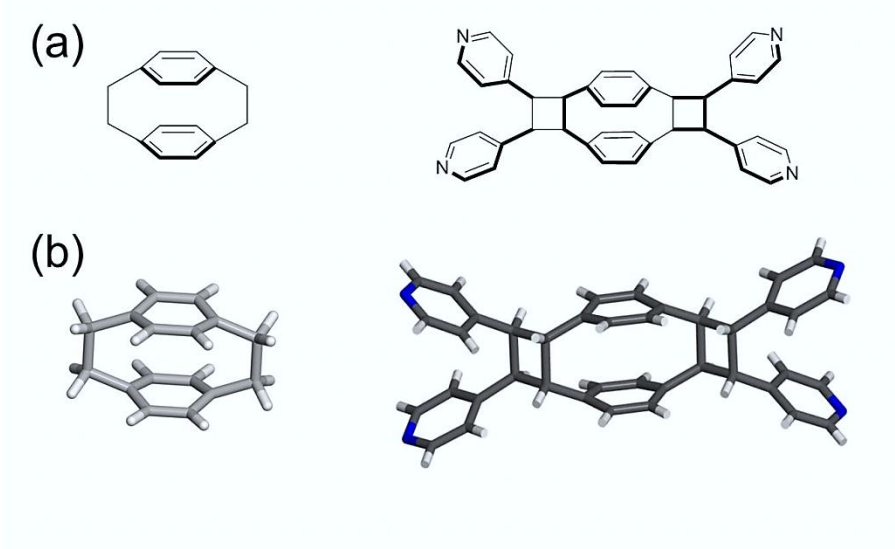

Figure 182: pCp and tpcp: (a) schematics and (b) X-ray crystal structures.

With this in mind, we report here the sonochemical preparation[139, 336] of nanocrystals of [2.2]paracyclophane (pCp) and the laterally-substituted derivative tetrakis(4-pyridylcyclobutyl)[2.2] paracyclophane (tpcp) (Figure 182).[96, 168] Originally studied by Cram,[282] and extensively developed by Hopf[283] and others,[283-287] pCp has garnered much interest owing to those unique properties[291-316] (e.g. optical, reactivity, chirality) conferred by the two co-facially stacked benzene rings by aliphatic bridges. Moreover, while both synthesis and materials aspects of pCp are of much continued interest, the generation of nanostructured pCp is underdeveloped. In this portion of the chapter, we demonstrate that while exclusive reprecipitation does not afford nanostructured pCp, the use of sonochemistry produces nanocrystals of sizes < 500 nm. Nanodispersions of the pCps are also shown to exhibit enhanced emission compared to solution. The emission is attributed to edge-to-face packing in the solid state that

promotes intermolecular interactions capable of maximizing interchromophore communication (Figure 183).[337]

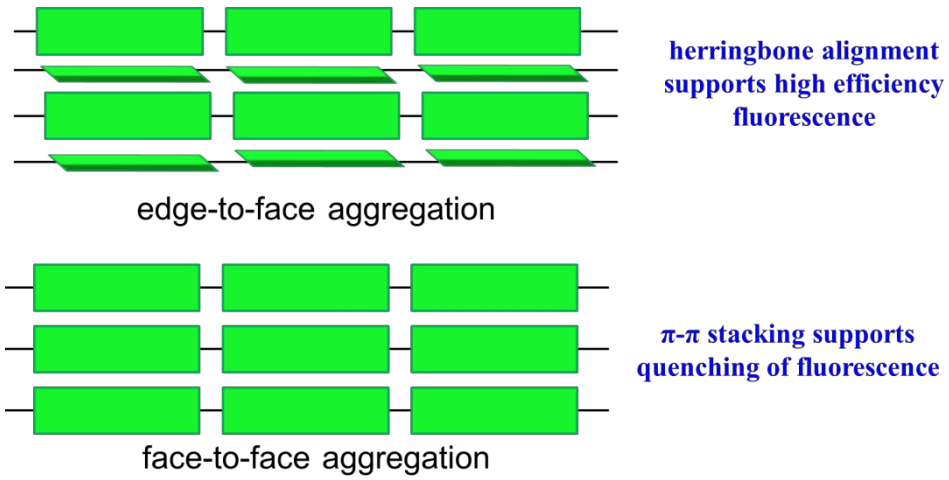

Figure 183: Solid-state packing motifs that influence the fluorescence efficiency of organic molecules.

6.10 Experimental

[2.2]Paracyclophane (pCp) was purchased from Carbosynth (Compton, Berkshire, UK). SDS was purchased from Sigma Aldrich Chemical Company (St. Louis, MO, USA). N,N-dimethylformamide, toluene, and ethanol were purchased from Fisher Scientific Company (Pittsburgh, PA, USA). tpcp was prepared as reported.[96] All chemicals were used without further purification.

PXRD data was collected using a Bruker D-5000 diffractometer equipped with a Bruker SOL-X energy-sensitive detector using CuK_α radiation (λ = 1.54056 Å). Particle size measurements were determined by a Zetasizer Nano ZS (Malvern, Southborough, MA) instrument at 25°C. The reported particle size and PDI values are averages of three measurements. SEM images were obtained using a Hitachi S-4800 with an accelerating voltage range of 2-5 kV. SEM samples were prepared by depositing each sample on a Si

wafer. Absorption and emission measurements were obtained using a HORIBA Jobin Yvon FluoroMax-4 (Edison, NJ, USA). All measurements were made on the as-prepared suspensions with a scan rate of 5 mm sec^{-1} and both slit widths set to 2 nm.

pCp Nanocrystal Synthesis: Nanocrystals of pCp were prepared by dissolving 150 mg of pCp in 5 mL of DMF. The solution was rapidly injected into 100 mL of distilled water at ambient temperature and sonicated for 5 mins in a cleaning bath (Branson 2510R-DTM). After sonication, the sample was filtered through an 8 μm membrane filter (Whatman Grade 2) and dried. The surfactant crystallization was performed with 0.021 M SDS as antisolvent.

tpcp Nanocrystal Synthesis: Nanocrystals of tpcp were prepared by dissolving 50 mg of pcp in 0.7 mL of DMF. The solution was rapidly injected into 100 mL of distilled water at ambient temperature and sonicated for 5 mins in a cleaning bath (Branson 2510R-DTM). After sonication, the sample was filtered through an 8 μm membrane filter (Whatman Grade 2) and dried. The surfactant crystallization was performed with 0.021 M SDS as the antisolvent.

6.11 Results

Our initial attempts to generate nanocrystals of pCp involved the reprecipitation method wherein pCp is dissolved in a hot polar solvent, which is followed by rapid injection into an antisolvent. pCp (0.15 g) was, thus, dissolved in toluene (7.0 mL) and rapidly injected into ethanol (100 mL). The resulting solid was analyzed using powder X-ray diffraction (PXRD) and scanning electron microscopy (SEM). SEM micrographs revealed large well-defined crystals of micrometer-sized dimensions, wherein the smallest crystals were on the order of 5 μm in both length and width (Figure 184a, b). The resulting microcrystals displayed a tetragonal morphology and were agglomerated as stacked crystals. An inspection of a PXRD pattern confirmed the solid to match the

reported structure of pCp,[338] which was evidenced by prominent peaks at 2θ = 15.0º, 16.1º, 25.9º, and 27.7º (Figure 184c).

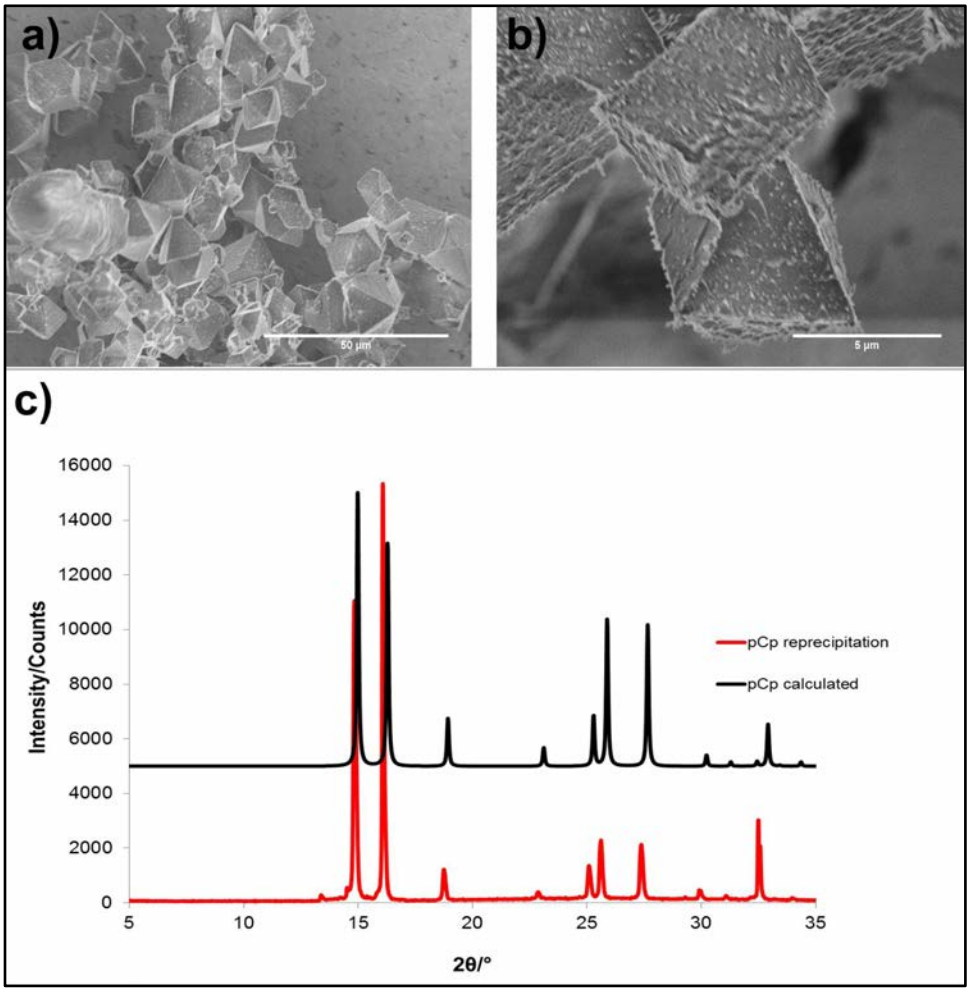

Figure 184: Analysis of pCp microcrystals: (a,b) SEM micrographs of microcrystals from reprecipitation and (c) PXRD diffractogram compared to calculated powder pattern of pCp.

To form nanocrystals of pCp, we next turned to a sonochemical approach. The method has been shown to generate crystals of nanoscale dimensions wherein more standard reprecipitation[339] experiments fail.[340] In our approach, low-intensity ultrasonic radiation using a sonication cleaning bath was applied in the crystal growth of pCp. In a

typical experiment, pCp (0.15 g) was dissolved in DMF (3.0 mL) and rapidly injected into water (100 mL) subjected to ultrasonic radiation. After 5 min of sonication, the suspension was vacuum filtered through an 8 μm membrane filter and analyzed using PXRD. The resulting diffractogram revealed the structure of the solid generated using sonochemistry to match that of pure pCp (Figure 185).

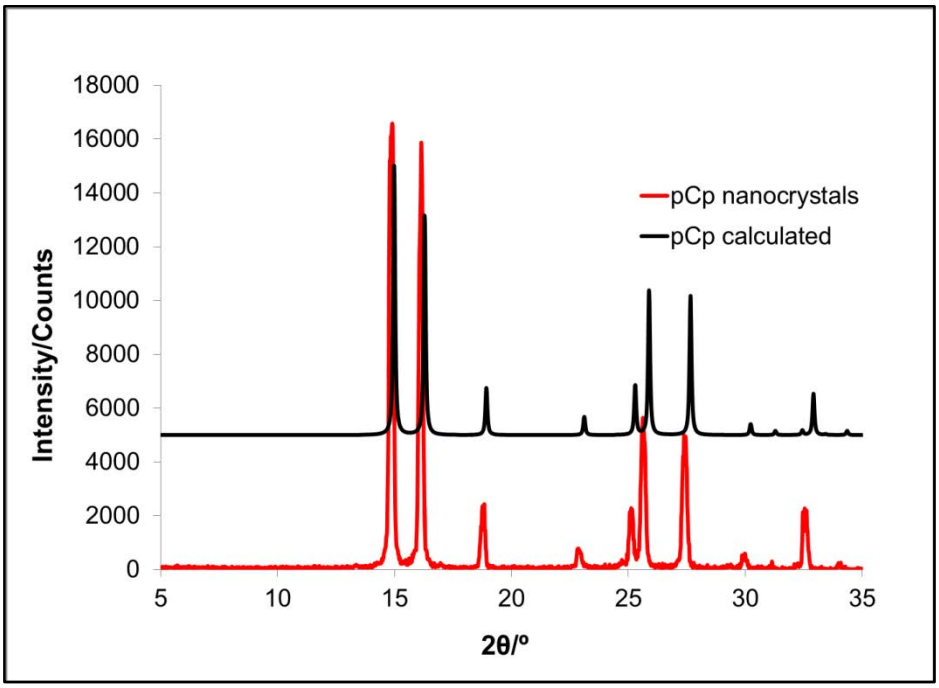

Figure 185: PXRD diffractogram of pCp treated with sonochemistry compared to calculated powder pattern of pure pCp.

SEM analysis of the solid obtained *via* sonochemistry confirmed the generation of nanometer-sized crystals of pCp. The crystals exhibited a spherical cube morphology,[341] with the smallest crystals displaying lengths and widths that range from 200 to 500 nm (Figure 186a,b). An aliquot of the original suspension generated using the sonochemistry was analyzed using dynamic light scattering (DLS). DLS measurements revealed average particle sizes of *ca.* 477 nm with a polydispersity index (PDI) of 0.146 (Figure 186c).

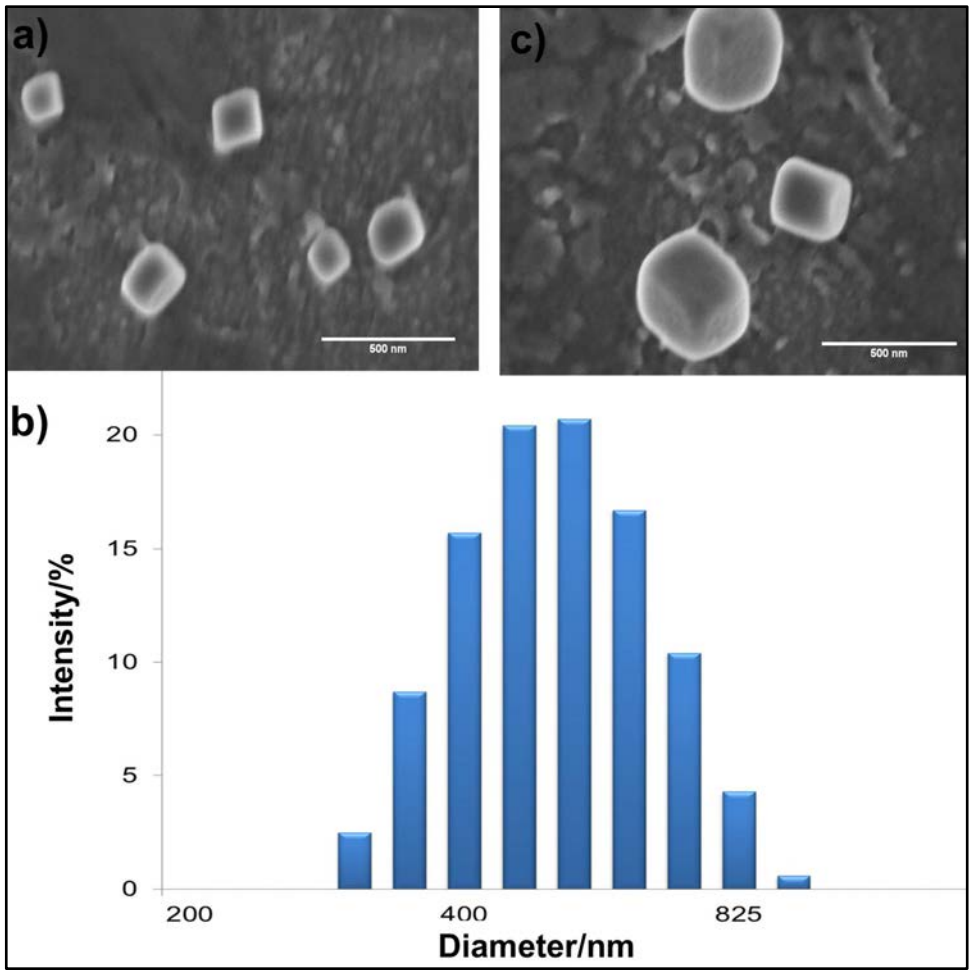

Figure 186: Analysis of pCp nanocrystals: (a, b) SEM micrographs of nanocrystals generated using sonochemistry and (c) particle size distribution.

We next turned to study possible influences of surfactant on nanocrystal formation. The introduction of a surfactant to generate nanomaterials can promote a decrease in particle size *via* the formation of micelles, where increases in nucleation rate are also realized.[342] Smaller particles could, thus, be expected in the presence of a surfactant.

Anionic sodium dodecyl sulfate (SDS) was employed as the surfactant, with water as antisolvent. In the experiment, pCp (0.15 g) was dissolved in DMF (3.0 mL) and rapidly injected into 0.021M aqueous SDS (100 mL) subjected to ultrasonic radiation for

5 minutes. Following vacuum filtration through an 8 μm filter, the solid was analyzed using PXRD and SEM, while an aliquot of the suspension was analyzed using DLS. SEM micrographs demonstrated the formation of spherical particles that range from 100 to 400 nm in diameter (Figure 187a-5). DLS measurements revealed particles with sizes of *ca*. 340 and a PDI of 0.270. The incorporation of the SDS, thus, resulted in an appreciable decrease in particle size of nanocrystalline pCp (Figure 187c).

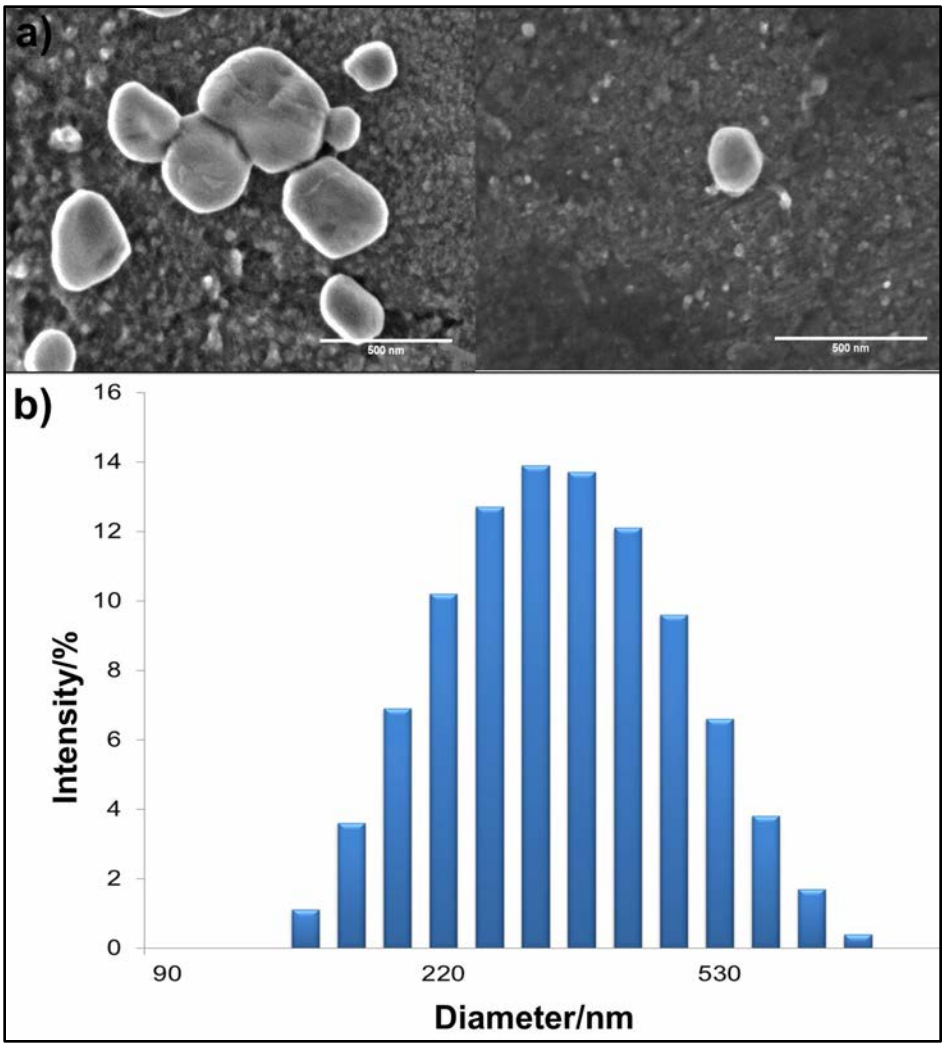

Figure 187: Analysis of pCp nanocrystals: (a,b) SEM micrographs of nanocrystals prepared using sonochemistry with the addition of SDS and (c) particle size distribution.

With the successful formation of nanocrystals of pCp achieved, we extended our efforts to nanocrystals of the laterally-substituted derivative tpcp. The pCp is achieved *via* a double [2+2] photodimerization conducted in the solid state.[96] Tpcp was, thus, dissolved in hot DMF and rapidly injected into water. Similar to our initial experiments involving pCp, SEM micrographs revealed large crystals of tpcp of rectangular morphology with lengths and widths of 15 μm and 4 μm, respectively (Figure 188a,b). PXRD (Figure 188c) confirmed the solid precipitate as pure crystalline tpcp.[343]

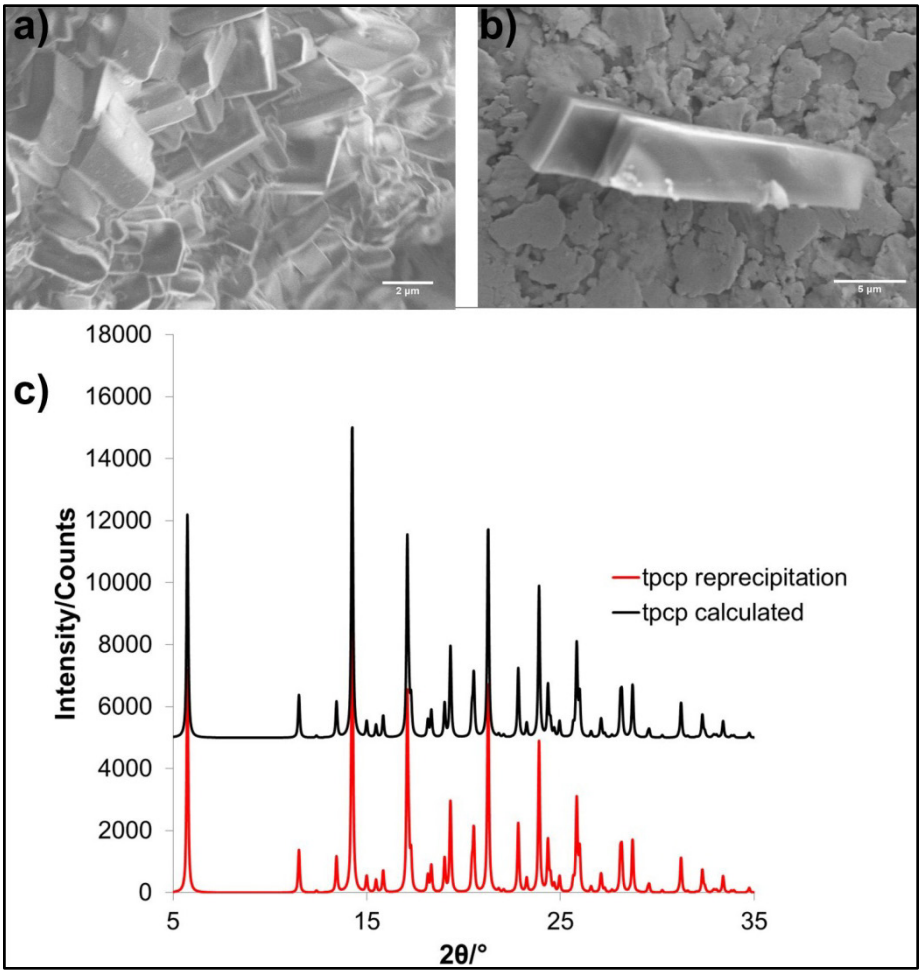

Figure 188: Analysis of tpcp microcrystals: (a, b) SEM micrographs of tpcp collected from reprecipitation and (c) PXRD diffractogram compared to the calculated powder pattern.

Sonochemistry was applied to generate nanocrystals of tpcp. The pCp (0.05 g) was dissolved in hot DMF (0.7 mL) and rapidly injected into water (100 mL) subjected to ultrasonic radiation. After 5 min of sonication, the suspension was filtered through an 8 μm membrane filter (Whatman) and analyzed using PXRD and SEM. An analysis of the PXRD pattern confirmed the solid generated using sonochemistry to match tpcp (Figure 189).

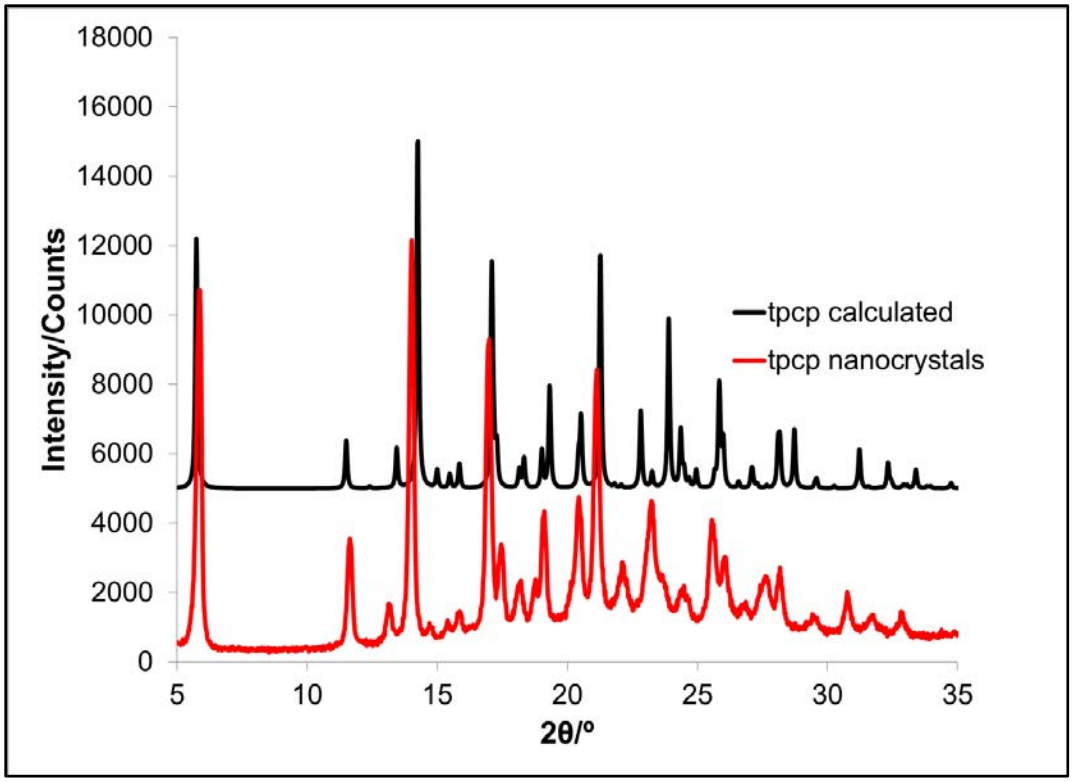

Figure 189: PXRD diffractogram of tpcp nanocrystals compared to the calculated powder pattern.

SEM analysis revealed the formation of tpcp nanocrystals. The smallest particles were spherical in shape, displaying sizes of *ca.* 250 nm (Figure 190a,b). When SDS was used as surfactant, particles on the order of 50 nm easily formed (Figure 190c,d). Thus, the incorporation of SDS resulted in an effective five-fold decrease in particle size. DLS

measurements, however, were inconclusive owing to rapid settling of the nanoparticles.[344] Indeed, the ζ-potential was determined to be -2.5 mV, which is consistent with aggregation of the small particles within the dispersion.[344]

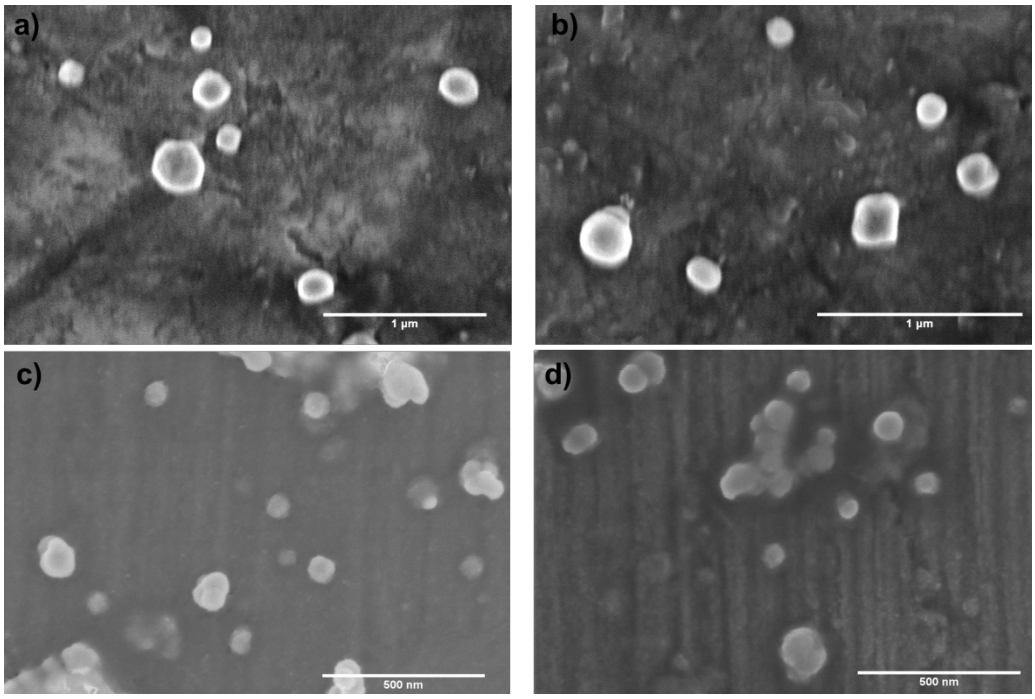

Figure 190: Nanocrystals of tpcp nanocrystals using (a,b) sonochemistry and (c,d) sonochemistry in the presence of the surfactant SDS.

Optical properties of nanosized pCp and tpcp were investigated next. Samples of pCp and tpcp obtained from the sonochemistry experiments were each examined as nanocrystalline suspensions in either water or an aqueous solution of SDS[345] and compared to dilute solutions of the same concentration. As reported, tpcp displays red-shifted excitation and emission in solution compared to pCp. The red-shift occurs despite a lack of continuous p-orbital conjugation. The fluorescence was attributed to the cyclobutane rings acting as efficient electron donors that promote internal charge transfer within the molecule.[169]

From our experiments, both pCp and tpcp were determined to exhibit more intense fluorescence as nanocrystal suspensions compared to dilute solution. While nanocrystalline pCp exhibited the same emission (356 nm) as pCp in solution, the nanoparticles without and in the presence of SDS displayed fluorescence *ca.* 40 times more intense. For tpcp, the nanocrystals were *ca.* 17 times more intense than dilute solution. The nanoparticles of tpcp also exhibited bathochromic emission to 490 nm in the presence of the SDS (Figure 191). The red shift can likely be attributed to hydrogen bonding of water molecules associated with SDS at the N-atoms of the pyridyl groups.[346] The presence of hydrogen bonds may also account for the significant decrease in particle size when both sonochemistry and SDS are used in tandem to facilitate the production of nanocrystals. A similar red shift has been observed for N-alkylated tpcp.[169]

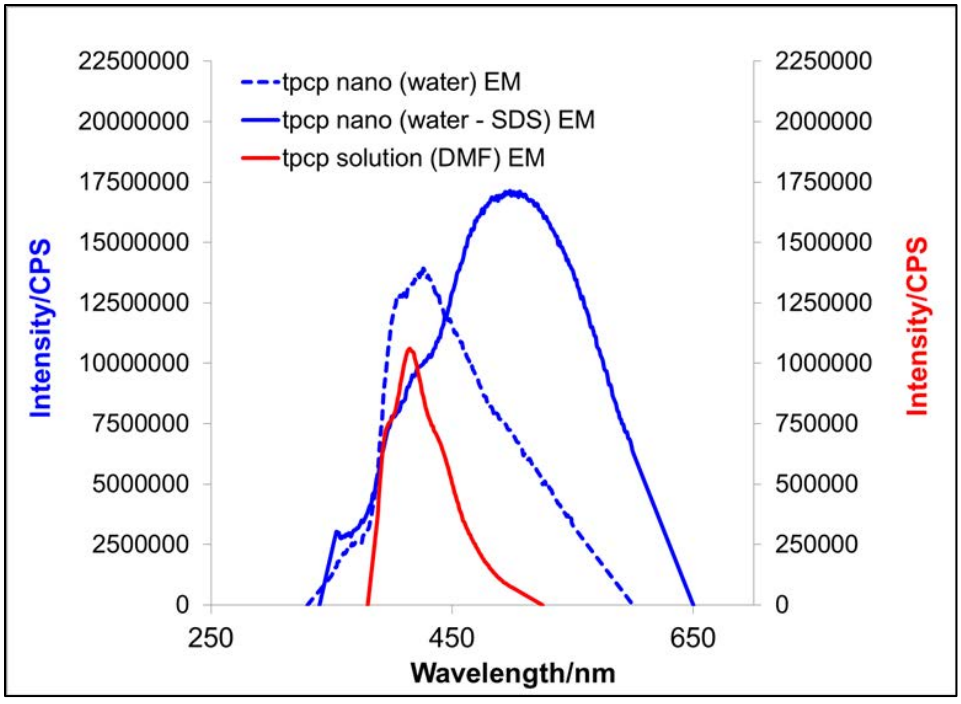

Figure 191: Emission spectra of tpcp nanocrystals compared to dilute solution (nanoparticles on primary axis and solution on secondary axis).

We also note that microsized crystals of pCp and tpcp also exhibited fluorescence more intense than solution yet significantly less (i.e. *ca.* 10 times less) than the nanocrystal suspension. The microcrystals of tpcp in the presence of SDS, in contrast to the nanocrystals, did not exhibit an appreciable red shift in fluorescence (Figure 192). Recent studies of pyrene micro- and nanostructures observed size and morphology-dependent fluorescence, suggesting that the relative blue shift obtained in larger rod-shaped crystals in comparison to nanoparticles can be attributed to different aggregation modes in the presence of SDS.[347] The lack of a red shift is also supportive of the influences of hydrogen bonding being appreciable along the surface of the nanocrystals.

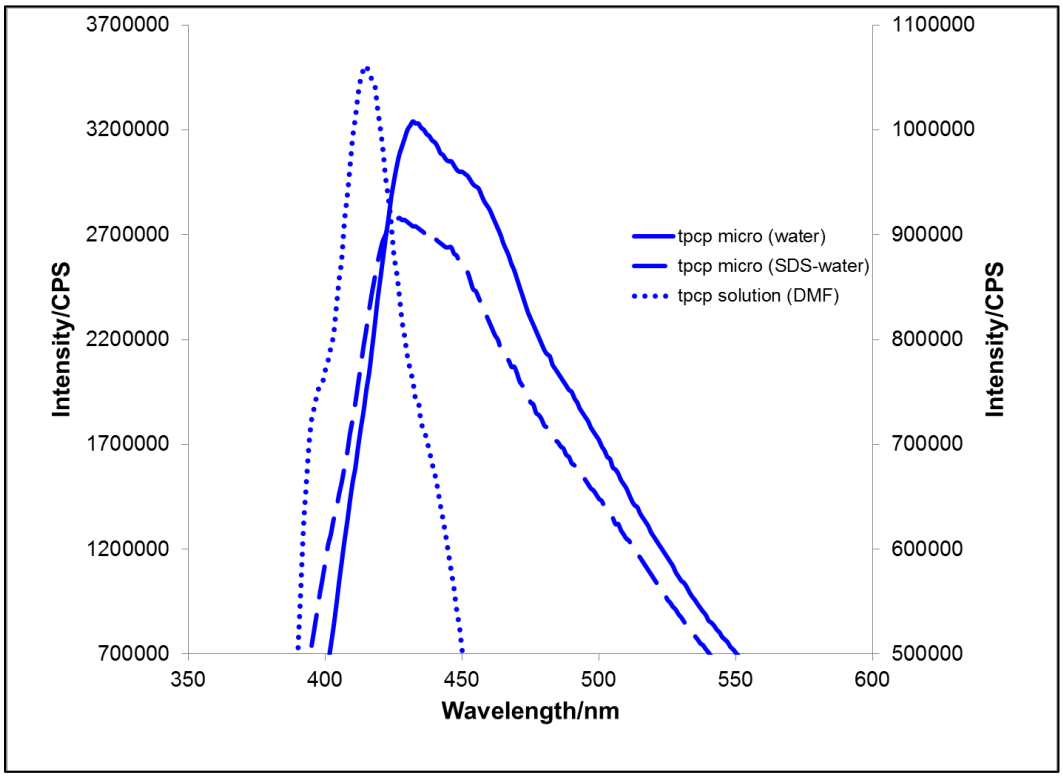

Figure 192: Emission spectra of tpcp microcrystals compared to dilute solution (nanoparticles on primary axis and solution on secondary axis).

6.12 Discussion

The enhanced fluorescence intensity of nanocrystalline pCp and tpcp, as well as the longer microcrystals, compared to solution can be attributed to aggregation behavior arising from minimal intermolecular π-overlap in the solid.[347] Fluorescence of organic chromophores is typically quenched by either by co-planarization at the molecular level[160] or intermolecular aggregation.[346] Given that pCp and tpcp possess two benzene rings covalently enforced in a face-to-face geometry, intermolecular forces in the solid can be expected to significantly impact fluorescence. Indeed, the solid-state packing of pCp[338] and tpcp[343] demonstrate that both molecules assemble in an edge-to-face, or herringbone, fashion (Figure 193).[349]

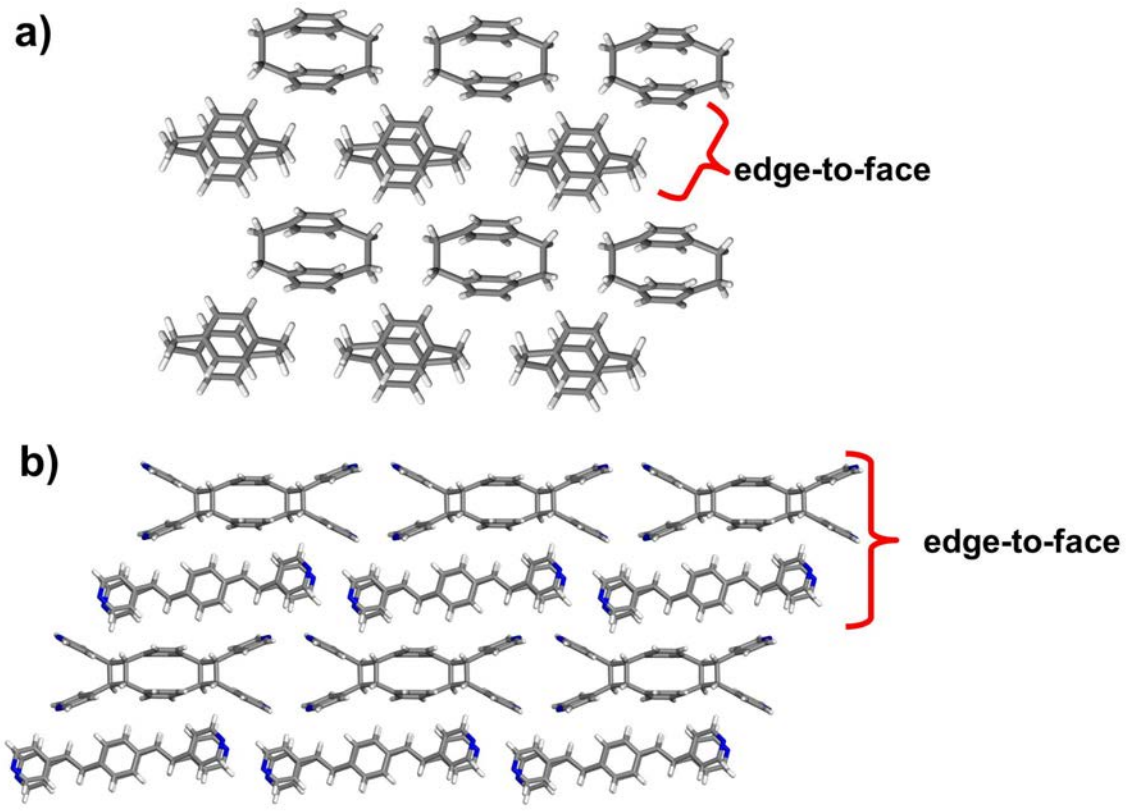

Figure 193: Edge-to-face packing of crystalline: (a) pCp and (b) tpcp.

Solid pCp and tpcp are composed of layers with molecules that lie offset and twisted by 90° and 76°, respectively. The edge-to-face interactions in the pCps are supported by (alkyl) C—H···π, (pyridine) C—H···N (pyridine), and (pyridine/benzene) C—H···π interactions. The combination of multiple hydrogen-bonding interactions increases the rigidity of the structures and can impact optical properties. This is particularly true for tpcp, wherein interactions involving the distal pyridines, effectively restrict the rotations of the pyridyl moieties and lead to an enhanced emission.[161] The resulting aggregates display a long-range ordered arrangement that is, thus, reflected in the emission behavior of the nanosuspensions. Indeed, herringbone arrangements are principal motifs in rigid pCp-based systems. In particular, edge-to-face packing is a prominent packing motif, suggesting that pCps can present a rare opportunity to enhance optoelectronic properties in lieu of covalent modification through the formation of organic nanocrystals.

6.13 Conclusion

In this chapter, we have demonstrated that laterally-substituted [2.2]cyclophanes exhibit unique optical properties, despite not being fully conjugated. Specifically, we show that the cyclobutanes act as strained donors that aid in shuttling electron density through the molecule, resulting in a nonconventional internal charge transfer (ITC) process. We also show that post-synthethic modification the covalent architecture results in red-shifted optical properties. In particular, quaternization of the distal pyridines facilitates the ICT, leading to large red-shifts in both excitation and emission for the entire series of cyclophanes. The resulting excitation and emission maxima are also approximately the same as exhibited by tetrasubstituted pCps that contain fully conjugated chromophores.

We have also investigated the impact of post-synthetic modification in the form of altering crystal size so as to attain pCps with different optical properties. We developed a

sonochemical method to prepare nanostructured pCps. The nanocrystals are on the order of 100-500 nm, and exhibit optical properties that differ compared to solution. Both nanostructured pCp and tpcp display more intense fluorescence, which is ascribed to an edge-to-face packing that effectively restricts intermolecular rotation being maintained in the nanocrystalline solid. In addition, we observed that tpcp nanocrystals exhibit a red-shifted emission as nanosuspensions, owing to the rapid formation of hydrogen-bonded aggregates in the presence of SDS.

CHAPTER 7: TOWARDS THE SOLID-STATE SYNTHESIS OF UNSYMMETRICAL CYCLOPHANES

A portion of this chapter has been published as part of a themed issue on [2.2]cyclophanes in the *Israel Journal of Chemistry*, and is adapted with permission from John Wiley and Sons, Copyright 2012 [E. Elacqua, T. Frisčić, L. R. MacGillivray, *Isr. J. Chem.* **2012**, *52*, 53.].

7.1 Introduction

There has been much work by chemists to design olefins that crystallize, with certainty, in geometries that are suitable for intermolecular [2+2] photodimerization reactions.[76, 83] The reaction results in the formation of two carbon-carbon single (C-C) bonds in a rigid, yet flexible, environment that can afford molecules that are otherwise unattainable in solution. That the reaction occurs in an environment that is solvent-free also means that the approach to synthesize molecules has relation to the field of green chemistry.[350]

That chemists aim to design olefins that crystallize to undergo photodimerizations in solids stems from pioneering work of Schmidt.[83] From numerous crystallographic studies of cinnamic acids, Schmidt delineated geometry criteria for the cycloaddition to occur in solids. In particular, it was determined that the reaction is topochemically controlled, being dictated by parallel alignment and overlap of C=C bonds with a separation distance < 4.2 Å (Figure 194). In addition to providing geometry criteria, Schmidt showed that the organization of olefins in solids is highly sensitive to subtle changes to molecular structure. More specifically, the organization of olefins, and more generally molecules, is 'unpredictably' influenced by the presence of functional groups or substituents. Homologous cinnamic acids were, thus, shown not to exhibit homologous reactivities. Effects of polymorphism were also shown to have a pronounced effect on packing and the resulting regiochemistry (e.g. head-to-head versus head-to-tail

photodimers) of the photodimerization. Such lack of reaction homology, and related effects of polymorphism, have meant that it is inherently difficult for chemists to perform covalent-bond-forming reactions in the solid state so as to synthesize molecules with similar synthetic 'freedoms' realized in solution. The challenge to control the organization of molecules in solids to control bulk physical properties such as reactivity has spurred on the field of crystal engineering.[16]

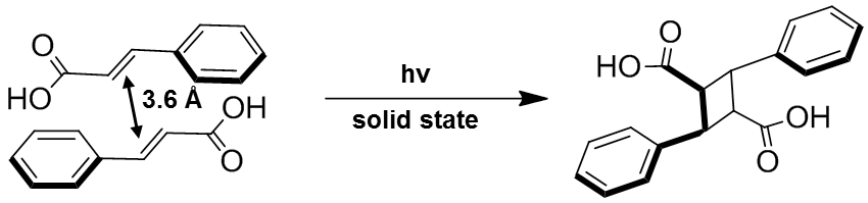

Figure 194: Solid-state [2+2] photocycloaddition of α-cinnamic acid, generating the head-to-tail truxillic acid product.

Although it is difficult to control reactivity in the solid state, cyclophanes have emerged as viable synthetic targets. Originally studied by Cram in the 1950's,[282] pCp remains of great interest to materials scientists,[289, 296, 302] owing to unique optical and electronic properties conferred by the two face-to-face benzene rings within the rigid covalent scaffold. X-ray crystal structure analyses of the parent pCp demonstrates the two stacked aromatic rings to assume a boat conformation, with the closest inter-ring C-C separations being shorter than the sum of van der Waals radii (2.78 Å).[351] Indeed, from a synthetic standpoint, it is the stacked geometry that makes pCp a 'natural' target for a solid-state reaction since two dienes separated by a phenyl spacer unit can be expected to undergo a double photoaddition to generate a pCp composed of peripheral cyclobutane units (Figure 195).

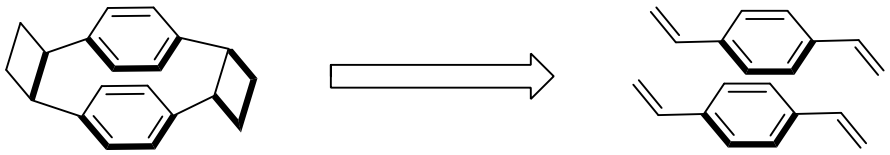

Figure 195: General method to produce a dicyclobutyl pCp from the [2+2] photodimerization of *p*-divinylbenzene.

A method to construct cyclobutane-bridged cyclophanes can involve a double [2+2] photodimerization of appropriate divinylbenzene derivatives. The result is a conformationally-rigid and highly-strained tricyclic product. Although the use of divinylbenzenes has been shown by Nishimura[352] to provide entries to the meta- and orthocyclophanes in solution (yields 0.5 to 40%), the method does not succeed in the case of pCp. Instead, only monocyclobutane derivatives form (Figure 196). The inability to form the pCp framework *via* double photodimerization in solution has been explained by a difficulty to organize two C=C bonds into close enough proximity for the second photodimerization that follows the formation of the first cyclobutane ring. The use of tethers (e.g. polyether) and pendent aromatic groups has, however, been shown to be fruitful in cases where reaction yields are particularly low.

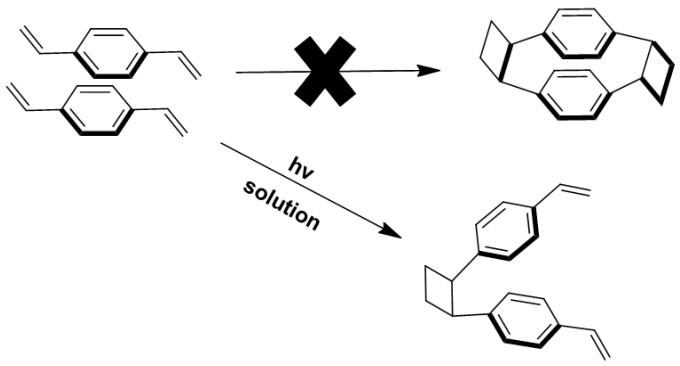

Figure 196: Solution-phase [2+2] photodimerization of *p*-divinylbenzene, affording exlusively the monocyclized product.

7.2 [2.2]Paracyclophanes in the Organic Solid State

Whereas studies on double [2+2] photodimerizations of dienes in the solid state,[352] although limited, had been previously reported, it was Hasegawa in 1987 that reported the first example of the formation of a pCp in a solid (Figure 196).[354] While studying the topochemical behavior of crystals of unsymmetrical distyryl diolefins, a mixed crystal of ethyl and propyl α-cyano-4-[2-(4-pyridyl)ethenyl]cinnamates (1:1 ratio) reacted quantitatively to give the tricyclic pCp (Figure 197). The photoreaction of the two diolefins occurred in a crystal-to-crystal transformation, as shown by X-ray powder diffraction analysis. The double cycloaddition was also demonstrated to proceed in a crystal phase different than each pure olefin, each of which formed a homopolymer. HPLC analysis of the reacted crystal was consistent with a double photodimerization that afforded three different pCps; specifically, two homodimers and one heterodimer.

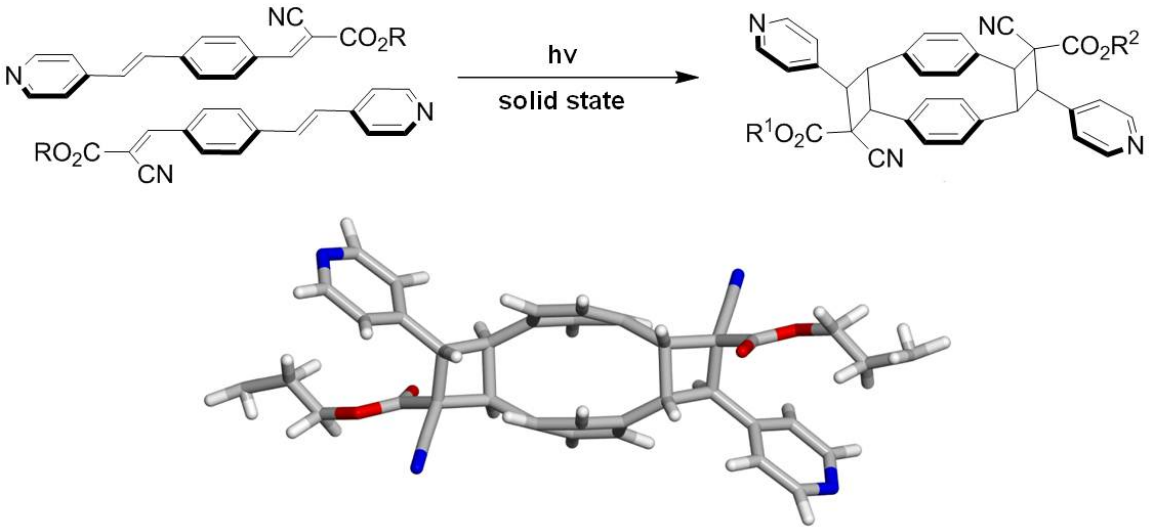

Figure 197: Solid-state [2+2] photodimerization of α-cyano-4-[2-(4-pyridyl)ethenyl]cinnamates to afford mixed pCp products.

A second approach to synthesize a pCp in the solid state was later reported by Moorthy in 2007.[355] While investigating the reactivity of 2-pyranone-annulated

derivatives of coumarin, two crystalline polymorphs of 4-methyl-7-styrylcoumarin were shown to undergo a double [2+2] photodimerization that afforded the tricyclic pCp (Figure 198). Needle and plate-like morphologies were obtained *via* crystallizations from mixtures of dichloromethane/chloroform with either xylene or petroleum ether, respectively. UV irradiation generated the pCp in 45% and 75% yield in the needles and plates, respectively. The lower yield in the needle morphologies was attributed to each layer being either reactive or nonreactive.

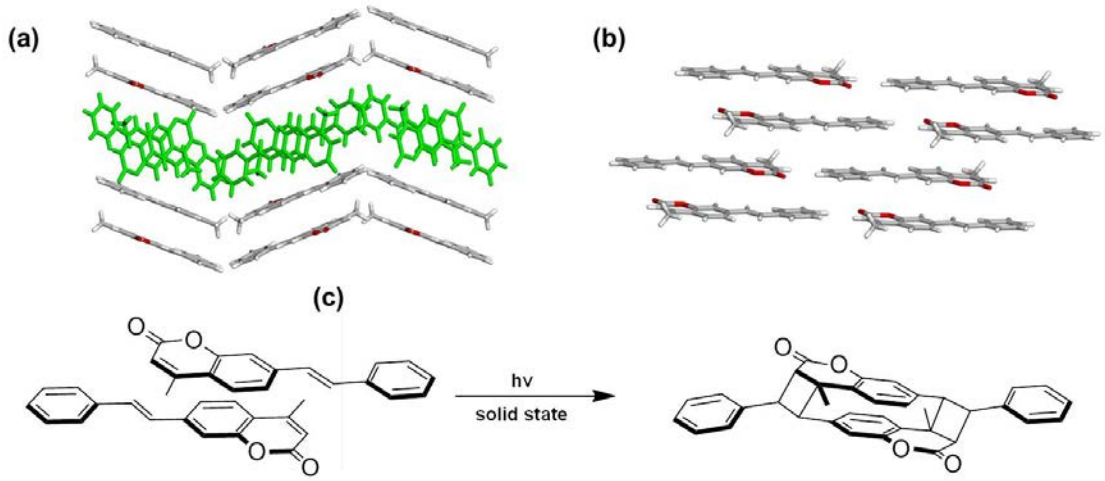

Figure 198: Solid-state [2+2] photodimerization of a coumarin derivative: (a) layers of the needle polymorph, (b) pairs of plate polymorph, and (c) reaction scheme.

Although pCps appear to be ideal solid-state targets, their accessibility suffers from the lack of control that is necessary to afford the strained structure. The approaches mentioned above, although they are quite successful in obtaining the deisred cyclophane products, suffer from a lack of design element and unpredictable crystal packing, causing the products to invariably form in the head-to-tail orientation.

Our use of hydrogen-bond templates[88] to direct the assembly and reactivity of olefins[76-77] originated from a general goal to control reactivity in the wake of vexatious effects of crystal packing.[16] By directing the photoreaction within a discrete molecular

assembly, the templates can organize olefins into positions that are both suitable to achieve topochemical control of the cycloaddition and be largely independent of effects of long-range packing.

In this chapter, we sought to synthesize unsymmetrical multifunctional [2.2]paracyclophanes in the solid state. Our strategy involves exploitation of our previously established strategy regarding a supramolecular protecting group, while maintaining a stilbenoid framework that could lead to enhanced reactivity by enabling pedal motion within our system. The resulting cyclophanes are expected to be of interest to materials scientists from an optoelectronic standpoint, as well as for post-synthetic modification and/or incorporation into metal-organic frameworks.

7.3 Experimental

All reagents and solvents used were reagent grade and commercially available. Potassium carbonate (anhydrous, 99%) and pyridine (≥99%) were purchased from Fisher Scientific Company (Pittsburgh, PA, USA). 4-Vinylpyridine (95%), 4-bromobenzaldehyde (99%), methyl (triphenylphosphoranylidene)acetate (98%), para-toluenesulfonaic acid monohydrate (98.5%), and dichloromethane (≥99.8%) were purchased from Sigma Aldrich Chemical (St. Louis, MO, USA). Ethanol (99.98%, absolute grade) and triethanolamine (≥99%) wer obtained from Pharmco-AAPER (Brookfield, CT, USA) and ACROS (Morris Plains, NJ), respectively. Dichloro bis(triphenylphosphine) palladium (II) was purchased from Frontier Scientific. 4-Vinylpyridine was distilled prior to use. All other reagents were used without further purification. Substituted resorcinols were purchased commercially or synthesized *via* standard literature preparations.

^{1}H NMR spectra were collected using a Bruker Avance 300 MHz or 400 MHz spectrometer using DMSO-d_6 as a solvent. Photoreactions were conducted using ultraviolet radiation from a 500 W medium-pressure mercury lamp in an ACE Glass

photochemistry cabinet. Co-crystals were finely ground using a mortar and pestle, and then placed between a pair of pyrex glass plates. The samples were irradiated in 10-hour periods and mixed between consecutive irradiations. The product formation was monitored using ^{1}H NMR spectroscopy. Upon completion of photoreaction, the products were isolated using basic extraction with $CHCl_3$.

Single crystal diffraction data was collected on a Nonius Kappa CCD single-crystal X-ray diffractometer at both room and low temperatures using MoK_α radiation (λ = 0.71073 Å). Data collection, cell refinement and data reduction were performed using *Collect*[197] and *HKL Scalepack*/*Denzo*,[198] respectively. Structure solution and refinement were accomplished using SHELXS-97[261] and SHELXL-97,[199] respectively. The structures were solved *via* direct methods. All non-hydrogen atoms were identified from the difference Fourier map within several refinement steps. All non-hydrogen atoms were refined anisotropically. Hydrogen atoms associated with carbon atoms were refined in geometrically constrained positions with isotropic thermal parameters $U_{iso}(H) = 1.5U_{eq}(C_{CH3})$ and $U_{iso}(H) = 1.2U_{eq}(C_{CH})$. Hydrogen atoms belonging to phenolic OH groups were and refined using a riding model with isotropic thermal parameters $U_{iso}(H) = 1.5U_{eq}(O_{hydroxy})$. Details of the structural analyses are summarized in Tables A23 - A24.

7.3.1 Synthesis of 4-[(E)-(pyridine-4-yl)ethenyl]benzaldehyde

The synthesis of 4-[(E)-(pyridine-4-yl)ethenyl]benzaldehyde was accomplished using a Heck reaction. 4-Bromobenzaldehyde (12.8 g, 0.0692 mol) was suspended in a mixture of triethanolamine (3 mL) and K_2CO_3 (solution, 114.5 g mol^{-1}, 250 mL). Dichloro bis(triphenylphosphine) palladium (II) (1.22 g, 25 mol %) was added to the solution. The solution was allowed to stir at 50º for 15 minutes, upon which 4-vinylpyridine (7.5 g, 0.0713 mol) was added slowly *via* syringe. The reaction was heated to reflux for an additional 40 hours. After cooling to room temperature, the solid was

filtered and refluxed in a minimal amount of pyridine for 2 hours. After reflux, the solution was cooled to room temperature, allowing for the product to crystallize out as light brown prisms, which were filtered, washed with aqueous ethanol, dried and used in the next step without further purification (10.5 g, 73 %): ^{1}H NMR (400 MHz, DMSO-d_6) δ/ppm = 10.0 (1H, s), 8.58 (dd, 2H), 7.96 (d, 2H), 7.86 (d, 2H), 7.65 (d, 1H), 7.62 (dd, 2H), 7.47 (d, 1H).

7.3.2 Synthesis of methyl-4-[(E)-(pyridine-4-yl)ethenyl]cinnamate (mpec)

Methyl-4-[(E)-(pyridine-4-yl)ethenyl]cinnamate (mpec) was synthesized utilizing Wittig-type conditions. Methyl (triphenylphosphoranlyidene) acetate (5.0 g, 0.015 mol) was dissolved in 100 mL dichloromethane. A solution of 4-[(E)-(Pyridine-4-yl)ethenyl]benzaldehyde (3.1 g, 0.0148 mol) in 50 mL of dichloromethane was then added slowly and subsequently heated to reflux for 16 hours. Upon cooling to ambient temperature, pTsOH (0.030 mol) was added with stirring to the CH_2Cl_2 solution. After stirring for 30 minutes, the acidified product was extracted with water (2x, 50mL), basified with K_2CO_3, and re-extracted with CH_2Cl_2 (2x, 50 mL). The solution was evaporated to yield an off-white solid free of the Ph_3P=O byproduct (3.1 g, 70%). ^{1}H NMR (400 MHz, DMSO-d_6): δ/ppm = 8.55 (dd, 2H), 7.72 (d, 2H), 7.68 (d, 2H), 7.64 (d, 1H), 7.57 (dd, d – overlapping, 3H), 7.34 (d, 1H), 6.67 (d, 1H), 3.73 (s, 3H).

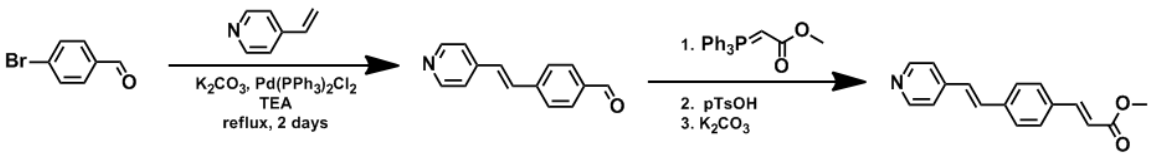

Figure 199: Synthesis of methyl-4-[(E)-(pyridine-4-yl)ethenyl]cinnamate (mpec) using Wittig chemistry.

Co-crystallization was performed by dissolving 100 mg of mpec and 0.17 mmol of a resorcinol in 10 mL EtOH. The solutions were heated slightly to facilitate dissolution, and then left to cool to room temperature. Upon further solvent evaporation, and within 4-7 days, each sample comprising contained either single crystals or a crystalline powder that was filtered, dried, and characterized using ^{1}H NMR spectroscopy.

7.4 Results

In preliminary studies with mpec, we have isolated and characterized four co-crystals, as well as the structure of the olefin itself, from our template switching. We have uncovered a template that produces a monocyclobutane product in quantitative yield, as well as uncovered a co-crystal system that affords the desired dicyclobutane product.

(1) mpec. The olefin methyl-4-[(E)-(pyridine-4-yl)ethenyl]cinnamate (mpec) crystallizes from EtOH in the monoclinic space group $P2_1/c$ with only one molecule in the asymmetric unit. The olefin self-assembles utilizing both C—H···N interactions between nearly orthogonal pyridines, and (alkoxy) C—H···O (carboxy) interactions. The C—H···N organize the olefins into an offset alignment (Figure 200), wherein both sets of olefins conform to Schmidt's criteria for a [2+2] photodimerization ($d_{C\cdots C}$ = 4.066 Å), and would be expected to afford an offset, yet head-to-head polycyclobutane product.

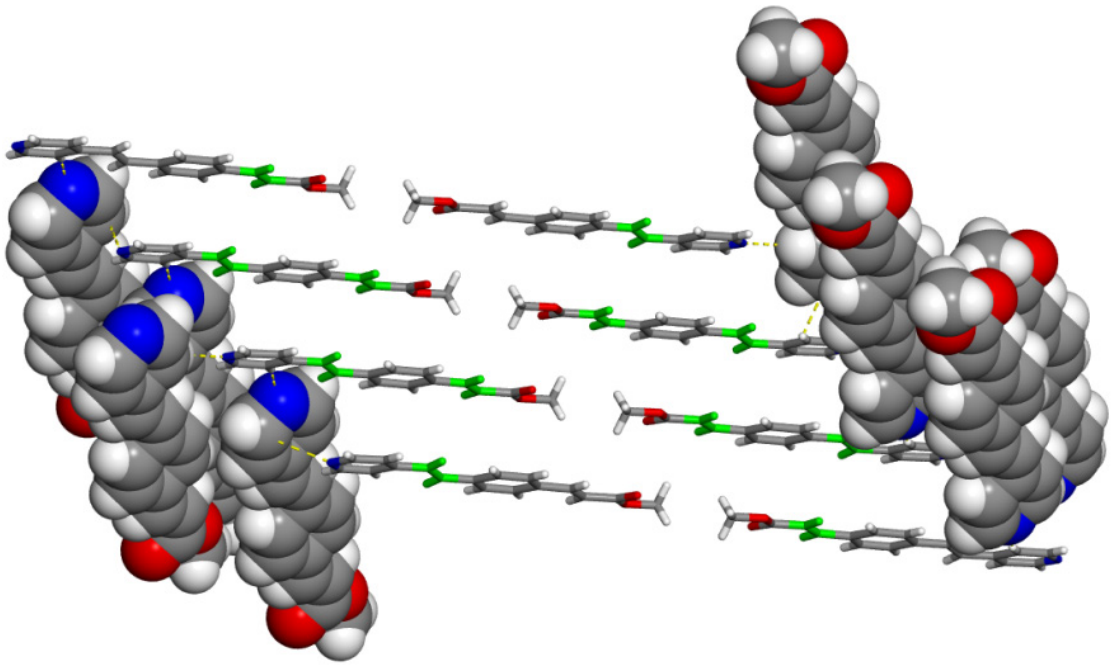

Figure 200: X-ray structure of mpec highlighting reactive olefins in green within extended structure.

(2) 2(mpec)·(4,6-diCl res). Co-crystals of the formulation 2(mpec)·(4,6-diCl res) crystallized from EtOH in the monoclinic space group $P2_1/c$ with one 4,6-diCl res and two molecules of mpec in the asymmetric unit. The components form a discrete assembly sustained by two O—H···N hydrogen bonds [O···N separations (Å): O1···N1 2.706(4), O2···N2 2.635(3)]. The C=C bonds adjacent to the pyridine rings were aligned and separated by 4.149 Å yet, however, the second pair of C=Cs adopted a crisscross conformation and was separated by 3.697 Å (Figure 201). The olefins between the assemblies were offset and antiparallel with a C···C separation of 4.980 Å. Additional interactions in the form of (alkenyl) C—H···Cl (res) and (pyridine) C—H···O (carboxy) contribute to the extended packing ($d_{C\cdots Cl}$ = 3.305 Å; $d_{C\cdots O}$ = 3.452 Å).

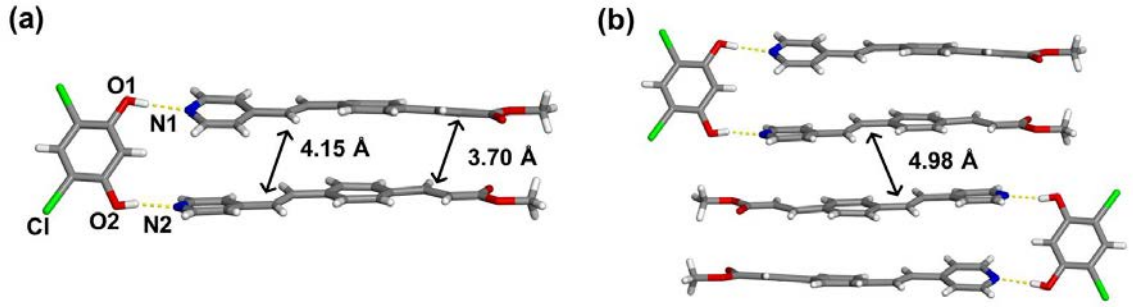

Figure 201: X-ray structure of 2(mpec)·(4,6-diCl res) highlighting (a) three-component assembly and (b) neighboring assemblies.

(3) 2(mpec)·(4,6-diI res). Co-crystals of the formulation 2(mpec)·(4,6-diI res) crystallized from EtOH in the triclinic space group $P\bar{1}$. A structure analysis revealed the formation of a discrete, three-component hydrogen-bonded assembly sustained by two O—H···N forces [O···N separations (Å): O1···N1 2.693(6), O2···N2 2.756(7)]. Both pairs of C=C bonds within an assembly were aligned and parallel, however, the C···C separations were 4.391 Å and 4.257 Å. The olefins between assemblies were offset and separated by 5.549 Å and 5.660 Å (Figure 202). The olefins within an assembly are twisted 18.32° away from each other, likely contributing to the higher C···C separation. Adjacent assemblies also interact through the formation of (res) I···O (carboxy) and (res) I···O (phenol) interactions ($d_{I\cdots O}$ = 3.186 Å; $d_{I\cdots O}$ = 3.416 Å).

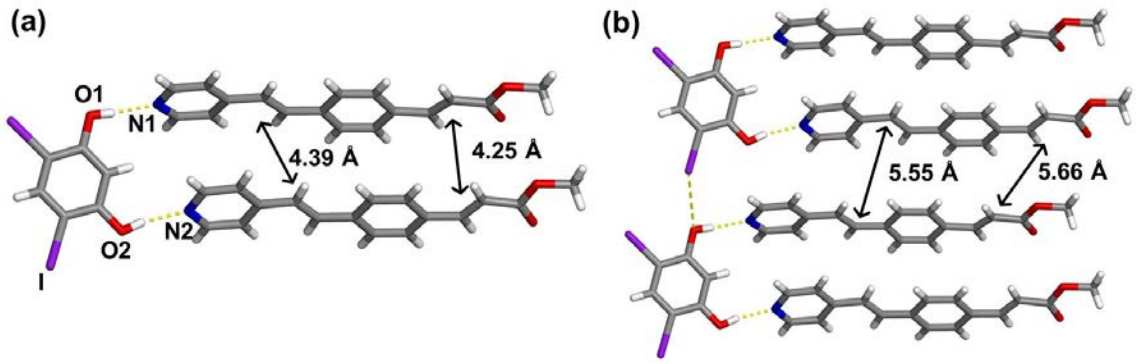

Figure 202: X-ray structure of 2(mpec)·(4,6-diI res) highlighting (a) three-component assembly and (b) neighboring assemblies.

(4) 2(mpec)·(4,6-diBr res). Co-crystals of the formulation 2(mpec)·(4,6-diBr res) crystallize from EtOH in the monoclinic space group $P2_1/n$ with one 4,6-diBr res and two molecules of mpec in the asymmetric unit. The molecules assemble to form a discrete three-component assembly sustained by two O—H···N hydrogen bonds [O···N separations (Å): O1···N1 2.647(6), O2···N2 2.709(6)]. Within each assembly, the first pair of C=C bonds are aligned with a C···C separation of 4.141 Å (Figure 203). The second pair of olefins is disordered over two sites (71/29), with the highest occupancy being crossed in relation to the stacked olefin in the assembly ($d_{C\cdots C}$ = 3.701 Å). The C=Cs between assemblies are arranged in an offset and antiparallel manner, being separated by 4.884 Å. The extended co-crystal packing contains (pyridine) C—H···O (carboxy) and (alkyl) C—H···Br (res) interactions between adjacent assemblies ($d_{C\cdots O}$ = 3.420 Å; $d_{C\cdots Br}$ = 3.719 Å).

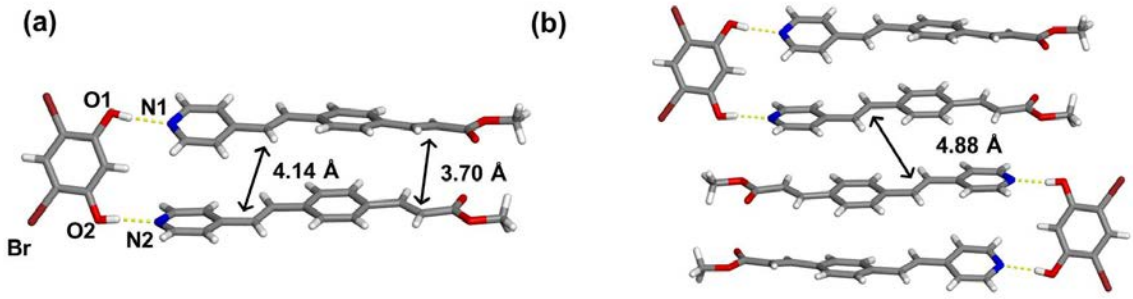

Figure 203: X-ray structure of 2(mpec)·(4,6-diBr res) highlighting (a) higher population three-component assembly and (b) neighboring assemblies.

(5) 2(mpec)·(4-Br res). 2(mpec)·(4-Br res) co-crystallizes from EtOH in the monoclinic space group $P2_1/c$ with one 4-Br res and two molecules of mpec in the asymmetric unit. The resulting three-component assembly is sustained by the formation of two O—H···N hydrogen bonds [O···N separations (Å): O1···N1 2.714(7), O2···N2 2.730(7)]. Within each assembly, the first pair of C=C bonds are aligned with a C···C separation of 3.745 Å (Figure 204), while the second pair of olefins is disordered over two sites (72/28), with the highest occupancy being crossed in relation to the stacked olefin in the assembly ($d_{C\cdots C}$ = 3.805 Å). In between the assemblies, the C=Cs are arranged in an offset and antiparallel manner, being separated by 4.864 Å. The extended packing contains additional (pyridine) C—H···O (carboxy) and (pyridine) C—H···O (alkoxy) interactions between adjacent assemblies ($d_{C\cdots O}$ = 3.420 Å, 3.778 Å; $d_{C\cdots O}$ = 3.394 Å).

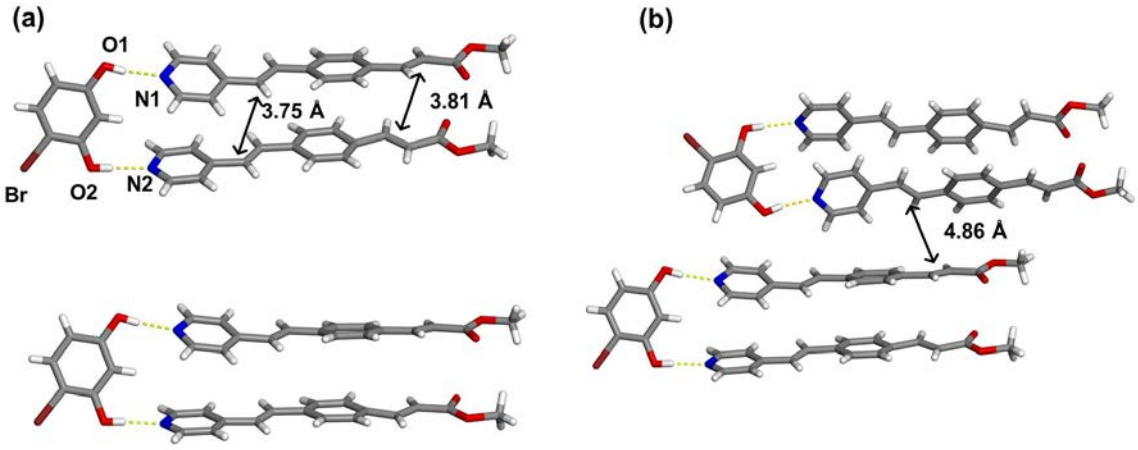

Figure 204: X-ray structure of 2(mpec)·(4-Br res) highlighting (a) three-component assemblies (higher occupancy and lower reactive occupancy) and (b) neighboring assemblies.

UV irradiation of of a powdered crystalline sample of 2(mpec)·(4-Br res) resulted in conversion to two products, one of which is the desired unsymmetrical cyclophane product. The photoconversion to the unsymmetrical cyclophane is evidenced by the two pairs of doublets centered at 4.7 and 4.3 ppm (Figure 205). Based on crystal structure analysis, the other product should be the monocyclobutane, wherein only the pair of olefins adjacent to the pyridines photoreact. The production of a monocyclobutane product is also consistent with the ^{1}H NMR signals of the remaining olefinic protons that shift slightly upfield to *ca.* 6.6 ppm.

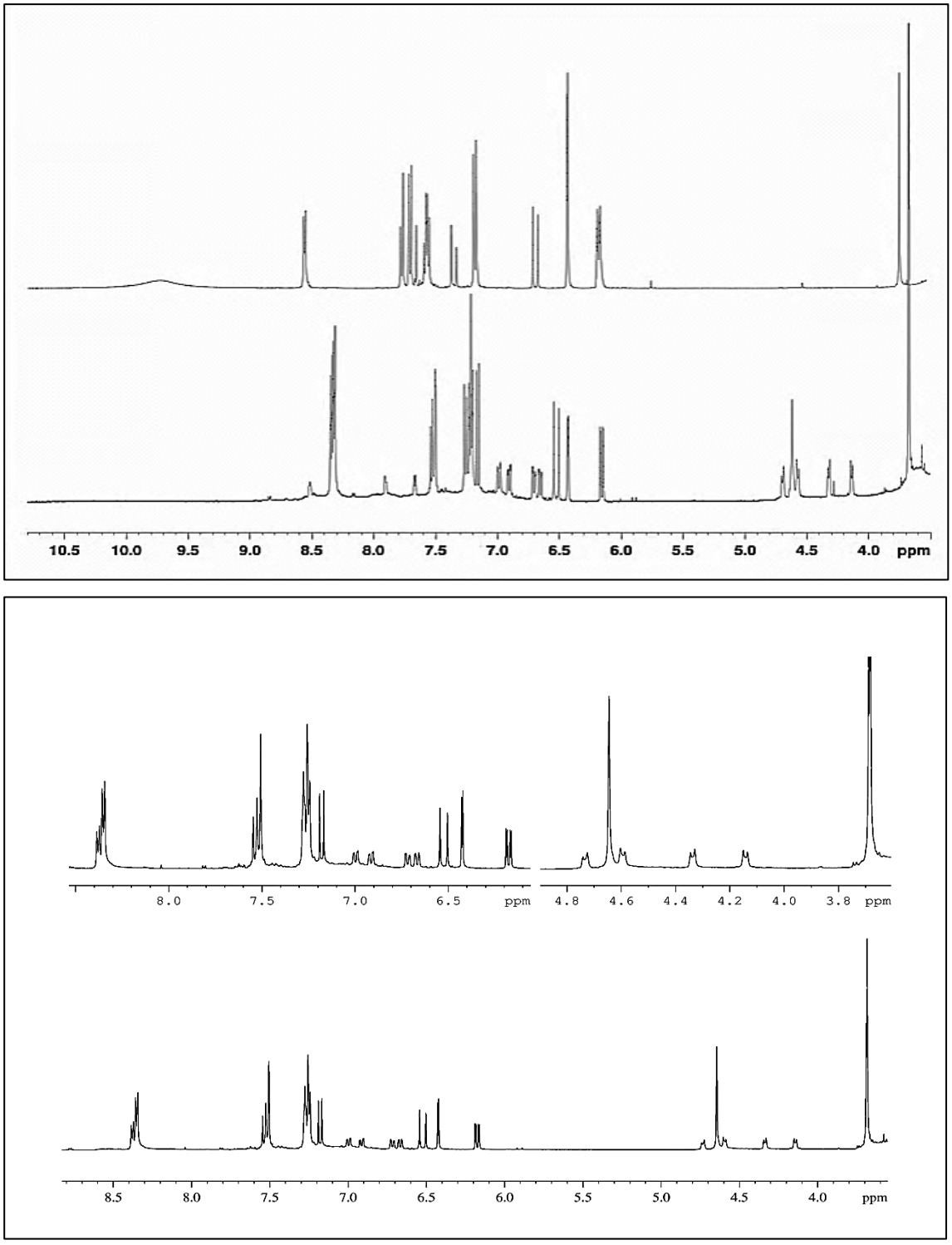

Figure 205: ^{1}H NMR spectra involving 2(mpec)·(4-Br res): (top, 300 MHz) overlay of 2(mpec)·(4-Br res) before and after UV-irradiation, and (bottom, 400 MHz) 2(mpec)·(4-Br res) after UV-irradiation with zoomed insets depicting aromatic and cyclobutane regions.

From our template switching, we also identified 4,6-diBr res as a template that affords a positive photoreaction. From analysis of a ^{1}H NMR spectrum before and after photoreaction, it appears as though the co-crystal formed undergoes quantitative conversion to a monocyclobutane product (Figure 206). The monocyclobutane formation is evidenced by the shifting of the olefinic protons upfield (6.5 ppm) as well as a single peak in the cyclobutane region *ca.* 4.7 ppm.

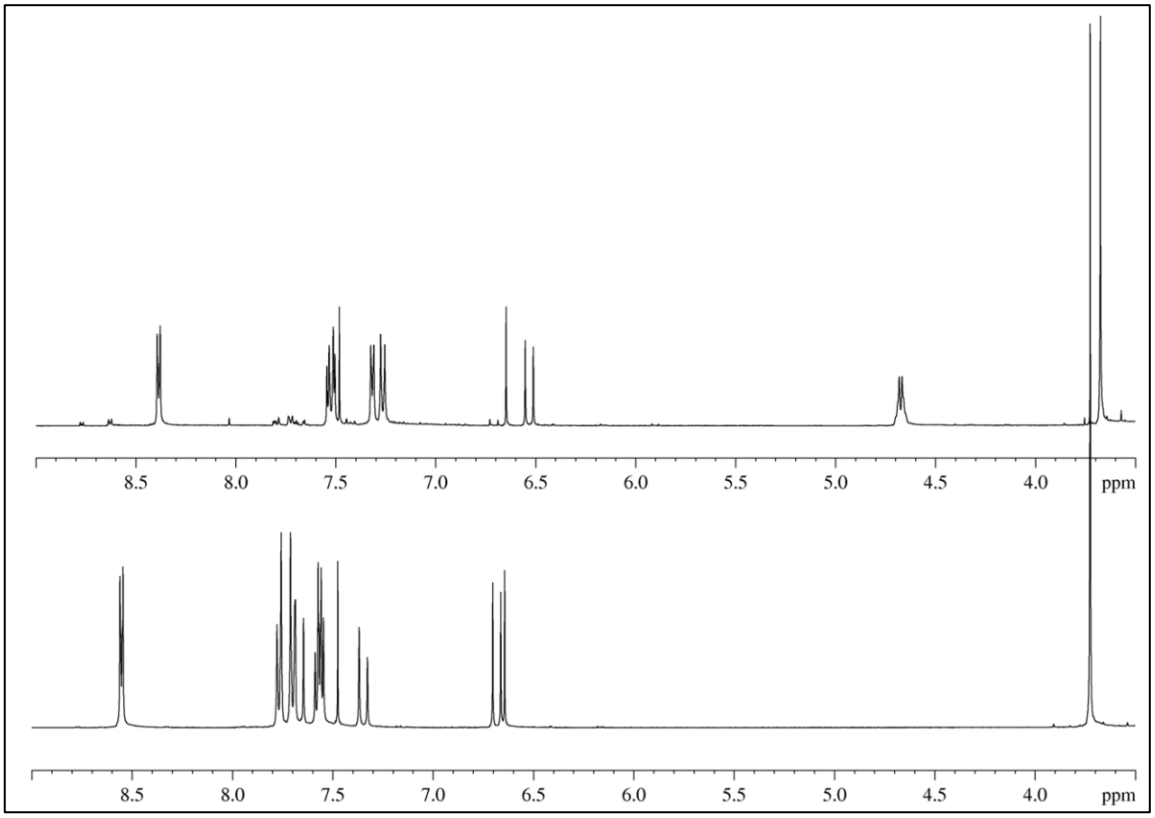

Figure 206: Comparison of the ^{1}H NMR spectrum of 2(mpec)·(4,6-diBr res) before and after UV-irradiation.

7.5 Conclusion

The production of unsymmetrical molecular targets in the solid state is of great interest in the context of post-synthetic modification, as well as for optoelectronic applications. Prior attempts to achieve the formation of unsymmetrical cyclophanes have

been lacking design elements and are thus, difficult to predict product distribution. We have demonstrated in this chapter how the application of our template switching approach can achieve the formation of an unsymmetrical paracyclophane in the solid state, wherein the utilization of a template provides control over the packing and affords a head-to-head product.

CHAPTER 8: CONCLUSIONS

The results presented in this thesis demonstrate the the use of highly-directional supramolecular interactions to achieve the formation of target architectures. Specifically, noncovalent interactions are utilized to form crystalline materials that differ in topologies, dimensionalities, connectivities, and properties (e.g. reactivity, optical). The crystalline materials are held together by either hydrogen bonding or metal coordination. In order to effectively mimic Nature and produce complex architectures with controlled self-assembly and precise molecular recognition elements, one must thoroughly understand how complementary molecules interact in the presence of multiple functional groups. Upon comprehending the complex interplay between supramolecular interactions and emergent properties, one can begin to carve the foundation for the design of functional architectures.

In chapter 2, the focus is placed on understanding molecular recognition and self-assembly as it relates to the formation of organic co-crystals and salts of sulfonamide-based pharmaceutical agents (PAs). To fully comprehend how different interactions can dictate structural changes, one must meticulously examine the geometries and topologies of the resultant solids. In doing so, we have recognized that not only do salts and co-crystals involving sulfa drugs differ in geometry, but some of the co-crystals appear to mimic salt-like geometries. Upon further analysis, we noted that the co-crystals comprised two tautomers with distinct polarities and relative energies, such that the higher energy form can be expected to exhibit salt-like characteristics. Specifically, all of the S–N lengths of the imidine – or higher energy and more polar tautomer – sit in between the S–N lengths of salts and the amidine tautomer. To our knowledge, this is the first attempt to assess a structural relationship of tautomers as related to the salt – co-crystal boundary. Our findings are significant in a field that strives to generate novel

robust solid forms that can exhibit enhanced physiochemical properties in lieu of salt formation.

In chapter 3, the focus is placed upon using co-crystallization to influence solid-state behavior of a chiral PA. Ibuprofen, a well known chiral drug, crystallizes as a racemate, wherein each crystal contains an equal amount of both enantiomers in a unit cell. By introducing a secondary complementary unit in the form of a bipyridine into the self-assembly process, we have been able to effectively alter the solid-state behavior, so as to generate both solid solution and conglomerate co-crystals. Not much is known about solid solutions, and thus, the formation of them should enable further analysis into their properties. Our studies have also resulted in the production of a co-crystal conglomerate. To our knowledge, this is the first co-crystal system with this behavior. Conglomerates are extremely important from a pharmaceutical, as well as synthetic, perspective since they ultimately result in chiral resolution without the need to form salts.

The exploitation of noncovalent forces has been utilized to confer reactivity upon multifunctional olefinic systems in chapters 4 and 5. In particular, we demonstrate how an unpredictable self-assembly process in the presence of multiple recognition elements can be rendered regioselective through the application of a supramolecular protecting group strategy. The strategy involves temporarily masking a hydrogen bond motif prior to self-assembly to afford a reactive unit. Upon [2+2] photoreaction, the motif can be unveiled to generate the desired architecture. Such a strategy is thought to be applicable in order to expand the range of target molecules that are deemed accessible *via* the organic solid state. In an effort to control self-assembly, and thus, reactivity, within more sterically-congested systems, we pursued the photodimerization of trisubstituted olefins, which are common molecular motifs in Nature. By having a broad range of supramolecular elements to confer solid-state reactivity, we are able to demonstrate the utility of stronger coordination bonds in achieving the desired self-assembly within

conformationally-flexible systems. To our knowledge, this is the first example of a [2+2] photodimerization in trisubstituted olefins *by design*.

In chapter 6, the foundation is placed upon the emergent properties of a series of [2.2]cyclophanes. Although cyclophanes are well-known hydrocarbons that possess unique properties, the number of ways to access and/or derivatize them synthetically remains underdeveloped. In this chapter, we examine a series of cyclophanes that were synthesized in the organic solid state in the context of optical properties. The molecules, contrary to our expectations, exhibit properties reflective of systems that engage in electronic communication despite the lack of continuous conjugation. We demonstrated that the strained cyclobutane rings promote interchromophore conjugation that leads to an unexpected internal charge transfer. Additionally, we have developed a method to produce nanocrystals of [2.2]paracyclophanes, with the nanocrystals exhibiting unique properties in comparison to their macromolecular counterparts.

In chapter 7, we aimed to extend our template strategy to unsymmetrical olefins that would afford multifunctional [2.2]paracyclophanes. We have demonstrated through preliminary results that co-crystallization and subsequent photodimerization affords the desired [2.2]paracyclophane, as well as a monocyclized product. Although not obtained in quantitative yields, this is the first example of a head-to-head unsymmetical [2.2]paracyclophane afforded in the organic solid state. It is expected to be of great interest in the development of functional porous networks and optical materials.

The entireity of this thesis represents the undeveloped interplay between traditional synthetic organic chemistry and supramolecular solid-state chemistry. The control and precision provided by the crystalline phase provides access to molecular targets with high fidelity and generally, stereospecifically, and in quantitative yields. In addition, the expansion to multifunctional targets, as well as molecules that are highly desirable in the context of emergent properties, bodes well for the continued development and exploitation of molecular recognition and solid-state self-assembly to generate novel

functional materials. Consequently, reactions conducted in organic co-crystals are promising modules to afford both simple and complex materials that exude desired properties and frameworks.

REFERENCES

1. a) K. C. Nicolaou, C. R. H. Hale, C. Nilewski, H. A. Ioannidou, *Chem. Soc. Rev*. **2012**, *41*, 5185. b) K. C. Nicolaou, D. Vourloumis, N. Winssinger, P. S. Baran, *Angew. Chem.* **2000**, *112*, 46; *Angew. Chem. Int. Ed.* **2000**, *39*, 44. c) E. J. Corey, A. K. Long, S. D. Rubenstein, *Science* **1985**, *228*, 408.

2. a) C. Vaxelaire, P. Winter, M. Christmann, *Angew. Chem.* **2011**, *16*, 3685; *Angew. Chem. Int. Ed.* **2011**, *50*, 3605. b) P. J. Hajduk, W. J. R. Galloway, D. R. Spring, *Nature* **2011**, *470*, 42.

3. a) J. D. Rocca, D. Liu, W. Lin, *Acc. Chem. Res.* **2011**, *44*, 957. b) Q. H. Cui, Y. S. Zhao, J. Yao, *J. Mater. Chem.* **2012**, *22*, 4136. c) N. Chandrasekhaur, R. Chandraeskar, *Angew. Chem.* **2012**, *124*, 3616; *Angew. Chem. Int. Ed.* **2012**, *51*, 3556.

4. a) W. Xie, C. D. Frisbie, *J. Phys. Chem. C* **2011**, *115*, 14360. b) G. Giri, E. Verplogen, S. C. B. Mannsfeld, S. Atahan-Evernk, D. H. Kim, S. Y. Lee, H. A. Becerril, A. Aspuru-Guzik, M. F. Toney, Z. Bao, *Nature* **2011**, *480*, 504. c) D. J. Lipomi, B. C.-K. Tee, M. Vosguertichian, Z. Bao, *Adv. Mater*. **2011**, *23*, 1771. d) A. N. Sokolov, S. Atahan-Evenk, R. Mondal, H. B. Akkerman, R. S. Sánchez-Carrera, S. Granados-Focil, J. Schrier, S. C. B. Mannsfeld, A. P. Soombely, Z. Bao, A. Aspuru-Guzik, *Nat. Commun.* **2011**, *2*, 1.

5. a) B. El Aroussi, S. Zebret, C. Brenard, P. Perrottet, J. Hamacek, *J. Am. Chem. Soc.* **2011**, *133*, 10764. b) K. Miyata, N. Nishiyama, K. Kataoka, *Chem. Soc. Rev.* **2012**, *41*, 2562. c) L. R. MacGillivray, *Angew. Chem.* **2012**, *124*, 1136; *Angew. Chem. Int. Ed.* **2012**, *51*, 1110.

6. L. Pauling, *J. Am. Chem. Soc.* **1931**, *53*, 1367.

7. a) D. A. Uhlenheuer, K. Petkau, L. Brunsveld, *Chem. Soc. Rev.* **2011**, *39*, 2817. b) D. Pijper, B. L. Feringa, *Soft Matter*, **2008**, *4*, 1349. c) J. Robertus, W. R. Browne, B. L. Feringa, *Chem. Soc. Rev.* **2010**, *39*, 354.

8. a) M. J. Wiester, P. A. Ulman, C. A. Mirkin, *Angew. Chem.* **2011**, *123*, 118; *Angew. Chem. Int. Ed.* **2011**, *50*, 114. b) K. Kirkorian, A. Ellis, L. J. Twyman, *Chem. Soc. Rev.* **2012**, *41*, 6138.

9. a) J.-M. Lehn, *Angew. Chem.* **1988**, *100*, 91; *Angew. Chem. Int. Ed.* **1988**, *27*, 89. b) J.-M. Lehn, *Supramolecular Chemistry*, Wiley-VCH, Weinheim, **1995**.

10. G. R. Desiraju, *Nature* **2001**, *412*, 397.

11. K. L. Wolf, H. Frahm, H. Harms, *J. Phys. Chem. B*, **1937**, *36*, 237.

12. C. B. Aakeröy, K. R. Seddon, *Chem. Soc. Rev.* **1993**, *22*, 97.

13. P. Metrangolo, *Chem. Eur. J.* **2001**, *7*, 2511.

14. J. Dunitz, *Pure Appl. Chem.* **1991**, *63*, 177.

15. M. O. Sinnokrot, C. D. Sherrill, *J. Phys. Chem. A*. **2006**, *110*, 10656.

16. G. R. Desiraju, *Angew. Chem.* **1995**, *107*, 2541; *Angew. Chem. Int. Ed.* **1995**, *34*, 2311.

17. a) T. Friščić, *Chem. Soc. Rev.* **2012**, *41*, 3493. b) N. Houbenov, J. S. Haataja, H. Iatrou, N. Hadjichristidis, J. Ruokolainen, C. F. J. Faul, O. Ikkala, *Angew. Chem.* **2011**, *123*, 2564; *Angew. Chem. Int. Ed.* **2011**, *50*, 2516. c) H.-Y.Gong, B. M. Rambo, W. Cho, V. W. Lynch, M. Oh, J. L. Sessler, *Chem. Commun.* **2011**, *47*, 5973.

18. a) J.-M. Lehn, *Angew. Chem,* **1990**, *102*, 1347; *Angew. Chem. Int. Ed.* **1990**, *29*, 1304. b) R. Buckley, C. D. Enekwa, L. D. Williams, N. V. Hud, *ChemBioChem*. **2011**, *12*, 2155. c) K. A. Nielsen, S. Bähring, J. O. Jeppesen, *Chem. Eur. J.* **2011**, *17*, 1101.

19. G. M. Whitesides, J. P. Mathais, C. T. Seto, *Science* **1991**, *254*, 1312.

20. R. G. Chapman, J. C. Sherman, *Tetrahedron*, **1997**, *47*, 15911.

21. E. Fisher, *Ber. Deutch. Chem.* **1893**, *2*, 267.

22. a) M. E. Belowich, C. Valente, R. A. Smaldone, D. C. Friedman, J. Thiel, L. Cronin, J. F. Stoddart, *J. Am. Chem. Soc.* **2012**, *134*, 5243. b) F. Zeng, S. C. Zimmerman, *Chem. Rev.* **1997**, *97*, 1681. c) P. A. Gale, *Acc. Chem. Res.* **2006**, *39*, 465.

23. S. Sivakova, S. J. Rowan, *Chem. Soc. Rev.* **2005**, *34*, 9-21.

24. P. J. Butler, *Philos. Trans. R. Soc. Lond. B*, **1999**, *354*, 537.

25. a) K.C. Nicolaou, E. J. Sorensen, *Classics in Total Synthesis*, Wiley-VCH; Weinheim, **1996**. b) K. C. Nicolaou, S. A. Snyder, *Classics in Total Synthesis II: More Targets, Strategies, Methods*, Wiley-VCH; Weinheim, **2003**.

26. a) E. J. Corey, *Chem. Soc. Rev.* **1988**, *17*, 111. b) E. J. Corey, *Angew. Chem.* **1991**, *103*, 469; *Angew. Chem. Int. Ed.* **1991**, *30*, 455.

27. E. J. Corey, *Pure Appl. Chem.* **1967**, *14*, 19.

28. a) K. C. Nicolaou, Y. Li, K. C. Fylaktakidou, H. J. Mitchell, H.-X. Wei, B. Weyershausen, *Angew. Chem.* **2001**, *113*, 3972; *Angew. Chem. Int. Ed.* **2001**, *40*, 3849. b) K. C. Nicolaou, B. S. Safina, M. Zak, S. H. Lee, M. Nevalainen, M. Bella, A. A. Estrada, C. Funke, F. J. Zécri, S. Bulat, *J. Am. Chem. Soc.* **2005**, *127*, 11159.

29. J. W. Steed, J. L. Atwood, *Supramolecular Chemistry*, 2nd Ed.; John Wiley & Sons; Hoboken, **2009**.

30. D. Braga, *Chem. Commun*. **2003**, 2751.

31. Selected references: a) T. F. A. de Greef, E. W. Meijer, *Aust. J. Chem.* **2010**, *63*, 596. b) T. Aida, E. W. Meijer, S. I. Stupp, *Science* **2012**, *335*, 813. c) J. S. Moore, *Curr. Opin. Colloid Interf. Sci.* **1999**, *4*, 108. d) S. I. Stupp, M. Keser, G. N. Tew, *Polymer* **1998**, *39*, 4505. e) E. Jahnke, I. Lieberwirth, N. Severin, J. P. Rabe, H. Frauenrath, *Angew. Chem.* **2006**, *118*, 5510; *Angew. Chem. Int. Ed.* **2006**, *45*, 5383. f) A. W. Bosman, L. Brunsveld, B. J. B. Folmer, R. P. Sijbesma, E. W. Meijer, *Macromol. Symp.* **2003**, *201*, 143. g) U. Mansfeld, A. Winter, M. D. Hager, R. Hoogenboom, W. Günther, U. S. Schubert, *Polym. Chem.* **2013**, *4*, 113.

32. a) S. J. Rowan, P. T. Mather, *Struct. Bond* **2008**, *128*, 119. b) T. Kato, M. Nakano, T. Moteki, Y. Uryu, S. Ujiie, *Macromolecules* **1995**, *28*, 8875. c) X. Feng, V. Marcon, W. Pisula, M. R. Hansen, J. Kilpatrick, F. Grozema, D. Andrienko, K. Kremer, K. Müllen, *Nature Mater.* **2009**, *8*, 421. d) T. Kato, T. Yasuda, Y. Kamikawa, M. Yoshio, *Chem. Commun.* **2009**, *7*, 729.

33. J.-M. Lehn, *Prog. Polym. Sci.* **2005**, *30*, 814.

34. a) J. D. Fox, S. J. Rowan, *Macromolecules* **2009**, *42*, 6823. b) L. S. Shimizu, *Polym. Int.* **2007**, *56*, 444. c) S. K. Yang, A. V. Ambade, M. Weck, *Chem. Soc. Rev.* **2011**, *40*, 129.

35. a) M. Weck, *Polym. Int.* **2007**, *56*, 453. b) J. M. Pollino, M. Weck, *Chem. Soc. Rev.* **2005**, *34*, 193.

36. a) W. C. Yount, D. M. Loveless, S. L. Craig, *J. Am. Chem. Soc.* **2005**, *127*, 14488. b) W. C. Yount, D. M. Loveless, S. L. Craig, *Angew. Chem.* **2005**, *117*, 2806; *Angew. Chem. Int. Ed.* **2005**, *117*, 2806. c) W. W. Gerhardt, A. J. Zucchero, C. R. South, U. H. F. Bunz, M. Weck, *Chem. Eur. J.* **2007**, *13*, 4467-4474. d) K. P. Nair, V. Breedveld, M Weck, *Macromolecules* **2008**, *41*, 3429. e) J. B. Beck, S. J. Rowan, *J. Am. Chem. Soc.* **2003**, *125*, 13922. f) S. Sivakova, D. A. Bohnsack, M. E. Mackay, P. Suwanmala, S. J. Rowan, *J. Am. Chem. Soc.* **2005**, 127*,* 18202.

37. J.-M. Lehn, *Polym. Int.* **2002**, *51*, 825.

38. M. Kotera, J.-M. Lehn, J.-P. Vigneron, *J. Chem. Soc. Chem. Commun.* **1994**, 197.

39. a) Z. Xu, E. J. Kramer, B. D. Edgecombe, J. M. J. Fréchet, *Macromolecules* **1997**, *30*, 7958. b) T. Kato, J. M. J. Fréchet, *J. Am. Chem. Soc*. **1989**, *111*, 8533. c) H. Kihara, T. Kato, T. Uryu, J. M. J. Fréchet, *Chem. Mater.* **1996**, *8*, 961. d) T. Kato, H. Kihara, U. Kumar, T. Uryu, J. M. J. Fréchet, *Angew. Chem*. **1994**, *106*, 126; *Angew. Chem. Int. Ed.* **1994**, *33*, 1644.

40. a) R. P. Sijbesma, E. W. Meijer, *Chem. Commun.* **2003**, 5. b) F. H. Beijer, H. Kooijman, A. L. Spek, R. P. Sijbesma, E. W. Meijer, *Angew. Chem.* **1998**, *110*, 79; *Angew. Chem. Int. Ed.* **1998**, *37*, 75.

41. a) S. A. Schmid, R. Abbel, A. P. H. J. Schenning, E. W. Meijer, L. M. Herz, *Phil. Trans. R. Soc. A*, **2012**, *370*, 3787. b) R. Abbel, C. Grenier, M. J. Pouderoijen, J. W. Stouwdam, P. D. L. G. Leclère, R. P. Sijbesma, E. W. Meijer, A. P. H. J. Schenning, *J. Am. Chem. Soc*, **2009**, *131*, 833.

42. T. Park, S. C. Zimmerman, *J. Am. Chem. Soc*, **2006**, *128*, 14236.

43. D. J. M. van Beek, A. J. H. Spiering, G. W. M. Peters, K. te Nijenhuis, R. P. Sijbesma, *Macromolecules* **2007**, *40*, 8474.

44. S. A. Schmid, R. Abbel, A. P. H. J. Schenning, E. W. Meijer, R. P. Sijbesma, L. M. Herz, *J. Am. Chem. Soc.* **2009**, *131*, 17696.

45. P. Y. W. Dankers, M. C. Harmsen, L. A. Brouwer, M. J. A. Van Luyn, E. W. Meijer, *Nature* **2005**, *4*, 568.

46. a) R. H. Grubbs, W. Tumas, *Science* **1989**, *243*, 907. b) S. T. Nguyen, L. K. Johnson, R. H. Grubbs, J. W. Ziller, *J. Am. Chem. Soc.* **1992**, *114*, 3974. c) R. R. Schrock, *Acc. Chem. Res.* **1990**, *23*, 158.

47. Selected references: a) M. Weck, B. Mohr, B. R. Maughon, R. H. Grubbs, *Macromolecules* **1997**, *30*, 6430. b) M. Weck, P. Schwab, R. H. Grubbs, *Macromolecules* **1996**, *29*, 1789. c) X. Zheng, C. W. Jones, M. Weck, *J. Am. Chem. Soc.* **2007**, *129*, 1105. d) A. V. Ambade, S. K. Yang, M. Weck, *Angew. Chem.* **1995**, *121*, 2938; *Angew. Chem. Int. Ed.* **1995**, *48*, 2894. e) S. K. Yang, A. V. Ambade, M. Weck, *J. Am. Chem. Soc.* **2010**, *132*, 1637.

48. a) H. Nakade, M. F. Ilker, B. J. Jordan, O. Uzun, N. L. LaPointe, E. B. Coughlin, V. M. Rotello, *Chem. Commun.* **2005**, 3271. b) R. Shenar, T. B. Norsten, V. M. Rotello, *Adv. Mater.* **2005**, *17*, 657. c) H. Xu, S. Sribastava, V. M. Rotello, *Adv. Polym. Sci.* **2007**, *207*, 179.

49. B. M. Mckenzie, S. J. Rowan, in *Molecular Recognition and Polymers: Control of Polymer Structure and Self-Assembly* (Eds: V. Rotello, S. Thayumanavan), John Wiley & Sons, Chichester, **2008**, pp. 157-178.

50. C. A. Schalley, in *Analytical Methods in Supramolecular Chemistry* (Ed: C. A. Schalley), Wiley-VCH, Weinheim, **2007**, pp. 1-16.

51. Selected references: a) R. Hoogenboom, U. S. Schubert, *Chem. Soc. Rev.* **2006**, *35*, 622. b) U. S. Schubert, C. Eschbaumer, *Angew. Chem.* **2002**, *114*, 3016; *Angew. Chem. Int. Ed.* **2002**, *41*, 2892. c) C.-A. Fustin, P. Guillet, U. S. Schubert, F. Gohy, *Adv. Mater.* **2007**, *19*, 1665. d) U. S. Schubert, M. Heller, *Chem. Eur. J.* **2001**, *7*, 5252.

52. Selected references: a) R. Shunmugam, G. J. Gabriel, K. A. Aamer, G. N. Tew, *Macromol. Rapid Comm.* **2010**, *31*, 784. b) R. Dobrawa, M. Lysetska, P. Ballester, M. Grüne, F. Würthner, *Macromolecules* **2005**, *38*, 1315. c) K. J. Calzia, G. N. Tew, *Macromolecules* **2002**, *35*, 6090. d) K. A. Aamer, G. N. Tew, *Macromolecules* **2004**, *37*, 1990. e) G. N. Tew, K. A. Aamer, R. Shumugam, *Polymer* **2005**, *46*, 8440.

53. J. R. Kumpfer, S. J. Rowan, *J. Am. Chem. Soc.* **2011**, *133*, 12866.

54. M. Burnworth, L. Tang, J. R. Kumpfer, A. J. Duncan, F. L. Beyer, G. L. Fiore, S. J. Rowan, C. Weder, *Nature* **2011**, *472*, 334.

55. Selected references: a) D. Pugh, A. A. Danopolus, *Coord. Chem. Rev.* **2007**, *251*, 610. b) R. B. Bedford, S. M. Draper, P. N. Scully, S. L. Welch, *New. J. Chem.* **2000**, *24*, 745. c) S. Gründemann, M. Albrecht, J. A. Loch, J. W. Faller, R. H. Crabtree, *Organometallics* **2001**, *20*, 5485. d) M. Poyatos, J. A. Mata, E. Falomir, R. H. Crabtree, E. Peris, *Organometallics* **2003**, *22*, 1110.

56. a) J. M. Pollino, M. Weck, *Synthesis* **2002**, *9*, 1277. b) J. M. Pollino, M. Weck, *Chem. Soc. Rev.* **2005**, *34*, 193. c) W. Gerhardt, M. Crne, M. Weck, *Chem. Eur. J.* **2004**, *10*, 2612. d) J. M. Pollino, L. P. Stubbs, M. Weck, *Macromolecules* **2003**, *36*, 2230. e) J. M. Pollino, M. Weck, *Org. Lett.* **2002**, *4*, 753. f) J. M. Pollino, K. P. Nair, L. P. Stubbs, J. Adams, M. Weck, *Tetrahedron* **2004**, *60*, 7205.

57. a) V. Piñón, III, M. Weck, *Langmuir* **2012**, *28*, 3279. b) K. P. Nair, V. Breedveld, M. Weck, *Macromolecules* **2011**, *44*, 3346.

58. a) J. J. Green, R. Langer, D. G. Anderson, *Acc. Chem. Res*. **2008**, *41*, 749. b) P. T. Corbett, J. Leclaire, L. Vial, K. R. West, J-L. Wietor, J. K. M. Sanders, *Chem. Rev*. **2006**, *106*, 3652. c) S. Otto, R. L. E. Ricardo, J. K. M. Sanders, *Science* **2002**, *297*, 667.

59. J. Maddox, *Nature* **1988**, *335*, 201.

60. a) G. R. Desiraju, *Acc. Chem. Res.* **2002**, *65*, 565. b) G. R. Desiraju, *Angew. Chem. Int. Ed.* **2007**, *46*, 8346. c) G. R. Desiraju, *Chem. Commun*, **1997**, 1475.

61. M. C. Etter, *J. Chem. Phys*. **1991**, *95*, 4601.

62. R. Robson, *Inorg. Nucl. Chem. Lett.* **1970**, *6*, 125.

63. M. Simard, D. Su, J. D. Wuest, *J. Am. Chem. Soc*. **1991**, *113*, 4696.

64. a) O. Ermer, *J. Am. Chem. Soc.* **1988**, *110*, 3747. b) M. Fujita, J. Yazaki, K. Ogura, *J. Am. Chem. Soc.* **1990**, *112*, 1546.

65. a) B. Moulton, M. J. Zaworotko, *Chem. Rev.* **2001**, *101*, 1629. b) S. Subramanian, M. J. Zaworotko, *Coord. Chem. Rev.* **1994**, *137*, 357. c) M. J. Zaworotko, *Angew. Chem.* **1998**, *110*, 1269; *Angew. Chem. Int. Ed.* **1998**, *37*, 1211.

66. a) D. Braga, F. Grepioni, *Acc. Chem. Res.* **2000**, *33*, 601. b) D. Braga, L. Brammer, N. R. Champness, *CrystEngComm.* **2005**, *7*, 1. c) D. Braga, L. Maini, F. Grepioni, *Angew. Chem.* **1998**, *110*, 2365; *Angew. Chem. Int. Ed.* **1998**, *37*, 2240.

67. a) L. R. MacGillivray, K. T. Holman, J. L. Atwood, *Cryst. Eng.* **1998**, *1*, 87. b) L. R. MacGillivray, *CrystEngComm* **2002**, *4* 37. c) L. R. MacGillivray, *CrystEngComm* **2004**, *6*, 77.

68. a) C. B. Aakeröy, A. M. Beatty, *Aust. J. Chem.* **2001**, *54*, 409. b) C. B. Aakeröy, *Acta Crystallogr.* **1997**, *B53*, 569. c) C. B. Aakeröy, A. M. Beatty, B. A. Helfrich, *Angew. Chem.* **2001**, *113*, 3340; *Angew. Chem. Int. Ed.* **2001**, *40*, 3240.

69. M. Eddaoudi, D. B. Moler, H. L. Li, B. L. Chen, T. M. Reineke, M. O'Keefe, O. M. Yaghi, *Acc. Chem. Res.* **2001**, *34*, 319.

70. a) Ö. Almarsson, M. J. Zaworotko, *Chem. Commun.* **2004**, 1889. b) P. Vishweshwar, J. A. McMahon, J. A. Bis, M. J. Zaworotko, *J. Pharm. Sci*. **2006**, *95*, 499. c) N. Schultheiss, A. Newman, *Cryst. Growth Des.* **2009**, *9*, 2950. d) A. V. Trask, *Mol. Pharm*, **2007**, *4*, 301.

71. a) O. R. Evans, W. Lin, *Acc. Chem. Res.* **2002**, *35*, 511. b) M. D. Hollingsworth, *Science* **2002**, *295*, 2410. c) G. R. Desiraju, *J. Mol. Struct*. **2003**, *656*, 5. d) F. Würthner, R. Schmidt, *ChemPhysChem* **2006**, *7*, 793.

72. a) J. C. Sumrak, A. N. Sokolov, L. R. MacGillivray, in *Self-Organized Organic Semiconductors: From Materials to Device Applications*, John Wiley & Sons, Hoboken, **2010**, pp. 1-19. b) A. N. Sokolov, T. Friščić, L. R. MacGillivray, *J. Am. Chem. Soc.* **2006**, *128*, 2806. c) P. P. Kapadia, L. R. Ditzler, J. Baltrusaitis, D. C. Swenson, A. V. Tivanski, F. C. Pigge, *J. Am. Chem. Soc.* **2011**, *133*, 8490.

73. a) J. R. Carlisle, M. Weck, in *Functional Organic Materials: Syntheses, Strategies and Applications* (Eds: J. J. Müller, U. H. F. Bunz), Wiley-VCH, Weinheim, **2007**, pp. 261-292. b) L. J. Prins, D. N. Reinhoudt, P. Timmerman, *Angew. Chem.* **2001**, *113*, 2446; *Angew. Chem. Int. Ed.* **2001**, *40*, 2382.

74. J. D. Dunitz, *CrystEngComm* **2003**, *5*, 506.

75. A. D. Bond, *CrystEngComm* **2007**, *9*, 833.

76. E. Elacqua, R. C. Laird, L. R. MacGillivray, in *Supramolecular Chemistry: From Molecules to Materials,* Vol. 6 (Eds: P. A. Gale, J. W. Steed), John Wiley & Sons, Chichester, **2012**, pp. 3153-3165.

77. L. R. MacGillivray, *J. Org. Chem.* **2008**, *73*, 3311.

78. a) S. J. Nehm, B. Rodríguez-Spong, N. Rodríguez-Hornedo, *Cryst. Growth Des.* **2006**, 6, 592. b) J. F. Remenar, S. L. Morrisette, M. L. Peterson, B. Moulton, J. M. MacPhee, H. Guzman, Ö. Almarsson, *J. Am. Chem. Soc*. **2003**, 125, 8456. c) S. L. Childs, L. J. Chyall, J. T. Dunlap, V. N. Smolenskaya, B. C. Stahly, G. P. Stahly, *J. Am. Chem. Soc.* **2004**, 126, 13335. d) D. P. McNamara, S. L. Childs, J. Giordano, A. Iarriccio, A. J. Cassiddy, M. S. Shet, R. Mannion, E. O'Donnell, A. Park, *Pharm. Res.* **2006**, 23, 1888. e) A. V. Trask, W. D. S. Motherwell, W. Jones, *Int. J. Pharm.* **2006**, 320, 114. g) S. Karki, T. Friščić, P. R. Laity, G. M. Day, W. Jones, *Adv. Mater.* **2009**, 21, 3905.

79. D. Yan, A. Delori, G. O. Lloyd, T. Friščić,G. M. Day, W. Jones, J. Lu, M. Wei, D. G. Evans, X. Duan, *Angew. Chem.* **2011**, *123*, 12691; *Angew. Chem. Int. Ed.* **2011**, *50*, 12483.

80. K. C. Nicolaou, S. A. Snyder, *Proc. Natl. Acad. Sci.* **2004**, *101*, 11929.

81. L. R. MacGillivray, G. S. Papaefstathiou, T. Friščić, T. Hamilton, D.-K. Bučar, Q. Chu, D. B. Varshney, I. G. Georgiev, *Acc. Chem. Res*. **2008**, *41*, 280.

82. a) V. Ramamurthy, K. Ventatesan, *Chem. Rev.* **1997**, *82*, 1. b) M. Nagarthinam, J. J. Vittal, *Chem. Commun.* **2008**, 438.

83. a) M. D. Cohen, G. M. J. Schmidt, *J. Chem. Soc.* **1964**, 2000. b) G. M. J. Schmidt, *Pure Appl. Chem.* **1971**, *27*, 647. c) G. M. J. Schmidt, *J. Chem. Soc.* **1964**, 2014.

84. G. R. Desiraju, *Angew. Chem.* **2007**, *44*, 8492; *Angew. Chem. Int. Ed.* **2007**, *46*, 8342.

85. a) K. V. Radha Kishan, G. R. Desiraju, *J. Org. Chem*. **1987**, *52*, 4640. a) J. H. Kim, S. M. Hubig, S. V. Lindeman, J. K. Kochi, *J. Am. Chem. Soc.* **2001**, *123*, 87. b) J. H. Kim, S. M. Hubig, S. V. Lindeman, J. K. Kochi, *J. Am. Chem. Soc*. **2001**, *123*, 87.

86. a) Y. Ito, H. Fujita, *J. Org. Chem.* **1996**, *61*, 5677. b) H. Ihmels, D. Leusser, M. Pfeiffer, D. Stalke, *Tetrahedron* **2000**, *56*, 6867. b) M. Horiguchi, Y. Ito, *J. Org. Chem.* **2006**, *71*, 3608.

87. a) T. R. Kelly, C. Zhao, G. J. Bridger, *J. Am. Chem. Soc.* **1989**, *111*, 3744. b) D. M. Bassani, V. Darcos, S. Mahony, J.-P. Desvergne, *J. Am. Chem. Soc.* **2000**, *122*, 8795. c) T. R. Kelly, G. J. Bridger, C. Zhao, C. *J. Am. Chem. Soc.* **1990**, *112*, 8024.

88. L. R. MacGillivray, J. L. Reid, J. A. Ripmeester, *J. Am. Chem. Soc.* **2000**, *122*, 7817.

89. a) D. G. Amiraskis, M. A. Garcia-Garibay, S. J. Rowan, J. F. Stoddart, A. J. P. White, D. J. Williams, *Angew. Chem.* **2001**, *113*, 4386; *Angew. Chem. Int. Ed.* **2001**, *40*, 4256. b) D. L. Caulder, K. N. Raymond, *Acc. Chem. Res.* **1999**, *32*, 975.

90. G. S. Papaefstathiou, A. J. Kipp, L. R. MacGillivray, *Chem. Commun.* **2001**, 2462.

91. N. Shan, W. Jones, *Tetrahedron Lett.* **2003**, *44*, 3687.

92. D. B. Varshney, X. Gao, T. Friščić, L. R. MacGillivray, *Angew. Chem.* **2006**, *118*, 662; *Angew. Chem. Int. Ed.* **2006**, *45*, 646.

93. L. R. MacGillivray, J. L. Reid, J. A. Ripmeester, G. S. Papaefstathiou, *Ind. Eng. Chem. Res.* **2002**, *41*, 4494.

94. B. R. Bhogala, B. Captain, A. Parthasarthy, V. Ramamurthy, *J. Am. Chem. Soc*. **2010**, *132*, 13434.

95. X. Gao, T. Friščić, L. R. MacGillivray, *Angew. Chem.* **2004**, *116*, 234; *Angew. Chem. Int. Ed*. **2004**, *43*, 232.

96. a) T. Friščić, L. R. MacGillivray, *Chem. Commun*. **2003**, 1306. b) T. Friščić, L. R. MacGillivray, *Aust. J. Chem*. **2006**, *59*, 613.

97. M. Khan, V. Enkelmann, G. Brunklaus, *Cryst. Growth Des*. **2009**, *9*, 2354.

98. R. Santra, K. Biradha, *CrystEngComm* **2008**, *10*, 1524.

99. T. Friščić, L. R. MacGillivray, *Chem. Commun*. **2005**, 5748.

100. X. Mei, S. Liu, C. Wolf, *Org. Lett*. **2007**, *9*, 2729.

101. T. Caronna, R. Liantonio, T. A. Logothetis, P. Metrangolo, T. Pilati, G. Resnati, *J. Am. Chem. Soc*. **2004**, *126*, 4500.

102. D.-K. Bučar, G. S. Papaefstathiou, T. D. Hamilton, Q. Chu, I. G. Georgiev, L. R. MacGillivray, *Eur. J. Inorg. Chem*. **2007**, *29*, 4559.

103. G. S. Papaefstathiou, Z. Zhou, L. Geng, L. R. MacGillivray, *J. Am. Chem. Soc.* **2004**, *126*, 9158.

104. a) Y.-F. Han, Y.-J. Lin, G.-L. Wang, G.-X. Jin, *Chem. Commun*. **2008**, 1807. b) W.-Z. Zhang, Y.-F. Han, Y.-J. Lin, G.-X. Jin, *Organometallics* **2010**, *29*, 2842.

105. Q. Chu, D. C. Swenson, L. R. MacGillivray, *Angew. Chem.* **2005**, *117*, 3635; *Angew. Chem. Int. Ed*. **2005**, *44*, 3569.

106. I. G. Georgiev, D.-K. Bučar, L. R. MacGillivray, *Chem. Commun*. **2010**, 4956.

107. A. Michaelides, S. Skoulika, M. G. Siskos, *Chem. Commun*. **2004**, 2418.

108. L. N. Toh, M. Nagarathinam, J. J. Vittal, *Angew. Chem.* **2005**, *117*, 2277; *Angew. Chem. Int. Ed*. **2005**, *44*, 2237.

109. G. S. Papaefstathiou, I. G. Georgiev, T. Friščić, L. R. MacGillivray, *Chem. Commun.* **2005**, 3974.

110. M. Nagarathinam, J. J. Vittal, *Angew. Chem.* **2006**, *118*, 4443; *Angew. Chem. Int. Ed.* **2006**, *45*, 4337.

111. M. Nagarathinam, J. J. Vittal, *Chem. Commun*. **2008**, 438.

112. A. M. P. Peedikakkal, J. J. Vittal, *Inorg. Chem.* **2010**, *49*, 10.

113. X.-H. Miao, L.-G. Zhu, *Dalton Trans.* **2010**, *39*, 1457.

114. A. Michaelides, S. Skoulika, M. G. Siskos, *CrystEngComm* **2008**, *10*, 817.

115. M. H. Mir, L. L. Koh, G. K. Tan, J. J. Vittal, *Angew. Chem.* **2010**, *122*, 400; *Angew. Chem. Int. Ed*. **2010**, *49*, 390.

116. J. F. Eubank, V. C. Kravtsov, M. Eddauodi, *J. Am. Chem. Soc.* **2007**, *129*, 5820.

117. D. Liu, Z.-G. Ren, H.-X. Li, J.-P. Lang, N.-Y. Li, B. F. Abrahams, *Angew. Chem.* **2010**, *122*, 4877; *Angew. Chem. Int. Ed*. **2010**, *49*, 4767.

118. A. Briceño, Y. Hill, T. Gonzalez, G. Dıaz de Delgado, *Dalton Trans*. **2009**, 1602.

119. Y. Hill, A. Briceño, *Chem. Commun*. **2007**, 3930.

120. A. M. P. Peedikakkal, J. J. Vittal, *Chem. Eur. J.* **2008**, *14*, 5329.

121. a) J. Hu, L. J. Barbour, G. W. Gokel, *New J. Chem*. **2004**, *28*, 907. b) G. W. Gokel, *Chem. Commun*. **2003**, *23*, 3251.

122. a) H. Koshima, A. Maeda, N. Masuda, T. Matsuura, T. Hirostu, K. Okada, H. Mizutari, Y. Ito, *Tetrahedron: Asymmetry* **1994**, *5*, 1415. b) H. Hosomi, Y. Ito, *Acta Crystallogr*. **2000**, *B56*, 682.

123. a) L. G. Kuz'mina, A. I. Vedernikov, S. K. Sazonov, N. A. Lobova, P. S. Loginov, J. A. K. Howard, M. V. Alfimov, S. P. Gromov, *Crystallogr. Rep*. **2008**, *53*, 428. b) E. V. Tulyakova, O. A. Federova, Y. V. Federov, A. V. Anisimov, *J. Photochem. Photobiol. A Chem*. **2008**, *200*, 90. c) L. G. Kuz'mina, A. I. Vedernikov, N. A. Lobova, A. V. Churakov, J. A. K. Howard, M. V. Alfimov, S. P. Gromov, *New J. Chem*. **2007**, *31*, 980. d) A. I. Vedernikov, S. P. Gromov, N. A. Lobova, L. G. Kuz'mina, Y. A. Strelenko, J. A. K. Howard, M. V. Alfimov, *Russ. Chem. Bull. Int. Ed*. **2005**, *54*, 1954.

124. G. K. Kole, G. K. Tan, J. J. Vittal, *Org. Lett*. **2010**, *12*, 128.

125. G. K. Kole, L. L. Koh, S. Y. Lee, S. Sung, J. J. Vittal, *Chem. Commun*. **2010**, *46*, 3660.

126. M. Linares, A. Briceño, *New J. Chem*. **2010**, *34*, 587.

127. K. S. Feldman, R. F. Campbell, *J. Org. Chem*. **1995**, *60*, 1924.

128. R. C. Grove, S. H. Malehorn, M. E. Breen, K. A. Wheeler, *Chem. Commun.* **2010**, *46*, 7322.

129. G. W. Coates, A. R. Dunn, L. M. Henling, J. W. Ziller, E. B. Lobkovsky, R. H. Grubbs, *J. Am. Chem. Soc.* **1998**, *120*, 3641.

130. a) G. R. Desiraju, R. Parthasarathy, *J. Am. Chem. Soc.* **1989**, *111*, 8725. b) J. H. Kim, S. M. Hubig, S. V. Lindeman, J. K. Kochi, *J. Am. Chem. Soc.* **2001**, *123*, 87.

131. a) O. K. Farha, J. Y. Hupp, *Acc. Chem. Res.* **2010**, *43*, 1166. b) R. A. Smaldone, R. S. Forgan, H. Furukawa, J. J. Gassensmith, A. M. Z. Slawin, O. M. Yaghi, J. F. Stoddart, *Angew. Chem.* **2010**, *122*, 8812; *Angew. Chem. Int. Ed.* **2010**, *49*, 8630. c) S. L. James, *Chem. Soc. Rev.* **2003**, *32*, 276. c) L. J. Murray, M. Dinča, J. R. Long, *Chem. Soc. Rev.* **2009**, *38*, 1294. d) N. L. Rosi, J. Kim, M. Eddaoudi, B. Chen, M. O'Keeffe, O. M. Yaghi, *J. Am. Chem. Soc.* **2005**, *127*, 1504.

132. a) J. C. Groen, L. A. A. Peffer, J. Pérez-Ramírez, *Micropor. Mesopor. Mat.* **2003**, *60*, 1. b) A. Taguchi, F. Schüth, *Micropor. Mesopor. Mat.* **2005**, *77*, 1. c) A. Corma, *Chem. Rev.* **1997**, *97*, 2373.

133. T. D. Hamilton, G. S. Papaefstathiou, L. R. MacGillivray, *CrsytEngComm* **2002**, *4*, 223.

134. G. S. Papaestathiou, L. R. MacGillivray, *Angew. Chem.* **2002**, *114*, 2174; *Angew. Chem. Int. Ed.* **2002,** 41, 2070.

135. G. S. Papaefstathiou, C. Milios, L. R. MacGillivray, *Micropor. Mesopor. Mat.* **2004**, *71*, 11.

136. G. S. Papaefstathiou, T. Friščić, L. R. MacGillivray, *J. Am. Chem. Soc.* **2005**, *127*, 14160.

137. a) T. Friščić, L. R. MacGillivray, *Z. Kristallogr.* **2005,** 220, 351. b) I. Halasz, *Cryst. Growth Des*. **2010**, 10, 2817.

138. a) S. M. Neville, G. J. Halder, K. W. Chapman, M. B. Duriska, P. D. Southon, J. D. Cashion, J.-F. Létard, B. Moubaraki, K. S. Murray, C. J. Kepert, *J. Am. Chem. Soc.* **2008**, *130*, 2869. b) T. K. Maji, G. Mostafa, R. Matsuda, S. Kitagawa, *J. Am. Chem. Soc.* **2005**, *127*, 17152. c) H. J. Park, M. P. Suh, *Chem. Eur. J.* **2008**, *14*, 8812.

139. D.-K. Bučar, L. R. MacGillivray, *J. Am. Chem. Soc.* **2006**, *129*, 32.

140. C. Karunatilaka, D.-K. Bučar, L. R. Ditzler, T. Friščić, D. C. Swenson, L. R. MacGillivray, A. V. Tizanski, *Angew. Chem.* **2011**, *123*, 8801; *Angew. Chem. Int. Ed.* **2011**, *50,* 8642.

141. Y. Qiu, Y. Chen, G. G. Z. Zhang, L. Liu, W. Porter, *Developing Solid Oral Dosage Forms: Pharmaceutical Theory & Practice*. 1st Ed.; Elsevier: New York, **2009**.

142. a) R. J. Bastin, M. J. Bowker, B. J. Slater, *Org. Process Res. Dev.* **2000**, 4, 427. b) S. L. Morissette, Ö. Almarsson, M. L. Peterson, J. F. Remenar, M. J. Read, A. V. Lemmo, S. Ellis, M. J. Cima, C. R. Gardner, *Adv. Drug Del. Rev.* **2004**, 56, 275. c) A. T. M. Serajuddin, *Adv. Drug Del. Rev.* **2007**, 89, 603.

143. J. Bernstein, *Polymorphism in Molecular Crystals*, Vol. 14, Oxford University Press: New York, **2002**.

144. a) C. B. Aakeröy, M. Fasulo, N. Schultheiss, J. Desper, C. Moore, *J. Am. Chem. Soc.* **1997**, *129*, 13772. b) A. D. Burrows, *Struct. Bond* **2004**, *104*, 55.

145. a) S. Karki, T. Friščić, W. Jones, W. D. S. Motherwell, *Mol. Pharm.* **2007**, *4* 347. b) T. Friščić, A. V. Trask, W. Jones, W. D. S. Motherwell, *Angew. Chem.* **2006**, *118*, 7708; *Angew. Chem. Int. Ed.* **2006**, *45*, 7546.

146. G. G. Z. Zhang, R. F. Henry, T. B. Borchardt, X. Lou, *J. Pharm. Sci.* **2007**, *96*, 990.

147. T. Friščić, W. Jones, *Cryst. Growth Des.* **2009**, *9*, 1621.

148. a) T. Friščić, L. Fábián, J. C. Burley, W. Jones, W. D. S. Motherwell, *Chem.Commun.* **2006**, 5009. b) J. Stojaković, B. S. Farris, L. R. MacGillivray, *Chem. Commun.* **2012**, *48*, 7958.

149. a) S. E. A. Gratton, S. S. Williams, M. E. Napier, P. D. Pohlhaus, Z. Zhou, K. B. Wiles, B. W. Maynor, C. Shen, T. Olafsen, E. T. Samulski, J. M. DeSimone, *Acc. Chem. Res.* **2008**, *41*, 1685. b) S. G. Kwon, T. Hyeon, *Acc. Chem. Res.* **2008**, *41*, 1696.

150. a) C. A. Fernandez, S. K. Nune, R. K. Motkuri, P. K. Thallapally, C. Wang, J. Liu, G. J. Exarhos, B. P. MacGrail, *Langmuir* **2010**, *26*, 18591. b) D. A. Stone, A. S. Tayi, J. E. Goldberger, L. C. Palmer, S. I. Stupp, *Chem. Commun.* **2011**, *47*, 5702. c) H. Oikawa, T. Onodera, A. Masuhara, H. Kasai, H. Nakanishi, *Adv. Polym. Sci.* **2010**, *231*, 147. d) A. Kaesar, A. P. H. J. Schenninc, *Adv. Mater.* **2010**, *22*, 2985. e) R. Klajn, J. F. Stoddart, B. A. Grzybowski, *Chem. Soc. Rev.* **2010**, *39*, 2203.

151. a) X. Hu, L. Zhao, C. Gao, *Colloid Polym. Sci.* **2011**, *289*, 1299. b) A. Pucci, G. Ruggeri, S, Bronco, F. Signori, F. Donati, M. Bernabò, F. Ciardelli, *Prog. Org. Coat.* **2011**, *72,* 21. c) S. B. Jo, W. H. Lee, L. Qiu, K. Cho, *J. Mater. Chem.* **2010**, *22*, 4244.

152. a) M.-L. Zheng, Q.-L. Tang, W.-Q. Chen, X.-M. Duan, *J. Nanosci. Nanotech.* **2009**, *9*, 1291. b) L. Zang, Y. Che, J. S. Moore, *Acc. Chem. Res.* **2008**, *41*, 1596. c) S.-J. Lim, B.-K. An, S. D. Jung, M.-A. Chung, S. Y. Park, *Angew. Chem.* **2004**, *116*, 6506; *Angew. Chem. Int. Ed.* **2004**, *43*, 6346.

153. B.-K. An, S.-K. Kwon, S.-D. Jung, S. Y. Park, *J. Am. Chem. Soc.* **2002**, *124*, 14410.

154. a) S. W. Thomas, G. D. Joly, T. M. Swager, *Chem. Rev.* **2007**, *107*, 1339. b) S.-J. Chung, K.-Y. Kwon, S.-W. Lee, J.-I. Jin, C. H. Lee, C. E. Lee, Y. Park, *Adv. Mater.* **1998**, *10*, 1112.

155. R. Deans, J. Kim, M. R. Machacek, T. M. Swager, *J. Am. Chem. Soc.* **2000**, *122*, 8565

156. M. Levitus, K. Schmieder, H. Ricks, K. D. Shimizu, U. H. F. Bunz , M. A. Garcia-Garibay, *J. Am. Chem. Soc.* **2001**, *123*, 4259.

157. G. Jones, II, C. Oh, *J. Phys. Chem.* **1994**, *98*, 2367.

158. J. Liu, J. W. Y. Lam, B. Z. Tang, *J. Inorg. Organomet. Polym.* **2009**, *19*, 249.

159. a) C. Zhao, Z. Wang, Y. Yang, C. Feng, A. Li, Y. Li, Y. Zhang, F. Bao, Y. Xing, X. Zhang, X. Zhang, *Cryst. Growth Des.* **2012**, *12*, 1227. b) Y.-X. Li, J. Jia, X.-T. Tao, *CrystEngComm* **2012**, *14*, 2843. c) Y. Dong, J. W. Y. Lan, A. Qin, J. Sun, J. Liu, Z. Li, J. Sun, H. H. Y. Sung, I. D. Williams, H. S. Kwok, B. Z. Tang, *Chem. Commun.* **2007**, 3255. d) Y. Qian, M. Cai, X. Zhou, Z. Gao, X. Wang, Y. Zhao, X. Yan, W. Wei, L. Xie, W. Huang, *J. Phys. Chem. C.* **2012**, *116*, 12187. e) H. Tong, Y. Dong, Y. Hong, M. Häussler, J. W. Y. Lan, H. H.-Y. Sung, X. Yu, J. Sun, I. D. Williams, H. S. Kwok, B. Z. Tang, *J. Phys. Chem. C.* **2007**, *111*, 2287.

160. a) J. Mei, J. Wang, J. Z. Sun, H. Zhao, W. Yuan, C. Deng, S. Chen, H. H. Y. Sung, P. Lu, A. Qin, H. S. Kwok, Y. Ma, I. D. Williams, B. Z. Tang, *Chem. Sci*. **2012**, *3*, 549. b) Z. Yan, H. Xu, S. Guang, X. Zhao, W. Fan, X. Y. Liu, *Adv. Funct. Mater.* **2012**, *22*, 345. c) M. L. Ferrer, F. del Monte, *J. Phys. Chem. B*. **2005**, *190*, 80. d) W. Wu, S. Ye, L. Xiao, Y. Fu, Q. Huang, G. Yu, Y. Liu, J. Qin, Q. Li, Z. Li, *J. Mater. Chem.* **2012**, *22*, 6374. e) H.-H. Fang, Q.-D. Chen, J. Yang, Z. Xia, B.-R. Gao, J. Feng, Y.-G. Ma, H.-B. Sun, *J. Phys. Chem. C.* **2010**, *114*, 11958. f) Y. Hong, J. W. Y. Lan, B. Z. Tang, *Chem. Commun*. **2009**, 4332. g) Q. Dai, W. Liu, L. Zeng, C.-S. Lee, J. Wu, P. Wang, *CrystEngComm* **2011**, *13*, 4617.

161. a) E. Cariati, R. Macchi, D. Roberto, R. Ugo, S. Galli, N. Masciocchi, A. Sironi, *Chem. Mater.* **2007**, *19*, 3704. b) S. Biswas, H.-Y Ahn, M. V. Bondar, K. D. Belfield, *Langmuir* **2012**, *28*, 1515.

162. E. Elacqua, D.-K. Bučar, R. F. Henry, G. G. Z. Zhang, L. R. MacGillivray, *Cryst. Growth Des.* **2013**. (DOI: 10.1021/cg301745x).

163. E. Elacqua, R. F. Henry, G. G. Z. Zhang, L. R. MacGillivray, *unpublished results*.

164. E. Elacqua, S. Chen, H. Xi, R. F. Henry, G. G. Z. Zhang, L. R. MacGillivray, *in preparation.*

165. E. Elacqua, P. Kaushik, R. H. Groeneman, J. C. Sumrak, D.-K. Bučar, L. R. MacGillivray, *Angew. Chem.* **2012**, *124*, 1061; *Angew. Chem. Int. Ed.* **2012**, *51*, 1037.

166. E. Elacqua, B. P. Loren, P. T. Jurgens, E. W. Reinheimer, L. R. MacGillivray, *in preparation*.

167. T. Friščić, S. Dutta, E. Elacqua, L. R. MacGillivray, *in preparation.*

168. E. Elacqua, T. Friščić, L. R. MacGillivray, *Isr. J. Chem.* **2012**, *52*, 53.

169. a) E. Elacqua, D.-K. Bučar, Y. Skvortsova, J. Baltrusaitis, M. L. Geng, L. R. MacGillivray, *Org. Lett.* **2009**, *11*, 5106. b) E. Elacqua, L. R. MacGillivray, *Eur. J. Org. Chem.* **2010**, 6883. c) E. Elacqua, P. T. Jurgens, D.-K. Bučar, J. Batrusaitis, L. R. MacGillivray, *unpublished results*.

170. E. Elacqua, R. H. Groeneman, B. P. Loren, L. R. MacGillivray, *unpublished results*.

171. E. Elacqua, P. T. Jurgens, J. Baltrusaitis, L. R. MacGillivray, *CrystEngComm* **2012**, *14*, 7567.

172. a) C. J. Pace, H. Zheng, R. Mylvaganam, D. Kim, J. Gao, *Angew. Chem.* **2012**, *124*, 107; *Angew. Chem. Int. Ed.* **2012**, *51*, 103. b) J. Zuckerman-Schpector, I. Haiduc, E. R. T. Tiekink, *Chem. Commun.* **2011**, *47*, 12682. c) A. Dey, M. T. Kirchner, V. R. Vangala, G. R. Desiraju, R. Mondal, J. A. K. Howard, *J. Am. Chem. Soc.* **2005**, *127*, 10545. d) R. S. Reddy, D. C. Craig, G. R. Desiraju, *J. Am. Chem. Soc.* **1996**, *118*, 4090.

173. a) P. Kavuru, D. Aboraryes, K. K. Arora, H. D. Clarke, A. Kennedy, L. Marshall, T. T. Ong, J. Perman, T. Pujari, L. Wojtas, M. J. Zaworotko, *Cryst. Growth Des.* **2010**, *10*, 3568. b) T. R. Shattock, K. K. Arora, P. Vishweshwar, M. J. Zaworotko, M. J. *Cryst. Growth Des.* **2008**, *8*, 4533. c) J. A. Bis, P. Vishweshwar, D. Weyna, M. J. Zaworotko, *Mol. Pharm.* **2007**, *4*, 401.

174. a) K. Bica, J. Shamshina, W. L. Hough, D. MacFarlane, R. D. Rogers, *Chem. Commun.* **2011**, *47*, 2267. b) A. Mukherjee, G. R. Desiraju, *Chem. Commun.* **2011**, *47*, 4090. c) D. Cinčić, T. Friščić, W. Jones, *J. Am. Chem. Soc.* **2008**, *130*, 7524.

175. a) A. V. Trask, W. D. S. Motherwell, W. Jones, *Cryst. Growth Des.* **2005**, *5*, 1013. b) C. C. Sun, H. Hou, *Cryst. Growth. Des.* **2008**, *8*, 1575. c) D.-K. Bučar, R. F. Henry, X. Lou, R. W. Duerst, L. R. MacGillivray, G. G. Z. Zhang, *Cryst. Growth Des.* **2009**, *9*, 1932. d) D.-K. Bučar, R. F. Henry, X. Lou, T. B. Borchardt, G. G. Z. Zhang, *Chem. Commun.* **2007**, 525.

176. a) A. J. Florence, A. Johnston, S. L. Price, H. Nowell, A. R. Kennedy, N. Shankland, N. *J. Pharm. Sci*. **2006**, *95*, 1918. b) A. J. Florence, C. K. Leech, N. Shankland, K. Shankland, A. Johnston, *CrystEngComm* **2006**, *8*, 746. c) W. W. Porter (III), S. G. Elie, A. J. Matzger, *Cryst. Growth Des.* **2008**, *8*, 14. d) M. Habgood, M. A. Deij, J. Mazurek, S. L. Price, J. H. ter Horst, *Cryst. Growth Des.* **2010**, *10*, 903.

177. N. A. Meanwell, N. A. *Annu. Rep. Med. Chem*. **2008**, *43*, 373.

178. a) N. R. Goud, N. J. Babu, A. Nangia, *Cryst. Growth Des.* **2011**, *11*, 1930. b) N. Brondel, E. J. A. Moynihan, K. N. Lehane, K. S. Eccles, C. J. Elcoate, S. J. Coles, S. E. Lawrence, A. R. Maguire, *CrystEngComm* **2010**, *12*, 2910. c) K. S. Eccles, C. J. Elcoate, S. P. Stokes, A. R. Maguire, S. E. Lawrence, *Cryst. Growth Des.* **2010**, *10*, 4243. d) K. S. Eccles, C. J. Elcoate, A. R. Maguire, S. E. Lawrence, *Cryst. Growth Des.* **2011**, *11*, 4433.

179. D. A. Haynes, J. A. Chisholm, W. Jones, W. D. S. Motherwell, *CrystEngComm* **2004**, *6*, 584.

180. a) D. A. Adsmond, D. J. Grant, *J. Pharm. Sci*. **2001**, *90*, 2058. b) G. L. Perlovich, A. M. Ryzhakov, V. V. Tkachev, L. K. Hansen, *Cryst. Growth Des.* **2010**, *11*, 1067.

181. a) M. R. Caira, *Mol. Pharm.* **2007**, *4*, 310. b) S. Ghosh, P. P. Bag, C. M. Reddy, *Cryst. Growth Des.* **2011**, *11*, 3489.

182. a) J. M. McIntosh, R. H. M. Robinson, F. R. Selbie, J. P. Reidy, H. Elliott Blake, L. Guttman, *Lancet,* **1945**, *246*, 97. b) E. Jawetz, Sulfonamides and Trimethoprim. In *Basic & Clinical Pharmacology*, 2nd ed.; (Ed: B. G. Katzung) Lange Medical Publications: Los Altos, **1984**, pp. 554-558.

183. a) M. Khan, M.; V. Enkelmann, G. Brunkalus, *J. Am. Chem. Soc.* **2010**, *132*, 5254. b) P. Vishweshwar, J. A. McMahon, J. A. Bis, M. J. Zaworotko, *J. Pharm. Sci.* **2006**, *3* 499. c) W. Jones, W. D. S. Motherwell, A. V. Trask, *MRS Bulletin,* **2006**, *31* 875. d) N. Shan, M. J. Zaworotko, *Drug Discov. Today,* **2008**, *13*, 440. e) C. B. Aakeröy, S. Forbes, J. Desper, J. *J. Am. Chem. Soc.* **2009**, *131*, 17048.

184. a) V. V. Joshi, R. K. Tiwari, T. C. Patel, T. P. Singh, *Indian J. Phys. A*. **1983**, *57A*, 79. b) H. S. Shin, G. S. Ihn, H. S. Kim, C. H. Koo, *J. Korean. Chem. Soc*. **1974**, *18*, 329.

185. a) B. Sarma, R. Thakuria, N. K. Nath, A. Nangia, *CrystEngComm*. **2011**, *13*, 3232. b) A. Nangia, *Cryst. Eng.* **2001**, *4*, 49. c) P. Vishweshwar, A. Nangia, V. M. Lynch, *Cryst. Growth Des.* **2003**, *3*, 783. d) Ö. Almarsson, M. J. Zaworotko, *Chem. Commun*. **2004**, 1889. e) G. R. Desiraju, *J. Chem. Sci.* **2010**, *122*, 667.

186. D.-K. Bučar, R. F. Henry, X. Lou, R. W. Duerst, T. B. Borchardt, L. R. MacGillivray, G. Z. Z. Zhang, *Mol. Pharm.* **2007**, *4*, 339.

187. a) S. G. Fleischman, S. S. Kuduva, J. A. McMahon, B. Moulton, R. Bailey Walsh, N. Rodríguez-Hornedo, M. J. Zaworotko, *Cryst. Growth Des.* **2003**, *3*, 909. b) S. L. Childs, N. Rodríguez-Hornedo, L. S. Reddy, A. Jayasankar, C. Maheshwari, L. McCausland, R. Shipplett, B. C. Stahly, *CrystEngComm* **2008**, *10*, 856.

188. pK_a values were calculated using a single point calculation in SPARC pK_a calculator (http://sparc.chem.uga.edu/sparc/)

189. CCDC refcodes: IRILUQ, HEKRUK, IRILOK, IRIMEB, IRIMEB01, QASHAX, XIFKUT, SMZTMP01, SORWIF, YOSMOI, RASSUZ, VIGVOW, YIZQAA, COVXIU, SACCAF, QASHAB, RIWLOY, YIDJIE, XOBCOH, HADNAB, SORWEB, VUGMIT, DAHNIJ, GEYSAE, GEYSAE01, HADMOO, PVVAWG01, VUGMOZ, XEXCAE, XEXCEI, SABDOQ, AWIJEW, EXAMUM, EXANAT, EXANEX, EXANIB, EXANOH, EXANUN, EXAPEZ, EXAPID, EXAPID01, EXAPUP.

190. a) S. L. Childs, G. P. Stahly, A. Park, *Mol. Pharm.* **2007**, *4*, 323. b) B. R. Bhogala, B. R. Basavoju, A. Nangia, *CrystEngComm* **2005**, *7*, 551. c) S. Mohamed, D. A. Tocher, M. Vickers, P. G. Karamertzanis, S. L. Price, *Cryst. Growth Des.* **2009**, *9*, 2881.

191. a) M. C. Etter, J. C. MacDonald, J. Bernstein, *Acta Crystallogr.* **1990**, *B46*, 256. b) J. Bernstein, R. E. Davis, L. Shimoni, N.-L. Chang, *Angew. Chem.* **1995**, *107*, 1708; *Angew. Chem. Int. Ed*. **1995**, *34*, 1555.

192. J. A. Bis, M. J. Zaworotko, *Cryst. Growth Des.* **2005**, *5*, 1169.

193. A. J. Cruz-Cabeza, C. R. Groom, *CrystEngComm* **2011**, *13*, 93.

194. a) A. R. Katritzky, C. D. Hall, B. E.-D. M. El-Gendy, B. Draghici, *J. Comput. Aided Mol. Des.* **2010**, *24*, 475. b) Y. C. Martin, *J. Comput. Aided Mol. Des.* **2010**, *23*, 693.

195. B. J. Coe, J. L. Harries, J. A. Harris, B. Brunschwig, S. J. Coles, M. E. Light, M. B. Hursthouse, *Dalton Trans.* **2004**, *18*, 2935.

196. *SaintPlus*, Bruker AXS Inc.: Madison, WI, USA, 1999.

197. R. W. W. Hooft, Nonius, BV, Delft, The Netherlands, 1998.

198. Z. Otwinowski, W. Minor, In *Methods in Enzymology*, Vol. 276 (Eds: C. W. Carter Jr. R. M. Sweet), Academic Press, New York, **1997**, pp. 307-326.

199. G. M. Sheldrick, *Acta Crystallogr.* **2008**, *A64*, 112-122.

200. I. J. Bruno, J. C. Cole, P. R. Edgington, M. Kessler, C. F. Macrae, *Acta. Crystallogr.* **2002**, *B58*, 389.

201. L. Infantes, L. Fábián, W. D. S. Motherwell, *CrystEngComm* **2007**, *9*, 65. b) A. J. Cruz-Cabeza, E. Pidcock, G. M. Day, W. D. S. Motherwell, W. Jones, *CrystEngComm* **2007**, *9*, 556. c) P. A. Wood, S. J. Borwick, D. J. Watkin, W. D. S. Motherwell, F. H. Allen, *Acta Crystallogr.* **2008**, *B64*, 393.

202. The reported inclusion complex of sulfamethazine and β-cyclodextrin (refcode: LILLUN) was excluded, since the compounds of interest were organic co-crystals, salts, or solvates. In addition, the reported complex of sulfamethazine and trimethoprim (refcode: SMZTMP) was excluded since the complex was incorrectly characterized as a co-crystal.

203. a) J. Rebek, Jr., B. Askew, M. Killoran, D. Nemeth, F.-T. Lin, *J. Am. Chem. Soc.* **1987**, *109*, 2426. b) J. Rebek, Jr., D. Nemeth, *J. Am. Chem. Soc.* **1986**, *108*, 5637. c) J. L. Sessler, C. M. Lawrence, J. Jayawickramarajah, *Chem. Soc. Rev.* **2007**, *36*, 314.

204. C. B. Aakeröy, A. Rajbanshi, Z. J. Li, J. Desper, *CrystEngComm* **2010**, *12*, 4231.

205. I.-J. Chen, A. D. MacKerell, Jr., *Theor. Chem. Acc.* **2000**, *103*, 483.

206. S. L. Childs, K. I. Hardcastle, *CrystEngComm* **2007**, *9*, 364.

207. a) M. C. Etter, *Acc. Chem. Res.* **1990**, *23*, 120. b) S. L. Childs, P. A. Wood, N. Rodríguez-Hornedo, L. S. Reddy, K. I. Hardcastle, *Cryst. Growth Des.* **2009**, *9*, 1869.

208. Selected examples: a) D. R. Weyna, T. Shattock, P. Vishweshwar, M. J. Zaworotko, *Cryst. Growth Des.* **2009**, *9*, 1106. b) I. D. H. Oswald, W. D. S. Motherwell, S. Parsons, *Acta Crystallogr*. **2005**, *B61*, 46. c) Z.-H. Zhang, X. Tan, S.-C. Chen, *Acta Crystallogr.* **2009**, *C65*, 457. d) I. D. H. Oswald, D. R. Allan, P. A. McGregor, W. D. S. Motherwell, S. Parsons, C. R. Pulham, *Acta Crystallogr.* **2002**, *B58*, 1057.

209. CCDC refcodes: AGOYOK, AGOYOK01, AMIDIJ, BOQDOA, COZKUL, DUCSAW, ITIQIL, MOYLOC, MOYMAP, MUPQAP, QAMRUS, VUJTAW, YUCQUJ, XUYJUX, XUYKIM, EPUQEM.

210. M. Remko, *J. Phys. Chem. A.* **2003**, *107*, 720.

211. G. Bettinetti, M. R. Caira, A. Callegari, M. Merli, M. Sorrenti, C. Tadini, *J. Pharm. Sci*. **2000**, *89*, 478.

212. H. Nakai, M. Takasuka, M. Shiro, *J. Chem. Soc. Perkin Trans. II,* **1984**, 1459.

213. M. R. Caira, G. Bettinetti, M. Sorrenti, L. Catenacci, *J. Pharm. Sci*. **2003**, *92*, 2164.

214. G. Guiseppetti, C. Tadini, G. Bettinetti, *Acta Crystallogr.* **1994**, *C50*, 1289.

215. J. Lu, A. J. Cruz-Cabeza, S. Rohani, M. C. Jennings, *Acta Crystallogr.* **2011,** *C67*, 306.

216. G. Bettinetti, N. Sardone, *Acta Crystallogr.* **1997**, *C53*, 594.

217. D. E. Lynch, P. Sandhu, S. Parsons, *Aust. J. Chem*. **2000**, *53*, 383.

218. M. R. Caira, *J. Crystallogr. Spectrosc. Res.* **1992**, *22*, 193.

219. M. R. Caira, *J. Crystallogr. Spectrosc. Res.* **1991**, *5*, 641.

220. R. Luccaciu, C. Ionescu, A. Wildervanck, M. R. Caira, *X-Ray Struct. Anal. Online* **2008**, *24*, x87.

221. M. R. Caira, *J. Chem. Crystallogr*. **1994**, *24*, 695.

222. A. K. Varma, R. K. Tiwari, *J. T. R. Chem.* **1999**, *6*, 13.

223. M. R. Caira, R. Mohamed, *Acta Crystallogr*. **1993**, *B49*, 760.

224. S. J. Coles, M. B. Hursthouse, T. A. Mayer, T. L. Threlfall, **2000**, University of Southampton, Crystal Structure Report Archive. (doi:10.3737/ecrystals.chem.soton.ac.uk/196 <http://dx.doi.org/10.3737/ecrystals.chem.soton.ac.uk/196>)

225. M. R. Caira, R. Mohamed, *Supramol. Chem.* **1993**, *2*, 201.

226. J. Rambaud, L. Maury, B. Pauvert, M. Audran, Y. Lasserre, G. Berge, J.-P. Declercq, *Acta Crystallogr.* **1985**, *C41*, 133.

227. N. Sardone, G. Bettinetti, M. Sorrenti, *Acta Crystallogr.* **1997**, *C53*, 1295.

228. H. M. Deutsch, D. G. VanDerveer, L. H. Zalkow, *Acta Crystallogr.* **1985**, *C41*, 1116.

229. U. Patel, M. Haridas, T. P. Singh, *Acta Crystallogr*. **1988**, *C44*, 1264.

230. J. M. Leger, S. Alberola, A. Carpy, *Acta Crystallogr.* **1977**, *B33*, 1455.

231. M. R. Caira, L. R. Nassimbeni, A. F. Wildervanck, *J. Chem. Soc. Perkin Trans. II,* **1995**, 2213.

232. E. Lu, N. Rodríguez-Hornedo, R. Suryanarayanan, *CrystEngComm* **2008**, *10*, 665.

233. M. Ghosh, A. K. Basak, S. K. Mazumdar, B. Sheldrik, *Acta Crystallogr.* **1991**, *C47*, 577.

234. CCDC refcodes: AWIJEW, COVXIU, EXAMUM, EXANAT, EXANEX, EXANIB, EXANOH, EXANUN, EXAPEZ, EXAPID, EXAPID01, EXAPUP, GEYSAE, GEYSAE01, RASSUZ, RIWLOY, SABDOQ, SORWEB, SORWIF, VIGVOW, VUGMIT, XEXCAE, XEXCEI, XOBCOH, YIZQAA.

235. R. K. Tiwari, M. Haridas, T. P. Singh, *Acta Crystallogr.* **1984**, *C40*, 655. (CCDC refcode: SLFNMD10)

236. CCDC refcodes: AWIJEW, EXAMUM, EXAPEZ, EXAPID, EXAPID01, EXAPUP.

237. a) H. Hosomi, S. Ohba, Y. Ito, *Acta Crystallogr.* **2000**, *C56*, e511. b) Q. Zheng, D. Wu, H. Ma, C. Shu, Y. Lia, C. Wang, *CrystEngComm* **2006**, *8*, 189. c) C. B. Aakeröy, J. Desper, J. F. Urbina, *CrystEngComm* **2005**, *7*, 193. d) T. W. Lee, J. P. K. Lau, L. Szeto, *Acta Crystallogr.* **2003**, *E59*, o942. e) M. Vinodu, I. Goldberg, *CrystEngComm* **2005**, *7*, 133. f) R. Moreno-Fuquen, J. Valderramanaranjo, A. M. Montaño, *Acta Crystallogr.* **1999**, *C55*, 218.

238. J. R. G. Sander, D.-K. Bučar, R. F. Henry, B. N. Giangiorgi, G. G. Z. Zhang, L. R. MacGillivray, *in preparation*.

239. M. W. Wong, R. Leung-Toung, C. Wentrup, C. *J. Am. Chem. Soc.* **1993**, *115*, 2465.

240. Amidine and imidine tautomers of SMT modeled using Spartan '10 (Wavefunction, Inc. Irvine, CA) software. Dipole moments and electrostatic potential maps obtained from equilibrium geometry of each tautomer using AM1 calculations.

241. M. Arijit, P. Grobelny, T. S. Thakur, G. R. Desiraju, *Cryst. Growth Des.* **2011**, *11*, 2637.

242. Y. R. Hristova, M. M. J. Smulders, J. K. Clegg, B. Breiner, J. R. Nitschke, *Chem. Sci.* **2011**, *2*, 638.

243. J. Jacques, A. Collet, S. H. Wilen, *Enantiomers, Racemates, and Resolutions,* Krieger Publishing Co.; Malabar, **1991**.

244. S. Chen, H. Xi, R. F. Henry, I. Marsden, G. Z. Z. Zhang, *CrystEngComm* **2010**, *12*, 1485.

245. a) J. F. McConnell, *Cryst. Struct. Comm.* **1974**, *73*, 3. b) N. Shankland, A. J. Florence, P. J. Cox, D. B. Sheen, S. W. Love, N. S. Stewart, C. C. Wilson, *Chem. Commun.* **1996**, 855. c) A. J. Romero, C. T. Rohodes, *Drug Dev. Ind. Pharm.* **1991**, *17*, 777. d) S. K. Dwivedi, S. Sattari, F. Jamali, A. G. Mitchell, *Int. J. Pharm*. **1992**, *87*, 95. e) A. J. Romero, C. T. Rohodes, *J. Pharm. Pharmacol*. **1993**, *45*, 258. f) A. Burger, K. T. Koller, W. M. Schiemeier, *Eur. J. Pharm. Biopharm*. **1996**, *42*, 142. g) Z. J. Li, M. T. Zell, E. J. Munson, D. J. Grant, *J. Pharm. Sci*. **1999**, *88*, 337. h) Z. J. Li, W. H. Ojala, D. J. Grant, *J. Pharm. Sci.* **2001**, *90*, 1523.

246. G. Z. Z. Zhang, S. Y. L. Paspal, S. Suryanarayanan, D. J. Grant, *J. Pharm. Sci.* **2003**, *92*, 1356.

247. R. D. B. Walsh, M. W. Bradner, S. Fleischman, L. A. Morales, B. Moulton, N. Rodriguez-Hornedo, M. J. Zaworotko, *Chem. Commun*. **2003**, 186-187.

248. Symphonix, Inel Corp. Artenary, France.

249. Jade, Version 6.5, Materials Data, Inc. Livermore, CA.

250. Roozeboom, H. W. B. *Z. Physik. Ch*. **1899**, *28*, 494.

251. N. L. Rosi, J. Eckert, M. Eddaoudi, D. T. Vodak, J. Kim, M. O'Keeffe, O. M. Yaghi, *Science* **2003**, *300*, 1127.

252. a) M. Zheng, C. Weng, S. Liu, W. Lin, *Chem. Sci.* **2012**, *3*, 2623. b) F. Song, C. Wang, W. Lin, *Chem. Commun.* **2011**, *47*, 8256.

253. K. E. deKrafft, Z. Xie, G. Cao, S. Tran, L. Ma, O. Z. Zhou, W. Lin, *Angew. Chem.* **2009**, *121*, 10085; *Angew. Chem. Int. Ed.* **2009**, *48*, 9901.

254. P. A. Clarke, W. H. C. Martin, *Annu. Rep. Prog. Chem. Sect. B.* **2003**, *99*, 84.

255. a) K. K. Tanabe, S. M. Cohen, *Chem. Soc. Rev.* **2011**, *40*, 498; b) T. Yamada, H. Kitagawa. *J. Am. Chem. Soc*. **2009**, *131*, 6312. c) R. K. Deshpande, J. L. Minnaar, S. G. Telfer, *Angew. Chem.* **2010**, *122*, 4702; *Angew. Chem. Int. Ed*. **2010**, *49*, 4598.

256. P. Gilli, L. Pretto, V. Bertolasi, G. Gilli, *Acc. Chem. Res*. **2009**, *42*, 33.

257. IR spectrum of solid **1b** is consistent with O—H···N hydrogen bonds (see: G. Saba, M. Bullock, J. L. Wood, *J. Mol. Struct.* **1976**, *30*, 151). We, and others (ref. 124), have been unsuccessful determining the X-ray structure of **1b**. Related isonicotinic acid assembles *via* O—H(acid)···N(pyr) hydrogen bonds, see: F. Takusagawa and A. Shimada. *Acta Crystallogr.* **1976**, *B32*, 1925.

258. M. Sedigh, M. A. Lipton, *Org. Lett.* **2005**, *7*, 1473.

259. a) T. R. Kelly, G. J. Bridger, C. Zhao, *J. Am. Chem. Soc.* **1990**, *112*, 8024; b) D. M. Bassani, V. Darcos, S. Mahony, J. -P. Desvergne, *J. Am. Chem. Soc.* **2000**, *122*, 8795.

260. a) J. Harada, K. Ogawa, *Chem. Soc. Rev.* **2009**, *38*, 2244. b) J. Harada, K. Ogawa. *J. Am. Chem. Soc.* **2001**, *123*, 10884.

261. G.M. Sheldrick, SHELXS-97, *Program for Crystal Structure Determination*; University of Göttingen: Germany, **1997**.

262. a) Rigaku Corporation, **1999**. b) CrystalClear Software User's Guide, Molecular Structure Corporation, **2000**. c) J. W. Pflugrath, *Acta Crystallogr.* **1999**, *D55*, 1718.

263. Rigaku (1998). REQAB. Rigaku Corporation, Tokyo, Japan.

264. A. Altomare, G. Cascarano, C. Giacovazzo, A. Guagliardi, M. Burla, G. Polidori, M. Camalli, *J. Appl. Cryst.* **1994**, *27*, 435.

265. M.C. Burla, R. Caliandro, M. Camalli, B. Carrozzini, G.L. Cascarano, L. De Caro, C. Giacovazzo, G. Polidori, R. Spagna, *J. Appl. Cryst.* **2005**, *38*, 381.

266. L. J. Barbour, *J. Supramol. Chem.* **2001**, *1*, 189.

267. a) A. L. Spek, PLATON, *A Multipurpose Crystallographic Tool*; Utrecht University: The Netherlands, **1998**. b) A. L. Spek, *J. Appl. Cryst.* **2003**, *36*, 7.

268. K. C. Agarwal, E. E. Knaus. *J. Heterocycl. Chem*. **1985**, *22*, 65.

269. M. -L. Boillet, C. Roux, J.-P. Audière, A. Dausse, J. Zarembowitch, *Inorg. Chem*. **1996**, *35*, 3975.

270. J. Harada, K. Ogawa, S. Tomoda, *Acta Crystallogr.* **1997**, *B53*, 662.

271. J. Harada, K. Ogawa, *J. Am. Chem. Soc.* **2004**, *126*, 3539.

272. D. B. Varshney, G. S. Papaefstathiou, *Chem. Commun.* **2002**, 1964.

273. T. D. Hamilton, D.-K. Bučar, L. R. MacGillivray, *New. J. Chem.* **2010**, *34*, 2400.

274. B. H. Northrop, Y. R. Zheng, K.-W. Chi, P. J. Stang, *Acc. Chem. Res*. **2009**, *42*, 1554.

275. a) M. Yoshizawa, J. K. Klosterman, M. Fujita, *Angew. Chem.* **2009**, *121*, 3470; *Angew. Chem. Int. Ed.* **2009**, *48*, 3418. (b) M. Fujita, M. Tominaga, A. Hori, B. Therrien, *Acc. Chem. Res.* **2005**, *38*, 371.

276. D. W. Johnson, F. Hof, P. M. Irvine, C. Nuckolls, J. Rebek, Jr., *Angew. Chem.* **2002**, *114*, 3947; *Angew. Chem. Int. Ed.* **2002**, *41*, 3793.

277. D. W. Johnson, K. J. Raymond, *Inorg. Chem.* **2001**, *40*, 5157.

278. a) E. J. Corey, J. A. Katzenellenbogen, G. H. Posner, *J. Am. Chem. Soc.* **1967**, *89*, 4245. b) H. M. R. Hoffman, J. Rabe, *J. Org. Chem.* **1985**, *50*, 3849. c) A. K. Chatterjee, D. P. Sanders, R. H. Grubbs, *Org. Lett.* **2002**, *4*, 1939.

279. D. Rodríguez, L. M. Quirós, J. A. Salas, *J. Biol. Chem.* **2004**, *279*, 8149.

280. a) K.-H. Pfoertner, G. Englert, P. Schoenholzer, *Tetrahedron* **1987**, *43*, 1321. b) V. Ramamurthy, K. Venkatesan, *Chem. Rev.*, **1987**, *87*, 433.

281. Selected examples: a) A. J. Zucchero, P. L. McGrier, U. H. F. Bunz, *Acc. Chem. Res.* **2010**, *43*, 397. b) M. Kivala, F. Diedrich, *Acc. Chem. Res.* **2009**, *42*, 235.

282. a) D. J. Cram, H. Steinberg, *J. Am. Chem. Soc*. **1951**, *73*, 5691. b) D. J. Cram, J. M. Cram, *Acc. Chem. Res*. **1971**, *4*, 204. c) H. Hopf, *Classics in Hydrocarbon Chemistry*; Wiley-VCH: Weinheim, **2000**.

283. P. Rademacher, In Modern Cyclophane Chemistry (Eds.: R. Gleiter, H. Hopf) Wiley-VCH: Weinheim, **2004**; pp. 274-287, and references therein.

284. a) A. Cipiciani, F. Fringuelli,O. Piermatti, F. Pizzo, R. Ruzziconi, *J. Org. Chem*. **2002**, *67*, 2665. b) T.-Z. Zhang, L.-X. Dai, X.-L. Hou, *Tetrahedron: Asymmetry* **2007**, *18*, 251. c) D. Y. Antonov, V. I. Rozenburg, T. I. Danilova, Z. A. Starikova, H. Hopf, *Eur. J. Org. Chem*. **2008**, *6*, 1038. d) B. Jiang, Y. Lei, X.-L. Zhao, *J. Org. Chem*. **2008**, *73*, 7833.

285. H. Hinrichs, A. J. Boydston, P. G. Jones, K. Hess, R. Herges, M. M. Haley, H. Hopf, *Chem. Eur. J*. **2006**, *12*, 7103.

286. Selected examples: a) Z. Pechlivanidis, H. Hopf, L. Ernst, *Eur. J. Org. Chem.* **2009**, *2*, 223. b) L. Bondarenko, I. Dix, H. Hinrichs, H. Hopf, *Synthesis* **2004**, *16*, 2751. c) L. Minuti, A. Taticchi, A. Marrocchi, S. Landi, E. Gacs-Baitz, *Tetrahedron Lett*. **2005**, *46*, 5735. d) A. Marrocchi, A. Taticchi, S. Landi, *Synthesis*. **2008**, *7*, 1045. e) A. Taticchi, L. Minuti, A. Marrocchi, D. Lanari, E. Gacs-Baitz, *Tetrahedron: Asymmetry* **2002**, *13*, 1331.

287. Selected examples: a) A. A. Aly, S. Ehrhardt, H. Hopf, I. Dix, P. G. Jones, *Eur. J. Org. Chem.* **2006**, *2*, 335. b) H. Hopf, H. Greiving, C. Beck, I. Dix, P. G. Jones, J.-P. Desvergne, H. Bouas-Laurent, *Eur. J. Org. Chem.* **2005**, *3*, 567. c) A. A. Aly, H. Hopf, L. Ernst, I. Dix, P. G. Jones, *Eur. J. Org. Chem*. **2006**, *13*, 3001.

288. H. Hopf, *Angew. Chem.* **2008**, *120*, 9954; *Angew. Chem. Int. Ed*. **2008**, *47*, 9808.

289. G. C. Bazan, *J. Org. Chem*. **2007**, *124*, 5182.

290. R. Gleiter, W. Schaefer, *Acc. Chem. Res*. **1990**, 23, 369.

291. L. Guyard, C. Dumas, F. Miomandre, R. Pansu, R. Renault-Méallet, P. Audebert, *New. J. Chem*. **2003**, *27*, 1000.

292. G. P. Bartholomew, G. C. Bazan, *Acc. Chem. Res*. **2001**, *34*, 30.

293. Several groups have studied 4-alkenyl[2.2]paracyclophane in the context of synthesis (see ref. 282a) and polymerizations (S. Iwatsuki, T. Itoh, M. Kubo, H. Okunu, *Polym. Bull.* **1994**, *32*, 27.); however, this is the first time the optical properties of such compounds have been extensively studied.

294. J. Zyss, I. Ledoux, S. Volkov, V. Chernyak, S. Mukamel, G. P. Bartholomew, G. C. Bazan, *J. Am. Chem. Soc*. **2000**, *122*, 11956.

295. a) G. C. Bazan, W. J. Oldham, Jr., R. J. Lachicotte, S. Tretiak, V. Chernyak, S. Mukamel, *J. Am. Chem. Soc*. **1998**, *120*, 9188. b) W. J. Oldham, Jr., Y.- J. Miao, R. J. Lachicotte, G. C. Bazan, G. C. *J. Am. Chem. Soc*. **1998**, *120*, 419.

296. A. Taticchi, A. Marrocchi, L. Minuti, S. Landi, E. Gacs-Baitz, *Heterocycles* **2006**, *68*, 1249.

297. S. Wang, G. C. Bazan, S. Tretiak, S. Mukamel, *J. Am. Chem. Soc*. **2000**, *122*, 1289.

298. H. Y. Woo, J. W. Hong, B. Liu, A. Mikhailovsky, D. Korystov, G. C. Bazan, *J. Am. Chem. Soc*. **2005**, *127*, 820.

299. J. W. Hong, B. S. Gaylord, G. C. Bazan, *J. Am. Chem. Soc*. **2002**, *124*, 11868.

300. Y. Morisaki, T. Ishida, Y. Chujo, *Macromolecules* **2002**, *35*, 7872.

301. Y. Morisaki, T. Ishida, H. Tanaka, Y. Chujo, *J. Polym. Sci*. **2004**, *42*, 5891.

302. Y. Morisaki, Y. Chujo, *Bull. Chem. Soc. Jpn*. **2005**, *78*, 288.

303. Y. Morisaki, F. Fujimura, Y. Chujo, *Organometallics* **2003**, *22*, 3553.

304. J. Oshita, A. Kunai, *Acta Polym*. **1998**, *49*, 379.

305. Y. Morisaki, N. Wada, Y. Chujo, *Polymer* **2005**, *46*, 5884.

306. Y. Morisaki, T. Murakami, Y. Chujo, *Macromolecules* **2008**, *41*, 5960.

307. Y. Morisaki, T. Murakami, T. Sawamura, Y. Chujo, *Macromolecules* **2009**, *42*, 3656.

308. G. P. Bartholomew, G. P.; Bazan, G. C. *J. Am. Chem. Soc*. **2002**, *124*, 5183-5196.

309. G. P. Bartholomew, M. Rumi, S. J. K. Pond, J. W. Perry, S. Tretiak, G. C. Bazan, *J. Am. Chem. Soc*. **2004**, *126*, 11529.

310. J. W. Hong, H. Y. Woo, B. Liu, G. C. Bazan, *J. Am. Chem. Soc*. **2005**, *127*, 7435.

311. Y. Morisaki, Y. Chujo, *Macromolecules* **2002**, *35*, 587.

312. Y. Morisaki, Y. Chujo, *Polym. Bull*. **2002**, *49*, 209.

313. For an example, see: M. Karikomi, C. Kitamura, S. Tanaka, Y. Yamashita, *J. Am. Chem. Soc.* **1005**, *117*, 6791.

314. U. Scherf, E. J. W. List, *Adv. Mater*. **2002**, *14*, 477.

315. L. Lin, Y. Morisaki, Y. Chujo, *J. Polym. Sci*. **2009**, *47*, 7003.

316. Y. Morisaki, Y. Chujo, *Bull. Chem. Soc. Jpn*. **2009**, *82*, 1070.

317. T. M. Selby, W. L. Meerts, T. S. Zwier, *J. Phys. Chem. A.* **2007**, *111*, 3697.

318. M. J. Frisch, G. W. T., H. B. Schlegel, G. E. Scuseria, M. A. Robb, J. R. Cheeseman, G. Scalmani, V. Barone, B. Mennucci, G. A. Petersson, H. Nakatsuji, M. Caricato, X. Li, H. P. Hratchian, A. F. Izmaylov, J. Bloino, G. Zheng, J. L. Sonnenberg, M. Hada, M. Ehara, K. Toyota, R. Fukuda, J. Hasegawa, M. Ishida, T. Nakajima, Y. Honda, O. Kitao, H. Nakai, T. Vreven, J. A. Montgomery, Jr., J. E. Peralta, F. Ogliaro, M. Bearpark, J. J. Heyd, E. Brothers, K. N. Kudin, V. N. Staroverov, R. Kobayashi, J. Normand, K. Raghavachari, A. Rendell, J. C. Burant, S. S. Iyengar, J. Tomasi, M. Cossi, N. Rega, J. M. Millam, M. Klene, J. E. Knox, J. B. Cross, V. Bakken, C. Adamo, J. Jaramillo, R. Gomperts, R. E. Stratmann, O. Yazyev, A. J. Austin, R. Cammi, C. Pomelli, J. W. Ochterski, R. L. Martin, K. Morokuma, V. G. Zakrzewski, G. A. Voth, P. Salvador, J. J. Dannenberg, S. Dapprich, A. D. Daniels, ; O. Farkas, J. B. F., J. V. Ortiz, J. Cioslowski, D. J. Fox, *Gaussian 09, Revision B.02*, Gaussian, Inc., Wallingford CT, **2009**.

319. T. Yanai, D. P. Tew, C. N. Handy, *Chem. Phys. Lett*. **2004**, *393*, 51.

320. a) E. Cances, B. Mennucci, J. Tomasi, *J. Chem. Phys.* **1997**, *107*, 3032. b) M. Cossi, V. Barone, B. Mennucci, J. Tomasi, J, *Chem. Phys. Lett*. **1998**, *286*, 253. c) B. Mennucci, J. Tomasi, *J. Chem. Phys.* **1997**, *106*, 5151.

321. T. Bruhn, K. Maksimenka, G. Bringmann, G. *SpecDis, Version 1.53*, **2012**.

322. http://www.chemcraftprog.com.

323. P. K. Bhowmik, A. K. Nedeltchev, H. Han, *Tetrahedron Lett*. **2007**, *48*, 5383.

324. M. B. J. Atkinson, S. V. S. Mariappan, D.-K. Bučar, J. Baltrusaitis, T. Friščić, N. G. Sinada, L. R. MacGillivray, *Proc. Natl. Acad. Sci.* **2011**, *108*, 10974.

325. The maximum excitation wavelengths for tetrakis-[(N-methyl)-4-pyridylcycobutyl][2.2]paracyclophane (N-methyl tpcp) and tetrakis-[(N-ethyl)-4-pyridylcycobutyl][2.2]paracyclophane (N-ethyl tpcp) are 422 and 427 nm, respectively.

326. P. Nandhikonda, S. Paudel, M. D. Heagy, *Tetrahedron* **2009**, *65*, 2173.

327. M. Shimizu, Y. Takeda, M. Higashi, T. Hiyama, *Angew. Chem.* **2009**, *121*, 3707; *Angew. Chem. Int. Ed.* **2009**, *48*, 3653.

328. a) X. Peng, L. Manna, W. Yang, J. Wickman, E. Scher, A. Kadavanich, A. P. Alivastos, *Nature* **2000**, *404*, 59. b) F. Kim, S. Connor, H. Song, T. Kuykendall, P. Yang, *Angew. Chem.* **2004**, *116*, 3759; Angew. *Chem. Int. Ed.* **2004**, *43*, 3673.

329. E. Kwon, H.-R. Chung, Y. Araki, H. Kasai, H. Oikawa, O. Ito, H. Nakanishi, *Chem. Phys. Lett*. **2007**, *441*, 106.

330. N. L. Rosi, C. A. Mirkin, *Chem. Rev.* **2005**, *105*, 1025.

331. C. Burda, X. Chen, R. Narayanan, M. A. El-Sayed, *Chem. Rev*. **2005**, *105*, 1025.

332. a) H. Kasai, Y. Yoshikawa, T. Seko, S. Okada, H. Oikawa, H. Matsuda, A. Watanabe, O. Ito, H. Totoyama, H. Nakanishi, *Mol. Cryst. Liq. Cryst.* **1997**, *294*, 173. b) H. Kasai, H. Kamatani, S. Okada, H. Oikawa, H. Masuda, H. Nakanishi, *Jpn. J. Appl. Phys.* **1996**, *34*, L221. c) H. Kasai, H. Kamatani, Y. Yoshikawa, S. Okada, H. Oikawa, A. Watanabe, O. Ito, H. Nakanishi, *Chem. Let.* **1997**, 1181. d) Y. Komai, H. Kasai, H. Hirakoso, Y. Hakuta, S. Okada, H. Oikawa, T. Adschiri, H. Inomata, K. Arai, H. Nakanishi, *Mol. Cryst. Liq. Cryst.* **1998**, *322*, 167. e) K. Baba, H. Kasai, S. Okada, H. Oikawa, H. Nakanishi, *Optical Mater.* **2002**, *21*, 591.

333. a) Y. S. Zhao, W. Yang, J. Yao, *Phys. Chem. Chem. Phys.* **2006**, *8*, 3300. b) Y. S Zhao, H. Fu, A. Peng, Y. Ma, D. Xiao, J. Yao, *Adv. Mater.* **2008**, *20*, 2859. c) H.-B. Fu, J.-N Yao, *J. Am. Chem. Soc.* **2001**, *123*, 1434. d) D. Xiao, L. Xi, W. Yang, H. Fu, Z. Shuai, Y. Fang, J. Yao, *J. Am. Chem. Soc.* **2003**, *125*, 6740.

334. C. J. Bhongale, C.-W. Chang, C.-S. Lee, E. W.-G. Diau, C.-S Hsu, *J. Phys. Chem. B.* **2005**, *109*, 13472.

335. S. Li, L. He, F. Xiong, Y. Li, G. Yang, *J. Phys. Chem. B.* **2004**, *108*, 10887.

336. a) J. H. Bang, K. S. Suslick, *Adv. Mater.* **2010**, *22*, 1039. c) J. R. G. Sander, D.-K. Bučar, R. F. Henry, G. G. Z. Zhang, L. R. MacGillivray, *Angew. Chem.* **2010**, *122*, 7442; *Angew. Chem. Int. Ed.* **2010**, *49*, 7284. d) B. W. Zeigler, K. S. Suslick, *J. Am. Chem. Soc.* **2011**, *133*, 14530.

337. a) Q. Mangalum, B. P. Morgan, J. M. Hanley, K. M. Jecen, C. J. McGill, G. A. Robertson, R. C. Smith, *Chem. Commun.* **2012**, *46*, 5136. b) D. Cornelis, E. Franz, I. Asselberghs, K. Clays, T. Verbiest, G. Koeckelberghs, *J. Am. Chem. Soc.* **2011**, *133*, 1317. c) J. W. Levell, W.-Y. Lai, R. J. Borthwick, S.-C. Lo, P. L. Burn, I. D. W. Samuel, *J. Phys. Chem. C.* **2011**, *115*, 25464. d) B. I. Ipe, K. G. Thomas, *J. Phys. Chem. B.* **2004**, *108*, 13265. e) F. Terenziani, V. Parthasarthy, A. Pla-Quintana, T. Maishal, A.-M. Caminade, J.-P. Majoral, M. Blanchard-Desce, *Angew. Chem.* **2009**, *121*, 8847; *Angew. Chem. Int. Ed.* **2009**, *48*, 8691.

338. CSD refcode: DXYLEN

339. a) H. Kasai, H. S. Nalwa, H. Oikawa, S. Okada, H. Matsuda, H. Minami, A. Kakuta, K. Ono, A. Mukoh, H. Nakanishi, *Jpn. J. Appl. Phys.* **1992**, *31*, 1132. b) H. S. Nalwa, H. Kasai, H. Kamatani, S. Okada, H. Oikawa, H. Matsuda, A. Kakuta, A. Mukoh, H. Nakanishi, *Adv. Mater.* **1993**, *5*, 758. c) H. Kasai, H. Oikawa, H. Nakanishi, *Organic Mesoscopic Chemistry* (Eds: H. Masuhara and F. C. Schryver), Blackwell Science, Oxford **1999**, pp. 145-170.

340. J. R. G. Sander, D.-K. Bučar, J. Baltrusaitis, L. R. MacGillivray, *J. Am. Chem. Soc.* **2012**, *134*, 6900.

341. Z. Shervani, Y. Ikushima, M. Sato, H. Kawanami, Y. Hakuta, T. Yokoyama, T. Nagasem H. Kuneida, K. Aramaki, *Colloid Polym. Sci.* **2008**, *286*, 403.

342. a) D. Horn, J. Rieger, *Angew. Chem.* **2001**, *113*, 4460; *Angew. Chem. Int. Ed.* **2001**, *40*, 4330. b) M. E. Matteucci, M. A. Hotze, K. P. Johnston, R. O. Williams, *Langmuir* **2006**, *22*, 8951.

343. CSD refcode: EHOTUQ

344. J. Choi, V. Reipa, V. M. Hitchins, P. L. Goering, R. A. Malinaskas, *Toxicol. Sci.* **2011**, *123*, 133.

345. We note that the pCp and tpcp samples prepared in 0.021 M SDS were also measured as a nanosuspension in that same medium.

346. a) P. H. Kwan, M. J. MacLachlan, T. M. Swager, *J. Am. Chem. Soc.* **2004**, *126*, 8638. b) T. E. Kasier, H. Wang, V. Stepanenko, F. Würthner, *Angew. Chem*. **2007**, *119*, 5637; *Angew. Chem. Int. Ed.* **2007**, *46*, 5541. c) T.-Q, Nguyen, R. Martel, P. Avouris, M. L. Bushey, L. Brus, C. Nuckolls, *J. Am. Chem. Soc.* **2004**, *126*, 5234. d) J. Waluk, *Acc. Chem. Res.* **2003**, *36*, 832.

347. X. Zhang, X. Zhang, W. Shi, X. Meng, C. Lee, S. Lee, *J. Phys. Chem.* **2005**, *109*, 18777.

348. a) S. A. Jenekhe, J. A. Osaheni, *Science* **1994**, *265*, 765. b) R. H. Friend, R. W. Gymer, A. B. Holmes, J. H. Burroughs, R. N. Marks, C. Taliani, D. D. C. Bradley, D. A. Dos Santos, J. L. Brédas, M. Lögdlund, W. R. Salaneck, *Nature* **1999**, *397*, 121.

349. J. Wang, A. Kulago, W. R. Browne, B. L. Feringa, *J. Am. Chem. Soc.* **2010**, *132*, 4191.

350. P. Anastas, J. Warner, *Green Chemistry: Theory and Practice*, Oxford University Press, New York, **1998**.

351. C. J. Brown, A. C. Farthing, *Nature* **1949**, *164*, 915.

352. J. Nishimura, Y. Nakamura, Y. Hayashida, T, Kudo, *Acc. Chem. Res.* **2000**, *333*, 679.

353. B. S. Green, G. M. J. Schmidt, *Tetrahedron Lett*. **1970**, 4249.

354. M. Maekawa, S. Kato, M. J. Hasegawa, *J. Am. Chem. Soc.* **1985**, *107*, 2788.

355. J. N. Moorthy, P. Venkatakrishmam, *Cryst. Growth Des.* **2007**, *7*, 713.

APPENDIX A: CRYSTALLOGRAPHIC TABLES

Table A-1: General and crystallographic data for co-crystals of sulfadiazine (SDZ).

Compound	**(SDZ)·(pico)**	**2(SDZ)·3(bipy)**	**2(SDZ)·(bpe)**	**2(SDZ)·(bpa)**
Chemical formula	$C_{16}H_{17}N_5O_2S$	$C_{50}H_{44}N_{14}O_4S_2$	$C_{16}H_{15}N_5O_2S$	$C_{16}H_{14}N_5O_2S$
Formula mass	343.41	969.11	341.39	340.38
Crystal system	triclinic	triclinic	triclinic	triclinic
Space group	$P\bar{1}$	$P\bar{1}$	$P\bar{1}$	$P\bar{1}$
a/Å	7.834(5)	10.7093(13)	5.6717(12)	5.734(3)
b/Å	9.005(5)	14.1126(17)	7.9548(17)	8.057(4)
c/Å	12.310(7)	15.9739(19)	18.104(4)	18.0163(10)
α/°	79.922(7)	90.1960(10)	98.292(4)	78.438(7)
β/°	83.513(6)	105.5040(10)	98.831(3)	81.646(8)
γ/°	70.167(6)	91.4720(10)	102.779(3)	77.011(7)
V / Å^3	803.0(8)	2325.5	785.832	796.62
$\rho_{(calcd)}$/ g cm^{-3}	1.420	1.384	1.443	1.419
T / K	100(2)	100(2)	100(2)	100(2)
Z	2	2	2	2
Radiation type	MoK_α	MoK_α	MoK_α	MoK_α
No. of reflections measured	7998	27441	9435	9490
No. of independent reflections	3225	10535	3726	3706
No. of reflections with $I > 2\sigma(I)$	2670	9224	3057	2671
R_{int}	0.0450	0.0205	0.0717	0.1351
R_1 ($I > 2\sigma(I)$)	0.0436	0.0343	0.0472	0.0495
$wR(F^2)$ ($I > 2\sigma(I)$)	0.1298	0.1098	0.1258	0.1315
R_1 (all data)	0.0536	0.0410	0.0587	0.0674
$wR(F^2)$ (all data)	0.1460	0.1249	0.1410	0.1545
Goodness of fit on F^2	1.067	0.930	1.058	0.863
CCDC number	847419	847416	847418	847417

Table A-2: General and crystallographic data for salts of SDZ.

Compound	**(4-ap$^+$)·(SDZ$^-$)**	**(dmap$^+$)·(SDZ$^-$)**	**(4-pypip$^+$)·(SDZ$^-$)**
Chemical formula	$C_{15}H_{16}N_6O_2S$	$C_{17}H_{20}N_6O_2S$	$C_{19}H_{23}N_7O_2S$
Formula mass	344.40	372.45	413.50
Crystal system	monoclinic	monoclinic	monoclinic
Space group	$P2_1/c$	$P2_1/n$	$P2_1/n$
a/Å	11.9647(13)	9.1978(10)	9.3362(13)
b/Å	8.6341(10)	15.1948(16)	15.684(2)
c/Å	15.8757(17)	13.3595(14)	13.6864(18)
α/°	90.00	90.00	90.00
β/°	95.112(5)	109.537(5)	105.497(4)
γ/°	90.00	90.00	90.00
$\rho_{(calcd)}$/ g cm^{-3}	1.400	1.406	1.422
V / Å^3	1633.5(3)	1759.61	1931.23
T / K	293(2)	293(2)	100(2)
Z	4	4	4
Radiation type	Mo K_α	Mo K_α	Mo K_α
No. of reflections measured	10799	11383	22717
No. of independent reflections	2882	3081	4714
No. of reflections with $I > 2\sigma(I)$	2397	2628	4107
R_{int}	0.0321	0.0241	0.0286
R_1 ($I > 2\sigma(I)$)	0.0371	0.0352	0.0354
$wR(F^2)$ ($I > 2\sigma(I)$	0.0983	0.1017	0.1088
R_1 (all data)	0.0475	0.0438	0.0421
$wR(F^2)$ (all data)	0.1041	0.1125	0.1208
Goodness of fit on F^2	1.063	1.079	0.867
CCDC number	852593	852594	847415

Table A-3: General and crystallographic data for co-crystals of SMT with bipyridines.

Compound	(SMT)·(bipy)·(CH_3CN)	(SMT)·(bpe)·(CH_3CN)	(SMT)·(bpa)·(CH_3CN)
Chemical formula	$C_{24}H_{25}N_7O_2S$	$C_{26}H_{27}N_7O_2S$	$C_{26}H_{25}N_7O_2S$
Formula mass	475.57	501.61	499.59
Crystal system	monoclinic	triclinic	triclinic
Space group	$P2_1/c$	$P\bar{1}$	$P\bar{1}$
a/Å	7.8552(19)	8.023(4)	8.0534(13)
b/Å	9.576(2)	9.510(5)	9.5214(16)
c/Å	31.243(8)	17.394(9)	17.305(3)
α/°	90.00	75.131(6)	75.571(2)
β/°	90.994(3)	88.730(7)	88.797(2)
γ/°	90.00	83.016(7)	80.744(2)
$\rho_{(calcd)}$/ g cm^{-3}	1.344	1.311	1.308
V / $Å^3$	2349.7(10)	1273.2(11)	1268.1(14)
T / K	100(2)	100(2)	100(2)
Z	4	2	2
Radiation type	Mo K_α	Mo K_α	Mo K_α
No. of reflections measured	26865	15067	14972
No. of independent reflections	5430	5884	5770
No. of reflections with $I > 2\sigma(I)$	4828	5099	5060
R_{int}	0.0839	0.0368	0.1049
R_1 ($I > 2\sigma(I)$)	0.0440	0.0504	0.0448
$wR(F^2)$ ($I > 2\sigma(I)$)	0.1178	0.1609	0.1266
R_1 (all data)	0.0503	0.0583	0.0499
$wR(F^2)$ (all data)	0.1279	0.1799	0.1315
Goodness of fit on F^2	1.095	0.723	1.055

Table A-4: General and crystallographic data for co-crystals of SMT with benzoic acids (1/2).

Compound	**(SMT)·(3-hba)**	**(SMT)·(4-hba)**	**(SMT)·(2,4-dhba)**	**(SMT)·(2,5-dhba)**
Chemical formula	$C_{19}H_{20}N_4O_5S$	$C_{19}H_{20}N_4O_5S$	$C_{19}H_{20}N_4O_6S$	$C_{19}H_{20}N_4O_6S$
Formula mass	416.45	416.45	432.45	432.45
Crystal system	orthorhombic	triclinic	triclinic	orthorhombic
Space group	Pbca	$P\bar{1}$	$P\bar{1}$	Pbca
a/Å	10.043(3)	7.9492(9)	7.963(3)	10.397(2)
b/Å	15.819(5)	9.3544(11)	9.460(3)	15.850(3)
c/Å	24.862(7)	13.2175(16)	13.915(4)	24.673(5)
α/°	90.00	74.1050(10)	73.714(4)	90.00
β/°	90.00	75.9110(10)	74.660(4)	90.00
γ/°	90.00	85.7810(10)	87.291(4)	90.00
$\rho_{(calcd)}$/ g cm^{-3}	1.401	1.509	1.481	1.413
V / Å^3	3950(2)	916.81(19)	969.9(5)	4066.0(14)
T / K	100(2)	100(2)	100(2)	100(2)
Z	8	2	2	8
Radiation type	Mo K_α	Mo K_α	Mo K_α	Mo K_α
No. of reflections measured	43752	10790	11481	44842
No. of independent reflections	4559	4179	4427	4634
No. of reflections with $I > 2\sigma(I)$	3871	3589	3676	3938
R_{int}	0.0522	0.0277	0.0820	0.0741
R_1 ($I > 2\sigma(I)$)	0.0488	0.0318	0.0544	0.0506
$wR(F^2)$ ($I > 2\sigma(I)$	0.1254	0.0956	0.1512	0.1280
R_1 (all data)	0.0584	0.0384	0.0647	0.0607
$wR(F^2)$ (all data)	0.1324	0.1028	0.1592	0.1349
Goodness of fit on F^2	1.069	0.718	1.057	1.101

Table A-5: General and crystallographic data for a salt and co-crystals of SMT with benzoic acids (2/2).

Compound	**(SMT+)·(2,6-dhba-)**	**(SMT)·(3,5-dhba)**	**(SMT)·(2-ata)**
Chemical formula	$C_{19}H_{20}N_4O_6S$	$C_{19}H_{20}N_4O_6S$	$C_{20}H_{21}N_5O_6S$
Formula mass	432.45	432.45	459.48
Crystal system	orthorhombic	monoclinic	monoclinic
Space group	Pbca	$P2_1/c$	$P2_1/c$
a/Å	10.4612(14)	7.8133(18)	7.062(2)
b/Å	15.292(2)	14.916(3)	16.506(5)
c/Å	25.609(3)	18.021(4)	17.644(5)
α/°	90.00	90.00	90.00
β/°	90.00	102.145(3)	101.145(4)
γ/°	90.00	90.00	90.00
$\rho_{(calcd)}$/ g cm^{-3}	1.403	1.399	1.512
V / Å^3	4096.7(9)	2053.2(8)	2017.9(11)
T / K	100(2)	100(2)	100(2)
Z	8	4	4
Radiation type	Mo K_α	Mo K_α	Mo K_α
No. of reflections measured	43907	23890	23393
No. of independent reflections	4699	4788	4637
No. of reflections with $I > 2\sigma(I)$	3268	3905	3265
R_{int}	0.0891	0.0907	0.0602
R_1 ($I > 2\sigma(I)$)	0.0435	0.0447	0.0445
$wR(F^2)$ ($I > 2\sigma(I)$)	0.1265	0.1243	0.1132
R_1 (all data)	0.0776	0.0540	0.0686
$wR(F^2)$ (all data)	0.1596	0.1326	0.1266
Goodness of fit on F^2	1.032	1.034	0.838

Table A-6: General and crystallographic data for co-crystals of SMT with amides.

Compound	**(SMT)·(4-pta)**	**(SMT)·(ba)**	**(SMT)·(4-aba)**	**(SMT)·(4-mba)·(H_2O)**
Chemical formula	$C_{18}H_{20}N_6O_2S_2$	$C_{19}H_{21}N_5O_3S$	$C_{19}H_{22}N_6O_3S$	$C_{20}H_{25}N_5O_5S$
Formula mass	416.52	399.47	414..49	447.51
Crystal system	Monoclinic	Monoclinic	Monoclinic	Triclinic
Space group	$P2_1/n$	$P2_1/c$	$P2_1/c$	$P\bar{1}$
a/Å	7.9134(7)	8.352(4)	24.767(16)	10.1739(9)
b/Å	24.681(2)	12.976(6)	7.942(5)	10.6410(10)
c/Å	10.1255(9)	17.293(9)	23.354(15)	10.7247(10)
α/°	90.00	90.00	90.00	77.5360(10)
β/°	96.7510(10)	94.113(7)	117.472(8)	70.0290(10)
γ/°	90.00	90.00	90.00	82.4470(10)
$\rho_{(calcd)}$/ g cm^{-3}	1.409	1.419	1.351	1.398
V / $Å^3$	1963.9(3)	1869.3(16)	4075(5)	1063.41(17)
T / K	100(2)	100(2)	100(2)	100(2)
Z	4	4	8	2
Radiation type	Mo K_α	Mo K_α	Mo K_α	Mo K_α
No. of reflections measured	22584	17613	37246	12292
No. of independent reflections	4491	4255	9298	4794
No. of reflections with $I > 2\sigma(I)$	3761	3877	7218	4413
R_{int}	0.0311	0.0513	0.0792	0.0152
R_1 ($I > 2\sigma(I)$)	0.0354	0.1065	0.1491	0.0332
$wR(F^2)$ ($I > 2\sigma(I)$	0.0905	0.2892	0.4179	0.0851
R_1 (all data)	0.0443	0.1116	0.1662	0.0359
$wR(F^2)$ (all data)	0.0961	0.2911	0.4179	0.0874
Goodness of fit on F^2	1.028	1.235	1.044	0.964

Table A-7: General and crystallographic data for co-crystals of ibu with bipyridines (1/2).

Compound	**2((±)-ibu)·(bpe)**	**2((+)-ibu)·(bpe)**	**2((±)-ibu)·(bpeth)**
Chemical formula	$C_{38}H_{46}N_2O_4$	$C_{38}H_{46}N_2O_4$	$C_{38}H_{48}N_2O_4$
Formula mass	594.79	594.79	596.81
Crystal system	triclinic	monoclinic	triclinic
Space group	$P\bar{1}$	$P2_1$	$P\bar{1}$
a/Å	5.893(5)	5.7726(13)	5.225(3)
b/Å	11.269(9)	51.194(13)	9.223(5)
c/Å	26.07(2)	11.479(3)	17.982(10)
α/°	84.646(15)	90.00	78.813(7)
β/°	87.251(13)	102.481(3)	82.303(7)
γ/°	78.723(14)	90.00	81.711(7)
$\rho_{(calcd)}$/ g cm^{-3}	1.169	1.193	1.184
V / Å^3	1690(2)	3312.3(14)	837.1(8)
T / K	100(2)	100(2)	100(2)
Z	4	4	2
Radiation type	MoKα	MoKα	MoKα
No. of reflections measured	17898	27285	9103
No. of independent reflections	7395	9409	3680
No. of reflections with $I > 2\sigma(I)$	4182	7780	2212
R_{int}	0.1309	0.0487	0.1386
R_1 ($I > 2\sigma(I)$)	0.1246	0.0673	0.0606
$wR(F^2)$ ($I > 2\sigma(I)$	0.3056	0.1713	0.1665
R_1 (all data)	0.2027	0.0814	0.1033
$wR(F^2)$ (all data)	0.3408	0.1875	0.1965
Goodness of fit on F^2	1.589	1.130	0.939

Table A-8: General and crystallographic data for co-crystals of ibu with bipyridines (2/2).

Compound	**2((±)-ibu)·(bph)**	**2((+)-ibu)·(2,2'-bpe)**	**2((±)-ibu)·(bpa)**	**((+)-ibu)·(2,4-bpe)**
Chemical formula	$C_{42}H_{50}N_2O_4$	$C_{19}H_{23}NO_2$	$C_{38}H_{44}N_2O_4$	$C_{25}H_{28}N_2O_2$
Formula mass	646.84	297.38	592.75	388.49
Crystal system	Triclinic	Monoclinic	Monoclinic	Monoclinic
Space group	$P\bar{1}$	$P2_1/c$	C2/c	$P2_1$
a/Å	5.809(3)	6.124(2)	32.404(4)	6.4557(9)
b/Å	11.716(6)	8.714(3)	5.8661(8)	9.5048(13)
c/Å	13.940(7)	30.992(10)	18.283(2)	17.457(2)
α/°	79.662(9)	90.00	90.00	90.00
β/°	81.549(9)	93.010(9)	110.3900(10)	99.910(2)
γ/°	78.805(9)	90.00	90.00	90.00
$\rho_{(calcd)}$/ g cm^{-3}	1.181	1.196	1.209	1.223
V / Å^3	909.4(8)	1651.5(9)	3257.6(7)	1055.2(3)
T / K	100(2)	100(2)	100(2)	100(2)
Z	1	4	4	2
Radiation type	MoKα	MoKα	MoKα	MoKα
No. of reflections measured	10410	18546	18377	12285
No. of independent reflections	4075	3788	3893	4796
No. of reflections with $I > 2\sigma(I)$	3334	3111	3159	4346
R_{int}	0.0378	0.0827	0.0307	0.0449
R_1 ($I > 2\sigma(I)$)	0.0434	0.0418	0.0396	0.0332
$wR(F^2)$ ($I > 2\sigma(I)$	0.1224	0.1246	0.1273	0.0937
R_1 (all data)	0.0538	0.0529	0.0529	0.0386
$wR(F^2)$ (all data)	0.1380	0.1374	0.1468	0.1027
Goodness of fit on F^2	0.839	0.882	1.094	0.769

Table A-9: General and crystallographic data for co-crystals of 1c and res templates (1/2).

Compound	**2(1c)·(res)**	**2(1c)·(4-Br res)**	**2(1c)·(4-Cl res)**	**2(1c)·(4,6-diCl res)**
Chemical formula	$C_{24}H_{24}N_2O_6$	$C_{24}H_{23}N_2O_6Br$	$C_{24}H_{23}N_2O_6Cl$	$C_{24}H_{22}N_2O_6Cl_2$
Formula mass	436.45	515.35	470.89	505.34
Crystal system	triclinic	Orthorhombic	Orthorhombic	triclinic
Space group	$P\bar{1}$	Pbca	Pbca	$P\bar{1}$
a/Å	8.1193(9)	14.804(3)	14.802(3)	7.3951(15)
b/Å	11.0270(12)	13.984(3)	14.010(3)	11.857(2)
c/Å	13.1397(14)	23.046(5)	23.198(5)	15.080(3)
α/°	106.197(5)	90.00	90.00	71.24(3)
β/°	92.247(5)	90.00	90.00	85.49(3)
γ/°	90.694(5)	90.00	90.00	82.61(3)
$\rho_{(calcd)}$/ g cm^{-3}	1.284	1.413	1.300	1.353
V / Å^3	1128.5(2)	4845.6(17)	4810.7(17)	1240.6
T / K	298(2)	293(2)	293(2)	293(2)
Z	2	8	8	2
Radiation type	MoKα	MoKα	MoKα	MoKα
No. of reflections measured	5323	39305	30112	10098
No. of independent reflections	3543	3598	2530	3542
No. of reflections with $I > 2\sigma(I)$	2409	2319	2251	2883
R_{int}	0.0256	0.0940	0.0524	0.0384
R_1 ($I > 2\sigma(I)$)	0.0529	0.0451	0.0485	0.0397
$wR(F^2)$ ($I > 2\sigma(I)$)	0.1375	0.0993	0.1083	0.0996
R_1 (all data)	0.0857	0.0825	0.0566	0.0510
$wR(F^2)$ (all data)	0.1574	0.1148	0.1126	0.1059
Goodness of fit on F^2	1.073	1.021	1.159	1.037
CCDC number	823833	-----	-----	-----

Table A-10: General and crystallographic data for co-crystals of 1c and res templates (2/2).

Compound	**2(1c)·(5-OCH_3 res)**	**2(1c)·(5-CO_2CH_3 res)**	**2(1c)·(5-F res)**
Chemical formula	$C_{25}H_{26}N_2O_7$	$C_{26}H_{26}N_2O_8$	$C_{24}H_{23}FN_2O_6$
Formula mass	466.48	494.49	454.44
Crystal system	monoclinic	monoclinic	orthorhombic
Space group	$P2_1/n$	$P2_1/n$	Pbca
a/Å	8.0652(16)	8.1808(16)	14.6296(16)
b/Å	22.284(5)	22.776(5)	13.5728(14)
c/Å	14.083(3)	14.130(3)	23.138(3)
α/°	90.00	90.00	90.00
β/°	105.25(3)	104.79(3)	90.00
γ/°	90.00	90.00	90.00
$\rho_{(calcd)}$/ g cm^{-3}	1.269	1.290	1.314
V / $Å^3$	2441.9(8)	2545.57	4594.4(9)
T / K	293(2)	293(2)	210(2)
Z	4	4	8
Radiation type	MoKα	MoKα	MoKα
No. of reflections measured	11379	21108	28322
No. of independent reflections	2590	3679	4038
No. of reflections with $I > 2\sigma(I)$	2138	3018	3163
R_{int}	0.0563	0.0555	0.0367
R_1 ($I > 2\sigma(I)$)	0.0522	0.0534	0.0384
$wR(F^2)$ ($I > 2\sigma(I)$	0.1361	0.1261	0.0953
R_1 (all data)	0.0645	0.0672	0.0536
$wR(F^2)$ (all data)	0.1452	0.1340	0.1018
Goodness of fit on F^2	1.049	1.071	1.028
CCDC number	-----	-----	798921

Table A-11: General and crystallographic data for co-crystals of 2c and res templates (1/3).

Compound	**2(2c)·(5-OCH_3 res)**	**2(2c)·(5-F res)**	**2(2c)·(5-CH_3 res)**	**2(2c)·(4-Br res)**
Chemical formula	$C_{37}H_{34}N_2O_7$	$C_{36}H_{31}N_2O_6F$	$C_{37}H_{34}N_2O_6$	$C_{36}H_{31}N_2O_6Br$
Formula mass	618.66	606.63	602.66	667.54
Crystal system	monoclinic	triclinic	monoclinic	triclinic
Space group	C2/c	$P\bar{1}$	C2/c	$P\bar{1}$
a/Å	23.045(5)	10.171(2)	21.346(3)	11.468(2)
b/Å	16.960(3)	11.595(2)	16.5889(18)	12.143(2)
c/Å	18.632(4)	14.156(3)	18.2708(19)	12.240(2)
α/°	90.00	72.73(3)	90.00	90.72(3)
β/°	99.21(3)	80.64(3)	98.868(5)	101.20(3)
γ/°	90.00	84.43(3)	90.00	108.44(3)
$\rho_{(calcd)}$/ g cm^{-3}	1.143	1.282	1.252	1.402
V / $Å^3$	7188(2)	1570.95	6392(13)	1581.16
T / K	293(2)	293(2)	298(2)	173(2)
Z	8	2	8	2
Radiation type	MoKα	MoKα	MoKα	MoKα
No. of reflections measured	27139	10203	18243	13696
No. of independent reflections	4818	3306	5608	4654
No. of reflections with $I > 2\sigma(I)$	3318	2574	3819	3447
R_{int}	0.0782	0.0627	0.0244	0.0442
R_1 ($I > 2\sigma(I)$)	0.0585	0.0477	0.0479	0.0380
$wR(F^2)$ ($I > 2\sigma(I)$	0.1403	0.1221	0.1332	0.0876
R_1 (all data)	0.0915	0.0622	0.0723	0.0589
$wR(F^2)$ (all data)	0.1571	0.1320	0.1469	0.0966
Goodness of fit on F^2	1.014	1.027	1.045	1.045
CCDC number	-----	-----	823835	-----

Table A-12: General and crystallographic data for co-crystals of 2c and res templates (2/3)

Compound	**2(2c)·(4-Cl res)**	**2(2c)·(4,6-diBr)**	**2(2c)·(4,6-diI)**
Chemical formula	$C_{36}H_{31}N_2O_6Cl$	$C_{36}H_{30}N_2O_6Br_2$	$C_{36}H_{30}N_2O_6I_2$
Formula mass	623.08	746.44	840.42
Crystal system	triclinic	triclinic	monoclinic
Space group	$P\bar{1}$	$P\bar{1}$	$P2_1/c$
a/Å	11.3651(12)	10.6510(12)	9.2806(10)
b/Å	12.1633(13)	11.2160(12)	20.263(3)
c/Å	12.2703(13)	14.2115(15)	18.1567(19)
α/°	90.398(5)	75.886(5)	90.00
β/°	100.483(5)	81.066(5)	98.896(5)
γ/°	108.302(5)	87.101(5)	90.00
$\rho_{(calcd)}$/ g cm^{-3}	1.310	1.524	1.655
V / Å^3	1579.79	1626.4(3)	3373.3(7)
T / K	298(2)	290(2)	296(2)
Z	2	2	4
Radiation type	MoKα	MoKα	MoKα
No. of reflections measured	10306	8907	17965
No. of independent reflections	5553	5715	5921
No. of reflections with $I > 2\sigma(I)$	3872	3725	4786
R_{int}	0.0210	0.0220	0.0272
R_1 ($I > 2\sigma(I)$)	0.0536	0.0447	0.0285
$wR(F^2)$ ($I > 2\sigma(I)$)	0.1566	0.0973	0.0564
R_1 (all data)	0.0761	0.0855	0.0430
$wR(F^2)$ (all data)	0.1717	0.1094	0.0599
Goodness of fit on F^2	1.075	0.978	1.016
CCDC number	823834	798920	836620

Table A-13: General and crystallographic data for co-crystals of 2c and res templates (3/3), and Na salt of 2a.

Compound	**2(2c)·(4,6-diCl)**	**2a Na^+ salt**
Chemical formula	$C_{36}H_{30}N_2O_6Cl_2$	$C_{56}H_{76}N_4O_{26}Na_4$
Formula mass	657.52	1313.17
Crystal system	triclinic	monoclinic
Space group	$P\bar{1}$	P21/c
a/Å	10.2757(11)	11.3215(12)
b/Å	11.4560(12)	8.2725(9)
c/Å	14.1516(15)	34.515(4)
α/°	75.356(5)	90.00
β/°	82.090(5)	96.947(5)
γ/°	85.142(5)	90.00
$\rho_{(calcd)}$/ g cm^{-3}	1.370	1.359
V / Å^3	1594.3(3)	3208.8(6)
T / K	293(2)	293(2)
Z	2	2
Radiation type	MoKα	MoKα
No. of reflections measured	10374	20539
No. of independent reflections	5596	5637
No. of reflections with $I > 2\sigma(I)$	4330	3496
R_{int}	0.0156	0.0636
R_1 ($I > 2\sigma(I)$)	0.0421	0.0454
$wR(F^2)$ ($I > 2\sigma(I)$	0.1149	0.103
R_1 (all data)	0.0584	0.0939
$wR(F^2)$ (all data)	0.1240	0.1172
Goodness of fit on F^2	1.071	1.016
CCDC number	827766	798922

Table A-14: General and crystallographic data for co-crystals and silver complexes of 3c.

Compound	**2(3c)·(4,6-diBr res)**	**$[Ag_2(3c)_4][OSO_2CF_3]_2$**	**$[Ag_2(3c)_4][ClO_4]_2$**
Chemical formula	$C_{22}H_{24}N_2O_6Br_2$	$C_{36}H_{36}N_4O_8S_2F_6Ag_2$	$C_{18}H_{18}N_2O_8ClAg$
Formula mass	594.26	1046.58	533.66
Crystal system	monoclinic	triclinic	triclinic
Space group	$P2_1/c$	$P\bar{1}$	$P\bar{1}$
a/Å	13.470(3)	8.2103(9)	7.9955(9)
b/Å	16.207(3)	11.4876(12)	10.5517(11)
c/Å	11.683(2)	12.9209(14)	13.3725(14)
α/°	90.00	72.572(5)	72.765(5)
β/°	94.84(3)	86.181(5)	88.932(5)
γ/°	90.00	78.560(5)	79.653(5)
$\rho_{(calcd)}$/ g cm^{-3}	1.553	1.265	1.124
V / Å^3	2541.4(9)	1139.6(2)	1059.3(2)
T / K	293(2)	293(2)	293(2)
Z	4	1	2
Radiation type	MoKα	MoKα	MoKα
No. of reflections measured	13154	7051	6230
No. of independent reflections	3158	4009	3688
No. of reflections with $I > 2\sigma(I)$	2528	3574	2791
R_{int}	0.0391	0.0176	0.0196
R_1 ($I > 2\sigma(I)$)	0.0304	0.0455	0.0428
$wR(F^2)$ ($I > 2\sigma(I)$	0.0687	0.1704	0.1073
R_1 (all data)	0.0449	0.0556	0.0649
$wR(F^2)$ (all data)	0.0743	0.1894	0.1168
Goodness of fit on F^2	1.049	1.297	1.062

Table A-15: General and crystallographic data for silver complexes of 3c and 3d.

Compound	**$[Ag_2(3c)_4][OTs]_2$**	**$[Ag(3d)][OMs]_\infty$**
Chemical formula	$C_{25}H_{25}N_2O_7SAg$	$C_{19}H_{21}N_2O_7SAg$
Formula mass	605.40	529.32
Crystal system	monoclinic	monoclinic
Space group	$P2_1/n$	C2/c
a/Å	7.1897(8)	24.705(3)
b/Å	24.156(3)	10.3568(11)
c/Å	15.0361(16)	19.835(3)
α/°	90.00	90.00
β/°	102.219(5)	127.393(5)
γ/°	90.00	90.00
$\rho_{(calcd)}$/ g cm^{-3}	1.576	1.734
V / Å^3	2552.2(5)	4032.1(9)
T / K	293(2)	293(2)
Z	4	8
Radiation type	MoKα	MoKα
No. of reflections measured	13841	14675
No. of independent reflections	4476	4800
No. of reflections with $I > 2\sigma(I)$	3676	4105
R_{int}	0.0305	0.0232
R_1 ($I > 2\sigma(I)$)	0.0385	0.0309
$wR(F^2)$ ($I > 2\sigma(I)$	0.1209	0.0724
R_1 (all data)	0.0511	0.0396
$wR(F^2)$ (all data)	0.1395	0.0765
Goodness of fit on F^2	1.211	1.042

Table A-16: General and crystallographic data for co-crystals and silver complexes of 4c.

Compound	**2(4c)·(4,6-diCl res)**	**$[Ag_2(4c)_4][OSO_2CF_3]_2$**
Chemical formula	$C_{36}H_{30}N_2O_6Cl_2$	$C_{31}H_{26}N_2O_7SF_3Ag$
Formula mass	657.52	735.48
Crystal system	monoclinic	triclinic
Space group	$P2_1/c$	$P\bar{1}$
a/Å	17.8352(18)	7.2744(8)
b/Å	16.0481(17)	11.8982(13)
c/Å	11.4935(12)	18.5901(19)
α/°	90.00	101.361(5)
β/°	92.343(5)	94.993(5)
γ/°	90.00	102.469(5)
$\rho_{(calcd)}$/ g cm^{-3}	1.329	1.496
V / Å^3	3286.9(6)	1526.1(3)
T / K	293(2)	293(2)
Z	4	1
Radiation type	MoKα	MoKα
No. of reflections measured	17595	10211
No. of independent reflections	5766	5496
No. of reflections with $I > 2\sigma(I)$	3660	3802
R_{int}	0.0351	0.0238
R_1 ($I > 2\sigma(I)$)	0.0768	0.0537
$wR(F^2)$ ($I > 2\sigma(I)$	0.2301	0.1408
R_1 (all data)	0.1195	0.0837
$wR(F^2)$ (all data)	0.2596	0.1608
Goodness of fit on F^2	1.107	1.027

Table A-17: General and crystallographic data for co-crystals and silver complexes of 3-Me-4-pyes (abbreviated 3M4P below) (1/2).

Compound	**2(3M4P)·(4,6-diI res)**	**(3M4P)·(5-CH_3 res)$_\infty$**	**[Ag (3M4P)$_2$][ClO_4]**
Chemical formula	$C_{28}H_{30}N_2O_6I_2$	$C_{17}H_{18}NO_3$	$C_{22}H_{26}N_2O_8ClAg$
Formula mass	744.34	284.32	589.77
Crystal system	orthorhombic	monoclinic	monoclinic
Space group	$P2_12_12_1$	$P2_1/c$	$P2_1/n$
a/Å	9.3929(10)	14.8281(16)	8.0242(9)
b/Å	16.7070(18)	7.5802(9)	27.927(3)
c/Å	19.414(2)	16.6818(18)	11.4710(12)
α/°	90.00	90.00	90.00
β/°	90.00	116.400(5)	106.315(5)
γ/°	90.00	90.00	90.00
$\rho_{(calcd)}$/ g cm^{-3}	1.623	1.124	1.588
V / Å^3	3046.6(6)	1679.5(3)	2467.0(5)
T / K	293(2)	293(2)	293(2)
Z	4	4	4
Radiation type	MoKα	MoKα	MoKα
No. of reflections measured	15543	9557	16710
No. of independent reflections	5356	2945	4336
No. of reflections with $I > 2\sigma(I)$	4079	1933	2955
R_{int}	0.0310	0.0384	0.0422
R_1 ($I > 2\sigma(I)$)	0.0356	0.0611	0.0497
$wR(F^2)$ ($I > 2\sigma(I)$	0.0925	0.1707	0.1451
R_1 (all data)	0.0641	0.0965	0.0769
$wR(F^2)$ (all data)	0.1261	0.1858	0.1612
Goodness of fit on F^2	1.118	1.086	1.064

Table A-18: General and crystallographic data for co-crystals and silver complexes of 3-Me-4-pyes (abbreviated 3M4P below) and 3-Me-4-pycb (2/2).

Compound	**$[Ag(3M4P)_2][OSO_2CF_3]$**	**$[Ag(3M4P)_2][OTs]\cdot[2H_2O]$**	**$[Ag(3\text{-}Me\text{-}4\text{-}pycb)][OTs]_\infty$**
Chemical formula	$C_{23}H_{26}N_2O_7SF_3Ag$	$C_{54}H_{70}N_2O_{16}S_2Ag_2$	$C_{54}H_{66}N_4O_{14}S_2Ag_2$
Formula mass	639.39	1310.99	1274.97
Crystal system	monolinic	triclinic	monoclinic
Space group	$P2_1/c$	$P\bar{1}$	$P2_1/c$
a/Å	8.0098(9)	7.5003(9)	14.1904(15)
b/Å	29.076(3)	20.087(3)	10.7068(12)
c/Å	11.9604(13)	22.145(3)	40.163(5)
α/°	90.00	104.648(5)	90.00
β/°	104.652(5)	93.042(5)	97.332(5)
γ/°	90.00	95.196(5)	90.00
$\rho_{(calcd)}$/ g cm^{-3}	1.576	1.409	1.399
V / Å^3	2694.9(5)	3204.6(8)	6052.2(12)
T / K	293(2)	293(2)	293(2)
Z	4	2	4
Radiation type	MoKα	MoKα	MoKα
No. of reflections measured	10912	19717	37422
No. of independent reflections	4590	11219	10624
No. of reflections with $I > 2\sigma(I)$	2842	5689	7645
R_{int}	0.0613	0.0334	0.0387
R_1 ($I > 2\sigma(I)$)	0.0542	0.0682	0.0868
$wR(F^2)$ ($I > 2\sigma(I)$)	0.1397	0.2166	0.2832
R_1 (all data)	0.0994	0.1327	0.1137
$wR(F^2)$ (all data)	0.1615	0.2562	0.3115
Goodness of fit on F^2	1.110	0.950	1.268

Table A-19: General and crystallographic data for silver complexes of 3-Me-3-pyes and 3-Me-3-pycb.

Compound	**$[Ag(3\text{-}Me\text{-}3\text{-}pyes)_2][OTs]_\infty$**	**$[Ag(3\text{-}Me\text{-}3\text{-}pyes)_2][ClO_4]$**	**$[Ag(3\text{-}Me\text{-}3\text{-}pycb)][ClO_4]_\infty$**
Chemical formula	$C_{27}H_{33}N_2O_7SAg$	$C_{22}H_{26}N_2O_8ClAg$	$C_{22}H_{26}N_2O_8ClAg$
Formula mass	637.48	589.77	589.77
Crystal system	monoclinic	monoclinic	triclinic
Space group	Cc	C2/c	$P\bar{1}$
a/Å	10.7441(11)	24.943(4)	9.2349(10)
b/Å	40.535(4)	12.134(2)	14.5838(16)
c/Å	7.5414(8)	8.3427(16)	18.8077(19)
α/°	90.00	90.00	78.847(5)
β/°	115.870(5)	97.545(9)	86.188(5)
γ/°	90.00	90.00	84.311(5)
$\rho_{(calcd)}$/ g cm^{-3}	1.433	1.565	1.586
V / Å^3	2955.2(5)	2503.1(7)	2470.0(5)
T / K	293(2)	293(2)	293(2)
Z	4	4	4
Radiation type	MoKα	MoKα	MoKα
No. of reflections measured	9484	7502	14383
No. of independent reflections	4910	2172	8627
No. of reflections with $I > 2\sigma(I)$	4488	981	5867
R_{int}	0.0201	0.1707	0.0252
R_1 ($I > 2\sigma(I)$)	0.0280	0.0885	0.0838
$wR(F^2)$ ($I > 2\sigma(I)$	0.0668	0.2129	0.2462
R_1 (all data)	0.0334	0.1993	0.1149
$wR(F^2)$ (all data)	0.0693	0.2531	0.2817
Goodness of fit on F^2	1.059	1.055	1.104

Table A-20: General and crystallographic data for co-crystals of 2-Me-4-pyes (abbreviated 2M4P below) (1/2).

Compound	**2(2M4P)·(4-Cl res)**	**2(2M4P)·(4,6-diCl res)**	**2(2M4P)·(4-Br res)**	**2(2M4P)·(4,6-diBr res)**
Chemical formula	$C_{28}H_{31}N_2O_6Cl$	$C_{28}H_{30}N_2O_6Cl_2$	$C_{28}H_{31}N_2O_6Br$	$C_{28}H_{30}N_2O_6Br_2$
Formula mass	527.00	561.44	571.46	650.36
Crystal system	triclinic	triclinic	monoclinic	triclinic
Space group	$P\bar{1}$	$P\bar{1}$	$P2_1/c$	$P\bar{1}$
a/Å	7.7155(8)	8.6933(9)	7.6230(8)	9.7663(10)
b/Å	9.3878(10)	9.5401(10)	9.5352(10)	10.6788(11)
c/Å	19.970(2)	18.1846(19)	40.665(4)	15.7631(16)
α/°	90.913(5)	96.959(5)	87.946(5)	99.296(5)
β/°	92.084(5)	91.314(5)	87.069(5)	104.339(5)
γ/°	105.762(5)	105.786(5)	72.908(5)	108.494(5)
$\rho_{(calcd)}$/ g cm^{-3}	1.259	1.297	1.500	1.481
V / Å^3	1390.6(2)	1438.1(3)	2820.9(5)	1458.0(3)
T / K	293(2)	293(2)	293(2)	293(2)
Z	2	2	4	2
Radiation type	MoKα	MoKα	MoKα	MoKα
No. of reflections measured	8366	4097	15364	9657
No. of independent reflections	4901	3340	9530	5127
No. of reflections with $I > 2\sigma(I)$	3273	2021	4621	4203
R_{int}	0.0231	0.0274	0.0459	0.0261
R_1 ($I > 2\sigma(I)$)	0.0663	0.0564	0.0613	0.0377
$wR(F^2)$ ($I > 2\sigma(I)$)	0.2164	0.1800	0.1601	0.1114
R_1 (all data)	0.0986	0.1062	0.1561	0.0489
$wR(F^2)$ (all data)	0.2505	0.2340	0.2214	0.1230
Goodness of fit on F^2	0.948	0.840	0.921	0.775

Table A-21: General and crystallographic data for silver complexes of 2-Me-4-pyes (abbreviated 2M4P below) and 2-Me-4-pycb (2/2).

Compound	**$[Ag(2M4P)_2][ClO_3]$**	**$[Ag_2(2M4P)_4][CO_2C_3F_7]_2$**	**$[Ag(2M4P)_2][OSO_2CF_3]$**	**$[Ag(2\text{-}Me4\text{-}pycb)][OSO_2CF_3]_\infty$**
Chemical formula	$C_{22}H_{26}N_2O_7ClAg$	$C_{26}H_{26}N_2O_6F_7Ag$	$C_{23}H_{26}N_2O_7SF_3Ag$	$C_{23}H_{26}N_2O_7SF_3Ag$
Formula mass	573.77	703.36	639.39	639.39
Crystal system	monoclinic	triclinic	triclinic	monoclinic
Space group	$P2_1/c$	$P\bar{1}$	$P\bar{1}$	$P2_1/c$
a/Å	11.5930(13)	8.9514(10)	9.1294(10)	15.7331(16)
b/Å	29.161(3)	13.3372(14)	12.3078(13)	18.4064(19)
c/Å	15.1584(16)	13.4983(14)	12.4687(13)	9.7973(10)
α/°	90.00	108.746(5)	79.179(5)	90.00
β/°	111.739(5)	90.495(5)	78.369(5)	93.949(5)
γ/°	90.00	103.150(5)	87.235(5)	90.00
$\rho_{(calcd)}$/ g cm^{-3}	1.601	1.578	1.576	1.501
V / Å^3	4760.0(9)	1480.2(3)	1347.8(2)	2830.2(5)
T / K	293(2)	293(2)	293(2)	293(2)
Z	8	2	2	4
Radiation type	MoKα	MoKα	MoKα	MoKα
No. of reflections measured	13982	9596	8534	16171
No. of independent reflections	4196	5196	4741	4980
No. of reflections with $I > 2\sigma(I)$	3202	3605	3959	3297
R_{int}	0.0200	0.0229	0.0144	0.0318
R_1 ($I > 2\sigma(I)$)	0.0646	0.0770	0.0476	0.1018
$wR(F^2)$ ($I > 2\sigma(I)$)	0.2212	0.2214	0.1540	0.2951
R_1 (all data)	0.0881	0.1019	0.0583	0.1411
$wR(F^2)$ (all data)	0.2495	0.2464	0.1692	0.3260
Goodness of fit on F^2	1.127	1.025	0.963	1.267

Table A-22: General and crystallographic data for tpcp-related crystals.

Compound	(tpcp-H$^+$)($^-$OTs)	(tpcp-H$^+$)($^-$CSA)	(Me-tpcp$^+$)(I$^-$)
Chemical formula	$C_{68}H_{64}N_4O_{12}S_4$	$C_{80}H_{96}N_4O_{12}S_4$	$C_{44}H_{44}N_4I_4$
Formula mass	1252.47	1433.85	1136.43
Crystal system	triclinic	triclinic	monoclinic
Space group	$P\bar{1}$	P1	$P2_1/n$
a/Å	9.9651(11)	13.0438(14)	13.4581(14)
b/Å	18.6737(19)	16.1244(17)	26.450(3)
c/Å	19.013(2)	22.165(3)	14.7209(16)
α/°	78.676(5)	84.993(5)	90.00
β/°	84.713(5)	89.849(5)	108.212(5)
γ/°	81.267(5)	67.290(5)	90.00
$\rho_{(calcd)}$/ g cm^{-3}	1.220	1.112	1.516
V / Å^3	3421.8(6)	4281.5(9)	4977.7(9)
T / K	293(2)	293(2)	293(2)
Z	2	2	4
Radiation type	MoKα	MoKα	MoKα
No. of reflections measured	21972	26829	24108
No. of independent reflections	12033	26137	6441
No. of reflections with $I > 2\sigma(I)$	6748	16226	2433
R_{int}	0.0464	0.0369	0.2530
R_1 ($I > 2\sigma(I)$)	0.1005	0.0964	0.1455
$wR(F^2)$ ($I > 2\sigma(I)$	0.2774	0.2466	0.3449
R_1 (all data)	0.1665	0.1578	0.3025
$wR(F^2)$ (all data)	0.3177	0.2826	0.4039
Goodness of fit on F^2	1.069	0.998	1.074

Table A-23: General and crystallographic data for mpec and co-crystals of mpec.

Compound	mpec	2(mpec)·(4,6-diCl res)	2(mpec)·(4,6-diI res)
Chemical formula	$C_{34}H_{30}N_2O_4$	$C_{40}H_{34}N_2O_6Cl_2$	$C_{40}H_{34}N_2O_6I_2$
Formula mass	530.60	709.59	892.49
Crystal system	monoclinic	monoclinic	triclinic
Space group	$P2_1/c$	$P2_1/c$	$P\bar{1}$
a/Å	5.9592(7)	10.0158(11)	8.9068(10)
b/Å	35.910(4)	11.2124(12)	9.120810)
c/Å	7.1216(8)	31.938(6)	24.124(3)
α/°	90.00	90.00	84.119(5)
β/°	114.635(5)	90.642(5)	87.145(5)
γ/°	90.00	90.00	69.163(5)
$\rho_{(calcd)}$/ g cm^{-3}	1.272	1.314	1.627
V / Å^3	1385.3(3)	3586.4(9)	1821.8(4)
T / K	293(2)	293(2)	293(2)
Z	2	4	2
Radiation type	MoKα	MoKα	MoKα
No. of reflections measured	5584	21436	9573
No. of independent reflections	2242	6299	6356
No. of reflections with $I > 2\sigma(I)$	1532	4486	4400
R_{int}	0.0253	0.0403	0.0236
R_1 ($I > 2\sigma(I)$)	0.0540	0.1789	0.0470
$wR(F^2)$ ($I > 2\sigma(I)$	0.2025	0.4426	0.1346
R_1 (all data)	0.0837	0.2102	0.0852
$wR(F^2)$ (all data)	0.2306	0.4655	0.1791
Goodness of fit on F^2	0.890	1.976	0.991

Table A-24: General and crystallographic data for mpec and co-crystals of mpec.

Compound	2(mpec)·(4,6-diBr res)	2(mpec)·(4-Br res)
Chemical formula	$C_{40}H_{34}N_2O_6Br_2$	$C_{40}H_{35}N_2O_6Br$
Formula mass	799.51	719.61
Crystal system	monoclinic	monoclinic
Space group	$P2_1/n$	$P2_1/c$
a/Å	10.0026(11)	10.3184(11)
b/Å	11.2197(12)	29.486(3)
c/Å	31.965(4)	11.3748(12)
α/°	90.00	90.00
β/°	90.694(5)	91.840(5)
γ/°	90.00	90.00
$\rho_{(calcd)}$/ g cm^{-3}	1.156	1.382
V / Å^3	3587.0(7)	3459.0(6)
T / K	293(2)	293(2)
Z	6	4
Radiation type	MoKα	MoKα
No. of reflections measured	19666	17274
No. of independent reflections	6311	5849
No. of reflections with $I > 2\sigma(I)$	3790	2443
R_{int}	0.0538	0.1003
R_1 ($I > 2\sigma(I)$)	0.0494	0.0860
$wR(F^2)$ ($I > 2\sigma(I)$)	0.1339	0.1909
R_1 (all data)	0.1065	0.2211
$wR(F^2)$ (all data)	0.1766	0.2233
Goodness of fit on F^2	0.956	1.013

APPENDIX B: ADDITIONAL CHARACTERIZATION DATA

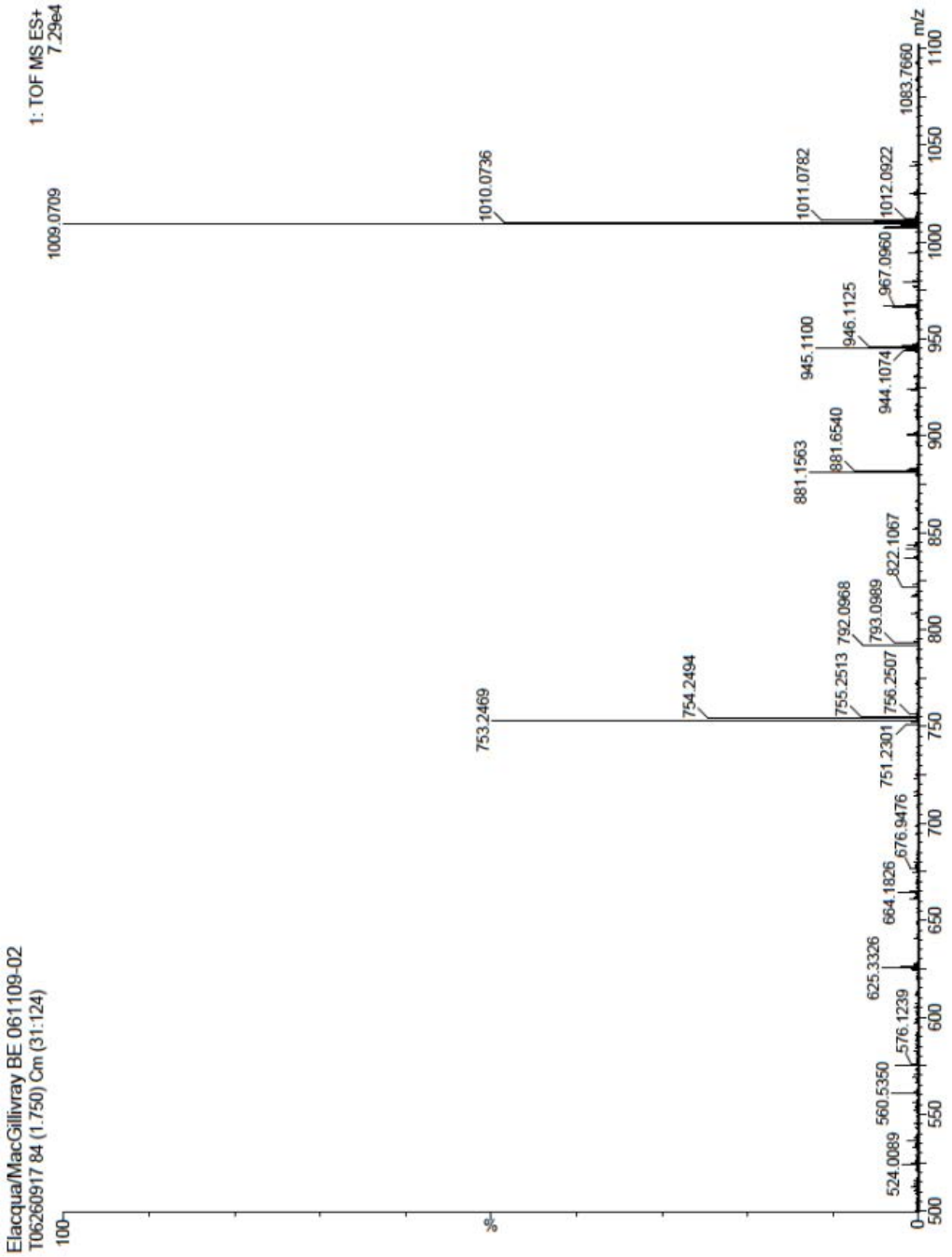

Figure B-1: Mass spectrum of N-methyl tpcp. The fragment at 1009.0709 m/z represents $C_{44}H_{44}N_4I_3$ (M-I).

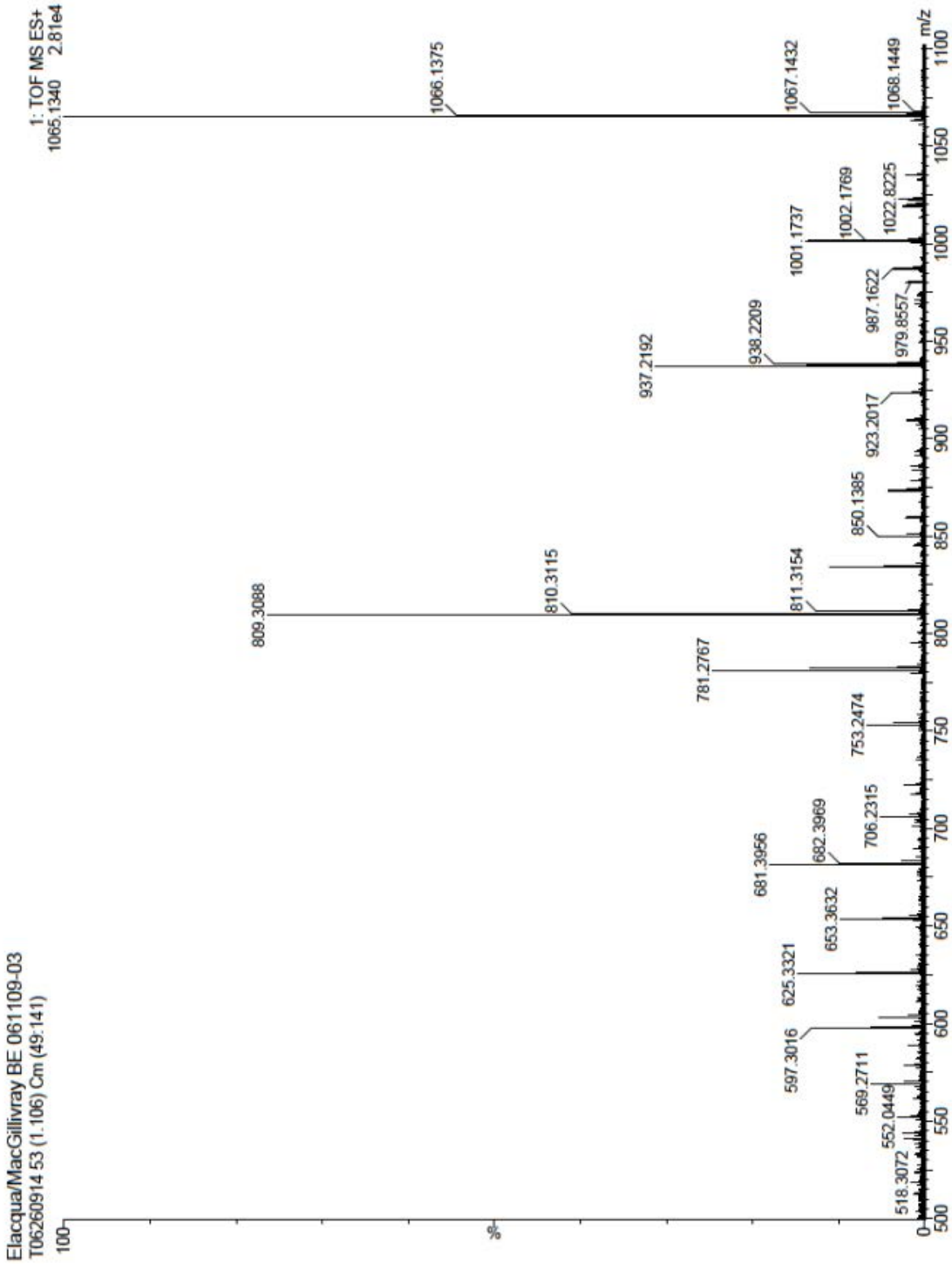

Figure B-2: Mass spectrum of N-ethyl tpcp. The fragment at 1065.134 m/z represents $C_{48}H_{52}N_4I_3$ (M-I).

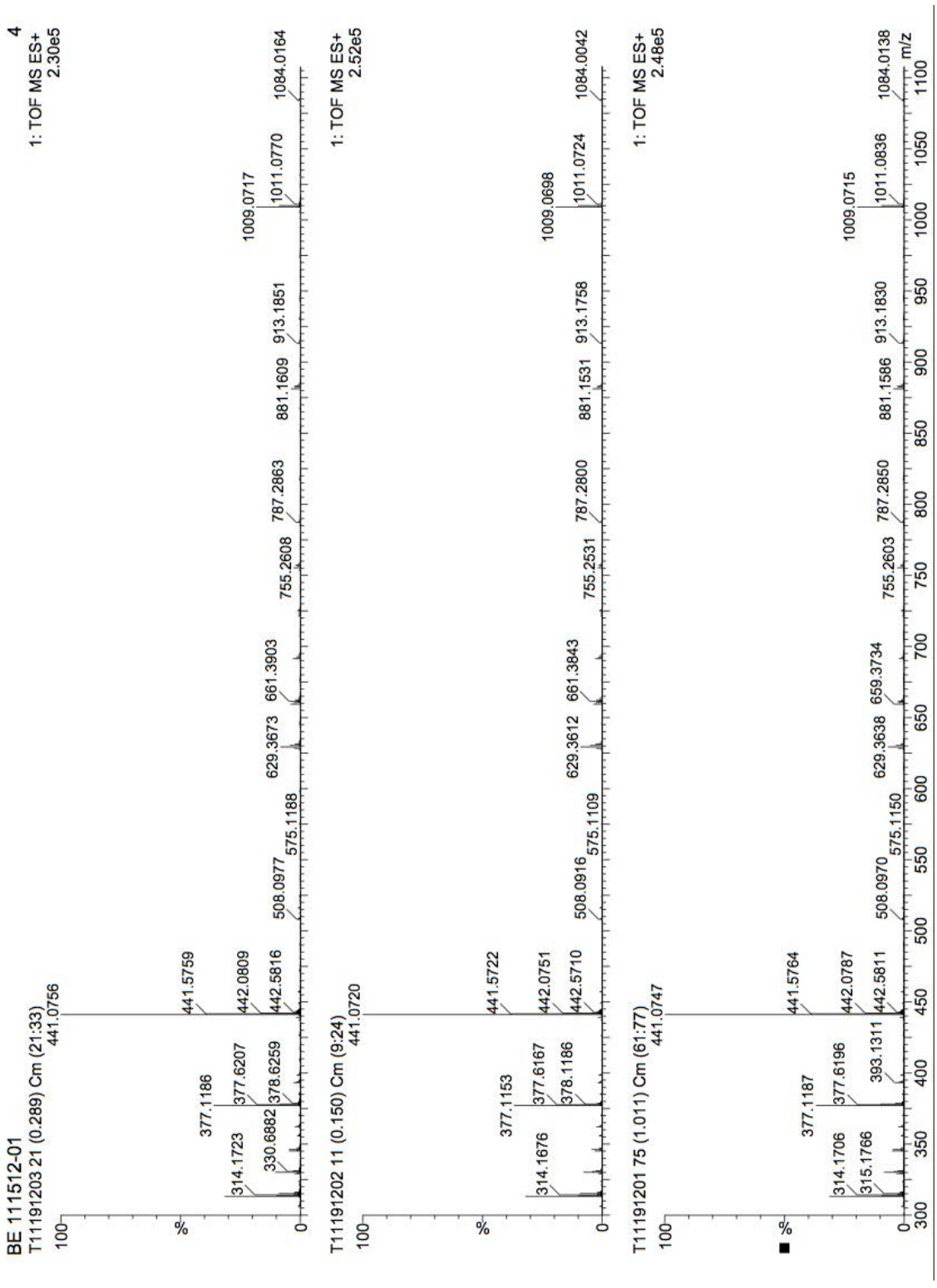

Figure B-3: Mass spectrum of N-methyl tpcp. The average fragment from the three trials was found to be 1009.071 m/z., representative of $C_{44}H_{44}N_4I_3$ (M-I).

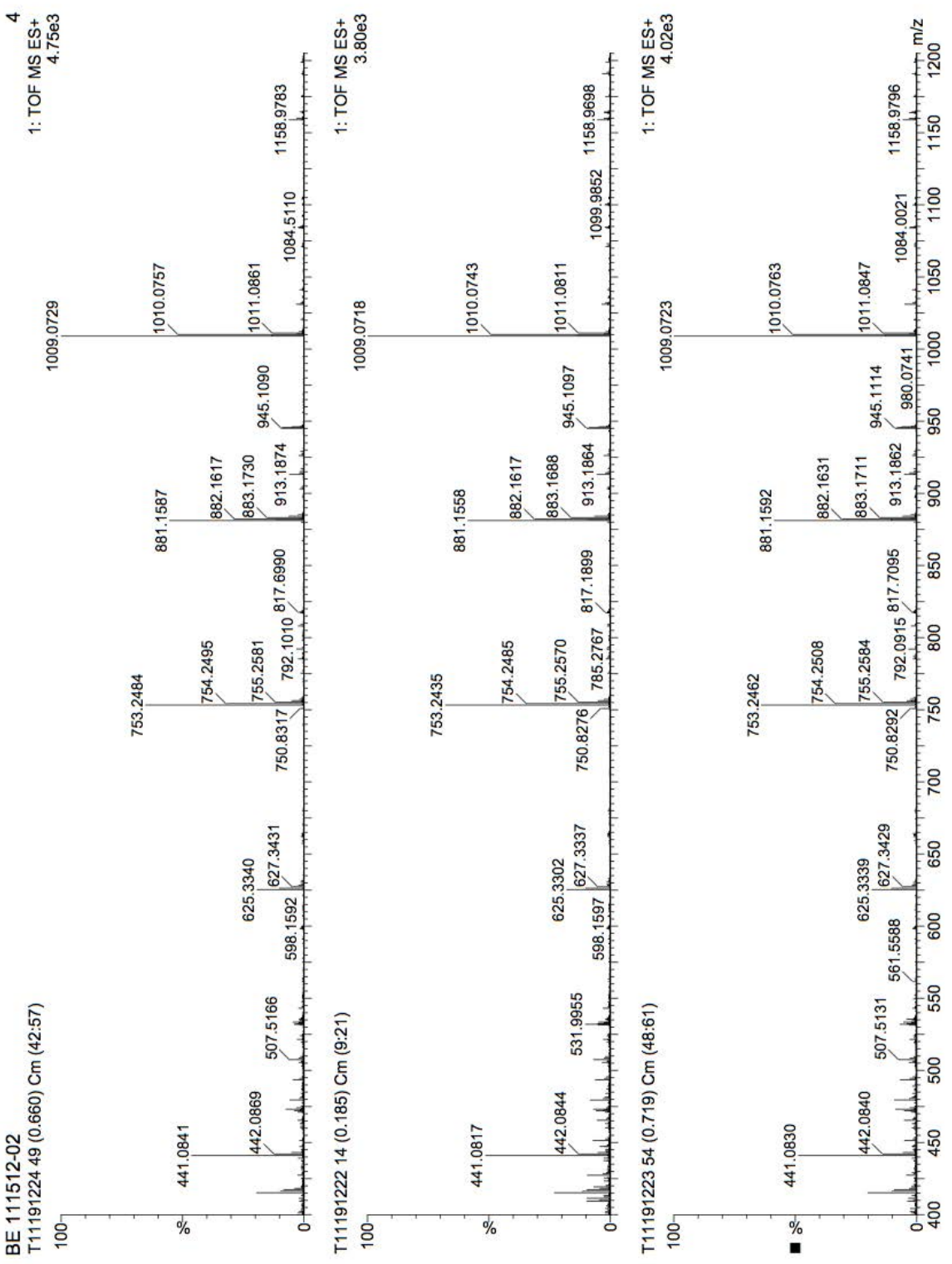

Figure B-4: Mass spectrum of N-methyl tpcm. The average fragment from the three trials was found to be 1009.072 m/z., representative of $C_{44}H_{44}N_4I_3$ (M-I).

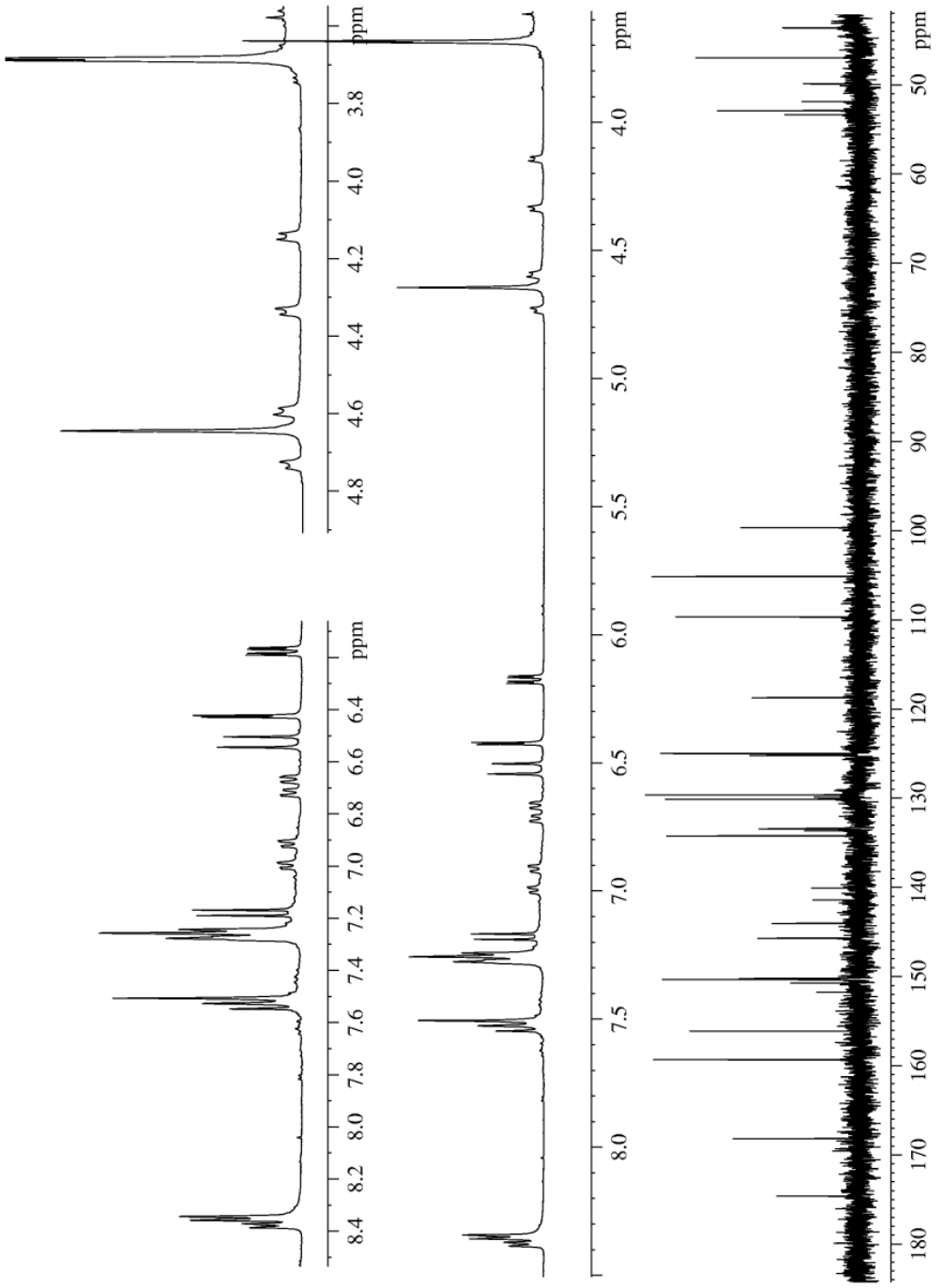

Figure B-5: Overlay of ^{1}H and ^{13}C NMR data for the photoreaction of 2(mpec)·(4-Br res). (Top = enlarged aromatic and cyclobutane regions).